ASME
SETTING THE STANDARD

Transactions of the ASME, Journal of Fluids Engineering (ISSN 0098-2202) is published monthly by The American Society of Mechanical Engineers, Three Park Avenue, New York, NY 10016. Periodicals postage paid at New York, NY and additional mailing offices.
POSTMASTER: Send address changes to Transactions of the ASME, Journal of Fluids Engineering, c/o THE AMERICAN SOCIETY OF MECHANICAL ENGINEERS, 22 Law Drive, Box 2300, Fairfield, NJ 07007-2300.
CHANGES OF ADDRESS must be received at Society headquarters seven weeks before they are to be effective. Please send old label and new address.
STATEMENT from By-Laws. The Society shall not be responsible for statements or opinions advanced in papers or ... printed in its publications (B7.1, Par. 3).

Journal of Fluids Engineering

Published Monthly by ASME

VOLUME 129 • NUMBER 5 • MAY 2007

TECHNICAL PAPERS

(Contents continued on inside back cover)

This journal is printed on acid-free paper, which exceeds the ANSI Z39.48-1992 specification for permanence of paper and library materials. ♾™
♻ 85% recycled content, including 10% post-consumer fibers.

(**Contents continued**)

Journal of Fluids Engineering **Volume 129, Number 5** **MAY 2007**

TECHNICAL BRIEF

DISCUSSION

ANNOUNCEMENT

The ASME Journal of Fluids Engineering is abstracted and indexed in the following:

Applied Science & Technology Index, Chemical Abstracts, Chemical Engineering and Biotechnology Abstracts (Electronic equivalent of Process and Chemical Engineering), Civil Engineering Abstracts, Computer & Information Systems Abstracts, Corrosion Abstracts, Current Contents, Ei EncompassLit, Electronics & Communications Abstracts, Engineered Materials Abstracts, Engineering Index, Environmental Engineering Abstracts, Environmental Science and Pollution Management, Excerpta Medica, Fluidex, Index to Scientific Reviews, INSPEC, International Building Services Abstracts, Mechanical & Transportation Engineering Abstracts, Mechanical Engineering Abstracts, METADEX (The electronic equivalent of Metals Abstracts and Alloys Index), Petroleum Abstracts, Process and Chemical Engineering, Referativnyi Zhurnal, Science Citation Index, SciSearch (The electronic equivalent of Science Citation Index), Shock and Vibration Digest, Solid State and Superconductivity Abstracts, Theoretical Chemical Engineering

Control of Vortex Shedding From a Bluff Body Using Imposed Magnetic Field

Sintu Singha

K. P. Sinhamahapatra

Department of Aerospace Engineering,
Indian Institute of Technology,
Kharagpur, India

S. K. Mukherjea
Department of Applied Mechanics,
Bengal Engineering and Science University,
Shibpur, India
e-mail: kalyanps@iitkgp.ac.in

The two-dimensional incompressible laminar viscous flow of a conducting fluid past a square cylinder placed centrally in a channel subjected to an imposed transverse magnetic field has been simulated to study the effect of a magnetic field on vortex shedding from a bluff body at different Reynolds numbers varying from 50 to 250. The present staggered grid finite difference simulation shows that for a steady flow the separated zone behind the cylinder is reduced as the magnetic field strength is increased. For flows in the periodic vortex shedding and unsteady wake regime an imposed transverse magnetic field is found to have a considerable effect on the flow characteristics with marginal increase in Strouhal number and a marked drop in the unsteady lift amplitude indicating a reduction in the strength of the shed vortices. It has further been observed, that it is possible to completely eliminate the periodic vortex shedding at the higher Reynolds numbers and to establish a steady flow if a sufficiently strong magnetic field is imposed. The necessary strength of the magnetic field, however, depends on the flow Reynolds number and increases with the increase in Reynolds number. This paper describes the algorithm in detail and presents important results that show the effect of the magnetic field on the separated wake and on the periodic vortex shedding process. [DOI: 10.1115/1.2717616]

Keywords: magnetohydrodynamics, Hartmann number, bluff body, vortex shedding, wake

1 Introduction

The flow over the bluff body is a common phenomenon in many engineering applications. For example, flows over tubular heat exchangers, suspension wires, pipelines, and suspension bridges, and so on. The so-called bluff bodies generate a particularly large and usually unsteady separated flow. When the bluff bodies have sharp edges on their circumferences, the flow separation is fixed by the sharp edges. The disturbed flows around all bluff bodies have the common feature of similar flow structures in the separated region despite differences in shape and the presence or absence of sharp edges. When the flow Reynolds number is small ($<40-50$), the laminar flow is characterized by a steady separation and a closed near wake within which the flow is recirculating. At higher Reynolds number the vortices "shed" alternately from the upper and the lower side of the body developing the famous Karman vortex street. The alternating eddies in this periodic laminar regime develop gradually to form a very long laminar wake. The periodic vortex shedding mechanism modifies the pressure distribution on the body periodically giving periodic forces in the streamwise and cross flow directions. The amplitude of the cross flow component is usually much higher, which often causes the body to vibrate along the cross flow direction. This "flow induced vibration" demands the attention regarding the material properties of the body to withstand the vibration. A method to control such flow-induced vibration is to control the vortex shedding and the separated zone behind the body in the desired direction such that the body can withstand the vibration with its own material properties. An imposed magnetic field in the transverse direction does the job satisfactorily when the fluid is electrically conducting.

The flow past a circular cylinder has drawn the attention of researchers for a very long time. However, the study of the flow around rectangular cylinders has also accelerated in the past few years. Davis and Moore [1] have reported a detailed study in the range of Reynolds number 100–2800. They have used a multidimensional version of the one-dimensional QUICKEST scheme due to Leonard [2]. Davis et al. [3] have studied the confined flow over rectangular cylinder to found that the confining walls have considerable effects on the flow characteristics. Frank et al. [4] have used the finite volume method with third order QUICK scheme to simulate the laminar flows past square cylinder. Okajima [5] has carried out a detailed experimental study of this flow problem in the range of Reynolds numbers 70–20,000.

The use of magnetic field in the cross-stream direction is a novel method of controlling the separated zone behind the body, which in turns help to reduce or eliminate the periodic vortex shedding and the resulting flow induced vibration if the fluid is conducting. The magnetohydrodynamic (MHD) effect on blood flow is described in Vardanyan [6]. Pal, Mishra, and Gupta [7] investigated MHD flow of an electrically conducting fluid in a slowly varying channel in the presence of a uniform transverse

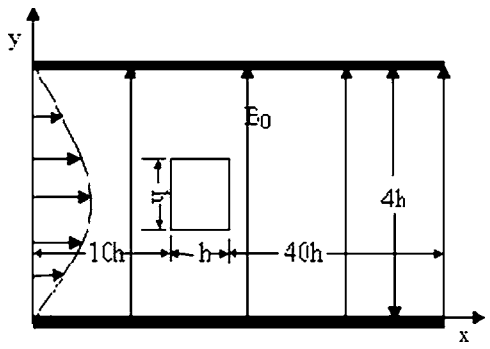

Fig. 1 A sketch of the flow problem (B_0 represents the uniform magnetic field)

Contributed by the Fluids Engineering Division of ASME for publication in the JOURNAL OF FLUIDS ENGINEERING. Manuscript received September 9, 2005; final manuscript received October 24, 2006. Assoc. Editor: Subrata Roy.

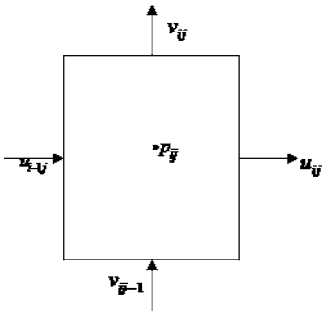

Fig. 2 The arrangement of the velocity components and pressure in a MAC cell

magnetic field. Midya, Layek, Gupta, and Mahapatra [8] investigated the magnetohydrodynamic effect on viscous flow in a channel with constriction.

In this paper, the incompressible viscous flows of an electrically conducting fluid around a square cylinder confined symmetrically between two parallel flat plates in the presence of a uniform transverse magnetic field is studied. A staggered grid arrangement has been employed to discretize the governing equations. A second order accurate explicit time integration scheme has been adopted to advance the velocity field in time. The study shows that the separation zone in terms of the wake length is decreased with the increase in magnetic field for steady flow cases ($\mathrm{Re} \leq 50$). The imposed magnetic field reduces the strength of the shed vortices and, hence, the flow asymmetry and lift amplitude in unsteady flows at higher Reynolds numbers ($\mathrm{Re} > 50$). Moreover, the unsteady flows at higher Reynolds numbers become steady when subjected to sufficiently strong magnetic field.

2 Flow Geometry and Governing Equations

The flow configuration considered in this paper is a two-dimensional incompressible viscous flow of electrically conducting fluid with conductivity σ and density ρ around a square cylinder of height h placed symmetrically between two flat plates as shown in Fig. 1. The electrical conductivity of the fluid (σ) is assumed to be constant. A parabolic velocity profile is given at the inlet of the channel. A uniform magnetic field B_0 is imposed along the cross-flow direction (Fig. 1).

Due to magnetohydrodynamic interactions, an induced electric field (E_z) is produced in the direction perpendicular to the plane of the flow, which in turn produces an induced magnetic field in the streamwise direction. It is assumed that the flows considered are of very small magnetic Reynolds number Re_m ($=\mu\sigma Vh$, where V is the characteristic velocity and μ is the permeability) and, hence, the induced magnetic field is negligible so that there is no distortion in the imposed uniform magnetic field [9]. It is also assumed that the magnetic field is not distorted near the body due to the difference in permeability and conductivity between the solid body and the conducting fluid. Thus, in essence, a short-circuited situation is assumed as if the induced current is taken through a stationary closed loop made of perfect conductor lying in the direction perpendicular to the stream, so that the induced electric field (E_z) becomes zero [9] and a net current $\sigma B_0 Q$ flows normal to the plane of the flow, where Q is the fluid volume flow rate. It is also assumed that the electric field due to the polarization of charges is also negligible. An elegant justification for these assumptions is given in Ref. [8] for the flow of a conducting fluid in a channel with constriction and is not reproduced here for brevity. The presence of a body in the flow, which usually will have a different conductivity, may, perhaps, reduce the accuracy of some of the assumptions. The induced magnetic and electric fields will alter the current flow and the current continuity needs to be taken into account for better accuracy. However, when the conductivities of the flowing fluid (e.g., molten sodium or mercury) and the cylinder material (e.g., steel or aluminum alloys) are nearly of the same order of magnitude, the induced electric and magnetic fields at low Hartmann numbers considered here will, probably, not be large enough to have a significant effect on the overall flow behavior. With this assumption, the current continuity is not considered in the present study and it is felt that the solution will be able to capture the qualitative features of the flow. With the consideration of the Lorentz forces due to the external magnetic field and the assumptions stated above the governing equations for two-dimensional Newtonian fluid in their nondimensional forms [8] are given by

Table 1 Variation of C_D, St, and C_{DP} for two grids

Grid size	C_D	St	C_{DP}
293×64	1.694	0.171	1.708
326×81	1.654	0.169	1.675

Table 2 Comparison of results at Re=250 without the magnetic field

Method	L	St	C_{DP}
Davis et al. [3]	$4h$	0.174	1.64
Present solution	$4h$	0.171	1.675

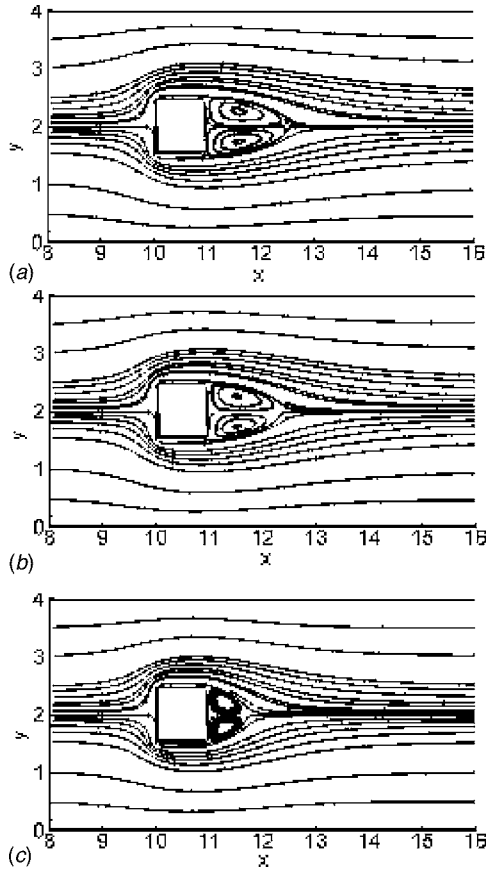

Fig. 3 Streamlines at Re=50: (*a*) *H*=0.0, (*b*) *H*=1.0, and (*c*) *H*=3.0

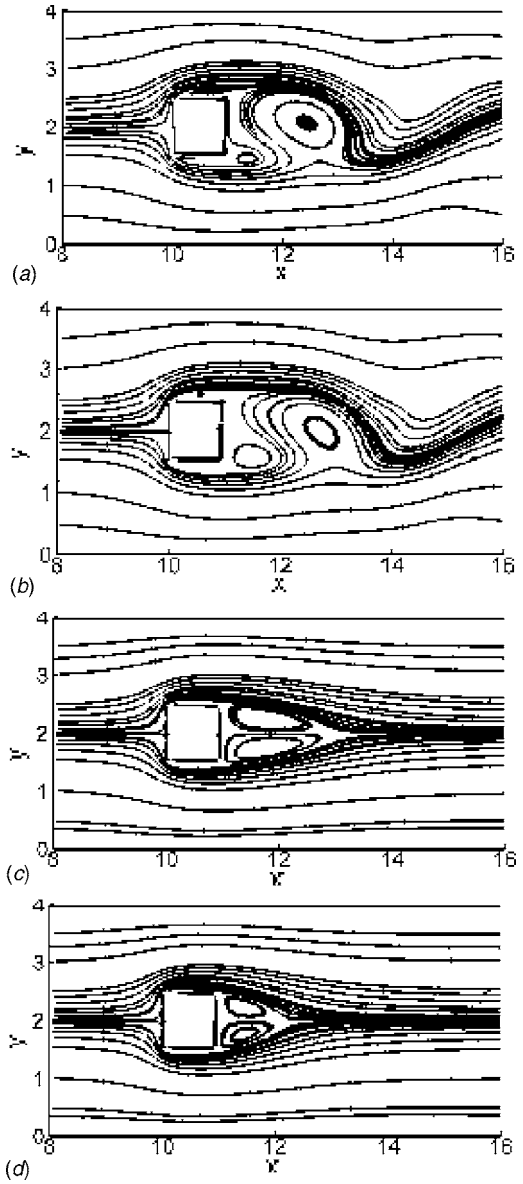

Fig. 4 Streamlines at Re=250: (*a*) *H*=0.0, (*b*) *H*=2.0, (*c*) *H* =5.0, and (*d*) *H*=7.0

Continuity equation:

$$\frac{\partial u_i}{\partial x_i} = 0 \tag{1}$$

Momentum equations:

$$\frac{\partial u_i}{\partial t} + \frac{\partial}{\partial x_j}(u_j u_i) = -\frac{\partial p}{\partial x_i} + \frac{1}{\mathrm{Re}}\frac{\partial^2 u_i}{\partial x_j \partial x_j} - \frac{H^2}{\mathrm{Re}} K_i u_i \tag{2}$$

where $K_1=1$ and $K_2=0$ and $\mathrm{Re}=Vh/\nu$ is the Reynolds number (ν is the kinematic viscosity, V is the characteristic velocity assumed as the velocity at the midsection of the inflow plane, h is the height of the square cylinder and is taken as the characteristic length of the flow) and $H=B_0 h\sqrt{\sigma/\rho\nu}$ is the Hartmann number.

Table 3 The required range of minimum Hartmann numbers that converts the unsteady flow (*H*=0) to a steady flow

Reynolds number	Range of *H*
150	2.0–3.0
200	3.0–4.0
250	4.0–5.0

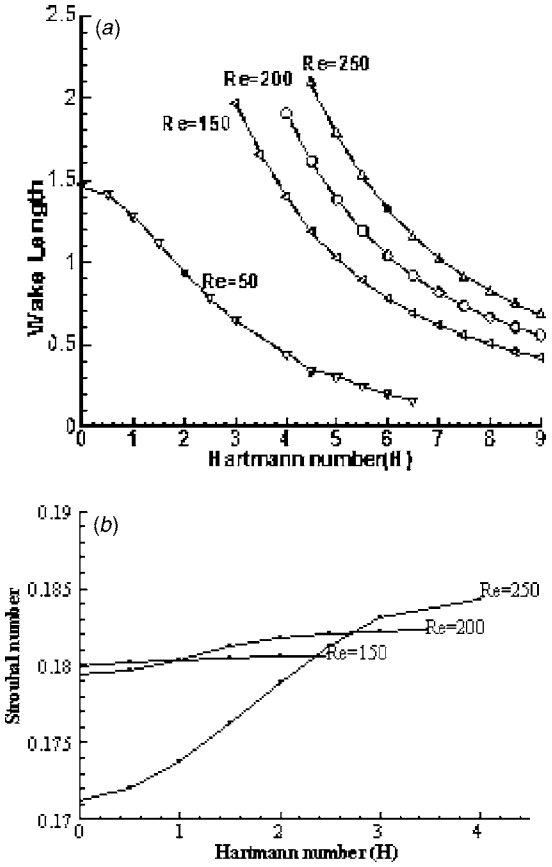

Fig. 5 Variation of (*a*) wake length and (*b*) Strouhal number with Hartmann number

3 Boundary Conditions

The impermeable no-slip boundary conditions are used on all the solid boundaries. A parabolic profile is assumed for the streamwise component of velocity (u_1) at the inlet, and the crosswise component of velocity (u_2) is taken as zero. At the outlet the crosswise component of velocity is calculated taking its gradient in the streamwise direction to be zero and the streamwise component of velocity is calculated from the continuity equation satisfied at the outflow boundary. It is further assumed that initially there is no flow inside the flow domain except at the inlet boundary.

4 Method of Solution

The nondimensional governing equations along with the boundary conditions are solved by the finite difference method. The discretization of the different terms of these equations are carried out on a nonuniform staggered grid, popularly known as the MAC (Marker and Cell) cell, proposed by Harlow and Welch [10]. The velocity components and pressure are arranged in a MAC cell as shown in Fig. 2.

A second order time accurate explicit Adams-Bashforth differencing scheme is used to advance the solution in time. The momentum equation is written using a space operator, J (containing convection and diffusion terms) as

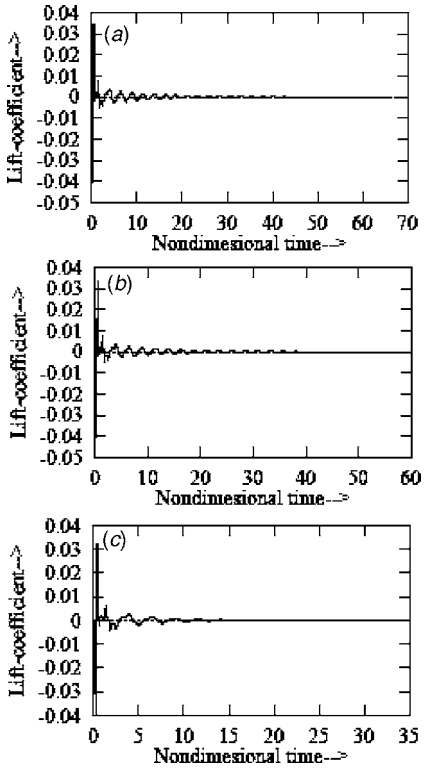

Fig. 6 Temporal growth of lift coefficient with respect to the nondimensional time (tV/h) at Re=50; (*a*) H=0.0, (*b*) H=1.0, and (*c*) H=3.0

$$\frac{\partial u_i}{\partial t} = J(u_i,u_j) - \frac{\partial p}{\partial x_i} - \frac{H^2}{\mathrm{Re}} K_i u_i \tag{3}$$

The velocity field is predicted using the second order time advancement scheme as in the following:

$$\frac{u_i^* - u_i}{\delta t} = \frac{3}{2} J(u_i,u_j)^n - \frac{1}{2} J(u_i,u_j)^{n-1} - \frac{\partial p^n}{\partial x_i} - \frac{H^2}{\mathrm{Re}} K_i u_i^n \tag{4}$$

The convective terms in the momentum equations are approximated by a combination of central difference and second upwind formulas. The diffusive terms are differenced by the conventional second order accurate 3-point central difference formulas.

The corrected solution for velocity and pressure are obtained by iterating

$$p^{n+1} \leftarrow p^n + p' \tag{5}$$

$$u_i^{n+1} \leftarrow u_i^* + \frac{\delta t}{\delta x_i} p' \tag{6}$$

where p' is computed by

$$p' = -r_0 \frac{\partial u_i^*}{\partial x_i} \Bigg/ \left[2\delta t \left(\frac{1}{\delta x_i^2} \right) \right] \tag{7}$$

r_0 is an over-relaxation factor and is taken as 1.2 for the computations reported here.

Hence, to advance the solution by one time level, the computational steps involved are as follows:

(a) The velocity and pressure fields (u_i^n, p^n) are initialized at

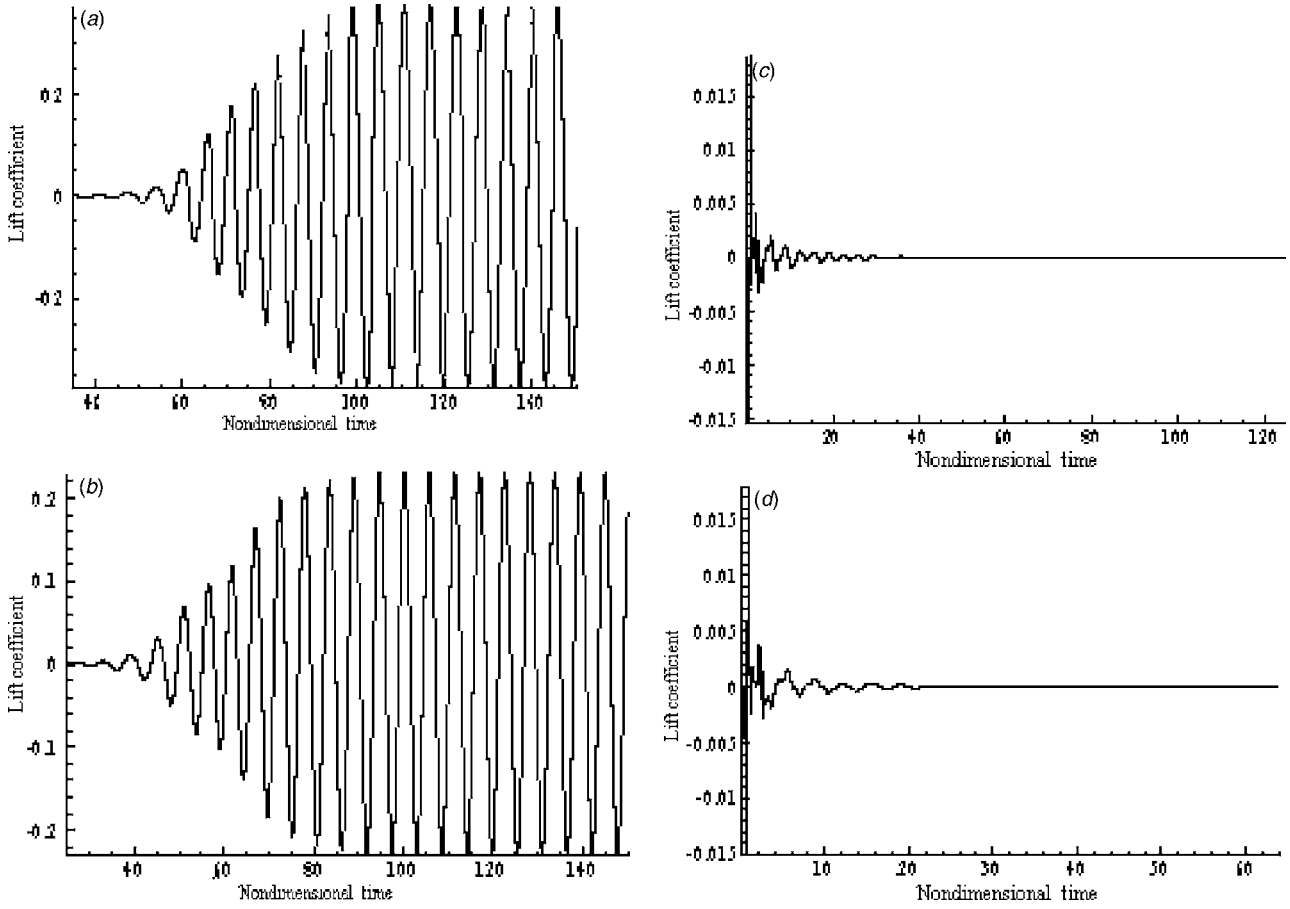

Fig. 7 Temporal growth of lift coefficient with respect to the nondimensional time (tV/h) at Re=250; (*a*) H=0.0, (*b*) H=2.0, (*c*) H=5.0, and (*d*) H=7.0

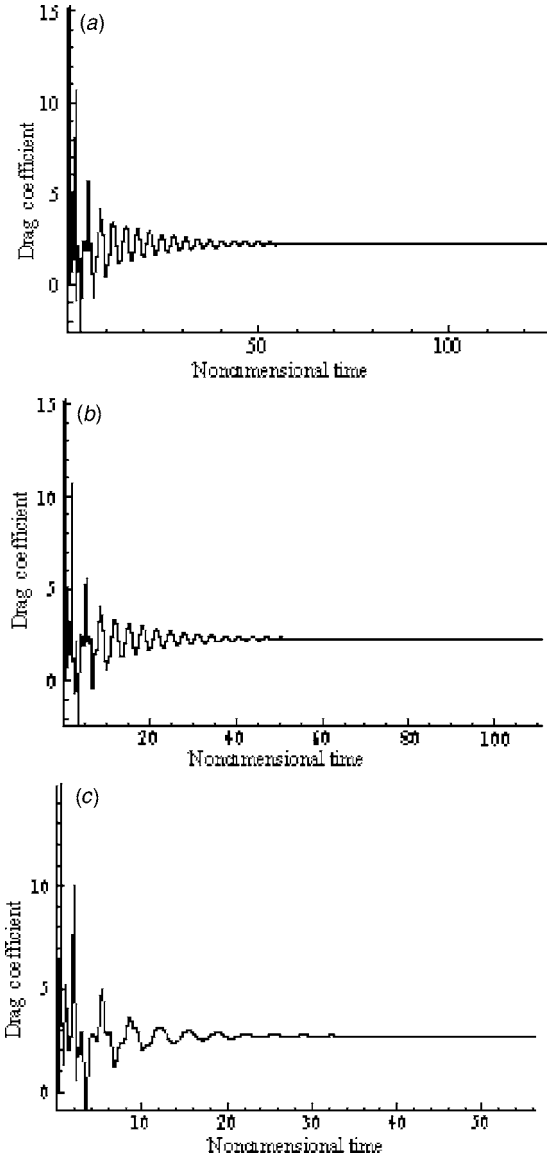

Fig. 8 Time history of the drag coefficient with respect to the nondimensional time (tV/h) at Re=50; (*a*) H=0.0, (*b*) H=1.0, and (*c*) H=3.0

each cell. These are either the solution of the previous level (nth level) or the prescribed initial conditions.

(b) The time step (δt) is calculated from the stability criteria.

(c) The velocity field is predicted using Eq. (4).

(d) The velocity and pressure fields are updated using Eqs. (5)–(7) iteratively.

(e) The maximum cell divergence of the velocity field is checked for its limit. When this condition is satisfied the solution is accepted as the velocity and pressure field at the $(n+1)$th time level. If the maximum divergence is not satisfactorily low the control moves to step (a), otherwise to step (f).

(f) The steady state convergence or limiting nondimensional time criterion is checked whether to stop the calculation. If not, then steps (a)–(f) are repeated for the next time level.

5 Results and Discussions

The numerical code developed by the authors using the algorithm described above has been used to solve the flow problem given in Fig. 1. The present study is confined to Reynolds number 50, 150, 200, and 250 with Hartmann numbers (H) ranging from 0.0 to 8.0.

A grid dependency study is made initially to verify the algorithm and the code. The computed results using two separate grids for the flow at a Reynolds number of 250 in the absence of a magnetic field are shown in Table 1. As seen in the table, there is no significant change in the various flow properties. Consequently, the grid with the resolution of 293×64 is adopted for all subsequent computations that are presented in this paper.

The computed result is compared with the benchmark solution due to Davis et al. [3] to validate the code developed. The comparison for the confined flow over the square cylinder at Reynolds number 250 and zero Hartmann number is presented in Table 2. The parameter L in the table represents the separation between the two confining plates and is taken as four times the cylinder height as in Davis et al. [3]. The frequency of oscillation of the lift coefficient (C_L) in terms of the dimensionless Strouhal number (fh/V) is found to be 0.171 in close agreement with the value of 0.174 obtained by Davis et al. [3]. The parameter f stands for the frequency of vortex shedding or time-dependent lift coefficient. Comparison of the average pressure drag coefficient (C_{DP}) also appears to be good.

Figures 3(*a*)–3(*c*) and Figs. 4(*a*)–4(*d*) show the streamlines of the flows at Reynolds number 50 and 250, respectively subjected to various imposed transverse magnetic fields. With zero Hartmann number (i.e., no magnetic field), the flow at Re=50 is a time-independent steady flow producing a closed wake attached to the rear face of the body, whereas the flow at Re=250 is an unsteady or time-dependent one producing a very long wake with alternate "shedding of vortices" from the top and bottom corners of the square. Figures 3(*a*)–3(*c*) show that the separation zone, characterized by the wake length, is reduced with the increase in Hartmann number. Figures 4(*a*)–4(*d*) show that the flow remains unsteady with periodic vortex shedding up to a certain Hartmann number beyond which the flow becomes steady with a closed wake and with a further increase in Hartmann number the wake length/separation zone is reduced. Since the strength of the shed vortices is reduced with the gradual increase of the Hartmann number, the flow asymmetry and, consequently, the amplitude of the lift coefficient decreases (Figs. 7(*a*) and 7(*b*)). With a further increase of the Hartmann number (Figs. 4(*c*) and 4(*d*)) the vortex shedding process is completely eliminated and the flow is steady, symmetric, and characterized by a closed wake and zero lift (Figs. 7(*c*) and 7(*d*)) as in very low Reynolds number flows. The range of minimum Hartmann numbers within which the periodic vortex shedding is totally suppressed and the initial unsteady flow converts to a steady flow at different Reynolds numbers are given in Table 3. Probably a unique value of the Hartmann number corresponding to a particular Reynolds number at which the periodic vortex shedding stops can be obtained if the computations are performed for several Hartmann numbers in the interval. But such attempts are not made in this study. From Table 3, it is seen that the unsteady flow at higher Reynolds numbers need a stronger magnetic field to become steady.

Figure 5(*a*) shows the variation of wake length with Hartmann number. It is clearly observed that at a fixed Reynolds number the wake length is significantly reduced with the increase in Hartmann number. The physical explanation for this fact is that the magnetic field in the transverse direction of the flow of a conducting fluid induces the Lorentz force in the upstream direction, which has a tendency to suppress the diffusion of vortices out of the wall and, hence, to shorten the wake. The same physical process, probably, also weakens the shed vortices and finally suppresses the shedding if the Lorentz force is strong enough. For Hartmann numbers less than its critical value (the minimum Hartmann number at which vortex shedding is suppressed completely), it is observed that while the length of the separated wake

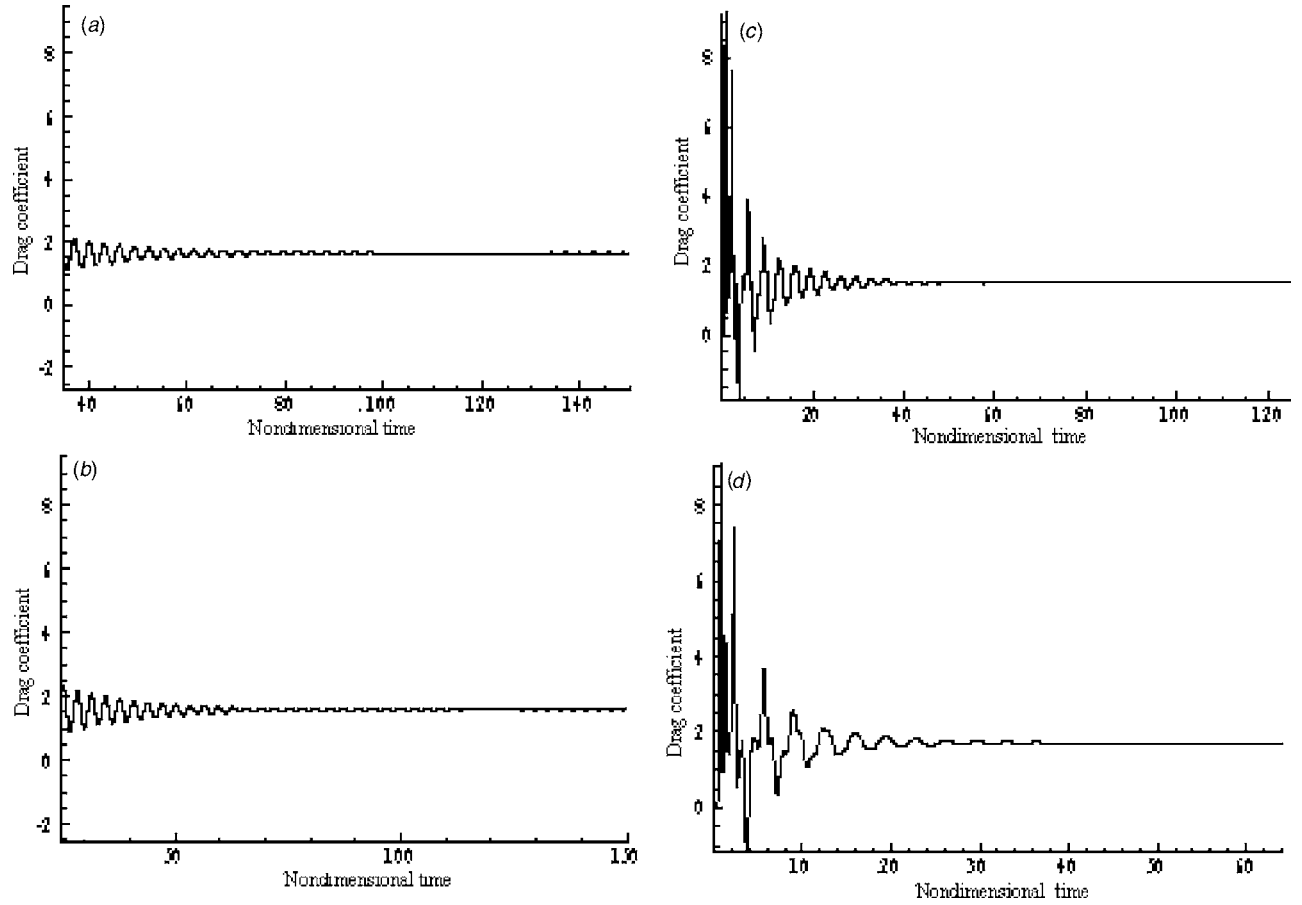

Fig. 9 Time history of the drag coefficient with respect to the nondimensional time (tV/h) at Re=250; (*a*) H=0.0, (*b*) H=2.0, (*c*) H=5.0, and (*d*) H=7.0

is decreased, the vortex shedding frequency is increased slightly as shown in Fig. 5(*b*). This effect seems to be more prominent at higher Reynolds numbers.

Figures 6(*a*)–6(*c*) and 7(*a*)–7(*d*) show the temporal variation of the lift coefficient at different Hartmann numbers for the Reynolds numbers of 50 and 250, respectively. Figures 6(*a*)–6(*c*) show that after the initial transient period, the average lift coefficient becomes a constant zero at the flow Reynolds number of 50, which indicate that in each case the flow has reached a time-independent steady state. However, the time to reach the steady state decreases with an increase in the Hartmann number. It is observed from Figs. 7(*a*)–7(*d*) that the flow remains unsteady (retaining the "shedding of vortices") up to a certain Hartmann number as stated earlier. It is interesting to note that even though the flow remain unsteady at H=2.0 (Fig. 7(*b*)) the amplitude of the sinusoidal lift coefficient has considerably decreased with respect to the "no imposed magnetic field" case (Fig. 7(*a*), H=0.0). This also implies that the strength of the shed vortices and the resulting flow asymmetry that essentially generates the lift has decreased. The same flow feature was also observed in the streamline plots in Figs. 4(*a*)–4(*d*). With a stronger magnetic field the periodic vortex shedding and the consequent unsteadiness and flow asymmetry are found to be eliminated completely, as can clearly be seen from Figs. 7(*c*) and 7(*d*), which show the lift coefficient time traces at H=5.0 and 7.0, respectively. So, it can be fairly concluded that the amplitude of cross flow vibration will be significantly reduced with an increase in Hartmann number and the vibration can be totally eliminated if the Hartmann number is increased sufficiently.

The time variations of the average drag coefficient at Reynolds numbers 50 and 250 with different Hartmann numbers are shown in Figs. 8(*a*)–8(*c*) and 9(*a*)–9(*d*), respectively. From Figs. 8(*a*)–8(*c*), it is observed that the average drag coefficient increases marginally with the increase in Hartmann number. It can, probably, be attributed to the fact that the increased amount of Lorentz force, due to the increase in Hartmann number, increases the pressure drop to keep on the flow with fixed discharge. This increase in pressure drop contributes to the increase in the pressure drag on the body when the flow is steady (as in case of Re=50). Figures 9(*a*)–9(*d*) present the temporal variation of the drag coefficient for the flow at Re=250 subjected to different magnetic field and it shows a very striking result. It can be observed very clearly that the average drag coefficient decreases marginally with an increase in the Hartmann number as long as the flow maintains its unsteadiness and alternate periodic vortex shedding. This marginal drop in drag force can be attributed to the weakened shed vortices that nullify the effect of increased pressure drop. But once the flow becomes steady due to sufficiently strong magnetic field, the average drag coefficient increases due to the increased pressure drop with a further increase in Hartmann number. The dependency of the average drag coefficient on the Hartmann number at different Reynolds number is presented in Fig. 10.

6 Conclusions

An explicit second order accurate finite difference code employing the pressure correction concept has been developed to study the incompressible laminar flow around a confined square cylinder subjected to an imposed uniform transverse magnetic field. The convective terms in the momentum equations are discretized using combined central and second upwind difference formulas and the diffusive terms are discretized using central dif-

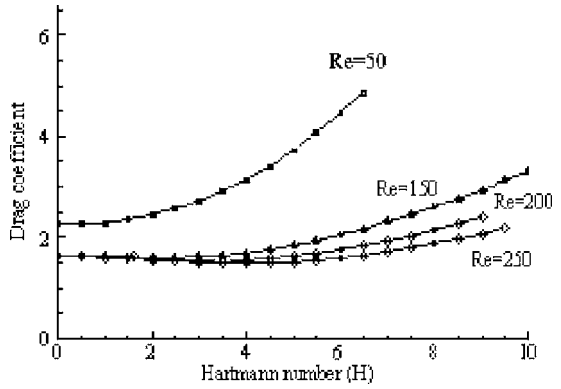

Fig. 10 Variation of the average drag coefficient with the Hartmann number

ference formulas. The fluid (liquid metal) is assumed to have a uniform electrical conductivity. The induced magnetic field is assumed to be negligible in comparison to the imposed magnetic field which is justified for MHD flows at very small magnetic Reynolds numbers.

The present study reveals the following effects of an imposed tranverse magnetic field on the flow around a square cylinder:

(i) In the steady separated, i.e., the closed near wake regime of the flow the wake length is reduced with an increase in Hartmann number.
(ii) In the periodic laminar wake regime the vortex shedding and unsteadiness in reduced as the Hartmann number is increased and if a sufficiently strong magnetic field is applied the periodic vortex shedding is completely eliminated. The limiting Hartmann number at which this phenomenon occurs is increased with the Reynolds number.
(iii) As the Hartmann number is increased the drag coefficient is decreased marginally in an unsteady flow but is considerably increased in a steady flow.
(iv) The amplitude of the periodic lift coefficient is decreased with an increase in Hartman number before it reaches a steady state value at the limiting Hartmann number.
(v) Low Reynolds number flows are less sensitive in terms of Strouhal number variation per unit change in Hartmann number.

Nomenclature

B_0 = uniform magnetic field
C_L = coefficient of lift
C_D = coefficient of drag
C_{DP} = coefficient of drag due to pressure
L = distance between the walls ($=4h$)
h = height of the square cylinder
H = Hartmann number ($=B_0 h\sqrt{\sigma/\rho\nu}$)
Re = Reynolds number ($=Vh/\nu$)
St = Strouhal number ($=fh/V$)
f = vortex shedding frequency
V = centerline velocity at inflow plane

References

[1] Davis, R. W., and Moore, E. F., 1982, "A Numerical Study of Vortex Shedding from Rectangles," J. Fluid Mech., **116**, pp. 475–506.
[2] Leonard, B. P., 1979, "A Stable and Accurate Convective Modeling Based on Quadratic Upstream Interpolation," Comput. Methods Appl. Mech. Eng., **19**, pp. 59–98.
[3] Davis, R. W., Moore, E. F., and Purtell, L. P., 1984, "A Numerical-Experimental Study of Confined Flow Around Rectangular Cylinders," Phys. Fluids, **27**, pp. 46–59.
[4] Frank, R., Rodi, W., and Schonung, B., 1990, "Numerical Calculation of Vortex-Shedding Flow Past Cylinders," J. Wind. Eng. Ind. Aerodyn., **35**, 227–257.
[5] Okajima, A., 1982, "Strouhal Numbers of Rectangular Cylinders," J. Fluid Mech., **123**, pp. 379–398.
[6] Vardanayan, V. A., 1973, "Effect of Magnetic Field on Blood Flow," Biofizika, **18**, pp. 491–496.
[7] Pal, B., Misra, J. C., Gupta, A. S., 1996, "Steady Hydromagnetic Flow in a Slowly Varying Channel," Proc. Natl. Inst. Sci. India, Part A, **66**(A), pp. 247–262.
[8] Midya, C., Layek, G. C., Gupta, A. S., and Mahapatra, R. T., 2003, "Magnetohydrodynamic Viscous Flow Separation in a Channel With Constriction," ASME J. Fluids Eng., **125**, pp. 952–962.
[9] Shercliff, J. A., 1965, *A Textbook of Magnetohydrodynamics*, Pergamon, NY, p. 147.
[10] Harlow, F. H., and Welch, J. E., 1965, "Numerical Calculation of Time Dependent Viscous Incompressible Flow of Fluid With Free Surface," Phys. Fluids, **8**, pp. 2182–2189.

Phase-Averaged PIV for the Nominal Wake of a Surface Ship in Regular Head Waves[1]

J. Longo

J. Shao

M. Irvine

F. Stern

IIHR-Hydroscience and Engineering,
College of Engineering,
University of Iowa,
Iowa City, IA 52242

Phase-averaged organized oscillation velocities (U,V,W) *and random fluctuation Reynolds stresses* $(\overline{uu},\overline{vv},\overline{ww},\overline{uv},\overline{uw})$ *are presented for the nominal wake of a surface ship advancing in regular head (incident) waves, but restrained from body motions, i.e., the forward-speed diffraction problem. A* $3.048\times3.048\times100$ m *towing tank, plunger wave maker, and towed, 2D particle-image velocimetry (PIV) and servo mechanism wave-probe measurement systems are used. The geometry is DTMB model 5415 (*$L=3.048$ m*,* $1/46.6$ *scale), which is an international benchmark for ship hydrodynamics. The conditions are Froude number* $\mathrm{Fr}=0.28$*, wave steepness* $Ak=0.025$*, wavelength* $\lambda/L=1.5$*, wave frequency* $f=0.584$ Hz*, and encounter frequency* $f_e=0.922$ Hz*. Innovative data acquisition, reduction, and uncertainty analysis procedures are developed for the phase-averaged PIV. The unsteady nominal wake is explained by interactions between the hull boundary layer and axial vortices and incident wave. There are three primary wave-induced effects: pressure gradients* $4\%U_c$*, orbital velocity transport* $15\%U_c$*, and unsteady sonar dome lifting wake. In the outer region, the uniform flow, incident wave velocities are recovered within the experimental uncertainties. In the inner, viscous-flow region, the boundary layer undergoes significant time-varying upward contraction and downward expansion in phase with the incident wave crests and troughs, respectively. The zeroth harmonic exceeds the steady-flow amplitudes by 5–20% and 70% for the velocities and Reynolds stresses, respectively. The first-harmonic amplitudes are large and in phase with the incident wave in the bulge region (axial velocity), damped by the hull and boundary layer and mostly in phase with the incident wave (vertical velocity), and small except near the free surface-hull shoulder (transverse velocity). Reynolds stress amplitudes are an order-of-magnitude smaller than for the velocity components showing large values in the thin boundary layer and bulge regions and mostly in phase with the incident wave.* [DOI: 10.1115/1.2717618]

1 Introduction

Procurement of detailed global and local flow benchmark experimental fluid dynamics (EFD) data for fluid physics, model development, and validation of Reynolds-averaged Navier-Stokes (RANS) ship hydrodynamics computational fluid dynamics (CFD) codes has been an ongoing effort since a ca. 1970 with data used periodically at workshops wherein codes are compared with each other and the data. Recent efforts have focused on modern tanker (KRISO VLCC, VLCC2), container (KRISO KCS), and surface combatant (DTMB 5415) hull forms and more challenging test cases, as per the Gothenburg 2000 Workshop [1] and Tokyo 2005 Workshop [2], the latter of which the present data is used. Kim et al. [3] and Lee et al. [4] provide steady-flow data for VLCC2 and KCS. The present interest is in DTMB 5415, for which data procurement has been part of an international collaboration between IIHR,[2] INSEAN,[3] and DTMB,[4] over the past 10 years. Initially steady-flow data are procured, including rigorous uncertainty analysis [5], identification of facility biases [6,7], mean flow map [8], steady nominal wake PIV [9], and propeller-hull interaction [10]. Subsequently, unsteady-flow data is procured, including wave breaking [11] and forward-speed diffraction forces, moment, and wave pattern [12,13]. The present paper concerns the forward-speed diffraction problem for unsteady PIV at the nominal wake of 5415. The most recent efforts have focused on free roll decay measurements with and without bilge keels [14–16].

In parallel, PIV studies for ship velocity fields have been conducted for various specialized purposes, as reviewed by Longo et al. [17]. Fu et al. [18] apply digital PIV and the autocorrelation evaluation method in a rotating arm basin to study dominant cross-flow separation induced by a 5.18 m submarine model in a turn. Dong et al. [19] apply film-based PIV with the autocorrelation method to investigate the bow flow of a 3.05 m ship model in a towing tank. PIV images at several axial stations in the bow wave highlight the cross plane vector fields and considerable vorticity entrained into the toe of the bow wave. Roth et al. [20] apply the digital PIV and the cross-correlation method to study the mean and turbulent bow flow of a 7.01 m ship model at several axial stations on the forebody including convergence tests on mean and turbulence variables and effects of interrogation window size on turbulence structure and statistics. Di Felice and De Gregorio [21] use the digital PIV and the cross-correlation method to investigate the turbulent wake of a 5.41 m ship model equipped with two, four-bladed propellers in a circulating water channel. By synchronizing the PIV recordings with the propeller shaft, phase-averaged velocities and vorticity are computed from several image pairs at a range of phase angles. Calcagno et al. [22] use 3D, stereoscopic PIV in a circulating water tunnel to investigate the turbulent propeller wake flow of a 6.096 m ship model equipped with a 0.222 m diameter, 5-bladed propeller. The phase-averaged data highlights the interactions of the turbulent wake of the hull and propulsor, tip vortex system, slipstream contraction, and strong diffusion and dissipation of the propeller blade wakes.

[1]Submitted ASME JFE: November 22, 2005; revision submitted June 29, 2006.
[2]IIHR-Hydroscience and Engineering, University of Iowa, Iowa, IA 52242.
[3]Italian Ship Model Basin, Rome, Italy.
[4]Naval Surface Warfare Center/Carderock Division, Bethesda, MD.
Contributed by the Fluids Engineering Division of ASME for publication in the JOURNAL OF FLUIDS ENGINEERING. Manuscript received November 22, 2005; final manuscript received September 28, 2006. Assoc. Editor James A. Liburdy.

Fig. 1 DTMB model 5512

Cotroni et al. [23] and Di Felice et al. [24] investigate the phase-averaged wake flow of two, four-bladed propellers in a cavitation tunnel using digital PIV, the cross-correlation evaluation method, and uncertainty assessment. Phase-averaged data are reported in sufficient detail to track the tip vortex systems including formation and breakdown with increasing downstream distance from the propeller disk. Judge et al. [25] investigate tip leakage vortices from a 0.8504 m diameter, three-bladed, ducted rotor with digital PIV and the cross-correlation evaluation method in a variable-pressure water tunnel. Similar studies that are more recent include PIV analysis of flow around a container ship model with a rotating propeller by Paik et al. [26] and three-component velocity field measurements of propeller wake using stereo PIV by Lee et al. [27].

Also of interest are unsteady PIV studies for more fundamental geometries and development of phase-averaging techniques. Lam and Leung [28] use phase-averaged PIV to study the asymmetric turbulent vortex shedding of a flat plate at high incidence. The vortex street is comprised of a train of leading edge vortices alternating with a train of trailing edge vortices. The trailing edge vortices possess higher peak vorticity and Reynolds stress production. The results at three angles of attack collapse into similar trends by using the projected plate width as the characteristic length scale. Konstantinidis et al. [29] use a conditional averaging approach to study the natural and forced turbulent wake of a circular cylinder. Inflow oscillations are shown to affect the vortex formation and shedding. Wernert and Favier [30] investigate principles of the phase-averaging technique for PIV with regard to convergence criterion with application to pitching airfoils oscillating through dynamic stall. In a series of papers (most recently [31]), unobstructed PIV within an axial turbopump using liquid and blades with matched refractive indices is used to study phase-averaged velocities and turbulence and average passage flow field and deterministic stresses. Wake-blade and wake-wake interactions induce flow nonuniformities, turbulent hot spots, and high deterministic stresses. Highest levels of phase-dependent unsteadiness and deterministic stresses are in the tip region induced by the tip vortex. Sung and Yoo [32] present a triple-decomposition method for three-dimensional phase averaging of PIV data in an investigation of large-scale coherent structures in a cylinder wake. The authors decompose the time-varying velocity signal into global mean, periodic mean, and residual random components followed by phase-averaging samples that are sorted into constant phase groups. Their procedures enable resolution of unsteady periodic flow coherent structures including secondary flow details. Druault et al. [33] implement a proper orthogonal decomposition (POD) method to recover the time information between successive PIV measurements which provides a continuous space-time description of the turbulent flow field within the tumble plane of in-cylinder engine flow. POD in conjunction with statistical analysis of the PIV data is particularly useful for unsteady periodic flow with some cycle-to-cycle variability as is present in internal combustion engines.

The motivation of the present study is to provide benchmark EFD data for advancement of ship hydrodynamics unsteady RANS codes from steady to unsteady flow. The forward-speed diffraction problem, i.e., ship advancing in regular head (incident) waves but restrained from motions is identified as a building block problem; since, in traditional potential flow strip theory approaches, the exciting forces for motions are the solution to the forward-speed diffraction problem. The ability of unsteady RANS for the forward-speed diffraction problem is viewed as a first step in merging the traditionally separate fields of resistance and propulsion with seakeeping and maneuvering and ultimately realization of simulation based design.

The approach is complementary CFD, EFD, and uncertainty assessment. CFD is used to guide EFD; EFD is used for validation and model development; and lastly CFD is validated and fills in sparse data for complete documentation and diagnostics of the flow. The EFD includes towing tank tests using DTMB model 5512 (length $L=3.048$ m geosym of DTMB model 5415) and nominal wake phase-averaged PIV and uncertainty analysis. The model geometry is shown in Fig. 1 and its parameters are given in Table 1. Test conditions are based on previous steady-flow PIV [9] and unsteady-flow force, moment and wave pattern [12,13] and phase-averaged regular head wave PIV [34] studies. The test conditions are selected to produce primarily a first harmonic linear response in the forces and moment and wave and flow fields. Previous [35] and concurrent [36] CFD studies are used for estimating the measurement regions and analysis of the data. Innovative data acquisition, reduction, and uncertainty analysis procedures are developed for the phase-averaged PIV, as part of the project. The complete descriptions of the test design, uncertainty analysis, and results are extensive and provided by Longo et al. [37].

2 Test Design

2.1 Facility, Coordinate System, Model, and Conditions. The tests are conducted in the IIHR towing tank, as shown in Fig. 2. The tank is 100 m long, 3.048 m wide, and 3.048 m deep, and equipped with a drive carriage and model trailer, plunger-type wave maker, automated wave dampener system, and wave-dampening beach. The wave dampeners enable 20 and 12 min intervals between unsteady and steady measurement carriage runs, respectively. These time intervals are determined to be sufficient based on visual inspection of the free surface and also on PIV data taken after steady and unsteady carriage runs such that the measured residual motions are less than the PIV uncertainties and close to the noise level of the measurement system. The noise level of the PIV system is previously determined from static (carriage speed $U_c=0$ m/s) and uniform flow ($U_c=1.53$ m/s) tests, as given in Table 2.

A right-handed Cartesian coordinate system fixed to the model is used with the origin at the intersection of the calm free surface and forward perpendicular of the model. The x, y, z axes are

Table 1 Geometric parameters for DTMB model 5512 and full scale

Parameter	Units	5512	Full scale
Linear scale ratio	⋯	46.59	1
Length, L	m	3.048	142.00
Beam, B	m	0.410	19.10
Draft, T	m	0.132	6.16
Wetted surface area, S	m^2	1.371	2975.66
Block coefficient, C_B	⋯	0.506	0.506

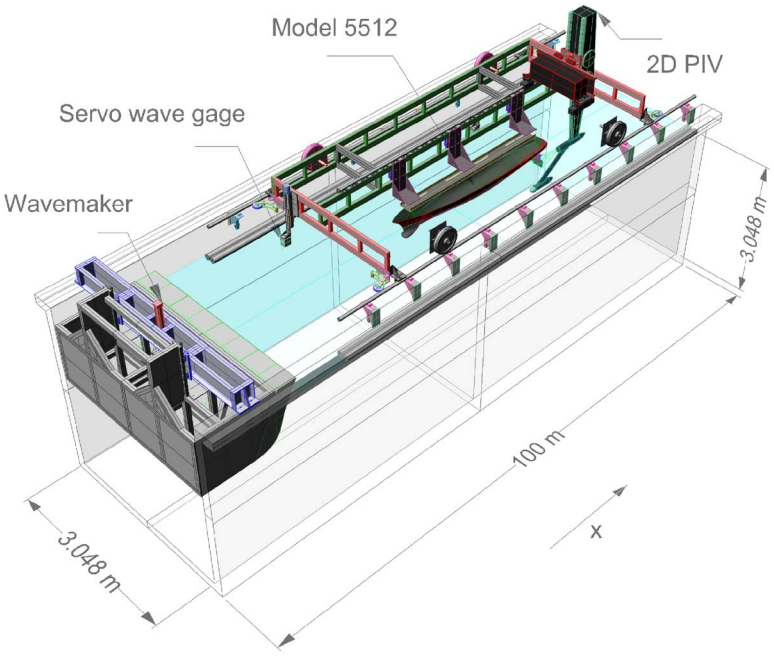

Fig. 2 IIHR facility and phase-averaged nominal wake experimental setup: towing tank, wave maker, DTMB model 5512, 2D PIV system, servo wave gage. Towing tank is not to scale in the *x* coordinate.

directed downstream, transversely to starboard, and upward, respectively. The coordinates, PIV velocities, and other variables of interest are nondimensional using L and U_c.

DTMB model 5512 is a fiber-reinforced Plexiglas geosym of DTMB model 5415, which is a 1:24.8 scale, $L=5.72$ m model ship conceived by the USA Navy as a preliminary design for a surface combatant ca. 1980 with a sonar dome bow and transom stern. To initiate transition to turbulent flow, a row of cylindrical studs of 1.6 mm height and 3.2 mm diameter are fixed with 9.5 mm spacing at $x=0.05$. The stud dimensions and placement on the model are in accordance with the recommendations by the 23rd ITTC [38].

Unsteady (with wave) and steady (without wave) tests are performed at carriage speed $U_c=1.53$ m/s, i.e., Froude number $\mathrm{Fr}=U_c/\sqrt{gL}=0.28$, which corresponds to the cruise speed for the full-scale ship. The model is rigidly fixed to the carriage with zero yaw and roll angle and towed at the dynamic sunk and trimmed condition [5], $\Delta FP=-0.00310L$, $\Delta AP=-0.000734L$. For unsteady tests, wavelength $\lambda=4.572$ m, wave frequency $f=0.584$ Hz, and wave steepness $Ak=0.025$, where f and Ak are defined in Eqs. (1) and (2), and A and g are wave amplitude and local gravity acceleration ($g=9.8031$ m/s^2), respectively,

$$f=\sqrt{\frac{g}{2\pi\lambda}} \tag{1}$$

$$Ak=A\frac{2\pi}{\lambda} \tag{2}$$

The encounter frequency is given by

$$f_e=\sqrt{\frac{g}{2\pi\lambda}}+\frac{U_c}{\lambda}=0.922\ \mathrm{Hz} \tag{3}$$

which is the dominant frequency of the unsteady response.

2.2 Data Acquisition and Reduction Methodology. The present interest is in PIV measurements of phase-averaged organized oscillation velocities (U,V,W) and random fluctuation Reynolds stresses $(\overline{uu},\overline{vv},\overline{ww},\overline{uv},\overline{uw})$, hereafter, referred to as phase-averaged (or simply) velocities and Reynolds stresses. The regular head wave primarily produces a first harmonic response; therefore, following [12,13], a Fourier series (FS) reconstruction is desired. The FS reconstruction is based on a fifth order least-squares regression (LSR) method used to interpolate the instantaneous measurements acquired at random phases for a continuous curve for all phases. There are three reasons for using this procedure: (1) it is difficult to synchronize the triggering of the PIV data acquisition with the phase of the regular head wave; (2) the uncertainty of the regular head wave frequency is large compared to the phase interval of data acquisition; and (3) the PIV data acquisition rate is not an integer fraction of the encounter frequency. The fifth order LSR is determined as a best fit to the data based on trial and error analysis using up to a tenth order LSR. After the experiments are completed and analyzed some limited testing is done using an arithmetic mean moving average method to test the accuracy of the LSR.

The data-reduction equation for an instantaneous PIV measurement is given in Eq. (4). L_{obj} is the width or height of the object plane in m (measurement area), L_{img} is the width or height of the CCD array of the digital camera in pixels, Δt is the time between successive PIV frames in s, and $S_{k,i}$ is the instantaneous particle displacement in pixels in a given interrogation area determined by the correlation software,

$$C_{k,i}=\frac{L_{\mathrm{obj}}}{L_{\mathrm{img}}\Delta t U_c}S_{k,i} \tag{4}$$

The axial U, transverse V, and vertical W velocities are given by $k=1,2,3$, respectively. In Eqs. (4)–(7) that follow, the measurement sample number is given by $i=1,\ldots,N_f$ where N_f is the number of valid measurements at a given grid point in a carriage run or group of carriage runs after filtering from a population of N_r PIV recordings. The instantaneous normal and shear Reynolds stresses are computed with Eqs. (5) and (6), respectively,

$$(c_k c_k)_i=(C_{k,i}-C_k)^2 \tag{5}$$

Table 2 Summary of steady and unsteady flow PIV uncertainty assessment results

Steady-flow PIV UA									
Term (X)	D_X (10^{-2})	B_X^2/U_X^2 (%)	P_X^2/U_X^2 (%)	U_X/D_x (%)	U_X/D_X[a] (%)	E (%)	U_E (%)	$U_c=0$[b]	$U_c=1$[c]
U	62.230	66.5	33.5	1.6	2.4	4.3	2.9	0.05	1.1
V	7.642	78.8	21.2	3.8	7.7	6.3	8.6	⋯	0.3
W	16.080	94.5	5.5	3.2	4.4	7.1	5.4	0.0004	0.08
$\overline{uu}$	4.611	42.6	57.4	2.6	4.7	3.5	5.4	0.00003	0.004
$\overline{vv}$	1.679	35.3	64.7	3.1	4.3	8.4	5.3		0.005
$\overline{ww}$	1.337	47.3	52.7	5.3	5.0	14.8	7.3	0.00002	0.004
$\overline{uv}$	0.909	25.3	74.7	5.9	4.1	5.4	7.2		0.005
$\overline{uw}$	1.200	20.0	80.0	2.6	5.8	5.7	6.4	0	0.0002

Unsteady-flow PIV UA								
Term (X)	D_X (10^{-2})	B_X (10^{-2})	B_X^2/U_X^2 (%)	P_X (10^{-2})	P_X^2/U_X^2 (%)	U_X (10^{-2})	U_X/D_x (%)	$\bar{X}_{\text{cnv}}$ (%)
U_0	57.825	0.415	55.9	0.370	44.1	0.560	1.0	0.2
V_0	7.452	0.071	32.8	0.101	67.2	0.124	1.7	0.8
W_0	15.921	0.062	17.9	0.133	82.1	0.147	0.9	0.3
$\overline{uu}_0$	0.552	0.054	90.8	0.019	9.2	0.058	10.5	0.9
$\overline{vv}_0$	0.239	0.038	91.5	0.011	8.5	0.039	16.5	2.2
$\overline{ww}_0$	0.203	0.021	97.4	0.003	2.6	0.021	10.5	0.9
$\overline{uv}_0$	0.135	0.036	97.2	0.006	2.8	0.037	27.4	2.0
$\overline{uw}_0$	0.184	0.020	99.4	0.002	0.6	0.021	11.2	1.0
U_1	9.320	0.286	77.2	0.156	22.8	0.326	3.5	1.1
V_1	3.636	0.064	30.8	0.096	69.2	0.116	3.2	1.8
W_1	3.761	0.048	47.5	0.050	52.5	0.070	1.9	1.5
$\overline{uu}_1$	0.349	0.038	91.6	0.013	8.4	0.040	11.4	1.9
$\overline{vv}_1$	0.077	0.025	90.3	0.008	9.7	0.026	34.4	12.3
$\overline{ww}_1$	0.077	0.015	97.3	0.003	2.7	0.015	19.8	3.0
$\overline{uv}_1$	0.056	0.025	93.6	0.006	6.4	0.026	45.4	8.2
$\overline{uw}_1$	0.084	0.015	99.0	0.001	1.0	0.015	17.4	3.0
γ_{U1}	628.319	2.545	29.6	3.852	70.4	4.623	0.8	0.5
γ_{V1}	628.319	2.468	14.2	6.073	85.8	6.555	1.0	1.1
γ_{W1}	628.319	3.409	27.2	5.583	72.8	6.541	1.0	1.4
$\gamma_{\overline{uu}_1}$	628.319	26.303	18.3	56.032	81.7	61.904	9.9	6.8
$\gamma_{\overline{vv}_1}$	628.319	21.803	13.9	54.275	86.1	58.490	9.3	5.7
$\gamma_{\overline{ww}_1}$	628.319	40.303	23.7	72.333	76.3	82.804	13.2	5.0
$\gamma_{\overline{uv}_1}$	628.319	12.881	18.8	26.743	81.2	29.683	4.7	9.9
$\gamma_{\overline{uw}_1}$	628.319	26.073	18.3	55.027	81.7	60.892	9.7	5.8

[a]Nominal wake uncertainty results from Gui et al. [9].
[b]Zero carriage speed test results.
[c]Uniform flow test results.

$$(c_m c_n)_i = (C_{m,i} - C_k)(C_{n,i} - C_k) \tag{6}$$

The axial $\overline{uu}$, transverse $\overline{vv}$, and vertical $\overline{ww}$ normal Reynolds stresses are given by $k=1,2,3$, respectively, in Eq. (5). The $\overline{uv}$ and $\overline{uw}$ shear Reynolds stresses are given by $m=1$, $n=2$ and $m=1, n=3$, respectively, in Eq. (6). $\overline{vw}$ is not obtainable with the 2D PIV system. For a steady-flow application, i.e., ship advancing into calm water, C_k in Eqs. (5) and (6) is the average velocity component determined with the average particle displacement component S_k as

$$C_k = \frac{L_{\text{obj}}}{L_{\text{img}}\Delta t U_c}\frac{1}{N_f}\sum_{i=1}^{N_f} S_{k,i} = \frac{L_{\text{obj}}}{L_{\text{img}}\Delta t U_c} S_k \tag{7}$$

For an unsteady-flow application, i.e., ship advancing into regular head waves, C_k in Eqs. (5) and (6) is a LSR polynomial X_{LSR}, where X_{LSR} is representative of the response of the unsteady velocity through one encounter period.

The data-reduction equation for the regular head wave elevation measurement is

$$\zeta_I(t_i) = \frac{z_I(t_i)}{L} \tag{8}$$

where $z_I(t_i)$ is the ith regular head wave elevation (dimensional) in a series of N_r sweeps of an analog-to-digital (A/D) card. This occurs synchronously with the acquisition of N_r PIV recordings. Equation (9) is the phase expression for the unsteady PIV measurements at $x=0.935$

$$\gamma_i = \gamma_{\zeta I_1} + 2\pi\frac{D}{\lambda} - 2\pi t_i f_e \tag{9}$$

The first term on the right-hand side is the first harmonic phase of the incident wave which is derived from $\zeta_I(t_i)$ at $t=0$ s (when data acquisition commences in the carriage run) at the position of a servo wave gage upstream of the PIV system. The second term on the right-hand side is the phase delay created by placing the servo wave gage upstream of the measurement area by a distance λ/D. The third term on the right-hand side is the phase delay associated with the regular time interval between successive PIV recordings. For this application, t_i is incremented by 133 ms since the PIV

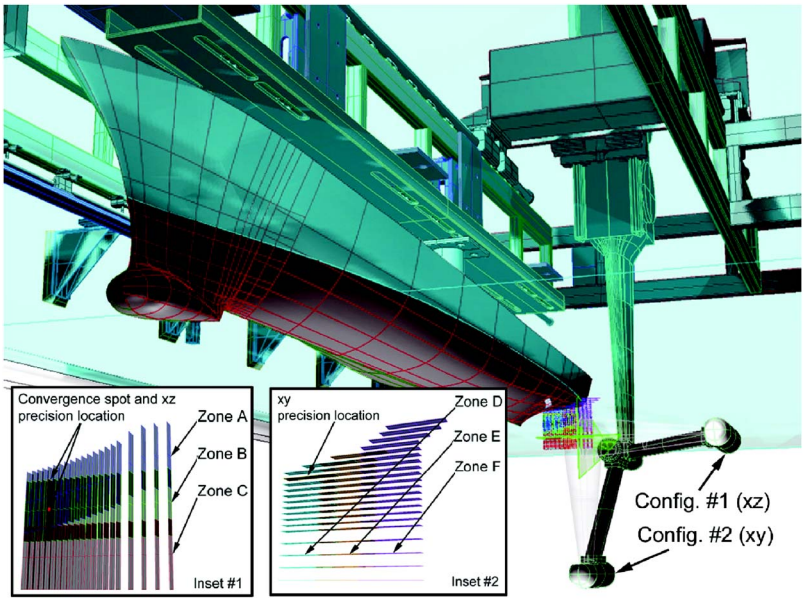

Fig. 3 PIV measurements at the nominal wake plane of DTMB model 5512 showing both configuration #1 *xz* and configuration #2 *xy* of the 2D PIV system. Inset #1 and #2 highlight the *xz* and *xy* measurement zones, respectively, and the convergence parameter and UA precision-limit locations.

system acquisition rate of vector fields is 7.5 Hz. This phase delay is expressed as a fraction of the encounter period $T=1/f_e$.

A numerical implementation of the method of least squares is used to compute the nth-order polynomial curve fits

$$X_{\mathrm{LSR},j} = a_0 + a_1(\gamma_j) + a_2(\gamma_j)^2 + \cdots + a_n(\gamma_j)^n \tag{10}$$

where $X_{\mathrm{LSR},j}$ and γ_j for $j=1,\ldots,360$ are the regression ordinate and abscissa, respectively, and the a's are regression coefficients which are functions of the variables in Eqs. (4)–(6) and (9). γ_j is used in the analysis to reconstruct the LSR model for whole phase angles in the range $\gamma_j=1-360$ deg.

A numerical implementation of the Nth-order FS model is used for representing a phase-averaged velocity or Reynolds stress polynomial curve fit

$$X_{\mathrm{FS},j} = \sum_{n=0}^{N} A_n \cos(2\pi n f_e t_j + \gamma_n) \tag{11}$$

where A_n and γ_n are nth-order harmonic amplitude and phase, respectively, t_j is the time in the encounter period for $j=1,\ldots,360$ when the FS is computed, and $\gamma_0=0$ deg. Summations are used to compute the FS coefficients in Eqs. (12) and (13), taking advantage of the fact that the LSR modeling is for 360 equidistant points over the encounter period T. The amplitude A_n and phase γ_n of the FS are expressed as

$$A_n = \frac{2}{360}\left[\left(\sum_{j=1}^{360} X_{\mathrm{LSR},j}\cos(2\pi f_e n t_j)\right)^2 + \left(\sum_{j=1}^{360} X_{\mathrm{LSR},j}\sin(2\pi f_e n t_j)\right)^2\right]^{1/2} \tag{12}$$

$$\gamma_n = \tan^{-1}\left[\left(-\sum_{j=1}^{360} X_{\mathrm{LSR},j}\sin(2\pi f_e n t_j)\right) \Big/ \left(\sum_{j=1}^{360} X_{\mathrm{LSR},j}\cos(2\pi f_e n t_j)\right)\right] \tag{13}$$

where the A_n's and γ_n's are the final, desired results for the present study.

2.3 Measurement Systems. The towed, 2D PIV system is designed and constructed by Dantec Dynamics and shown in Figs. 2 and 3. The PIV hardware components (hydrodynamic strut, laser, light-guiding arm, light-sheet optics, digital camera) are assembled on a massive 2D, computer-controlled traversing system capable of automated movement along the transverse y and vertical z axes. Movements in the x coordinate are manual. The strut is pressurized, partly submerged, and contains a 20 mJ, dual cavity Nd:yag laser and light-guide arm for steering 532 nm beams through the light-sheet optics, which is housed in a submerged, streamlined torpedo. The digital camera is a one-megapixel 1008×1018 pixels cross-correlation camera fitted with an f/1.4 50 mm lens that views the light sheet from a distance of 50 cm through a 90 deg mirror. The maximum object-plane size with the 50 mm lens is 7.5×7.5 cm^2, however, smaller areas can be utilized to realize a number of advantages which will be discussed later. The camera is housed in a separate submerged, streamlined

torpedo. Light-sheet and camera torpedoes are joined with a rigid, streamlined ministrut such that the light sheet is orthogonal to the viewing axis of the camera. Figure 3 shows the system configured to measure in two modes. In the first, the ministrut is horizontal and velocities (U,W) and Reynolds stresses $(\overline{uu},\overline{ww},\overline{uw})$ are acquired in vertical xz planes. In the second, the ministrut is rotated downward through 90 deg whereby velocities (U,V) and Reynolds stresses $(\overline{uu},\overline{vv},\overline{uv})$ are acquired in horizontal xy planes. Synchronization of the laser and camera, image processing, and acquisition of towing carriage speed are performed with the Dantec Dynamics PIV 2000 vector processor which is equipped with a four-channel, 12-bit A/D card. Data acquisition and parameter settings are facilitated with an IBM-compatible, Windows NT PC equipped with a National Instruments GPIB card and Dantec Dynamics v.3.11 Flowmanager software. Results in the form of vector maps are displayed real-time at a rate of 7.5 Hz. Unsteady data are phase-locked to the regular head wave elevation by connection of a servo wave probe to the PIV A/D board. The probe monitors the regular head wave from a distance $D=4.42$ m upstream of the measurement area. The servo probe is a ±5 cm, precalibrated Kenek wave probe with a resolution of 0.1 mm and 1:1 frequency response up to 5 Hz for the present incident wave amplitudes. Silver-coated hollow glass spheres with a density of 1600 $\mathrm{kg/m^3}$ and an average diameter of 15 μm are used as seed particles. These particles have demonstrated very good light-reflectance for PIV image capture and adequate suspension capability. Additionally, the particles are capable of following sinusoidal motions with frequencies up to 1375 Hz.

The second measurement system is used for monitoring and measuring the carriage speed and servo wave probe output for each data-acquisition run. It is composed of a DOS PC, IIHR-fabricated speed circuit, and Kenek servo wave gauge. The speed circuit hardware includes an 8000-count optical encoder affixed to a wheel of the drive carriage through a pair of chain-driven sprockets and a digital-to-analog converter. A detailed uncertainty analysis of the IIHR speed circuit has estimated the uncertainty in U_c of $U_{Uc}=0.25\%$ for towing speeds corresponding to Fr=0.28 with model 5512 [5].

2.4 Data Acquisition and Reduction Procedures. The measurement area dimensions are 192×1018 pixels (14.3×74.9 mm) or 18% of the total field of view. Advantages of this measurement area include previous use by Gui et al. [9], real-time data throughput for accurate vector map time stamping, and reduction of amplitude and phase errors at the periphery of the image plane [39]. Other PIV data acquisition parameters include 32×32 pixel interrogation areas, 50% overlap in both coordinates, and window-offsetting 8 pixels in the axial coordinate. A Gaussian window function is used in the correlations. With the above settings, the measurement grid is 11×62 vectors. PIV image pairs or recordings are taken at 133 ms intervals or 7.5 Hz. The time between successive PIV images is $\Delta t=490$ μs. Measurements are taken at several measurement area locations within six zones. For measurements in the vertical plane, 21 measurement area locations are used in zones A, B, C (Fig. 3, inset #1). For measurements in the horizontal plane, 16, 17, and 21 measurement area locations are used in zones D, E, and F (Fig. 3, inset #2), respectively. All zones are centered axially on the nominal wake plane and cover the region of interest in the yz cross plane predicted by a RANS solution [36] for the current test conditions, i.e., $x=0.935$; $-0.06\leqslant y\leqslant 0$; $-0.06\leqslant z\leqslant 0$. Zones are arranged to provide adequate overlap for measurement-continuity checks across zone boundaries, i.e., 28–80% between zones A and B, 28% between zones B and C, and 32% between zones D, E, F. Zone A sets the nearest measurement locations to the model through placement of the top interrogation area at $x=0.935$ adjacent to the hull surface. This ensures a minimum distance of 1.2 mm between the center of the nearest interrogation area and the hull surface or $y^+=70$ based on a friction velocity estimate from flat plate data. For the unsteady cases, regular head wave data is taken $D=4.42$ m upstream of the measurement area midpoint. U_c and $\zeta_I(t)$ are sampled on the DOS PC for 10 s at a rate of 410 Hz.

Data acquisition procedures were initiated by at-rest reference voltages for U_c and $\zeta_I(t)$. Time is allowed for waves to travel the length of the tank after which the carriage is started and accelerates through 10 m to a constant speed. Data acquisition commences after traveling another 10 m for 27 s or 42 m through the tank after which the carriage is decelerated. A single carriage run produces 200 PIV recordings. The wave elevation at $t=0$ s on the first PIV recording determines the initial phase of the regular head wave. Ten and six carriage runs are made for unsteady and steady cases, respectively. Prior to initiating the test program, a convergence study sets the required number of carriage runs that yield converged zeroth and first harmonic amplitude and phases. The study focuses on convergence histories and running means for a single measurement area in the viscous flow (zone B, plane 05). The convergence parameter is defined by

$$X_{\mathrm{cnv}}=\frac{(X_n-X_{n-1})}{D_X}\times 100\% \tag{14}$$

where X_n for $n=2,\ldots,N_f$ is any phase-averaged velocity or Reynolds stress. Equation (14) evaluates successive changes in the value of X at a given grid point as a percentage of the dynamic range D_X for increasing numbers of valid PIV samples at that grid point. Convergence is considered to be achieved for values of X_{cnv} that are within the uncertainty level U_X of X. At the test program conclusion, a more extensive convergence study is undertaken to evaluate the convergence parameter (14) of all phase-averaged velocities and Reynolds stresses at all measurement areas and grid points. Results indicate average convergence parameter values of 1.0%, 4.1%, and 4.5% for zeroth and first harmonic amplitudes and first harmonic phase, respectively, as shown in Table 2.

Unsteady and steady data are postprocessed with FORTRAN programs that are written and run on a Windows PC. Unsteady data are phase averaged by processing batches of PIV and corresponding DOS data files acquired at single light sheet positions. From a batch, f_e is computed from PIV-sampled ζ_I for each carriage run followed by FS analysis which yields ζ_{I1} and $\gamma_{\zeta I1}$ at $t=0$ s. f_e, $\gamma_{\zeta I1}$, and D are then used in Eq. (9) to compute the specific phase angle of all vector maps in each carriage run (Fig. 4(*a*)). The following procedures are used at all grid points in the measurement area. Data are sorted on the phase angle from 0 to 2π (Fig. 4(*b*)) and then filtered with a two-stage range filter and 2D median filter to remove spurious vectors (Figs. 4(*b*) and 4(*c*)). Because there is no penalty in the phase-averaging process, rejected vectors are not replaced. A fifth order LSR curve is fit to the filtered data, which represents the phase-averaged unsteady response through one encounter period. Then, a tenth order FS is computed from the LSR curve fit to obtain the harmonic amplitudes and phases of the phase-averaged response (Fig. 4(*d*)). Phase-averaged Reynolds stresses are computed in the range $0-2\pi$ as differences between the instantaneous velocities and the FS reconstruction of the velocities. Similarly as with the organized oscillations, a fifth order LSR is fit to the random fluctuations followed by a tenth order FS. Convergence histories for zeroth and first harmonic amplitude and first harmonic phase are computed and monitored at seven locations longitudinally across the measurement area. When all raw data is processed as per the above procedures, constant y or z data are patched across zone boundaries and five passes of a moving-average filter is applied across the range of y or z values to remove high-frequency noise in the patch regions. The three-dimensional flow field at the nominal wake plane is constructed through linear interpolation of xz and xy data to a standard 150×150 grid in the region $-0.06\leqslant y\leqslant 0$, $-0.06\leqslant z\leqslant 0$. Animations of the velocities and Reynolds

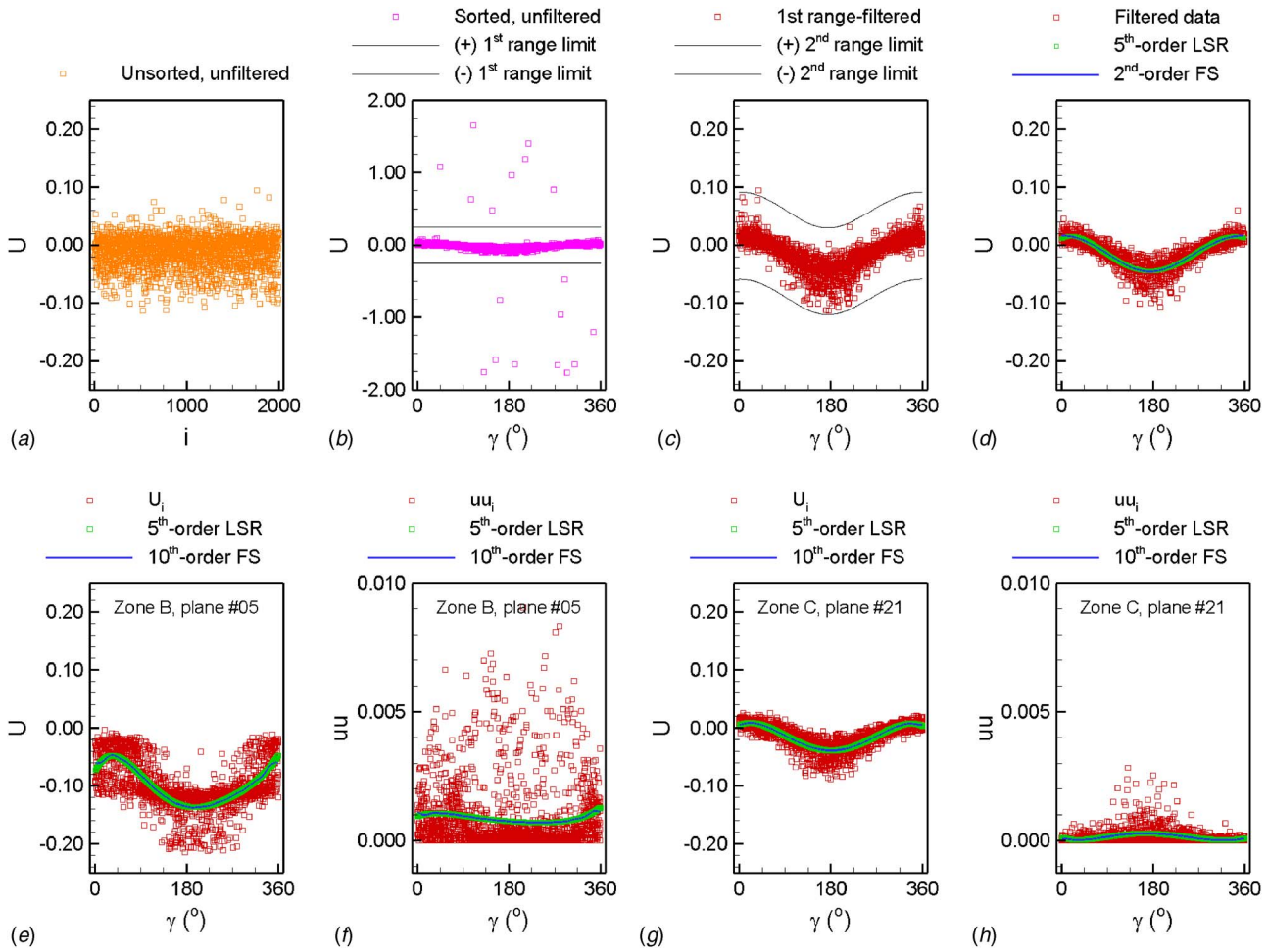

Fig. 4 Typical unsteady PIV data-reduction procedures: (*a*) unsorted, unfiltered data; (*b*) phase-sorted, unfiltered data and first stage range-filter limits; (*c*) first stage range-filtered data and second stage range-filter limits; (*d*) range- and median-filtered data with LSR curve fit and FS expansion of LSR curve fit; (*e*) mean axial velocity response and LSR and FS in the *xz* precision limit measurement area; (*f*) axial normal stress response and LSR and FS in the *xz* precision limit measurement area; (*g*) mean axial velocity response and LSR and FS in the external flow; (*h*) axial normal stress response and LSR and FS in the external flow.

stresses are generated with Eq. (11).

At the test program conclusion, an analysis is made of the data reduction LSR interpolation procedure by comparison with interpolation using an arithmetic mean based on a moving average method where averages between 3 deg and 358 deg are based on local averages between ±2 deg. The differences for the first harmonic amplitude and phase are within the measurement uncertainties. The differences for the second harmonic amplitude are fairly large but although not estimated the uncertainty is also expected to be large such that reanalysis of all the data is not deemed necessary.

3 Uncertainty Analysis

Original development of uncertainty analysis procedures for steady PIV measurements is undertaken as part of the commissioning procedures for the IIHR towed, 2D PIV system and documentation of the quality of nominal wake data [9]. Techniques for reduction of PIV cross-correlation evaluation bias with window functions are also developed [40]. Subsequently, uncertainty analysis procedures are developed for unsteady forces and moment and wave field data [12,13] and extended for present unsteady PIV measurements by Longo et al. [41]. More recently, improvements are made to directly account for the bias errors in the LSR representation of the unsteady PIV data.

Measurement uncertainties for the steady velocities and Reynolds stresses are provided in Table 2 including original values from [9]. The current results are considered satisfactory and show 1–3% reduced uncertainties over previous values for 6–8 variables with $\overline{ww}$ and $\overline{uv}$ 0.3% and 1.8% higher, respectively, than previously. Reductions are a result of improved repeatability of the measurements, which lowers the precision limits and thereby U_X. For the velocities, more than half of the uncertainty is attributed to the bias limits, whereas, the precision limits are dominant in the Reynolds stress uncertainties. This result is expected since the signal to noise ratio of the Reynolds stresses is lower in comparison to that of the velocities, thus making the repeatability of the Reynolds stress result more difficult.

The unsteady uncertainty analysis determines the final uncertainties in the phase-averaged velocities and Reynolds stresses FS reconstruction. A summary of the bias and precision limits, total uncertainties, and global convergence is given in Table 2. A comprehensive accounting of the uncertainties in the final results should consider the uncertainties in the LSR and FS models which are caused by uncertainties in the original measured variables from Eqs. (4)–(6) and (9). The original measured variables themselves are functional relations of several variables as shown in Eqs. (4) and (9), each of which contains systematic errors. Systematic errors in the variables of Eqs. (4) and (9) propagate

through the LSR and FS models and into the harmonic amplitudes and phases. The specific uncertainty analysis methodology adopted for the unsteady PIV measurements follows Coleman and Steele [42]. The methodology provides a framework for comprehensive estimation of uncertainties associated with the LSR curve fitting and is also adapted for the estimation of uncertainties associated with the FS reconstructions. Equations (4)–(6) for $i=1,\ldots,N_f$ are written in functional form as

$$X_i = f\{S_{k,i}, L_{\text{obj}}, L_{\text{img}}, \Delta t, U_c, \gamma_{\zeta I_1}, D, \lambda, t_i, f_e, y, z\} \tag{15}$$

The derivatives in the LSR and FS bias limits are evaluated numerically with a perturbation method. The method is implemented for any variable by perturbing the nominal LSR or FS by 1% in either the ordinate or abscissa, the LSR or FS is recomputed, and the differences between the perturbed and nominal LSR are summed at whole phase angles from $\gamma_I = 1$ deg, …, 360 deg. For $S_{k,i}$ and t_i, this method is also applied sequentially over all $i=1,\ldots,N_f$. Systematic uncertainties in the FS associated with errors in the y and z coordinate positions of the measurement area are accounted for by evaluating the spatial derivatives of the variables and combining them with B_y and B_z. To avoid accounting twice for systematic uncertainties associated with f_e, this term is omitted for FS analysis as the LSR analysis previously included effects of f_e. Bias limits are averaged over 31 grid points along the midlines of the xz and xy measurement areas that are chosen for the uncertainty analysis (Fig. 3 inset #1, 2). These lines are coincident with the nominal wake of model 5512.

The precision limits of the FS results are determined with an end-to-end, multiple-test method. Ten converged steady and unsteady datasets are obtained at zone B, plane 05 ($y=-30.48$ mm, $z=-53.34$ mm) and zone D, plane 14 ($y=0$ mm, $z=-53.34$ mm). These locations are within the boundary layer and near the steady-flow peak values of turbulent kinetic energy (Fig. 3 inset #1, 2). As stated above, only 31 points at $x=0.935$, or 5% of the total number of grid points in each measurement area are considered in the analysis. This procedure is followed because these points are coincident with the nominal wake plane and good representatives of the total population of measurement area grid points. The converged datasets are spaced evenly in time through the course of the experiments to account for factors that influence variability of the measurements such as ambient motions in the tank water, traverse errors in the y, z coordinates, and laser-power and seeding changes.

Referring to Eq. (15), there are 12 elemental biases. Five ($B_{Sk,i}$, B_{Lobj}, B_{Limg}, $B_{\Delta t}$, B_{ti}) are estimated based on manufacturers specifications, whereas the other seven (B_{Uc}, $B_{\gamma\zeta I1}$, B_D, B_λ, B_{fe}, B_y, B_z) are estimated either by previous uncertainty analysis, calibration or empirical tests. B_{Uc} is estimated based on previous uncertainty analysis, as already mentioned. $B_{\gamma\zeta I1}$ and B_{fe} are estimated based numerical tests to determine the minimum phase and frequency resolution of the FS and FFT subroutines, respectively. B_D is estimated from a set of three measurements between the servo wave gauge needle and the center of the measurement area with a tape measure. B_λ is estimated with an independent experiment for direct measurement of λ using two servo wave gauges separated a known distance axially in the tank. B_y and B_z are estimated with the manufacturer's accuracy specifications of the y, z traverses and imaging tests of location markers on the hull and the free surface.

The largest bias for the axial and vertical velocity amplitudes is B_{Lobj}, whereas the second largest is B_{Uc} and B_λ, respectively. The largest and second largest biases for the transverse velocity amplitudes are B_λ and B_z. For the transverse and vertical velocity amplitudes B_y also has a significant contribution. The largest and second largest biases for the Reynolds stress amplitudes are either $B_{Sk,i}$ or B_λ. The largest and second largest biases for both the velocity and Reynolds stress phase angles are B_z and B_y, respectively. The other six biases B_{Limg}, $B_{\Delta t}$, $B_{\gamma\zeta I1}$, B_D, B_{ti}, B_{fe} are relatively small contributing $\leqslant 1\%$ to the total bias limit. Large B_{Lobj} is due to accuracy of the PIV calibration. Large B_{Uc} is due to the accuracy of the carriage speed circuit. Large B_λ, B_z, and B_y are due to the large sensitivity coefficients associated with these biases. Lastly, large $B_{Sk,i}$ is due to the accuracy of the PIV evaluation algorithm.

Table 2 summarizes the bias and precision limits as percentages of the total uncertainty along with the total uncertainty as a percentage of the dynamic range. The bias limit is largest for the axial velocity amplitudes, whereas the precision limit is largest for the transverse and vertical velocity amplitudes. However, both bias and precision limits contribute significantly. The bias limits are much larger than the precision limits for the Reynolds stress amplitudes. The precision limit amplitudes are much larger than the bias limits for both velocity and Reynolds stress phases. The weaker signal to noise ratio for the transverse and vertical velocities accounts for their larger precision limits. The total uncertainties for the velocity amplitudes and phases are of similar magnitude as the steady-flow amplitude estimates; therefore, they are considered satisfactory. The total uncertainties for the Reynolds stress amplitudes and phases are larger than their steady-flow amplitude estimates, but still considered satisfactory in view of the complexity and difficulty making such measurements. The average convergence parameter for velocity and Reynolds stress amplitudes and phases is less than its respective uncertainty for most cases, except for some of the Reynolds stress phases. The uncertainty analysis suggests that the total uncertainty can be reduced in many cases by reduction in various elemental biases and in some cases additional data acquisition.

4 Results

Of primary interest is the phase-averaged velocity and Reynolds stress nominal wake measurements for surface combatant 5512 in regular head waves. However, to put the work in perspective it is useful to first review steady nominal wake, regular head wave unsteady elevation and phase-averaged velocities, unsteady forces and moments, and phase-averaged wave field for the same conditions as for the present results. The summary is also useful for those who wish to use the data for validation of simulation methods.

4.1 Steady Nominal Wake. Steady-flow nominal wake data are retaken as part of the project and compared with [9] steady PIV results in order to validate newly developed data acquisition and data reduction procedures. Quantitative comparisons are made including consideration of the data uncertainties. The data are also compared with [5] 5-hole pitot tube measurements for the same facility and model and also for two other facilities using larger geometrically similar models and again with consideration to the uncertainties [6]. The overall comparisons enable error and uncertainty estimates for the current ability to measure steady ship velocity fields. Another reason for retaking the data is to map a larger region of the nominal wake plane and take data for both steady and unsteady flow at the same measurement locations facilitating direct comparisons between the steady and unsteady measurements. Lastly, it is useful to review the steady flow prior to discussing the unsteady-flow results.

4.1.1 Error/Uncertainty Estimates for Ship Velocity Fields. As discussed in the preceding sections there are many factors that affect the accuracy of steady PIV measurements. Quantitative comparisons of present D_1 and D_2 [9] measurements including consideration of uncertainty estimates enable an assessment of unaccounted for bias errors. The comparison error $E=D_1-D_2$ and uncertainty $U_E=\sqrt{U_{D_1}^2+U_{D_2}^2}$ are defined. For $|E|\leqslant U_E$, the differences are within the uncertainty of the measurement system and the data are validated at the interval U_E. For $|E|>U_E$, the differences are greater than the uncertainty of the measurement system indicating unaccounted for bias errors with E itself a better esti-

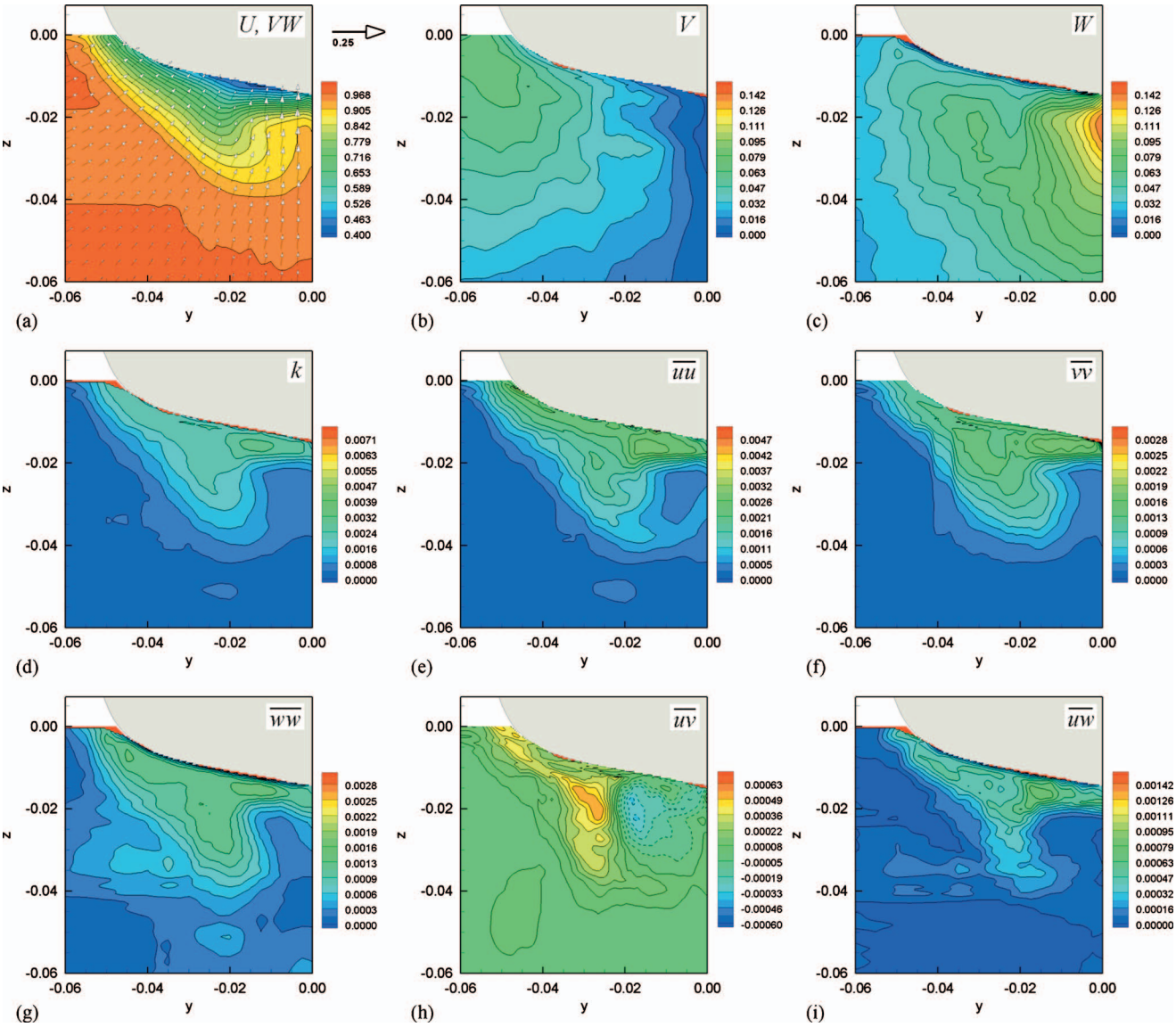

Fig. 5 Steady-flow mean velocities and Reynolds stresses

mate of the uncertainty in the measurements. The present and previous data are interpolated onto a common 50×50 grid with dimensions of $-0.0475\leqslant y\leqslant 0, -0.045\leqslant z\leqslant -0.0025$ and E is evaluated at all grid points, as summarized using average values in Table 2. U, W, $\overline{vv}$, and $\overline{ww}$ comparison errors are larger than U_E indicating unaccounted for bias errors and that their respective E intervals should be used as improved uncertainty estimates. Previous steady PIV results are compared with [5] 5-hole pitot tube data in [9]; for U and $W|E|>U_E$ with $E=4.2\%$ and 7.9%, respectively, whereas for $V|E|\leqslant U_E=8.9\%$. Gui et al. [9] shows that differences are likely due to biases from the use of a pitot probe for flow with velocity gradients. IIHR 5-hole pitot tube data are compared with INSEAN and DTMB 5-hole pitot data for 5415 in [6]. For V and $W|E|>U_E$ with $E=4.1\%$ and 7.7%, respectively, whereas for $U|E|\leqslant U_E=3.9\%$. No clear trend is observable regarding differences between facilities, model size, or 5-hole pitot versus PIV measurement systems, i.e., the differences between each are of similar magnitudes. The overall conclusion is that steady nominal wake uncertainties are no worse than $(U,V,W,\overline{uu},\overline{vv},\overline{ww},\overline{uv},\overline{uw})=(4.3\%,\ 8.9\%,\ 7.9\%,\ 5.4\%,\ 8.4\%,\ 14.8\%,\ 7.2\%,\ 6.4\%)$. Evaluation and comparison of axial vorticity indicates similar patterns between facilities and measurement systems, but even larger differences than for the mean velocities.

4.1.2 Mean Velocities and Reynolds Stresses. The steady nominal wake is shown in Fig. 5. The flow pattern is explained by interactions between the hull boundary layer and sonar dome (near center plane) and after body shoulder (near mid girth) outboard rotating axial vortices, as displayed by the INSEAN mean-flow map on the fore and after body and in the near wake. For $x=0$, 0.1, 0.2, and 0.4, mostly thin boundary layer development is observed along the mid girth with thickening near the free surface and keel. Near-keel axial velocity contours have an elliptical shape with a long axis parallel to the center plane, which is correlated with similarly shaped axial vorticity contours. For $x=0.6$, there is a gradual thickening of the boundary layer. Near-keel axial velocity contours have an elliptical shape rotated such that the long axis is parallel with the hull bottom, which is again correlated with similarly shaped axial vorticity contours, but with two distinct regions of high vorticity. For $x=0.8$ and 0.935 (nominal wake plane) axial velocity contours are hook shaped with a bulge in the boundary layer near $\frac{3}{4}$ girth and a thin boundary layer

near the keel, which is correlated with hooked and elliptical (long axis parallel to the calm water plane) axial vorticity contours, respectively. For $x=1.0$, 1.1, and 1.2, the bulge in the axial velocity contours becomes parallel to the wake center plane.

For the nominal wake, inboard of the axial vortex center $(y,z)=(-0.02,-0.02)$ and near the center plane, high momentum fluid is transported towards the hull thinning the boundary layer, whereas outboard of the vortex center low momentum fluid is transported away from the hull thickening the boundary layer. The appearance is a bulge in the axial velocity contours. The cross-plane vectors are towards the hull with 45 deg and 90 deg angle to the hull outboard and inboard of the bulge and vortex center. At the axial vortex center $\omega_x \approx 7$ and $U \approx 65\% U_c$. The turbulent kinetic energy and Reynolds stresses correlate with the axial velocity and vorticity contours with large values especially in the thin boundary layer near the hull bottom and center plane but also in the bulge region. Maximum values for $(\sqrt{k}, \sqrt{\overline{uu}}, \sqrt{\overline{vv}}, \sqrt{\overline{ww}})$ are 5.4%, 5.3%, 4.1%, and $3.7\% U_c$. Normal Reynolds stresses are anisotropic with $\overline{uu} > \overline{vv} > \overline{ww}$. Magnitudes and trends are consistent with a flat plate boundary layer at $z/\delta=0.5$. At the vortex center, the normal Reynolds stresses are more isotropic, i.e., $(\sqrt{\overline{uu}}, \sqrt{\overline{vv}}, \sqrt{\overline{ww}})$ are 4.3%, 3.3%, and $3.2\% U_c$. $\overline{uv}$ is negative in regions of positive $\partial U/\partial y$ and positive in regions of negative $\partial U/\partial y$ with maximum values of $\sqrt{\overline{uv}}=2.4\% U_c$. $\overline{uw}$ is similar but correlates with $\partial U/\partial z$ with a maximum value of $\sqrt{\overline{uw}}=2.8\% U_c$. The mean and turbulent nominal wake flow pattern shows similarity to the boundary layer and turbulence structure in the presence of common downstreamwise vortex pairs [43,44]. The similarities include thinning and thickening of the boundary layer inboard and outboard of the vortex, respectively; up wash of low momentum fluid, high turbulence outboard of the vortex; isotropic normal Reynolds stresses in the vortex core; and large Reynolds shear stresses in the up wash region.

4.2 Regular Head Wave Elevation and Velocities. The regular head wave elevations have been studied in conjunction with commissioning the plunger wave maker [45] and measurements of the forces and moments and wave pattern [12,13]. Longo et al. [45] show that the regular head waves follow linear plunger wavemaker theory with nonlinear effects within the uncertainty estimates, except for extreme conditions. Gui et al. [12,13] provide updated uncertainty estimates for regular head wave amplitude (0.7% dynamic range), wave frequency (2.7% dynamic range), and encounter frequency (0.4% dynamic range), which are applicable for the present conditions.

In preparation for the present experiments, stationary and towed PIV phase-averaged regular head wave measurements are made to develop data acquisition and reduction procedures and document the velocities, including comparisons with linear 2D progressive wave theory [34]. For a progressive wave traveling in the positive x direction, the incident wave elevation and axial and vertical velocities are

$$\zeta_I(x,t) = A\cos(kx - 2\pi f_e t) \tag{16}$$

$$U(x,z,t) = 1 + \frac{2\pi f A}{U_c} e^{kz}\cos(kx - 2\pi f_e t) \tag{17}$$

$$W(x,z,t) = \frac{2\pi f A}{U_c} e^{kz}\sin(kx - 2\pi f_e t) \tag{18}$$

Note that for the current conditions the maximum values of nondimensional wave amplitude and velocities are 0.006 and 0.046, respectively. Admittedly, the wave amplitude and wave-induced velocities are small and only somewhat larger than their estimated uncertainties; however, as shown below by comparison with theory they are arguably well resolved.

The average difference between the measured elevation and theory is 1.4%, which is larger than the uncertainty estimated at 0.7%. Tests to measure the wavelength using two wave probes have shown an average $\bar{\lambda}=4.654$ m which is 1.7% longer than the dispersion relation predicts $\lambda=4.575$ m for small-amplitude, deep-water waves. Based on the average measured wavelength and first harmonic amplitude, $Ak=0.024$.

Average differences between phase-averaged regular head wave velocities experiment and theory are computed for three vertical-plane measurement areas having 682 grid points each. For the U component, average differences are 1.2%, 0.9%, and 0.8% for $U_{0_T}-U_{0_E}$, $U_{1_T}-U_{1_E}$, and $\gamma_{U1_T}-\gamma_{U1_E}$, respectively, and for the W component, averaged differences are 0.1%, 0.9%, and 2.0% for $W_{0_T}-W_{0_E}$, $W_{1_T}-W_{1_E}$, and $\gamma_{W1_T}-\gamma_{W1_E}$, respectively. The average differences are all well within the noise levels of the U and W zeroth and first harmonics in Table 2. The first harmonic amplitude of V is an order-of-magnitude smaller than that for U or W. The second harmonics for the axial and vertical velocities are two orders-of-magnitude smaller than their first harmonics. The second harmonic for the transverse velocity is an order-of-magnitude smaller than its first harmonic. Reynolds stresses responses are small, but distinct trends are apparent. Axial $\overline{uu}$ and vertical $\overline{ww}$ normal stresses show increases when magnitudes of their corresponding velocities are maximum/minimum, which indicates a second-harmonic response. In fact, the second harmonic amplitudes are larger than the first for all three normal Reynolds stresses, 105%, 152%, and 140%, respectively, for $\overline{uu}$, $\overline{vv}$, and $\overline{ww}$. The amplitude of the transverse normal Reynolds stress is relatively small compared with the axial and vertical components. Shear stresses $\overline{uv}$ and $\overline{uw}$ roughly correlate with $\overline{uu}$ and $\overline{ww}$, respectively. Although the uncertainty in the measurement of the second harmonics is expected to be large there is a clear trend of large second-harmonic response for the Reynolds stresses.

4.3 Unsteady Forces and Moment. Gui et al. [12,13] study resistance C_T and heave C_H forces and pitch moment C_M for 5512 for a wide range of Fr, Ak, and λ, including the present conditions, as shown in Fig. 6 and Table 3. Figure 6 includes corresponding wave elevations ζ_I and running mean values and FFT for all four variables. Running means display statistical convergence for all four time histories. Dominant FFT frequencies for incident wave frequency (0.584 Hz) and the encounter frequencies of the forces and moments (~0.922 Hz) closely correspond with the imposed conditions. The difference between the steady and twice the zeroth harmonic is referred to as added resistance and is $9\% C_T$. The first harmonic is 1.38% of the steady C_T and the second harmonic is 2.7% of the first harmonic. The phase angles for maximum C_T, C_H, and C_M correspond to wave crests at $x=0.1$, 0.39, and 0.003, respectively, i.e., for crests on the fore body for the resistance and pitch moment and near the mid body for the heave force.

4.4 Phase-Averaged Wave Field. Gui et al. [12,13] also study the phase-averaged wave field for the present conditions, including near $(-0.2 \leq x \leq 1.3,\ 0 \leq y \leq 0.082)$ and far $(-0.2 \leq x \leq 1.3,\ 0.082 \leq y \leq 0.392)$ field regions using capacitance wire and servo mechanism wave gauges, respectively. The results are combined providing zeroth harmonic amplitude and first harmonic amplitude and phase results. RMS near field wave elevations are also measured in the transom region. Note that the incident wave amplitude A is 43% of the dynamic range of the steady wave pattern. The zeroth harmonic wave pattern is within estimated uncertainties of the previously measured steady wave pattern [5] displaying Kelvin-type transverse and diverging waves for a slender ship. The maximum first harmonic amplitude is $1.7A$. A large amplitude crest line and low amplitude trough line diverge from the fore body shoulder ($x=0.35$) and transom corner, respectively, with a 24.5 deg angle to the hull center plane. The former leads and the latter lags the incident wave by $\pi/3$. The diffraction wave is defined as the difference between the first harmonic response and incident wave and has a maximum amplitude of 40% of the unsteady free surface elevations. The RMS for steady and un-

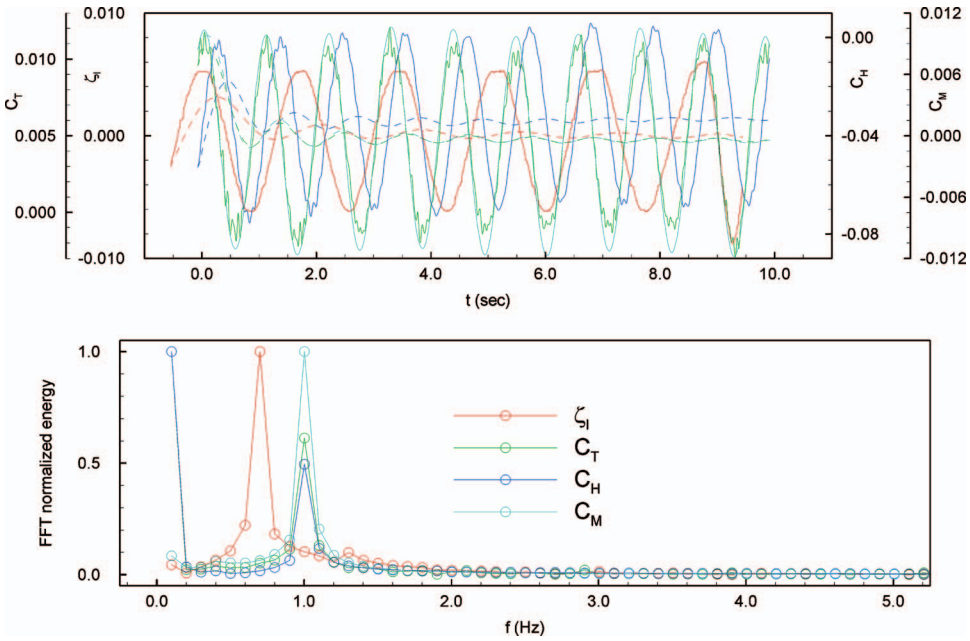

Fig. 6 Time histories (top, solid lines) and running averages (top, dashed lines) of ζ_I, C_T, C_H, and C_M for $Ak=0.025$, $\lambda=4.572$ m, Fr=0.28. FFTs (bottom) highlight regular head wave and encounter frequencies.

steady flow has similar patterns and maximum values in a narrow region close to the center plane extending $0.1L$ aft. Away from the center plane the RMS is larger for unsteady rather than steady flow.

4.5 Unsteady Nominal Wake. There are three primary effects on the boundary layer and wake due to the regular head wave. The wave-induced pressure gradients cause accelerations/decelerations of the axial and vertical velocities similarly as the regular head wave, but with the possibility of under/over shoots and phase leads/lags. In the outer region, the axial and vertical velocities are in phase and $\pi/2$ out of phase with the wave elevation, respectively, with a magnitude of oscillations $3-4.3\%U_c$ from bottom to top of measurement area. The wave-induced particle trajectories transport fluid axially and vertically with amplitude Ae^{kz} in phase with the wave elevation. The effects of axial transport are likely small, but the effects of vertical transport are significant since the transport distance of 0.01 is a large fraction of the boundary layer thickness in the nominal wake plane such that velocity oscillations are $15\%U_c$. Lastly, the wave induces a time varying ±2.8 deg angle of attack on the sonar dome resulting in unsteady sonar dome vortices with wavelength $U_c/f_e=0.54$, as shown by complementary CFD [36].

4.5.1 Zeroth Harmonic and Streaming. The zeroth harmonic response shows significant differences from the steady flow (Fig. 5), which is highlighted by streaming defined as the difference between twice the zeroth harmonic and steady amplitudes. Figure 7 displays streaming for the velocity components, turbulent kinetic energy, and Reynolds stresses normalized by the steady amplitude dynamic range. The maximum amplitudes are 5–20% and 70%, respectively, which are considerably larger than the uncertainties for steady and zeroth harmonic amplitudes. Amplitudes correspond to steady streaming motion induced by the incident wave and superimposed on the steady-flow pattern. The patterns for the velocity components correlate with the steady axial vorticity. The axial velocity shows increases in the bulge region and decreases in the thin boundary layer region outboard and inboard, respectively, of the vortex center. Note that the bulge and thin boundary layer regions correspond to the up and down wash regions, respectively, mentioned earlier in discussing the similarity between the steady nominal wake and boundary layer in the presence of common down stream wise vortex pairs. The transverse velocity shows small increases and large decreases above and be-

Table 3 Fourier series reconstruction of the regular head wave and forces and moment coefficients

Term	ζ_I (cm)	C_T	C_H	C_M
f (Hz)	0.584	0.924	0.918	0.919
X_{stdy} (×2)	⋯	0.884e−02	−0.633e−01	−0.187e−02
X_0	−0.969e−01	0.926e−02	−0.680e−01	−0.118e−02
X_1	0.177e+01	0.608e−02	0.356e−01	0.108e−01
X_2	0.675e−01	0.167e−03	0.183e−03	0.909e−05
X_{add}	⋯	0.402e−03	⋯	⋯
γ_1 (deg)	246.9	−46.9	243.4	−36.7
	$\zeta_{I,\text{crest}}$ in relation to the ship model			
$x_{\max}$ (nd)	⋯	0.100	0.390	0.003
$x_{\min}$ (nd)	⋯	0.849	1.140	0.752

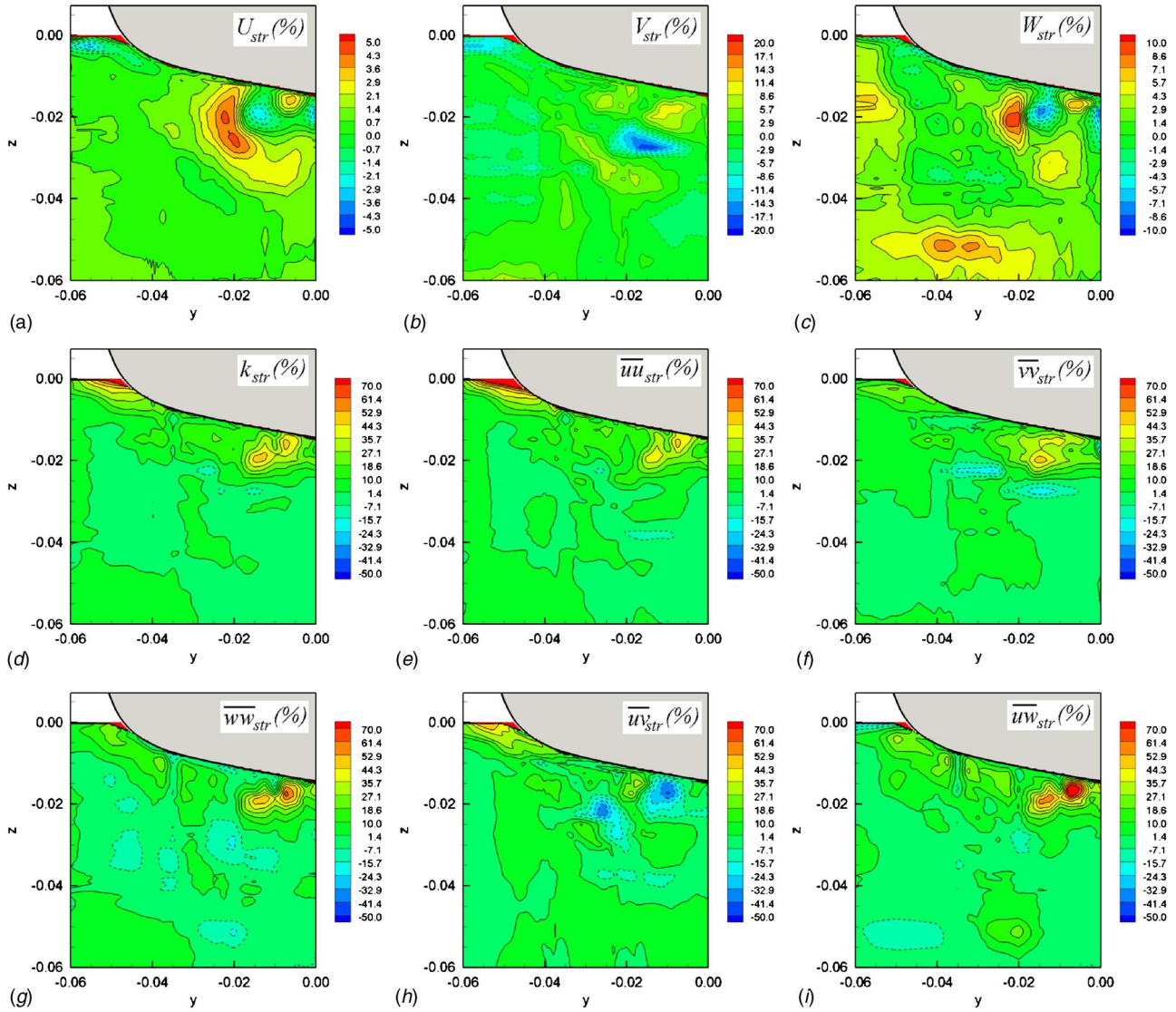

Fig. 7 Differences in zeroth harmonic amplitude and steady-flow variables as a percentage of the steady variable dynamic range [streaming=$(X_0 - X_{stdy})/D_X \times 100\%$]

low the vortex center, whereas the vertical velocity shows increases and decreases outboard and inboard of the vortex center, which combine to produce a streaming axial vortex with center coincident with the steady axial vortex but with opposite (inboard) rotation. The turbulent kinetic energy and Reynolds stresses show positive values in the thin boundary layer region where steady values are a maximum, except $\overline{uv}$ which shows negative values in the thin boundary layer and bulge region where steady values are negative and positive, respectively. Thus, there are three overall effects of the regular head wave on the time mean flow in comparison to the steady flow. The axial velocity is larger in the bulge region. The axial vorticity is reduced with center shifted downwards and towards the center plane $(y,z)=(-0.03,-0.015)$. The normal stresses and $\overline{uw}$ are larger and the $\overline{uv}$ Reynolds stresses is smaller positive/larger negative in the thin boundary layer/bulge regions. The increases in the Reynolds stresses are substantial and much larger than their respective uncertainties.

4.5.2 First and Second Harmonics. Figures 8 and 9 provide first harmonic amplitude and phase, respectively, for the velocity components, turbulent kinetic energy, and Reynolds stresses. The axial and vertical velocity first harmonic amplitude and phase on the outer edge of the measurement region $(y=-0.06)$ recovers the uniform stream, regular head wave values. In regions where the first harmonic amplitudes are small the phase is indeterminate; therefore, when the amplitude is less than 10% of the maximum value the phase is set to the edge values, 0, $\pi/3$, and $-\pi/2$ for (U,V,W) and $-\pi$, $-\pi$, $-\pi/2$, $-\pi$ and 0 for $(\overline{uu},\overline{vv},\overline{ww},\overline{uv},\overline{uw})$.

The axial velocity first harmonic amplitude shows very large amplitudes in the bulge and thin boundary layer regions similarly but with even larger amplitudes than the streaming. The former is in phase and the latter $-\pi$ out of phase with the incident wave. These large amplitudes are attributed to the wave-induced vertical transport of low momentum fluid downward at wave troughs and high momentum fluid upward at wave crests, which results in contraction and expansion of the boundary layer in phase with the wave in the bulge region and $-\pi$ out of phase with the wave in the thin boundary layer region.

The vertical first harmonic amplitude shows zero response under the hull near the center plane, small response in bulge and thin boundary layer region, and regular head wave/uniform flow in the outer region indicating the hull and boundary layer has a significant damping effect on the wave-induced vertical velocities. The phase is the same as for the regular head wave vertical velocity $-\pi/2$, except in the bulge and thin boundary layer region where it

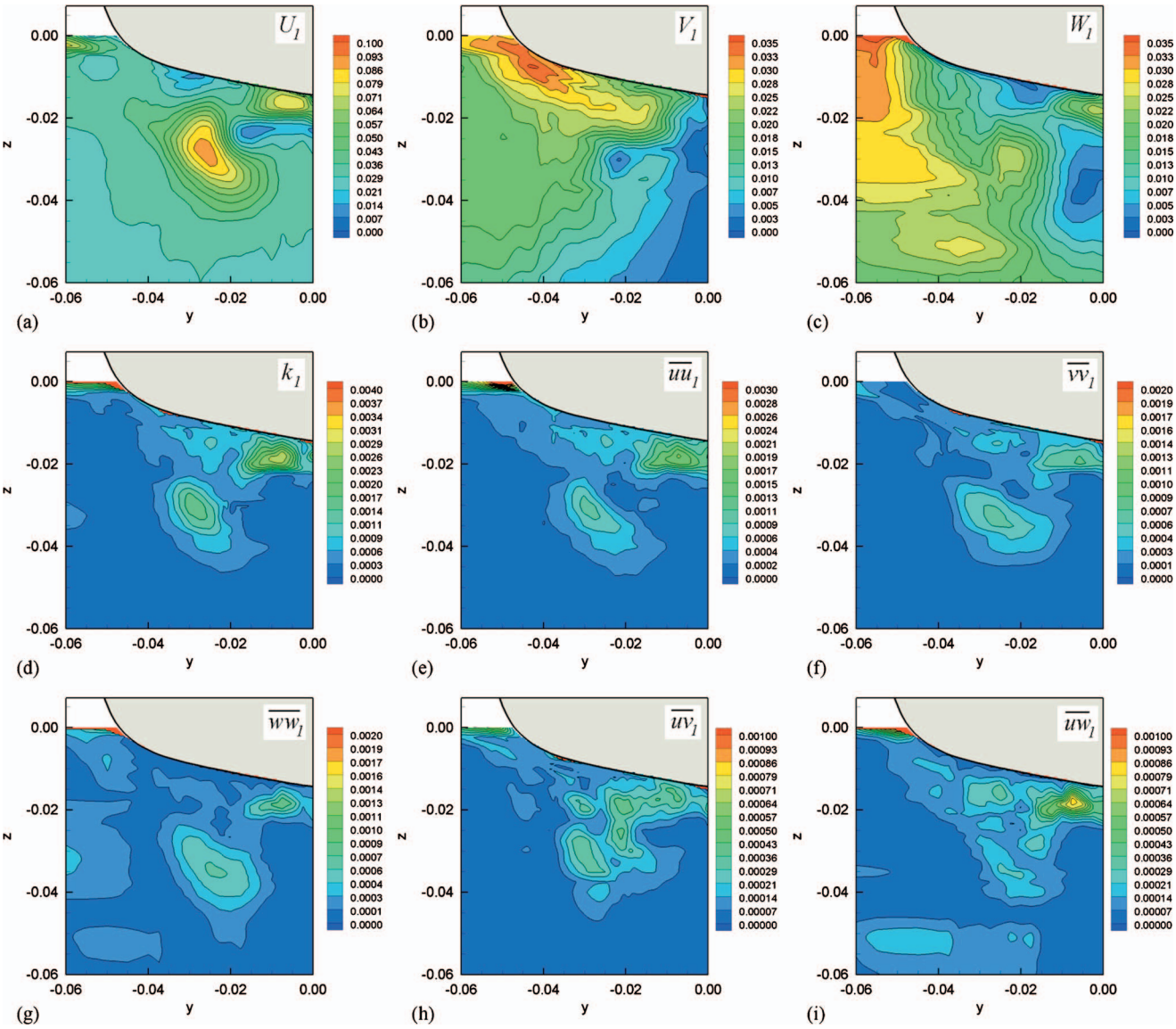

Fig. 8 First harmonic amplitude (nondimensional) for phase-averaged velocities and Reynolds stresses

is in phase with the wave.

The transverse first harmonic amplitude shows zero response under the hull near the center plane (by symmetry it should be identically zero on the center plane), small response in the outer region, and fairly large (similar order wave-induced velocities) at the hull shoulder near the free surface where a finger of large values is evident. The phase is $\pi/3$. Near the steady vortex center, the phase abruptly changes from π to $-\pi$, but the amplitudes are small. The V_1 response is explained by continuity with $\partial U/\partial x$ small and $\partial V/\partial y = -\partial W/\partial z$. As W increases positively, V moves away from the hull and center plane. Therefore, W and V must be somewhat in phase with each other (at least we know they would be exactly in phase with each other if the hull is infinitely long with parallel sides). In consideration of the ship coordinate system, we might expect $\pi/2$ phase for V since the phase for W is $-\pi/2$, i.e., equal magnitude but opposite sign. However, we observe $\pi/3$. The departure from $\pi/2$ may be due to the curvature of the hull, i.e., the three-dimensional effect of the hull.

Turbulent kinetic energy and Reynolds stresses first harmonic amplitudes are two/one orders-of-magnitude smaller than the $U/(V,W)$ velocities showing the largest values in the bulge and thin boundary layer regions. Although the Reynolds stresses amplitudes are less than their uncertainties their patterns are distinct and seemingly reasonable. The phase is mostly the same as for the regular head wave, except in the bulge region where it is π out of phase.

The second harmonic amplitudes are mostly an order-of-magnitude smaller than the first harmonic amplitudes showing the largest values in the bulge and thin boundary layer regions.

4.5.3 Fourier Series-Reconstructed Time Histories. Figure 10 shows reconstructed time histories of the axial velocity contours with cross plane vectors at $t/T = 0, \frac{1}{4}, \frac{1}{2}, \frac{3}{4}$ including a profile view (top row) of 5512 with superimposed wave profiles at the same t/T. The vectors include total FS reconstruction (middle row) and first harmonic (bottom row). The reference vectors are color-coded to the superimposed wave profiles. The contours and vectors support conclusions from the preceding section. The large increases (expansion) and decreases (contraction) in the boundary layer thickness are in phase with the regular head wave and wave-induced axial velocities. The regular head wave-induced vertical velocities are evident in the outer region and damped in the inner region and are $-\pi/2$ out of phase with the regular head wave. Large regular head wave-induced transverse velocities are dis-

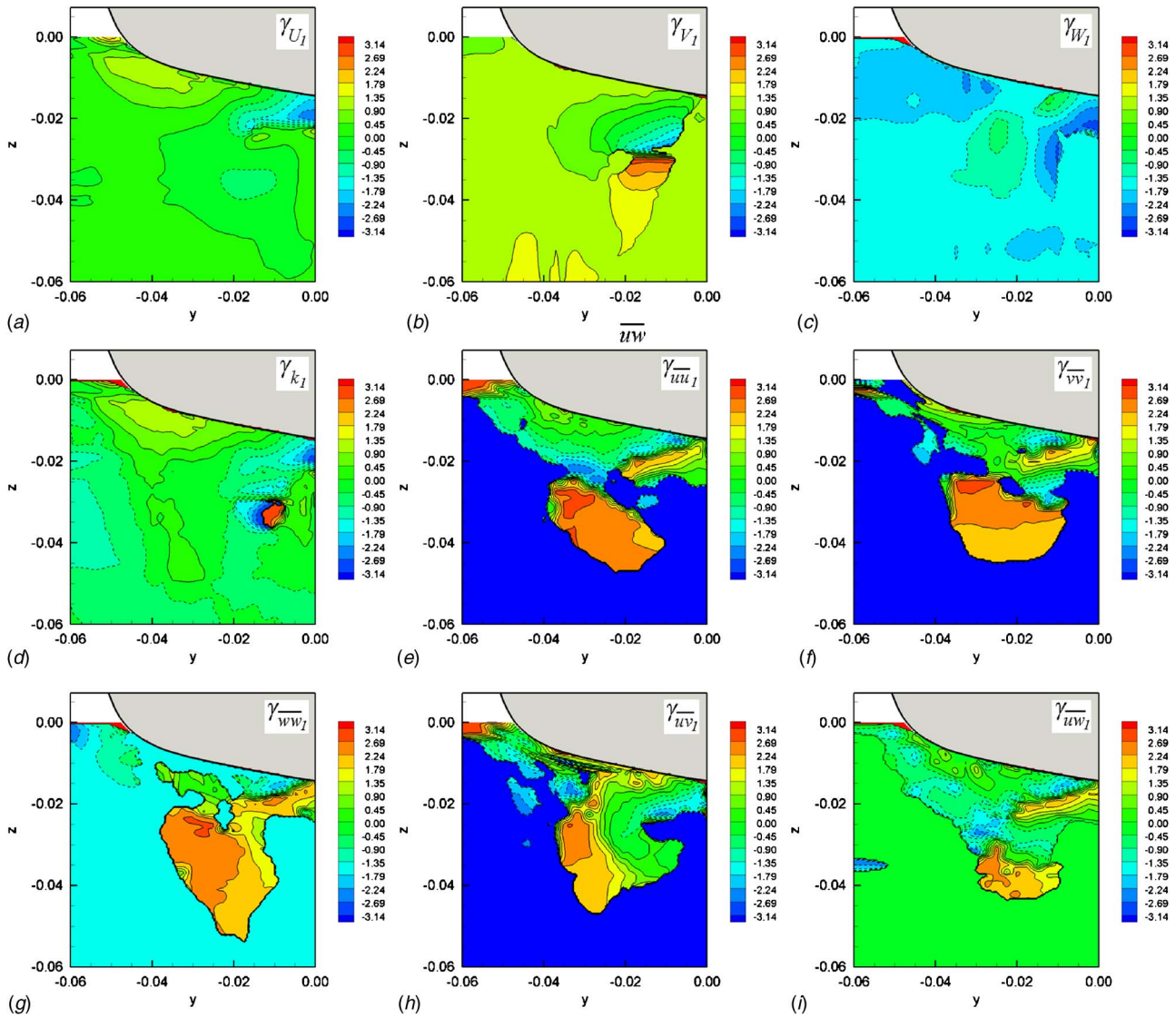

Fig. 9 First harmonic phase (radians) for phase-averaged velocities and Reynolds stresses

played at the hull shoulder and near free surface with a phase of $\pi/3$. Total FS reconstruction cross plane vectors are 45 deg to the hull and oscillating clockwise after a wave crest passes $x=0.935$ and then counterclockwise after a wave trough passes $x=0.935$. First harmonic vectors more clearly define the regular head wave-induced oscillations in V and W showing small values everywhere for a wave crest and trough at $x=0.935$, large downward flow toward the center plane for decreasing wave elevation at $x=0.935$, and large upward flow away from the center plane for increasing wave elevation at $x=0.935$.

5 Conclusions

The present results for phase-averaged organized oscillation velocities (U,V,W) and random fluctuation Reynolds stresses $(\overline{uu},\overline{vv},\overline{ww},\overline{uv},\overline{uw})$ for the nominal wake of a surface ship advancing in regular head waves, but restrained from body motions, are important in documenting the unsteady ship boundary layer response. In conjunction with previous studies in the same facility using the same ship model and conditions for regular head wave elevation and velocity, unsteady forces and moment, and phase-averaged wave field provide valuable benchmark data for validation of ship-hydrodynamics simulation methods. Innovative data acquisition, reduction, and uncertainty analysis procedures are developed for the phase-averaged PIV, as part of the project. Use of towed PIV and focus on phase-averaged variables and Fourier reconstructions including uncertainty assessment is unique.

Comparisons of steady-flow results with previous steady PIV and 5-hole pitot tube measurements for the same geometry and conditions including other facilities enable an overall assessment of the current ability to measure steady ship velocity fields. The steady nominal wake is explained by interactions between the hull boundary layer and sonar dome and after body shoulder outboard rotating axial vortices thinning and thickening the boundary layer inboard and outboard of the vortex center. The appearance is a mid-girth bulge in the axial velocity contours, cross plane vectors towards the hull, and maximum Reynolds stresses in the thin boundary layer and bulge regions. The unsteady nominal wake is explained by interactions between the hull boundary layer and axial vortices and regular head wave with three primary wave-induced effects: pressure gradients $4\%U_c$, orbital velocity transport $15\%U_c$, and unsteady sonar dome lifting wake. In the outer region, the uniform flow, incident wave velocities are recovered within the experimental uncertainties. In the inner, viscous-flow region, the boundary layer undergoes significant time-varying upward contraction and downward expansion in phase with incident wave crests and troughs, respectively. The difference between

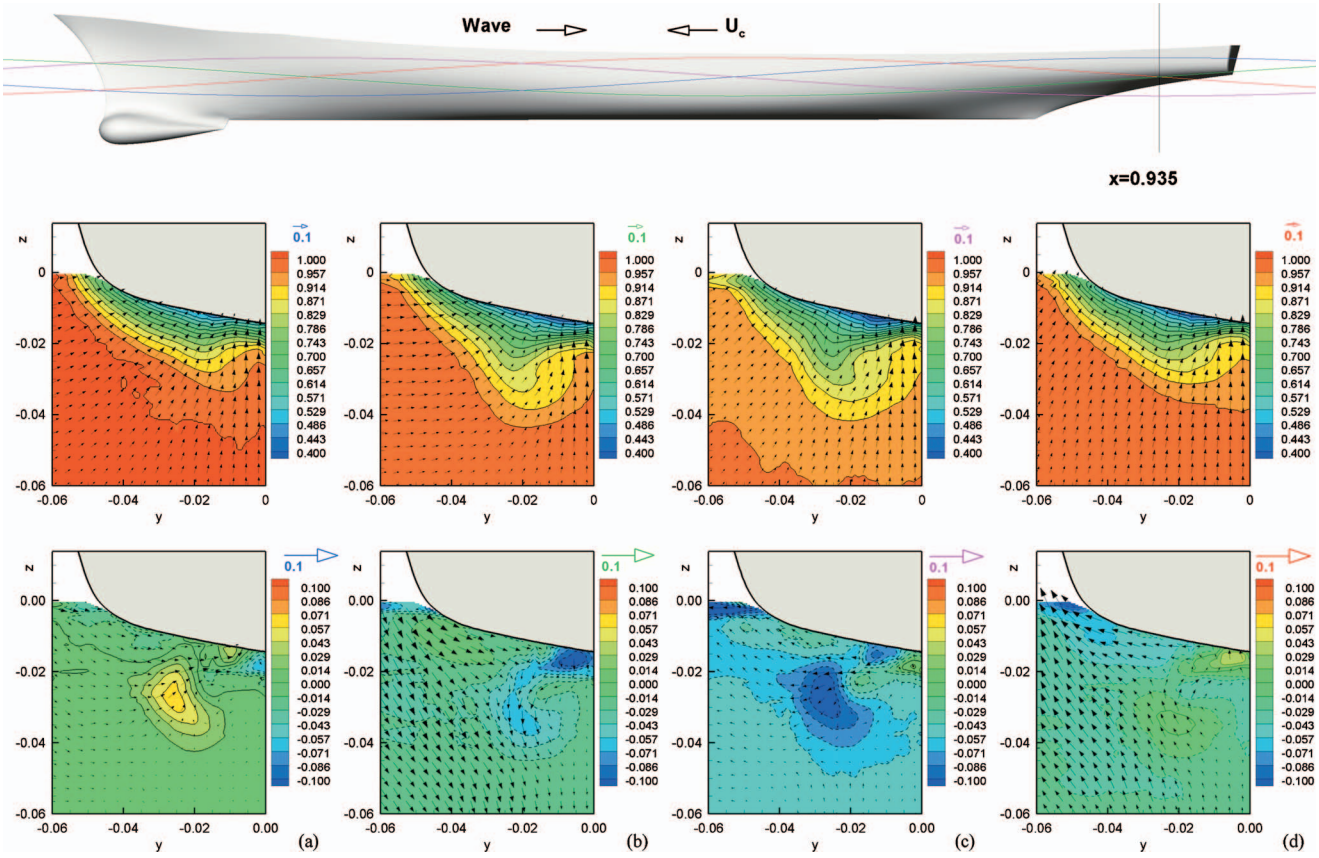

Fig. 10 FS reconstruction of unsteady nominal wake *U* contours and *VW* vectors at quarter periods for total magnitude (middle) and first harmonic (bottom): (*a*) *t*/*T*=0; (*b*) *t*/*T*=1/4; (*c*) *t*/*T*=1/2; (*d*) *t*/*T*=3/4. Reference vectors are color-coded to the regular head waves (top).

twice the zeroth harmonic and steady amplitudes is referred to as streaming and shows 5–20% and 70% maximum amplitudes for the velocities and Reynolds stresses, respectively. The overall effect is larger axial velocity in the bulge region, reduced axial vorticity with center shifted downwards and towards the center plane, and larger normal stresses and $\overline{uv}$ but smaller $\overline{uw}$ Reynolds stresses. The axial velocity first harmonic amplitude is large in the bulge region and small in the thin boundary layer region. The former is in phase and the latter π is out of phase with the incident wave. The vertical first harmonic amplitude is small except in the outer region indicating the hull and boundary layer has a damping effect on the wave-induced vertical velocities. The phase is the same as the incident wave vertical velocity, except near the center plane where it is π out of phase. The transverse first harmonic amplitude also is small except at the hull shoulder near the free surface where a finger of large values is evident with a phase of $\pi/3$. Reynolds stress amplitudes are an order-of-magnitude smaller than the velocities showing the largest values in the bulge and thin boundary layer regions with mostly the same phase as the incident wave.

The CFD Tokyo Workshop 2005 includes 5 test cases. The first is calm water bare hull resistance for the fixed condition for KCS (test case 1.1, 11 entries), 5415 (test case 1.2, 11 entries), and KVLCC2 (test case 1.4, 13 entries) and free to sink and trim condition for 5415 (test case 1.3, 1 entry). The second is calm water self-propelled condition for KCS (test case 2; 4 entries). The third is calm water static drift condition for KVLCC2 (test case 3; 16 entries). The fourth is the incident-wave, forward-speed diffraction condition for 5415 (test case 4; 4 entries) for which the present data are used. In addition, grid dependence is studied for the KVLCC2 (test case 5, 11 entries). The CFD codes are challenged by the free to sink and trim, self-propelled, and forward-speed diffraction conditions, as indicated by so few entries. Test case 4 does not make use of all the present data, but only includes comparisons for zeroth harmonic amplitude and first harmonic amplitude and phase, resistance and heave forces, pitch moment, and phase-averaged wave field and nominal wake velocities, and in the latter cases Fourier series reconstructions at quarter period time intervals. Even partial use of the present data proves useful in evaluating the capabilities of the CFD codes for unsteady flow. The agreement is in part impressive, but achieved collectively since some codes perform better/worse for different variables.

Future experiments of the present kind surely will be even more complex as CFD matures for more realistic and smaller scale simulations. For ship hydrodynamics, motions, maneuvering, and self-propelled trajectories are of interest, including global and local variables. Even with current advancements in stereo PIV measurement systems for both free surface and velocity fields, such experiments remain a formidably resourceful challenge. Adding to this challenge are the requirements for smaller and smaller scales demanding yet higher data rates and resolution.

Acknowledgment

This research is sponsored by the Office of Naval Research under Grants Nos. N00014-96-1-0018 under the administration of Dr. E.P. Rood and N00014-01-1-0073 under the administration of Dr. Pat Purtell whose support is greatly appreciated. Special thanks are extended to the University of Iowa mechanical engineering undergraduates Tanner Kuhl and Ben Orozco for their efforts in the data acquisition.

Nomenclature

$(c_k c_k)_i$ = instantaneous normal stress; $k=1$ (uu), $k=2$ (vv), $k=3$ (ww)
$(c_m c_n)_i$ = instantaneous shear stress; $m=1$, $n=2$ (uv), $m=1$, $n=3$ (uw)
$\overline{uv}$, $\overline{uw}$ = shear stresses
$\overline{uu}$, $\overline{vv}$, $\overline{ww}$ = normal stresses in the x,y,z coordinates, respectively
A = wave amplitude, m
$a_0,\ldots,a_n$ = least-squares regression coefficients
Ak = wave steepness
A_n = nth-order harmonic amplitude
AP = aft perpendicular
B = model beam, m
B_X = bias limit of variable X
C_B = block coefficient
C_H = heave coefficient
C_k = average PIV velocity component over $i=N_f$ samples; $k=1(U)$, $k=2(V)$, $k=3(W)$
$C_{k,i}$ = Instantaneous PIV velocity component; $k=1(U)$, $k=2(V)$, $k=3(W)$
C_M = pitch moment coefficient
C_T = total resistance coefficient
D = distance between an upstream wave gauge and PIV measurement area center, m
D_X = dynamic range of variable X
E = comparison error between data 1 (D_1) and data 2 (D_2)
f = wave frequency, Hz
f_e = encounter frequency, Hz
FP = forward perpendicular
Fr = Froude number
g = gravity constant, 9.8031 m/s^2
k = wave number, m^{-1}
L = model length, m
L_{img} = width or height of the image plane, pixel
L_{obj} = width or height of the object plane, m
n = Fourier series order
N_f = number of valid PIV samples after filtering from a population of N_r samples
N_r = number of PIV recordings
P_X = precision limit of variable X
S = model surface area, m^2
S_k = average particle displacement over $i=N_f$ samples, pixel
$S_{k,i}$ = instantaneous particle displacement, pixel
T = model draft, m; also encounter period, s
t = time, s
U,V,W = axial, transverse, vertical fluid velocities, respectively
U_c = carriage speed, m/s
U_X = uncertainty of variable X
X = any measured variable
x,y,z = axial, transverse, vertical coordinates, respectively
X_0 = zeroth harmonic amplitude of variable X
X_1 = first harmonic amplitude of variable X
X_2 = second harmonic amplitude of variable X
X_{cnv} = convergence of variable X
X_{FS} = FS reconstruction of the variable X
X_{LSR} = least-squares regression reconstruction of variable X
y^+ = inner wall variable
z_I = incident wave elevation, m
Δt = time between successive PIV frames, s
δ = boundary layer thickness
γ_i = phase angle of the ith PIV recording, radian
γ_n = nth order phase, radian
λ = wavelength, m
ω_x = axial vorticity
ζ_I = incident wave elevation

References

[1] Larsson, L., Stern, F., and Bertram, V., 2003, "Benchmarking of Computational Fluid Dynamics for Ship Flows: The Gothenburg 2000 Workshop," J. Ship Res., **47**(1), pp. 63–81.
[2] Hino, T., 2005, CFD Workshop Tokyo Workshop 2005, National Maritime Research Institute.
[3] Kim, W. J., Van, S. H., and Kim, D.-H., 2001, "Measurement of Flows Around Commercial Ship Models," Exp. Fluids, **31**(5), pp. 567–578.
[4] Lee, S.-J., Kim, H.-R., Kim, W.-J., and Van, S.-H., 2003, "Wind Tunnel Tests on Flow Characteristics of the KRISO 3,600 TEU Container Ship and 300K VLCC Double-Deck Ship Models," J. Ship Res., **47**(1), pp. 24–38.
[5] Longo, J., and Stern, F., 2005, "Uncertainty Assessment for Towing Tank Tests With Example for Surface Combatant DTMB Model 5415," J. Ship Res., **49**(1), pp. 55–68.
[6] Stern, F., Longo, J., Penna, R., Olivieri, A., Ratcliffe, T., and Coleman, H., 2000, "International Collaboration on Benchmark CFD Validation Data for Naval Surface Combatant," *Invited Paper Proceedings of the 23rd ONR Symposium on Naval Hydrodynamics*, Val de Reuil, France.
[7] Stern, F., Olivieri, A., Shao, J., Longo, J., and Ratcliffe, T., 2005, "Statistical Approach for Estimating Intervals of Certification or Biases of Facilities or Measurement Systems Including Uncertainties," J. Fluids Eng., **127**, pp. 604–610.
[8] Olivieri, A., Pistani, F., Avanzini, A., Stern, F., and Penna, R., 2001, "Towing Tank Experiments of Resistance, Sinkage and Trim, Boundary Layer, Wake, and Free Surface Flow Around a Naval Combatant INSEAN 2340 Model," IIHR Report No. 421, Iowa Institute of Hydraulic Research, University of Iowa, 56 pp.
[9] Gui, L., Longo, J., and Stern, F., 2001, "Towing Tank PIV Measurement System, Data and Uncertainty Assessment for DTMB Model 5512," Exp. Fluids, **31**, pp. 336–346.
[10] Ratcliffe, T. J., Mutnick, I., and Rice, J., 2001, "Stern Wave Topography and Longitudinal Wave Cuts Obtained on Model 5415, With and Without Propulsion," NSWCCD-50-TR-2000/028, Bethesda, Maryland.
[11] Olivieri, A., Pistani, F., Wilson, R., Benedetti, L., La Gala, F., Campana, E. F., and Stern, F., 2004, "Froude Number and Scale Effects and Froude Number 0.35 Wave Elevations and Mean-Velocity Measurements for Bow and Shoulder Wave Breaking of Surface Combatant DTMB 5415," IIHR Report No. 441, IIHR-Hydroscience and Engineering, University of Iowa, p. 62.
[12] Gui, L., Longo, L., Metcalf, B., Shao, J., and Stern, F., 2001, "Forces, Moment, and Wave Pattern for Surface Combatant in Regular Head Waves-Part 1: Measurement Systems and Uncertainty Assessment," Exp. Fluids, **31**, pp. 674–680.
[13] Gui, L., Longo, L., Metcalf, B., Shao, J., and Stern, F., 2002, "Forces, Moment, and Wave Pattern for Naval Combatant in Regular Head Waves-Part 2: Measurement Results and Discussions," Exp. Fluids, **32**, pp. 27–36.
[14] Felli, M., Di Felice, F., and Lugni, C., 2004, "Experimental Study of the Flow Field Around a Rolling Ship Model," Proceedings of the 25th ONR Symposium on Naval Hydrodynamics, St. John's, Newfoundland, Canada.
[15] Bishop, R., Atsavapranee, P., Percival, S., Shan, J., and Engle, A., 2004, "An Investigation of Viscous Roll Damping Through the Application of Particle-Image Velocimetry," Proceedings of the 25th ONR Symposium on Naval Hydrodynamics, St. John's, Newfoundland, Canada.
[16] Irvine, M., Longo, J., and Stern, F., 2004, "Towing-Tank Tests for Surface Combatant for Free Roll Decay and Coupled Pitch and Heave Motions," Proceedings of the 25th ONR Symposium on Naval Hydrodynamics, St. John's, Newfoundland, Canada.
[17] Longo, J., Gui, L., and Stern, F., 2004, "Ship Velocity Fields," *PIV and Water Waves, Advances in Coastal and Ocean Engineering*, World Scientific, Singapore.
[18] Fu, T. C., Atsavapranee, P., and Hess, D. E., 2002, "PIV Measurements of the Cross-Flow Wake of a Turning Submarine Model (ONR Body-1)," in Proceedings of the 25th ONR Symposium on Naval Hydrodynamics, Fukuoka, Japan, pp. 154–166.
[19] Dong, R. R., Katz, J., and Huang, T. T., 1997, "On the Structure of Bow Waves on a Ship Model," J. Phys. (Paris), Colloq., **346**, pp. 77–115.
[20] Roth, G. I., Mascenik, D. T., and Katz, J., 1999, "Measurements of the Flow Structure and Turbulence Within a Ship Bow Wave," Phys. Fluids, **11**, pp. 3512–3523.
[21] Di Felice, F., and De Gregorio, F., 2000, "Ship Model Wake Analysis by Means of PIV in Large Circulating Water Channel," in Proceedings of the 10th International Offshore and Polar Engineering Conference, Seattle, WA, pp. 392–397.
[22] Calcagno, G., Di Felice, F. D., Felli, M., and Pereira, F., 2002, "Propeller Wake Analysis Behind a Ship by Stereo PIV," in Proceedings of the 24th ONR Symposium on Naval Hydrodynamics, Fukuoka, Japan, pp. 112–127.
[23] Cotroni, A., Di Felice, F., Romano, G. P., and Elefante, M., 2000, "Investigation of the Near Wake of a Propeller Using Particle Image Velocimetry," Exp. Fluids, **29**, pp. S227–S236.

[24] Di Felice, F., Romano, G., and Elefante, M., 2000, "Propeller Wake Analysis by Means of PIV," in Proceedings of the 23rd ONR Symposium on Naval Hydrodynamics, Val de Reuil, France, pp. 493–510.
[25] Judge, C. Q., Oweis, G. F., Ceccio, S. L., Jessup, S. D., Chesnakas, C. J., and Fry, D. J., 2001, "PIV Measurements of a Tip Leakage Vortex," Proceedings of the 26th American Towing Tank Conference, Glen Cove, New York.
[26] Paik, B. G., Lee, C. M., and Lee, S. J., 2004, "PIV Analysis of Flow Around a Container Ship Model With a Rotating Propeller," Exp. Fluids, **36**, pp. 833–846.
[27] Lee, S. J., Paik, B. G., Yoon, J. H., and Lee, C. M., 2004, "Three-Component Velocity Field Measurements of Propeller Wake Using a Stereoscopic PIV Technique," Exp. Fluids, **27**, pp. 575–585.
[28] Lam, K. M., and Leung, M. Y. H., 2005, "Asymmetric Vortex Shedding Flow Past an Inclined Flat Plate at High Incidence," Eur. J. Mech. B/Fluids, **24**, pp. 33–48.
[29] Konstantinidis, E., Balabani, S., and Yianneskis, M., 2005, "Conditional Averaging of PIV Plane Wake Data Using a Cross-Correlation Approach," Exp. Fluids, **39**, pp. 38–47.
[30] Wernert, P., and Favier, D., 1999, "Considerations About the Phase Averaging Method With Application to ELDV and PIV Measurements Over Pitching Airfoils," Exp. Fluids, **27**, pp. 473–483.
[31] Uzol, O., Chow, Y.-C., Katz, J., and Meneveau, C., 2003, "Average Passage Flow Field and Deterministic Stresses in the Tip and Hub Regions of a Multistage Turbomachine," J. Turbomach., **125**, pp. 714–725.
[32] Sung, J., and Yoo, J. Y., 2001, "Three-Dimensional Phase Averaging of Time-Resolved PIV Measurement Data," Meas. Sci. Technol., **12**, pp. 655–662.
[33] Druault, P., Guibert, P., and Alizon, F., 2005, "Use of Proper Orthogonal Decomposition for Time Interpolation From PIV," Exp. Fluids, **39**, pp. 1009–1023.
[34] Longo, J., Shao, J., Irvine, M., Gui, L., and Stern, F., 2004b, "Phase-Averaged Towed PIV Measurements for Regular Head Waves in a Model Ship Towing Tank," *PIV and Water Waves, Advances in Coastal and Ocean Engineering*, World Scientific, Singapore.
[35] Rhee, S. H., and Stern, F., 2001, "Unsteady RANS Method for Surface Ship Boundary Layer and Wake and Wave Field," Int. J. Numer. Methods Fluids, **37**, pp. 445–478.
[36] Carrica, P., Wilson, R., and Stern, F., 2006, "Unsteady RANS Simulation of the Ship Forward-Speed Diffraction Problem," Comput. Fluids, **35**, pp. 545–570.
[37] Longo, J., Shao, J., Irvine, M., and Stern, F., 2005, "Phase-Averaged Nominal Wake for Surface Ship in Regular Head Waves," IIHR Report No. 447, IIHR-Hydroscience and Engineering, The University of Iowa, 68 pp.
[38] ITTC, 2002, "ITTC Recommended Procedures," 23rd International Towing Tank Conference, Venice, Italy.
[39] Longo, J., Shao, J., Irvine, M., Gui, L., and Stern, F., 2002, "Phase-Averaged Towed PIV Measurements for Regular Head Waves in a Model Ship Towing Tank," Proceedings of the PIV and Modeling Water Wave Phenomena, Cambridge, UK.
[40] Gui, L., Longo, J., and Stern, F., 2001, "Biases of PIV Measurement of Turbulent Flow and the Masked Correlation-Based Interrogation," Exp. Fluids, **30**, pp. 27–35.
[41] Longo, J., Shao, J., Irvine, M., Gui, L., and Stern, F., 2002, "Phase-Averaged PIV for Surface Combatant in Regular Head Waves," Proceedings of the 24th ONR Symposium on Naval Hydrodynamics, Fukuoka, Japan.
[42] Coleman, H. W., and Steele, G. W., 1999, *Experimentation and Uncertainty Analysis for Engineers*, 2nd ed., Wiley, 275 pp.
[43] Pauley, W. R., and Eaton, J. K., 1988, "Experimental Study of the Development of Longitudinal Vortex Pairs Embedded in a Turbulent Boundary Layer," AIAA J., **26**(7), pp. 816–823.
[44] Pauley, W. R., and Eaton, J. K., 1989, "Boundary Layer Turbulence Structure in the Presence of Embedded Streamwise Vortex Pairs," Proceedings of the Seventh Symposium on Turbulent Shear Flows, Stanford University, Stanford, CA.
[45] Longo, J., Rhee, S.-H., Kuhl, D., Metcalf, B., Rose, R., and Stern, F., 1998, "IIHR Towing-Tank Wave maker," Proceedings of the 25th ATTC, Iowa City, IA.

M. Boutazakhti[1]
e-mail: Mohamed.Boutazakhti@utoronto.ca

P. E. Sullivan

M. J. Thomson

Mechanical and Industrial Engineering,
University of Toronto,
Toronto, Canada

I. Yimer
Institute for Aerospace Research,
National Research Council,
Canada

Flow Downstream of a Cluster of Nine Jets

This work is an experimental investigation of the flow downstream of a low emission nozzle. The nozzle is a 3×3 square matrix of nine small swirling air jets, has a design swirl number of 0.8, and operates at a Reynolds number of 40,000. Particle image velocimetry (PIV) was used to map the velocity field under nonburning and atmospheric conditions for the first 18 jet diameters downstream of the nozzle exit plane. Seeding was liquid injected into the air stream and drops were sized to filter out those larger than 3×3 pixels. The results showed that the cluster blends into a single jet-like flow 12 jet diameters downstream with the axial component of the velocity displaying self-similar properties. Lateral jet interaction slows the decay of the axial component of the velocity and jet expansion in the developed region while accelerating the decay of the radial component. [DOI: 10.1115/1.2720451]

1 Introduction

The key to reducing combustion nitrogen oxides (NO_x) and carbon monoxide (CO) emissions is fast and thorough mixing of fuel and air. Multipoint lean direct injection (LDI) nozzles improve mixing and atomization by injecting fuel in small amounts through multiple injection ports, where each nozzle contains dozens of small swirling jets. This paper examines the flow downstream of a matrix of nine small swirling air jets. Combustion studies reported in the literature show multipoint lean direct injection (LDI) nozzles have lower emissions compared to ordinary nozzles [1,2]. To date, there have been no detailed investigations of the nozzle flow or the effect of lateral jet interaction. A detailed understanding of the flow is necessary to understand the role of chemistry, mixing, and atomization to emission performance and to model these nozzles. While there are many previous studies of clusters of jets reported in the literature [3–7], their results cannot be extrapolated to the flow configuration examined here as the jets are nonswirling and the arrangements are cluster specific.

Axisymmetric turbulent free jets have been widely studied. The extent of the potential core in these flows depends on the jet exit conditions. When the boundary layer upstream of the jet exit plane is thin, the core region can be substantial, whereas when the flow is turbulent upstream of the injection point the potential core shrinks considerably. The core region can be as short as $x_{3c}/D=7$, or extend beyond $x_{3c}/D=200$; where x_{3c} is the position downstream measured from the exit plane and D is the round jet diameter [8].

The growth rate of jets with differing initial conditions is not constant which is inconsistent with the assumption of asymptotic independence. It was found that by including a finite mass source and a new length scale L, the jet width δ scales as $\delta \sim x_3(x_3/L)^n$, where x_3 is the position downstream of the exit of the jet and the exponent, n, is an arbitrary constant [9]. Although these previous results were derived for nonswirling round jets, the literature shows that some of the conclusions are applicable to swirling jets as well [10–12]. The azimuthal velocity component in a swirling jet introduces a radial pressure gradient that affects the development of the shear layer, weakens the organized structures, and favors the growth of random turbulence enhancing spreading, mass entrainment, and shear layer growth rates for swirling jets compared to nonswirling ones [13].

Swirling free jets experience a sudden expansion just after the exit and the rate of initial expansion is proportional to the degree of swirl. The centerline velocity decays exponentially as, x_3^{-n}, where the exponent depends on swirl and decreases with increasing swirl intensity [10]. Axial velocity profiles of jets with swirl intensity as high as $S_N=0.68$ reached a self-preserving regime similar to nonswirling jets [12].

Multiple jet flows are widely used in combustion systems to enhance fuel atomization and mixing. Studies show that far from the jet exit plane, the flow from a cluster of round non-swirling jets has velocity profiles similar to those of a single jet issuing from a single source [3–7].

For nonswirling jet clusters, as the jets merge laterally, the peak velocity at the outer jets shifts towards the central jet axis. After merging, the velocity profiles have a single jet-like shape. Computational investigations of nonswirling jet clusters using the k-ϵ turbulence model predict a single jet-like shape of the merged flow profile but fail to correctly predict the curvature, because of the inability of the standard k-ϵ model to predict flows with strong streamline curvature [7]. The merged single jet-like flow, resulting from a cluster of nonswirling jets, reaches a spreading rate similar to the single jet, after a negligible spreading rate in the merger region [4,6]. Far downstream, the merged flow displays self-similar behavior with a slightly slower spreading rate compared to a single jet [5].

There are no studies of clusters of swirling jets reported in the literature. This work studies the flow downstream of a 3×3 square matrix of nine small swirling air jets (Fig. 1) with a design swirl number of 0.8 and a Reynolds number of 40,000 based on the air pressure drop across the nozzle and the swirl cup diameter. Particle image velocimetry (PIV) measurements were conducted under nonburning conditions at atmospheric temperature and pressure to map the velocity field. The study covered the first 21 jet diameters downstream of the cluster exit plane.

The objectives of this study were:

1. Characterize the velocity profile; and
2. Investigate the effect of lateral jet interaction on the flow field.

Because of the small size of the nozzle, seeding the airflow with solid particles for the PIV experiments was impossible. Instead, liquid was injected into the air stream and a particle sizing MATLAB routine was developed to identify liquid drop size and filter those larger than 3×3 pixels for fluid phase velocity measurements.

[1]Corresponding author. Presently at: Techint Goodfellow Technologies Inc.

Contributed by the Fluids Engineering Division of ASME for publication in the JOURNAL OF FLUIDS ENGINEERING. Manuscript received April 5, 2005; final manuscript received October 3, 2006. Assoc. Editor: Theodore Heindel.

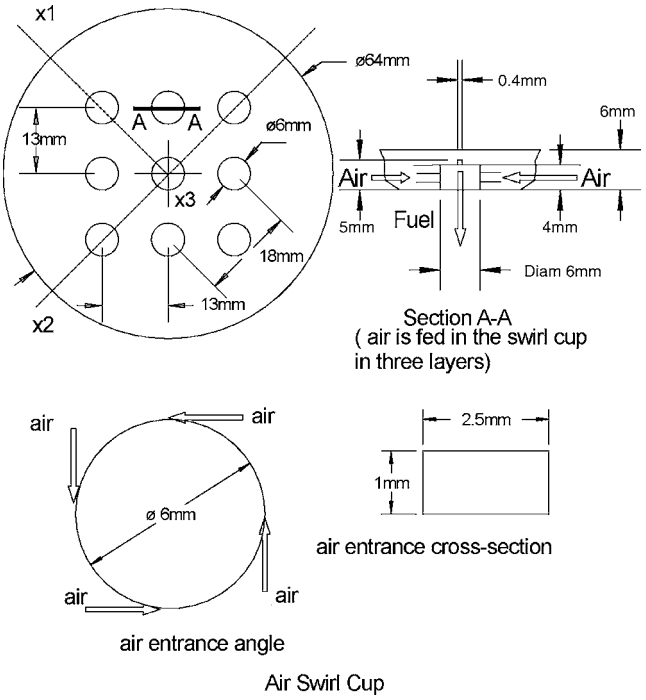

Fig. 1 Macrolamination nozzle

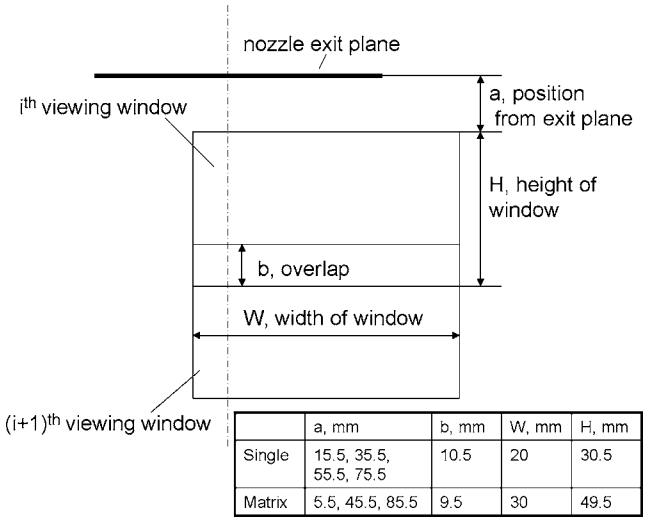

	a, mm	b, mm	W, mm	H, mm
Single	15.5, 35.5, 55.5, 75.5	10.5	20	30.5
Matrix	5.5, 45.5, 85.5	9.5	30	49.5

Fig. 2 PIV viewing widows

2 Experimental Setup

The nine swirling jets matrix flow was produced using a macrolamination Parker Hannifin nozzle (Fig. 1) operated at 13 g/s of air. To evaluate the effect of adjacent jets interaction on the flow field, measurements were made for a single jet (operated at one ninth of the previous flow rate) and the full matrix of nine jets.

The nozzle was mounted in an enclosed vertical booth. The measurements were done using a LaVision Particle Image Velocimetry (PIV) system. MIL-PRF-7024 type II (nozzle calibrating fluid) was injected between 0.11 and 0.32 g/s into the air hose 1 m upstream of the nozzle inlet plane for seeding. A particle sizing MATLAB algorithm was used to preprocess the PIV images and remove large liquid droplets retaining droplets smaller than 3×3 pixels and using them to measure the gas phase velocity.

2.1 Nozzle and Vertical Test Booth. The nozzle had nine air blast fuel injectors (Fig. 1) made from a series of flat metallic sheets diffusion bonded together. The air and fuel channels were chemically etched into the metal. For each jet, the air issues into a 4 mm deep, 6 mm diameter recess acting as a radial air swirl cup. Air exhausts into three swirling layers through four 1 mm $\times$2.5 mm rectangular ports in each layer. All the air jets swirl in the same direction with a design air swirl number value is $S_N=0.8$.

The nozzle was mounted in a vertical test booth 375 mm wide with an octagonal cross section. The nozzle could be positioned in the horizontal x_1 and x_2 directions as well as the vertical direction x_3 (Fig. 1). The enclosure had a rectangular Plexiglas 80 $\times$100 mm viewing window for optical access. Parker Hannifin Ball screw systems and Compumotor step motors with a repeatability within 0.025 mm were used for motion in the x_1, x_2, and x_3 directions. The overall repeatability of the translation including the railings and frame was estimated to be 0.1 mm and the system was computer controlled. The booth enclosure was operated at atmospheric temperature and pressure.

2.2 Particle Image Velocimetry (PIV) Setup. A LaVision PIV was used with a 120 mJ, 16 Hz dual cavity New wave, Gemini PIV 15 Nd:YAG laser operated at 532 nm wavelength. The power supply and the laser rods are water cooled. The camera was a 1280×1024 pixel FlowMaster3S (PCO Sensicam, VGA) CCD camera operated in double-frame, single exposure mode and the images were processed with a cross-correlation algorithm. After the first laser flash, the CCD camera transfers the first image to the frame buffer (on-chip storage zone). While the first frame is read out, the CCD records the second frame and remains sensitive during the time required to transfer the first frame from the frame buffer. The readout time determines the exposure time for the second frame, 125 ms for the FlowMaster3S camera. The exposure time for the first frame is factory set to 10 μs. The time interval Δt between two successive laser pulses was 6 μs.

Adaptive multipass PIV with decreasingly smaller size interrogation area was used where the initial interrogation window sizes was 128×128 pixels and the final interrogation window size was 64×64 pixels. The final size was the smallest possible for the seeding density used. The cross-correlation algorithm operated with an overlap of 25% to increase the final output vector map density. A three point Gaussian correlation peak fit was used to evaluate the displacement with subpixel accuracy. Two independent Gaussian distributions were fitted to the correlation peak in the x_1 and x_3 directions; the accuracy was 0.1 pixel [14].

Figure 2 is the position and size of the viewing windows used to capture the PIV images. A specific viewing window pattern was used for each of the flow configurations (single and matrix) and the details of these windows are given in the table accompanying Fig. 2. A larger field of view imposing a lower spatial resolution was used for the full matrix case to cover the central jet as well as the corner jet. The nine jet matrix flow was probed from $x_3/D\sim2$ to 20 with a spatial resolution $\Delta x=2.3$ mm. The viewing windows contained the axis of the central jet. For the single jet, the flow field was mapped from $x_3/D\sim3$ to 17.6 with a spatial resolution $\Delta x=1.4$ mm.

3 PIV Image Preprocessing

Prior to cross correlating the raw images, the PIV images were preprocessed to filter out large drops. The algorithm allowed digital sizing of the images of the drops, the construction of filters for small and large drops, and the filtering of the original raw images to extract the images containing only small drops.

Figure 3(*a*) is an enlarged view of a raw PIV image with a wide range of droplet sizes. Figures 3(*b*) and 3(*c*) are the resulting large and small droplet images, respectively, obtained using a cut-off drop size of 3×3 pixel.

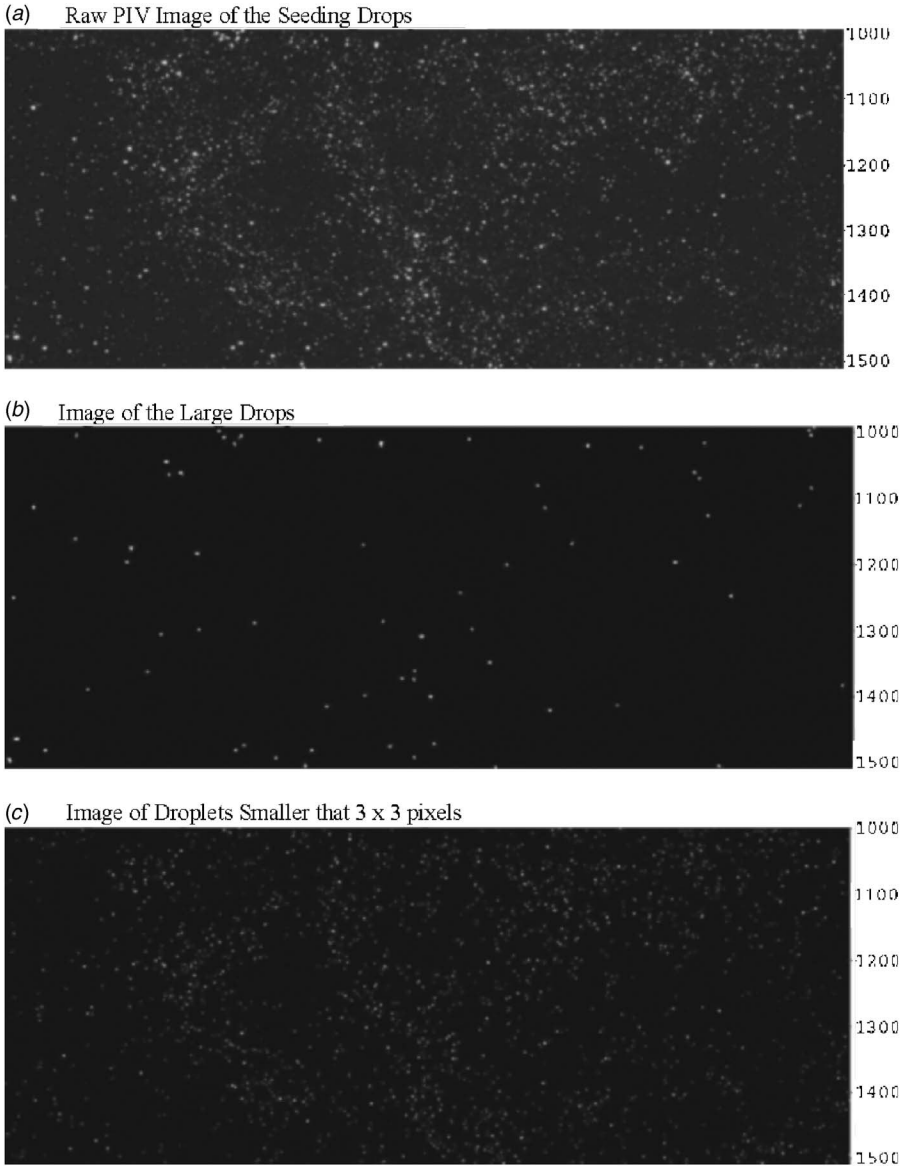

Fig. 3 PIV images of the seeding drops

The procedure followed and detailed in the flowchart in Fig. 4 was

1. Binary conversion;
2. Droplet identification;
3. Filtering out of large droplets; and
4. Computation of separate images of large and small drops.

To assist in droplet identification, all pixels whose intensity was smaller than a predefined threshold were set to zero. Pixels with intensities larger than the threshold are set to 1. The camera has a 10 bit dynamic range with a background noise level at 30 counts and because of this a fixed threshold of 40 counts was used to preprocess the images.

The droplet identification function uses a connectivity parameter that requires either two pixels to share an edge or a corner to be considered connected. The second connectivity parameter is more conservative when the aim is to leave out large droplets and was used in this work.

The properties of the identified droplets were evaluated. Due to diffraction a straightforward conversion of a droplet pixel size into the actual physical size for droplets smaller than 20 μm was not possible. Particle size in the intensity matrix used for cross-correlation and its impact is discussed in detail in the literature [14]. The correlation matrix is based on the local intensity and using particle sizes smaller than 3×3 pixels results in poor dynamic and spatial resolutions and is at its worse for particle sizes below 1 pixel scale. Above 3×3 pixels, the correlation is no better; the 3×3 pixels size is an ideal balance to address these considerations. All droplets with a bounding box larger than 3×3 were defined as large. A filter set to 0 at the location of the large droplets was computed and applied to the original image to remove large particles. A similar filtering process was used to identify small droplets.

4 Experimental Setup Assessment

The number of the PIV realizations used to compute the velocity field was determined by storage limitations. Experimental checks were performed to confirm the accuracy of the mean velocity components and the statistical accuracy of the measurements. The axial component of the velocity was compared against

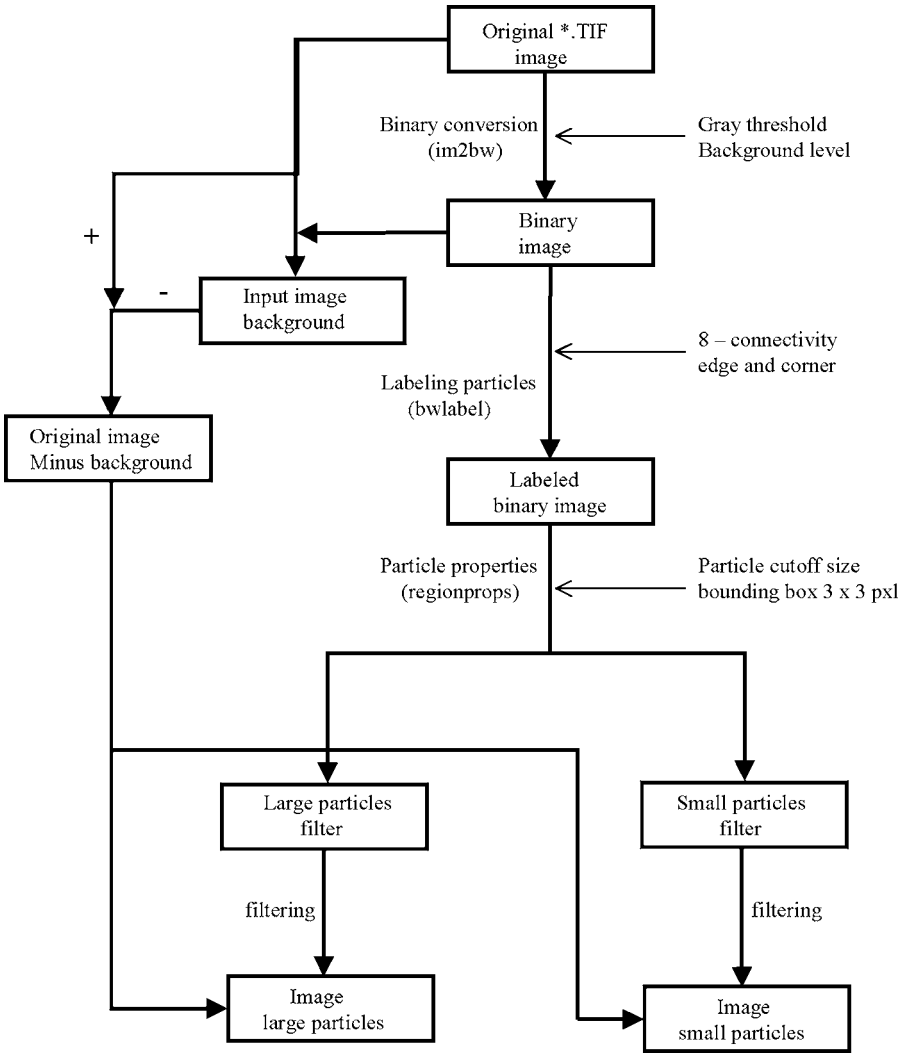

Fig. 4 Image preprocessing algorithm diagram

an independent measurement of the axial component of the velocity obtained using phase Doppler particle anemometry for droplets smaller than 5 μm.

For U_3, the convergence coefficient calculated using i PIV realizations is

$$C^i_{U_3} = 100\frac{U_3^{i+1} - U_3^i}{U_3^i} \tag{1}$$

where U_3^i ($i=1-N$, where N is the total number of PIV realizations) is the velocity average calculated using the first i realizations of the instantaneous velocity.

For both the radial and axial velocity, the maximum value of $C^N_{U_i}$ was 5%. For the mean of the axial component, the maximum value for the convergence coefficient was $C^N_{U_3}=1\%$. Figure 5 is a sample convergence curve for the mean axial velocity U_3. The total number of PIV realizations was $N=1170$. The x axis represents the number of samples i ($1<i<1170$) used to compute U_3. The y axis is the associated convergence coefficient, $C^i_{U_3}$, calculated using i samples. Figure 6 is the statistical accuracy across the matrix diagonal at different positions downstream for the axial average component and is of the order of $\sim$1% at the center and increases in the outer region to 4%. Figure 7 compares the axial velocity measured with PIV and phase Doppler particle anemometry (PDPA) using 5 μm calibrating fluid drops for the downstream position $x_3/D=3$ with an agreement within $\sim$2% and the error on the mean axial velocity is smaller than 5%.

5 Results and Discussion

5.1 Centerline Axial Velocity Decay. A logarithmic profile of the centerline axial velocity component U_3 for the nine jets configuration is shown in Fig. 8. The horizontal axis is x_3/D from 3 to 21. The vertical axis is the centerline axial velocity for the central jet. There are two regions where the decay is linear:

1. The merger region from $x_3/D=5$ to 10; and
2. The developed region from $x_3/D=12$ to 21.

For each of these regions, the axial centerline velocity is [9]

$$U_{3,\max} \sim \left(\frac{x_3}{D}\right)^{-m} \tag{2}$$

where m is the slope of the profile; $m_{m1}=0.19$ and $m_{m2}=0.46$ for the merger and the developed region, respectively. The centerline velocity decay rate is slower in the merger region than in the developed region. In the merger region, the central jet entrains high momentum air from the adjacent jets. As the lateral jets merge, more air from the surroundings is entrained and the central jet axial velocity decay rate increases consequently. The normalized lateral length scale $\delta/D \sim (x_3/D)^m$ measures jet expansion

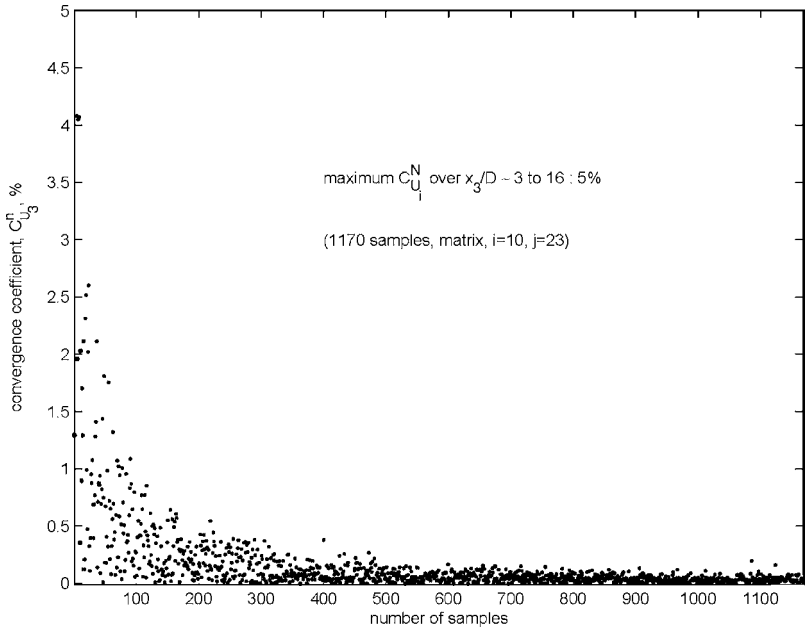

Fig. 5 Sample convergence curve for average velocity

[9]. The surrounding eight jets from which the central jet entrains in the merging region, $x_3/D=5-10$, confines jet expansion in that region to less than $1.5D$.

While the axial velocity profile of the central jet in the matrix has a maximum at the center, the single jet axial velocity has a local minimum and maximum is off the jet axis; a common feature of swirling jets (presented later in Figs. 12 and 13). The logarithmic centerline axial velocity decay for the single jet is shown in Fig. 9. As seen with the nine jets, the logarithmic profile has two linear regions. After an initial slow linear decay rate, the centerline axial velocity decay increases past $x_3/D=8$. In the slow decay region, the effect of the quiescent air entrainment on the axial velocity is mostly absorbed by the fast decay of the velocity maximum (at $x_r=7$ mm from the centerline) and is not seen along the centerline. Downstream of $x_3/D=8$, the centerline decay rate is faster as the decay rate of the maximum decreases and the effect of entrainment reaches the centerline. The values of m (Eq. (2)) for the single jet are $m_{s1}=0.14$ and $m_{s2}=0.69$ for the slow and fast decay regions, respectively. The initial decay rate is slow and

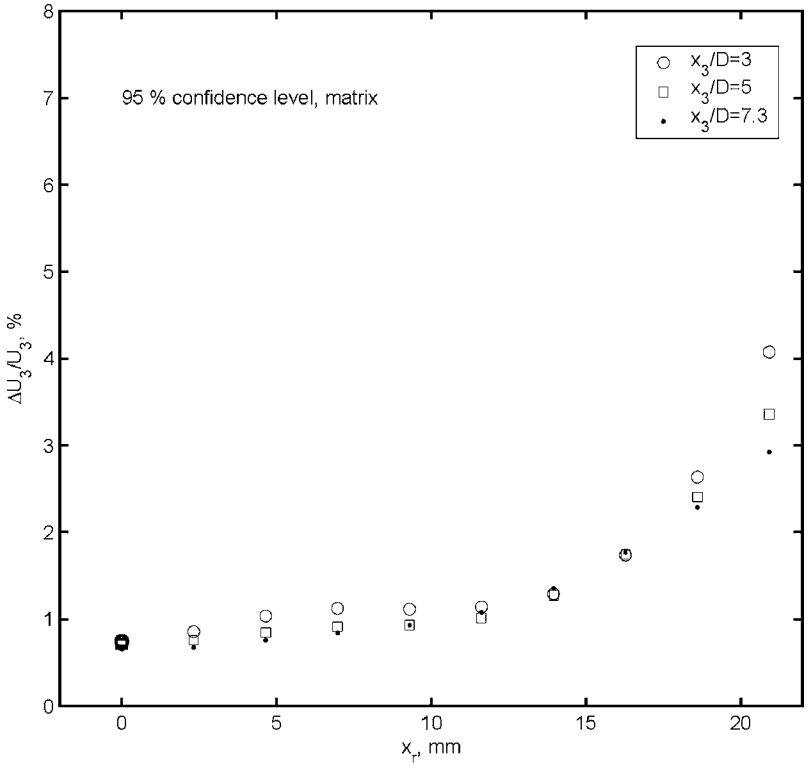

Fig. 6 Statistical accuracy, axial velocity

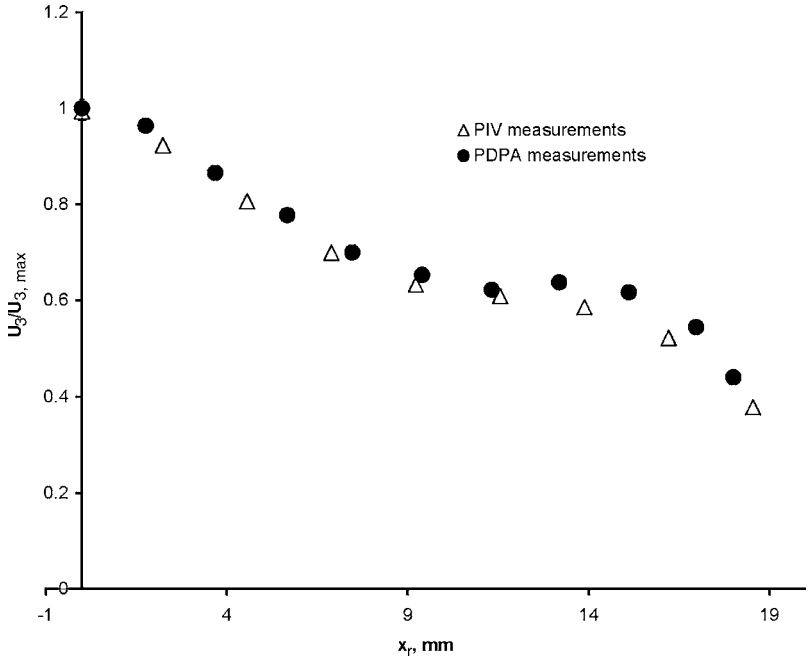

Fig. 7 Comparison of PIV and PDPA Measurements, $x_3/D=3$

similar to the rate for the nine jets. The expansion is limited to less than $1.5D$ within the first 8 diameters downstream. In the downstream region, the expansion is faster and the lateral size of the jet is almost double the jet size for the nine jets. The values of the coefficients m for the single jet and the matrix are summarized in Table 1.

Lateral jet interaction slows the spreading rate of the jet in the developed region due to the entrainment of higher momentum air from the surrounding jets. Within the first 20 diameters downstream both flows have two expansion rates. The difference between the two stages is due to jet-jet interaction for the nine jets flow and to swirl for the single jet. Similar results are reported in the literature. It was found that the spreading rate of cluster jets is smaller than a single jet in the first 20 diameters downstream [4]. The investigation of the interaction between two jets with variable spacing showed a slower spreading rate for the combined jet [5].

5.2 Mean Velocity Field. The profiles of the axial velocity for the matrix at different x_3/D positions downstream in the merger region ($x_3/D<10.5$) are shown in Fig. 10. The axial velocity is normalized with the corresponding maximum axial velocity $U_{3,\max}$ for each downstream position x_3/D. The horizontal axis is the position along the diagonal. The central and the corner jet axis are situated at $x_r=0$ and 18 mm, respectively. The profiles at $x_3/D=3$ and 5 display, in addition to a maximum at $x_r=0$ corresponding to the central jet, a local maximum between $x_r=14$ and

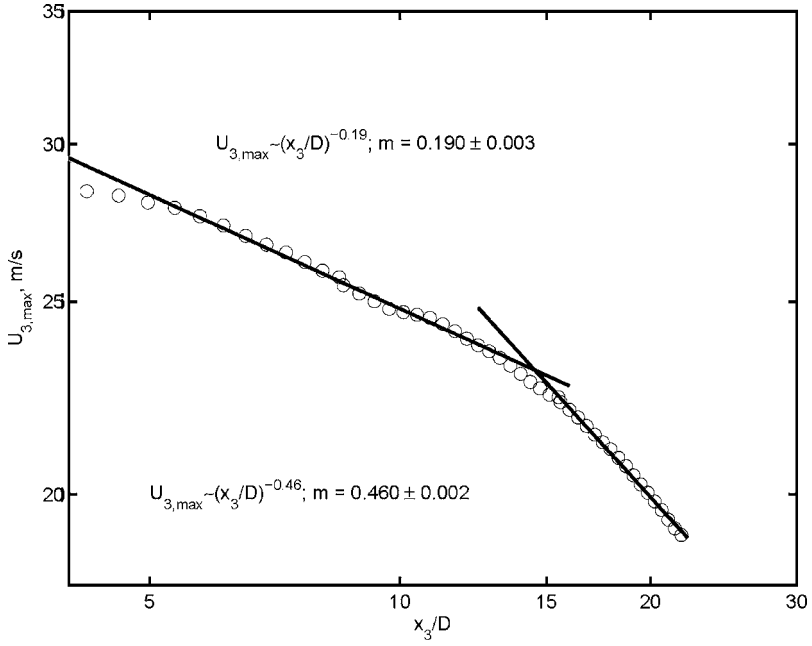

Fig. 8 Exponential decay of centerline axial velocity for the cluster

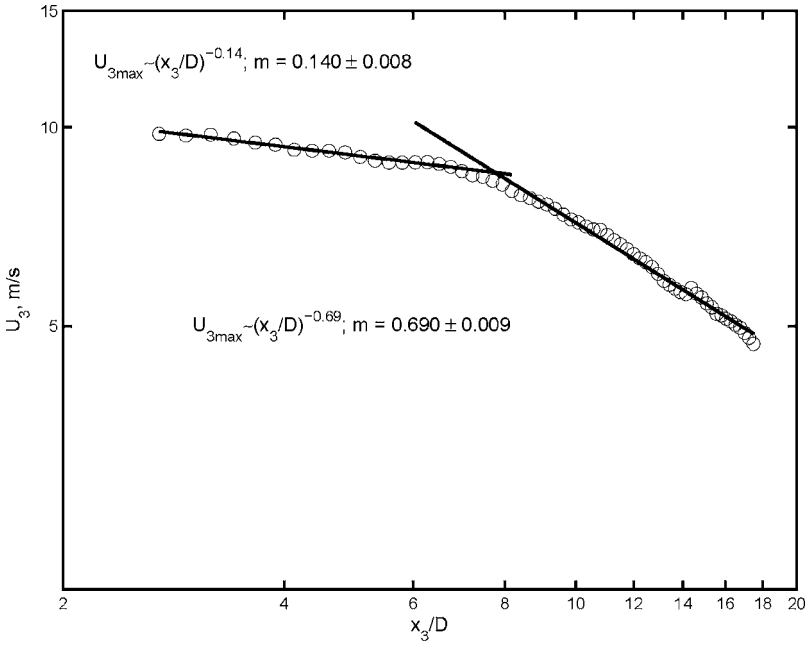

Fig. 9 Exponential decay of centerline axial velocity for the single jet

12 mm. The local maximum corresponds to the corner jet exiting at the radial position $x_r=18$ mm. The outer jets are entrained into the central jet moving the local maximum towards the nozzle centerline as the flow moves downstream. The axial velocity slowly decreases in the immediate vicinity of the two maximums while for most of the region between the two maximums it increases as the flow moves downstream into the merger region because high momentum air from the corner jet is entrained into the central region. Similar results for clusters of nonswirling air jets where the location of the local maximum moves towards the center of the main flow as the jets move downstream were reported in the literature [4,5,7].

Table 1 Values of m ($\delta \sim x_3^m$)

Region	x_3/D	m
Merger, matrix	5–10	0.19
Slow expansion, single jet	3–8	0.14
Developed, matrix	12–21	0.46
Fast expansion, single jet	8–17	0.69

The profiles broaden as the central velocity decreases and the velocity at the tails increases as more surrounding air is entrained. In the developed region ($10.5<x_3/D<21.4$), the axial velocity profiles resemble those of a single nonswirling round jet similar to the observations cited in the literature for clusters of nonswirling jets [4,5]. Figure 11 is the profile of the normalized axial velocity. The normalized radial position x_r/δ is plotted versus the normalized velocity $U_3/U_{3,\max}$. $\delta=x_3^m$ was used for scaling. The normalized profiles collapse onto a single curve within the region corre-

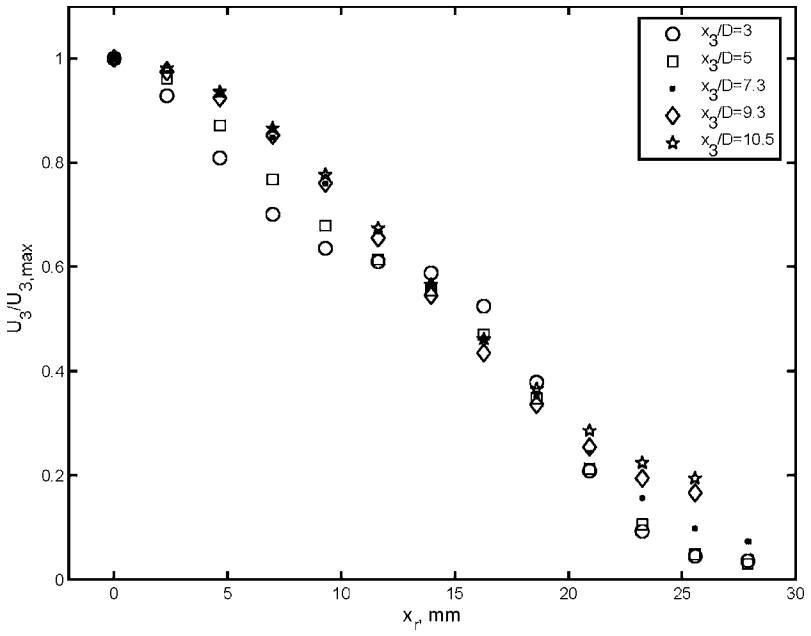

Fig. 10 Axial velocity profiles in the merging region of the cluster

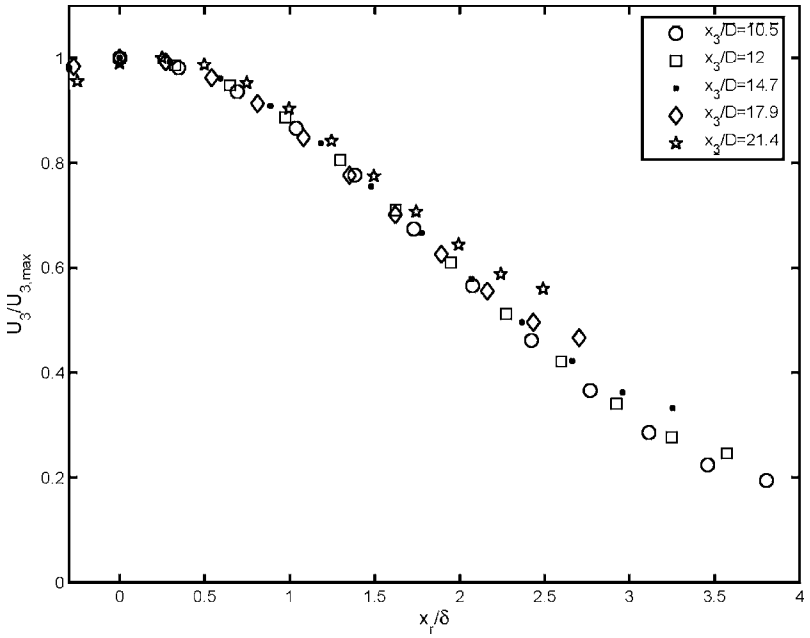

Fig. 11 Cluster self-preserving profiles in the developed region

sponding to $x_r=0-18$ mm, with a slight divergence at the ends. The self-preserving behavior is similar to the results reported in the literature for twin nonswirling jets [5].

Figures 12 and 13 are the axial velocity profiles for a single jet in the slow and fast expansion regions, respectively. Unlike the profiles of the central jet in the matrix, the axial velocity profiles over the entire downstream distance examined ($x_3/D=3.7-16.8$) have a local minimum at the centerline. The profiles were normalized with the corresponding values of the velocity at the centerline $U_{3,\text{cent}}$ for each x_3/D position. The minimum at the centerline decreases from $x_3/D=3.7$ to 16.8; the decrease is initially slow while the maximum, located at approximately the same position $x_r=8$ mm through the first phase, and drops off quickly. In the fast expansion region, the local minimum decay accelerates and the maximum decreases continuously while shifting to increasing values x_r as the flow moves downstream. At $x_3/D=16.8$, the local centerline minimum is still apparent in the profile.

The radial velocity profiles for the matrix are shown in Fig. 14. The profiles are from $x_3/D=2.3$ to 3.4. For positions further downstream, the radial velocity is less than the displacement measurement limit (0.1 pixel, corresponding to 0.5 m/s). The region between $x_r=0$ and $x_r=18$ mm has flow from the central jet directed in the positive direction of x_r and from the corner jet di-

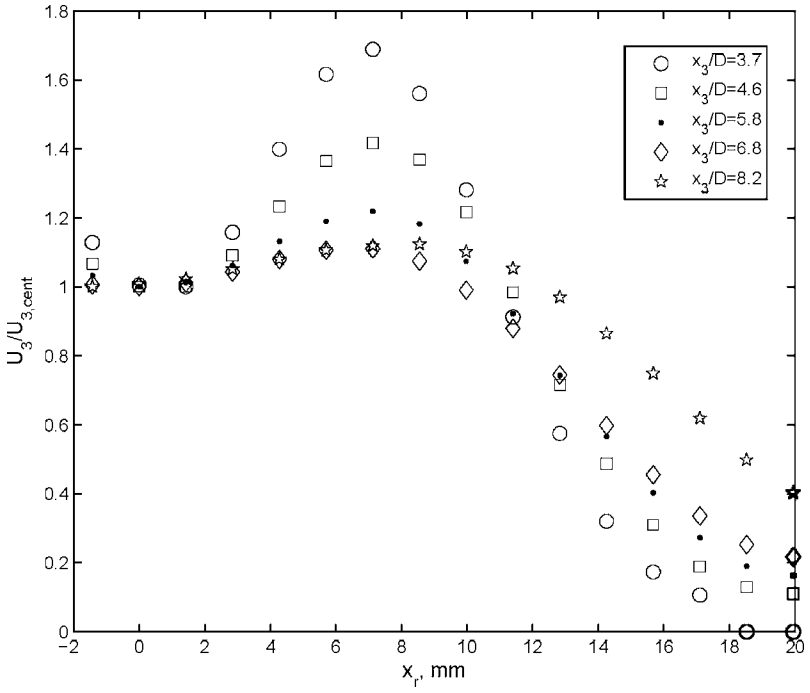

Fig. 12 Single jet axial velocity in the near field

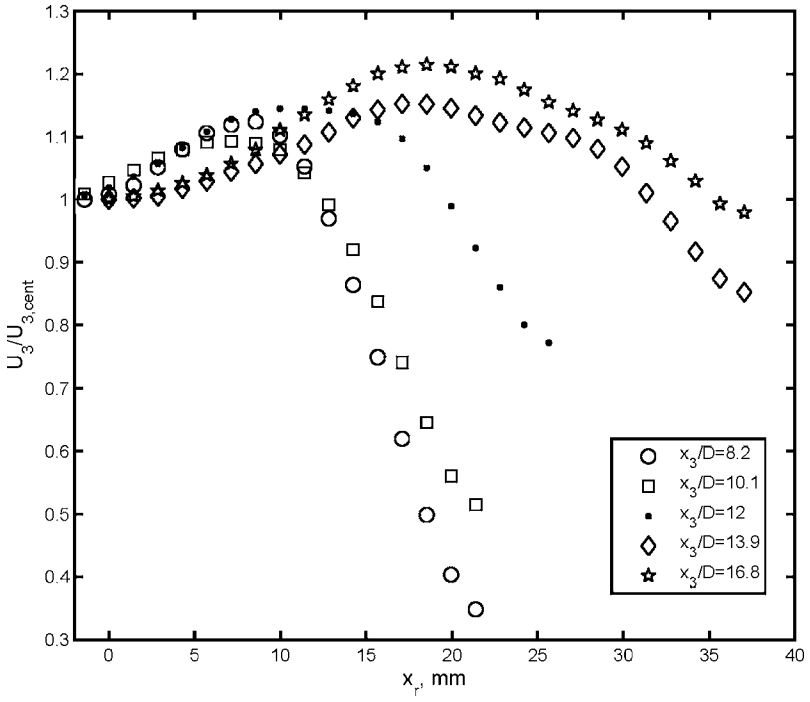

Fig. 13 Single jet axial velocity in the far field

rected in the negative direction of x_r.

The radial profiles display three distinct parts: a region corresponding to the central jet expansion (x_r=0–9 mm), a region corresponding to the outward expansion of the corner jet (x_r =18 mm and larger), and the region $9<x_r<18$ with negative radial velocity (first profile in Fig. 14). The negative radial velocity slowly decreases as the central jet expands. Figure 14 shows that by x_3/D=2.7 the radial velocity of the air issuing from the corner jet and directed towards the centerline is overcome by the expanding central jet and is practically zero.

6 Conclusion

Aside from combustion emission performance studies reported in the literature [1,2], there are no detailed investigations of the flow downstream of multipoint lean direct injection nozzles. These detailed studies are necessary for numerical modeling and improving our understanding of the physical mechanisms involved in the performance of these nozzles. Unlike clusters of nonswirling jets, there are no swirling jets cluster studies reported in the literature.

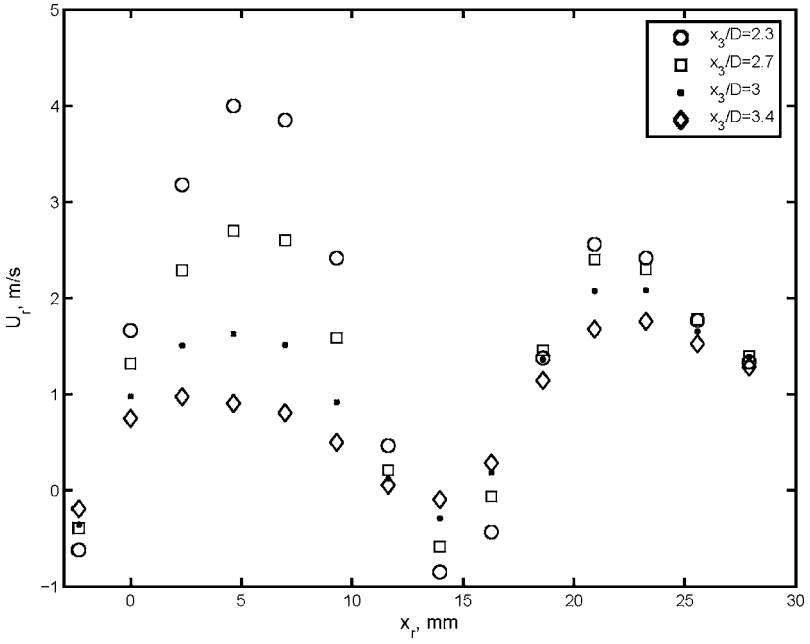

Fig. 14 Radial velocity profiles for the cluster

A drop sizing algorithm filtered large spray drops from the PIV images allowing measurement of the gas-phase velocity field. The mean velocity measurements agree within 2% of the same profiles collected using phase Doppler anemometry in the central region of the flow field where the PDPA measurements are most reliable.

The flow field of the cluster displays two distinct regions: the merger region ($x_3/D<10$) and the developed region ($x_3/D>12$). In the merger region, the characteristics of the individual jets are still visible and the expansion rate of the central jet is slowed. In the developed region the cluster blends into a single jet-like flow with the axial component of the velocity field displaying self-preserving properties. This flow behavior is similar to the behavior of clusters of nonswirling jets reported in the literature.

Lateral jet interaction:

1. Slows the expansion rate of the jet and the decay of the axial component of the velocity in the developed region; and
2. Accelerates the decay of the radial velocity and creates recirculation regions between jets just downstream of the nozzle exit.

Acknowledgment

The authors gratefully acknowledge the support of the Natural Sciences and Engineering Research Council of Canada (NSERC), the Ontario Graduate Scholarship Program (OGS), and the National Research Council of Canada (NRC). The experiments were done at the Aerodynamics Laboratory, Institute for Aerospace Research at the National Research Council, Ottawa. The nozzle used in the investigation was provided by Parker Hannifin-USA.

Nomenclature

D = air cup diameter, 6 mm

U_r, U_3 = mean radial and axial velocities, respectively

S_N = swirl number, $S_N=T_M/RA_M$, where R is the radius of the jet, and T_M and A_M are the axial fluxes of the angular and axial momentum, respectively [15]

x_r, x_3 = radial and axial position, respectively

$\delta\sim x_3(x_3/L)^n$ = jet length scale at the position x_3

m = exponent of the jet growth rate, $\delta/D\sim(x_3)^m$

References

[1] Mansour, A., Straub, D. L., Benjamin, M., and Richards, G. A., 2000, "Application of Macrolamination Technology to Lean Premixed Combustion," Proceedings of ASME Turbo Expo 2000, Germany.

[2] Tacina, R., Wey, C., Laing, P., and Mansour, A., 2001, "A low NO_x Lean Direct Injection Multipoint Integrated Module Combustion Concept for Advanced Aircraft Gas Turbine," Proceedings of ASME Turbo Expo 2001, Portugal.

[3] Yimer, I., Becker, H. A., and Grandmaison, E. W., 1996, "Development of Flow From Multiple-Jet Burner," Can. J. Chem. Eng., **74**, pp. 840–851.

[4] Raghunathan, S., and Reid, I. M., 1981, "A Study of Multiple Jets," AIAA81-4015.

[5] Moustafa, G. H., 1993, "Experimental Investigation of High-Speed Twin Jets," AIAA J., **32**(11), pp. 2320–2322.

[6] Hardalupas, Y., and Whitelaw, J. H., 1996, "Interaction Between Sprays From Multiple Coaxial Airblast Atomizers," J. Fluids Eng., **118**, pp. 762–771.

[7] Yimer, I., Becker, H. A., and Grandmaison, E. W., 2001, "The Strong-Jet/Weak-Jet Problem: New Experiments and CFD," Combust. Flame, **124**, pp. 481–502.

[8] Schetz, J. A., 1984, *Foundations of Boundary Layer Theory for Momentum, Heat and Mass Transfer*, Prentice-Hall.

[9] George, W. K., 1989, "The Self-Preservation of Turbulent Flows and its Relation to Initial Conditions and Coherent Structures," *Advances in Turbulence*, Hemisphere.

[10] Mathur, M. L., and MacCallum, N. R. L., 1967, "Swirling Air Jets Issuing From Vane Swirlers. Part 1: Free Jets," J. Inst. Fuel, May, pp. 214–237.

[11] Mathur, M. L., and MacCallum, N. R. L., 1967, "Swirling Air Jets Issuing From Vane Swirlers. Part 2: Enclosed Jets," J. Inst. Fuel, June, pp. 238–245.

[12] Grandmaison, E. W., and Becker, H. A., 1982, "Turbulent Mixing in Free Swirling Jets," Can. J. Chem. Eng., **60**, pp. 76–93.

[13] Panda, J., and McLaughlin, D. K., 1994, "Experiments on the Instablilities of a Swirling Jet," Phys. Fluids, **6**(1), pp. 263–276.

[14] Marxen, M., Sullivan, P. E., Loewen, M. R., and Jahne, A., 2000, "Comparison of Gaussian Particle Center Estimators and the Achievable Measurement Density for Particle Tracking Velocimetry," Exp. Fluids, **29**, pp. 145–153.

[15] Lefebvre, A. H., 1999, *Gas Turbine Combustion*, 2nd ed., Taylor & Francis.

Nejla Mahjoub Said
e-mail: Nejla.Mahjoub@fsm.rnu.tn

Sabra Habli

Hatem Mhiri

Laboratoire de Mécanique des Fluides et Thermique,
Ecole Nationale d'Ingénieurs de Monastir,
Route de Ouardanine 5020 Monastir, Tunisie

Hervé Bournot

Georges Le Palec

Equipe IMFT,
Institut de Mécanique de Marseille,
UNIMECA, 60 rue Joliot-Curie,
Technopôle de Château-Gombert,
13453 Marseille Cedex 13, France

Flow Field Measurement in a Crossflowing Elevated Jet

Structural features resulting from the interaction of a turbulent round jet issuing transversely into a uniform stream are described with the help of flow visualization and the PIV technique. The jet exits from a rigidly mounted pipe projecting at a distance from the floor of a tunnel. The aim of the present work is to investigate the flow structure in the near-field jet-pipe exit. Jet-to-crossflow velocity ratios from 0.375 to 3 were revealed at Reynolds numbers from 1660 to 6330. Flows in the vertical symmetry plane and horizontal plane across the jet-wake, jet-exit, and pipe-wake regions are investigated. The measured velocity fields present quantitative characteristics of the streamlines, vortices, and topological features of the flow structures. In particular, the origin and formation of the vortices in the wake are described and shown to be fundamentally different from the well-known phenomenon of vortex shedding from solid bluff bodies.
[DOI: 10.1115/1.2717614]

Keywords: wind tunnel experiments, particle image velocimetry, laser tomography visualization, jet in crossflow

Introduction

The growing awareness of environmental pollution and the attempts to curb it have made the study of jets exhausting into a crossflow of great interest. Chimney stack exhaust smoke into a wind, cooling tower plumes, discharges of warm water from pipes laid out on the ocean bed, and pollutant discharges into a river are a few such examples. Other examples of gaseous jets in a crossflow are the lift jets of V/STOL aircraft taking off and landing in strong wind, the injection of fuel into combustion chambers, and the cooling jets on turbine blades.

The jet in a crossflow is a flow with a wide range of applications owing to its ability to mix two streams of fluid efficiently. It is characterized by a strong three-dimensional flow field, complex interactions between two streams of fluids (i.e., jet fluid and crossflow fluid), and several interacting flow regions (i.e., the crossflow, the jet, the wake behind the jet, the pipe/orifice flow, and the wall boundary layer). In the case of the jet in a crossflow discharged from an elevated source (e.g., a pipe or stack), the wake behind the stack presents an additional important flow region.

The mean statistical properties of jets emitted into crossflows from ground-level sources have been examined in the literature both from an experimental and numerical point of view (e.g., Keffer et al. [1], Kamotani et al. [2], Andreopoulos et al. [3], Crabb et al. [4], Fric et al. [5], Mahjoub Saïd et al. [6]). Attention was focused on the ground-level case. Examinations of elevated sources are still rare.

Andreopoulos [7] presented measurements of velocity fluctuation statistics in the jet-pipe of a jet in a crossflow situation for various values of the jet-pipe-to-crossflow velocity ratio. The results of this work show that at high velocity ratios the pipe flow is very weakly affected by the crossflow.

Andreopoulos [8,9] measured velocity profiles and statistical turbulence properties, both in the bent jet and the far wake region of a cooling tower, at low jet-to-wind velocity ratios. Strong interaction among the bent plume, cooling tower, and wake-like region behind the cooling tower and jet were discussed. However, details of the flow structures in the near-wake region were not reported due to limitations of the instruments they employed.

Measurements of velocity and temperature field and flow visualization results are reported by Andreopoulos [10]. The experimental program included a flow visualization study and mean and fluctuating velocity and temperature measurements with multiwire probes and thermocouples. Coherent structures in the form of jet-like, wakelike, or mushroom-type vortices have been observed. The measurements showed that there is a strong interaction between the bending jet and the wake of the cooling tower, which is basically responsible for the downwash effect.

Results which support the idea that the jet also sheds some of its vorticity in the case of the ground-level source are given by Lozano et al. [11]. Eiff et al. [12] have shown continuous vortices extending from the stack-wake into the jet-wake.

Smith et al. [13] studied the mixing of the round jet normal to a uniform crossflow for a range of $R=5-25$. The results concern structural events of the vortex interaction region, and mixing and mean centerline concentration decay in the near and far field. Their work shows deep penetration of free-stream fluid into the upper edge of the jet. They also show jet fluid penetrating the wake structures from $R=10$ to $R=15$, a feature which persists as high as $R=200$. They report that the scalar centerline decay is faster in the near field compared to that in the far field. They conclude that in the near field, the counter-rotating vortex pair (CVP) itself does not enhance mixing.

Eiff et al. [14] clarified how the basically vertical vortices in the jet-wake (the jet-wake vortices) interact with the vortices in the stack-wake (the stack-wake vortices) below, but at this point there is no work known to us that suggests how these jet-wake vortices evolve in the region above the lower jet-wake region.

Turbulent transverse jets at high jet-to-crossflow blowing ratios have been investigated by Hasselbrink et al. [15], using both analytical and experimental techniques, with the primary goal of understanding the overall structure of the velocity field, and how it is influenced by combustion heat release. Algebraic scaling laws for the simplest case of nonreacting jets at high R were developed.

Su et al. [16] note that even though a number of applications of jets in a crossflow involve mixing, the body of work devoted to mixing of jets in a crossflow is relatively small. Applying PLIF and PIV in nitrogen as jet fluid-into-air crossflowing, Su et al.

Contributed by the Fluids Engineering Division of ASME for publication in the JOURNAL OF FLUIDS ENGINEERING. Manuscript received August 28, 2005; final manuscript received October 14, 2006. Review conducted by Joseph Katz.

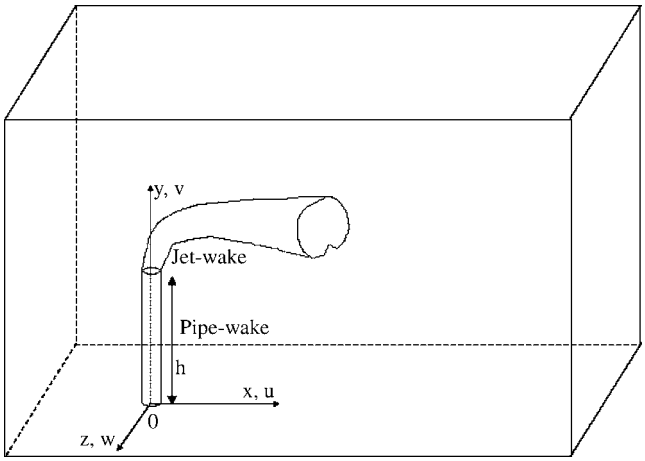

Fig. 1 Definition sketch

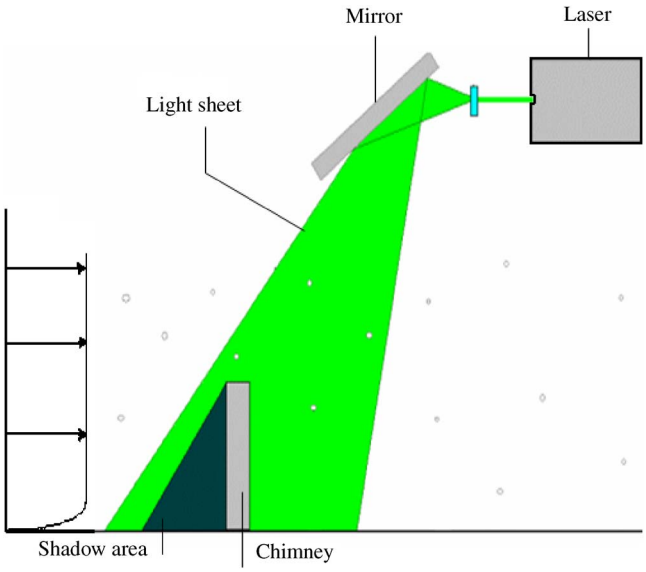

Fig. 2 Experimental setup: PIV

mapped the velocity and scalar fields in the center plane and at various positions off the center plane. All measurements are made at a single jet-to-crossflow velocity $R=5.7$ and jet exit Reynolds number Re=5000. Cross-stream profiles of scalar concentration and velocity magnitude show that the flow becomes asymmetric very near the nozzle exit, with excess values in the wake region of the flow. The results from their experiments were used to provide a comprehensive view of the scalar field.

Haven et al. [17] conducted a series of experiments to investigate the effects of the jet geometry on film cooling, and one of the cases they considered is an elliptic jet in a crossflow. While they have uncovered certain flow differences between the elliptic and circular jet geometries, their findings are restricted to very low velocity ratio only, with maximum $R=2$, since they are primarily interested in the situation where the deflected jets stay close to the cooling surface.

Gopalan et al. [18] examine the flow structure and associated wall pressure fluctuations caused by the injection of a round, turbulent jet into a turbulent boundary layer (water-into-water). The velocity ratio R varies from 0.5 to 2.5 and the Reynolds number is 1.9×10^4. Their results consist of sample instantaneous flow structures, distributions of mean velocity, vorticity and turbulence intensity in planes perpendicular and parallel to the wall.

The digital particle image velocimetry (DPIV) technique has been used to investigate the flow fields of an elliptic jet in a crossflow (water-into-water) by New et al. [19]. Two different jet orientations are considered: one with the major axis of the ellipse aligned with the crossflow and the other with the major axis normal to the crossflow. Their results show regular pairing of leading-edge vortices when the major axis of the jet is aligned with the crossflow.

Mahjoub Said et al. [6] numerically analyzed a jet subjected to a transverse turbulent flow. They examined the efficiency of the various usual turbulence closure models (the k-ε standard model, the k-ε R.N.G. model, the realizable k-ε model, and the second-order model) in describing the behavior of the flow in its various regions. They also studied the flow behavior and examined the influence of R (velocity ratio $R=v_0/u_\infty$) on the dispersion of the jet.

The emitted jet bends over into the crossflow direction, as shown in Fig. 1. On the downstream or lee side of the jet, a wake region is formed. In the case of a ground-level source, this wake region (the jet-wake) interacts with the ground-level boundary layer. In the case of the elevated source, the jet-wake interacts with the wake behind the pipe (the pipe-wake).

Measurements at stations closer to the exit of the elevated jet are more difficult to undertake owing to the existence of a recirculating zone, high turbulence intensities, and the angle of the main flow.

In order to understand the flow patterns of a plume issued from an elevated jet into a crossflow at large plume-to-wind velocity ratios, we conducted a series of experiments using a Particle Image Velocimetry (PIV) technique and laser tomography visualization. The visualized flow patterns and measured velocities on the vertical and horizontal symmetric planes are presented to illuminate the interactions between the crossflow, plume, and elevated jet. The results may offer engineers an extra consideration for practical application of plume dispersion.

Using a PIV technique and laser tomography visualization, we examined the wake regions of the pipe and plume at levels near the top of the pipe. The complex geometry of these structures in the wake of the plume as well as their interaction with the plume as it bends over after emission, is discussed. In this paper we describe the Kelvin-Helmholtz vortex structures. We have also established that the Karman-type vortex structures in the jet-wake, which we refer to as jet-wake vortices, extend to just below the centerline of the jet on each side of the symmetry plane of the flow.

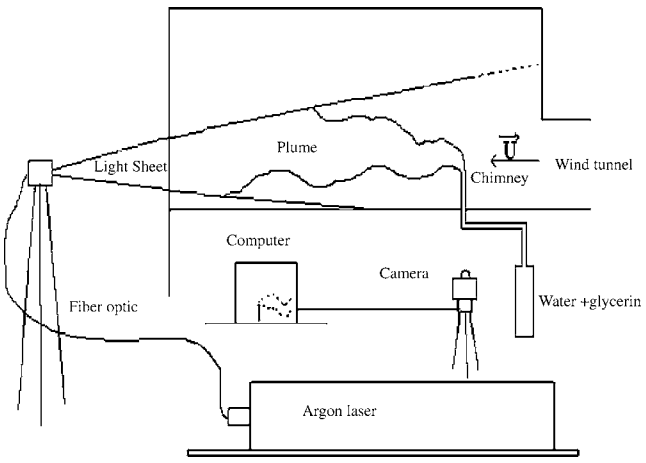

Fig. 3 Experimental setup: Tomography laser

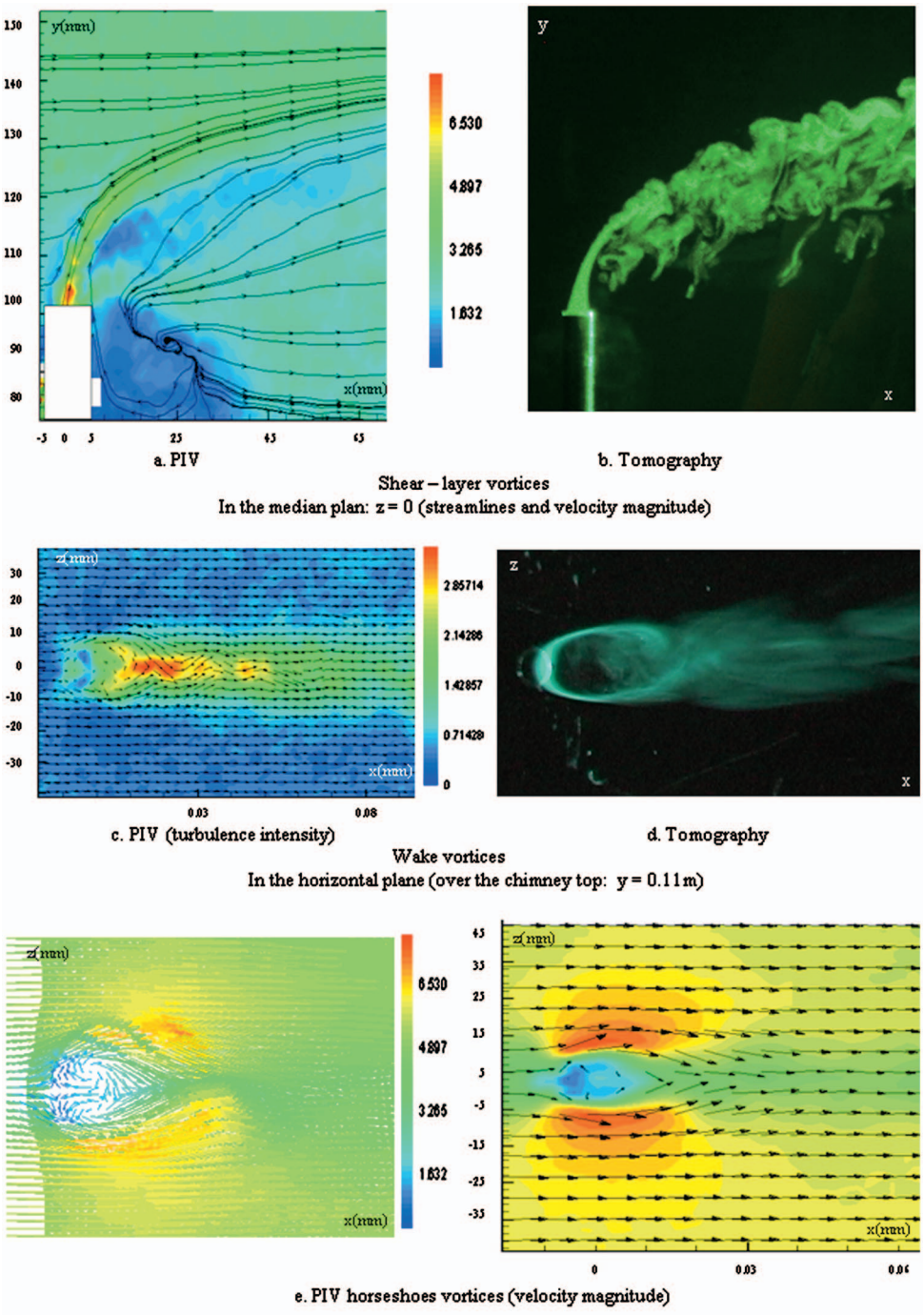

Fig. 4 Different types of vortical structure associated with the transverse-jet near field, $u_\infty = 3\ \mathrm{m\ s^{-1}}$, $v_0 = 8\ \mathrm{m\ s^{-1}}$, Re = 5330

Experimental Method

Measurements were carried out in a wind tunnel. This tunnel had a test section with a speed range of about 0–16 m s^{-1}. The experiments were performed in an open circuit discharging to the atmosphere outside the laboratory and with a parallel-sided, closed working section 3 m in length and 0.2 m × 0.3 m in cross section. For optical access, it has a side made of Pyrex; the interior of the wind tunnel is painted black to reduce reflections. In all experiments, the crossflow is seeded with oil droplets of approximately 0.8 μm diameter, and introduced at the ambient temperature into the tunnel nozzle. The turbulence intensity level of the crossflow was less than 0.2%. The jet was produced by means of a smooth pipe 0.1 m in length (h), 12 mm external diameter and 10 mm internal diameter (d) through which air at constant temperature was discharged. The pipe was positioned at the upstream end (20 cm from the tunnel nozzle) and along the centerline of the tunnel oriented perpendicularly to the crossflow.

The velocity profile at the pipe exit is measured using a low-density particle tracking technique. The jet is seeded with approximately 1 μm diameter glycerin particles (seeding density ≈ 30 particles ml^{-1} of pure jet fluid).

The origin of the wake coordinate system is fixed on the axis of the pipe. The x axis is directed downstream, the y axis is perpen-

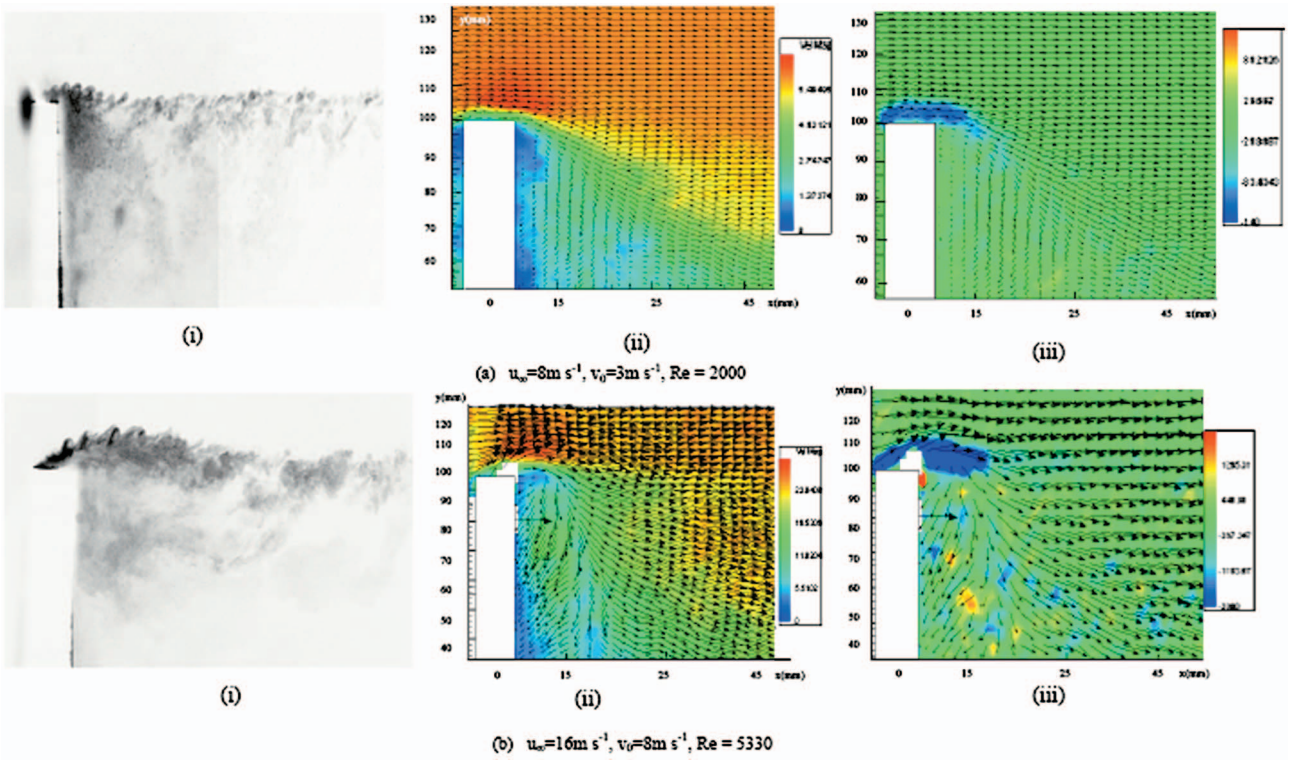

Fig. 5 (*i*) **Flow visualization;** (*ii*) **mean velocity field;** (*iii*) **mean vorticity field,** $R<1$

dicular (defined as transverse) to the flow direction and the pipe axis, and the z axis lies along the axis of the pipe (defined as spanwise).

Experimental Study by the PIV Method (Particle Image Velocimetry). The Particle Image Velocimetry system (Fig. 2) is based upon a TSI PowerView system, including a 50 mJ dual

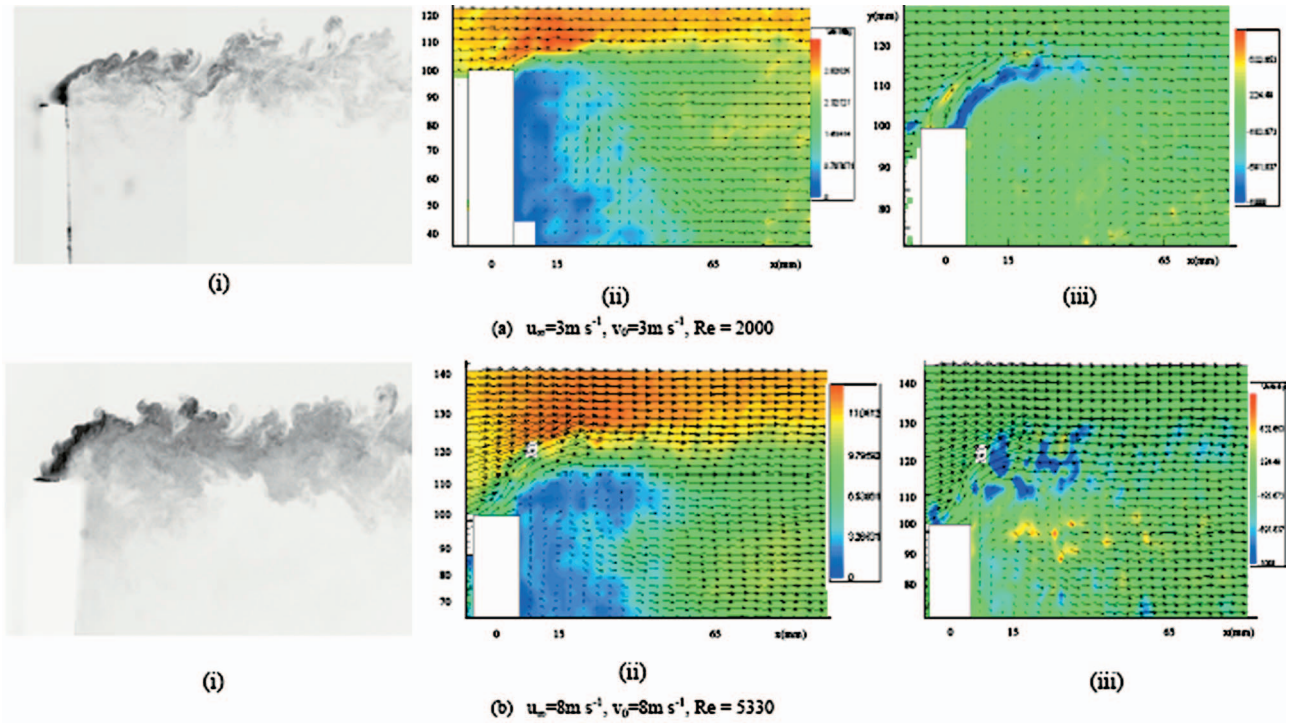

Fig. 6 (*i*) **Flow visualization;** (*ii*) **mean velocity field;** (*iii*) **mean vorticity field,** $R=1$

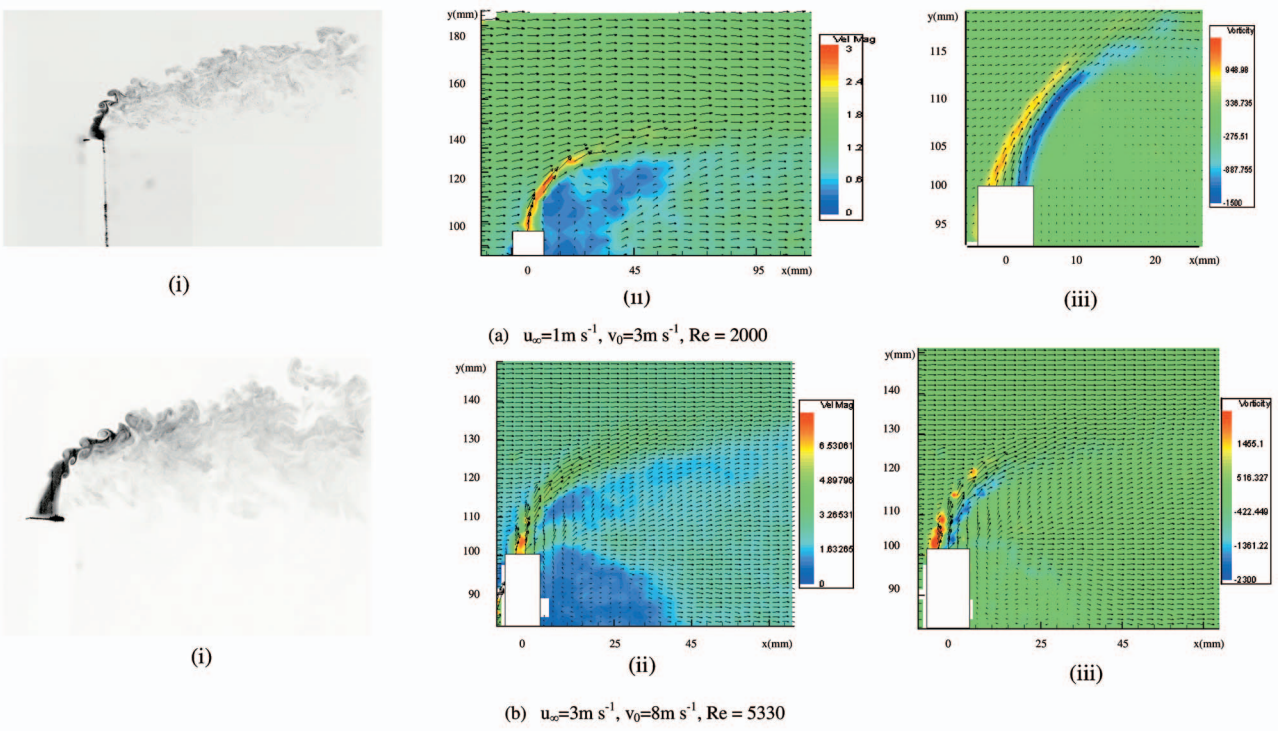

Fig. 7 (*i*) Flow visualization; (*ii*) mean velocity field; (*iii*) mean vorticity field, $R>1$

YAG laser which produces two plan luminous pulses, the duration of one ranging from 5×10^{-9} to 10^{-8} s, a PowerView 4 M high resolution cross-correlation camera (2 k×2 k resolution, 12 bits), a synchronizer and "Insight" Windows-based software for acquisition, processing, and postprocessing. This software allows the synchronization of pulsations according to the observed phenomena, and the adjustment of the time step between two images. This time step was 70 μs. In order to avoid errors, the velocity vectors were calibrated at 130 μm/pixel and limited to the representation of the velocity field in the regions where the luminance was strong enough.

Laser pulses from an ND-YAG (Neodymium-Doped Yttrium Aluminum Garnet) laser were expanded to form a thin light sheet using a cylindrical lens. The light sheet was brought from the top of the wind tunnel using a 45 deg mirror. Because of this arrangement, a shadow area upstream from the pipe was created where it was impossible to take measurements.

The light scattered from the seeded particles was captured and the resulting scattering signal is collected by an interline transfer CCD camera. The camera was oriented perpendicular to the plane of the sheet. The frame transfer capability of this camera allows each of the two closely spaced laser sheet pulses to be captured in a separate image. The collected images were transferred to the control computer. A target image was used to provide accurate scaling of the flow.

However, after the vector field is initially processed, filters are applied to the data to eliminate spurious vectors, and these vectors are linearly interpolated. Then the vector field is reprocessed. This permits the use of the cross-correlation PIV algorithm [20], which eliminates directional ambiguity and yields improved resolution over single-image autocorrelation techniques. In this way, the in-plane loss-of-correlation is minimized, and therefore the chance of valid vector detection is maximized.

Once an ensemble of instantaneous vector fields has been obtained from a set of images, several postprocessing calculations are made. Raw data are cast from pixel units into physical coordinates, and turbulence statistics and derived quantities such as vorticity and strain rate are calculated, using custom software. The final fields were averages performed with 50 successive acquisitions [12,21].

The uncertainties were about 5%. The estimates were inferred from estimated inaccuracies in the calibration data and from the observed scatter in the measurements.

The velocity profile of the main flow was measured with a hot wire anemometer together with a high precision electronic pressure transducer. With the help of an on-line micropressure calibration system, the uncertainty in the freestream velocity was estimated to be as large as 3% of a reading.

Experimental Study by Laser Tomography Visualization. For flow visualization, we used a 5 W continuous argon ion laser, a fiberoptic light sheet generator, and a standard video camera (Fig. 3). A spectra-physics 5 W argon-ion laser coupled with beam-steering optics and a cylindrical prism provided the laser sheet to visualize the cross sections of the deflected jet. A CCD color video camera was used to record the flow field to a recorder, and still images were captured via a frame grabber in a workstation. The visualization allows a quantitative analysis of the plume such as Kelvin-Helmholtz instabilities, the different vorticities, and the plume behavior downstream from the nozzle. Flow visualization was also used to determine jet trajectories and flow widths. We also decided to make a horizontal light sheet in the wind tunnel in order to visualize the three-dimensional aspects of the plume.

The results presented in this study correspond only to the dynamic aspect of the problem.

Results and Discussion

Consider a pipe of diameter d, which emits air containing particles of glycerin. The plume is subjected to a transverse flow. The ratio between the two velocities, $R=v_0/u_\infty$, is obtained by varying u_∞ (the crossflow free-stream velocity) and v_0 (the jet velocity). Consideration is given to an unsteady, three-dimensional flow.

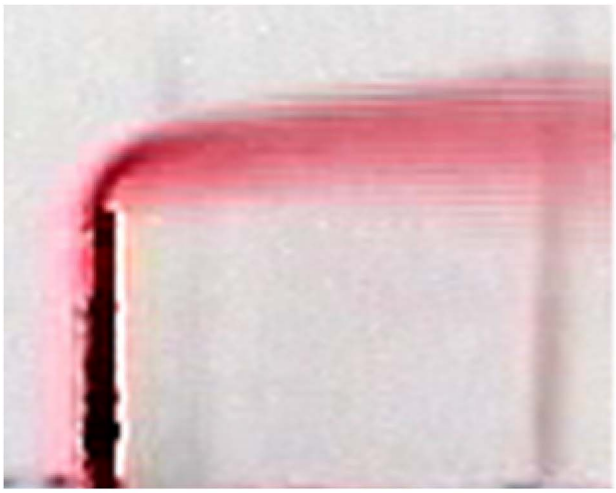

$u_\infty=3ms^{-1}, v_0=8ms^{-1}$, R =2.666

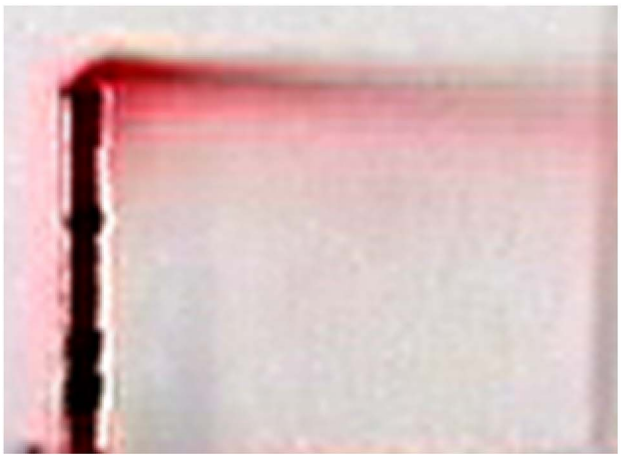

$u_\infty=8ms^{-1}, v = 8m\ s^{-1}$, R =1

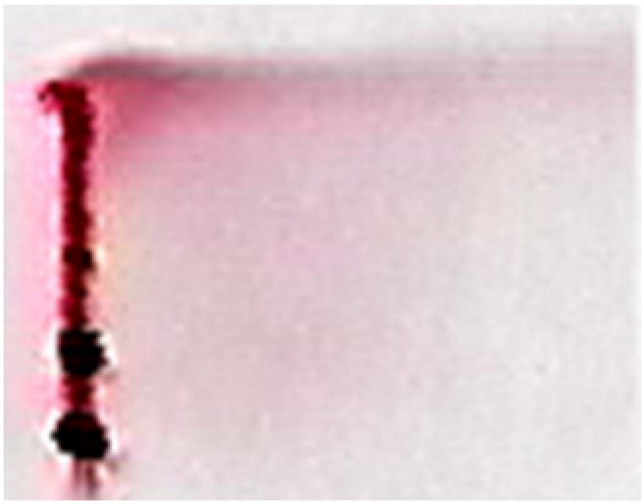

$u_\infty=16ms^{-1}, v_0=8ms^{-1}$, R =0.5

(Laser Tomography Visualization)

Fig. 8 Crossflow effects, Re=5330

Complex flow behaviors are the results of the interactions between the downwash effect, which is induced by the crossflow passing over the pipe exit, the up-shear effect induced by the issuing plume, and the wakes behind the plume and the pipe.

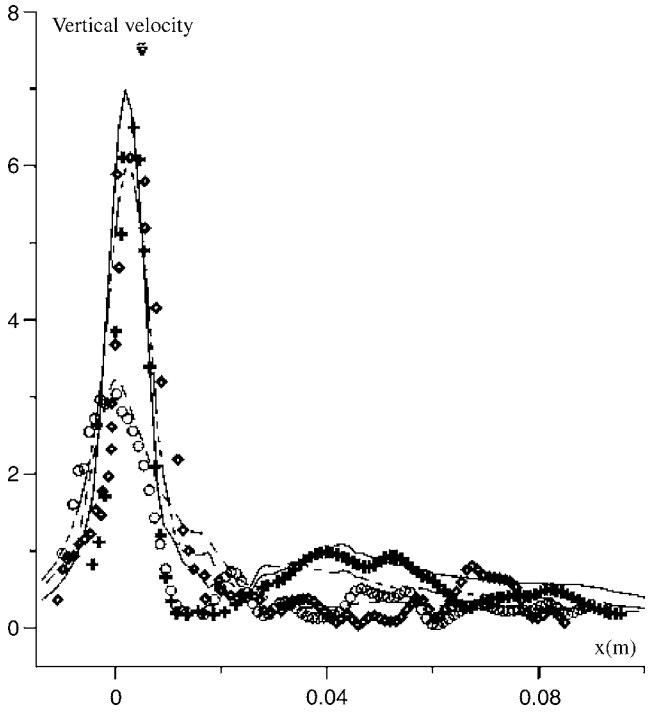

Fig. 9 Mean $\tilde{v}$-velocity profiles above the exit jet at y=0.11 m for v_0= 9.5 m s^{-1} and various u_∞

The emitted plume bends over into the crossflow direction. On the downstream or lee side of the plume, a wake region is formed. In the case of a ground-level source, this wake region (the plume wake) interacts with the ground-level boundary layer; interesting details of this interaction have recently been given by Mahjoub Saïd et al. [6]. In the case of the elevated source (Mahjoub Saïd et al. [22]); the plume wake interacts with the wake behind the pipe (pipe wake).

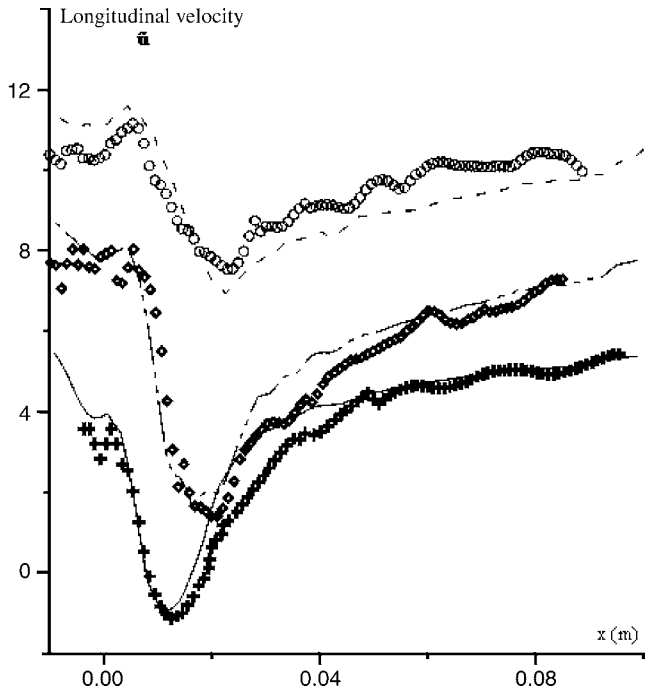

Fig. 10 Mean $\tilde{u}$-velocity profiles above the exit jet at y =0.11 m for v_0= 9.5 m s^{-1} and various u_∞

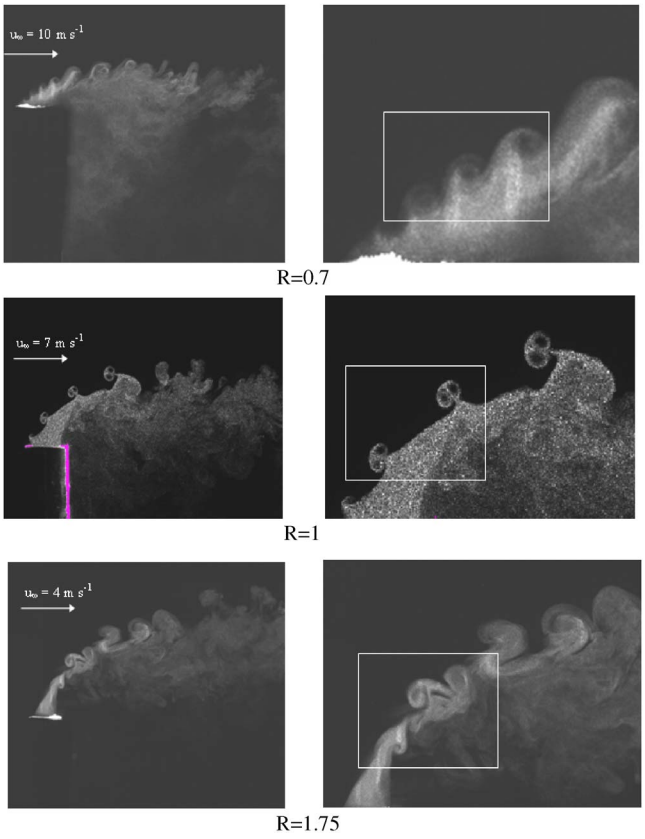

Fig. 11 Kelvin-Helmholtz structures for different velocity ratio (PIV), at v_0=7 ms^{-1} and Re=3600

Four types of coherent structure can be discerned in the near field of the jet, where the three-dimensional interaction between the jet and crossflow is most intense. We begin by presenting a brief review of these structures before addressing the wake in particular. Illustrated in Fig. 4 are the following: the jet shear-layer vortices; the wake vortices; the system of horseshoe vortices; and the counter-rotating vortex pair. Two of these, the shear-layer vortices and the wake vortices, are intrinsically unsteady; the other two, i.e., the horseshoe vortices and the vortex pair, have mean-flow definition although they may also have unsteady components. The instability of Benard-Von-Karman generates an alley of contrarotating swirls in quincunxes (in zig-zag), which are formed alternately on the right and on the left pipe.

Figure 4(*a*) shows the time-averaged streamlines on the symmetry plane. Streamlines emanate from the leading and trailing edges of the jet-exit. Streamlines indicate the motion of the crossflow fluid. Streamlines entering the domain from the crossflow boundary, upstream of the jet, appear to bend in the direction of the jet fluid and almost merge with the leading edge boundary of the jet. These streamlines must account for the upstream side entrainment of the jet. In addition, the jet entrains fluid on the downstream side, and the source of this entrainment is the node observed in the vicinity. The presence of this node has been well documented (e.g., Kelso et al. [23]). The local flow field acts as a source in the symmetry plane (note the streamlines fanning out across the plane) and a sink in the horizontal plane (the streamlines pass round the jet and converge toward this node). Due to this dual behavior, this point is sometimes termed the "saddle-node." The intensity of this (downstream side) entrainment is high.

In the pipe wake of Fig. 4(*a*), the bifurcation line separates the flow field into reverse and forward flow regions and the source point is a critical point in topological terms. The flows emitting from the source point are coming from the lateral flows, which originate from the recirculation bubble formed when the crossflow passes over the pipe. The recirculation bubble in the wake is subjected to the interaction of the downwash effect induced by the crossflow passing over the pipe tip and the up-shear effect induced by the jet flows.

In addition to the annular swirls which develop at the periphery of the jet, we can observe the presence of a horseshoe swirl which surrounds most of the opening of ejection while extending to the swirls from the wake. The view of horseshoe vortices wrapping around the base of a jet issuing from a pipe into a crossflow is shown in Fig. 4(*e*). This shows that the origin and formation of the vortices in the wake are fundamentally different from the well-known phenomenon of vortex shedding from solid bluff bodies.

The jet coming out of the pipe is bent by the cross stream while the latter is deflected by the jet in the normal and lateral directions. An important characteristic of the flow is that the shear layer emanating from the upstream edge of the pipe is considerably thicker than that emanating from the downstream edge of the pipe (lee side).

The study of the Reynolds number effects shows many important dynamics features, while the study of the velocity ratio R indicates a considerable difference between low and high bending jets (Figs. 5–7).

The trailing edge moves towards the leading edge forming a partial "ring" of jet fluid around the crossflow. However, the progression rate appears slower at the higher Reynolds number. As long as the jet accelerates, the trailing edge continues to move closer to the leading edge. The Reynolds number has a noticeable effect on the instabilities on the jet edges. When Reynolds numbers increase, the instabilities become noticeable. The photographs in Figs. 5–7 show "rollers" on the top and bottom edges of the jet. The shear is greatest at the top and bottom edges of the jet. This results in the Kelvin-Helmholtz instability mechanism are active on these edges. These photographs (Figs. 5–7(*i*)) clearly demonstrate that the instability intensifies as the Reynolds number is increased. In these images, jet fluid is seen to penetrate the wake structures to an increasing depth with increasing velocity ratio.

In Fig. 5(*ii*), where the value of the velocity ratio is lower than 1 ((*a*) R=0.375; (*b*) R=0.5), we note a downwash of the plume in the downstream region of the pipe. The effluents are sucked into the wake zone which develops in the downstream region of the pipe. The plume flows only within the wake formed by the ambient flow over the pipe. A downwash of the flow occurs behind the pipe. We note for the low velocity ratio the pipe and the bent-over jet interacts strongly in a mutual way.

Figure 7(*ii*) shows a sequence of equidistant vortices at the plume/ambient flow interface rotating along counterclockwise motions ((*a*) R=3; (*b*) R=2.666). Visualizing a sequence of images allowed us to observe that these vortical patterns had a translation velocity parallel to the interface. It also appears that in the lower section of the plume, similar vortical patterns were formed, but their rotation very logically takes place in the opposite direction, as this constitutes a resting-flow zone. In the wake zone, we can notice the disorderly formation of vortical patterns.

Figures 5–7(*iii*) show contours of the mean vorticity field on the symmetry plane, along with a velocity vector passing through the median plane (vertical section) at various R. The red color designates the positive values of vorticity (clockwise rotation of local flows), while the blue color designates the negative values of vorticity (counterclockwise rotation of local flows). The vector represents the velocity magnitudes. The vectors are superimposed on the isovorticity contours in order to compare the vorticity-concentrated locations with the features of the flow structures.

In the reverse-flow region of the jet-wake, the interaction between the up-shear effect, induced by the jet near the pipe exit, and the traction effect, induced by the bent-jet, causes the streamlines to turn counterclockwise, and thus causes negative vorticity

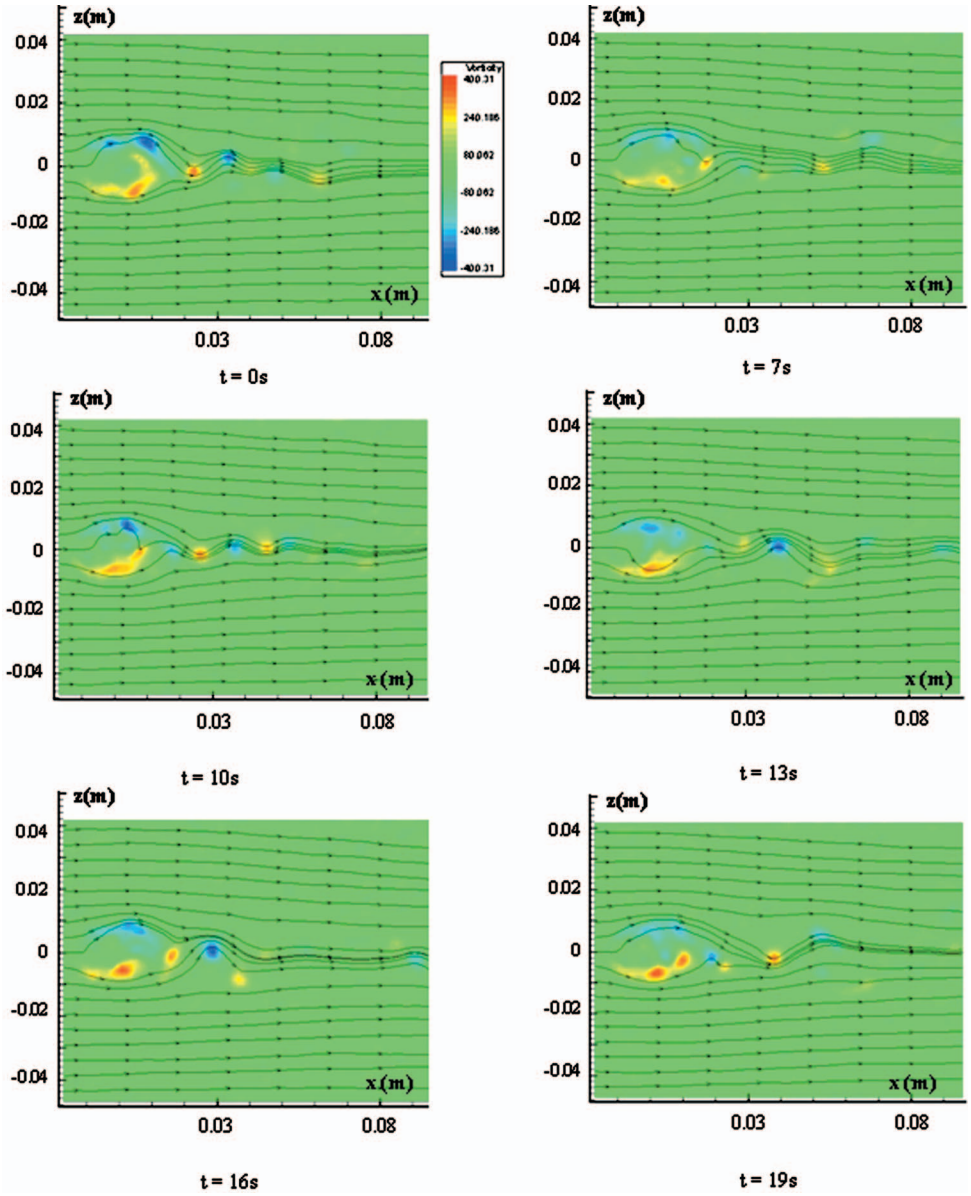

Fig. 12 Cross-sectional vorticities of the flow downstream elevated jet and their wakes (v_0 =3 ms^{-1}, u_∞=1 ms^{-1}, Re=2000)

contours to appear there. In the reverse flow regimes of the pipe wake, all the vorticity contours are positive because all the streamlines turn clockwise.

The position of the center of this recirculation zone, which is not a closed recirculation zone, in the longitudinal direction depends strongly on the Reynolds number Re, while its position is a function of the velocity ratio. As the Reynolds number increases the center is formed closer to the pipe, while as the velocity ratio decreases it moves upward.

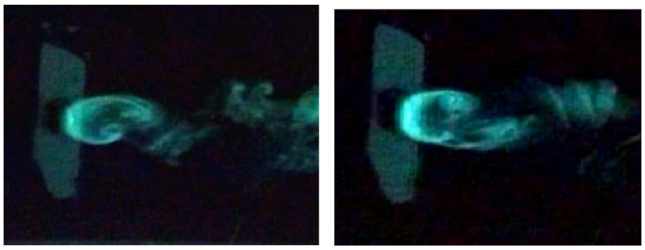

Fig. 13 Cross-sectional views, 1 cm above the pipe exit

In Fig. 8 we present by laser tomography visualization the effect of transverse velocity. The jet is ejected at v_0=8 m s^{-1} for various cross-stream velocities (u_∞). The Reynolds number is Re=5330.

These visual displays allowed us to observe that the ambient flow greatly affects the jet's flow, the main factor determining the jet's shape being the exhaust velocity/wind velocity ratio.

When the velocity of the wind tunnel increases, the jet curves until it becomes almost horizontal to the ground. When the wind tunnel has a velocity (u_∞=3 m s^{-1}, 8 m s^{-1}) lower than or equal to the jet's velocity (v_0=8 m s^{-1}), the jet trajectory spreads and tends to bend down more quickly as the velocity of the wind tunnel increases (u_∞=16 m s^{-1}).

We have compared our experimental data with numerical re-

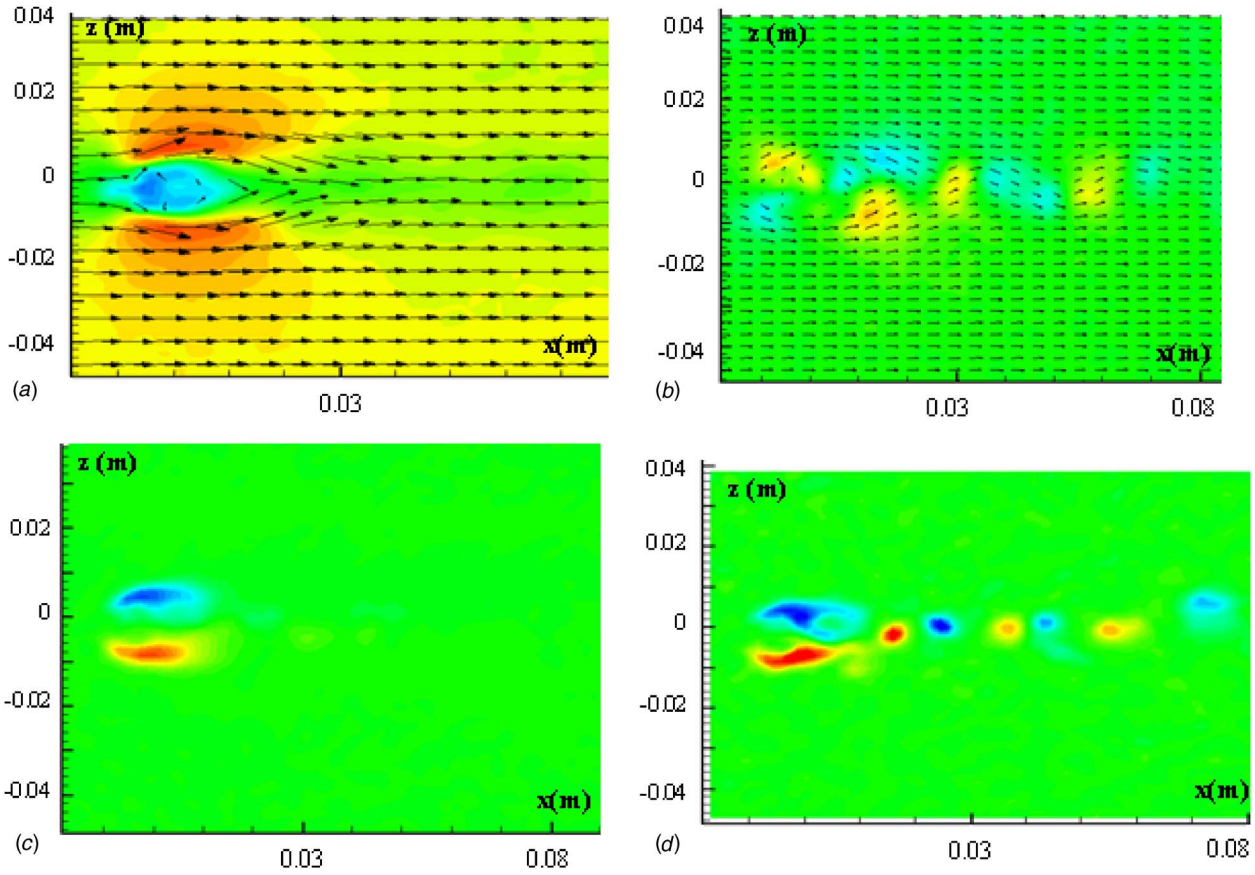

Fig. 14 (*a*) **Mean velocity field;** (*b*) **instantaneous** $\tilde{v}$**-velocity;** (*c*) **mean vorticity field;** (*d*) **instantaneous vorticity** (v_0 **=3 ms**$^{-1}$, u_∞**=1 ms**$^{-1}$, **Re=2000**)

sults obtained by Mahjoub et al. [22] and good qualitative agreement and reasonable quantitative agreement on most features are noted.

The numerical results presented herein for the elevated jet is obtained from a second-order turbulence closure model [6].

The evolution profiles of vertical and longitudinal velocity are displayed in Figs. 9 and 10 for various velocity ratios. Trajectory data are obtained from the ensemble-averaged contour plots of the side-view images, where each average is obtained from 50 instantaneous images acquired at the same tunnel run conditions. The profiles presented here are defined to be the locus of points in the $z=0$ plane at $y=0.11$ m (0.01 m above the exit of the pipe).

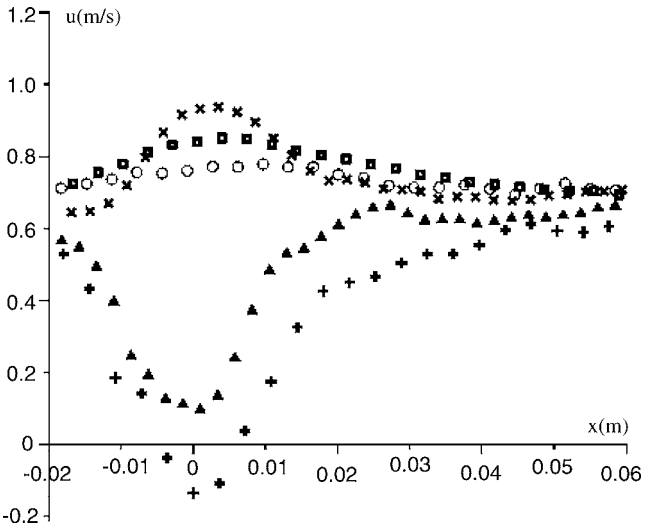

Fig. 15 Mean $\tilde{u}$**-velocity profiles for** u_∞**=1 m s**$^{-1}$ **and** v_0 **= 2.5 m s**$^{-1}$ **at** y**=0.11 m and Re=1660 (at various sections** z)

In these figures we compare the mean vertical velocity $\tilde{v}$ and the longitudinal evolution of the mean velocity $\tilde{u}$ for a vertical plane corresponding to $x=0.11$ m at $v_0=9.5$ m s^{-1} and various $\tilde{u}$ (6.5 m s^{-1}, 9.5 m s^{-1}, 12 m s^{-1}) versus x. We observe that the jet penetrates further into the cross stream, and the wake region in the lee of the jet is large when the velocity ratio increases. This causes significant inflow towards the symmetry plane.

For a low velocity ratio ($\approx$0.8), the bending over happens so quickly that shortly downstream of the exit the vertical velocity in the jet is nearly zero.

We note that the longitudinal velocity is lowest at the center of the wake region. The jet deflection is an indication of the entrainment rate of the crossflow by the jet in the near field. Based on this argument, it is reasonable to say that with a relatively larger streamwise deflection, high velocity ratio jets have a higher near-field entrainment rate than low velocity ratio jets.

At the exhaust area of the pipe, we observe a typical turbulent pattern called Kelvin-Helmholtz instabilities (Fig. 11). This phenomenon appears when the flow is subjected to shearing between two fluids, which slip one over the other at different velocities. This instability leads to the formation of a "swirling sheet" within the mixing-zone between the two fluids. Depending on wind velocity, these patterns turn clockwise or counterclockwise. In fact, the rotational direction depends on the R factor. This is clearly visible in Fig. 11, the value of the velocity ratio being lower than 1, equal to 1, and greater than 1, respectively.

This photograph clearly shows the jet shear-layer vortices,

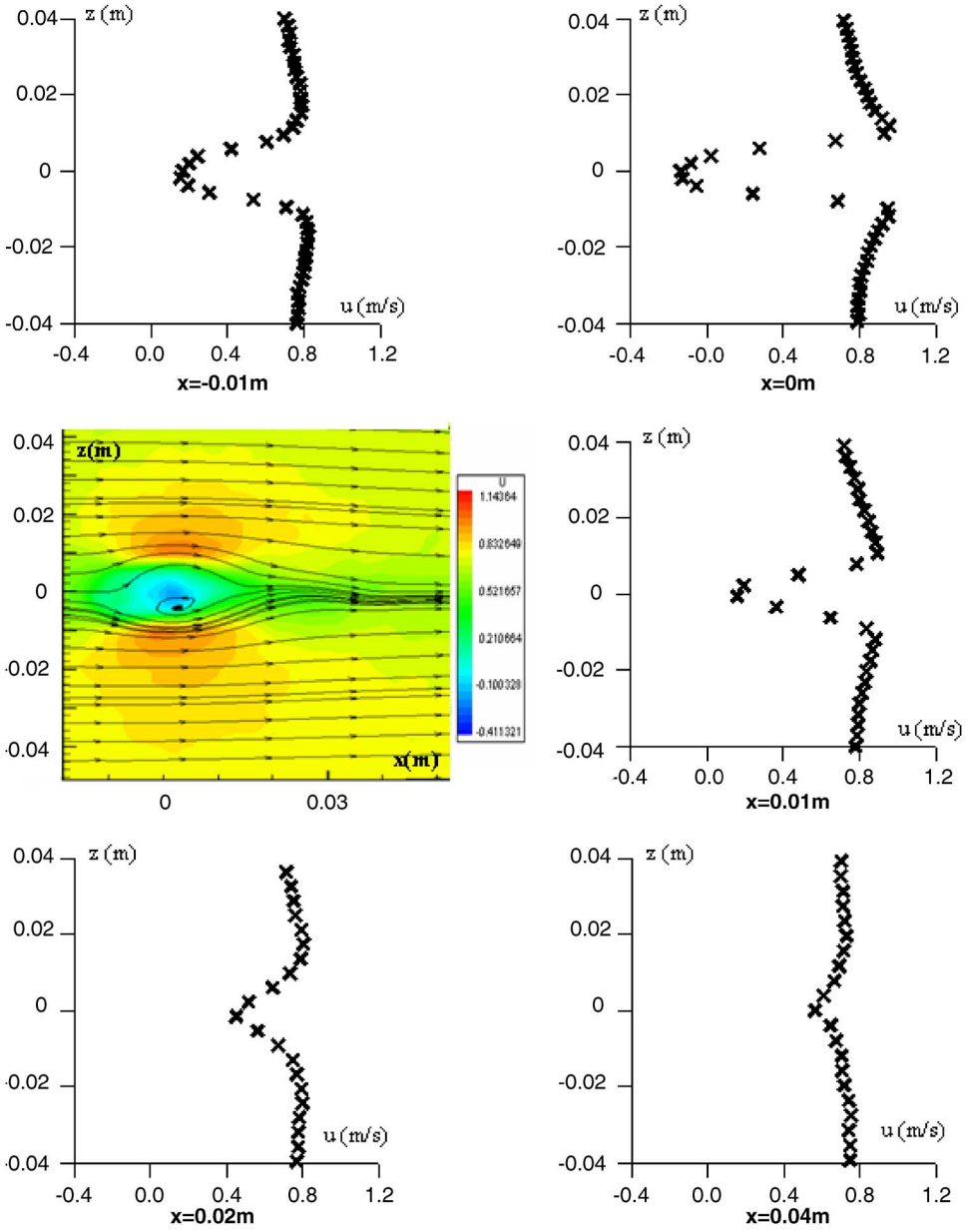

Fig. 16 Mean $\tilde{u}$-velocity profiles for $u_\infty = 1$ m s^{-1} and $v_0 = 2.5$ m s^{-1} at $y = 0.11$ m and Re = 1660 (at various sections x)

which dominate the initial portion of the jet and which are the result of the Kelvin-Helmholtz instabilities of the annular shear layer that separates from the edge of the jet orifice. The shear layers coming out of the pipe roll up at two different locations, at the upwind side and at the lee side of the pipe.

We present the field in the case when wind velocity is greater ($u_\infty = 10$ m s^{-1}) than exhaust velocity ($v_0 = 7$ m s^{-1}) at Re = 3600 and $R = 0.7$. This result shows the presence of vortices with a clockwise rotational direction.

However, it should be pointed out that the presence of vortices at the plume/wind tunnel flow interface is observed in Fig. 11 ($R = 1$) when the velocities of the two flows are similar, and so the formation of vortices take place in the two directions. The fact that the two flows do not have the same direction creates at the interface an instability which itself generates vortices with a counterclockwise and a clockwise rotational direction at the plume interface. One striking feature of this flow is the appearance of mushroom-type vortices that are very regular.

Figure 11 demonstrates a rolling up of the shear layer, particularly evident in the upstream boundary of the jet, where the velocity ratio was relatively high, $R = 1.75$, and the Reynolds number Re = 3600. This rolling up starts to take place at about $1d$ above the exit and persists to about $4d$ downstream along the jet path. The windward side of the jet is decelerated with respect to the lee side in the very near field and this results in a stretching of the vortex lines. Further downstream, and in particular after the bending over of the jet, the upper side of the jet is accelerated with respect to the lower side, resulting in a compression of the vortex lines. The vortices on the lee side of the jet disappear very quickly while the others on the upwind side of the pipe persist much longer before they break down to turbulence.

Figure 12 shows sectional instantaneous views of transverse jet wakes for six different instances. The wake vortices are perhaps the most intriguing structures in the near field. They have some characteristics which are similar to wake vortices of solid cylin-

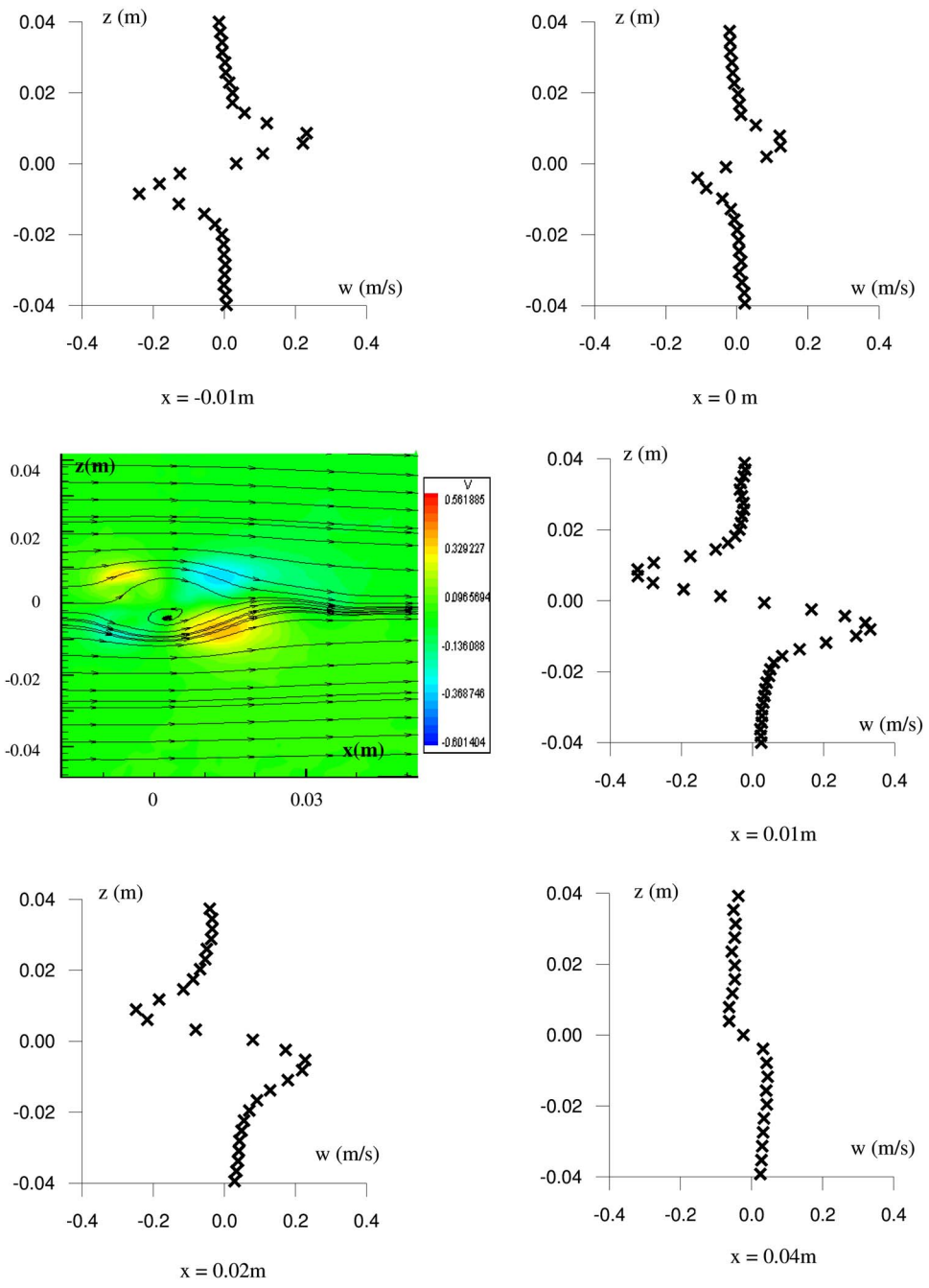

Fig. 17 Mean $\tilde{w}$-velocity profiles for u_∞=1 m s^{-1} and v_0= 2.5 m s^{-1} at y=0.11 m and Re=1660 (at various sections x)

ders, but differences between the jet (a fluid) and the cylinder (a solid) as obstacles to the crossflow suggest significant differences in how the wake vortices should form.

Furthermore, if the "wake" is defined as the region downstream of the jet, between the jet and the pipe, it can immediately be seen that this is fundamentally different from a bluff-body wake.

Downstream of the jet, there appears to be a quiescent region with low vorticity (shown in blue). Further downstream, the flow contains larger scale features which move slowly in the direction of the crossflow.

Figure 13 shows sectional views of transverse jet wakes. The photographs show the path of the crossflow around the pipe and its entrainment into the wake. In each photograph the jet, near the right side of the photograph, issues toward the viewer, and the crossflow is from right to left. In each case, at least one horseshoe vortex is seen to wrap around the pipe near the orifice. Downstream from the orifice, further structure is seen in the near-pipe wake. The wakes show structures staggered from side to side.

Instantaneous realizations of the jet velocity field are very different from the corresponding ensemble-averaged fields. Figure 14 shows typical mean and instantaneous side-view images through the y=0.11 m plane of an R=3.

In this figure, the velocity vectors and the vorticity pattern on the horizontal plane (y=0.11 m) are shown. A recirculation zone is found in the jet-wake between the forward and aft stagnation

points which are located on the symmetry axis $z=0$ m. Inside the recirculation zone, along the symmetry axis, reverse flows evolve from the aft stagnation point and go towards the forward stagnation point.

The elevated jet generates vorticity for its own wake, of one sign on one side and of opposite sign on the other side.

On the whole, the Karman vortex gradually grows up in the shear layer and moves towards the wake centerline. Just after passing through the wake bubble, it starts to move fast. As it goes downstream, it gets away from the centerline slightly and then turns to the centerline again. Finally, it moves parallel to the x axis. The paths of vortices shed at upper and lower sides meet together at the reattachment point. Far downstream, the lock-on makes the vortex remain much closer to the centerline. Thus, it appears that the upper and lower vortex streets are formed into a line.

The longitudinal velocity $\tilde{u}$ has been measured for $u_\infty = 1$ m s^{-1}, $v_0 = 2.5$ m s^{-1} at $y=0.11$ m and Re=1660. Figure 15 shows mean $\tilde{u}$ velocity profiles versus longitudinal coordinate x, at five spanwise positions z. We note that the recirculation region behind the jet is formed at $x=0.0075$ mm ($0.75\,d$) in the center plane ($z=0$) and extends for a length of approximately one diameter. The recirculation is formed as a result of the combined blockage of the jet and vortex structure.

Figures 16 and 17 present mean velocity profiles for different locations of longitudinal positions. The profiles were presented at the $y=0.11$ m plane as functions of the distance z (lateral coordinate). These figures show important characteristics of the jet in the initial stages.

The mean $\tilde{u}$-velocity profiles show a peak that is the result of jet fluid. The peak is reduced in size at $x=0.75d$ and it disappeared forward of the recirculation region.

The mean $\tilde{w}$ velocity profiles show two peaks. These are evidence of the jet forming the characteristic vortex pair and balancing out the wake developed by the free stream around the jet; on the centerline, w is zero suggesting that the slower moving elements of fluid have a high probability of being entrained upward into the underside of the jet.

The mean velocity values quantify the width of the wake.

Conclusion

Simultaneous tomography laser and particle image velocimetry (PIV) yield measurements of three-dimensional elevated jet fluid velocity fields in turbulent crossflowing jets. The jet-to-crossflow velocity ratios were in the range 0.375–3, covering a range of jet exit Reynolds numbers from 1660 to 6330. The measurements are focused on the near-field region of the jet. The configuration studied, which has the jet nozzle, protrudes into the uniform region of the tunnel flow. The jet nozzle is a simple pipe.

The flow field of an elevated jet in a crossflow is dominated primarily by the complex interactions among the jet-wake, pipe-wake, up-shear effect of the jet and the downwash effect, which is induced when a crossflow passes over the pipe-tip.

The streamline patterns on the horizontal planes show nonclosed recirculation zones of different topological structures in different characteristic flow regions due to the strong three-dimensional effect.

According to R values, the development of Kelvin-Helmholtz peripheral instabilities is noticed. The spacing between vortices can be regular. The pattern's rotational direction is imposed by the value of R. We have also described the Karman-type vortex structures.

Nomenclature

d = internal diameter of the jet, m
h = jet height, m
H_T = wind tunnel height, m
k = kinetic energy of turbulence, m^2 s^{-2}
R = velocity ratio v_0/u_∞
Re = Reynolds number $v_0 d/\nu$
Re_F = Reynolds number $u_\infty H_T/\nu$
$\tilde{u}$, $\tilde{v}$, $\tilde{w}$ = velocity components along x, y, and z directions, m s^{-1}
x, y, z = coordinates, m

Subscripts

∞ = Condition in crossflow
o = entry of jet

References

[1] Keffer, J. F., and Baines, W. D., 1963, "The Round Turbulent Jet in a Cross-wind," J. Fluid Mech., **15**, pp. 481–496.
[2] Kamotani, Y., and Greber, I., 1972, "Experiments on a Turbulent Jet in a Crossflow," AIAA J., **10**, pp. 1425–1429.
[3] Andreopoulos, J., and Rodi, W., 1984, "Experimental Investigation of Jets in a Crossflow," J. Fluid Mech., **138**, pp. 93–127.
[4] Crabb, D., Durao, D. F. G., and Whitelaw, J. H., 1981, "A Round Jet Normal to a Crossflow," ASME J. Fluids Eng., **103**, pp. 142–152.
[5] Fric, T. F., and Roshko, A., 1994, "Vortical Structure in the Wake of a Transverse Jet," J. Fluid Mech., **279**, pp. 1–47.
[6] Mahjoub Saïd, N., Mhiri, H., El Golli, S., Le Palec, G., and Bournot, Ph., 2003, "Three-Dimensional Numerical Calculations of a Jet in an External Cross Flow: Application of Dispersion of Pollutants," ASME J. Heat Transfer, **125**, pp. 510–522.
[7] Andreopoulos, J., 1982, "Measurements in a Jet-Pipe Flow Issuing Perpendiculalarly into a Cross Stream," J. Fluids Eng., **104**, pp. 493–499.
[8] Andreopoulos, J., 1986a, "Wind Tunnel Experiments on Cooling Tower Plumes, Part I: In Uniform Cross Flow," ASME, Paper No. 86-WA/HT-31.
[9] Andreopoulos, J., 1986b, "Wind Tunnel Experiments on Cooling Tower Plumes, Part I: In Non-Uniform Cross Flow of Boundary Layer Type," ASME, Paper No. 86-WA/HT-32.
[10] Andreopoulos, J., (1989), "Wind Tunnel Experiments on Cooling Tower Plumes: Part 1—In Uniform Crossflow," J. Heat Transfer, **111**, pp. 941–948.
[11] Losano, A., Smith, S. H., Mungal, M. G., and Hanson, R. K., 1994, "Concentration Measurements in a Transverse Jet by Planar Laser-Induced Fluarescence of Acetone," AIAA J., **32**, pp. 218–322.
[12] Eiff, O. S., Kawall, J. G., and Keffer, J. F., 1995, "Lock-in of Vortices in the Wake of an Elevated Round Turbulent Jet in a Crossflow," Exp. Fluids, **19**, pp. 203–213.
[13] Smith, S. H., and Mungal, M. G., 1998, "Mixing, Structure and Scaling of the Jet in Crossflow," J. Fluid Mech., **357**, pp. 83–122.
[14] Eiff, O. S., and Keffer, J. F., 1995, "Limits of the Lock-in Mechanism in a Round Turbulent Jet Emitted From an Elevated Source," 15th Canadian Congress on Applied Mechanics, University of Victoria, Victoria, British Colombia.
[15] Hasselbrink, E. F. Jr., and Mungal, M. G., 2001, "Transverse Jets and Jet Flames. Part 2. Velocity and OH Field Imaging," J. Fluid Mech., **443**, pp. 27–68.
[16] Su, L. K., and Mungal, M. G., 2004, "Simultaneous Measurement of Scalar and Velocity Field Evolution in Turbulent Crossflowing Jets," J. Fluid Mech., **513**, pp. 1–45.
[17] Haven, B. A., and Kurosaka, M., 1997, "Kidney and Anti-Kidney Vortices in Crossflow Jets," J. Fluid Mech., **352**, pp. 27–64.
[18] Gopalan, S., Abraham, B. M., and Katz, J., 2004, "The Structure of a Jet in Cross Flow at Low Velocity Ratios," Phys. Fluids, **16**(6), pp. 2067–2087.
[19] New, T. H., Lim, T. T., and Luo, S. C., 2004, "A Flow Field Study of an Elliptic Jet in Cross Flow Using the DPIV Technique," Exp. Fluids, **36**(4), pp. 604–618.
[20] Hasselbrink, E. F., 1999, "Transverse Jets and Jet Flames: Structure, Scaling and Effects of Heat Release," Ph.D. thesis, Stanford University, Stanford, CA.
[21] Knapp, Y., Bertrand, E., and Mouret, F., 2003, "2D-PIV Measurements of the Pulsatile Flow in a Left Heart Simulator," Proceedings of PSFVIP-4, June 3–5, 2003, Chamonix, France.
[22] Mahjoub, Said N., Mhiri, H., Le Palec, G., and Bournot, Ph., 2005, "Experimental and Numerical Analysis of Pollutant Dispersion From a Chimney," Atmos. Environ., **39**, pp. 1727–1738.
[23] Kelso, R. M., Lim, T. T., and Perry, A. E., 1996, "An Experimental Study of Round Jets in Crossflow," J. Fluid Mech., **306**, pp. 111–144.

An Experimental Study of Artificially-Generated Turbulent Spots Under Strong Favorable Pressure Gradients and Freestream Turbulence

M. I. Yaras
Mechanical and Aerospace Engineering,
Carleton University,
Ottawa, Ontario, Canada

This paper presents experimental results on the internal flow structure of turbulent spots, and examines the sensitivity of this structure to streamwise acceleration rate and freestream turbulence. Measurements were performed on a flat plate, with two levels of freestream acceleration rate and three levels of freestream turbulence. The turbulent spots were generated artificially at a fixed distance from the test-surface leading edge, and the development of the spot was documented through hotwire measurements at three streamwise locations. The measurements were performed at multiple spanwise locations to allow observation of the three-dimensional spatial structure of the turbulent spot and the temporal evolution of this structure. Analysis of the perturbation velocity and rms velocity fluctuations provides insight into the variations of the streaky streamwise-velocity structure within the turbulent spot, with a focus on the effects of freestream acceleration rate and turbulence level. [DOI: 10.1115/1.2717608]

Introduction

The appearance of turbulent spots within a laminar boundary layer was first observed by Emmons [1], who developed a model for the statistical properties of such spots. Subsequently, Elder [2] suggested that breakdown into a turbulent spot is dependent on local conditions only, and is essentially independent of flow Reynolds number and local boundary-layer thickness. While a critical Reynolds number is required to amplify small disturbances within a laminar boundary layer, this is not a prerequisite for the generation of a turbulent spot by a strong disturbance. The experiments of Wygnanski et al. [3] established the average shape of a turbulent spot, and provided physical arguments on the processes responsible for the growth of the spot. The commonly observed shape of a turbulent spot in the streamwise/spanwise and streamwise/wall-normal planes is shown schematically in Fig. 1. During the growth of the turbulent spot, fluid appears to be entrained from both the local irrotational freestream and the surrounding laminar boundary layer [4]. Through measurements on the symmetry plane of a turbulent spot, Cantwell et al. [5] observed the outer part of the rear (upstream) interface and the lower part of the front (downstream) interface of the turbulent spot to be regions of particularly significant entrainment. Wygnanski et al. [3] and Cantwell et al. [5] reported the overhang region at the front interface of the turbulent spot to be many boundary-layer thicknesses long on the spot centerline. Based on the fact that the turbulence in the overhang region does not extend all the way to the surface, this region was argued to develop through a sweeping action over the slower laminar flow near the wall. Gad-El-Hak et al. [6] measured the wall-normal growth rate of the turbulent spot to be very similar to that observed in a turbulent boundary layer. Additionally, the authors argued that the spreading of a turbulent spot parallel to the surface is not limited to turbulent entrainment. In classical turbulent entrainment, the turbulent region characterized by random three-dimensional vortical flow structures is bounded by irrotational nonturbulent fluid, hence the entrainment process must be by direct contact, i.e., by local diffusion of vorticity. The rotational nature of the laminar boundary-layer fluid surrounding a turbulent spot allows for the possibility of mechanisms in addition to the diffusion of vorticity to participate in the spreading of the turbulent spot. The mechanism that is thought to have a substantial contribution to the transverse growth of turbulent spots is the destabilization of the rotational fluid surrounding the turbulent spot in a laminar boundary layer (e.g., [6–8]).

Through visualization experiments, Gad-El-Hak et al. [6] observed that in the upper portion of the turbulent spot, at about two boundary-layer thicknesses from the surface, the streamwise and spanwise length scales of the turbulence eddies within the spot were roughly equal to the boundary-layer thickness. In the streamwise/wall-normal plane, the turbulent spot was observed to contain many eddy structures with a preferred inclination in the downstream direction. Flow visualization studies such as those of Elder [2], Cantwell et al. [5], and Gad-el-Hak et al. [6] revealed the presence of low-speed streaks upstream of the rear edge of the turbulent spot. These streaks have been found to have approximately the same spanwise spacing as found in turbulent boundary layers, and display streamwise coherence. Sankaran et al. [9] suggested that the wall-attached legs of hairpin vortices in turbulent spots would provide such a streak formation mechanism, which would be analogous to the pairs of counter rotating vortices in turbulent boundary layers that have been argued to be the source of the streaks. The recent three-dimensional particle-image-velocimetry measurements of artificially-generated turbulent spots by Schröder and Kompenhans [10] provide quantitative evidence for the presence of well-organized longitudinal streaks inside turbulent spots, together with an organized vorticity field that supports earlier hypotheses regarding the presence of hairpin vortices. Schröder and Kompenhans observed these flow structures to be more orderly than those encountered deep in turbulent boundary layers. Similar streaky structures were observed in the bottom portion of artificially-generated turbulent spots by Makita and Nishizawa [11] using rakes of I- and X-hotwire probes. These authors argued for the presence of hairpin vortices, the induced upwash and downwash velocities of which lead to the formation

Contributed by the Fluids Engineering Division of ASME for publication in the JOURNAL OF FLUIDS ENGINEERING. Manuscript received November 15, 2005; final manuscript received September 13, 2006. Review conducted by Joseph Katz.

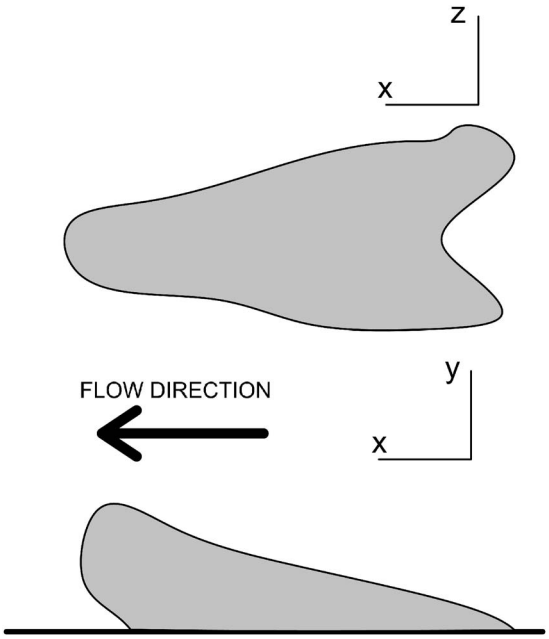

Fig. 1 Approximate shape of turbulent spots

of streaks in the streamwise velocity field. The authors observed the number of streaks to increase as the spot grew while propagating downstream, and noted that the wingtips of the spots maintained a streamwise velocity defect regardless of the change in the number of streaks within the spot.

In a natural setting, turbulent spots develop in close vicinity of each other. It is therefore of interest to establish the effect of the mutual interaction of spots on their internal structure and growth rate. Zilberman et al. [12] measured the interaction of a turbulent spot with a turbulent boundary layer created by a row of spherical trips, and concluded that the turbulent spot retains its identity, displaying an internal turbulence structure similar to that of the outer region of a turbulent boundary layer, with little loss in intensity. Makita and Nishizawa [11] studied the merging of two artificially-generated spots, and observed that the merging of the spot wingtips containing low-speed streaks leads to a stronger upwash in that region, with the resultant unstable inflectional profile producing spanwise vortical structures around the top of the merged region.

While the majority of the attention on turbulent spots has focused on their internal structure and spreading rates [13], the flow region immediately behind (upstream) a turbulent spot, first studied by Schubauer and Klebanoff [14], is also of interest, for an increased stability is observed in this flow region relative to the local undisturbed laminar conditions. This calming effect is thought to be the result of the velocity profile behind the trailing edge of the turbulent spot deviating from the undisturbed profile in a manner that is consistent with the aforementioned mechanism associated with a streaky streamwise velocity distribution in the turbulent spot, hence affecting the stability of this region of flow.

It is evident from this brief survey that a considerable body of literature exists on turbulent spots. However, a clear and consistent picture on the substructures prevailing in turbulent spots and on the dominant mechanism of transverse spreading is yet to be achieved. The present experimental study has been undertaken to provide further evidence on the internal structure of turbulent spots, and to determine the extent of modification in this structure due to variations in free-stream turbulence and streamwise acceleration rate.

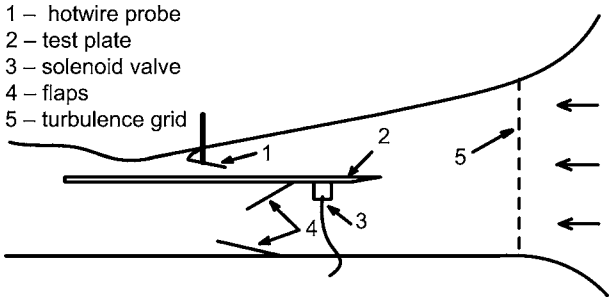

Fig. 2 Test section configuration

Experimental Setup and Data Processing

The experiments were performed in a closed-circuit wind tunnel on a flat and smooth test plate of 1220 mm length and 762 mm width, made of 25.4 mm-thick medium density fiber (MDF) board (Fig. 2). The leading edge of the test surface consists of a 50.8 mm long aluminum section, mounted onto the test plate such that its top surface is aligned with the top surface of the test plate. The aluminum attachment has an elliptic leading edge of 15.9 and 3.2 mm axis dimensions, and is machined to a 15 deg knife edge from its lower side. Streamwise pressure gradients are imposed on the test surface using a contoured wall that forms the ceiling of the test section. This test configuration has been used extensively by the author's research group in studies of attached and separated boundary-layer transition. For the present test cases, over the 750 mm length of the test surface starting from the leading edge, the contoured ceiling was set to converge towards the test surface at an angle of 11.0 deg, as shown in Fig. 2.

Turbulent spots were created by injecting puffs of air perpendicular to the test surface through a 0.75 mm-diameter hole located at a distance of 100 mm from midspan of the test plate and 200 mm from the test-plate leading edge. Compressed air supplied to a solenoid valve mounted under the test plate was used to generate the puffs of air, and the valve was triggered at a frequency of 0.9 Hz with a square-wave pulse of 9.6 ms duration.

Since the streamwise flow blockage due to the solenoid valve under the plate is localized, a deflector plate of the same height as the solenoid valve was mounted to the test plate just downstream of the valve to produce a spanwise-uniform flow blockage. A second flap mounted on the floor (Fig. 2) was set to an angle such that the stagnation point was shifted slightly towards the working side of the test plate on the elliptic leading edge. Through measurements with a miniature seven-hole pressure probe, the flow incidence at the test-plate leading edge was confirmed to be uniform to within 0.5 deg along the span of the plate.

The streamwise velocity component in the boundary layer and in the freestream was measured using a single-sensor hotwire probe, with a tungsten sensor of 1.3 mm length and 5 μm diameter. The signal from the hotwire anemometer was sampled at a rate of 10,600 Hz, and was low-pass filtered with a cutoff frequency of 3800 Hz prior to digitization. At each measurement location, 75 records of velocity samples were acquired, with the start of each record of 4096 samples being synchronized with the turbulent-spot trigger. The sampling frequency of 10,600 Hz and the sample count of 4096 yields a measurement duration of close to 0.4 s for each record, which was sufficient to track the turbulent spot at the measurement plane farthest along the test surface. The trigger frequency of 0.9 Hz yielded a time-interval just over 1 s between data records, which ensured that the boundary-layer developing on the test surface recovered from the passing of a turbulent spot before the next spot was generated.

The artificially-generated turbulent spots were measured at streamwise locations 250 mm, 400 mm, and 500 mm downstream of the location where the disturbance was introduced to the flow periodically. At each of these three streamwise measurement loca-

tions, the flow was traversed in the direction normal to the test surface, with the axis of the hotwire probe oriented at a shallow angle to the test surface (Fig. 2). In each traverse, measurements were performed at 80 points clustered towards the test surface over a traverse distance that measured several multiples of the local undisturbed boundary-layer thickness to capture the turbulent spot completely. At each of the three streamwise measurement locations, the traverse normal to the test surface was repeated at a series of spanwise locations. Based on the expectation that, in ensemble-averaged form, the turbulent spot is to approximate a laterally-symmetric structure with respect to its centerline, the spanwise measurement stations were placed in the range of $z=-12.5$ mm to $z=62.5$ mm, with $z=0$ mm coinciding with the spanwise location of the disturbance used to produce the turbulent spot. The traverse locations were placed 5 mm apart in the spanwise direction, with the exception of three of the traverses centered at $z=0$ mm, which were spaced at 2.5 mm.

The structure of the artificially-generated turbulent spots was studied through the ensemble-averaged perturbation and rms fluctuation in the streamwise velocity component. The perturbation velocity was obtained by subtracting from the ensemble-averaged local flow velocity the undisturbed laminar velocity that would have prevailed at that position in the absence of a turbulent spot

$$\tilde{u}(x,y,z,t) = \frac{\hat{u}(x,y,z,t) - u_\ell(x,y,z)}{u_{\text{ref}}} \tag{1}$$

where $\hat{u}$ is the ensemble-averaged streamwise velocity, u_{ref} is the freestream reference velocity measured 25 mm from the leading edge of the test surface and at the spanwise location where the turbulent spots were created, and u_ℓ is the undisturbed laminar velocity determined by time-averaging the velocity trace from the moment of trigger of the data acquisition process, which was synchronized with the production of the disturbance, until the turbulent spot arrived at the measurement location. The ensemble averaging of the velocity-time traces was performed over 75 data records, which was found to be sufficient for statistical convergence. The use of the ensemble-averaged velocity in the calculation of the perturbation velocity serves to remove the high frequency fluctuations, yielding a smooth perturbation velocity field due to the presence of the turbulent spot in the laminar boundary layer.

The rms fluctuation in the streamwise velocity component was determined through

$$u'(x,y,z) = \sqrt{\frac{\sum_n (u(x,y,z,t) - \hat{u}(x,y,z,t))^2}{n}} \tag{2}$$

where n is the number of samples in each data record.

Test Conditions

The freestream reference velocity at $(x,y,z)=(25,25,0$ mm) was 3.0 m/s and 4.4 m/s, which correspond to flow Reynolds numbers based on the test-plate length ($L=1.22$ m) of 245,000 and 350,000, respectively. The flow Reynolds number was kept constant to within ±5000 during the measurements, with the variations being caused primarily by slight drifts in the rotational speed of the wind-tunnel fan. For each of the flow Reynolds numbers, measurements were performed at three levels of free-stream turbulence, as documented in Table 1. The tabulated freestream turbulence intensity, Tu_{ref}, and integral length scale of turbulence, Λ, were quantified 10 mm upstream of the test-plate leading edge, and were confirmed to be uniform in the spanwise and test-plate-normal directions well beyond the spatial range that may affect the development of the artificially-generated turbulent spots. The integral length scale of turbulence was calculated from the single-sensor hotwire data using the frozen-eddy approximation. The moderate-Tu and high-Tu conditions were realized through turbulence grids installed at the exit plane of the wind-tunnel contraction, 500 mm upstream of the test-plate leading edge. Each turbulence grid consists of a 3.175 mm-thick perforated aluminum plate with nonstaggered square holes. The turbulence grid for the moderate-Tu case consists of a 3.175 mm thick perforated aluminum plate with nonstaggered 12.7 mm × 12.7 mm square holes of 15.88 mm spacing, yielding an open area ratio of 0.64. The turbulence grid for the high-Tu case consists of a 3.175 mm thick perforated aluminum plate with nonstaggered 25.4 mm × 25.4 mm square holes of 31.75 mm spacing, yielding an open area ratio of 0.64. The low-Tu case did not utilize a turbulence grid; accordingly, the integral length scale of turbulence in this instance is observed to scale on the cross-sectional dimensions of the wind tunnel at the test section.

Table 1 Freestream reference turbulence intensity and length scale

	Re_L	Tu_{ref} (%)	Λ_{ref} (mm)
Low-Tu	245,000	0.97	771
	350,000	0.90	728
Moderate-Tu	245,000	3.07	34
	350,000	2.75	36
High-Tu	245,000	5.43	16
	350,000	5.18	19

The streamwise variation of the freestream acceleration parameter, $\eta = \nu/u_e^2 du_e/dx$, is shown in Fig. 3. These results correspond to the low-Tu condition, and were confirmed to remain essentially the same for the moderate-Tu and high-Tu conditions. Between the streamwise location where the disturbance is produced, $x=200$ mm, and the last streamwise location of measurements, $x=700$ mm, the acceleration parameter is observed to remain fairly constant at about 3×10^{-6} and 4.5×10^{-6} for the high and low flow Reynolds numbers, respectively. These values of the acceleration parameter correspond to pressure gradients that have been categorized in the published literature on turbomachinery-blade aerodynamics as strongly favorable. Moretti and Kays [15] observed the onset of relaminarization of turbulent boundary layers to occur when the acceleration parameter reaches a critical value of 3.5×10^{-6}. This is consistent with the range of 2.5×10^{-6}–3.5×10^{-6} suggested by Jones and Launder [16] and the value of 3.0×10^{-6} reported by Escudier et al. [17]. The conditions for the present experiments are thus in the range where a turbulent boundary layer would begin to relaminarize, and this

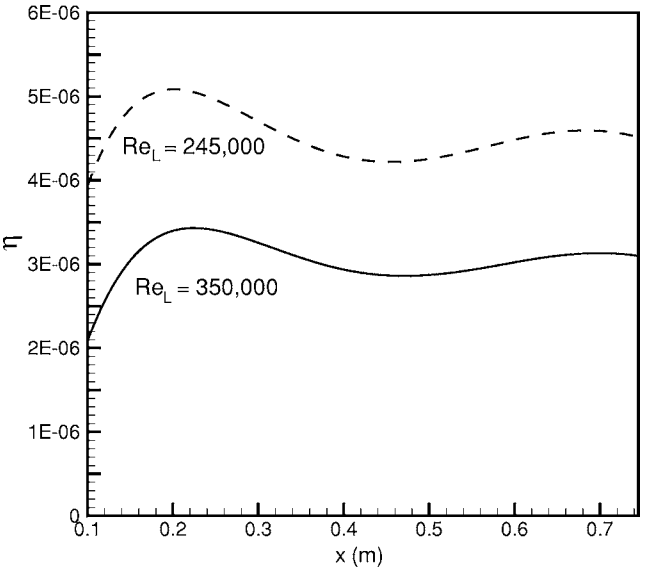

Fig. 3 Streamwise variation of acceleration parameter

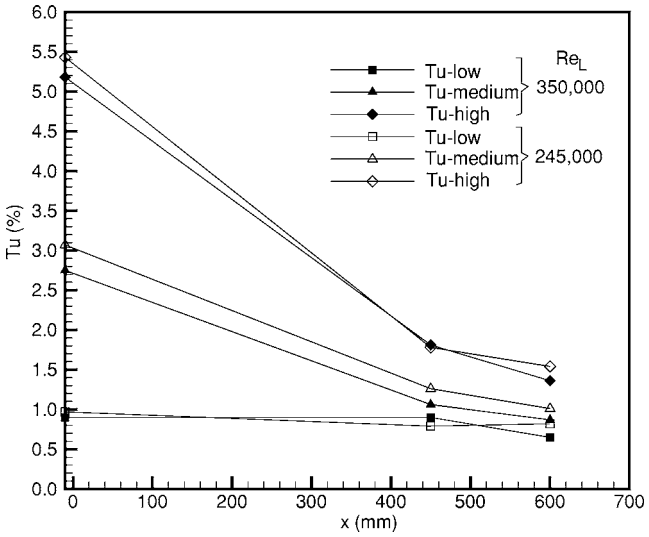

Fig. 4 Streamwise variation of freestream turbulence intensity

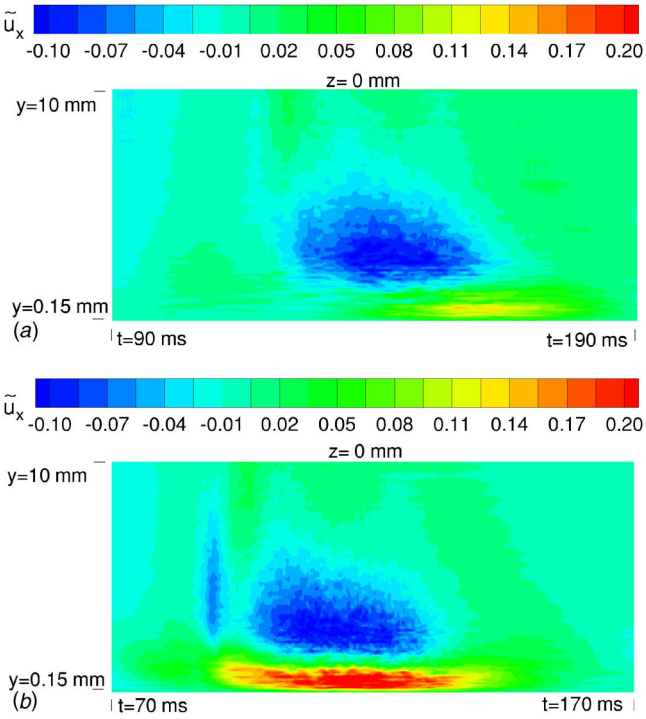

Fig. 5 Distribution of perturbation velocity (*y-t* plane) (*a*) $\eta=4.5\times10^{-6}$; (*b*) $\eta=3.0\times10^{-6}$, low Tu, $x=600$ mm

choice was made with the expectation that the substructures in the artificially-generated turbulent spots would be more organized if they are to mimic the trends observed in the substructures prevailing in the inner region of turbulent boundary layers, as will be discussed in the next section of the paper. Given the strongly stabilizing influence of the streamwise acceleration rate of the two test cases, the puffs of air had to be injected from the test surface at a high velocity (approximately 35 m/s) for consistent generation of a turbulent spot in each instance.

The ceiling geometry was not altered between the two flow Reynolds numbers, hence the observed variation in the acceleration parameter between the two test cases is the direct result of altering the flow Reynolds number in the test section. The simultaneous variation in the flow Reynolds number and the acceleration parameter may potentially create difficulties in isolating the effects of the two parameters on the turbulent-spot characteristics. Nonetheless, the respective variations in the two parameters are complementary in the sense that a reduction in flow Reynolds number is accompanied by an increase in the streamwise acceleration rate, with both trends expected to promote stability of the boundary layer.

The streamwise variation of freestream turbulence is presented in Fig. 4. As a result of the strong streamwise acceleration of the flow over the test surface, the freestream turbulence in the moderate-Tu and high-Tu cases is observed to decrease considerably with streamwise distance, particularly up to the first streamwise location of measurements at $x=450$ mm. The rate of decrease of Tu with streamwise distance is observed to increase with the level of turbulence prevailing at the leading edge. Consequently, a significant reduction with streamwise distance is observed in the differences amongst the turbulence intensity levels of the three cases. It is therefore important to bear in mind that the variations in the turbulent-spot characteristics observed in this study are caused by changes in the freestream turbulence level that are in a streamwise-averaged sense considerably less than those implied by the differences amongst the reference turbulence intensity values at the leading edge given in Table 1. While the turbulence intensity for the low-Tu and moderate-Tu cases is observed to reach similar values towards the last streamwise location of measurements, this does not necessarily amount to similar *level* of freestream disturbance in these two cases, for they differ in the integral length scale of turbulence, as listed in Table 1.

At the noted flow Reynolds numbers, freestream turbulence levels and streamwise pressure gradients, in the absence of the artificial disturbance used to generate turbulent spots, the boundary layer on the test surface remained laminar over the measured portion of the test plate. With the edge of the boundary layer taken as the location with a streamwise velocity that is 99% of the local freestream velocity, the undisturbed boundary-layer thickness for the flow Reynolds number of 245,000 varied from 4.0 mm at $x=450$ mm to 3.2 mm at $x=700$ mm. The corresponding thicknesses for the higher flow Reynolds number were determined to be 3.5 mm and 2.5 mm. These values correspond to the low-Tu case. As freestream turbulence was increased from low-Tu to high-Tu, the undisturbed laminar boundary thickness increased by about 2 mm at $x=450$ mm and about 0.5 mm at $x=700$ mm, owing to increased mixing at the edge of the boundary layer facilitated by the freestream turbulence eddies.

Results and Discussion

The perturbation velocity distribution in the x-t plane along the centerline ($z=0$) of the turbulent spot is shown in Fig. 5. Elapsed time is displayed on the abscissa, with $t=0$ corresponding to the injection of a puff of air into the flow at $x=200$ mm. Figure 6 illustrates the perturbation velocity distribution in the y-z plane, at an instant when the turbulent spot is about halfway through the measurement plane. Figures 7 and 8 contain the rms velocity-fluctuation fields corresponding to the perturbation velocity fields of Figs. 5 and 6, respectively. Figure 9 shows the rms velocity distribution at $y=0.8$ mm, which is about 25% of the undisturbed local boundary-layer thickness from the test surface. The results presented in these figures correspond to the second streamwise measurement station located at $x=600$ mm, two streamwise acceleration rates, and low freestream turbulence conditions. It is to be noted that the relative scaling of the axes in these plots distorts the streamwise, spanwise, and wall-normal proportions of the turbulent spot, and are chosen as such to most clearly illustrate the structure of the spot.

The perturbation velocity and rms velocity-fluctuation distributions in the x-t plane at the spot centerline (Figs. 5 and 7) display a conventional shape of a turbulent spot, with a height that is about twice the local boundary-layer thickness, and an overhang region on one side of the spot. The shape of the spot in the t-z

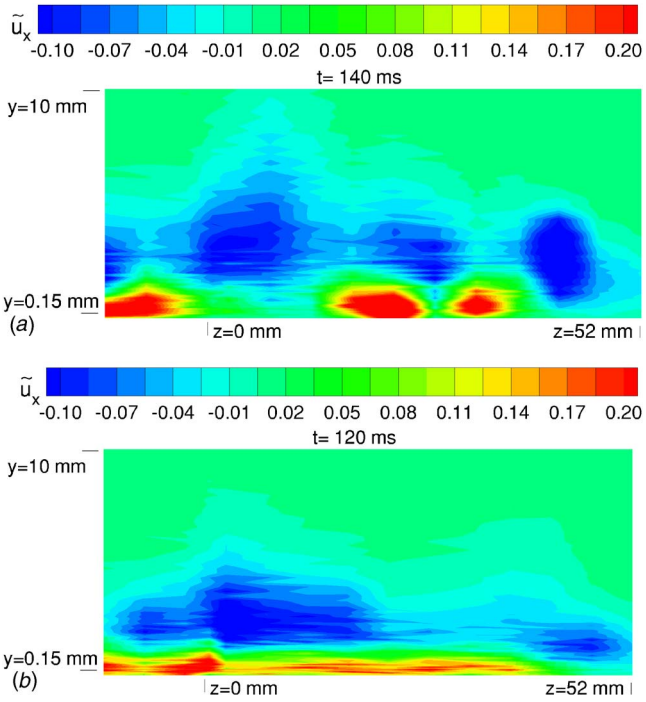

Fig. 6 Distribution of perturbation velocity (*y-z* plane) (*a*) $\eta = 4.5\times10^{-6}$; (*b*) $\eta = 3.0\times10^{-6}$, low Tu, $x = 600$ mm

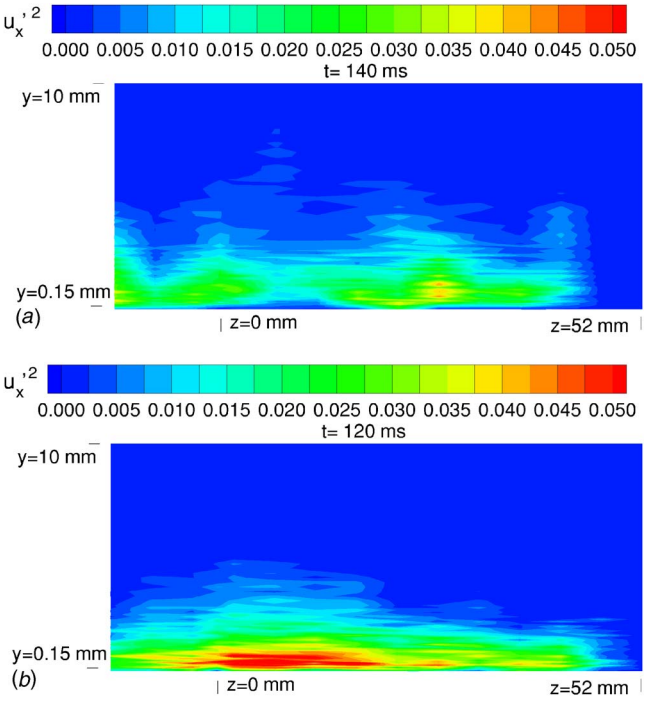

Fig. 8 Distribution of rms velocity fluctuation (*y-z* plane) (*a*) $\eta = 4.5\times10^{-6}$; (*b*) $\eta = 3.0\times10^{-6}$, low Tu, $x = 600$ mm

plane, observed through rms-velocity contours (Fig. 9), again follows the conventional pattern of an approximate arrowhead. Interestingly, however, the pointed end of the approximate arrowhead is on the trailing rather than leading side of the turbulent spot. This is in contrast with most previously published studies where the arrowhead is observed to point in the downstream direction.

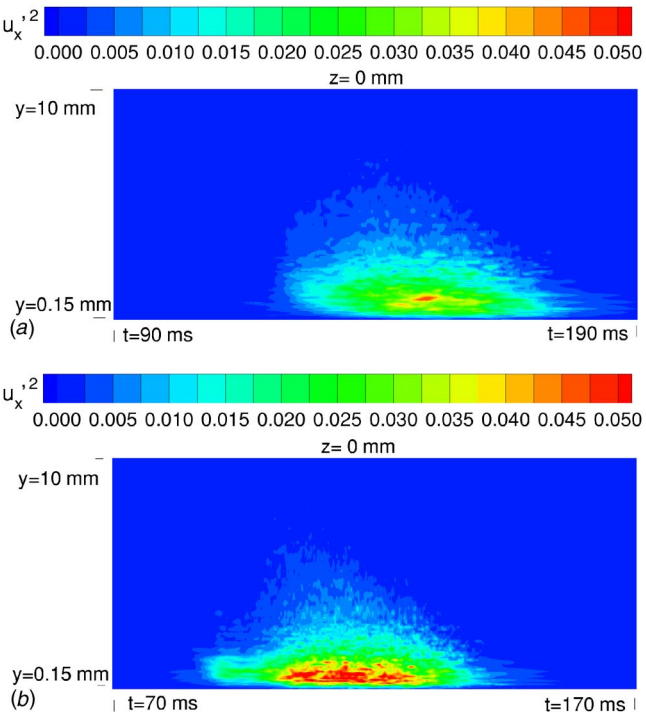

Fig. 7 Distribution of rms velocity fluctuation (*y-t* plane) (*a*) $\eta = 4.5\times10^{-6}$; (*b*) $\eta = 3.0\times10^{-6}$, low Tu, $x = 600$ mm

The present observation is consistent with the measurements of Zhong et al. [18] and the direct numerical simulations of Wu et al. [19], who observed upstream-pointing arrowhead shapes for turbulent spots generated through the influence of freestream disturbances in the form of wakes. Wu et al. provided an explanation for this difference on the basis of whether the disturbance that is the source of the turbulent spot originates near the surface or near the edge of the boundary layer. When the disturbance originates at the edge of the boundary layer, the resultant parcel of fluid particles

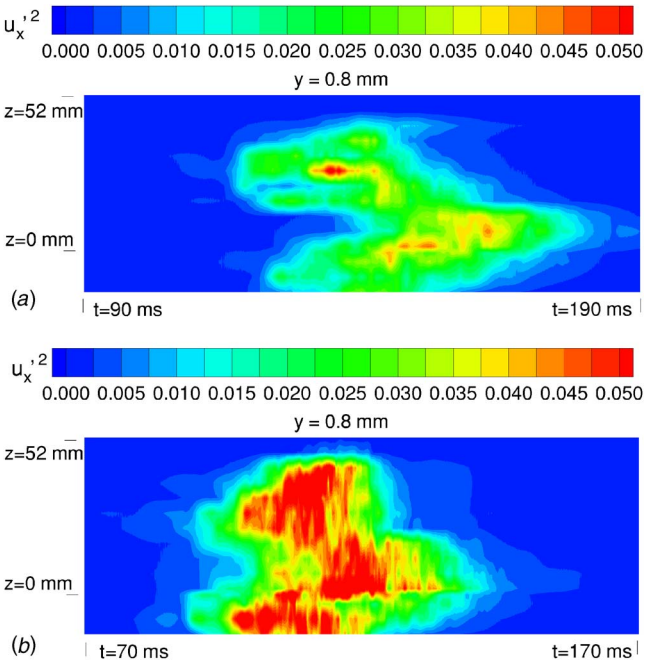

Fig. 9 Distribution of rms velocity fluctuation (*t-z* plane) (*a*) $\eta = 4.5\times10^{-6}$; (*b*) $\eta = 3.0\times10^{-6}$, low Tu, $x = 600$ mm

that are put into a turbulent motion by the disturbance convect in the downstream direction at a velocity that is faster than the fluid deeper in the local boundary layer. Thus, in a frame of reference that moves at the average streamwise velocity of the local boundary-layer fluid, the parcel of disturbed fluid propagates in the downstream direction as it spreads transversely. The time that is available for lateral spreading of the disturbance in this frame of reference increases with downstream distance. As a result, one expects the lateral extent of the turbulent region to increase with downstream distance, yielding an arrowhead shape in the t-z plane that points in the upstream direction. In the case where the disturbance of the fluid particles initiates at the surface, the parcel of disturbed fluid particles convect in the upstream direction when viewed in the above-noted reference frame. Thus, the time available for transverse spreading of the spot into the local undisturbed boundary-layer fluid increases in the upstream direction, yielding a shape in the t-z plane that approximates a downstream-pointing arrowhead.

In the present study, a puff of air injected from the test surface in the direction perpendicular to the surface serves as the disturbance for creating the turbulent spot. With the disturbance originating at the test surface, as per the aforementioned argument, one would expect the arrowhead to point downstream, hence contradicting the present experimental result. The explanation for this apparent contradiction likely resides in the fact that the puffs of air were of high velocity (approximately 35 m/s), which was found to be necessary to create turbulent spots consistently under the stabilizing influence of the strong favorable streamwise pressure gradients in the present experiments. The total momentum of the puff of air dictated by the size of the discharge hole and the discharge velocity was observed to be sufficient for this disturbance to travel from the test surface to well beyond the edge of the local boundary layer. As such, the present configuration yields a disturbance that essentially spans across the entire thickness of the boundary layer at the location of the injection hole, and as a result, either scenario for the orientation of the arrowhead shape of the turbulent spot in the z-t plane becomes plausible. Since the turbulent spots of the present study were observed to consistently have the upstream-pointing arrowhead shape, it appears that the disturbance of the boundary layer in its outer region dominates the process of breakdown into a turbulent spot, possibly in part due to the greater mean-flow kinetic energy that is available for conversion into turbulence energy in that region of the boundary layer.

The perturbation velocity field in the y-t plane (Fig. 5) displays a well-known distribution inside the turbulent spot, with a relatively larger region of negative perturbation residing above a narrower region of positive perturbation next to the surface. When this perturbation velocity field is viewed in the y-z plane, the higher streamwise acceleration case (Fig. 6(a)) reveals a more nonuniform spanwise distribution of the low- and high-perturbation velocity zones, with the two zones following an alternating pattern. Based on a recent experimental investigation of turbulent spot structures at a flow Reynolds number similar to those of the present study and using multiplane stereo particle image velocimetry, Schröder and Kompenhans [10] proposed a conceptual model of the interior of a turbulent spot as consisting of well-organized substructures in the form of longitudinal streaks in the streamwise velocity field with strong shear layers prevailing between the streaks, the destabilization of which appear to lead to the formation of hairpin-like vortices, which in turn reinforce the streaky flow structure, similar to the coherent structures observed in the inner region of turbulent boundary layers. The spanwise distribution of the perturbation velocity in Fig. 6(a) is consistent with the longitudinal velocity streaks observed by Schröder and Kompenhans in their instantaneous velocity vector fields. The fact that the low-velocity streaks in the present study consistently reside above the high-velocity streaks supports Schröder and Kompenhans' postulate that the formation of these streaks is coupled with the presence of coherent structures in the form of hairpin vortices, the legs of which reside in the shear regions between the high and low-speed streaks. These hairpin vortices would be expected to be inclined in the downstream direction under the action of the wall-normal streamise-velocity gradient. As a result, the velocity induced by each of these hairpin vortices between its two legs would result in upward transfer of low momentum fluid leading to the formation of the low-velocity streak away from the surface, and the downward velocity induced on either side of the hairpin vortex would provide the high momentum fluid that feeds the high-velocity streaks on either side of the hairpin vortex. The fact that distinct streaks are observed in the perturbation velocity field, the computation of which involves ensemble averaging, suggests the hairpin vortices within the turbulent spot to maintain a well-organized pattern in their spanwise and streamwise arrangement. While the low-velocity streaks are spatially broader than the high-velocity streaks (Fig. 6(a)), the peak velocity perturbation in the low-velocity streaks is noted to be half of the peak velocity perturbation observed in the high-velocity streaks. It is also important to point out that the outermost streak along the wingtip of the turbulent spot is consistently a low-velocity streak. This is suggestive of a unique asymmetric—one-legged—shape for the vortical coherent structures that are positioned along the wingtip. As reviewed in the Introduction, the rate of lateral spreading of turbulent spots is too high to be explained by the turbulent diffusion process alone. It has been suggested that the presence of a turbulent spot within the rotational fluid of a laminar boundary layer promotes instability leading to breakdown in the vicinity of the turbulent spot. Recently, Chong and Zhong [13] highlighted the reduction in the fullness of the local velocity profile caused by the arrival of the wingtip of a turbulent spot, with the dip observed in the profile being the direct result of the presence of negative perturbation velocity along the wingtip. While this alteration of the boundary-layer velocity profile may be considered to be in the right direction as far as more favorable conditions for instability is concerned, the presence of well-organized coherent vortical structures of asymmetric shape along the wingtips of turbulent spots as implied by the present results may also play a role in the instability induced by the turbulent spot in its vicinity. Further work is needed to reveal the details of this instability mechanism.

The perturbation velocity distribution in the y-z plane for the lower streamwise acceleration rate (Fig. 6(b)) displays a more uniform spanwise distribution of the negative and positive perturbation regions, with no evidence of an alternating pattern between the two regions. This is in fact the more common observation of the perturbation velocity field in other studies of turbulent spots, such as the recent work of Chong and Zhong [13]. The observation may be explained by greater variations in the spanwise position of the streamwise-velocity streaks from one measurement cycle to the next, for such variations would result in spanwise smearing of these streaks when they are viewed through ensemble-averaged data such as the perturbation velocity. For the case of lower streamwise acceleration, the notably higher level of rms velocity fluctuations within the high-perturbation velocity region of the turbulent spot in Figs. 7(b), 8(b), and 9(b) is consistent with this argument of streak meandering. In turbulent boundary layers, low-velocity streaks near the surface have been observed not to remain straight, but meander in the spanwise direction over ranges comparable to the streak width [20]. Furthermore, through simulations Piomelli et al. [21] observed that as the streamwise acceleration rate is increased to initiate relaminarization in a turbulent boundary layer, the velocity streaks become more elongated with fewer undulations resulting from significant decreases in spanwise fluctuations compared to the streamwise fluctuations. This observation is consistent with the present results in the turbulent spot, where the streaky pattern in the ensemble-averaged perturbation velocity distribution becomes more distinct with increasing streamwise acceleration rate.

When measured in wall units, the spacing of the low velocity streaks in Fig. 6(a) corresponds to $\lambda_z^+ \approx 250$, with the friction ve-

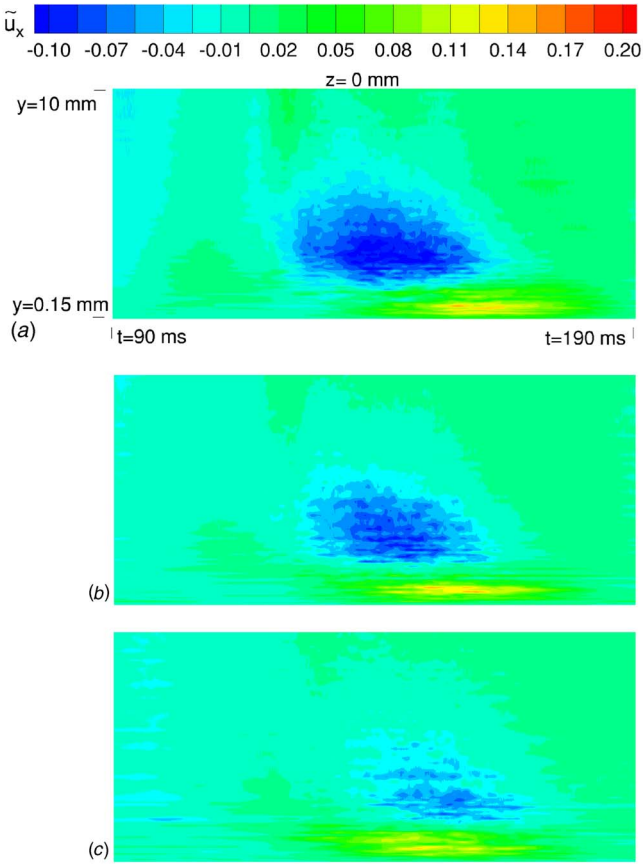

Fig. 10 Distribution of perturbation velocity (*y-t* plane) (*a*) low Tu; (*b*) moderate Tu; (*c*) high Tu, $\eta=4.5\times10^{-6}$, $x=600$ mm

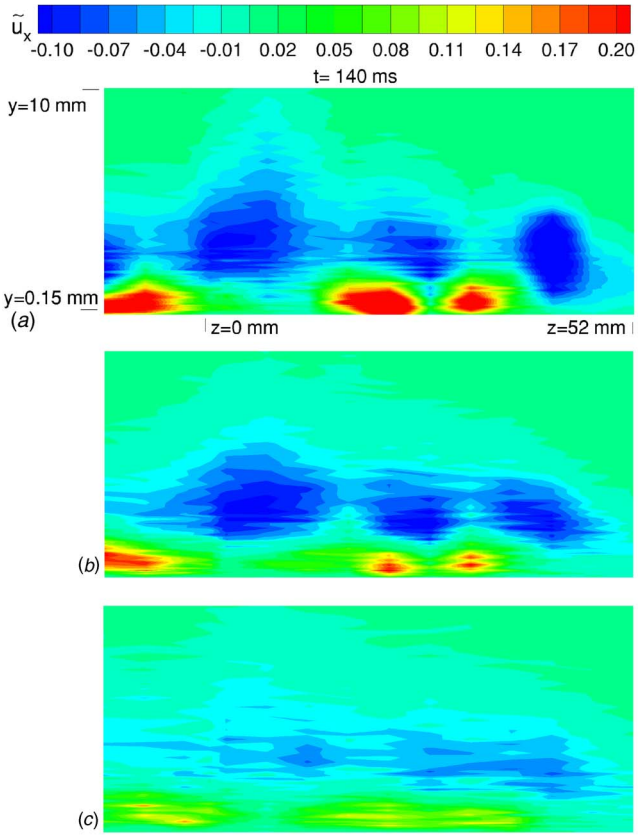

Fig. 11 Distribution of perturbation velocity (*y-z* plane) (*a*) low Tu; (*b*) moderate Tu; (*c*) high Tu, $\eta=4.5\times10^{-6}$, $x=600$ mm

locity calculated on the basis of the local wall shear stress in the undisturbed laminar boundary layer. Despite the fact that the friction velocity is calculated based on the local laminar velocity field, this value is higher than the low-velocity streak spacing in turbulent boundary layers, which has a mean value of $\lambda_z^+\approx100$ and a lognormal probability distribution with a dense range around the mean extending from about $\lambda_z^+\approx60$ to 180 [22], independent of flow Reynolds number [22] and streamwise pressure gradients [23]. However, in instances where the stabilizing influence of favorable streamwise pressure gradients is sufficiently high to initiate relaminarization of a turbulent boundary layer, the streak spacing has been found to increase two- to threefold [23,24]. The strong favorable pressure gradients in the present study may therefore provide a plausible explanation for the relatively large spanwise spacing of the streaks in the measured turbulent spots.

The favorable agreement between the present trends in the streaks of the turbulent spots and of those measured in the inner region of turbulent boundary layers, with respect to the sensitivity of their spanwise meandering and spanwise spacing to streamwise acceleration, is suggestive of a fundamental similarity between the coherent hairpin-like vortical structures in transitioning and turbulent boundary layers.

Comparison of the perturbation velocity fields in the turbulent spot for the low, moderate and high freestream turbulence cases at $x=600$ mm (Figs. 10 and 11), shows weakening of the perturbation as the freestream turbulence intensity is increased. Despite the smaller magnitudes of the velocity perturbations, the streaky structure is noted to remain generally in tact. This suggests that the hairpin vortices that are argued to play a key role in the formation of the streaks under low freestream turbulence conditions maintain their fundamental structure and spatial pattern at higher levels of freestream turbulence.

Velocity fluctuations within the turbulent spot increase as the freestream turbulence intensity is increased, especially in regions where spatial gradients in the perturbation velocity field are relatively high (Figs. 12–14). Given that these velocity fluctuations are relative to the ensemble-averaged velocity, this trend is suggestive of increased meandering (spanwise oscillation) of the streaks in the ensemble-averaged velocity field of the turbulent spot with increasing freestream turbulence. This meandering is likely part of the reason for the smearing and reduced magnitude of velocity perturbations associated with the streaks in the ensemble-averaged velocity distribution (Figs. 10 and 11) as freestream turbulence intensity is increased. Increased meandering of the streaky structures with increasing freestream turbulence would also mean that the highly organized spatial distribution of hairpin vortices inferred in the turbulent spot at low freestream turbulence conditions would be disturbed, which in turn may reduce the collective induced effect of these vortices, thereby weakening the streaky structures. The integral length scale of the freestream eddies, given in Table 1, is similar to the lateral spacing of the streaky structures for the high-turbulence case, and is about twice the lateral spacing of the streaky structures in the moderate-turbulence case. Freestream eddies that are of the order of the spacing of the streaky structures, as in the present cases, are likely to be more effective in disrupting the organization of the rows of hairpin vortices associated with the streaky velocity field, than eddies that are either much smaller than the spacing of the streaks, or compare with or exceed the overall size of the turbulent spot.

In Figs. 12–14, the extent of velocity fluctuations in the turbulent spot are noted to increase considerably as freestream turbu-

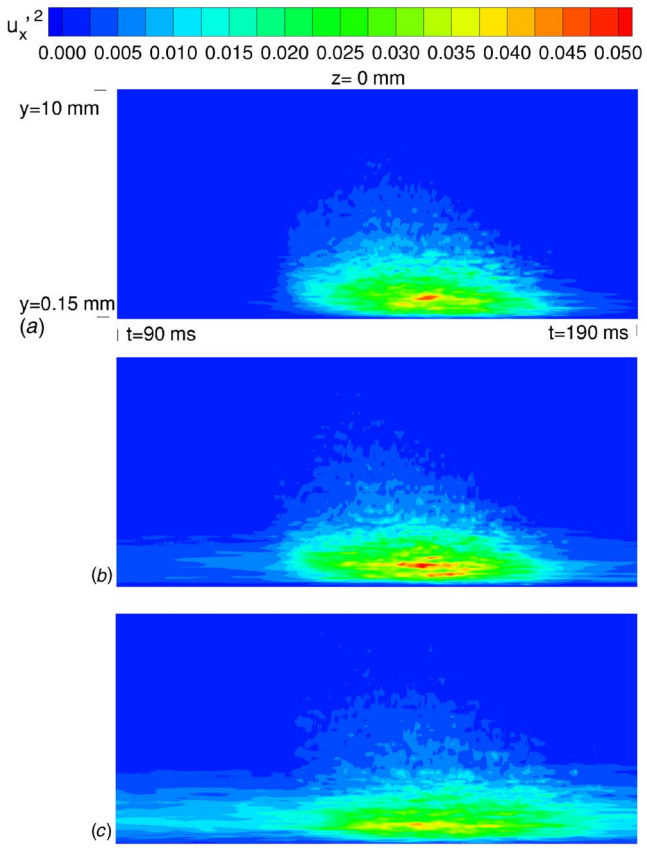

Fig. 12 Distribution of rms velocity fluctuation (*y-t* plane) (*a*) low Tu; (*b*) moderate Tu; (*c*) high Tu, $\eta=4.5\times10^{-6}$, $x=600$ mm

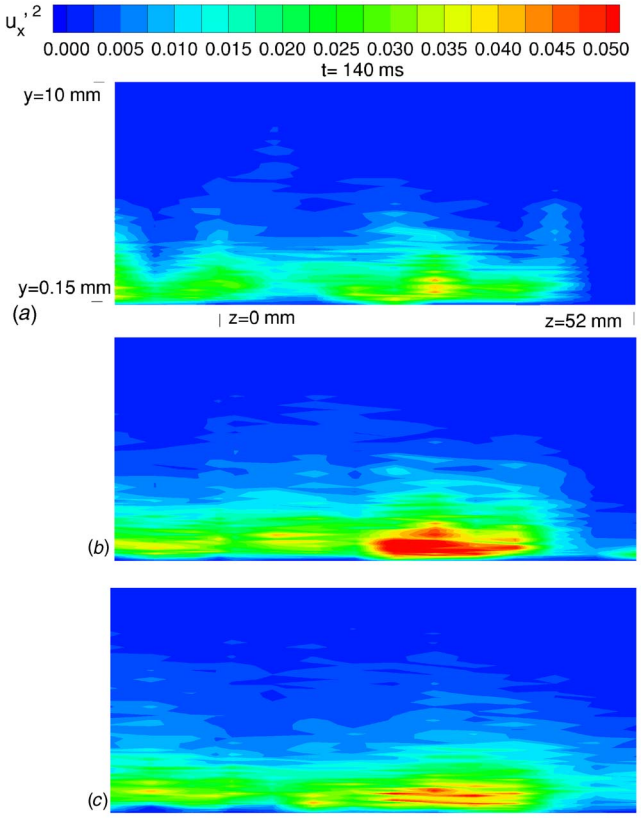

Fig. 13 Distribution of rms velocity fluctuation (*y-z* plane) (*a*) low Tu; (*b*) moderate Tu; (*c*) high Tu, $\eta=4.5\times10^{-6}$, $x=600$ mm

lence intensity is raised from low to moderate, but this trend reverses with further increase in the intensity of freestream turbulence. This reversal in trend is caused by the fact that for the high-turbulence case, the streaky structures appearing in the ensemble-averaged velocity field are considerably weaker than in the moderate-turbulence case, and thus the magnitude of the velocity fluctuations that result from their meandering is correspondingly lower.

The approximate arrowhead shape of the turbulent spot noted in Fig. 14(*a*) at low freestream turbulence is not retained at the higher levels of freestream turbulence (Figs. 14(*b*) and 14(*c*)). Instead, multiple longitudinal protrusions are observed in the rms velocity-fluctuation field on the leading and trailing sides of the turbulent spot, which are visible for both the moderate and high freestream turbulence levels. The spanwise locations of these protrusions are noted to correspond to the high-velocity streaks in the perturbation velocity field (Figs. 11(*b*) and 11(*c*)), which is expected based on the proximity of the *z-t* plane shown in Fig. 14 to the surface, and suggests the presence of an organized pattern of hairpin vortices well beyond the region of the turbulent spot that is identified through the perturbation-velocity field. It is also worth noting that as the freestream turbulence is increased, the emergence of these longitudinal trailing- and leading-edge protrusions in the rms velocity-fluctuation field is consistent with the manifestation of greater rms velocity fluctuations in the region of high-perturbation-velocity streaks halfway along the length of the turbulent spot (Figs. 13(*b*) and 13(*c*) versus Fig. 13(*a*)).

Comparison of the perturbation velocity fields for the low, moderate and high freestream turbulence cases at $x=600$ mm, in the *y-t* plane, as illustrated in Fig. 10, suggests a slightly lower streamwise convection rate for the turbulent spot in the high freestream turbulence case. For the low, moderate and high freestream turbulence cases, the lateral location of the turbulent-

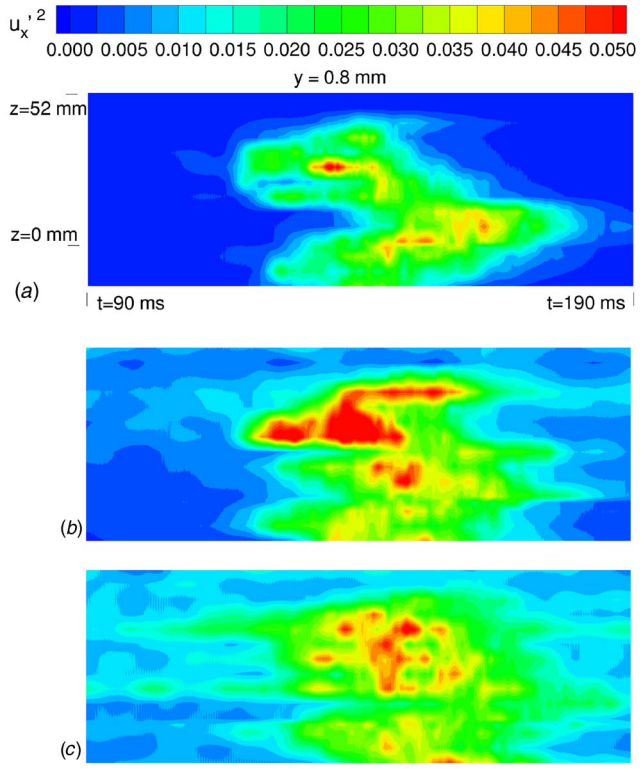

Fig. 14 Distribution of rms velocity fluctuation (*t-z* plane) (*a*) low Tu; (*b*) moderate Tu; (*c*) high Tu, $\eta=4.5\times10^{-6}$, $x=600$ mm

spot wingtip, as observed in the perturbation velocity fields at $x=600$ mm, in the y-z plane (Fig. 11), are very similar to each other. The same was observed to be true at the remaining streamwise measurement locations of $x=450$ mm and $x=750$ mm. This result suggests that the lateral spreading rate is not affected to a noticeable extent by the current variations in the freestream turbulence level. Given the significant effect of freestream turbulence on the internal structure of the turbulent spot and on the shape of its interface with the surrounding laminar fluid, the observed insensitivity of the spot transverse spreading rate to variations in freestream turbulence is not obvious. It is quite plausible that any changes that occur in the way the turbulent spot interacts with the surrounding boundary-layer fluid as freestream turbulence is increased are dominated by the highly stabilizing influence of the strong favorable streamwise pressure gradients of the present test cases. Thus, more experimentation covering a wider range of streamwise acceleration rates is needed to draw general conclusions regarding the effects of freestream turbulence on the convection and spreading rates of turbulent spots.

Conclusions

The structure of an artificially-generated turbulent spot has been studied experimentally under strongly favorable pressure gradients and three levels of freestream turbulence.

The results demonstrate the presence of a streaky structure of streamwise velocity in the turbulent spot, with high- and low-velocity streaks following an alternating pattern in the spanwise direction, the turbulent spot being consistently terminated by a low-velocity streak at the wingtip, and the high-velocity streaks residing closer to the wall than the low-velocity streaks. This pattern provides strong support for the presence of hairpin-like vortices that are spread through the turbulent spot in a well-organized pattern. Based on the sensitivity of the streaky pattern to the freestream streamwise rate of acceleration, the spanwise meandering of the streaks in the turbulent spot is argued to decrease with increasing streamwise acceleration. The spanwise spacing of the streaks is found to be somewhat higher than those observed in the inner region of turbulent boundary layers, and this difference is argued to be the result of the stabilizing influence of strong favorable streamwise pressure gradients. The favorable agreement between the present trends in the streaks of the turbulent spots and of those measured in the inner region of turbulent boundary layers, with respect to the sensitivity of their spanwise meandering and spanwise spacing to streamwise acceleration, is suggestive of a fundamental similarity between the coherent hairpin-like vortical structures in transitioning and turbulent boundary layers.

The magnitude of the velocity perturbations associated with the streaky structure is observed to decrease with increasing freestream turbulence. This is accompanied by considerable increase in the spanwise meandering of the streaks. Despite the noted effect of freestream turbulence on the internal structure of the turbulent spot, its effect on the transverse spreading and streamwise convection rates of the spot were observed to be insignificant over the measured range of freestream turbulence levels. This result is suggested to be at least partly due to the stabilizing influence of the strong favorable streamwise pressure gradients on the laminar boundary layer.

Finally, through comparison of the present results with published literature, the streamwise direction of the arrowhead shape of the turbulent spot is shown to depend on whether the disturbance is introduced near the wall or near the edge of the boundary layer. In the instance where the disturbance is introduced across the thickness of the boundary layer, as in the present study, the scenario associated with a boundary-layer-edge disturbance is observed to dominate.

Acknowledgment

The author gratefully acknowledges the financial support of Pratt and Whitney Canada.

Nomenclature

L = test-plate length, $L=1220$ mm
n = number of samples in each data record
Re_L = flow Reynolds number based on test-surface length and u_{ref}
Tu = freestream turbulence intensity
$\mathrm{Tu}_{\mathrm{ref}}$ = reference turbulence intensity at $x=-10$ mm
u = instantaneous streamwise velocity
u_l = laminar streamwise velocity
$\hat{u}$ = ensemble-averaged streamwise velocity component
$\tilde{u}$ = streamwise component of perturbation velocity, Eq. (1)
u' = rms streamwise velocity fluctuation, Eq. (2)
u_e = boundary-layer edge velocity
u_{ref} = freestream velocity measured at $y=25$ mm, $z=0$ mm, 25 mm downstream of the test-surface leading edge
u_τ = friction velocity, $u_\tau=(v(du_l/dy))_{y=0}^{1/2}$
η = streamwise acceleration parameter, $\eta=(v/u_e^2)\times(du_e/dx)$
x,y,z = streamwise, surface-normal and spanwise coordinates; $x=200$ mm, $z=0$ mm at the location of disturbance
λ_z^+ = spanwise spacing of low-speed streaks, normalized by u_τ/v
v = kinematic viscosity
Λ_{ref} = integral length scale of freestream turbulence at $x=-10$ mm

References

[1] Emmons, H. W. 1951, "The Laminar-Turbulent Transition in a Boundary Layer," J. Aeronaut. Sci., **18**, pp. 490–498.
[2] Elder, J. W. 1960, "An Experimental Investigation of Turbulent Spots and Breakdown to Turbulence," J. Fluid Mech., **9**, pp. 235–246.
[3] Wygnanski, I., Sokolov, M., and Friedman, D. 1976, "On a Turbulent Spot in a Laminar Boundary Layer," J. Fluid Mech., **78**, pp. 785–819.
[4] Coles, D., and Barker, S. J. 1975, "Some Remarks on a Synthetic Turbulent Boundary Layer," in *Turbulent Mixing in Nonreactive and Reactive Flows*, S. N. B. Murthy, ed., Plenum Press, New York, 0.75pp. 285–293.
[5] Cantwell, B., Coles, D., and Dimotakis, P. 1978, "Structure and Entrainment in the Plane of Symmetry of a Turbulent Spot," J. Fluid Mech., **87**, pp. 641–676.
[6] Gad-El-Hak, M., Blackwelder, F., and Riley, J. J. 1981, "On the Growth of Turbulent Regions in Laminar Boundary Layers," J. Fluid Mech., **110**, pp. 73–95.
[7] Charters, A. C. 1943, "Transition Between Laminar and Turbulent Flow by Transverse Contamination," NACA Technical Note No. 891.
[8] Corrsin, S., and Kistler, A. L. 1955, "Free-Stream Boundaries of Turbulent Flows," NACA Report No. 1244.
[9] Sankaran, R., Sokolov, M., and Antonia, R. A. 1988, "Substructures in a Turbulent Spot," J. Fluid Mech., **197**, pp. 389–414.
[10] Schröder, A., and Kompenhans, J. 2004, "Investigation of a Turbulent Spot Using Multi-Plane Stereo Particle Image Velocimetry," Exp. Fluids, **36**, pp. 82–90.
[11] Makita, H., and Nishizawa, A. 2001, "Characteristics of Internal Vortical Structures in a Merged Turbulent Spot," J. Turbul., **2**, pp. 1–14.
[12] Zilberman, M., Wygnanski, I., and Kaplan, R. 1977, "Transitional Boundary Layer Spot in a Fully Turbulent Environment," Phys. Fluids, **20**, pp. 258–271.
[13] Chong, T. P., and Zhong, S. 2003, "On the Three-Dimensional Structure of Turbulent Spots," ASME Paper No. GT-2003-38435.
[14] Schubauer, G. B., and Klebanoff, P. S. 1956, "Contributions on the Mechanics of Boundary Layer Transition," NACA Report No. 1289.
[15] Moretti, P. H., and Kay, V. M. 1965, "Heat Transfer in Turbulent Boundary Layer With Varying Free-Stream Velocity and Varying Surface Temperature—An Experimental Study," Int. J. Heat Mass Transfer, **8**, pp. 1187–1202.
[16] Jones, V. P., and Launder, B. E. 1972, "Some Properties of Sink-Flow Turbulent Boundary Layers," J. Fluid Mech., **56**, pp. 337–351.
[17] Escudier, M. P., Abdel-Hameed, A., Johnson, M. W., and Sutcliffe, C. J. 1998, "Laminarization and Retransition of a Turbulent Boundary Layer Subjected to a Favourable Pressure Gradient," Exp. Fluids, **25**, pp. 491–502.
[18] Zhong, S., Kittichaikarn, C., Hodson, H. P., and Ireland, P. T. 1998, "Visualization of Turbulent Spots Under the Influence of Adverse Pressure Gradients," *Proceeding of the 8th International Conference on Flow Visualization*, Italy.
[19] Wu, X., Jacobs, R. G., Hunt, J. C. R., and Durbin, P. A. 1999, "Simulation of Boundary Layer Transition Induced by Periodically Passing Wakes," J. Fluid

Mech., **398**, pp. 109–153.
[20] Kline, S. J., and Robinson, S. K. 1988, "Quasi-Coherent Structures in the Turbulent Boundary Layer: Part I. Status Report on a Community-Wide Summary of the Data," Near Wall Turbulence, 1988 Zoran Zarić Memorial Conference, S. J. Kline and N. J. Afghan, ed.
[21] Piomelli, U., Balaras, E., and Pascarelli, A. 2000, "Turbulent Structures in Accelerating Boundary Layers," J. Turbul., **1**, pp. 1–16.
[22] Smith, C. R., and Metzler, S. P. 1983, "The Characteristics of Low-Speed Streaks in the Near-Wall Region of a Turbulent Boundary Layer," J. Fluid Mech., **129**, pp. 27–54.
[23] Schraub, F. A., and Kline, S. J. 1965, "A Study of the Structure of the Turbulent Boundary Layer With and Without Longitudinal Pressure Gradient," Report No. MD-12, Thermosciences Division, Stanford University.
[24] Talamelli, A., Fornaciari, N., Westin, K. J. A., and Alfredsson, P. H. 2002, "Experimental Investigation of Streaky Structures in a Relaminarizing Boundary Layer," J. Turbul., **3**, pp. 18–30.

Development of a Nozzle-Flapper-Type Servo Valve Using a Slit Structure

Kenji Kawashima

Chongho Youn

Toshiharu Kagawa
e-mail: kkawashi@pi.titech.ac.jp

Precision and Intelligence Laboratory,
Tokyo Institute of Technology,
4259 Nagatsuta, Midori-ku,
Yokohama, Kanagawa Prefecture, 226-8503
Japan

Pneumatic servo valves play a significant role in power transmission and system control using a pressurized gas. When pressurized air passes through servo valves, noise and pressure fluctuations are often experienced at the downstream side, and such fluctuations limit the value's efficiency. In this paper, a novel four-port nozzle-flapper-type servo valve using a slit structure instead of an orifice plate is proposed. The slit structure maintains a laminar flow condition, and this provides an opportunity for the minimization of the noise and pressure fluctuations. The slit structure is fabricated using etching technology. The flow characteristics of the slit are investigated theoretically and experimentally in order to evaluate the design specifications and characteristics of the valve. The experimental results indicated that the noise level decreased by approximately 15 dB *and could reduce the pressure fluctuation by 75%, compared with the previous valve. It is felt that the valve is more effective than many current valves.* [DOI: 10.1115/1.2717617]

1 Introduction

Pneumatic servo systems, such as actuators in process automation systems [1], or suspensions to isolate vibration [2], have been widely used in industry. The main reason for this is that air has several advantageous properties, namely, compressibility, high power ratio, and clean energy power transmission, and nonmagnetism.

Pneumatic servo valves are needed in systems to transmit power through a gas under pressure and to control the system. When pressurized air passes through a valve, considerable noise and pressure fluctuation occur at the downstream side. This is not favorable for precision pressure control. Therefore, reduction of noise and pressure fluctuation originating from the valve are required.

These phenomena have been investigated both analytically and experimentally [3,4]. In addition, several methods, such as the use of diffusers [5], wrapping pipe with sound-damping materials [6], changing the plug structure [7], and the use of silencers [8] have been developed to reduce noise and pressure fluctuation.

However, with these methods, when the flow rate increases, the flow might become turbulent. In some cases, sonic flow occurs even when the pressure ratio is lower than 0.528. Turbulent and sonic flow can generate considerable noise and shock waves.

In this paper, we have developed a slit structure that can maintain a laminar flow. The noise and pressure fluctuation are reduced by using the structure. A novel nozzle-flapper-type servo valve using a slit structure is proposed. The slit structure is fabricated and installed in the valve instead of an orifice. The slit structure is contained in Sec. 2, and the characteristics of the slit are investigated in Sec. 3. The procedure used to design the valve is described in Sec. 4. Finally, the effects of the noise and pressure fluctuation on the valve are investigated experimentally.

2 Newly Developed Slit Structure

Figure 1 shows a schematic drawing and Fig. 2 shows a 3D sectional cut view of the developed structure. The slit structure consists of three elements, an upper disk, a case, and a lower disk.

The upper part of Fig. 1 shows the top view of the lower disk. The disk consists of a lower surface of the radial slit and an exhaust port. The lower part of Fig. 1 shows the cross section of the structure. The upper disk consists of a flow inlet and an upper surface of the radial slit. The case covers the upper and lower disk.

The compressed air enters from the center of the upper disk and is exhausted outward through the radial slits to the port. Etching technology is used to make very small slits and makes the flow laminar. The parameters of the fabricated slit structure are listed in Table 1. Slit structures having three different heights were constructed. The gap of the return path is comparatively large compared to that of the slit.

3 Characteristics of the Slit Structure

The flow rate characteristics of the slit structure are investigated theoretically under the assumptions that the flow is laminar and passes through the slit under isothermal conditions.

The relationship between the pressure drop dP and the average flow velocity $\bar{u}$ is given by the next equation

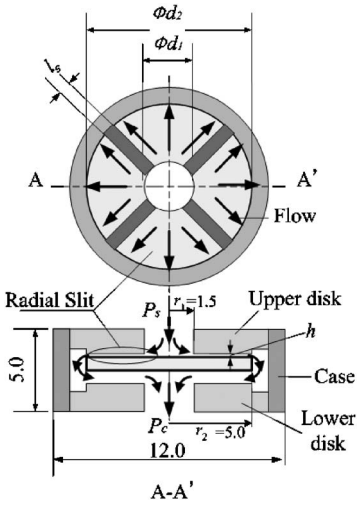

Fig. 1 Drawing of the slit structure

Contributed by the Fluids Engineering Division of ASME for publication in the JOURNAL OF FLUIDS ENGINEERING. Manuscript received November 11, 2005; final manuscript received November 6, 2006. Review conducted by Kenneth Breuer.

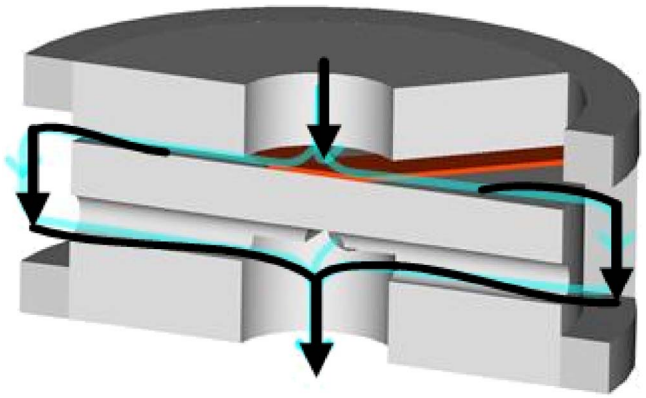

Fig. 2 3D sectional cut view of the developed slit

$$dP = -\frac{12\mu\bar{u}}{h^2}dr \tag{1}$$

which comes from the Navier-Stokes equation of steady state laminar flow between parallel plates [9]. In Eq. (1), μ stands for the viscosity of the air and h is the height of the parallel slit. The following equation is obtained from the continuity equation:

$$(\bar{u}A\rho)_{r_1} = (\bar{u}A\rho)_r \quad r_1 \leqslant r \leqslant r_2 \tag{2}$$

where $\bar{u}$, A, and ρ are the velocity, the cross-sectional area, and density with respect to radii r_1 and r accordingly.

Using the state equation of gases

$$P = \rho R\theta \tag{3}$$

such that $\rho = P/R\theta$ where R and θ are the gas constant and average temperature of air, respectively. Equation (1) now takes the form

$$\bar{u}_r = \frac{(\bar{u}A\rho)_{r_1}}{(A\rho)_r} = \frac{(\bar{u}AP)_{r_1}}{(AP)_r} \tag{4}$$

The effective area of the slit A_r at radius r is given by the following equation:

$$A_r = h(2\pi r - 4l_s) \tag{5}$$

where l_s indicates the width of the spacer used to maintain the height. Substituting Eq. (4) into Eq. (1) yields the following equation:

$$\frac{dP}{dr} = -\frac{12\mu(\bar{u}AP)_{r_1}}{h^2(AP)_r} \tag{6}$$

The pressure drop in the slit is given as

$$\Delta P = \int_{r_1}^{r_2} dP \tag{7}$$

The extra pressure drop ΔP_i must be considered in the inlet region [10]. This is evaluated using the following equation:

$$\Delta P_i = \xi\frac{\rho\bar{u}_{r_1}^2}{2} \tag{8}$$

where ξ is the friction coefficient, whose value 0.45 was chosen to approximately match the experimental results. If the flow rate G is given, the inlet average velocity $\bar{u}_{r_1}$ is obtained from the equation

Table 1 Parameters of the slit structure

d_1 (mm)	d_2 (mm)	l_s (mm)	h (μm)
3	10	1	30, 45, 60

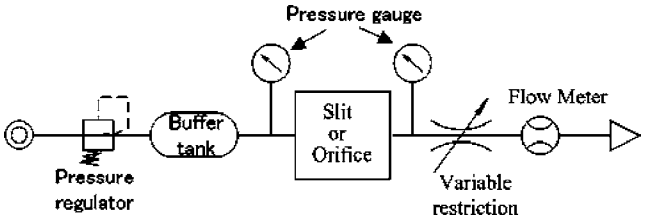

Fig. 3 Experimental apparatus to measure flow characteristics

$G = (\rho\bar{u}A)_{r_1}$. As a result, the total pressure drop ΔP_{total} is given by adding the losses in the slit ΔP and the losses associated with the inlet region ΔP_i,

$$\Delta P_{\text{total}} = \Delta P + \Delta P_i \tag{9}$$

The flow characteristics of the slit were calculated by Eq. (9) using the parameters listed in Table 1. The supply pressure was set at 500 kPa, and the volumetric flow rate $Q = G/\rho$ was obtained by varying the outlet pressure.

The characteristics were measured experimentally in advance using the experimental apparatus shown in Fig. 3. The outlet pressure was varied by a restriction downstream of the slit. The pressure and flow rate were measured using a pressure gauge (Nagano Keiki Co,. LTd., AA10-121) with an uncertainty of 0.5% and a gas flow meter (Shinagawa corp. DC-2C) with an uncertainty of 2%.

The flow characteristics are shown in Fig. 4. The plotted data show the experimental results and the solid lines show the results of calculation. The results clarify that the experimental and calculated results agree well when the downstream pressure is higher than 400 kPa. Almost the same results were obtained with the different supply pressures. Therefore, it became clear that the calculation is effective for designing the slit when the pressure drop is less than 100 kPa.

4 Newly Developed Servo Valve Using the Slit Structure

In the pneumatic position and force control systems, nozzle-flapper-type servo valves are normally used. This is because the valve has high precision and a quick response due to their simple construction. A high sensitivity and wide frequency range can be achieved with the valve.

Pressure control systems with nozzle-flapper elements are generally approximated to a first order lag system to the input current assuming an isothermal state change for the air in the load chamber [11,12].

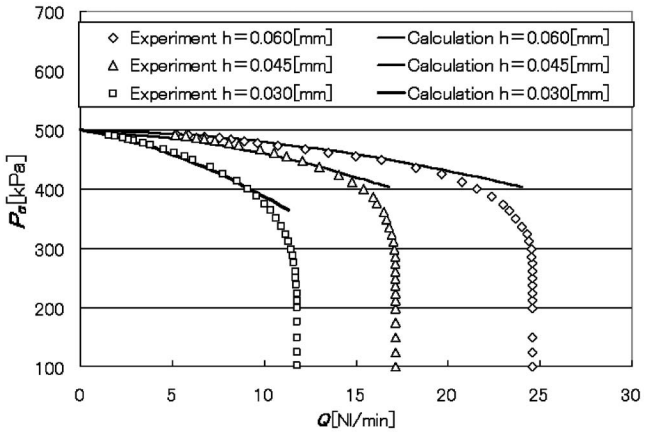

Fig. 4 Flow characteristics of the slit structure

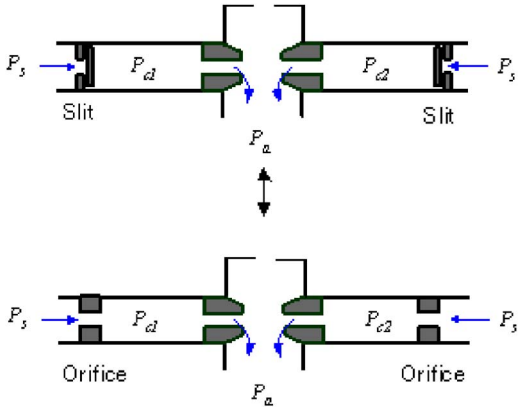

Fig. 5 Structure of four-port nozzle-flapper type servo valve (top: proposed valve; bottom: ordinal valve)

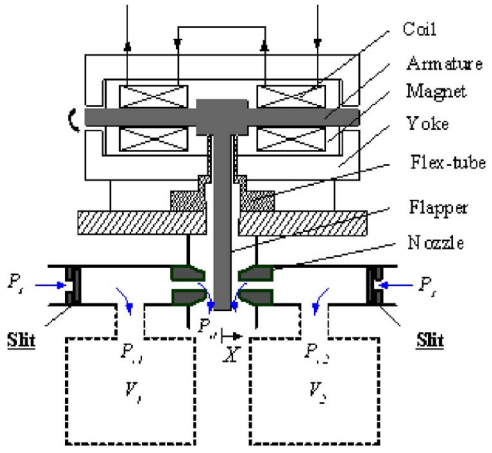

Fig. 7 Developed four-port nozzle-flapper-type servo valve with a slit structure

A four-port nozzle-flapper-type servo valve using the newly developed slit structure was proposed. The slit structure was fabricated and installed in the valve in place of an orifice, as shown in Fig. 5.

4.1 Design Procedure. The procedure used to determine the inner diameter, the outer diameter and the height of the slit structure in developing the servo valve is explained as follows:

First, the valve was designed under the required control pressure P_c and the maximum flow rate G at a supply pressure. The laminar flow in the slit is maintained. In this regional, the Reynolds number R_e

$$R_e = \frac{Gl_h}{\mu A} \leqslant 2300 \tag{10}$$

where l_h is the characteristic length given by

$$l_h \cong 4\frac{2\pi r_2 h}{2(2\pi r_2 + h)} \cong 2h \quad (r_2 \gg h) \tag{11}$$

Therefore, the following equation is derived from Eqs. (5), (10), and (11):

$$\frac{2G}{\mu(2\pi r_2 - 4l_s)} \leqslant 2300 \tag{12}$$

As a result, the outer diameter of the slit $d_2 = 2r_2$ is determined from Eq. (12).

The following equation is given by substituting Eq. (5) into Eq. (6) and transforming Eq. (7),

$$\int_{r_1}^{r_2} PdP = \int_{r_1}^{r_2} \frac{-12\mu(\bar{u}AP)_{r_1}}{2h^3(\pi r - 2l_s)} dr \tag{13}$$

As a result, the next equation is derived from Eqs. (8), (9), and (13),

$$P_c = \sqrt{P_s^2 - \frac{12\mu R\theta_a G}{h^3\pi} \ln\left(\frac{2r_2 - 2l_s/\pi}{2r_1 - 2l_s/\pi}\right)} + 0.45\frac{G^2}{8h^2(\pi r_1 - 2l_s)^2} \tag{14}$$

When the maximum flow rate is $G = 3.45 \times 10^{-4}$ kg/s and the width of the spacer is $l_s = 1.0 \times 10^{-3}$ m, the outer diameter of the slit d_2 must be larger than 6.5×10^{-3} m from Eq. (12) since the viscosity of air at 293 K is $\mu = 18.09 \times 10^{-6}$ Pa·s. As a result, the outer diameter $d_2 = 1.0 \times 10^{-2}$ m is selected in order to make the slit small.

When the supply pressure P_s and control pressure P_c are given as 500 kPa and 450 kPa, respectively, the relationship between the height h and the inner diameter d_1 is shown in Fig. 6. The inner diameter becomes larger as the height of the slit becomes thinner. The height h was set to 0.06 mm, and the inner diameter d_1 was set to 3.0 mm, as shown by the dotted line in Fig. 6, in consideration of the difficulty of the fabrication.

Finally, the Reynolds number at the inlet region is calculated in order to confirm that the flow is maintained as laminar. Based on a previous study, the velocity is known to decrease in the slit because the flow channel gradually increases [13]. The Reynolds number is approximately 1500 at the inlet region. Therefore, it is confirmed that the flow remains laminar. This slit structure was used in the new servo valve.

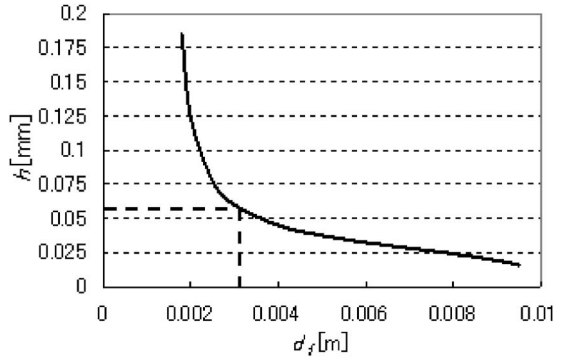

Fig. 6 Relationship between the height and the inner diameter of the slit structure

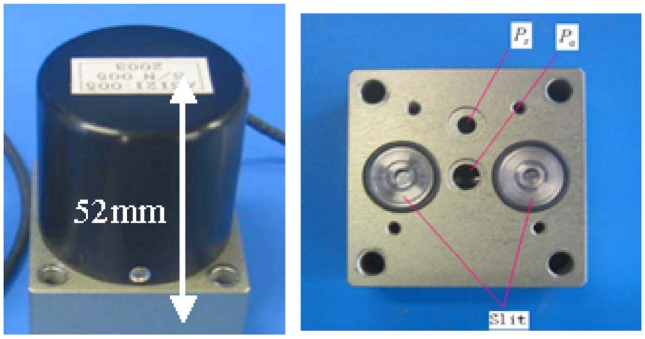

Fig. 8 Photograph of the developed four-port nozzle-flapper-type servo valve (left: overall view; right: bottom side)

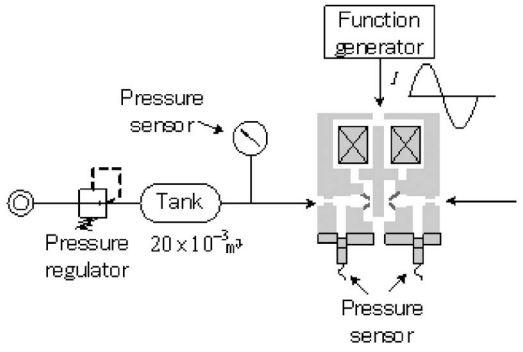

Fig. 9 Experimental apparatus

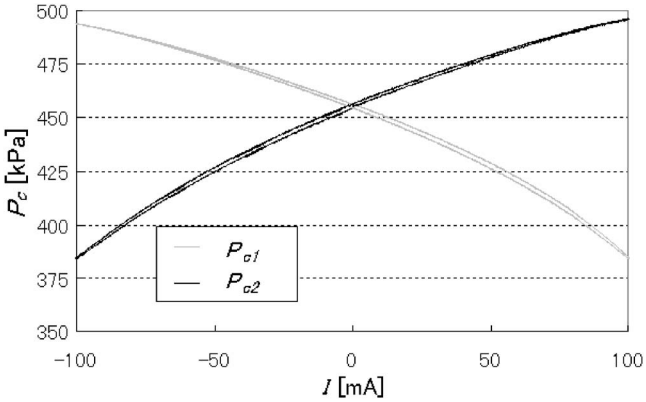

Fig. 11 Static characteristics of the developed servo valve

4.2 Developed Nozzle-Flapper-Type Serve Valve. The newly developed four-port nozzle-flapper-type servo valve is shown in Fig. 7. The valve has two supply ports, two control ports, and an exhaust port. The slit structures were installed instead of orifice plates at the supply ports. In the figure, P_s and P_a denote the supply pressure and atmospheric pressure, respectively. The armature-flapper is moved by a torque motor consisting of a coil and vertically arranged magnets. Movement of the flapper changes the distances between the flapper and the nozzles, which creates different pressures, P_{c1} and P_{c2}, in the control ports. In the steady state, the differential pressure, $\Delta P = P_{c1} - P_{c2}$, is proportional to the input current when the control ports are closed.

Figure 8 shows a photograph of the newly developed valve. The slit structure was installed in the servo valve. The height, width, and length of the valve are 52 mm, 43 mm, and 43 mm, respectively. The size of the valve is almost the same as a conventional servo valve.

5 Characteristics of the Servo Valve

5.1 Static Characteristics. The static characteristics of the servo valve were investigated experimentally. The experiments were performed at a constant ambient temperature of 293 K and a supply pressure of 500 kPa.

The experimental apparatus is shown in Fig. 9. The pressure sensors (TOYODA Co,. Ltd., PMS-5M2-1M), having a frequency response of up to 5 kHz with the uncertainty of 0.5% were attached directly to the control ports. The steady-state control pressures of the previous valve and the developed valve, P_{c1} and P_{c2}, were plotted against input current I, as shown in Figs. 10 and 11. With both of the control ports closed, the input current was varied using a sine waveform varying between ±100 mA at 1/120 Hz.

Figure 11 indicates that even if some hysteresis exists, there is an almost linear relationship between the input current and the differential pressure. The results are approximately the same as for a previous servo valve [12].

5.2 Dynamic Characteristics. The frequency response was obtained by superimposing a 5 mA swept sinusoidal current on a biased zero input current and is summarized in the bode diagram shown in Fig. 12. The inputs were the currents to the valve and the outputs were the pressures at the control port. From this bode diagram we can see that the gains descended to 3 dB at approximately 100 Hz.

The flow rate transfer dynamic characteristics of the slit structure are considered. Numerous studies have been conducted on flow rate dynamic characteristics in narrow pipes and thin slits [10,14]. The dynamic characteristics can be evaluated by a dimensionless quantity called the Womersley number W_n, which presents the ratio of frequency f to the viscosity μ [15]. When $W_n \leqslant 1$, the flow becomes pseudostatic; this means that the dynamic characteristics of f is treated as the same as the steady flow. With the slit used in this research for the condition of $f=100$ Hz and $P_c=500$ kPa, we have

$$W_n = l_h \sqrt{\frac{2\pi f \rho}{\mu}} \cong 0.16 \qquad (14')$$

This estimation guarantees that the slit structure used in this research has enough response.

The result shown in Fig. 11 is approximately the same as a conventional nozzle-flapper type servo valve [12]. The response is dominated by the movement of the flapper.

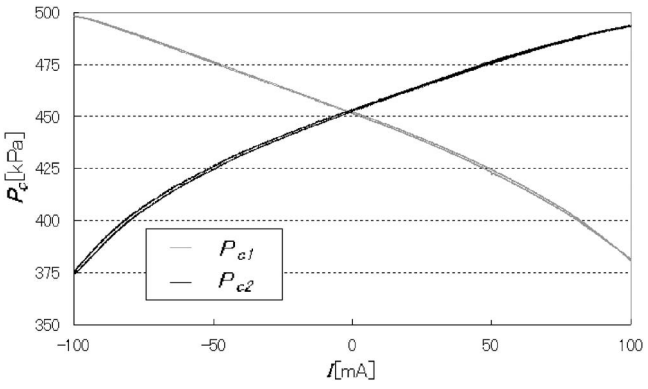

Fig. 10 Static characteristics of the previous servo valve

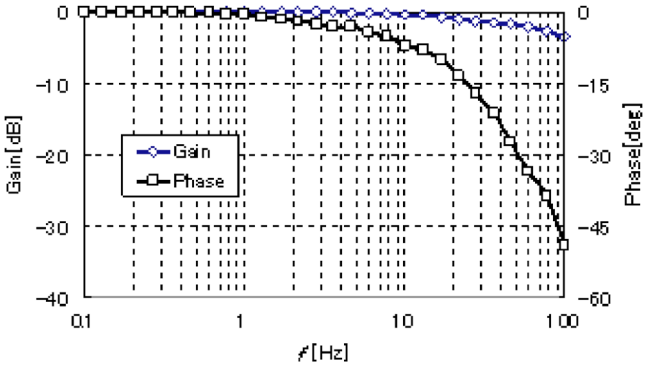

Fig. 12 Frequency response of the differential pressure measured at 0 mA dc input superimposed by a ±5 mA sinusoid

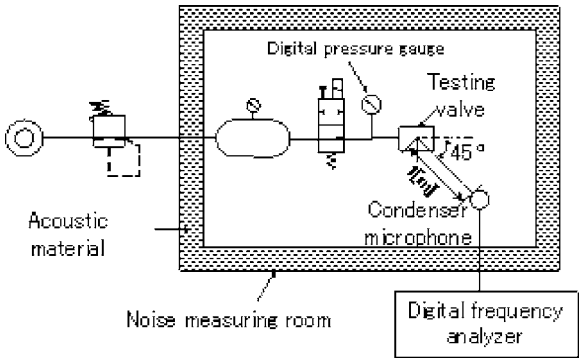

Fig. 13 Experimental system to measure noise

5.3 Noise Level. The noise level of the valve was measured using the room shown in Fig. 13, according to the Japanese Industrial Standards (JIS) exhaust sound reducing characteristics [16]. The room is covered with acoustic material in order to maintain the background noise level at 30 dB. A condenser microphone was placed in the room at an angle of 45 deg from the center axis of the valve. The distance from the valve to the microphone was 1.0 m. The noise level was measured by the microphone, and the sound spectrum was analyzed with a digital frequency analyzer settled outside the noise measuring room.

The noise levels of the previous servo valve, which used orifice plates, and the newly developed valve with the slit structure were compared. We confirmed in advance that the flow characteristics of both valves were approximately the same.

The experiment was performed by maintaining the current input to the valve at 0 mA and varying the supply pressure. The experimental results are shown in Fig. 14. The results indicate that the noise level decreased approximately 15 dB in the newly developed valve.

5.4 Pressure Fluctuation. The pressure fluctuation at the control ports of the previous and newly developed valves was measured by attaching a chamber to the port. The volume of the chamber was 1.0×10^{-4} m^3 and the supply pressure was set to 500 kPa. The input to the valve was 0 mA. The average pressure in the chamber was 455 kPa under this condition. The differential pressure between the pressure 455 kPa, which was given by a precision regulator, and the pressure in the chamber was measured using a differential pressure sensor.

The experimental results are shown in Fig. 15. Pressure fluctuation with an amplitude of 40 Pa was observed in the previous valve, whereas that of the newly developed valve was only 10 Pa. The newly developed valve reduced the pressure fluctuation by 75%, as compared with the previous valve. The root mean square values of the pressure for the previous valve $\Delta P_{\mathrm{rms\_prev}}$ and the new valve $\Delta P_{\mathrm{rms\_new}}$ were calculated from the data shown in Fig. 15. Then, we obtained $20\log(\Delta P_{\mathrm{rms\_new}}/\Delta P_{\mathrm{rms\_prev}})$. The value was −18.4 dB which has high relationship between the results shown in Fig. 14. We confirmed that the same tendency could be observed even when the average pressure was changed.

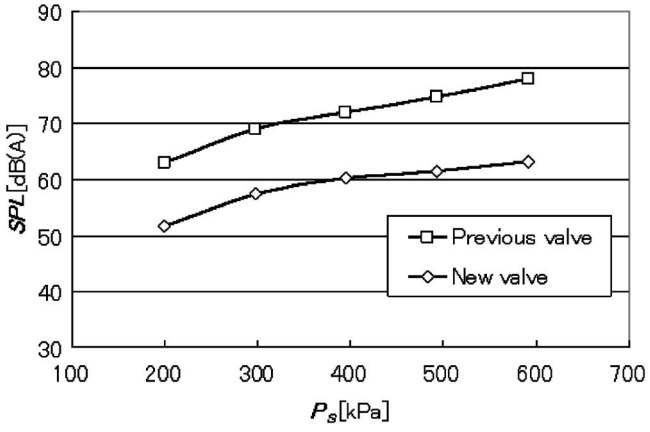

Fig. 14 Noise level of previous valves and the present valve

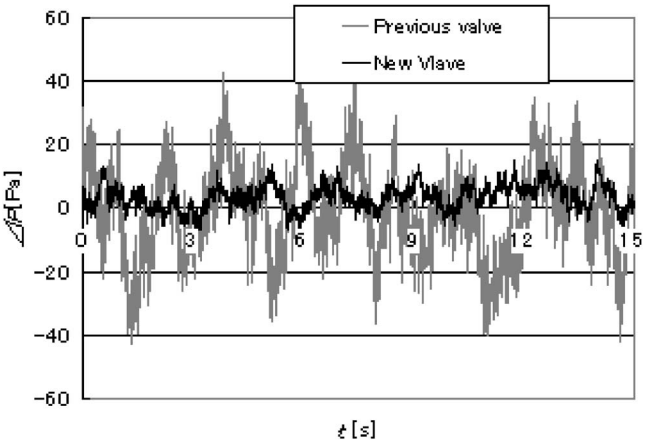

Fig. 15 Fluctuation of pressure

6 Conclusion

This paper proposed a new four-port nozzle-flapper-type servo valve using slit structures instead of orifice plates. The slit structure was fabricated using etching technology and the flow characteristics of the slit were investigated both theoretically and experimentally. In addition, the design procedure of the valve was developed. The valve was then constructed, and its characteristics were measured. The results indicated that the noise level decreased by approximately 15 dB and could reduce the pressure fluctuation by 75%, compared with the previous valve. The effectiveness of the newly developed valve was thus demonstrated.

Acknowledgment

The authors are grateful to Professor H. Muramatsu of Numazu College of Technology and Mr. K. Sasaki of PSC Co. Ltd., for their advice and support.

References

[1] Barber, A., 1997, *Pneumatic Handbook*, 8th ed., Elsevier Advanced Technology.
[2] Wakui, S., 2003, "Incline Compensation Control Using an Air-Spring Type Isolated Apparatus," Precis. Eng., **27**, pp. 170–174.
[3] Lighthill, M. J., 1952, "On Sound Generated Aerodynamically 1: General Theory," Proc. R. Soc. London, Ser. A, **211**, pp. 564–587.
[4] Reethof, G., 1988, "A Theoretically Based Valve Noise Prediction Method for Compressible Fluids," ASME J. Vib., Acoust., Stress, Reliab. Des., **108**, pp. 329–338.
[5] Boger, H. W., 1971, "Designing Valves and Downstream Devices as Low Noise Packages," Heat./Piping/Air Cond., **43**(10), pp. 82–86.
[6] Bell, L. H., and Bell, D. H., 1993, *Industrial Noise Control*, Marcel Dekker Inc., New York.
[7] Amini, A., and Owen, I., 1995, "A Practical Solution to the Problem of Noise and Fluctuation in a Pressure-Reducing Valve," Exp. Therm. Fluid Sci., **10**, pp. 136–141.
[8] Davies, P. O. L. A., Harrison, M. F., and Collins, H. J., 1997, "Acoustic Modeling of Multiple Path with Experimental Validations," J. Sound Vib., **200**(2), pp. 195–225.
[9] Nakayama, Y., and Boucher, R. F. B., 1999, *Introduction to Fluid Mechanics*, Butterworth-Heinemann.
[10] Stone, C. R., and Wright, S. D., 1994, "Nonlinear and Unsteady Flow Analysis of Flow in a Viscous Flowmeter," Trans. Inst. Meas. Control (London), **16**(3), pp. 128–141.

[11] Kagawa, T., 1985, "Heat Transfer Effects on the Frequency Response of a Pneumatic Nozzle Flapper," ASME J. Dyn. Syst., Meas., Control, **107**, pp. 332–336.
[12] Wang, T., Cai, M., Kawashima, K., and Kagawa, T., 2005, "Model of a Nozzle-Flapper Type Pneumatic Servo Valve Including the Influence of Flow Force," Int. J. Fluid Power, **6**, pp. 33–43.
[13] Youn, C., Kawashima, K., and Kagawa, T., 2003, "Fundamental Analysis of Super Low Noise Control Restriction for Compressible Fluid," The 18th I.C.H.P., pp. 387–394 September (2003).
[14] Kawashima, K., Kato, T., Yamazaki, Y., Yanagisawa, M., and Kagawa, T., 2005, "Development of Slit Type Pressure Differentiator Using an Isothermal Chamber," Meas. Sci. Technol., **16**, pp. 1150–1156.
[15] Womersley, J. R., 1952, "Method for the Calculation of Velocity Rate of Flow and Viscous Drag in Arteries When the Pressure Gradient is Known," J. Physiol. (London), **127** pp. 553–563.
[16] JIS B8379, The pneumatic silencer, pp. 653–657 (1995) in Japanese.

A Quasi-Analytical Method for Fluid Flow in a Multi-Inlet Collection Manifold

Ephraim M. Sparrow

Jimmy C. K. Tong

Laboratory for Heat Transfer
and Fluid Flow Practice,
Department of Mechanical Engineering,
University of Minnesota,
Minneapolis, MN

John P. Abraham
Laboratory for Heat Transfer
and Fluid Flow Practice,
School of Engineering,
University of St. Thomas,
St. Paul, MN

This paper sets forth a fully validated quasianalytical method for determining the fluid flow in a multi-inlet collection manifold. The method is based on first principles, which are the conservation laws for mass and momentum. Although it is necessary to use numerical means to extract results from the model, the solution task is accomplished by the use of a spreadsheet, without the need for complex software or large computer assets. The validation of the method was achieved by comparing the key results with those from a numerically exact simulation. The comparison included both local results and global results. For the local results, the accuracy of the model was found to be in the 1% range, while the global results from the model were accurate to about 4%. The investigated manifold was a case study drawn from a problem involving thermal management of electronic equipment, in which an array of coldplates discharged spent air into the manifold. It was found, from both the quasianalytical method and the numerical simulation, that there is a variation in the per-coldplate flowrate due to axial pressure variations in the manifold. These pressure variations can be attributed to the streamwise acceleration of the manifold flow due to the accumulation of the flow entering the manifold from the coldplate array. The utility of the quasianalytical method was further demonstrated by applying it to a number of other cases. In particular, the method was used to design a manifold capable of producing a uniform mass flowrate through all of its ports.
[DOI: 10.1115/1.2717620]

1 Introduction

Manifolds are a significant component in a wide variety of fluid-flow systems. Two types of commonly occurring manifolds may be identified. One type, the distribution manifold, is a chamber in which there is a single fluid inlet and numerous fluid exits. The other, the collection manifold, has numerous fluid inlets and a single fluid exit. In practice, distribution and collection manifolds are used in tandem. The interconnection between the manifolds is made by flow passages which extend from the exits of the distribution manifold to the inlets of the collection manifold.

Despite the fact that manifolds have been a significant component of fluid-flow systems for at least a century, they continue to be the subject of continuing research because of their involvement in devices based on new technologies. In this regard, it is relevant to examine the recent literature to assess the application areas in which manifolds play a significant role. Perhaps the most outstanding new technology in which manifolds have an essential role is fuel cells [1–4]. The advent of microfabrication techniques has enabled the creation of microdimension fluid-flow devices that involve manifolds [5–10]. Chemical assessment, analysis, and reaction devices frequently make use of fluid–flow manifolds [11,12]. The most enduring and still most common application of manifolds is in automotive and other propulsion devices [13–19]. Manifolds are widely used for flow distribution and collection in heat exchangers [6,20,21]. Polymer processing equipment may also incorporate manifolds for distribution of the liquid melt in dies [22]. This brief review underscores the importance of manifolds in contemporary technology and testifies to the need for continued research.

The performance of manifold systems is usually quantified by the degree of uniformity of the flowrates in the respective interconnecting passages and the overall pressure drop across the system. In the manifold design problem, these metrics of performance are needed prior to the fabrication and installation of the manifold system. Owing to the complexity of the patterns of fluid flow in manifold systems, numerical simulation appears to be an attractive means of evaluating these metrics. However, experience has shown [23] that even when a supercomputer is employed for the numerical work, several days of computer time may be required to obtain a single solution. A primary cause of the computational burden is that many manifold problems involve multiple dimensional scales of flow which must be resolved.

There is therefore ample motivation for the development of models capable of providing highly accurate results for the performance metrics without the need for the powerful computer assets required for direct numerical simulation. The major goal of this paper is the development and implementation of such a model. To establish the accuracy of the model, a complementary numerical simulation has been performed. The numerical simulation not only serves as a standard for comparison, but it provides a rich harvest of new results in addition to the performance metrics. In particular, the simulation results reveal details of the manifold flow field that appear to not have been previously demonstrated in the published literature.

The main approach to be used here is to frame the development of the method in terms of a case study. In addition, a second application of the method has been set forth in Appendix B and literature citations to other successful implements are provided.

The method is developed here in connection with the thermal management of a heat-generating airborne radar system. The physical situation to be investigated is pictured in Fig. 1. As seen there, a 20-inlet collection manifold is fed by the discharge of an array of air-cooled coldplates whose purpose is to absorb the energy dissipated by electronic equipment. The air coolant is taken from the surrounding ambient. Each inlet of the collection manifold is mated with a corresponding coldplate. The flow-pressure drop characteristic of each individual coldplate is identical to the others and is known from a separate experimental determination [23]. What is unknown is the rate of fluid flow passing through the individual coldplates. That flowrate is determined in part by the

Contributed by the Fluids Engineering Division of ASME for publication in the JOURNAL OF FLUIDS ENGINEERING. Manuscript received March 13, 2006; final manuscript received October 5, 2006. Assoc. Editor: Malcolm J. Andrews.

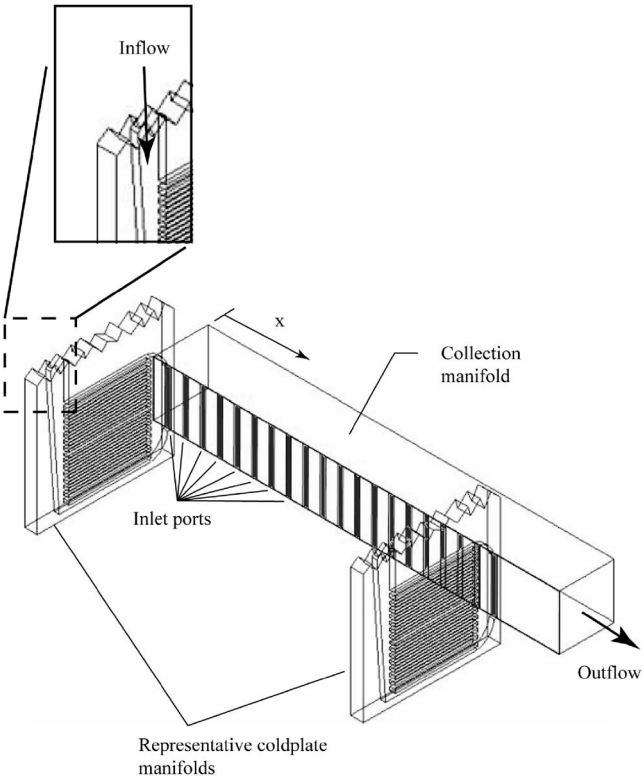

Fig. 1 Pictorial diagram of the collection manifold

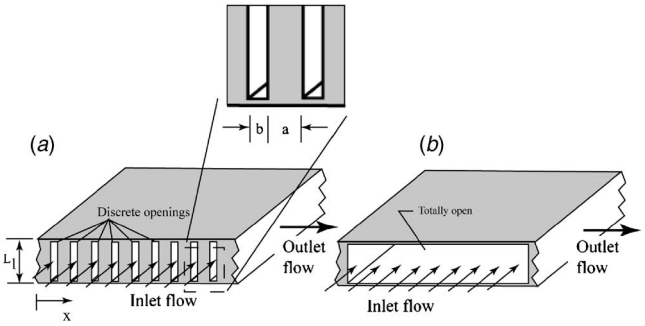

Fig. 2 A typical section of the multiport collection manifold. (*a*) Actual configuration with discrete openings and (*b*) quasi-analytical model with totally open inlet face.

characteristics of the flow within the collection manifold. The knowledge of the individual flowrates is critical to the proper design of the thermal management system.

In addition to determining the aforementioned individual flowrates, the overall pressure drop experienced by the system, including both the coldplates and the collection manifold, will be obtained from the analysis. As mentioned earlier, the model will be complemented by numerical simulation whose results will be compared with those of the analysis. In addition, a number of important features of the flow field within the collection manifold will be revealed by the numerical results.

2 Quasianalytical Model and its Solution

The model is based on the laws of momentum and mass conservation. The basis of the model will now be described. The starting point of the modeling effort is conveyed by Figs. 2(*a*) and 2(*b*). The first of these figures shows a collection manifold illustrating a cluster of fluid-inlet ports. Each inlet port is separated from its neighbors by a section of the manifold wall. For the model, Fig. 2(*b*) shows the inlet ports smeared so as to occupy the entire length of the side wall. This approximation is intended to eliminate the discrete nature of the inflow to the multiport collection manifold and replace it by a continuous inflow. It will be shown later that this approximation has a negligible effect on the quality of the results.

The analysis focus on the control volumes is pictured in Figs. 3(*a*) and 3(*b*). In Fig. 3(*a*), the control volume is shown in place in the collection manifold, where the dashed lines indicate the walls of the collection manifold upstream and downstream of the control volume. This control volume is used for the application of the conservation of the mass principle. In deference to industry standards, the conservation principle will be applied to the volumetric flowrate Q with the understanding that the density is assumed to be constant. The extension of the analysis to variable density fluids is straightforward.

As seen in Fig. 3(*a*), the air enters the control volume at a volumetric flowrate $Q(x)$ and leaves at a rate $Q(x+dx)$. In addition, air enters through the lateral surface of the control volume at a rate $dQ_{\text{coldplate}}$, where the subscript coldplate denotes the inflow of fluid from the coldplates. The mass balance on the control volume for steady-state conditions is

$$Q(x) + dQ_{\text{coldplate}} = Q(x + dx) \tag{1}$$

The quantity $[Q(x+dx)-Q(x)]$ is equal to $(dQ/dx)dx$, so that

$$\frac{dQ}{dx}dx = dQ_{\text{coldplate}} \tag{2}$$

For the application of the momentum conservation principle, it is convenient to use the diagram of Fig. 3(*b*). The leftmost portion of Fig. 3(*b*) depicts the flow of momentum through the control volume while the rightmost portion shows a side view of the control volume with the pressure forces indicated. For the steady state, the balance between the x direction forces and the change of x momentum yields, in terms of the notation of the figure,

$$[p(x) - p(x + dx)]A = (\rho QU)_{x+dx} - (\rho QU)_x \tag{3}$$

Note that the friction pressure drop has been omitted from this equation. It has been demonstrated in [24] that in an accelerating flow such as that which occurs in the present collection manifold, the acceleration-based pressure drop totally dominates the friction-based pressure drop. This assertion will be verified by an a posteriori numerical comparison of the two pressure drops. Since $U=Q/A$, this equation becomes

$$-\frac{dp}{dx} = \frac{\rho}{A^2}\frac{dQ^2}{dx} \tag{4}$$

or

$$\frac{d}{dx}[p_{\text{amb}} - p(x)] = \frac{\rho}{A^2}\frac{dQ^2}{dx} \tag{5}$$

in which the quantity p_{amb} denotes the pressure in the ambient from which the air is drawn. The pressure difference $[p_{\text{amb}} - p(x)]$ is responsible for drawing air from the ambient through the coldplate system and into the multiport collection manifold.

A formal integration of Eq. (5) yields

$$p_{\text{amb}} - p(x) = \frac{\rho}{A^2}Q^2 + \text{Const} \tag{6}$$

The constant of integration can be evaluated by making use of the condition that at $x=0$ (the upstream end of the collection manifold), $Q=0$ and $p(x)=p(0)$, so that

$$p_{\text{amb}} - p(x) = \frac{\rho}{A^2}Q^2 + [p_{\text{amb}} - p(0)] \tag{7}$$

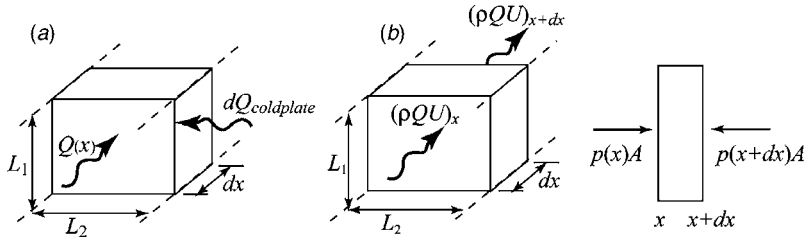

Fig. 3 (*a*) Mass conservation and (*b*) momentum conservation for the control volume of the quasianalytical model

To eliminate the pressure difference $[p_{amb}-p(x)]$, reference is made to the experiments [23] described in the Appendix. In those experiments, the pressure drop across a representative coldplate was measured. The measured pressure drops were well correlated as a function of the volumetric flowrate of the coldplate by

$$p_{amb} - p(x) = C(Q_{coldplate})^n \tag{8}$$

where C and n are constants to be stated later when numerical results are presented, and $Q_{coldplate}$ is the volumetric flow per coldplate. The combination of Eqs. (7) and (8) leads to

$$Q_{coldplate} = (1/C)^{1/n}\left\{\frac{\rho}{A^2}Q^2 + [p_{amb} - p(0)]\right\}^{1/n} \tag{9}$$

The quantity $Q_{coldplate}$ is actually delivered to an opening such as one of those depicted in Fig. 2(*a*). The area through which this delivery is made is $(L_1 \times b)$. For the present model, it has been assumed that the flowrate $Q_{coldplate}$ is smeared across the area $[L_1 \times (a+b)]$ that is depicted in Figs. 2(*a*) and 2(*b*). Therefore, for the present model, the volumetric flowrate per unit length $(dQ_{coldplate}/dx)$ entering the manifold through a smeared inlet is

$$\frac{dQ_{coldplate}}{dx} = \frac{Q_{coldplate}}{a+b} \tag{10}$$

The combination of this equation with the mass conservation equation, Eq. (2), yields

$$Q_{coldplate} = \frac{dQ}{dx}(a+b) \tag{11}$$

Finally, the elimination of $Q_{coldplate}$ between Eqs. (9) and (11) leads to

$$\frac{dQ}{dx} = \frac{(1/C)^{1/n}}{(a+b)}\left\{\frac{\rho}{A^2}Q^2 + [p_{amb} - p(0)]\right\}^{1/n} \tag{12}$$

This is a first-order, nonlinear, ordinary differential equation for $Q(x)$. As a prerequisite for a solution, one boundary condition is required. That boundary condition is that the flowrate at the downstream end of the collection manifold be equal to a prescribed total flowrate Q_{total} or, formally,

$$Q = Q_{total} \quad \text{at } x = 20 \times (a+b) \tag{13}$$

This boundary condition cannot be implemented directly because Eq. (12) already contains an unknown constant $p(0)$. In view of this, the solution strategy was to guess a value of $p(0)$ and integrate from $x=0$ to $x=20\times(a+b)$. If the resulting value of Q at $x=20\times(a+b)$ is not equal to the given value Q_{total}, another guess is made for $p(0)$, and the procedure is repeated. By using this strategy, a number of solutions were obtained for parametric values of $[p_{amb}-p(0)]$. These solutions will be displayed later, after the numerical simulation is formulated and solutions are obtained from it.

3 Numerical Simulation and its Solution

A second approach to solving the problem in question is to use direct numerical simulation. The physical situation is once again conveyed by Fig. 1. In contrast to the foregoing model, no simplifying assumptions are made in the numerical simulation. In particular, the discrete inlets are treated as such.

The numerical simulation is based on the three-dimensional Reynolds-Averaged-Navier-Stokes (RANS) equations for turbulent flow, which are

x direction:

$$\rho\left(u\frac{\partial u}{\partial x} + v\frac{\partial u}{\partial y} + w\frac{\partial u}{\partial z}\right) = -\frac{\partial p}{\partial z} + \frac{\partial}{\partial x}\left(\mu_{eff}\frac{\partial u}{\partial x}\right) + \frac{\partial}{\partial y}\left(\mu_{eff}\frac{\partial u}{\partial y}\right) + \frac{\partial}{\partial z}\left(\mu_{eff}\frac{\partial u}{\partial z}\right) \tag{14}$$

y direction:

$$\rho\left(u\frac{\partial v}{\partial x} + v\frac{\partial v}{\partial y} + w\frac{\partial v}{\partial z}\right) = -\frac{\partial p}{\partial y} + \frac{\partial}{\partial x}\left(\mu_{eff}\frac{\partial v}{\partial x}\right) + \frac{\partial}{\partial y}\left(\mu_{eff}\frac{\partial v}{\partial y}\right) + \frac{\partial}{\partial z}\left(\mu_{eff}\frac{\partial v}{\partial z}\right) \tag{15}$$

z direction:

$$\rho\left(u\frac{\partial w}{\partial x} + v\frac{\partial w}{\partial y} + w\frac{\partial w}{\partial z}\right) = -\frac{\partial p}{\partial z} + \frac{\partial}{\partial x}\left(\mu_{eff}\frac{\partial w}{\partial x}\right) + \frac{\partial}{\partial y}\left(\mu_{eff}\frac{\partial w}{\partial y}\right) + \frac{\partial}{\partial z}\left(\mu_{eff}\frac{\partial w}{\partial z}\right) \tag{16}$$

In these equations, the velocity components, u, v, and w, respectively, correspond to the Cartesian coordinates, x,y, and z. The fluid properties ρ and μ are regarded as constants, and the effective viscosity, μ_{eff}, is defined as

$$\mu_{eff} = \mu + \mu_t \tag{17}$$

In order to proceed, it is necessary to select a turbulence model. On the basis of the authors' prior experience with turbulent flows, the renormalization group (RNG) k-ε model is believed to be appropriate for the nature of the flow under consideration, and this was the model adopted.

The accuracy of a numerical simulation depends critically on the solution domain chosen, which is the physical space in which the numerical calculations are performed. It is necessary to place the boundaries of the solution domain at locations where definitive information about either the velocity or the pressure is available. In particular, in the problem under consideration, the downstream boundary of the domain must be displaced beyond the 20th inlet in order to enable a proper closure to be imposed. For this reason, the boundary was positioned downstream of the 20th inlet by a distance 3.5 times the modular length $(a+b)$. At that boundary, the total volumetric flowrate, Q_{total}, was specified.

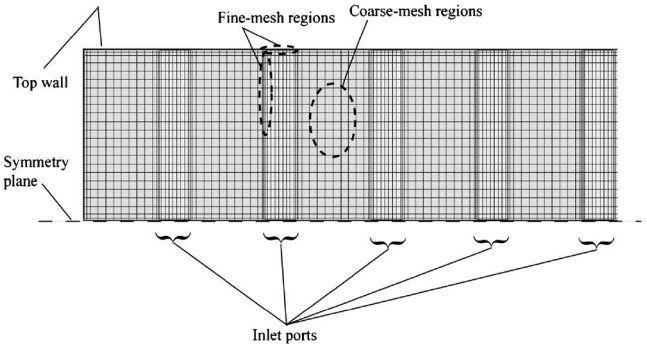

Fig. 4 Details of the mesh at the vertical sidewall in which the inlet ports are situated

At all the solid boundaries internal to the manifold, the velocity components were set equal to zero. At each of the inlets, special care had to be taken because the individual flowrates at the respective inlets were not known a priori. The method adopted was to define a flow resistance, R, in accordance with the definition,

$$V_{\text{inlet}} = \frac{Q_{\text{coldplate}}}{A_{\text{inlet}}} \equiv \frac{[p_{\text{amb}} - p(x)]^{1/n}}{R} \tag{18}$$

The resistance may be evaluated by the use of Eq. (8), which gives

$$R = A_{\text{inlet}} C^{1/n} \tag{19}$$

3.1 Computational Grid. The numerical computations were performed with FLUENT/ICEPAK software. To establish the accuracy of the solutions, a mesh-independence study was performed. To best utilize the available nodal capacity of the computer resources, a plane of symmetry halfway between the top and bottom walls of the manifold was recognized. For the mesh-independence study, separate solutions were run with 350,000 nodes and 600,000 nodes. A comparison of the results from these solutions indicated agreement to better than 1%. In addition to the use of a very fine grid as witnessed by a large number of nodes, the deployment of the nodes was carefully allocated. In particular, nodes were concentrated at the inlets in the wall of the manifold in order to permit the flow to turn and enter the mainflow without unnatural impediment.

An illustration of the deployment of the mesh is presented in Fig. 4. This figure shows the grid as it would be viewed by an observer looking head-on at the duct sidewall that contains the inlet ports. The upper boundary of the diagram is the top wall of the manifold while the lower boundary is the symmetry plane. Of special relevance is the periodic pattern of grid deployment that is based on the need for a finer grid at those locations that are immediately adjacent to the respective inlet ports. Also noteworthy is the finer grid adjacent to the upper and left-hand boundaries of the display. This grid refinement reflects the fact that those boundaries are walls. Grid refinement is also evident at the lower boundary; however, refinement is truly not necessary there because the lower boundary is a symmetry plane. The software itself is responsible for that refinement.

As a further measure of the accuracy of the numerical results, it is noteworthy that all of the residuals, which are metrics of convergence of the numerical calculations, were 10^{-6} or smaller.

4 Results and Discussion

4.1 Overall Pressure Drop. From the standpoint of design, a quantity of major practical importance is the overall pressure drop between the inlets of the coldplates and the downstream end of the collection manifold. These results are presented in Fig. 5. In that figure, the results from the solution are plotted as a solid line, while those from the numerical simulation are represented as discrete data points. The results correspond to the case-study conditions:

(a) $a=0.4$ in. (cm), $b=0.16$ in. (cm)
(b) $L_1=L_2=1.75$ in. (cm)
(c) $C=6.754\times10^{-6}$, units consistent with $[p_{\text{amb}}-p(x)]$ in Pa and Q in m^3/min, Eq. (8)
(d) $n=1.62$, Eq. (8)
(e) Air properties at STP

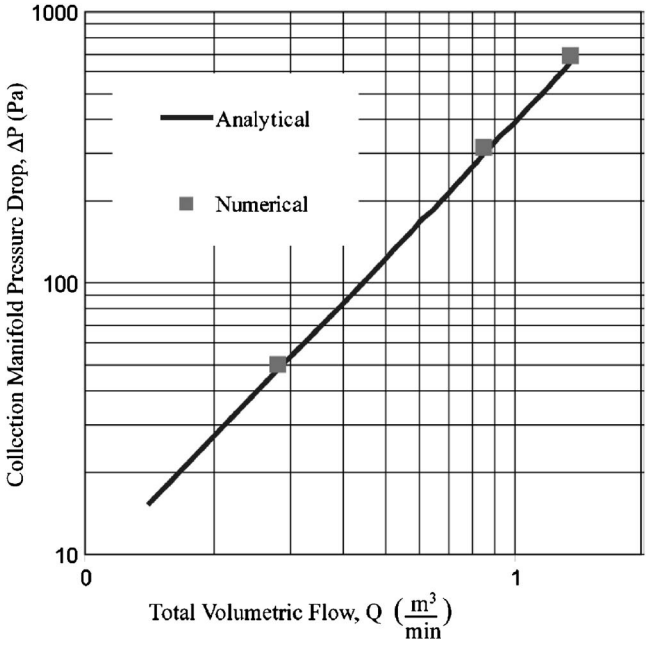

Fig. 5 Overall pressure drop predictions from the quasianalytical and numerical simulation models

Inspection of Fig. 5 reveals a remarkable level of agreement between the results from the quasianalytical and simulation solutions, the average deviation being 4.3%. This finding establishes the validity of the quasianalytical model as a competent tool for prediction of accurate results for technically important quantities such as the overall pressure drop. This outcome enables the method, with its great ease of application, to be used instead of the more demanding numerical simulation.

4.2 Per-Inlet Volumetric Flowrates. A much more demanding test of the quasianalytical model is its ability to predict the volumetric flowrates entering the manifold through the respective inlets. A bar graph, Fig. 6, has been prepared to assess the quality of the per-inlet predicted results, with the numerical solutions used as a standard. In the figure, the per-inlet volumetric flowrate is plotted as a function of the inlet number, with inlet number 1 being the most upstream. At each of the inlets, there are two bars, respectively, corresponding to the predictions of the quasianalytical solution (black bar) and the numerical simulation (gray bar). The results conveyed in Fig. 6 are for the highest investigated flowrate, 1.35 m^3/min. This flowrate was chosen for the display of the result because it is expected to be the most demanding test of the quasianalytical model and because it is believed to induce the largest end-to-end nonuniformities in the per-inlet flowrates.

An overview of Fig. 6 reveals outstanding agreement between the results corresponding to the two solution methods, with an average deviation of 1.1%. This remarkable agreement provides further reinforcement of the conclusion that is drawn from Fig. 5. Taken together, the comparisons shown in these figures give con-

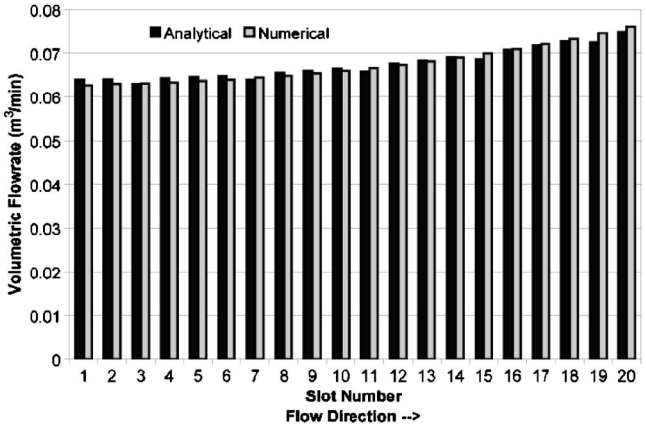

Fig. 6 Per-inlet volumetric flowrates for the quasianalytical model and the numerical simulation

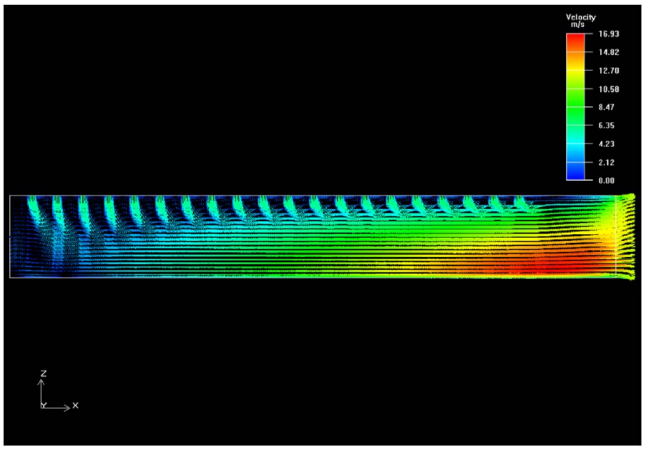

Fig. 7 Vector diagram of the pattern of fluid flow extracted from the numerical simulation corresponding to a total volumetric flowrate of 1.35 m^3/min

clusive evidence of the capability of the quasianalytical method to provide results whose accuracy is well within that required for engineering application.

The remarkable agreement between the results also validates the neglect of frictional effects in the quasianalytical model. In this regard, it may be noted that the numerical simulation includes frictional effects.

Figure 6 also provides other results that are significant for engineering design. The ideal performance of the system consisting of the coldplates and the collection manifold is a per-coldplate flowrate that is the same for all coldplates. Since the per-coldplate flowrate is identical to the per-inlet flowrate, Fig. 6 can be used to assess the deviations from the ideal. For the quasianalytical model, the standard deviation of the predicted per-coldplate flowrate from a strictly uniform flowrate is 5%. The corresponding standard deviation for the results of the numerical simulation is 6%. Any deviation from strict uniformity can give rise to thermal nonuniformities among the individual coldplates. However, it is believed that the aforementioned nonuniformities in the rate of fluid flow are tolerable.

Another interesting finding from both of the solutions is the fact that the per-inlet flowrate increases toward the downstream end of the collection manifold. This behavior is due to the acceleration-based pressure decrease in the streamwise direction. This decrease gives rise to an increase in the pressure difference $[p_{amb}-p(x)]$, which is the driving force for fluid flow through the individual coldplates.

4.3 Other Applications of the Present Method. The satisfactory accuracy of the results provided by the quasianalytical method identified in the preceding section is by no means an isolated finding. In that regard, it is relevant to cite two other fluid-flow applications where the method has been employed with equally good outcomes. One of these applications is related to the utilization of solar energy, and the other is concerned with the design of fabric ducts.

The solar-energy application was motivated by the desire to utilize the energy trapped in solar-heated attic spaces. The utilization scheme was implemented by the placement of an air-to-water heat exchanger in the attic space. The function of the exchanger is to heat water for either domestic or swimming-pool service. To fulfill this function, it is necessary for hot air to be collected uniformly from the entire attic space and delivered to the heat exchanger. The air collection and delivery functions are performed by a single permeable-walled duct.

To accomplish the uniform collection of air from the attic, it was necessary for the permeability of the duct wall to vary in a very specific manner along its length. The quasianalytical method set forth in this paper was employed to determine the permeability distribution. A duct with that permeability distribution was constructed and subsequently evaluated experimentally. To verify the predictions of the model, the static pressure was measured at 50 axial locations along the 7.62 m length of the duct. The comparison of the data with the predictions is presented in Fig. 6 of [24], where excellent agreement prevails. The quality of the comparison is especially important because it is based on a local quantity rather than on an overall or average quantity.

Fabric ducts are gaining increasing acceptance because they provide spatially continuous ventilation at very moderate sound levels. From the standpoint of design, a fabric duct can be considered as a distribution manifold with a very large number of exit apertures.

For the proper design of fabric duct systems, it is necessary to know the inlet pressure that is required to maintain the duct in the fully inflated state from end to end. A predictive theory was developed based on the model in this paper to enable the inlet pressure to be calculated. Well over 100 fabric duct systems have been designed on this basis, and all have functioned in accordance with the predicted pressure specification.

4.4 Patterns of Fluid Flow. Insights into the patterns of fluid flow within the collection manifold are provided by examination of vector diagrams extracted from the numerical simulations. An illustration of the information conveyed by such diagrams is provided by Fig. 7 which corresponds to the flowrate of 1.35 m^3/min. That diagram reveals the flow pattern in the symmetry plane as viewed from above. The most remarkable feature seen in this figure is the jet-like structures issued from individual inlets. These jets experience strong interactions with the axial stream created by the confluence of the individual jets. These interactions are most evident near the downstream end of the manifold. In that zone, the axial stream is so strong that it is able to bend the jets. On the other hand, the axial stream is prohibited by the incoming jets from penetrating too close to the inlet-containing wall.

Of particular note in Fig. 7 is the seemingly anomalous behavior of the first of the jets. That jet exhibits considerable curvature despite the fact that the axial stream has not yet developed. To investigate this behavior, the flow pattern at the upstream end of the manifold is magnified and displayed in Fig. 8. It can be seen from the figure that there is a unique recirculation zone that is situated just upstream of the first inlet. That recirculation zone displaces the jet passing through the first inlet and is thereby responsible for the curvature of the jet. None of the succeeding jets is subjected to such a recirculation zone.

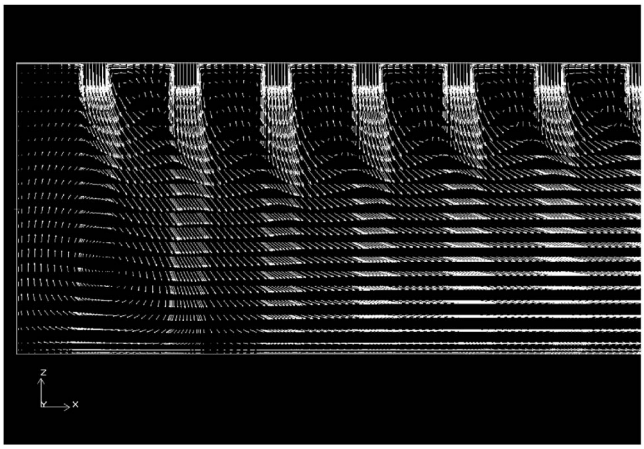

Fig. 8 Magnification of the flow pattern at the upstream end of the manifold

5 Concluding Remarks

The goal of this work was to establish the efficacy of a quasianalytical method for predicting fluid-flow results in complex systems such as a multi-inlet manifold. In addition, as demonstrated in Appendix B, the method can be used as a design tool.

The method is based on first principles, which are the laws of momentum and mass conservation. The attainment of results requires the solution of a first-order, nonlinear, ordinary differential equation. In some cases, it may be necessary to use numerical means to actually solve that equation. In that case, the solution task is accomplished by the use of a spreadsheet, without the need for complex software or large computer assets. This is in contrast to the substantial resources required for the implementation of the numerical simulation method, which was used here to validate the results based on the quasianalytical model.

Two types of results from the quasianalytical model are compared with corresponding results from the numerical simulation. The first quantity to be compared is the overall system pressure drop. For this quantity, the average deviation of the predicted results from those of the simulation is 4.3%. A much more demanding test of the quasianalytical model is the prediction of the per-inlet flowrates, which may be regarded as a local result. The deviation of the quasianalytical predictions, averaged over all 20 inlets of the manifold, was found to be only 1.1% relative to those of the numerical simulation. The collective conclusion drawn from these comparisons is that the quasianalytical model is capable of providing results of practical relevance at levels of accuracy that are well within those needed for engineering design.

The per-coldplate flowrates (which are identical to the per-inlet flowrates) were found to increase moderately in the streamwise direction. This increase can be attributed to the acceleration-based pressure drop caused by the continuous inflow of fluid from the coldplates to the manifold.

The inflows from the coldplates to the manifold give rise to a succession of jets arranged along the inlet wall of the manifold. In general, the jets situated in the downstream region of the manifold are deflected in the streamwise direction by the ever-increasing axial flow. The jet at the upstream-most inlet also experiences streamwise deflection that, however, is caused by a strong recirculation zone rather than by the axial flow.

On the basis of the case study presented in this paper, plus the cited references in Sec. 4.3 and the analysis set forth in Appendix B, it may be concluded that the quasianalytical method of this paper has merit both as a predictive and design tool.

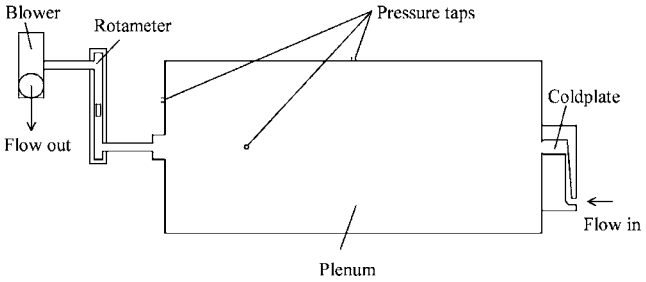

Fig. 9 Schematic of coldplate experiment

Acknowledgment

Support of H. Birali Runesha and the Supercomputing Institute for Digital Simulation and Advanced Computation at the University of Minnesota is gratefully acknowledged.

Appendix A

An experimental apparatus was fabricated [23] to facilitate the measurement of the pressure drop across a representative coldplate as a function of the volumetric flowrate. A schematic diagram of the test setup is shown schematically in Fig. 9. The apparatus is operated in the suction mode to properly simulate the physical situation treated in the paper proper and displayed in Fig. 1.

Air from the temperature-controlled laboratory is drawn into the inlet cross section of the coldplate. From the inlet, the air flows successively through a distribution manifold, an array of parallel channels, and a collection manifold, all of which constitute the coldplate. The air exiting the coldplate discharges as a jet into a very large airtight plenum chamber, where its velocity is reduced to virtually zero without material pressure recovery. The chamber is equipped with three taps to measure the static pressure. At the downstream end of the chamber, the extracted air passes successively through a calibrated rotameter and a centrifugal blower, and is then discharged into the laboratory.

Pressure drop data were collected for a number of preselected values of the volumetric flowrate. The measured pressure drop was read as the difference between the ambient and plenum pressures. This pressure difference includes the acceleration-based pressure drop between the ambient and the coldplate inlet and the pressure drop across the coldplate proper. Note that in the absence of pressure recovery in the plenum, the measured pressure difference is equal to the static pressure drop between the ambient and the exit cross section of the coldplate. This ambient to plenum pressure drop was measured by means of a micromanometer capable of resolving 0.001 in. of the water column.

The data and the least-squares correlation are displayed in Fig. 10 on log-log coordinates. The correlating line is seen to be an excellent representation of the data.

Appendix B: Another Application of the Quasianalytical Method

To illustrate the versatility of the quasianalytical method described in the main body of the paper, this method will be used here to determine a means for achieving the same flowrate through all the coldplates that comprise the system pictured in Fig. 1. In the original analysis of this system described in the paper, the exit cross-sectional area $A_{cp,e}$ of each coldplate was equal to the cross-sectional area of the corresponding inlet port A_{port} in the manifold. Furthermore, all the coldplates had the same exit cross-sectional area. For the study to be performed in this appendix, the uniformity of the coldplate exit areas will be retained, but the inlet port cross-sectional areas will be allowed to vary to enable the per-port inflow to be uniform.

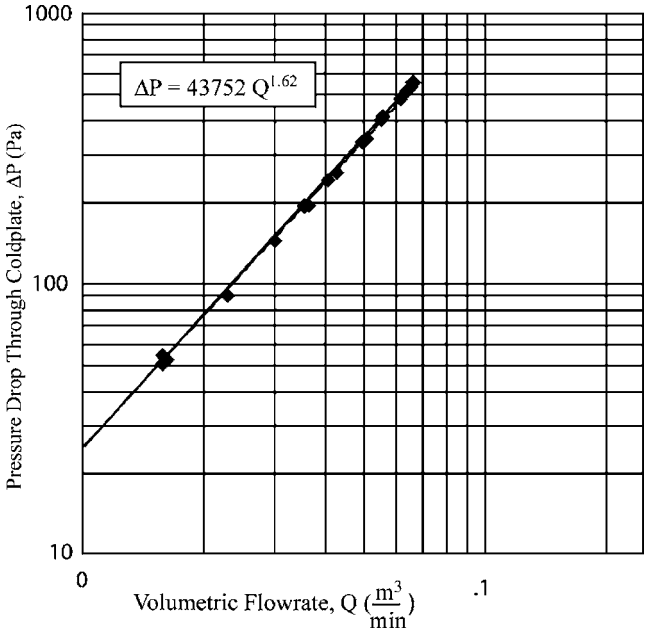

Fig. 10 Pressure drop of a typical coldplate obtained from an experiment

To begin the analysis, it is useful to introduce some additional nomenclature. Let $p_{cp,e}$ denote the pressure at the exit of a coldplate and p_{port} denote the pressure immediately downstream of the corresponding inlet port. Then,

$$p_{amb} - p_{port} = (p_{amb} - p_{cp,e}) + (p_{cp,e} - p_{port}) \tag{B1}$$

The first term on the right-hand side of this equation is equal to

$$C(Q_{coldplate})^n \tag{B2}$$

that follows from Eq. (6). For the second term on the right-hand side in Eq. (B1), a model based on the well-established orifice-flow equation is used. That model is expressed by

$$Q_{coldplate} = C_D A_{cp,e} \sqrt{\frac{2(p_{cp,e} - p_{port})}{\rho(\alpha - 1)}} \tag{B3}$$

where C_D is a discharge coefficient and α is

$$\alpha = (A_{cp,e}/A_{port})^2 \tag{B4}$$

The right-hand side of Eq. (B1) can be evaluated using Eqs. (B2) and (B3), with the result

$$p_{amb} - p_{port} = C(Q_{coldplate})^n + \frac{\rho(\alpha - 1)}{2}\left(\frac{Q_{coldplate}}{C_D A_{cp,e}}\right)^2 \tag{B5}$$

Then, in accord with the model used in the paper proper, p_{port} is equated to $p(x)$. After this substitution, differentiation of Eq. (B5) yields

$$\frac{dp}{dx} - \left(\frac{Q_{coldplate}}{C_D}\right)^2 \frac{\rho}{A_{port}^3}\frac{dA_{port}}{dx} \tag{B6}$$

where note has been taken that $dQ_{coldplate}/dx = 0$.

Another equation for dp/dx is provided by Eq. (4). When dp/dx is eliminated from Eqs. (4) and (B6), there follows

$$-\frac{1}{A^2}\frac{dQ^2}{dx} = \left(\frac{Q_{coldplate}}{C_D}\right)^2 \frac{1}{A_{port}^3}\frac{dA_{port}}{dx} \tag{B7}$$

In this equation, A is the constant cross-sectional area of the collection manifold, and Q is the volumetric flow passing through the manifold at an axial station x. Furthermore,

$$Q(x) = (x/L)Q_{total} \tag{B8}$$

and

$$Q_{total} = NQ_{coldplate} \tag{B9}$$

where N is the number of coldplates, and L is the axial length of the manifold.

After substitution of Eqs. (B8) and (B9) into Eq. (B7), there is

$$-\frac{dA_{port}}{A_{port}^3} = \left(\frac{C_D N}{AL}\right)^2 d(x^2) \tag{B10}$$

Integration of this equation and subsequent application of the boundary condition that $A_{port} = A_{port,0}$ at $x = 0$ leads to

$$\frac{1}{2}\left(\frac{A}{A_{port}}\right)^2 = \frac{1}{2}\left(\frac{A}{A_{port,0}}\right)^2 + (C_D N)\left(\frac{x}{L}\right)^2 \tag{B11}$$

This equation indicates that the attainment of a uniform per-coldplate flowrate requires that A_{port} decreases along the length of the collection manifold.

References

[1] Koh, J. H., Seo, H. K., Lee, C. G., Yoo, Y. S., and Lim, H. C., 2003, "Pressure and Flow Distribution in Internal Gas Manifolds of a Fuel-Cell Stack," J. Power Sources, **115**, pp. 54–65.

[2] Venkataraman, R., and Farooque, M., 2004, "Study of the Gas Flow Distribution and Heat Transfer for Externally Manifolded Fuel Cell Stack Module Using Computational Fluid Dynamics Method," J. Fuel Cell Sci. Technol., **1**, pp. 49–55.

[3] Schenone, C., 2005, "Gas Distribution for Molten Carbonate Fuel Cells," *Proceedings of the First European Fuel Cell Technology and Applications Conference*, December, 2005.

[4] Biao, Z., Kui, J., and Peng, Q., 2006, "Liquid Water Transport in Parallel Serpentine Channels With Manifolds on Cathode Side of PEM Fuel Cell Stack," J. Power Sources, **154**, pp. 124–137.

[5] Amador, C., Gavriilidis, A., and Angeli, P., 2004, "Flow Distribution in Different Microreactor Scale-Out Geometries and the Effect of Manufacturing Tolerances and Channel Blockage," Chem. Eng. J., **101**, pp. 379–390.

[6] Tonomura, O., Tanaka, S., and Hasimoto, I., 2004, "CFD-Based Design of Manifolds in Fin-Plate Microdevices," Chem. Eng. J., **101**, pp. 397–402.

[7] Eason, C., Dalton, T., and Slattery, O., 2005, "Direct Comparison Between Five Different Microchannels," Heat Transfer Eng., **26**, pp. 89–98.

[8] Furlani, E., 2005, "Thermal Modulation and Instability of Newtonian Liquid Microjets," 2005 NSTI Technology and Trade Show, pp. 668–671.

[9] Tonkovich, A., Kuhlmann, D., and Yuschak, T., 2005, "Microchannel Technology Scale-Up to Commercial Capacity," Chem. Eng. Res. Des., **83**, pp. 634–639.

[10] Emerson, D. R., Cieslicki, K., and Barber, R. W., 2006, "Biomimetic Design of Microfluidic Manifolds Based on a Generalized Murray's Law," Lab Chip, **6**, pp. 447–454.

[11] Nozal, O., Arce, L., and Valcarcel, M., 2004, "Rapid Determination of Trace Levels of Tetracyclines in Surface Water Using a Continuous Flow Manifold Coupled to a Capillary Electrophoresis System," Anal. Chim. Acta, **517**, pp. 89–94.

[12] Yebra-Biurrun, M., Moreno-Cid, A., and Cancela-Perez, S., 2005, "Fast On-Line Ultrasonic-Assisted Extraction Coupled to a Flow-Injection Atomic Absorption Spectrometric System for Zinc Determination in Meat Samples," Talanta, **66**, pp. 691–695.

[13] Kale, S., and Ganesan, V., 2004, "Investigation of the Flow Field in the Various Regions of the Intake Manifold of a S.I. Engine," Ind. J. Eng. Mater. Sci., **11**, pp. 85–92.

[14] Persoons, T., Van den Blick, E., and Fausto, S., 2004, "Study of Pulsating Flow in Close-Coupled Catalyst Manifolds Using Phase-Locked Hot-Wire Anemometry," Exp. Fluids, **36**, pp. 217–232.

[15] D'Errico, G., and Onorati, A., 2006, "Thermo Fluid-Dynamic Modeling of a Six-Cylinder Spark Ignition Engine With a Secondary Air-Injection System," International Journal of Engine Research, **7**, pp. 1–16.

[16] Cylkis, P., and Hendla, R., 2005, "Influence of Real Gas Model on the Simulation of Pressure Pulsations in the Reciprocating Compression Manifold," Archives of Thermodynamics, **26**, pp. 21–35.

[17] Ma, F., Choi, J., and Yang, V., 2005, "Thrust Chamber Dynamics and Propulsion Performance of Single-Tube Pulse Detonation Engines," J. Propul. Power, **21**, pp. 512–526.

[18] Xu, B., Liang, F., and Cai, S., 2005, "Numerical Analysis and Visualization of Natural Gas Jet With Multi-Point, Ignition System," Chin. J. Mech. Eng., **18**, pp. 550–554.

[19] Ryu, J., Cheong, C., and Lee, S., 2005, "Computation of Internal Aerodynamic Noise from a Quick-Opening Throttle Valve Using Frequency-Domain Acoustic Analogy," Appl. Acoust., **66**, pp. 1278–1308.
[20] Hrnjak, P. S., 2004, "Flow Distribution Issues in Parallel Flow Heat Exchangers," ASHRAE Trans., **110**, Part 1, pp. 301–306.
[21] Vist, S., 2004, "Two-Phase Flow Distribution in Compact Heat Exchanger Manifolds," Exp. Therm. Fluid Sci., **28**, pp. 209–215.
[22] Wu, T., Jiang, B., and Bi, C., 2006, "Nonisothermal Comprehensive 3D Analysis of Polymer Melts in a Coat-Hangar Die," Polym. Eng. Sci., **46**, pp. 406–415.
[23] Tong, J. C. K, 2006, "Development of Systematic Solution Methodologies for the Fluid-Flow Manifold Problem," Ph.D. thesis, University of Minnesota, Minneapolis, MN.
[24] Sparrow, E. M., Sipple, J., and Palmer, E., 1995, "Enhanced Applications of Attic-Collected Solar Energy," *Proceedngs of the 1995 Annual Conference of the American Society of Solar Energy*, pp. 342–347.

LES Simulation of Backflow Vortex Structure at the Inlet of an Inducer

Nobuhiro Yamanishi
Japan Aerospace Exploration Agency,
Ibaraki 305 8505, Japan
e-mail: yamanishi.nobuhiro@jaxa.jp

Shinji Fukao
Mitsubishi Heavy Industries,
Hyogo 676 8686, Japan
e-mail: shinji_fukao@mhi.co.jp

Xiangyu Qiao
ANSYS,
Kanagawa 220 6216, Japan
e-mail: xiangyu.qiao@ansys.com

Chisachi Kato
The University of Tokyo,
Tokyo 153 8505, Japan
e-mail: ckato@iis.u-tokyo.ac.jp

Yoshinobu Tsujimoto
Osaka University,
Osaka 560 8531, Japan
e-mail: tujimoto@me.es.osaka-u.ac.jp

Turbopump inducers often have swirling backflow under a wide range of flow rates because they are designed with a certain angle of attack even at the design point in order to attain high cavitation performance. When the flow rate is decreased, the backflow region extends upstream and may cause various problems by interacting with upstream elements. It is also known that the backflow vortex structure occurs in the shear layer between the main flow and the swirling backflow. Experimental studies on the backflow from an inducer have given us insight into the characteristics of backflow vortex structure, but the limited information has not lead to the complete understanding of the phenomena. Numerical studies based on Reynolds-averaged Navier-Stokes (RANS) computations usually deteriorate when the flow field of interest involves large-scale separations, as shown by a previous study by Tsujimoto et al. (2005). On the other hand, the numerical approach using the Large Eddy Simulation (LES) technique has the potential to predict unsteady flows and/or flow fields that include regions of large-scale separation much more accurately than RANS computations does in general. The present paper describes the application of the LES code developed by one of the authors (Kato) to further understand the backflow vortex structure at the inlet of an inducer. First, the internal flow of the inducer was simulated, as a way to evaluate the validity of the proposed method, under a wide range of inlet flow coefficients. The static pressure performance and the length of the backflow region was compared with measured values, and good agreement was obtained. Second, using the validated LES code, the fundamental characteristics of the backflow vortex was investigated in detail. It was found that the backflow vortices are formed in a circumferentially twisted manner at the boundary between the swirling backflow and the straight inlet flow. Also, the backflow vortices rotate in the same direction as the inducer, but with half of the circumferential flow velocity in the backflow region. Another finding was that the backflow region expands toward the center of the flow field and the number of vortices decrease, as the flow coefficient decreases. To the best of our knowledge, this is the first computation of the backflow at the inducer inlet to achieve quantitative agreement with measured results, and give new findings to the complicated three-dimensional structure of the backflow, which was very limited under experimental studies. [DOI: 10.1115/1.2717613]

Keywords: inducer, CFD, large eddy simulation, swirling backflow, vortex

Introduction

Applying an inducer for a rocket turbopump operating at high rotational speeds and low NPSH is a common method to prevent head drop of the main pump impeller at cavitating conditions. Although the inducer is a simple helical shaped axial pump, complex internal flow occurs because of its relatively long chord length. For this reason, many interesting phenomena occur at cavitating and noncavitating conditions. It is well known that backflow takes place at the outer region close to the inducer blade at low flow coefficients, similar to other turbopumps, creating vortices and shaft vibrations. Inducers often have swirling backflow under a wide range of flow rates because they are designed with a certain angle of attack even at the design point in order to attain high cavitation performance. Chebayevsky and Petrov [1] have shown that backflow occurs below about a half of incidence free flow rate.

Experimental studies on the backflow from an inducer have given us insight into the characteristics of backflow vortex structures (Tsujimoto et al. [2–4]). Backflow from the inducer has a swirl velocity of about 20–30% of the inducer tip velocity and a backflow vortex structure is formed at the boundary between swirling backflow and straight main flow, as illustrated in Fig. 1. The pressure at the core of a backflow vortex is lower than the ambient pressure due to the centrifugal force on the vortical flow which results in cavitation if the core pressure becomes lower than the vapor pressure. This is called backflow vortex cavitation. In addition to blade surface and backflow vortex cavitations, tip leakage cavitation occurs for inducers with tip clearance. With these types of cavitation, the flow in an inducer presents a very complicated three-dimensional structure. Since experimental results give limited information, numerical simulation plays an important role to further understand such complicated flow phenomena.

Although the internal flow of an inducer is essentially unsteady, the steady Reynolds-averaged Navier-Stokes (RANS) equations were used as the governing equations in recent studies (Hosangadi et al. [5], Dorney et al. [6], and Kimura et al. [7]). However, because the RANS equations are in terms of time averages, RANS computations has inherent limitations in predicting the unsteady nature of a flow field. Solutions from the RANS equations usually deteriorate when the flow field of interest involves the large-scale separations that are often encountered in internal flows in turbomachinery particularly at off-design points. Such limitations were experienced by Tsujimoto et al. [4], in which the backflow vortex

Contributed by the Fluids Engineering Division of ASME for publication in the JOURNAL OF FLUIDS ENGINEERING. Manuscript received August 25, 2005; final manuscript received September 28, 2006. Assoc. Editor: Akira Goto.

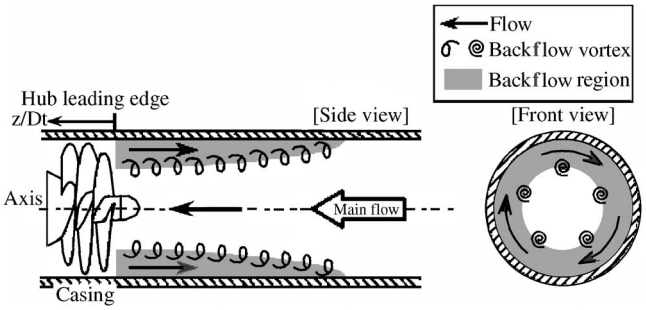

Fig. 1 Schematic of backflow vortex

structure appeared at the early stage of their computations, but eventually died away. As a result, previous studies using RANS-based computations have discussed the backflow region, but none have shown quantitative agreement with experimental results. Further, none have reached the point of discussing details of the backflow vortex structure. On the other hand, large-eddy simulation (LES), in which turbulent eddies of a scale larger than the computational grid are directly computed, has the potential to predict unsteady flows and/or flow fields that include regions of large-scale separation much more accurately than RANS-based computation does in general. Results obtained by LES computations should reproduce numerous features of the backflow vortex at the inlet of the inducer.

In the present paper, the backflow vortex structure at the inlet of an inducer is studied by using the LES technique. Kato et al. [8,9] have recently developed a simulation code based on the LES technique incorporated with a multi-frame-of-reference dynamic overset grid approach to take full account of unsteady internal flows of a mixed-flow pump. The present paper describes the application of this code to further understand the backflow vortices at the inlet of an inducer. First, the internal flow of the inducer will be simulated, as a way to evaluate the validity of the proposed method, under a wide range of inlet flow coefficients. The static pressure peformance and the length of the backflow region will be compared with measured values. Second, using the verified LES code, the fundamental characteristics of the backflow vortex will be investigated in detail. The simulated results are expected to give clear understanding of the complicated three-dimensional structure, which was very limited with experimental studies.

In what follows, first, the configuration of the test inducer is given. Second, the governing equations of the flowfield and the numerical method, including the finite element formulations, computational mesh, and boundary conditions will be explained. Third, the computed head-flow characteristics will be compared with experimental results. Finally, the backflow vortex structure will be discussed, together with numerically and experimentally obtained results of propagation velocity, number of vortices, and radial position of vortices.

Configuration of Test Inducer

The geometry of the test inducer is shown in Fig. 2. The basic design of the inducer is similar to the one used in a rocket engine liquid oxygen turbopump. It has three helical blades with 95.5 deg sweep back leading edge and a tip diameter of 149.8 mm. The inlet blade angle is 7.5 deg and the discharge blade angle is 9.0 deg at the tip. The design flow coefficient is 0.078, as shown in Table 1.

Numerical Method

Governing Equations. Most current computational methods for flow simulations of turbomachinery use the Reynolds averaged Navier-Stokes (RANS) equations as the governing equations. RANS-based computations have inherent limitations in predicting

Fig. 2 Inducer geometry

the unsteady nature of the flow fields as well as predicting large scale separations which often occur at off-design points. The proposed method therefore uses the LES technique which directly computes turbulent eddies larger than the grid size while the effects of smaller eddies are modeled. The governing equations used in the present study are the spatially-filtered Navier-Stokes equations represented in the Cartesian coordinates.

The effects of those eddies that are not resolved by the grid (subgrid scale eddies) are modeled by the following equations:

$$\nu_{\mathrm{SGS}} = (C_S\Delta)^2(2\bar{S}_{ij}\bar{S}_{ij})^{0.5} \tag{1}$$

$$\bar{S}_{ij} = \frac{1}{2}\left(\frac{\partial \bar{u}_i}{\partial x_j} + \frac{\partial \bar{u}_j}{\partial x_i}\right) \tag{2}$$

Here, ν_{SGS} is the subgrid scale kinematic viscosity and S_{ij} is the strain rate tensor. The value of model coefficient C_S is fixed to 0.15 (Standard Smagorinsky Model, SSM [10]), which is a standard value for flows with large separation. The grid-filter size Δ is computed as the cubic root of the volume of each finite element. The value of ν_{SGS} is modified near the wall by multiplying the grid-filter Δ with the following Van-Driest wall-damping function f:

$$f = 1 - \exp\left(-\frac{y^+}{A^+}\right) \tag{3}$$

Finite Element Formulations. A streamline-upwind formulation [11] is used to discretize the governing equations of the flow field. This formulation is based on the explicit Euler's method, but shifts the spatial residuals of the governing equations in the upstream direction of the local flow. The magnitude of this shift is one half of the time increment multiplied by the magnitude of the local flow velocity. This shift exactly cancels out the negative numerical dissipation that is otherwise the result of applying Euler's method, and guarantees stability and the accuracy of solu-

Table 1 Design parameters of the test inducer

Number of blades	3
Tip diameter (D_t)	149.8 mm
Inlet tip blade angle	7.5 deg
Outlet tip blade angle	9.0 deg
Tip solidity	1.91
Tip gap	0.50 mm
Design flow coefficient	0.078

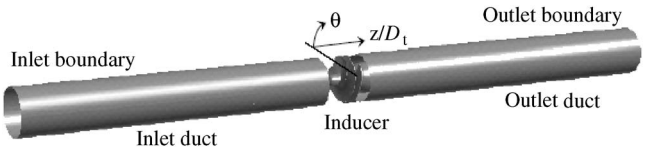

Fig. 3 Computational region

tions. The proposed formulation essentially possesses second-order accuracy in terms of both time and space, and has been successfully applied to the LES of internal flows [11].

Computational Mesh and Boundary Conditions. The computational model used in this study consists of three sets of meshes each of which is dedicated to the inlet, the test inducer, and the outlet as shown in Fig. 3. The number of grid points is approximately 430,000 for the inlet, 2,000,000 for the inducer, and 50,000 for the outlet, which totals to about 2,480,000 grid points (Fig. 4). The grid points for the inlet mesh are relatively large because the backflow vortices must be resolved.

The boundary conditions were given as follows. At the upstream boundary of the inducer, a uniform velocity distribution was given. No prerotation was given, and the inlet boundary layer was not considered in the present study. At the downstream boundary of the discharge mesh, which is located 1000 mm downstream of the inducer exit, the fluid traction was assumed zero in all three directions. On the solid walls, a no-slip boundary condition was prescribed with the Van-Driest damping function. Note that the wall is moving in the negative direction in the rotational frame of reference on the casing liner of the inducer mesh. Thus the wall is at rest when it is viewed from the stationary frame of reference. The grid resolution near the wall surface was not necessarily fine enough for full credit to be given to the use of the no-slip wall boundary condition. However, since no reliable stress wall boundary conditions that can be applied to complex turbulent flows have been proposed for LES, the no-slip wall condition was used in the present study. The minimum grid size was approximately 5 in wall units, in the wall normal direction.

The time increment of the computation was set such that 20,000 time steps corresponded to one revolution of the inducer. Starting from an initial flow field where all the velocity components and the static pressure were set to zero, the flow field in the inducer developed within about 40–50 revolutions of the inducer and reached a statistical equilibrium state thereafter. The establishment of the equilibrium flow state was judged from fluctuations in velocity and static pressure at four representative points and those in the static and total heads of the pump. The total pump head was calculated by averaging the flow field.

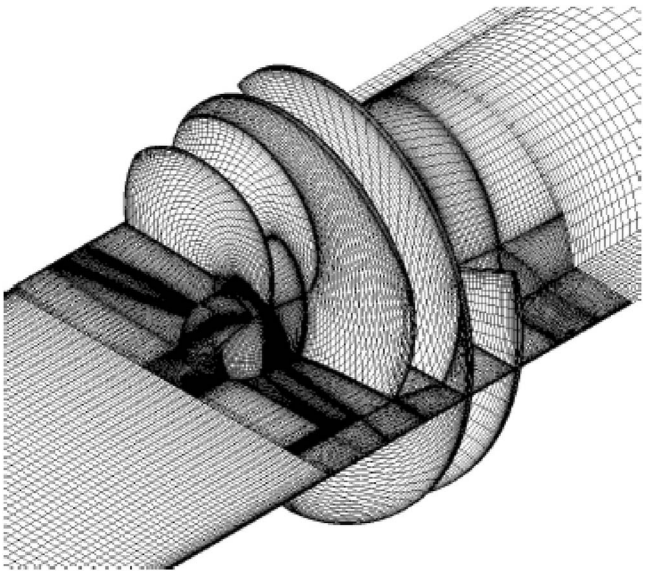

Fig. 4 Computational mesh

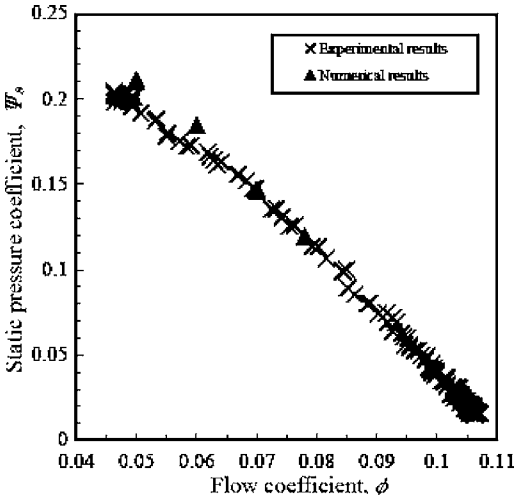

Fig. 5 Static pressure performance

Computed Head-Flow Characteristics

Static pressure head of the inducer was evaluated as the difference of the static pressure measured at upstream and exit of the inducer. The pressure head was computed from the average of 5 inducer revolutions after the flow field developed. The computational time required for the flow field to develop was 50 revolutions for $\phi=0.05$ and 0.06, 45 revolutions for $\phi=0.07$, and 42 revolutions for $\phi=0.078$.

Figure 5 is the comparison of head-flow characteristics. The experimental results were obtained from water tunnel experiments carried out by Tsujimoto et al. at $N=4000$ rpm [2]. We can confirm that the computed pump heads agree fairly well with the measured values. We should also note that an inflexion point exists around $\phi=0.07$ in the measured values. According to measurements using tufts and bubble tracers, at $\phi=0.07$, the rotating backflow region reaches upstream to the pressure transducer that measures the inlet pressure, and extends further upstream as the flow coefficient decreases. Thus, the inlet pressure is measured

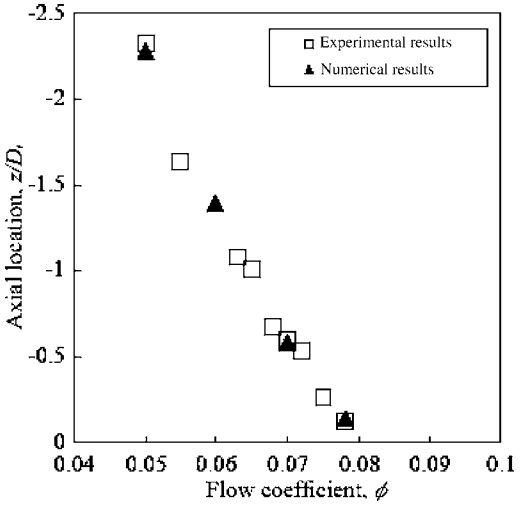

Fig. 6 Axial location of upstream edge of backflow

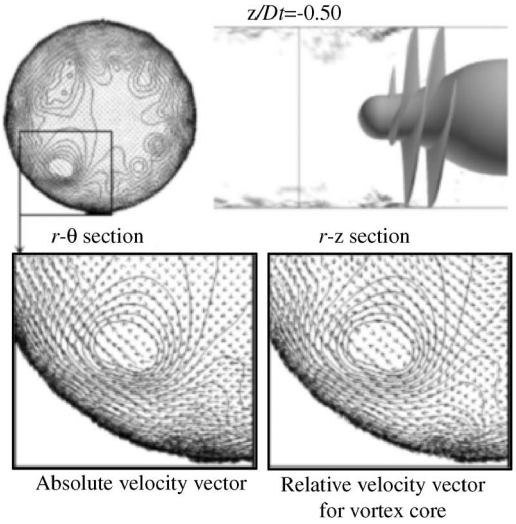

Fig. 7 Pressure contours and velocity vector in the r-θ cross section at $z/D_t=-0.50$ ($\phi=0.06$, after 55 revolutions)

higher than expected due to the flow rotation, which in result gives a lower pressure coefficient in the measurements. Such results indicate that an accurate prediction of the backflow region is the key to obtain good agreement at low flow coefficients.

Backflow Region

Based on the visualization of computational results, the upstream edge locations of the backflow region were measured and compared with experimental results, as shown in Fig. 6. The experimental results were obtained from water tunnel experiments carried out by Yokota et al. at $\sigma=0.05$ and $N=3000$ rpm [3]. Here, the origin ($z=0$) is at the inducer leading edge on the hub. The upstream edges of the backflow region of both results show good agreement, with backflow appearing at design flow coefficient and gradually increasing its length with the decrease of flow coefficient. Previous studies using RANS-based computations have discussed the backflow region, but none have achieved quantitative agreement with experimental results. Results obtained by LES computations agree well with experiments, reproducing measured backflow vortex lengths. It is apparent that unsteady flows that include regions of large-scale separation can be predicted accurately by using the LES technique, verifying our numerical approach.

Backflow Vortex Structure

An example of the backflow vortex obtained from our LES-based computation is shown in Fig. 7. Here, pressure contours and velocity vectors in an r-θ cross section at $z/D_t=-0.50$ for $\phi=0.06$ is shown. The lower left hand figure might show that the vortex center is slightly shifted towards the center of the cross section compared to the pressure minimum, but the use of absolute velocity vectors is misleading because the vortices are actually moving. On the contrary, the lower right hand figure used relative velocity vector to the vortex core, showing that a pressure minimum exists at the vortex center. Further discussions on backflow vortex will be based on the understanding that a vortex exists at the pressure minimum.

Next, the backflow vortex at the shear layer between the main flow and the swirling backflow at $\phi=0.06$ after 55 revolutions is shown in Fig. 8. The contours in the r-θ cross section at $z/D_t=-1.6$ to -0.40 are axial velocity contours with negative values ($u_z/U_t<0$). The isopressure surface at $C_p=-0.020$ is also shown. In Fig. 9, the circumferential velocity and pressure distribution at various axial locations are presented. First, the axial velocity contours indicate that the backflow region exists close to the duct

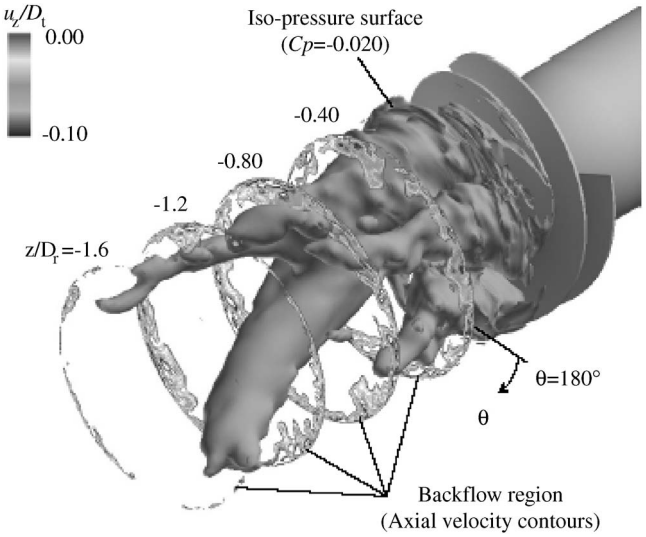

Fig. 8 Backflow vortex at the shear layer between main flow and swirling backflow ($\phi=0.06$, after 55 revolutions)

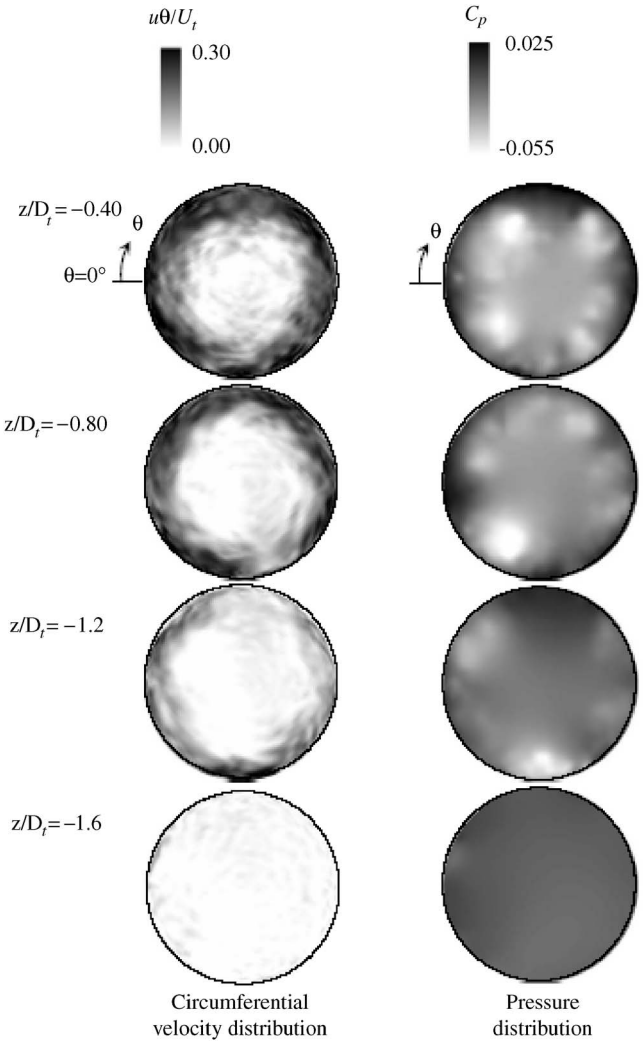

Fig. 9 Circumferential velocity and pressure distribution at various axial locations ($\phi=0.06$, after 55 revolutions)

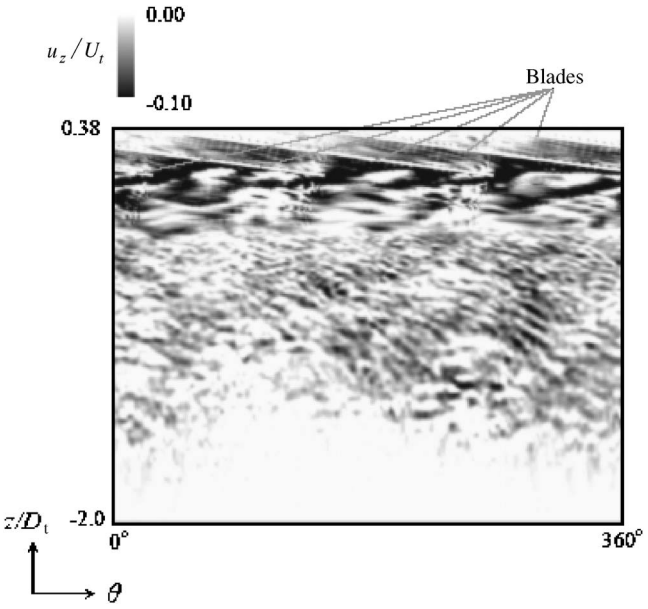

Fig. 10 Axial velocity distribution at r/D_t=0.50 (tip) (ϕ=0.06, after 55 revolutions)

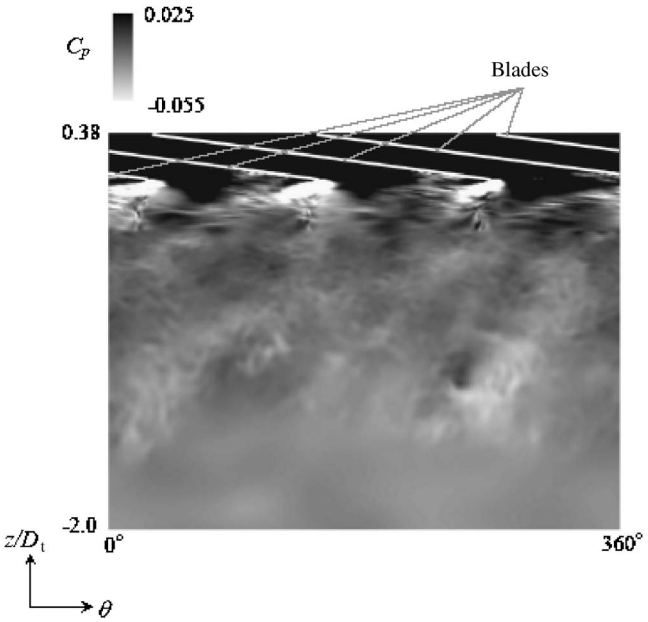

Fig. 11 Pressure distribution at r/D_t=0.50 (tip) (ϕ=0.06, after 55 revolutions)

wall. The axial velocity contours and the low pressure surfaces also denote that vortices appear at the backflow region ($u_z/U_t < 0$), which is consistent with previous studies pointing out that backflow vortex structure is formed at the boundary between swirling backflow and straight normal flow. Next, as the cross section shifts upstream, the area with circumferential velocity decreases in the radial direction, and the low pressure region approaches closer to the duct wall. When Figs. 8 and 9 are compared, the area with circumferential velocity is larger than the area with negative axial velocity, showing that the swirling backflow gives angular momentum to the straight inlet flow. Overall, the twisted isopressure surface of Fig. 8 and the rotating low pressure region of Fig. 9 indicates that the backflow vortex appears in a twisted manner.

Figure 10 is the axial velocity distribution at the θ-z cross section near the duct wall from $z/D_t=-2.0$ to 0.38. The shaded area in the figure has negative axial velocities. Figure 11 is the C_p distribution at the same cross section. By defining the tip of the backflow region by Fig. 10, it is apparent that low pressure regions in Fig. 11 expands to the tip of the backflow region. This indicates that the tip touches the duct wall. Also, the low pressure regions are inclined from axial direction, suggesting the twisted geometry of backflow vortices.

Figure 12 is the rotational process of the backflow vortex at ϕ=0.06 from the 54th revolution to the 55th revolution. The increment between each image is one-tenth of a revolution. The vortices which appear in the pressure contours at $z/D_t=-0.50$ show that 2–4 large vortices rotate in the same direction with the inducer, along with several small vortices.

Figures 13 and 14 are the backflow vortex at ϕ=0.05 and 0.07. It is clear that the number, position, and strength of the vortices have a strong correlation with the inlet flow coefficient. Further discussion on this relation, along with comparison with experimental results will be carried out in the following section.

Propagation Velocity of the Backflow Vortex

Figure 15 is a comparison of the angular propagation velocity and maximum circumferential velocity of the backflow vortex. Both are normalized by the angular velocity of the inducer. Experimental data were obtained at N=3000 rpm and σ=0.05 by visualizing the vortices with cavitation bubbles and measuring it with a laser displacement sensor. We have confirmed that the cavitation bubbles have no direct effect on the vortices at such condition [3]. The average value of the experimental data is plotted in the figure. For the numerical data, the average of the vortices appearing on the $z/D_t=-0.18$ cross section is plotted. At ϕ =0.078, the vortices appearing at the $z/D_t=-0.10$ cross section is averaged because the backflow is short. Numerical data are obtained by sampling the flow field for five inducer revolutions, after the flow field is at a statistical equilibrium. The experimental and

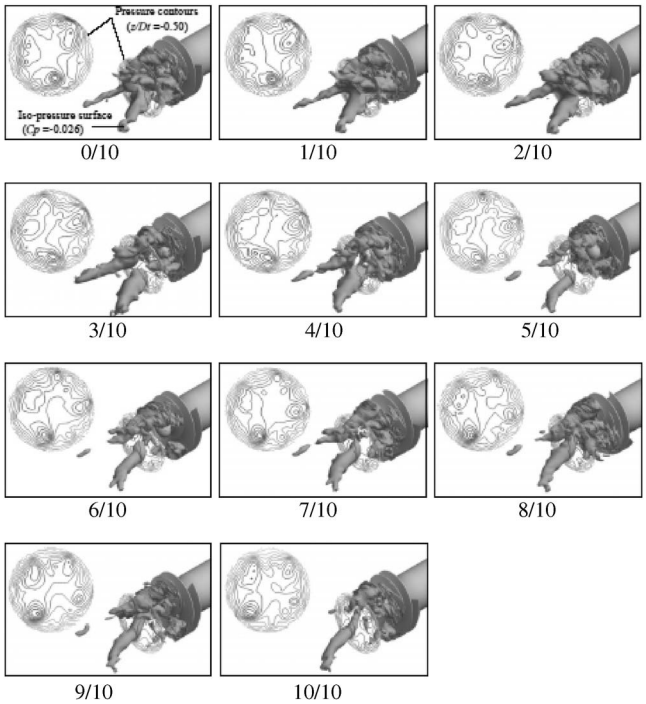

Fig. 12 Rotation process of backflow vortex (ϕ=0.06, from 54 to 55 revolutions)

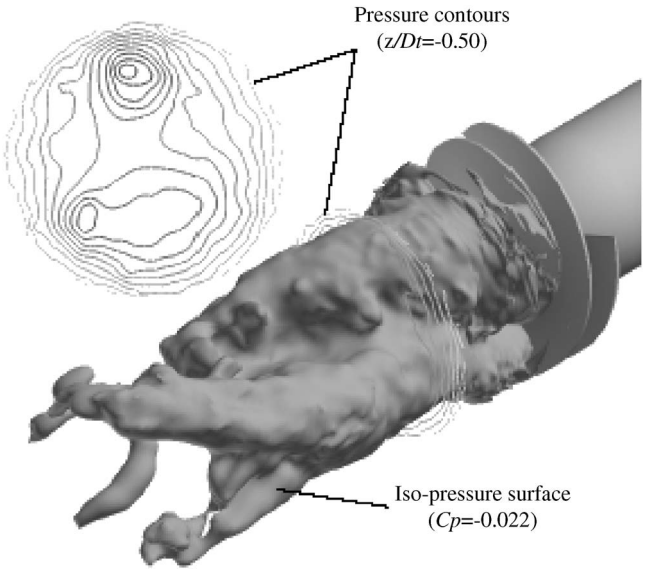

Fig. 13 Backflow vortex (ϕ=0.05, after 55 revolutions)

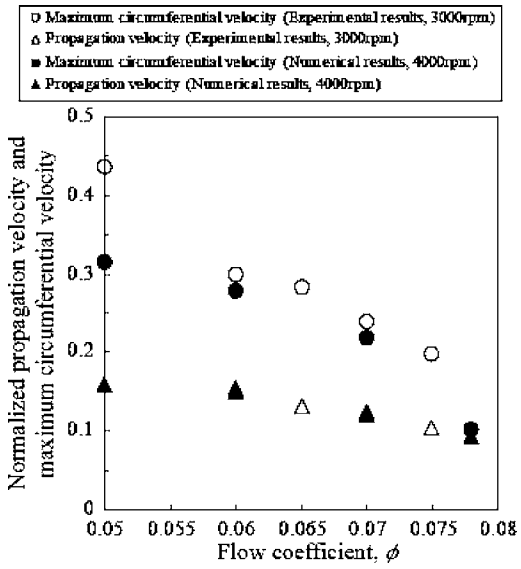

Fig. 15 Normalized propagation velocity and maximum circumferential velocity (z/D_t=−0.18, except for ϕ=0.078: z/D_t=−0.10)

numerical data show fairly good agreement where the propagation velocity is about half the maximum circumferential velocity.

Number of Backflow Vortices

Figure 16 is the number of backflow vortices observed at each flow coefficient. Experimentally, the number of vortices is counted by dividing the pass rate of the vortices by the propagation velocity. The pass rate is measured by a laser displacement sensor at the z/D_t=−0.18 cross section. A high speed video camera is also used for counting. The results obtained by the laser displacement sensor was plotted with its maximum (upper bar), minimum (lower bar), and average (X) value because of its variance. Numerical data was obtained by simply counting the average number of vortices at the z/D_t=−0.18 cross section. Both results have a certain range of variance because the number of vortices changes with time, as shown previously. The numerical and experimental data show qualitative agreement, with the number of vortices decreasing as the flow coefficient decreases. The numerical results give smaller variance.

According to a 2D stability analysis by Yokota et al. [3], the maximum number of the vortices is a function of vortex radial position: larger number of vortices can exist stably if the vortices are located closer to the outer wall. The decrease of the number of vortices associated with the decrease of the flow rate is caused by the fact that the radial position of the vortices is shifted inward with the decrease of the flow rate, as typically shown in Fig. 17.

Radial Position of Backflow Vortex

Figure 17 presents the radial position of the backflow vortex projected on to the meridional plane. The experimental results are averages of measured data at N=3000 rpm and σ=0.05. The numerical results are the averaged radial position of the vortices at each axial location. Both results show that as the flow coefficient decreases, the backflow region extends upstream and expands toward the center of the flow field.

Conclusions

Large-eddy simulation (LES), in which turbulent eddies of a scale larger than the computational grid are directly computed, has the potential to predict unsteady flows and/or flow fields that include regions of large-scale separation much more accurately than RANS-based computation does in general. The present paper described the application of the LES-based computational code developed by Kato et al. to further understand the backflow vortices at the inlet of an inducer. First, the internal flows of the inducer

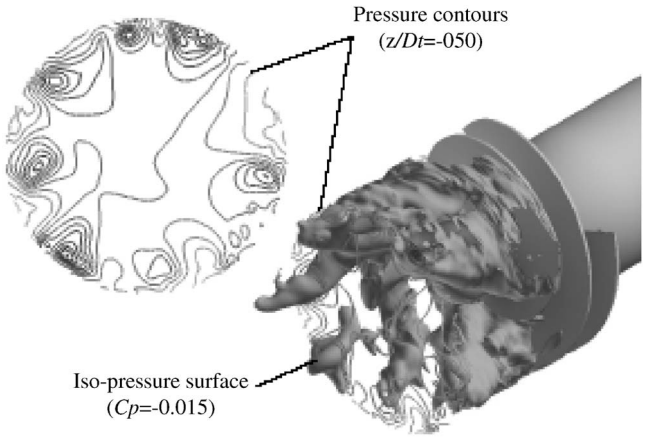

Fig. 14 Backflow vortex (ϕ=0.07, after 45 revolutions)

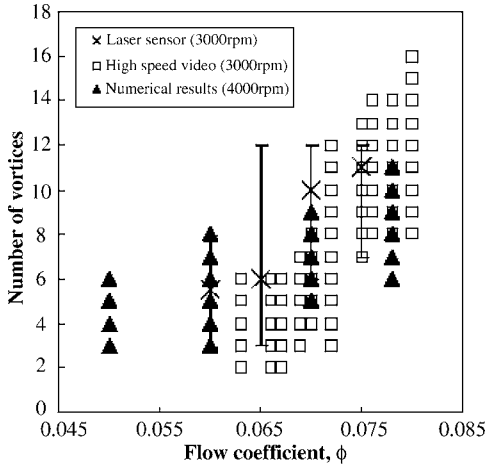

Fig. 16 Number of vortices

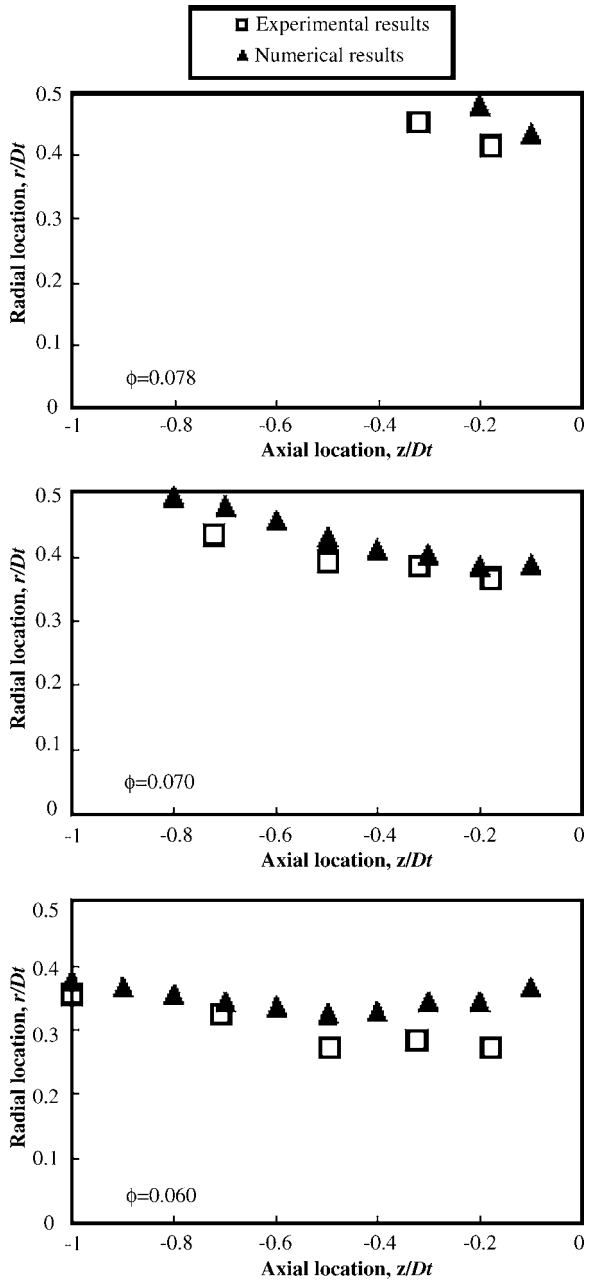

Fig. 17 Profile of vortex filaments projected to the meridional plane

are simulated, as a way to evaluate the validity of the proposed method, under a wide range of inlet flow coefficients. The static pressure peformance and the length of the backflow region was compared with measured values, and good agreement was obtained. Second, using the verified LES code, the fundamental characteristics of the backflow vortex was investigated in detail. As expected, the simulated results gave insight into the complicated three-dimensional structure of the backflow vortex. The results obtained from numerical analysis can be summarized as follows:

1. The backflow region extends upstream as the flow coefficient decreases.
2. The backflow vortices are formed in a circumferentially twisted manner at the boundary between the swirling backflow and the straight inlet flow.
3. The backflow vortices rotate in the same direction as the inducer, but with half of the circumferential velocity in the backflow region.
4. The backflow region expands toward the center of the flow field and the number of vortices decrease, as the flow coefficient decreases.

Previous studies using RANS-based computations have discussed the backflow region, but none have shown quantitative agreement with experimental results. Further, none have reached the point to discuss details of the backflow vortex structure. Results obtained by LES computations agree well with experiments, reproducing numerous features of the backflow vortex, as shown in this paper. To the best of our knowledge, this is the first computation of the backflow at the inducer inlet to achieve quantitative agreement with measured results, and give new findings to the complicated three-dimensional structure of the backflow, which was very limited under experimental studies.

It has been shown by experiments (Yamamoto [12]) that the response of backflow vortex structure to the flow rate fluctuation has an important effect on cavitation instabilities. Based on the good agreements with experiments examined in the present paper, the code is now being applied to the case with flow rate fluctuation to clarify the mechanisms of backflow response.

Acknowledgment

The authors would like to express their sincere gratitude to Mr. A. Ishimaru, Mr. T. Nagata, and Mr. H. Nakai for their contributions to this paper.

Nomenclature

D_t = inducer tip diameter, m
N = inducer rotational speed, rpm
p = static pressure, Pa
p_v = vapor pressure, Pa
r = radial position, m
u_z = meridional velocity, m/s
u_θ = circumferential velocity, m/s
U_t = inducer tip speed, m/s

Greek Symbols

ν = kinematic viscosity
$\sigma=(p_{\text{in}}-p_v)/(\rho U_t^2/2)$ = cavitation number
$\phi=u_{\text{in}}/U_t$ = flow coefficient
$\Psi_s=(p_{\text{out}}-p_{\text{in}})/(\rho U_t^2)$ = static pressure coefficient
$C_p=(p-p_{\text{in}})/(\rho U_t^2/2)$ = nondimensional pressure

Subscripts

in = inlet
out = outlet
SGS = subgrid scale

References

[1] Chebayevsky, V. F., and Petrov, V. I., 1973, "Cavitational Characteristics of High-Rotational Inducer and Centrifugal Pumps," *Mashinostroyeniye*, Moscow (in Russian).
[2] Tsujimoto, Y., Yoshida, Y., Maekawa, Y., Watanabe, S., and Hashimoto, T., 1997, "Observations of Oscillating Cavitation of an Inducer," ASME J. Fluids Eng., **119**(4), pp. 775–781.
[3] Yokota, K., Kurahara, K., Kataoka, D., Tsujimoto, Y., and Acosta, A., 1999, "A Study of Swirling Backflow and Vortex Structure at the Inlet of an Inducer," JSME Int. J., Ser. B, **42**(3), pp. 451–459.
[4] Tsujimoto, Y., Horiguchi, H., and Qiao, X., 2005, "Backflow From Inducer and its Dynamics," ASME FEDSM2005-77381.
[5] Hosangadi, A., Ahuja, V., and Ungewitter, R. J., 2006, "Numerical Study of a Flat Plate Inducer: Comparison of Performance in Liquid Hydrogen and Water," AIAA2006-5070.
[6] Dorney, D., Griffin, L., Marcu, B., and Williams, M., 2006, "Unsteady Flow Interactions Between the LH2 Feed Line and SSME LPFP Inducer," AIAA2006-5073.

[7] Kimura, T., Yoshida, Y., and Shimagaki, M., 2006, "Relation Between Geometries of Inducer Inlet and Backflow and Vortex Structures," AIAA2004-4022.
[8] Kato, C., Shimizu., H., and Okamoto, T., 1999, "Large Eddy Simulation of Unsteady Flow in a Mixed-Flow Pump," ASME FEDSM99-7802.
[9] Kato, C., Mukai, H., and Manabe, A., 2002, "LES of Internal Flows in a Mixed-Flow Pump With Performance Instability," ASME FEDSM2002-31205.
[10] Smagorinsky, J., 1963, "General Circulation Experiments With Primitive Equations," Mon. Weather Rev., **91**, pp. 99–164.
[11] Kato, C., Kaiho, M., and Manabe, A., 2003, "An Overset Finite-Element Large-Eddy Simulation Method With Applications to Turbomachinery and Aeroacoustics," ASME J. Appl. Mech., **70**, pp. 32–43.
[12] Yamamoto, K., 1992, "Instability in a Cavitating Centrifugal Pump (3rd Report, Mechanism of Low-Cycle System Oscillation)," Trans. Jpn. Soc. Mech. Eng., Ser. B, **58**, pp. 180–186 (in Japanese).

Direct Numerical Simulation of Bubbly Flows and Application to Cavitation Mitigation

Tianshi Lu
e-mail: tlu@bnl.gov

Roman Samulyak

Computational Science Center,
Brookhaven National Laboratory,
Upton, NY 11973

James Glimm
Department of Applied Mathematics and Statistics,
Stony Brook University,
Stony Brook, NY 11794-3600

The direct numerical simulation (DNS) method has been used to the study of the linear and shock wave propagation in bubbly fluids and the estimation of the efficiency of the cavitation mitigation in the container of the Spallation Neutron Source liquid mercury target. The DNS method for bubbly flows is based on the front tracking technique developed for free surface flows. Our front tracking hydrodynamic simulation code FronTier is capable of tracking and resolving topological changes of a large number of interfaces in two- and three-dimensional spaces. Both the bubbles and the fluid are compressible. In the application to the cavitation mitigation by bubble injection in the SNS, the collapse pressure of cavitation bubbles was calculated by solving the Keller equation with the liquid pressure obtained from the DNS of the bubbly flows. Simulations of the propagation of linear and shock waves in bubbly fluids have been performed, and a good agreement with theoretical predictions and experiments has been achieved. The validated DNS method for bubbly flows has been applied to the cavitation mitigation estimation in the SNS. The pressure wave propagation in the pure and the bubbly mercury has been simulated, and the collapse pressure of cavitation bubbles has been calculated. The efficiency of the cavitation mitigation by bubble injection has been estimated. The DNS method for bubbly flows has been validated through comparison of simulations with theory and experiments. The use of layers of nondissolvable gas bubbles as a pressure mitigation technique to reduce the cavitation erosion has been confirmed.
[DOI: 10.1115/1.2720477]

Keywords: bubbly flow, front tracking, cavitation mitigation

1 Introduction

Wave propagation in bubbly fluids has attracted investigators for many decades because of its special properties. Bubbly fluids have the unique feature that even a minute bubble concentration (volume fraction less than one percent) significantly increases the compressibility of the system. The system transports energy at a speed considerably lower than the sound speeds in both phases as a result of the energy exchange between the liquid and the bubbles. When additional effects such as vaporization and condensation play a role, e.g., in cavitating flows, further phenomena, still little understood, are superimposed upon the basic behavior of bubbly flows. The rich internal structure of bubbly flows endows the medium strikingly complex behavior.

One of the reasons for the study of bubbly flows is their wide applications ranging from hydraulic engineering to high energy physics experiments. In particular, we are interested in a recent application of bubbly fluids in the mitigation of cavitation damages in the Spallation Neutron Source (SNS) [1], which will be discussed in details in Sec. 5. Another important motivation is to connect the microscopic behavior of individual bubbles to the macroscopic behavior of the mixed medium that one directly observes. Since the microstructure in this case is made up of a complex substructure, the task is much more complicated than that of classical kinetic theory.

The wave propagation in bubbly fluids has been studied using a variety of mathematical models. Significant progress has been achieved in the study of systems consisting of noncondensable gas bubbles [2–5] and of vapor bubbles [6,7]. The treatment of the kinetic and thermal properties of the medium, e.g., the compressibility of the liquid and the thermal conduction, by different authors varies. But they shared a common feature that the two phases were not separated explicitly, i.e., the bubble radius and concentration were considered as functions of time and space. The Rayleigh-Plesset equation or the Keller equation governing the evolution of spherical bubbles has been used as the kinetic connection between the bubbles and fluid. These models include many important physical effects in bubbly systems such as the viscosity, the surface tension, and thermal conduction. Numerical simulations of such systems requires relatively simple algorithms and are computational inexpensive.

Nevertheless, homogenized models treat the system as a pseudofluid and cannot capture all features of the rich internal structure of the bubbles. They exhibit sometimes large discrepancies with experiments [4] even for systems of noncondensable gas bubbles. Their range of validity is limited to small void fraction and small amplitude waves. These models are also not suitable if the bubbles are distorted severely by the flow or even fission into smaller bubbles, as it may happen in cavitating and boiling flows [8,9]. The direct numerical simulation (DNS) method, which solves the full nonlinear system of compressible fluid dynamics equations in every component of the multiphase domain, is potentially free of these deficiencies. DNS is based on techniques developed for free surface flows. Welch [10] numerically investigated the evolution of a single vapor bubble using the interface tracking method. Juric and Tryggvason [11] simulated the boiling flows using the incompressible flow approximation for both liquid and vapor and a simplified version of interface tracking. 3D simulations of very large volume fraction fluids using a method of front tracking with incompressible liquid approximation was also reported [12]. In this paper, we perform DNS simulations of small void fraction bubbly fluids using front tracking for compressible fluid equations. Our FronTier code is capable of tracking and resolving topological changes of a large number of interfaces in two- and three-

Contributed by the Fluids Engineering Division of ASME for publication in the JOURNAL OF FLUIDS ENGINEERING. Manuscript received September 28, 2005; final manuscript received October 25, 2006. Review conducted by Joseph Katz.

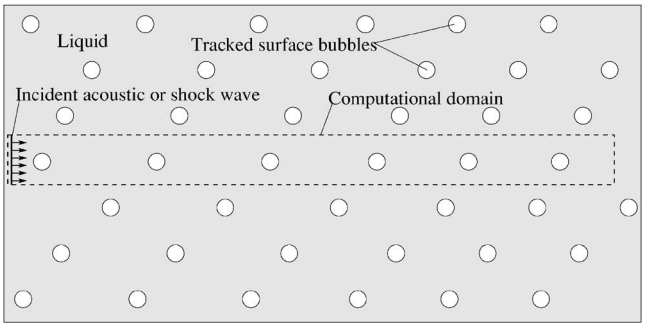

Fig. 1 Schematic of the numerical experiments on the propagation of linear and shock waves in bubbly fluids

dimensional spaces. A homogeneous approach to multiphase flows has also been developed in the FronTier code and compared to the DNS approach [13,14]. In this paper, both the bubbles and the fluid are compressible because we are interested in the speed of wave propagations. We simulated the propagation of acoustic and shock waves in bubbly fluids with small void fraction and compared them to the theory and experiments. After the validation of the FronTier based DNS method for bubbly flows, it was applied to the engineering problem of cavitation mitigation in the Spallation Neutron Source, which involves bubbly flows of relatively large void fraction.

The paper is organized as follows: Sec. 2 presents the governing system of equations and main conclusions of the homogenized model of bubbly flows, and Sec. 3 gives the description of the numerical method. In Sec. 4 we present the results of the DNS on linear and shock wave propagation in bubbly fluids along with the comparison to the theory and the experiments. In Sec. 5, after the description of the SNS and the bubble injection technique for the cavitation mitigation, the cavitation is estimated in two steps. First the pressure wave propagation in the mercury target of the SNS is simulated using the front tracking method, then the collapse pressure of cavitation bubbles is calculated by solving the Keller equation under the ambient pressure whose profile has been obtained in the first step. The efficiency of the cavitation mitigation is estimated by comparing the average collapse pressure with and without injected bubbles. Finally, we conclude the paper with a summary of our results in Sec. 6.

2 Mathematical Formulation

2.1 Governing System of Equations. In the DNS method, we study bubbly fluids as a system of one-phase domains separated by explicit interfaces (see Fig. 1). Namely we solve the system of Euler's equations

$$\frac{\partial \rho}{\partial t} = -\nabla \cdot (\rho \mathbf{u}) \tag{1}$$

$$\rho\left(\frac{\partial}{\partial t} + \mathbf{u} \cdot \nabla\right)\mathbf{u} = -\nabla p \tag{2}$$

$$\rho\left(\frac{\partial}{\partial t} + \mathbf{u} \cdot \nabla\right)e = -p\,\nabla \cdot \mathbf{u} \tag{3}$$

$$p = p(\rho, e) \tag{4}$$

separately in each gas bubble and in the ambient liquid subject to the liquid-gas interface conditions. Here $\mathbf{u}$, ρ, and e are the velocity, density, and the specific internal energy of the fluid, respectively, and p is the pressure. The continuity of pressure and normal velocity is satisfied at the liquid-gas interface. If the surface tension is important as in surface instability problems, we modify the pressure interface condition by adding a pressure jump due to the surface tension and local curvature. In simulations presented in this paper, the surface tension was neglected as it is important only for bubbles of a submicron size. Gas bubbles in simulated fluids are much larger. Notice that we have also neglected the viscosity and heat conduction in fluid equations. These effects are often important in the dynamics of bubbly flows, and will be included in future simulations. We use the polytropic equation of state (EOS) model for gas bubbles,

$$p = (\gamma - 1)\rho e$$

where γ is the ratio of specific heats, and the stiffened polytropic EOS for the ambient liquid

$$p = (\gamma_l - 1)\rho(e + e_\infty) - \gamma_l p_\infty$$

which models tension by allowing negative pressure values. Experimentally measurable liquid properties such as the sound speed and specific heats can be used to calculate the parameters γ_l, p_∞, and e_∞.

2.2 Wave Equations in Homogenized Models. Since some of our results are compared to the homogenized theory of bubbly fluids, we present in this section main equations. The theory on bubbly flows is based on the homogenized model, in which the fluid and bubbles are treated as a single mixed phase, opposed to the two separated phases in the direct numerical simulations. In compressible fluids with gas bubbles, the conservation of mass and momentum in one spatial dimension give

$$\frac{1}{\rho_f c_f^2}\frac{\partial p}{\partial t} + \frac{\partial u}{\partial x} = \frac{\partial \beta}{\partial t}$$

$$\frac{\partial(\rho u)}{\partial t} + \frac{\partial(\rho u^2 + p)}{\partial x} = 0$$

where β is the bubble volume fraction, ρ is the averaged density of the mixed phase that equals $\rho_f(1-\beta)+\rho_g\beta$, and p is the averaged pressure. The bubble oscillation in weakly compressible fluids is governed by the Keller equation [15–17], which is an extension of the Rayleigh-Plesset equation,

$$\left(1 - \frac{1}{c_f}\frac{dR}{dt}\right)R\frac{d^2R}{dt^2} + \frac{3}{2}\left(1 - \frac{1}{3c_f}\frac{dR}{dt}\right)\left(\frac{dR}{dt}\right)^2 = \frac{1}{\rho_f}\left(1 + \frac{1}{c_f}\frac{dR}{dt} + \frac{R}{c_f}\frac{d}{dt}\right)(p_B - p) \tag{5}$$

The p in Eq. (5) coincides with the average pressure in the conservation laws to the lowest order in β [18]. p_B is the liquid pressure at bubble surface. The bubble pressure p_g is approximately uniform except for sound waves of frequency far above the resonance. For air bubbles of diameter 0.1 mm and above, the thermal diffusivity $\nu = \kappa/(\rho c_p) \ll \omega R^2$ except for sound waves of frequency far below resonance (κ, ρ, and c_p are the heat conductivity, density and specific heat with fixed pressure for the gas, respectively). Therefore the bubbles are almost adiabatic for near-resonant sound waves. For bubbles consisting of a γ-law gas,

$$p_g R^{3\gamma} = \text{constant}$$

Neglecting the viscosity, the difference between p_g and p_B is from the surface tension,

$$p_g = p_B + \frac{2\sigma}{R}$$

2.2.1 Linear Waves. The following dispersion relation for linear sound waves in bubbly fluids was derived from the wave equations [5]:

$$\frac{k^2}{\omega^2} = \frac{1}{c_f^2} + \frac{1}{c^2}\frac{1}{1 - i\delta\dfrac{\omega}{\omega_B} - \dfrac{\omega^2}{\omega_B^2}} \tag{6}$$

where ω_B is the resonant frequency of single bubble oscillation, δ is the damping coefficient accounting for the various dissipation mechanisms. c_f is the sound speed in bubble free fluid and c is the sound speed in the low-frequency limit, which is given by

$$\frac{1}{c^2} = (\beta\rho_g + (1-\beta)\rho_f)\left(\frac{\beta}{\rho_g c_g^2} + \frac{1-\beta}{\rho_g c_f^2}\right)$$

where ρ_g and ρ_f are the densities of the gas and the fluid, c_g and c_f are the sound speeds of the two phases. For adiabatic bubbles,

$$c = \sqrt{\frac{\gamma p}{\beta\rho_f}}$$

$$\omega_B = \frac{1}{R}\sqrt{\frac{3\gamma p}{\rho_f}} \tag{7}$$

Chapman and Plesset [19] formulated δ as the sum of the acoustic, viscous, and thermal contributions. It has been pointed out by Prosperetti et al. [18,20] that δ depends on the frequency of the sound wave. Nevertheless, Eq. (6) has been widely used for the dispersion relation. The dispersion relation for near-resonant sound waves measured in different experiments [21–23] agreed with the theoretical predictions.

2.2.2 Shock Waves. The shock profile in the bubbly fluid evolves into a smooth steady form in contrast to the sharp discontinuity in the pure fluid. The steady state shock speed was obtained from the Rankine-Hugoniot relation [4]

$$\frac{1}{U^2} = \frac{1}{c_f^2} + \rho_f\frac{\beta_b - \beta_a}{P_a - P_b} \tag{8}$$

where subscripts a and b stand for ahead and behind the shock front. Since heat conduction and surface tension is neglected, $P_a\beta_a^\gamma = P_b\beta_b^\gamma$. The evolution into a steady wave can take very long time and distance, and the unsteady waves move at higher velocities [4]. The shock profiles were measured for various gas bubbles by Beylich and Gülhan [2], to which our simulation results will be compared.

3 Numerical Method

In this paper, we study bubbly fluids as a system of one-phase domains separated by free interfaces using FronTier, a front tracking compressible hydrodynamics code. Front tracking is an adaptive computational method in which a lower dimensional moving grid is fit to and follows distinguished waves in a flow. The front propagates according to the dynamics around it (i.e., Lagrangian) while the regular spatial grid is fixed in time (i.e., Eulerian). The discontinuities across the interfaces are kept sharp so as to eliminate the interfacial numerical diffusion which plagues traditional finite difference schemes.

The implementation of the front tracking method in the FronTier code has been described in details by Glimm et al. [24]. Here we formulate the main ideas. In each time step, the front is propagated first, then the interior states are updated. For the front propagation, each point of the interface is propagated in the normal direction, and the states on either side of the interface are evolved according to the solution of the nonlocal Riemann problem. The hyperbolic solver has three steps: slope reconstruction, prediction using local Riemann solver, and correction by nonlocal solver. Then the states on the propagated fronts are updated in the tangential direction while the fronts are fixed. After that the fronts are tested for intersection and then untangled or redistributed if necessary to resolve the topological change or the clustering/sparsity of grid points on the interfaces due to front contract/expand.

For the subsequent interior state update, FronTier uses high resolution shock-capturing hyperbolic schemes on a spatial grid. Among the various shock capturing methods currently implemented in FronTier, a second order monotone upwind scheme for conservation laws (MUSCL) scheme developed by Van Leer and adapted for FronTier by Chern was used for the simulation here. MUSCL scheme is similar to the piecewise parabolic method [25], and detailed descriptions can be found in Collela's paper [26], and the references therein. The two-pass implementation currently being used in FronTier, namely, first *regular* cells then *irregular* cells update, is well documented [24]. Different equation of state models are used for gas/vapor bubbles and the ambient fluid.

FronTier can handle multidimensional wave interactions in both two- [27] and three- [28] dimensional spaces. Although computationally intensive, front tracking is potentially very accurate in treating many physical effects in bubbly flows, such as the compressibility of the fluid, surface tension and viscosity. Since the FronTier code is capable of tracking simultaneously a large number of interfaces and resolving their topological changes, many effects that are difficult to handle in mathematical models for bubbly flows are now naturally included in the simulations, e.g., the bubbles' deviation from sphericity, bubble-fluid relative motion, bubble merge/fissure and bubble size/spatial distribution. This approach has numerous potential advantages for modeling the phase transitions in boiling and cavitation flows. We have implemented a model for the phase transitions induced mass transfer across free interfaces [29]. FronTier is implemented for distributed memory parallel computers.

For the application of FronTier to the simulation of bubbly flows, the region around a long column of bubbles (tens to hundreds) has been chosen as the computational domain, as shown in Fig. 1. Two approximations were used in the simulations. The flow inside the column was assumed to be axisymmetric and the influence from the neighboring bubbles was included by treating the domain boundary as a reflecting wall, which is called the Neumann boundary in FronTier. Thus the wave propagation in bubbly flows was reduced to an axisymmetric two-dimensional problem. An extensive introduction to the FronTier code for axisymmetric flows is available [24].

We have shown that the assumption of axial symmetry is adequate for the study of the main features of the wave propagation in bubbly fluids. This conclusion is based on the comparison of our numerical results with theoretical and experimental data presented in the next section. The axisymmetric assumption is exact for the scattering of the planar wave by an isolated column of bubbles that are initially spherical. The Neumann boundary condition for the modeling of the presence of other bubbly layers is strong because scattered pressure waves are only partially reflected. As a contrast, the scattering theory, on which the Keller equation is based, completely neglects the reflection between bubbles and the secondary scattering. Therefore the scattering theory only holds for the case of small β such that bubble interaction is negligible. For moderate β, the secondary scattering cannot be neglected, and the Neumann boundary condition between adjacent bubbles is a better approximation.

4 Simulation Results on Bubbly Flows

In this section, we present the results of the DNS of the linear and shock wave propagations in bubbly fluids. Since the void fraction is small (0.02% for linear waves, 0.25% for shock waves), the homogenized model is expected to be valid. The dispersion relation measured from simulations is compared with theoretical predictions in Sec. 4.1. Shock speed values measured from simulations are compared to steady-state values, and shock profiles for various gas bubbles are compared to experimental data [2] in Sec. 4.2.

4.1 Linear Waves. To compare the simulation results with the

Table 1 Phase velocities (V) and attenuation coefficients (α) from the simulation and the theory. λ is the wavelength in pure water. V and α are the simulation results, V_{th} and α_{th} are the theoretical predictions from Eq. (6) with $\delta=0.7$. $R=0.06$ mm, $\beta=0.02\%$.

λ (cm)	f (kHz)	V (cm/ms)	V_{th} (cm/ms)	α (dB/cm)	α_{th} (dB/cm)
0.5	290	155	153	2.2	0.9
1.0	145	183	194	5.7	5.0
1.5	96.7	220	274	18.4	20.7
2.0	72.5	160	173	28.5	30.9
2.5	58.0	100	100	21.8	29.4
2.75	52.7	75	84	18.9	25.2
3.0	48.3	68	75	17.8	20.4
4.0	36.3	62	68	10.7	8.5
5.0	29.0	66	69	3.9	4.4

theory, we measured the dispersion relation. Writing down the complex wave number k in Eq. (6) as $k=k_1+ik_2$, we have

$$e^{i(kx-\omega t)} = e^{-k_2 x} e^{i(k_1 x-\omega t)}$$

from which the phase velocity of the sound wave is defined as

$$V = \frac{\omega}{k_1} \tag{9}$$

and the attenuation coefficient α in dB per unit length is defined as

$$\alpha = 20 \log_{10} e \cdot k_2 \tag{10}$$

The bubble radius in the simulation was $R=0.06$ mm. From Eq. (7), we have

$$f_B = \frac{\omega_B}{2\pi} = \frac{1}{2\pi R}\sqrt{\frac{3\gamma p}{\rho_f}} = 54.4 \text{ kHz}$$

We simulated the sound waves of frequencies ranging from 30 to 300 kHz. The volume fraction was $\beta=0.02\%$. The amplitude of the pressure wave was chosen to be 0.1 bar, one tenth of the ambient pressure. The linearity was ensured by performing numerical simulations with sound waves of half amplitude which gave virtually the same dispersion relation. For each frequency, the sound wave of up to eight wavelengths was propagated from the pure fluid into the bubbly region. The cross-sectional averaged pressure in the bubbly region was recorded at selected times and positions, from which the phase velocity and the attenuation coefficient were measured. The phase velocity was obtained by measuring the propagation speed of the first pressure node in the bubbly region. The envelope of the oscillating pressure wave was plotted and the attenuation coefficient was measured in the 1 cm long bubbly fluid region next to the incident plane by fitting the envelope to an exponential curve. A shorter region was used for the frequency with the strongest attenuation ($\lambda=2$ cm).

The phase velocities and attenuation coefficients measured from the simulations are listed in Table 1 along with theoretically predicted values. Theoretical values were calculated using the damping coefficient $\delta=0.7$ in Eq. (6). There are various theoretical and empirical formulas for the damping coefficient [5], several of them giving value under 0.1. The parameters in our simulations is closest to those in experiment of Fox et al. [21], who used the empirical value of 0.5 for the damping coefficient. The measured dispersion relation was compared to the theoretical curve in Fig. 2(*a*). It can be seen that the simulation agrees well with the theory. However, the point in Fig. 2(*a*) with frequency about 100 kHz has a large deviation from the theoretical value. Most likely the deviation is due to the dependence of δ on the frequency, especially near the resonance [18,20].

The grid resolution for most of our simulations on linear wave propagations was 100 grids per millimeter. To ensure the accuracy of the simulation results, a mesh refinement check has been carried out. Figure 3 shows a typical result. It can be seen that the results were reasonably accurate at the default grid resolution (100 grids/mm). The one-dimensional grid on the bubble surface, which is the explicitly tracked fluid interface, was more refined, and the circumference of a bubble in the simulation was discretized into 50 points. The approximation of a cylindrical domain has been justified by varying the aspect ratio of the cylinder containing a bubble, which confirms that the dispersion relation only

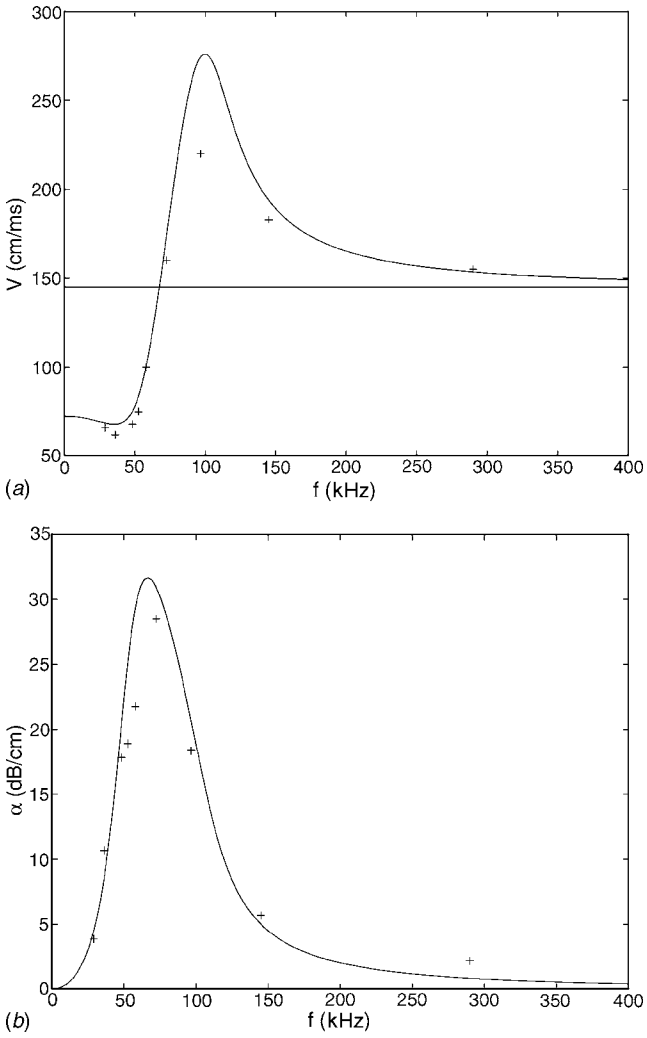

Fig. 2 Comparison of the dispersion relation between the simulation and the theory. $R=0.06$ mm, $\beta=0.02\%$. (*a*) The phase velocity; (*b*) the attenuation coefficient. In both figures, the crosses are the simulation data and the solid line is the theoretical prediction from Eq. (6) with $\delta=0.7$. The horizontal line in (*a*) is the sound speed in pure water.

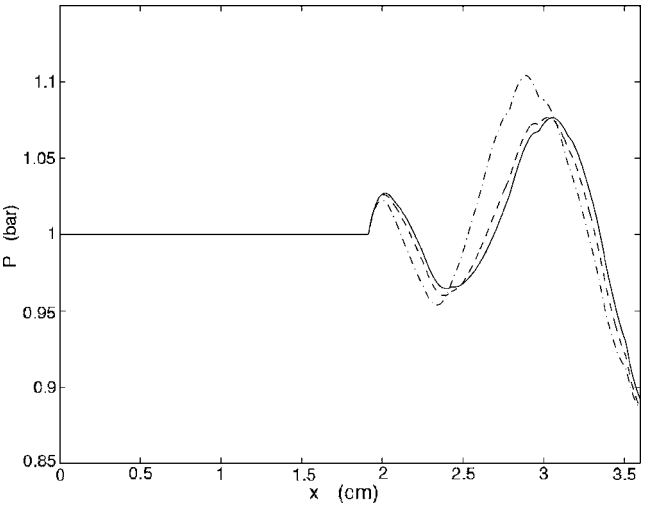

Fig. 3 The pressure profile in bubbly water 23 μs after the incidence of the sound wave with a wavelength of 1 cm in pure water. The default resolution used in the simulations was 100 grids/mm, under which the bubble radius R=0.06 mm corresponds to 6 grids. The solid line is the default resolution of 100 grids/mm, the dashed-dotted line is 50 grids/mm, the dashed line is 200 grids/mm.

depends on the void fraction, i.e., the ratio of the bubble volume over the cylinder volume, but not on the aspect ratio.

4.2 Shock Waves. Beylich and Gülhan [2] studied the propagation of shock waves in glycerol filled with bubbles of various gases. We carried out numerical simulations using their experimental settings. We have also varied the sound speed in the pure fluid to measure the corresponding shock speeds and compared them to the steady-state values given by Eq. (8). In the simulations, the pressure behind the shock was either fixed at the boundary or set as the initial pressure in an air layer next to the bubbly fluid. The results from the two methods have been compared and found to be very close.

The measured shock speeds are listed in Table 2. The speeds were measured about 10 cm away from the shock incident plane. It is seen from the table that the measured shock speeds differ from the steady state values by less than 15%. The reason for the deviation is that the shock waves in simulations had not reached the steady state.

The shock profiles were measured at 1.0 m away from the shock incident plane as in the experiments of Beylich et al. [2]. The shock profiles for SF_6 bubbles of volume fraction 0.25% are plotted in Fig. 4. These figures show that the pressure in the bubbly fluid oscillated after the passage of the shock front. The oscillation amplitude from the simulation was close to the experimental value. However the oscillation period from the simulation was 28% shorter than the experimental value.

There were several sources of error that could be responsible for the deviation. The main source of error was numerical dissipation at the bubble surface. The default grid resolution for the simulations on shock wave propagation was 100 grids per centimeter, and the bubble circumference contains about 100 points. It has been found that increasing resolution only slightly changed the oscillation amplitude and period. Other sources of error include the axisymmetric approximation and the Neumann boundary condition on the domain wall. It is worth mentioning that the oscillation period calculated by Watanabe et al. [4] based on the homogenized model was also about 1/4 shorter than the experimental value.

The shock profiles with various gas bubbles and different volume fractions were measured and they agreed with the experiments as well. The oscillation amplitude was found to be smaller for gas with larger polytropic index γ, and the oscillation period was longer for larger bubble volume fraction β, both of which agreed with the experiments. As a summary, the shock velocity measurement agreed well with the theory, while the shock profiles agreed with the experiment qualitatively and partly quantitatively.

According to Noordzij and van Wijngaarden [30], waveforms observed during the propagation of shocks in bubbly liquids can be classified into three types, referred to as A-, B-, and C-type waves. The highly oscillatory A-type waveform is usually found near the boundary at which the shock is introduced. The other two represent later stages in the evolution of the wave. As pointed out by Watanabe and Prosperetti [4], the heat exchange between bubbles and liquid plays an important role in the formation of B- and C-type shocks. Due to the negligence of heat diffusion in our simulations, we only observed A-type shocks. Our simulations agreed with Beylich and Gülhan's experiments [2], in which they

Table 2 Shock speeds measured from the simulations are compared to the steady state values. β_a is the bubble volume fraction ahead of the shock, P_b is the pressure behind the shock, U and U_{th} are the measured shock speed and corresponding steady-state value given by Eq. (8). p_a=1.11 bar, ρ_f=1.22 g/cm^3, R_a=1.15 mm.

Gas (γ)	c_f (m/s)	β_a (%)	P_b (bar)	U (m/s)	U_{th} (m/s)
SF_6(1.09)	1450	0.25	1.9	26.20	25.40
SF_6(1.09)	458	0.25	1.9	22.52	22.48
SF_6(1.09)	145	0.25	1.9	13.47	12.64
N_2(1.4)	1450	0.25	1.7	25.56	26.68
N_2(1.4)	458	0.25	1.7	22.21	23.35
N_2(1.4)	145	0.25	1.7	12.29	12.79
He(1.67)	1450	0.25	1.9	25.68	30.01
He(1.67)	458	0.25	1.9	22.69	25.49
He(1.67)	145	0.25	1.9	13.52	13.11
SF_6(1.09)	1450	2.17	1.8	8.72	8.52
SF_6(1.09)	458	2.17	1.8	8.04	8.39
SF_6(1.09)	145	2.17	1.8	7.10	7.35
N_2(1.4)	1312	2.17	1.8	8.60	9.42
N_2(1.4)	458	2.17	1.8	9.09	9.25
N_2(1.4)	145	2.17	1.8	7.80	7.92
He(1.67)	1450	1.04	1.9	13.92	14.96
He(1.67)	458	1.04	1.9	12.70	14.29
He(1.67)	145	1.04	1.9	9.70	10.44

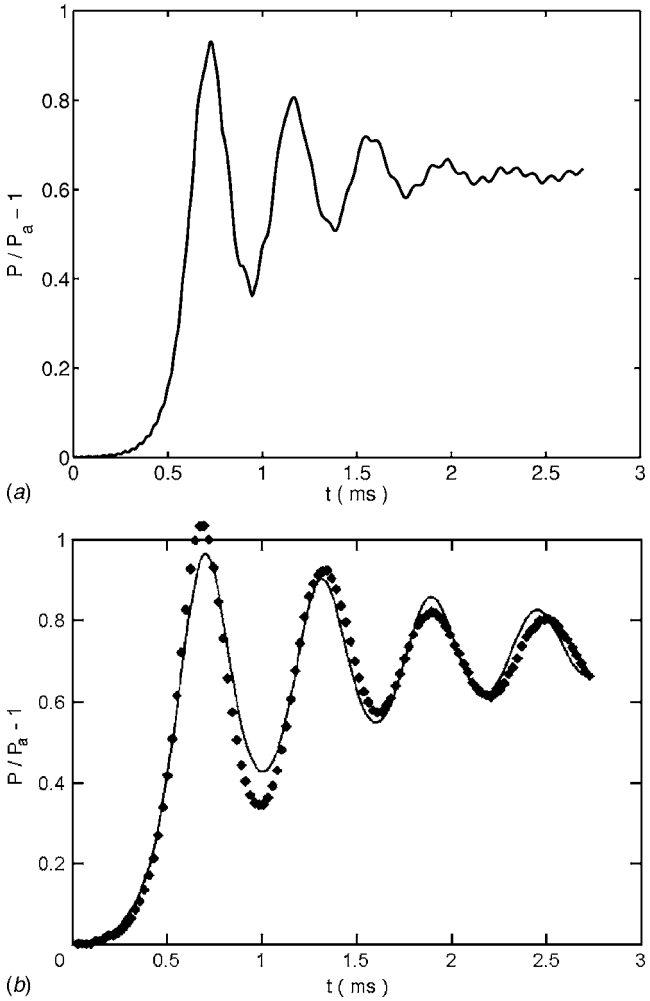

Fig. 4 The shock profiles in glycerol filled with SF_6 bubbles. The parameters in the simulations were from the experiments [2]. P_a=1.11 bar, P_b=1.80 bar, ρ_f=1.22 g/cm^3, R_a=1.15 mm, γ =1.09, and β=0.25%. The top figure is from the simulation, the bottom one is from the experiment. The curves in the experimental figure is the original fitting with artificial turbulent viscosity [2].

only published data on A-type shocks. We have already implemented a heat diffusion algorithm in FronTier [31], and will explore all types of shock profiles in the future.

5 Application of Bubbly Flows to Cavitation Mitigation

The comparison of simulation results with theory and experiments in the previous section validated the FronTier based DNS method for bubbly flows. The DNS method is used in this section to study the cavitation reduction problem in the Spallation Neutron Source target container. The DNS method is well suited for the description of bubbly flows in the SNS target since large void fraction fluids and very strong pressure waves make the applicability of the homogenized theory questionable. Section 5.1 introduces the design of the SNS target and the associated fluid dynamical issue. The method of approach is described in Sec. 5.2. Section 5.3 analyzes the simulation results on the pressure wave propagation in the pure and bubbly mercury. In Section 5.4, the collapse pressure of cavitation bubbles is calculated. Lastly, the efficiency of cavitation mitigation by bubbly injection is estimated in Sec. 5.5.

5.1 Spallation Neutron Source. The Spallation Neutron Source (SNS) is an accelerator-based neutron source being built at Oak Ridge National Lab. The SNS will provide the most intense pulsed neutron beam in the world for scientific research and industrial development. In the SNS, 800 MeV proton beams bombarding the mercury target in a steel container deposit totally 2.1 kJ of energy per pulse in less than 300 ns which results in the rapid pressure increase in the mercury (see Fig. 5). The peak deposited energy density is 19 J/cm^3, corresponding to 500 bar in mercury. The subsequent pressure waves induces severe cavitation on the container, so much so that the lifetime of the container was only two weeks with 1 MW proton pulses at the frequency of 60 Hz [1]. In order to mitigate the cavitation erosion, research is being done on the evaluation of cavitation-resistant materials and coatings. It has also been suggested that the injection of nondissolvable gas bubbles into the container could absorb the energy of the pressure wave. Our goal is to estimate the efficiency of the cavitation mitigation by the bubble injection method.

The SNS target prototype tested at the Los Alamos National Laboratory is a cylinder of 10 cm diameter and 30 cm length [1]. The pressure in the target is about 1 bar in the absense of the proton beam. After the proton beam bombards the target, the pressure rises in the mercury almost instantaneously compared to acoustic time scales. The pressure distribution, as shown in Fig. 5, has a Gaussian profile in the transverse direction with σ=1.0 cm and an exponential attenuation along the axis. The pressure profile can be approximated as

$$P_0(r,z) = 500e^{-r^2-0.1z} \text{ bar} \tag{11}$$

where r and z are in cm, and the origin of the z axis is the window where proton beams enter. When nondissolvable gas bubbles are injected into the container, the bubble pressure has little change after the proton pulse and it remains about 1 bar.

5.2 Method of Approach. Before we compare the cavitation erosion in pure and bubbly mercury, a brief introduction to the mechanism of cavitation damage and the method we used to quantify it is given in this section. Cavitation is the process in which bubbles, consisting of vapor and noncondensable gas, form, expand, and collapse in the fluid according to the surrounding pressure which decreases and increases rapidly. Vapor bubbles are formed when the pressure falls below the saturated vapor pressure of the fluid at the ambient temperature or some critical pressure smaller than the corresponding saturation pressure [32]. They implode when the fluid pressure rises back above the saturated vapor pressure or when the bubbles move into a region with higher pressure. If the bubble is close to the container wall, the shock wave from the rebound of the collapse erodes the wall as in the SNS target container.

The attenuation of the pressure wave during the rebound phase of the cavitation bubbles has been studied extensively [33]. The pressure of the rebounded wave that hits the container wall can be used to quantify the cavitation erosion. Since it is proportional to the first collapse pressure of cavitation bubbles, we only need to compare the average collapse pressure in the pure mercury and the bubbly mercury for the estimation of the cavitation mitigation efficiency. In order to calculate the collapse pressure, we need to know how the cavitation bubbles grow and collapse under the pressure wave in the container. Since the collapsed bubble size (<0.1 μm) is less than a millionth of the container size (10 cm), it is difficult to directly simulate the evolution of cavitation bubbles in the entire container. Instead we estimated it in two steps.

First, we simulated the propagation of pressure waves in the container caused by the initial pressure distribution given by Eq. (11). The simulation was carried out for both the pure mercury and mercury containing nondissolvable gas bubbles. For the simulation of the bubbly mercury, the bubble surfaces were tracked explicitly via the front tracking method described in the previous

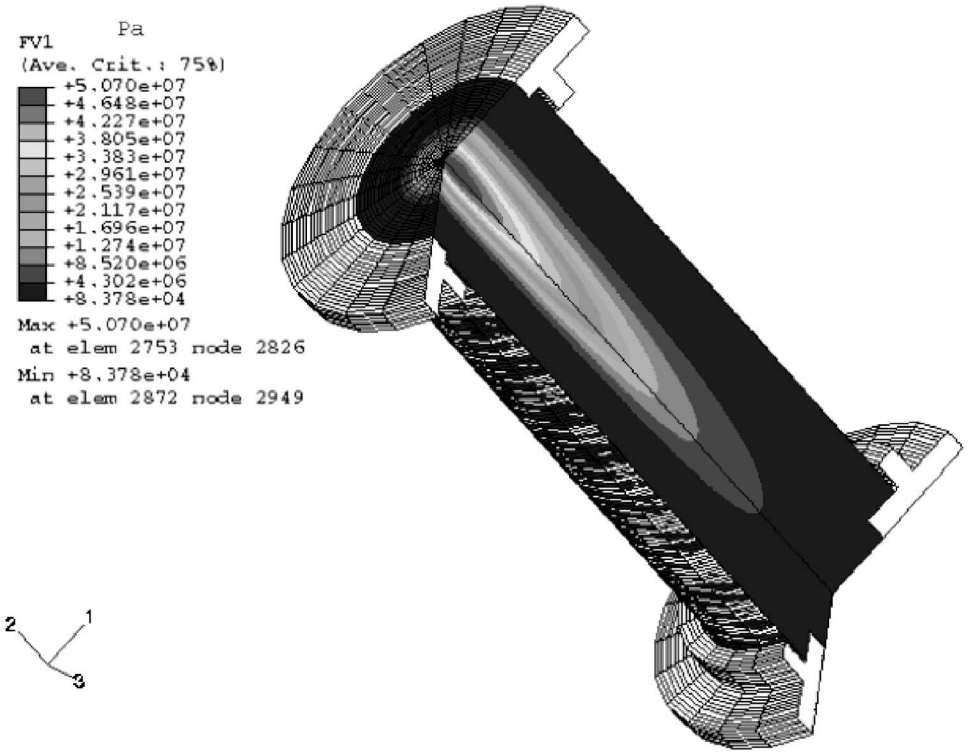

Fig. 5 The pressure distribution right after a pulse of proton beams in the mercury target of the Spallation Neutron Source (courtesy of SNS experimental facilities, Oak Ridge National Lab)

sections. The pressure relaxation caused by the cavitation was ignored in the simulation of pressure waves in the container. We assumed that the growth and collapse of cavitation bubbles is uncorrelated, namely, that the far field liquid pressure for a cavitation bubble is not significantly perturbed by relaxation waves from neighboring cavitation bubbles. Since the distribution of cavitation centers is unknown for mercury under such conditions, accounting for pressure relaxation processes would contain a large amount of uncertainty.

In the second step, the collapse pressure of cavitation bubbles was calculated by solving the Keller equation (Eq. (5)) under the liquid pressure whose profile was obtained in the first step. A cavitation bubble consists of vapor and noncondensable gas. Due to the liquid-vapor phase transition, the partial vapor pressure in a bubble remains negligible compared to the amplitude of pressure waves in the SNS target, while the partial pressure of the gas (typically air) changes violently. As a result, it suffices to calculate the growth and collapse of cavitation bubbles that consist only of air for the estimation of the collapse pressure.

5.3 Pressure Wave Propagation in the Container. Inferred from Eq. (11) for the initial pressure distribution, the strongest pressure oscillation and consequently the most severe cavitation might be located at the center of the entrance window, which was confirmed by the simulation. Therefore we compared the pressure profile at the window center in the pure and bubbly mercury. The pressure profile in the pure mercury is shown in Fig. 6(*a*), while the pressure profile in the mercury filled with air bubbles is shown in Fig. 6(*b*).

It is readily seen that, as expected, the pressure decayed much faster in the bubbly mercury, since bubbles absorbed the energy from pressure waves and spread it away from the entrance window. The pressure oscillation in the bubbly mercury was also more rapid due to reflections between the window and bubbles. The typical decay time in both cases is shorter than the period between two proton pulses at the-frequency of 60 Hz. Both profiles can be approximately described by the following formula:

$$P_w(t) = P_{w0} e^{-(t/\tau)} \cos\left(\frac{2\pi t}{T}\right) \tag{12}$$

where P_{w0} is the pressure oscillation amplitude on the window right after the bombard of the proton pulse, τ is the inverse of the attenuation rate, and T is the oscillation period. Numerical values of the coefficients are $P_{w0}=500$ bar, $\tau=0.94$ ms, $T=70$ μs for pure mercury and $P_{w0}=600$ bar, $\tau=50$ μs, $T=12$ μs for mercury filled with air bubbles of radius 1.0 mm and volume fraction 2.5%.

We compared the result of direct numerical simulations with that of the multiple scattering theory introduced in Sec. 2.2. The homogenized wave equations in Sec. 2.2 were solved numerically in the longitudinal direction of the chamber, with the initial liquid pressure given by Eq. (11) rather than a sinusoidal profile as for acoustic waves. As widely recognized [3,18], the equations in Sec. 2.2 are valid for small void fractions and accurate up to the first order of β. In our simulation for the SNS problem, $\beta=2.5\%$, which is not very small. Therefore, the simulation results could be different from the theoretical predictions based on homogenized wave equations. Indeed we found discrepancies, for example, for injected air bubbles of radius 1.0 mm and volume fraction 2.5%, the simulation showed an oscillation with period $T=12$ μs, while the homogenized wave equations gave a period of 15.4 μs. The simulated frequency is higher due to the nonlinear effect of a finite void fraction. In another example, where $\beta=0.53\%$ and $R=0.5$ mm, the simulation had an oscillation period $T=16$ μs, while the theory gave a period of 17.6 μs, which is still different but closer to the simulation result because the void fraction is smaller in this case. Another reason for the discrepancy is the high frequency of the pressure wave in the liquid. The wave equations

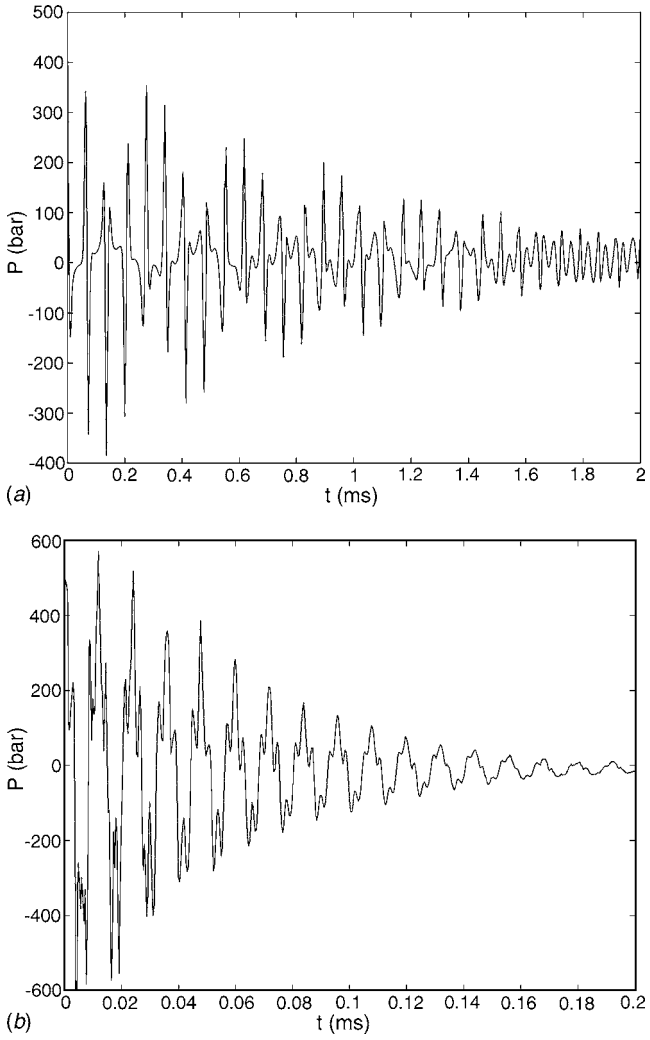

Fig. 6 The pressure profile at the center of the entrance window. (*a*) The pure mercury. (*b*) The mercury injected with noncondensable gas bubbles of radius 1.0 mm and volume fraction 2.5%.

in Sec. 2.2 were derived for sound waves with $\lambda \gg R$. In the SNS problem, the energy deposition from the proton beam increases the liquid pressure to about 500 bar at the entrance window, while the pressure in the injected bubbles remains around 1 bar. At finite bubble volume fraction, the induced pressure wave has a wavelength of the same order as the bubble radius. These effects make DNS a valuable method in the study of the SNS problem and a more general class of bubbly flows.

The accuracy of the results has been guaranteed by mesh refinement check. Thanks to the relatively large void fraction, we were able to use higher resolution in simulations of bubble layers in SNS than in those of linear and shock waves. Due to the exponential decay of proton beams along their path, the energy deposition has longitudinal attenuation as indicated by Eq. (11). In the presence of the attenuated deposition, standing wave does not form in the container, which is confirmed by numerical simulations. Furthermore, simulations showed that the longitudinal attenuation was strengthened by injected bubbles due to energy absorption, such that a 3-cm layer of bubbles near the entrance window is effectively the same as a chamber full of bubbles in terms of pressure damping.

5.4 Collapse Pressure of Cavitation Bubbles. The second step is the calculation of the collapse pressure of cavitation bubbles. The Keller equation for the bubble growth and collapse in the weakly compressible liquid was used for that purpose. With the ambient liquid pressure obtained in the first step, the closed system of equations is

$$\left(1-\frac{1}{c_f}\frac{dR}{dt}\right)R\frac{d^2R}{dt^2}+\frac{3}{2}\left(1-\frac{1}{3c_f}\frac{dR}{dt}\right)\left(\frac{dR}{dt}\right)^2 = \frac{1}{\rho_f}\left(1+\frac{1}{c_f}\frac{dR}{dt}+\frac{R}{c_f}\frac{d}{dt}\right)(p_B-p)$$

$$p_g = p_B + \frac{2\sigma}{R}$$

$$p_g R^3 = p_{g0} R_0^3$$

The p in the equation above is the difference between the ambient pressure and the vapor pressure of mercury in the bubble, however the latter is much smaller in our case and can be neglected. In the last equation, the gas pressure in the bubble is associated with the bubble radius by the isothermal relation, which is valid for most of the cavitation bubbles in the target and especially during their evolution stages after the formation and before the collapse. To estimate the range of initial bubble sizes for our numerical studies, recall that the cavitation bubble grows from a nucleus whose radius is bounded below by the stability condition [32,34]

$$\frac{4\sigma}{3R_0} < -p$$

For liquid mercury, $\sigma = 0.48$ kg/s^2, in SNS a typical tension of 100 bar gives $R_0 > 0.065$ μm. Therefore it is reasonable to assume that the initial radius of most cavitation bubbles in the SNS are below 1 μm, which justifies the isothermal relation for the bubbles.

The pressure waves in both the pure and bubbly mercury have an attenuating sinusoidal form. Since the attenuation is much slower than the period of oscillation, we calculated the overall collapse pressure of cavitation bubbles by using a purely sinusoidal pressure wave for one period and summing up all periods with the attenuating amplitude. The purely sinusoidal time-wise fluctuation of pressure has the following form:

$$p(t) = P\sin\left(\frac{2\pi t}{T}+\phi_0\right) \tag{13}$$

where ϕ_0 is the initial phase when a cavitation bubble starts to grow from a nucleus. ϕ_0 must be within $[-\pi, 0]$ because for the bubbles to grow the initial pressure must be below the saturated pressure of mercury, which is almost 0 compared to the pressure wave in the SNS target.

The typical bubble size evolutions with various ϕ_0 are shown in Fig. 7. It is interesting to notice that the bubble does not always collapse—the bubbles beginning to grow at $\phi_0 < -0.8\pi$ continues to grow after a period. Although they may collapse after two or more periods according to the Keller equation, the associated collapse pressure is smaller since the ambient pressure has attenuated. On the other hand, for ϕ_0 within $[-0.8\pi, 0]$ a bubble collapses within about a period. We are only interested in the first collapse because it produces the largest pressure peak and after that the bubble often fissures into a cloud of tiny bubbles and the Keller equation no longer applies [32]. Figure 8 shows the dependence of the first collapse pressure P_c on ϕ_0. It is seen that the collapse pressure is highest for ϕ_0 around -0.63π, and the average collapse pressure $\overline{P_c}$ is roughly one half of the peak value at $\phi_0 = -0.63\pi$.

Neglecting the surface tension and the viscosity, which is justified by the high pressure wave in the liquid, the Keller equation becomes a purely acoustic equation so that P_c is a function of $R_0/c_f T$. In prescribed ambient pressure wave, P_c is a function of R_0 and p_{g0}, and we observed that P_c depends only on the gas

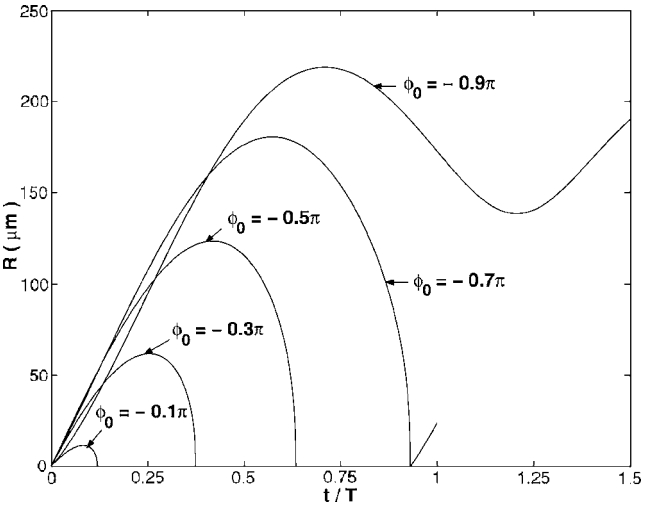

Fig. 7 Bubble size evolution with different ϕ_0. R_0=1.0 μm, p_{g0}=0.01 bar, P=100 bar, T=20 μs.

content $p_{g0}R_0^3$ as long as $p_{g0} \ll P$. Combining the two observations, we see that $\overline{P_c}$ is a function of P and $p_{g0}(R_0/c_fT)^3$. In fact, in the range of $P<10$ kbar and $T<1$ ms, an empirical formula for $\overline{P_c}$ with P, T as variables and p_{g0}, R_0 as parameters was obtained

$$\overline{P_c}(P,T) \doteq \frac{1}{2}P_c(P,T,\phi_0=-0.63\pi) \doteq \frac{93.0}{2}\left(\frac{P}{\rho_f c_f^2}\right)^{1.25}\left(\frac{p_{g0}}{\rho_f c_f^2}\left(\frac{R_0}{c_f T}\right)^3\right)^{-0.50} \text{ kbar} \quad (14)$$

with errors less than 1%. The result agreed with the fact that the higher rate of stressing the fluid is experiencing, the higher tension can be sustained. In the bubble injection regime, the period of pressure oscillation T decreases which in turn reduces the cavitation bubble collapse pressure.

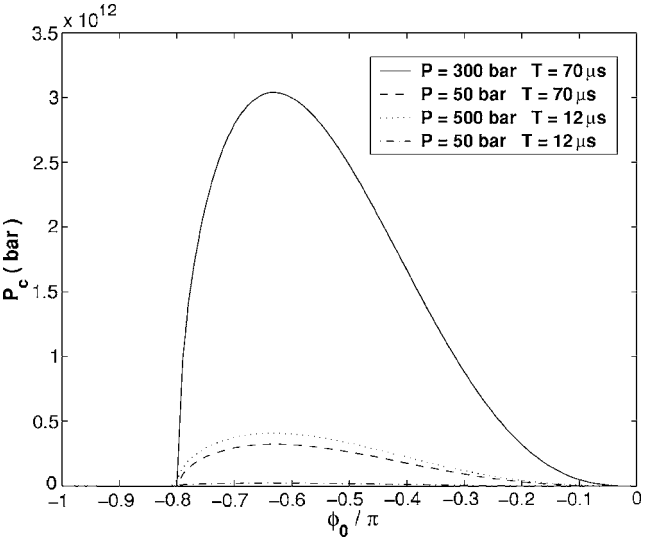

Fig. 8 The first collapse pressure P_c versus ϕ_0 under the sinusoidal pressure waves with different amplitude P and period T. The solid line and the dashed line correspond to the pure mercury, the dotted line and the dashed-dotted line correspond to the mercury filled with air bubbles of radii 1.0 mm and volume fraction of 2.5%.

5.5 Efficiency of Cavitation Damage Mitigation. Our goal is to evaluate the mitigation of the cavitation damage by the bubble injection, i.e., to find the ratio between the overall impact on the container from the collapses of cavitation bubbles in the pure mercury and the mercury with nondissolvable gas bubbles. As mentioned in Sec. 5.2, we needed only to compare the average collapse pressure $\overline{P_c}$. It is worth pointing out that, according to Eq. (14), $\overline{P_c}$ can be factored into two parts, one depending on P and T, and the other one on p_{g0}, R_0. This implies that the ratio between the two cases (with and without bubble injection) is *independent* of the size of the initial nucleus and amount of gas in it as long as $p_{g0} \ll P$.

To estimate quantitatively the efficiency of the cavitation mitigation on the entrance window by the bubble injection, we found the average collapse pressure in each period and took the sum over all the periods of the attenuating sinusoidal pressure wave given in Eq. (12). In other words, we defined

$$S = \sum_{n=0}^{\infty} \overline{P_c}(P_w(nT),T) = \sum_{n=0}^{\infty} \overline{P_c}(P_{w0}e^{-(nT/\tau)},T) \quad (15)$$

where the summand is the average collapse pressure in the nth period. The overall cavitation damage is proportional to S. The ratio of S in pure mercury and S in bubbly mercury was defined to be the mitigation efficiency, i.e.,

$$E(\beta,R) = \frac{S(\beta=0)}{S(\beta,R)} \quad (16)$$

where β and R are the volume fraction and mean radius of the injected bubbles. Combining Eqs. (14) and (15), we obtain

$$S \doteq KP_{w0}^{1.25}T^{1.50}\sum_{n=0}^{\infty} e^{-1.25(nT/\tau)} = K\frac{P_{w0}^{1.25}T^{1.50}}{1-e^{-1.25T/\tau}} \quad (17)$$

where K is a coefficient depending only on the cavitation nucleus and cancels in E.

Using the data in the paragraph following Eq. (12), we found that $E(\beta=2.5\%, R=1.0 \text{ mm})=32.7$. Varying β and R in the simulation of pressure wave propagation we can easily measure the corresponding efficiency. For example, when $\beta=0.53\%$ and $R=0.5$ mm, we found $P_{w0}=450$ bar, $\tau=44$ μs, $T=16$ μs. From Eqs. (16) and (17), $E(0.53\%, 0.5 \text{ mm})=42.9$.

Therefore, we have confirmed the mitigation of cavitation through the injection of nondissolvable gas bubbles. The bubbles absorb/disperse the energy and rapidly attenuate the pressure on the entrance window of the SNS target so that the cavitation lasts for much shorter time. The simulation results will be compared to experimental data from the SNS group on bubble injection and cavitation mitigation once they are available.

6 Conclusion

Through the comparison of numerical simulations with experiments and theoretical predictions on the propagation of acoustic and shock waves in bubbly fluids, the direct approach to the simulation of bubbly flows using the method of front tracking and the FronTier code has been validated. The method has a variety of current and prospective applications, such as Rayleigh-Taylor instability [35,36] and cavitating flows [29]. For cavitating flows, the dynamics of vapor bubble phase boundaries was resolved in the simulations of atomization of a high speed jet, and the tracking of the bubble surfaces was extended to dynamically created bubbles.

The pressure wave relaxation in bubbly mercury in the SNS target has been investigated numerically using the FronTier hydro code. The estimation of cavitation bubble collapse pressure under periodic ambient pressure has been carried out systematically. The efficiency of the mitigation of overall cavitation damage by the injection of bubbles has been calculated. The overall cavitation

damage has been found to be reduced by more than an order of magnitude through the injection of gas bubbles with volume fraction of order 1%. Therefore the use of layers of nondissolvable gas bubbles as a pressure mitigation technique to reduce the cavitation erosion has been confirmed.

Acknowledgment

We thank John Haines and Bernie Riemer for fruitful discussions of SNS related problems. This manuscript has been authored in part by Brookhaven Science Associates, LLC, under Contract No. DE-AC02-98CH10886 with the U.S. Department of Energy. The United States Government retains, and the publisher, by accepting the article for publication, acknowledges, a world-wide license to publish or reproduce the published form of this manuscript, or allow others to do so, for the United States Government purpose.

References

[1] Riemer, B., et al., 2002, "Status Report on Mercury Target Related Issues," Technical Report No. SNS-101060100-TR0006-R00, Oak Ridge National Laboratory, TN.
[2] Beylich, A. E., and Gülhan, A., 1990, "On the Structure of Nonlinear Waves in Liquids With Gas Bubbles," Phys. Fluids A, **2**(8), pp. 1412–1428.
[3] Caflisch, R. E., Miksis, M. J., Papanicolaou, G. C., and Ting, L., 1985, "Effective Equations for Wave Propagation in Bubbly Liquids," J. Fluid Mech., **153**, pp. 259–273.
[4] Watanabe, W., and Prosperetti, A., 1994, "Shock Waves in Dilute Bubbly Liquids," J. Fluid Mech., **274**, pp. 349–381.
[5] van Wijngaarden, L., 1972, "One-Dimensional Flow of Liquids Containing Small Gas Bubbles," Annu. Rev. Fluid Mech., **4**, pp. 369–396.
[6] Finch, R. D., and Neppiras, E. A., 1973, "Vapor Bubble Dynamics," J. Acoust. Soc. Am., **53**, pp. 1402–1410.
[7] Hao, Y., and Prosperetti, A., 1999, "The Dynamics of Vapor Bubbles in Acoustic Pressure Fields," Phys. Fluids, **11**(8), pp. 2008–2019.
[8] Ceccio, S. L., and Brennen, C. E., 1991, "Observations of the Dynamics and Acoustics of Traveling Bubble Cavitation," J. Fluid Mech., **233**, pp. 633–660.
[9] Kuhn de Chizelle, Y., Ceccio, S. L., and Brennen, C. E., 1995, "Observations and Scaling of Traveling Bubble Cavitation," J. Fluid Mech., **293**, pp. 99–126.
[10] Welch, S. W., 1995, "Local Simulation of Two-Phase Flows Including Interface Tracking With Mass Transfer," J. Comput. Phys., **121**, pp. 142–154.
[11] Juric, D., and Tryggvason, G., 1998, "Computation of Boiling Flows," Int. J. Multiphase Flow, **24**, pp. 387–410.
[12] Delale, C. F., Nas, S., and Tryggvason, G., 2005, "Direct Numerical Simulation of Shock Propagation in Bubbly Liquids," Phys. Fluids, **17**, pp. 121705–121708.
[13] Samulyak, R., Lu, T., and Prykarpatskyy, Y., 2004, "Direct and Homogeneous Numerical Approaches to Multiphase Flows and Applications," Lect. Notes Comput. Sci., **3039**, pp. 653–660.
[14] Samulyak, R., Prykarpatskyy, Y., Lu, T., Glimm, J., Xu, Z. L., and Kim, M. N., 2006, "Comparison of Heterogeneous and Homogenized Numerical Models of Cavitation," Int. J. Multiscale Comp. Eng., **4**, pp. 377–390.
[15] Keller, J. B., and Kolodner, I. I., 1956, "Damping of Underwater Explosion Bubble Oscillations," J. Appl. Phys., **27**, pp. 1152–1161.
[16] Keller, J. B., and Miksis, M. J., 1980, "Bubble Oscillations of Large Amplitude," J. Acoust. Soc. Am., **68**, pp. 628–633.
[17] Prosperetti, A., and Lezzi, A. M., 1986, "Bubble Dynamics in a Compressible Liquid. Part 1. First-Order Theory," J. Fluid Mech., **168**, pp. 457–478.
[18] Commander, K. W., and Prosperetti, A., 1989, "Linear Pressure Waves in Bubbly Liquids: Comparison Between Theory and Experiments," J. Acoust. Soc. Am., **85**(2), pp. 732–746.
[19] Chapman, R. B., and Plesset, M. S., 1971, "Thermal Effects in the Free Oscillation of Gas Bubbles," ASME J. Basic Eng., **93**, pp. 373–376.
[20] Prosperetti, A., Crum, L. A., and Commander, K. W., 1988, "Nonlinear Bubble Dynamics," J. Acoust. Soc. Am., **83**, pp. 502–514.
[21] Fox, F. E., Curley, S. R., and Larson, G. S., 1955, "Phase Velocity and Absorption Measurements in Water Containing Air Bubbles," J. Acoust. Soc. Am., **27**(3), pp. 534–539.
[22] Macpherson, J. D., 1957, "The Effects of Gas Bubbles on Sound Propagation in Water," Proc. Phys. Soc. London, Sect. B, **70**, pp. 85–92.
[23] Silberman, E., 1957, "Sound Velocity and Attenuation in Bubbly Mixtures Measured in Standing Wave Tubes," J. Acoust. Soc. Am., **29**(8), pp. 925–933.
[24] Glimm, J., Grove, J., and Zhang, Y., 2002, "Interface Tracking for Axisymmetric Flows," SIAM J. Sci. Comput. (USA), **24**(1), pp. 208–236.
[25] Collela, P., and Woodward, P., 1984, "The Piecewise Parabolic Method (PPM) for Gas-Dynamics," J. Comput. Phys., **54**, pp. 174–201.
[26] Collela, P., 1985, "A Direct Eulerian MUSCL Scheme for Gas Dynamics," SIAM (Soc. Ind. Appl. Math.) J. Sci. Stat. Comput., **6**(1), pp. 104–117.
[27] Glimm, J., Grove, J., Lindquist, B., McBryan, O. A., and Tryggvason, G., 1988, "The Bifurcation of Tracked Scalar Waves," SIAM (Soc. Ind. Appl. Math.) J. Sci. Stat. Comput., **9**, pp. 61–79.
[28] Glimm, J., Grove, J., Li, X. L., and Tan, D. C., 2000, "Robust Computational Algorithms for Dynamic Interface Tracking in Three Dimensions," SIAM J. Sci. Comput. (USA), **21**, pp. 2240–2256.
[29] Xu, Z. L., Kim, M. N., Lu, T., Oh, W., Glimm, J., Samulyak, R., Li, X. L., and Tzanos, C., 2006, "Discrete Bubble Modeling of Unsteady Cavitating Flow," Int. J. Multiscale Comp. Eng., **4**, pp. 601–616.
[30] Noordzij, L., and van Wijngaarden, L., 1974, "Relaxation Effects, Caused by Relative Motion, on Shock Waves in Gas-Bubble/Liquid Mixture," J. Fluid Mech., **66**, pp. 115–143.
[31] Lu, T., 2005, "Direct Numerical Simulation of Bubbly Flows and Interfacial Dynamics of Phase Transitions," Ph.D. thesis, http://pubweb.bnl.gov/users/tlu/www
[32] Brennen, C. E., 1995, *Cavitation and Bubble Dynamics*, Oxford University Press, Oxford.
[33] Hickling, R., and Plesset, M. S., 1964, "Collapse and Rebound of a Spherical Bubble in Water," Phys. Fluids, **7**(1), pp. 7–14.
[34] Arndt, R. E. A., 1981, "Cavitation in Fluid Machinery and Hydraulic Structures," Annu. Rev. Fluid Mech., **13**, pp. 273–328.
[35] Glimm, J., Grove, J., Li, X. L., Oh, W., and Sharp, D. H., 2001, "A Critical Analysis of Rayleigh-Taylor Growth Rates," J. Comput. Phys., **169**, pp. 652–677.
[36] Jin, H., Liu, X. F., Lu, T., Cheng, B., Glimm, J., and Sharp, D. H., 2005, "Rayleigh-Taylor Mixing Rates for Compressible Flow," Phys. Fluids, **17**, pp. 024104–024113.

Near-Field Flow Measurements of a Cavitating Jet Emanating From a Crown-Shaped Nozzle

Stephane Poussou

Michael W. Plesniak

Department of Mechanical Engineering,
Purdue University,
West Lafayette, IN 47907

The effect of a crown-shaped nozzle on cavitation is studied experimentally in the near-field of a 25 mm diameter (D) water jet at $Re_D = 2 \times 10^5$ using particle image velocimetry (PIV) and high speed shadowgraphy recorded with a 5000 fps digital camera. The objectives are to passively control the jet flow structure and to examine its consequences on the physical appearance of cavitating bubbles. The experiments are performed in a closed-loop facility that enables complete optical access to the near-nozzle region. The cavitating and noncavitating mean velocity fields are obtained up to three nozzle diameters downstream and compared to those of a companion round nozzle. PIV measurements are taken in two distinct azimuthal planes passing through the tip and bottom points of the crown nozzle edge. The data include shear layer momentum thickness and vorticity thickness, spanwise vorticity distribution and streamwise normal Reynolds stress. Significant deviation from an axisymmetric shear layer is observed in the noncavitating flow consistently up to one diameter downstream, after which identical asymptotic conditions are achieved in both round and crown-shaped nozzles. Maximum magnitudes of spanwise vorticity and streamwise normal Reynolds stress are the highest downstream of the nozzle tip edges under noncavitating conditions. Significant modifications in trends and magnitudes are observed for the shear layer momentum thickness under cavitating conditions up to one diameter downstream. Qualitative flow visualization reveals that bubble growth occurs at different conditions depending on azimuthal location. Bubbles, in the form of elongated filaments, are the dominant structures produced downstream of the valley edges of the nozzle with an inclination of 45 deg with respect to the direction of the flow, and are observed to persist with significant strength up to two diameters downstream. These filaments are stretched between periodic larger-scale, spanwise bubbly clusters distorted in the shape of the nozzle outlet. The tip edges produce cavitating bubbles under conditions similar to that of a classical round nozzle. In summary, it was demonstrated that passive control of turbulent structures in the jet does impact the cavitation process. [DOI: 10.1115/1.2717615]

1 Introduction

This paper presents an experimental investigation of a water jet at relatively high Reynolds number emanating from a conically tapered, crown-shaped nozzle and explores its effect on cavitation in the near-field flow. Cavitation phenomena occur when a gaseous cavity is subject to a local pressure equal to or lower than the vapor pressure [1]. Unstable growth of the nucleus is followed by catastrophic collapse, which is a source of acoustic vibration and erosion if near a solid boundary. Levels of pressure sufficiently low for inception are possible within shear flows in the cores of vortical structures [2,3]. A cavitation number is typically defined by $\sigma \equiv (P - P_v)/(\frac{1}{2}\rho U_\infty^2)$, where P is the mean static pressure, P_v is the vapor pressure, and ρ is the density of the liquid, and U_∞ is the jet velocity. The onset of cavitation in a submerged jet was studied experimentally by Gopolan et al. [4] in a 50 mm diameter (D) round jet at $\mathrm{Re}_D = 5 \times 10^5$. When the boundary layer was initially laminar, inception occurred in the cores of strong streamwise vortices in the near-field ($x/D < 0.55$) with inception indices of 2.5, with bubbles in the form of inclined "cylinders." When the boundary layer was tripped, inception was delayed downstream ($x/D \approx 2$) with inception indices of 1.7, in the form of distorted "spherical" bubbles found in the cores of spanwise vortex rings. Their study showed that cavitation inception is sensitive to the initial state of the shear layer and the vortical structure of the near-field flow. Trends of the incipient cavitation number with jet velocity, nozzle size or nuclei content are still under investigation, as reported in the review of Arndt [3].

Promotion of cavitation in submerged jets is a practical means to improve the efficiency of processes such as medical disinfection or material cutting. Passive control at the nozzle exit, e.g., modifying the outlet geometry, can alter the underlying structure of the near-field flow and subsequently affect cavitation in the shear layer. Nozzles of indeterminate origin are nozzles with a round cross section but in which the axial projection of the outlet edge varies around the circumference [5]. Different outlet geometries have been studied to attempt perturbing the development of vortex rings by injecting longitudinal vorticity at the origin of the shear layer. Webster and Longmire [6] performed experiments on inclined nozzles and observed an influence of the nozzle exit plane angle on pairing process, vortex rings inclination, shear layer growth, along with deviations from axisymmetric spreading. Longmire et al. [7] studied crown-shaped nozzles for both forced and unforced flows and reported significant azimuthal asymmetry. Observations were explained by the presence of longitudinal vortices attached to typical vortex rings, causing different entrainment of ambient fluid according to azimuthal location. Shu et al. [8] investigated the formation of pairs of counter-rotating streamwise vortices in crown-shaped nozzles. They showed that incursion of ambient fluid downstream of the bottom edges at the nozzle outlet resulted in radial excursion of jet fluid by vortex pairs downstream of the tip edges due to reorganization of vortex pairs and corresponding to Biot-Savart self-induction.

Contributed by the Fluids Engineering Division of ASME for publication in the JOURNAL OF FLUIDS ENGINEERING. Manuscript received August 30, 2005; final manuscript received October 30, 2006. Assoc. Editor: Georges L. Chahine.

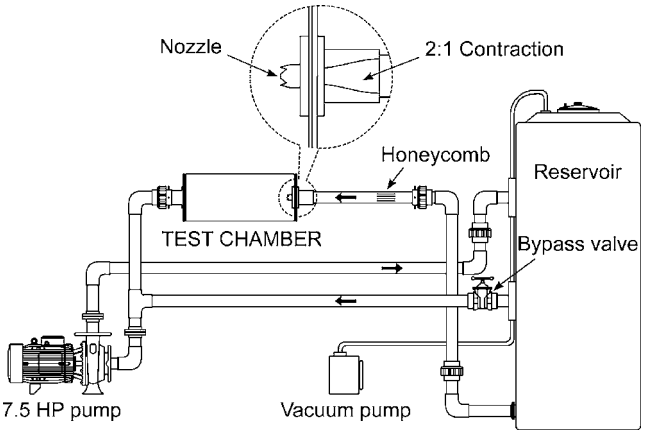

Fig. 1 Schematic of the experimental facility

In this paper, particle image velocimetry (PIV) is used to examine the velocity field downstream of a crown-shaped nozzle in the near-nozzle region. High speed shadowgraphy is used to visualize the growth of freestream nuclei. Considerations of bubble collapse and values of cavitation inception numbers are beyond the scope of the present paper. Our objective is to investigate the effect of a crown-shaped geometry on the near-field flow of a jet at developed cavitating conditions and visualize whether the alterations of the flow field are substantial enough to affect nuclei growth. It is hypothesized that longitudinal vortices formed downstream of the nozzle bottom edges contribute to cavitation in the near-nozzle region. To date, experimental studies have not investigated the influence of a change in nozzle edge geometry on the cavitation process at large-scale and/or small-scale. This question will be addressed by the present paper through experimental observation of a cavitating jet emanating from a crown-shaped nozzle. Our measurements show that the development of the shear layer is altered by the nozzle geometry, and inclined elongated bubbles are observed in the cores of secondary vortices downstream of valley edges and coexist with bent spanwise primary vortices up to approximately one diameter downstream. Specific objectives of this paper include: (i) comparison of the velocity fields of a round and a crown-shaped nozzle under noncavitating and developed cavitating conditions; (ii) qualitative comparison of visual occurrence of cavitation between a round and a crown-shaped nozzle.

2 Experimental Setup and Procedure

2.1 Flow Facility and Crown-Shaped Nozzle. The experiments were performed in a closed-loop water jet-cavitation facility shown schematically in Fig. 1. The cylindrical test chamber is made of acrylic to allow complete optical access and is entirely filled with water. Its dimensions are 23 cm in diameter by 60 cm in length. The flow is driven by a 7.5 HP centrifugal pump (12 l/s) located downstream and 1 m below the nozzle to avoid cavitation from freestream nuclei produced by the pump itself. The flow rate through the test chamber is measured with an ultrasonic flowmeter (GE Panametrics TransPort, Model PT878) and regulated with a bypass valve located between the pump inlet and the reservoir. Closing the bypass valve produces a drop of pressure inside the test chamber and increased suction through the nozzle. The resulting jet velocity varies with the inside pressure. The facility allows only growth of nuclei inside the test chamber. The jet mean velocity at the nozzle exit plane, U_∞, is fixed at 7 m/s and 11 m/s when the flow is not cavitating and cavitating, respectively. The Reynolds number based on jet diameter is 1.5×10^5 and 2.5×10^5, corresponding to cavitation indices of 2.6 and 0.4, respectively. The dissolved oxygen content is 8 mg/l for all experiments and is measured with a dissolved oxygen meter (Extech Instruments, Model 407510). Water in the facility contains only naturally present nuclei and is kept at rest in the reservoir at 0.2 bar below atmospheric pressure before each run for an extended period, typically 3 h. Nuclei content of the flow within the facility cannot be directly controlled and is not monitored during a run. Honeycombs are used to reduce swirl and freestream turbulence upstream of the nozzle. The jet has a diameter $D=2.54$ cm and issues from a smooth fifth order polynomial contraction of 2:1 diameter ratio.

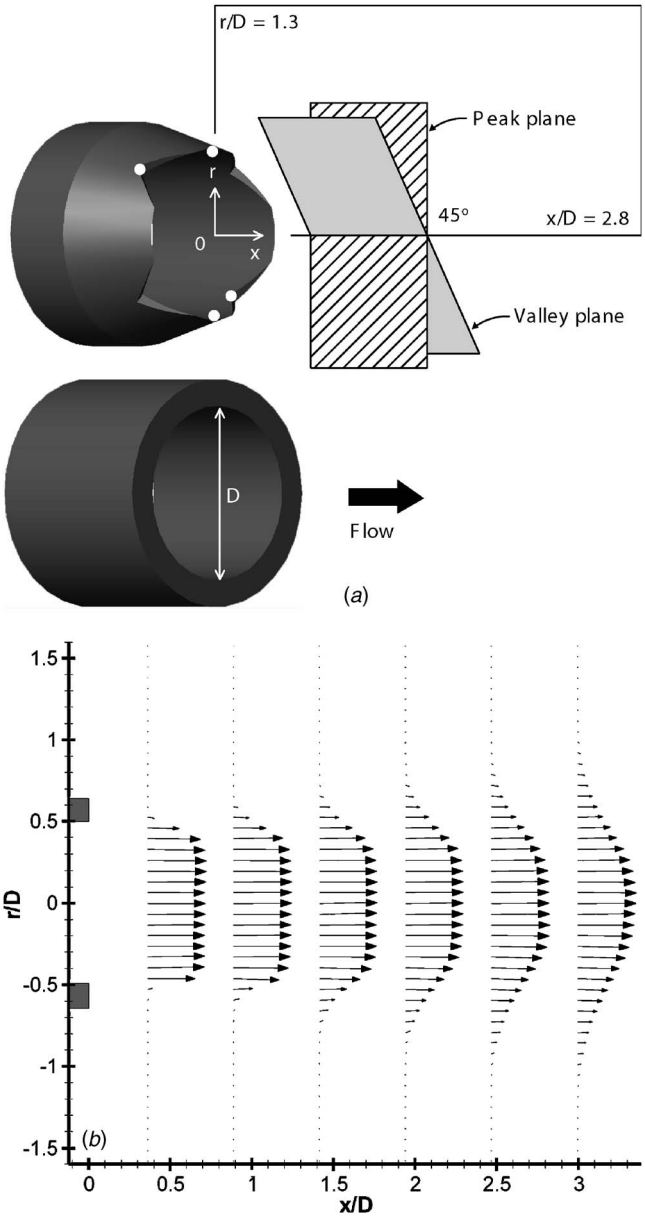

Fig. 2 (*a*) (*i*) Schematic representation of the crown-shaped and round nozzles; (*ii*) planes and region of PIV measurements. (*b*) PIV mean velocity field of the round nozzle under noncavitating conditions.

Two different 2.6 mm long nozzles are used in the experiments, as shown in Fig. 2(*a*). The 4-point conically tapered crown-shaped nozzle has an initial wall thickness of 3.8 mm. The depth of the valleys from the exit edge is 8 mm and the angle is 90 deg. Conical tapering starts at a distance 14.7 mm from the exit edge.

2.2 Particle Image Velocimetry System. All of the PIV measurements are recorded in the near-field of the nozzle exit (from

$x/D=0$ to 2.8 and from $r/D=0$ to 1.3) as indicated by the coordinate system (x,r) in Fig. 2(*a*). The origin of the coordinate system is located at the intersection between the jet centerline and the exit plane. The laser sheet is produced by a dual-head, frequency-doubled Nd:YAG laser capable of 300 mJ/pulse. The laser sheet coincides with the vertical azimuthal plane passing through the centerline of the nozzle. Because of the asymmetry in the crown-shaped nozzle, two different azimuthal planes are studied: the "peak" plane includes two points diametrally located at the top of the nozzle exit edge, while the "valley" plane includes two points diametrally located at the bottom of the nozzle exit edge, as indicated in Fig. 2(*a*). The nozzle is rotated accordingly to the selected plane of interest. Images of the jet shear layer are recorded using a 2048×2048 pixels, 12-bit gray-level digital camera (TSI Powerview, Model 630149-G). Analysis of the vector field is performed with a commercial FFT-based algorithm (TSI, Insight 5.1) using cross-correlation, and validated with a median filter. The window size is 64×64 pixels (2.5×2.5 mm) and grid size is 32×32 pixels to allow 50% overlap between adjacent windows. The corresponding vector density is 128 vectors/cm^2. Under noncavitating conditions, silver-coated hollow glass spheres are used to seed the water. These particles have a mean diameter of 13 μm and a specific gravity between 1.6 and 1.7. Under cavitating conditions, neutrally buoyant fluorescent particles of 20 μm diameter are used. These particles are dye-colored (rhodamine 6G and dichlorofluorescein) and emit light at 573 nm wavelength. A notch interference filter is installed in front of the CCD sensor inside the camera to reject light emitted by bubbles and transmit only fluorescent light from the seeding particles. Both types of particles have a Stokes number of the order of 0.01 and thus can be considered as tracers in the flow. The dimensions of the cylindrical test chamber and the location of the interrogation region near the centerline are such that radial measurements do not require correction for optical distortion by the cylindrical interface when comparing the flow fields between the two nozzles.

2.3 High Speed Shadowgraphy Setup. Flow visualization using shadowgraph illumination is used to investigate the physical appearance and motion of cavitating bubbles. Instantaneous images are captured using a high speed camera (NAC Memrecam, Model fx6000) with a shutter speed of 1/5000 s. The framing rate is 3000 images per second at 1280×344 pixels resolution and 5000 images per second at 640×344 pixels resolution. Because air bubbles tend to accumulate on top of the test chamber, the flow field is imaged from below. Backlighting is produced by an opaque white screen illuminated by a 500 W lamp placed opposite to the camera. Recirculation of large bubbles in the vicinity of the jet reduces the image quality. However those bubbles move considerably slower than the freestream nuclei embedded within the shear layer. Thus, cavitating structures are distinguished without ambiguity from background shapes by viewing sequences of images frame by frame.

2.4 Experimental Uncertainty. For each experimental configuration, a typical ensemble of 2000 instantaneous PIV realizations is averaged to achieve convergence of higher order statistics and streamwise normal Reynolds stress. A small fraction of vectors ($<5\%$) in the (x,r) plane vector field is discarded by filtering because of unpaired particles owing to out-of-plane motions arising from three-dimensionality. Under cavitating conditions, some velocity vectors cannot be determined wherever bubbles are present in the PIV image, those locations are not utilized to compute the mean velocity field. The uncertainty in particle displacement is estimated to be less than $\pm2\%$ based on the pixel resolution of the image. Pixel displacement error is combined with processing errors at a 95% confidence interval following the method of Moffat [9] to yield an uncertainty in the measured streamwise mean velocity of $\pm3\%$, cross-stream mean velocity of $\pm30\%$, maximum mean spanwise vorticity of $\pm5\%$ and streamwise normal Reynolds stress of $\pm4\%$. Detailed calculations are available in Poussou [10].

3 Structure of the Near-Field Flow of the Jet

PIV measurements are taken in the near-field flow of the crown-shaped nozzle from $x/D=0$ to 2.8 and from $r/D=0$ to 1.3, and compared to those of the reference round nozzle. The mean velocity field measured for the round nozzle under noncavitating conditions is provided in Fig. 2(*b*). The Reynolds number for each configuration—round nozzle, peak plane, and valley plane—is $\mathrm{Re}_D=1.5\times10^5$ under noncavitating conditions ($U_\infty=7$ m/s and $\sigma=2.6$) and $\mathrm{Re}_D=2.5\times10^5$ under cavitating conditions ($U_\infty=11$ m/s and $\sigma=0.4$). For consistency in the plots, a specific symbol is assigned to each configuration: ○ for the round jet, △ for the peak plane, and ▽ for the valley plane.

3.1 Shear Layer Momentum Thickness. The normalized momentum thickness of the shear layer, θ/D, is calculated as

$$\frac{\theta}{D}\equiv\int_0^\infty\frac{u}{U_\infty}\left(1-\frac{u}{U_\infty}\right)\frac{1}{D}dr \tag{1}$$

and averaged over the lower and upper halves of the jet. Under noncavitating conditions shown in Fig. 3 (*a,i*), the jet momentum thickness of the round nozzle, peak plane, and valley plane each exhibit linear growth at an identical rate of $d\theta/\mathrm{dx}=0.038$, which compares favorably to 0.037 measured by Hussain and Zedan [11] in the boundary layer initially tripped of a round air jet at $\mathrm{Re}_D=1.4\times10^5$. The valley plane has the highest values of θ/D which are 0.011 greater than the other cases because in this plane, the shear layer forms at the bottom point of the valley $0.3D$ upstream of the origin of the coordinate system $x/D=0$. The cross-sectional exit plane containing the peaks was chosen as the origin for the coordinate system because we investigate possible interactions between the structures in peak and valley planes downstream of this location. Under cavitating conditions shown in Fig. 3 (*a,ii*), the growth rate for the round nozzle is reduced to 0.033. The momentum thickness in the valley plane grows faster than that of the round nozzle up to $x/D=1$ and stabilizes downstream at the same growth rate as the round nozzle. The momentum thickness in the valley plane continues to be higher than in the round nozzle over the entire region of measurement. In the peak plane, the momentum thickness is higher than that of the round nozzle by a constant difference up to approximately $x/D=1$, after which the growth rate decreases. The deviations observed along the peak curve are due to low density of seeding particles within the cavitating shear layer. Figure 3(*b*) displays the differences in the thickness evolution induced by cavitation for each configuration. The trends of the round nozzle and valley plane are very similar, as shown in Figs. 3(*b,i*) and 3(*b,iii*). The presence of developed cavitation does not yield significant changes in shear layer growth rate, which is consistent with O'Hern [2], and Iyer and Ceccio [12]. The peak plane exhibits in Fig. 3(*b,ii*) a large deviation of quasi-constant amplitude upstream of approximately $x/D=1$ under cavitating conditions. Thus, measurements of the momentum thickness in the developed cavitating shear layer suggest that near $x/D=1$, substantial changes occur in vortical structure and bubble growth.

3.2 Maximum Spanwise Vorticity. The normalized magnitude of the spanwise vorticity (perpendicular to the plane of the light sheet), $\omega/(U_\infty/D)$, is computed for each configuration over the entire region of measurement. The corresponding maximum values found at each x/D are averaged over the lower and upper halves of the jet, and the resulting value is plotted versus axial distance from the origin. Under noncavitating conditions shown in Fig. 4(*a,i*), the peak and valley planes have higher spanwise vorticity than the round nozzle up to $x/D=1$. The peak plane exhibits the largest magnitude, followed by the valley plane whose vortic-

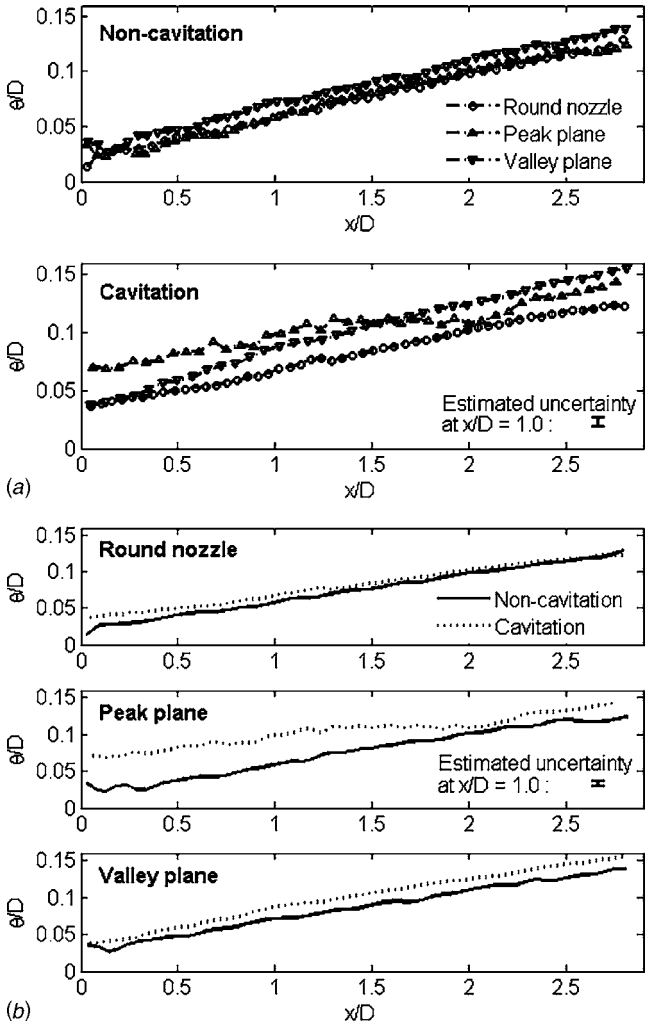

Fig. 3 (*a*) **Streamwise development of the normalized momentum thickness (*i*) without cavitation and (*ii*) with cavitation. (*b*) Streamwise development of the normalized momentum thickness of the (*i*) round nozzle, (*ii*) peak plane, and (*iii*) valley plane.**

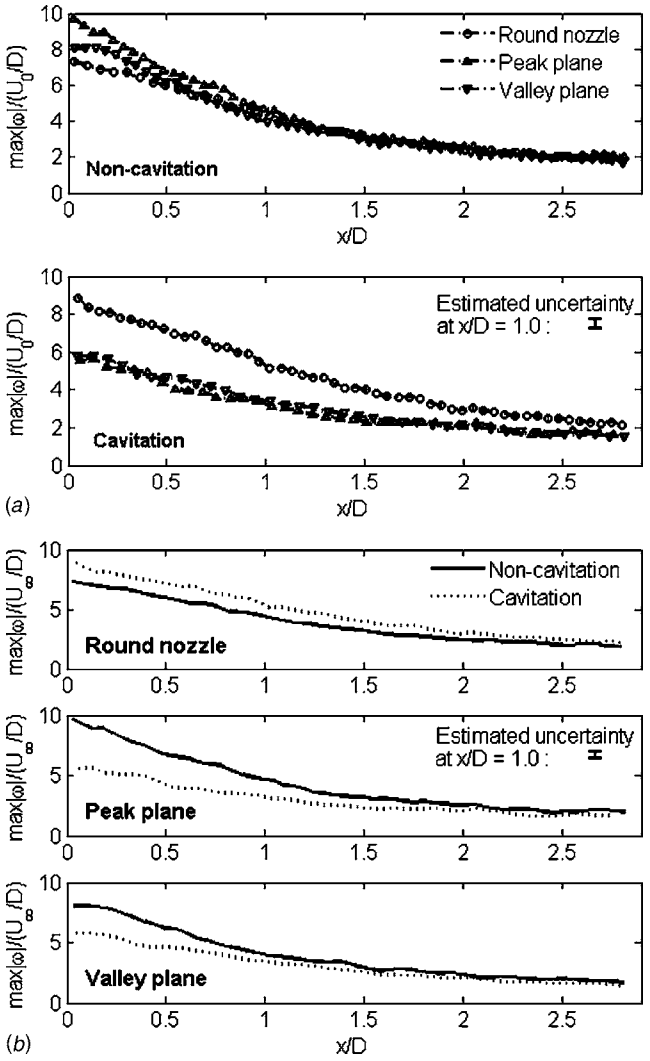

Fig. 4 (*a*) **Streamwise development of the normalized maximum spanwise vorticity (*i*) without cavitation and (*ii*) with cavitation. (*b*) Streamwise development of the normalized maximum spanwise vorticity of the (*i*) round nozzle, (*ii*) peak plane, and (*iii*) valley plane.**

ity has decayed because turbulent mixing in this plane starts upstream of $x/D=0$. Downstream of $x/D=1$, all three configurations achieve the same asymptotic conditions. Under cavitating conditions shown in Fig. 4(*a,ii*), the peak and valley planes have identical evolution over the measurement region with vorticity magnitudes significantly lower than that of the round nozzle. Comparison of the vorticity evolution without and with cavitation are plotted in Fig. 4(*b*). For the round nozzle, the presence of cavitation does not induce significant changes in trend and magnitude, whereas the peak and valley plane experience major changes upstream of $x/D\approx 1$ before asymptoting downstream. These measurements of the maximum spanwise vorticity suggest that the cavitating flows are different in the two nozzles upstream of $x/D\approx 1$.

3.3 Shear Layer Vorticity Thickness. The normalized vorticity thickness of the shear layer, δ_ω/D, is estimated by the following expression:

$$\frac{\delta_\omega}{D} \equiv \frac{1}{|\omega|_{\max}} \int_o^\infty |\omega| \frac{1}{D} dr \tag{2}$$

and averaged over the lower and upper halves of the jet. Under noncavitating conditions shown in Fig. 5(*a,i*), all three configurations exhibit similar trends and magnitudes. This is consistent with the previous observation of the evolution of the momentum thickness in Sec. 3.1. The round nozzle shows a growth rate, $d\delta_\omega/dx=0.175$ between $x/D=1$ and 2.5. Brown and Roshko [13] reported values of the growth rate between 0.145 and 0.22 in a one-stream planar mixing layer. Our value for the present axisymmetric shear layer is in agreement, because curvature effects on shear layer growth are not significant in the very near-field flow. Under cavitating conditions, shown in Fig. 5(*a,ii*), the peak and valley planes both exhibit a common trend for the vorticity thickness that is significantly higher than that of the round jet, as expected from the evolution of the maximum vorticity described in the previous section. The round nozzle has a lower growth rate for its vorticity thickness when cavitation occurs, which is consistent with the evolution of the momentum thickness.

3.4 Normal Reynolds Stress in the Streamwise Direction. The turbulent fluctuations of the velocity in the streamwise direction are estimated by substracting the mean jet velocity from the instantaneous streamwise velocity. The resulting mean normal Reynolds stress $\langle u'^2 \rangle$ is averaged over the lower and upper halves of the jet and normalized by U_∞^2. Under noncavitating conditions, shown in Fig. 6(*a,i*), the peak plane shows the highest values of

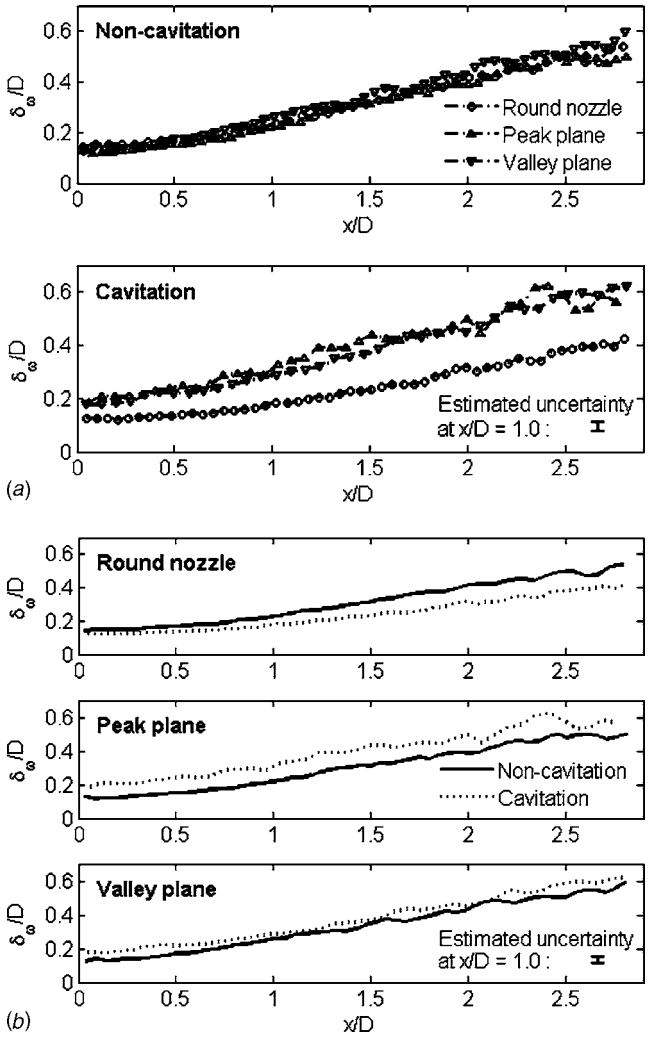

Fig. 5 (*a*) **Streamwise development of the normalized vorticity thickness** (*i*) **without cavitation and** (*ii*) **with cavitation.** (*b*) **Streamwise development of the normalized vorticity thickness of the** (*i*) **round nozzle,** (*ii*) **peak plane, and** (*iii*) **valley plane.**

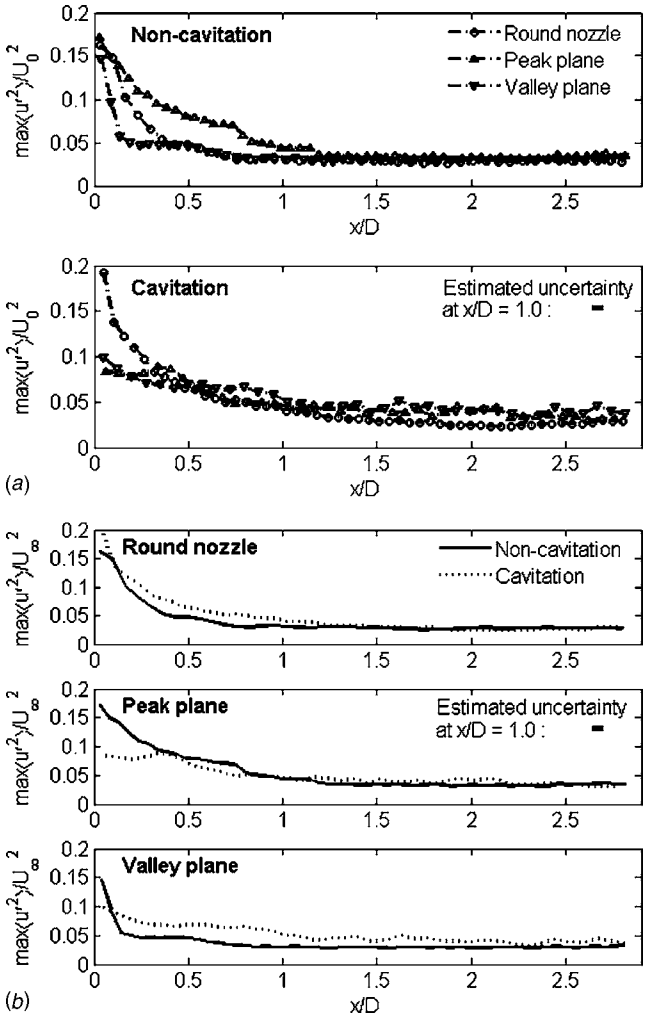

Fig. 6 (*a*) **Streamwise development of the normalized maximum normal stress** (*i*) **without cavitation and** (*ii*) **with cavitation.** (*b*) **Streamwise development of the normalized maximum normal stress of the** (*i*) **round nozzle,** (*ii*) **peak plane, and** (*iii*) **valley plane.**

normal stress up to $x/D=1$, reaching values 65% larger than that of the round nozzle at $x/D=0.5$. All configurations reach the same asymptotic value of 0.029. The measurements reported by Hussain and Zedan [11] for the velocity fluctuation intensity in an axisymmetric boundary layer initially tripped yield a streamwise normal Reynolds stress of 0.031. Our observed decreasing trends agree with those reported by Bell and Mehta [14], and Browand and Latigo [15]. Both studies reported asymptotic values of 0.027 downstream of a plane shear layer, in favorable agreement with the present value, and highest values of the order of 0.06 at the origin, whereas maximum values reported herein are significantly higher than 0.1. These measurements under noncavitating conditions of the normal streamwise stress suggest significant azimuthal deviation in the peak plane compared to the round nozzle. Under cavitating conditions shown in Fig. 6(*a,ii*), peak and valley planes collapse onto the same curve and reach a similar plateau in the very near-field flow. From the uncertainty estimation, no conclusion is possible on the relative differences between peak and valley planes.

3.5 Summary of PIV Data. Under noncavitating conditions, the growth rate of the shear layer is approximately the same for the round and crown-shaped nozzles, although the shear layer thicknesses are different. The modified jet lacks axisymmetry, as indicated by the momentum thickness being larger in the valley plane. The spanwise vorticity produced by the crown-shaped nozzle reaches higher magnitudes than in the round nozzle, which can be explained by the tapered exit of the crown-shaped nozzle. The peak plane shows higher levels of streamwise normal Reynolds stress up to one diameter downstream.

Under cavitating conditions, the changes observed for the vorticity magnitude and normal stress in each configuration at a particular location ($x/D=1$) suggest an interaction of the vortical structures produced by the peaks and the valleys. The spanwise vorticity and normal stress follow the same evolution in trend and magnitude in both peak and valley planes. The round nozzle does not undergo significant modifications contrary to the crown-shaped nozzle, suggesting that cavitation occurs differently in the two nozzles.

The differences in flow physics induced by cavitation might be explained by the hypothesis of Belahadji et al. [16]. They suggest that the rate of vortex stretching can be decoupled from the rotation rate in a streamwise vortex because of gas phase trapped in the core, allowing streamwise velocity fluctuations to be decoupled from spanwise fluctuations. Iyer and Ceccio [12] further explained that the pressure in the core of a cavitating vortex can remain constant because vortex stretching results only in more vaporization while the core diameter remains constant. They ob-

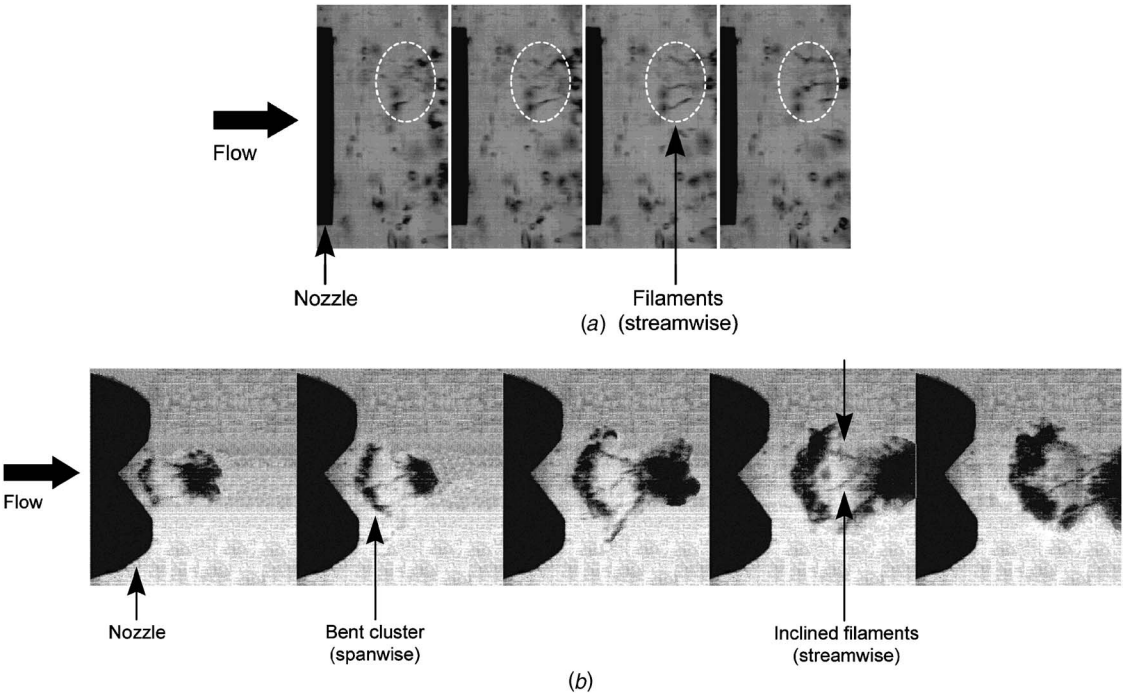

Fig. 7 (*a*) **High speed photograph sequence showing bubble growth downstream of the round nozzle (0.3 ms interval between each image at 0.2 ms exposure time, viewed from left to right).** (*b*) **High speed photograph sequence showing bubble growth downstream of a valley in the crown-shaped nozzle (0.3 ms time interval between each image at 0.2 ms exposure time, viewed from left to right).**

served that the development of vortical structures in the shear layer is not significantly affected by the presence of cavitation and averaged velocities are conserved. The use of the PIV technique is also affected by the presence of cavitation, because of the complex interactions between seeding particles and bubbles.

4 Visualization of Bubble Growth

High speed shadowgraphy was used to investigate the shape and orientation of the bubbles within the shear layer and to provide information on the physical effect of the crown-shaped geometry on cavitation. The cavitating conditions correspond to those in which PIV measurements were acquired. A visual method is used in this study to provide a qualitative description of bubble growth. Rigorous determination of incipient cavitation indices is beyond the scope of this investigation. As pointed out by Arndt [3], visual observation (with the naked eye) of cavitating bubbles can be misleading, as nuclei within large coherent structures can be activated in smaller eddies and migrate by convection.

In the round nozzle case, expansion of single freestream nuclei was observed in the cores of streamwise vortices at an axial distance between $x/D=0.4$ and 0.6 as illustrated in Fig. 7(*a*). Those observations are consistent with Gopolan et al. [4], reporting inception at $x/D=0.55$. Observations also showed aggregation of nuclei downstream in larger-scale spanwise structures that started to roll-up at $x/D\approx 1$ at a wavelength of $0.4D$, compared to $0.25D-0.3D$ in a cavitating smooth jet [4]. Vortex pairing was observed about $x/D=2$ and 4, thus suggesting a wavelength of $1.6D$ at the end of the potential core at $x/D\approx 5$. This value agrees with the wavelength $1.6D$ of the helical mode in a turbulent round jet calculated by Michalke [17]. The convection axial velocity of the vortex rings was measured to be $u/U_\infty=0.57$, yielding an estimation for the Strouhal number based on diameter of $\mathrm{St}_D=0.35$.

In the crown-shaped nozzle downstream of the peaks, spanwise bubbly clusters of relatively large scale (>3 mm) were produced with size and wavelength akin to that of the round nozzle. Growth of freestream nuclei was visually observed within streamwise vortices at the axial location $x/D=0.6$, similar to the location reported for the round nozzle, followed by roll-up of spanwise vortices at $x/D\approx 1$.

Downstream of the valleys, one observation was the typical periodic formation of large-scale spanwise vortices bent in a shape following the edge of the valley as shown in Fig. 7(*b*). In this figure, a large air bubble is entrained within the shear layer at the bottom point of a valley and its fragmentation provides enough nuclei to make low-pressure structures visible. The downstream-most round blob and curved bubbly structure observed near the edge form during different phases of the Kelvin-Helmholtz vortex shedding process. The more uniform structure occurs in the vicinity of a "braid region," whereas the curved shape is associated with the spanwise vortex ring passage. As they are convected downstream to regions of lower pressure, the curved vortices expand in the azimuthal direction and the curvature progressively decreases. This observation is consistent with that of Longmire et al. [7] reporting significant distortion of large-scale vortex rings of smoke produced by a two-peak crown-shaped nozzle. A second observation was the repetitive production of smaller-scale vortices by the inclined edges of the valley up to $x/D=0.5$, in the form of filaments oriented inward the jet with ends attached to the larger structures convected downstream. Their major axis was in the plane formed by the edges of the valley, forming a 45 deg angle with the direction of the flow. These structures were visualized by single continuous, elongated gaseous cylinders with a well-defined interface, suggesting low levels of pressure. They were observed to pair and persist downstream with significant strength until $x/D=2.5$. The two types of structures are schematically illustrated in Fig. 8. These observations can be interpreted based on the results of Shu et al. [8]. Incursion of surrounding quiescent fluid into the jet was observed at the bottom points of the valleys because of local pressure minima (Longmire et al. [7]), resulting in the formation of counter-rotating pairs of streamwise vortices. In the present experiment, this incursion process suggests that pairs of inclined vortex filaments can be created downstream of

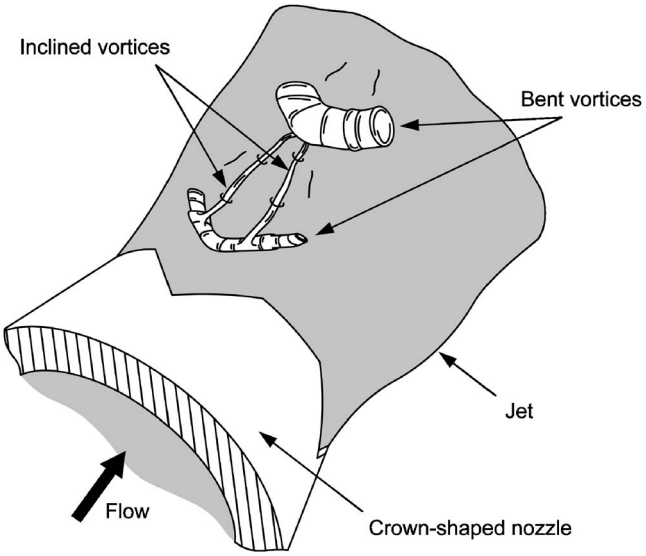

Fig. 8 Schematic of the gas phase structures observed downstream of the valleys

the valleys and stretched in the braid region between two consecutive large-scale spanwise, as shown in Fig. 8, further reducing the core diameter and local pressure to levels sufficiently low to activate freestream nuclei. These secondary structures compete with the formation of vortex rings downstream of the valleys, explaining why fewer large-scale structures were observed downstream of the valleys than downstream of the peaks. In summary, visual observations suggest that the crown-shaped nozzle introduces strong longitudinal vorticity in the shear layer in the form of inclined vortices. It is precisely these secondary vortices produced by the valleys that are of particular interest in control of cavitation inception, as secondary vortices have been found to have a profound effect on nuclei activation in the near-field flow of a round jet (Gopolan et al. [4]).

A time-averaged view of the near-field flow (Fig. 9) confirms that bubbles growth within visible large-scale structures follows the geometry of the nozzle outlet. Downstream of the peaks, bubbles reached macroscopic size at a distance of $0.6D$ from the edge compared to $0.25D$ downstream of the valleys.

Instantaneous photographs (Fig. 10) of large air bubbles entrained within the shear layer at the bottom point of valleys

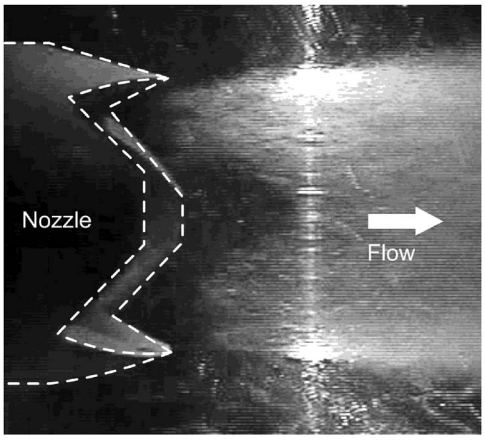

Fig. 9 Time-averaged view (30 ms exposure time) of the cavitating jet emanating from the crown-shaped nozzle. Illumination by a laser beam crossing the shear layer along a vertical diameter.

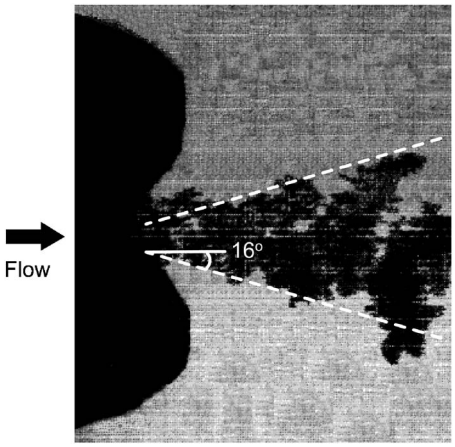

Fig. 10 Instantaneous photograph showing breakdown and azimuthal expansion of a large bubble being entrained within the shear layer at the bottom of a valley

showed fragmentation into smaller bubbles and azimuthal expansion inside the shear layer at an angle of 16 deg measured from the direction of the flow. The angle suggests that the perturbations downstream of the two points where a valley meets the exit plane can intersect downstream of the nozzle at an estimated distance of $0.9D$, which is close to the characteristic distance $x/D=1$ noted in the PIV measurements. This is consistent with the present observation of measured quantities (vorticity, Reynolds stress) reaching same asymptotic values in both the round and crown-shaped cases, which suggests a reorganization of the shear layer vortical structure downstream of $x/D \approx 1$. Shu et al. [8] also reported that the shear layer momentum thickness of a jet at $\mathrm{Re}_D=1\times10^4$ underwent significant deviations downstream of $x/D=1$, which they explained by reorganization of streamwise vortices.

5 Summary and Conclusions

A 25 mm diameter jet emanating from a crown-shaped nozzle at $\mathrm{Re}_D=2\times10^5$ was studied under noncavitating conditions (cavitation index $\sigma=2.6$) and cavitating conditions ($\sigma=0.4$) and compared to a reference classical round jet. Under noncavitating conditions, the modified shear layer lacked axisymmetry depending on azimuthal location. Downstream of the peaks, the shear layer achieved maximum values of the streamwise normal Reynolds stress, which were 65% greater than those measured in the round nozzle, as well as higher spanwise vorticity levels. The growth rate of the shear layer was not significantly altered by the crown-shaped geometry although its thickness was. When cavitation occurred, the magnitudes and trends of the spanwise vorticity and streamwise normal Reynolds stress were affected in similar manners downstream of the peaks and valleys. The main finding of this investigation is the particular effect of the nozzle outlet geometry on the physical appearance of cavitating bubbles and their evolution. Although bubble growth downstream of the peaks was similar to that observed in a classical round nozzle, cavitation occurred downstream of the valleys in the cores of strong secondary inclined vortices. Bubbles resembled small-scale, elongated cylinders oriented 45 deg with respect to the flow direction and were contained in the plane formed by the edges of the valley. Spanwise larger-scale bubbly structures were significantly bent, approximately following the shape of the nozzle outlet. These results suggest that the introduction of longitudinal vorticity at the exit of the crown-shaped nozzle profoundly alters the structure of the shear layer in the near-nozzle region up to one diameter downstream, and contributes to the formation of secondary inclined vortices that are known to determine cavitation inception. Thus,

passive control of turbulent structures in the shear layer of a developing jet emanating from a crown-shaped nozzle has potential for control of the cavitation process.

References

[1] Brennen, C. E., 1995, *Cavitation and Bubble Dynamics*, Oxford University Press, Oxford, UK.

[2] O'Hern, T. J., 1990, "An Experimental Investigation of Turbulent Shear Flow Cavitation," J. Fluid Mech., **215**, pp. 365–391.

[3] Arndt, R. E. A., 2002, "Cavitation in Vortical Flows," Annu. Rev. Fluid Mech., **34**, pp. 143–175.

[4] Gopalan, S., Katz, J., and Knio, O., 1999, "The Flow Structure in the Near Field of Jets and its Effect on Cavitation Inception," J. Fluid Mech., **398**, pp. 1–43.

[5] Wlezien, R. W., and Kibens, V., 1986, "Passive Control of Jets With Indeterminate Origins," AIAA J., **24**, pp. 1263–1270.

[6] Webster, D. R., and Longmire, E. K., 1997, "Vortex Dynamics in Jets From Inclined Nozzles," Phys. Fluids, **9**, pp. 655–666.

[7] Longmire, E. K., Eaton, J. K., and Elkins, C. J., 1992, "Control of Jet Structure by Crown-Shaped Nozzles," AIAA J., **30**, pp. 505–512.

[8] Shu, F., Plesniak, M. W., and Sojka, P. E., 2005, "Indeterminate-Origin Nozzles to Control Jet Structure and Evolution," J. Turbul., **6**(26), pp. 1–18.

[9] Moffat, R. J., 1988, "Describing the Uncertainties in Experimental Results," Exp. Therm. Fluid Sci., **1**, pp. 3–17.

[10] Poussou, S. B., 2004, "Cavitation Inception in the Near-Field of Jets Emanating From Crown-Shaped Indeterminate Origin Nozzles," M.S. thesis, Purdue University, West Lafayette, IN.

[11] Hussain, A. K. M. F., and Zedan, M. F., 1978, "Effects of the Initial Condition on the Axisymmetric Free Shear Layer: Effects of the Initial Momentum Thickness," Phys. Fluids, **21**, pp. 1100–1112.

[12] Iyer, C. O., and Ceccio, S. L., 2002, "The Influence of Developed Cavitation on the Flow of a Turbulent Shear Layer," Phys. Fluids, **14**, pp. 3414–3431.

[13] Brown, G. L., and Roshko, A., 1974, "On Density Effects and Large Structure in Turbulent Mixing Layers," J. Fluid Mech., **64**, pp. 775–816.

[14] Bell, J. H., and Mehta, R. D., 1990, "Development of a Two-Stream Mixing Layer From Tripped and Untripped Boundary Layers," AIAA J., **28**, pp. 2034–2042.

[15] Browand, F. K., and Latigo, B. O., 1979, "Growth of the Two-Dimensional Mixing Layer From a Turbulent and Nonturbulent Boundary Layer," Phys. Fluids, **22**, pp. 1011–1019.

[16] Belahadji, B., Franc, J. P., and Michel, J. M., 1995, "Cavitation in the Rotational Structures of a Turbulent Wake," J. Fluid Mech., **287**, pp. 383–403.

[17] Michalke, A., 1965, "On Spatially Growing Disturbances in an Inviscid Shear Layer," J. Fluid Mech., **23**, pp. 521–544.

Large-Eddy Simulation With Simplified Collisional Microdynamics in a High Reynolds Number Particle-Laden Channel Flow

Anna Chtab
CORIA-UMR 6614,
University of Rouen,
Site Universitaire du Madrillet,
76801 Saint-Etienne du Rouvray, France

Mikhael Gorokhovski[1]
LMFA UMR 5509,
Ecole Centrale de Lyon,
36 avenue Guy-de-Collongue,
69134 Ecully Cedex, France
e-mail: mikhael.gorokhovski@ec-lyon.fr

Computing high Reynolds number channel flows laden by heavy solid particles requires excessive CPU resources to calculate interparticle collisions. Since the frequency of these collisions is high, the kinematic details of each elementary collision may not be essential when calculating particle statistics. In this paper, the dynamics of a particle with a phase trajectory that is discontinuous (due to collisions) is simulated using a hypothetical "noncolliding" particle moving along a trajectory smoothed over interparticle collisions. The statistical temperature of this particle is assumed to be in equilibrium with the statistical "temperature" of the resolved turbulence. This simplified microdynamic is introduced into ballistic calculations of particles within the framework of the "two-way" LES approach. The simulation was conducted specifically to compare the velocity statistics of the hypothetical particle with statistics yielded by measurements in the gas/particle channel flow and by the LES/particle approach where binary collisions were simulated. This paper shows that, by assuming the universality of collisional microdynamics, one may predict the experimental observation and the results of detailed simulations without requiring supplementary CPU resources to compute the binary collisions.
[DOI: 10.1115/1.2717619]

Keywords: particle and turbulent flow, interparticle collisions, LES/particle approach

Introduction

High Reynolds number turbulent flows with immersed particles occur in many industrial applications, including particulate transport, pollution control, and pulverized coal combustion. This practical interest led to laboratory studies of interaction between particles and carrier turbulent flow. One interdependent phenomena of this interaction is the effect of interparticle collisions. Extensive experimental studies of a high-Reynolds number turbulent channel flow, laden by 70 μm copper particles, were conducted by Kulick, Fessler, and Eaton [1], and Fessler, Kulick, and Eaton [2]. These studies observed that in this flow, (i) particles did not effectively change the mean velocity of the flow; (ii) the particles' velocity profile had a particularly flattened form; and (iii) particles attenuated the gas phase turbulence. These interesting results motivated Benson and Eaton [3] to carry out an additional experimental investigation using 150 μm glass particles. This study considered two channel wall types: a wall with a specified roughness, and a wall assumed to be perfectly smooth. In the channel with rough walls, they reproduced the results reported by Kulick et al. [1]. However, in the channel with smooth walls, the particle effects were less pronounced. This was explained by the scattering effect of wall roughness; due to irregular rebounding from the rough wall, the frequency of interparticle collisions near the wall may be substantially increased, initiating the redistribution of particle velocities across the channel. The experiment of Kussin and Sommerfeld [4] in a narrow horizontal channel with rough walls emphasized the role of particle cross-channel rebounding from rough walls. This effect decreased the averaged transport velocities of particles and increased the fluctuations across the channel. However, Sommerfeld and Kussin [5] showed that effect of particle rebounding across the channel becomes weaker with increase of high of the channel.

Developing CFD codes for predicting turbulent two-phase flow behavior is needed for experimental investigation and will aid in the design of industrial systems. Modeling particle-particle collisions is of primary importance for providing accurate predictions and effectively using CPU resources.

During the past several years, it has been recognized (Moin and Kim [6]) that the large eddy simulation (LES) approach with the universality assumption at small-scale turbulence provides accurate local estimates of statistical quantities for high-Reynolds number turbulent gas flow. Recently, Saveliev and Gorokhovski [7] used renormalization-group transformation to show that, in the LES approach, turbulent viscosity appears from the cumulative contribution of the molecular viscosity term and not as a result of averaging of the nonlinear term in the Navier-Stokes equation. The momentum transport from flow to particles can be predicted accurately by applying the LES approach for flow computation with immersed solid particles (Simonin et al. [8]; Boivin et al. [9]; Apte et al. [10]). The experimental study of Kulick et al. [1] motivated Wang and Squires [11] to validate this approach for high-Reynolds number channel gas-particle flow. The LES was combined with Lagrangian tracking of round particles dragged by resolved fluid motion. Wang and Squires [11] showed that the computed velocity of the gas-phase flow corresponds well with experimental data. However, in the near-wall region, the computed particle velocity differed strongly from the measured velocity. The lack of a model for interparticle collision was considered a likely cause of this discrepancy. The LES of the moderate Reynolds number turbulent gas-particle channel flow by simulating

[1]Corresponding author.

Contributed by the Fluids Engineering Division of ASME for publication in the JOURNAL OF FLUIDS ENGINEERING. Manuscript received February 17, 2006; final manuscript received October 25, 2006. Assoc. Editor: Paul Durbin.

interparticle collision was performed by Simonin et al. [12] and Vance and Squires [13]. This study showed that particle-particle collisions may substantially modify the wall-normal transport of particles. Particles lagged the flow in the central region of the channel and led the fluid close to the wall. After Wang and Squires's paper [11], the LES of Yamamoto et al. [14] was also specifically conducted to model the Kulick's et al. [1] experiment. In addition to the approach of Wang and Squires [11], Yamamoto et al. [14] simulated the interparticle collision. In this computation, the particle mean and fluctuating velocities successfully predicted the experimental profiles of Kulick et al. [1], especially regarding the velocity gradients. In these papers, the collision process was described by a series of binary collisions with a potential for hard sphere interaction. Collision occurrences were treated either using the Monte Carlo approach (Alder and Wainwright [15] and Bird [16]) or deterministically (Tanaka and Tsuji [17]). If the number of particles is sufficiently large and the collision events are correctly detected, these models are highly accurate. On the other hand, as mentioned by Vance and Squires [13], computing interparticle collisions is very expensive, requiring significantly more CPU resources than gas flow computations. This expense provides motivation to simplify the simulation of interparticle collisions. In the approach, proposed by Sommerfeld [18,19] (see also Sommerfeld [20], and references therein), each tracking particle is also subjected to two hard sphere collisions. However, the collision partner is chosen stochastically where the parameters of the hypothetic partner are sampled from a presumed distribution. The weakness of Sommerfeld's approach is that the moments of this distribution must be known from experimental observations or preliminary computations.

The objective of our paper is to introduce and verify the universal character assumption of interparticle collisions in highly turbulent shear flows without kinematic simulating of binary hard sphere collisions.

Usually, the dynamics of colliding particles are formulated in the framework of the Boltzmann-type equation. Each Lagrangian realization of a particle group corresponds to the number density of points in the phase space, which determines the distribution function at the given moment (Dukowicz [21]; Gorokhovski and Saveliev [22]). As time increases, these points form the trajectories, which are discontinuous due to interparticle collisions. Problems computing such trajectories are well-known: (i) the unity vector in the direction of two-body postcollisional relative velocity must be prescribed (Landau and Lifshitz [23]); and (ii) the computational time step must be very small (Bird [16]). At the same time, the strong impact of interparticle collisions on the flow motion, mentioned in [12,14,17–20], implies that the frequency of these collisions is high. Then it is natural to simplify the microdynamics of interparticle collisions. One may introduce a hypothetical "noncolliding" particle that moves along the "smoothed over all particle-particle collisions" trajectory. In modern kinetic theory, the hypothetical particle with "effective" collisional dynamics is interpreted by renormalizing the Boltzmann equation (Saveliev and Nanbu [24]). The phase density of smoothly moving hypothetical particles, governed by the renormalized Boltzmann equation, corresponds exactly to the solution of the original Boltzmann equation.

This paper introduces the formulation of hypothetical particle motion by using a simple approximation; the statistical particle "temperature" is in local "thermodynamic equilibrium" with resolved turbulence. In terms of LES/two-way coupling, our objective was to compare the computed velocity statistics with the measured one in experiments of Kulick et al. [1] and Benson and Eaton [3]. This paper also compares the numerical predictions with those obtained by the LES/particle computation, in which the binary collisions are simulated (Yamamoto et al. [14]). The paper addresses the question: "Can the computational model, based on simplified collisional microdynamics, match the measurements with the same predictability as Yamamoto's et al. [14] approach?"

2 Simulation Overview

2.1 Motion of a Hypothetical Particle. Consider the dispersed two-phase turbulent flow as a system of interacting Lagrangian fluid and solid particles that evolves over time. The kinetic description for particles with position $\vec{\mathbf{r}}(x_1,x_2,x_3)$ and velocity $\vec{\mathbf{v}}(\mathbf{v}_1,\mathbf{v}_2,\mathbf{v}_3)$ is specified by the distribution function of particles $f(\vec{\mathbf{r}},\vec{\mathbf{v}},t)$ in the six-dimensional space; for solid particles, $f_p(\vec{\mathbf{r}}_p,\vec{\mathbf{v}}_p,t)$ and fluid particles, $f_g(\vec{\mathbf{r}}_g,\vec{\mathbf{v}}_g,t)$. For solid particles, we write the Boltzmann equation in the following form:

$$\frac{\partial f_p}{\partial t}+\vec{\mathbf{v}}_p\cdot\frac{\partial f_p}{\partial \vec{\mathbf{r}}_p}=I(f_p,f_p)+I(f_p,f_g) \tag{1}$$

where two collision operators on the right-hand side, $I(f_p,f_p)$ and $I(f_p,f_g)$, characterize collisions between solid particles and collisions between solid and Lagrangian fluid particles, respectively. Assuming a hard sphere collision with a prescribed efficiency, the first operator in Eq. (1) is usually modeled by the Monte Carlo method. The form of the second operator is principally unknown. The total number of solid particles does not change due to collisions; the total momentum of solid particles is also unchanged due to the solid-solid collision, i.e.,

$$\int d^3\mathbf{v}_p I(f_p,f_p)=0 \tag{2}$$

$$\int d^3\mathbf{v}_p I(f_p,f_g)=0 \tag{3}$$

$$\int d^3\mathbf{v}_p I(f_p,f_p)\mathbf{v}_p=0 \tag{4}$$

However,

$$\int d^3\mathbf{v}_p I(f_p,f_g)\mathbf{v}_p\neq 0 \tag{5}$$

Introducing the solid particles number density, n_p, and the particle velocity averaged by f_p, $\langle\mathbf{v}_p\rangle_{f_p}=(1/n_p)\int d^3\mathbf{v}_p f_p\mathbf{v}_p$, the classical kinetic approach (Landau and Lifshitz [23]) assumes the solid-solid particle collision frequency to be high enough that the correlation of velocities can be identified with the particle temperature of ordinary statistical mechanics, T_p,

$$\langle\mathbf{v}'_{p\alpha}\mathbf{v}'_{p\beta}\rangle_{f_0}=\frac{1}{3}\langle\mathbf{v}'^2_p\rangle_{f_M}\delta_{\alpha\beta}=\frac{T_p}{m_p} \tag{6}$$

where f_M is the Maxwellian distribution, m_p is the solid particle mass, and $\delta_{\alpha\beta}$ is the Kronecker delta.

Multiplying Eq. (1) by the particle velocity, integrating over all these velocities, and using Eq. (6) yields

$$\frac{d\langle\mathbf{v}_{p,\beta}\rangle_{f_p}}{dt}=-\frac{1}{n_p}\frac{\partial}{\partial x_\beta}\left(\frac{n_pT_p}{m_p}\right)+\frac{1}{n_p}\int\mathbf{v}_{p,\beta}I(f_p,f_g)d^3\mathbf{v}_{p,\beta} \tag{7}$$

This motion equation is averaged over all irregularities: the first term on the right-hand side represents an integrated effect of interparticle collisions; the second term implies the mean rate of the particle mean velocity change due to all particle-turbulence interactions. These terms must be modeled. The second term in Eq. (7) is modeled by the interaction with resolved turbulent flow,

$$(\langle\mathbf{v}_{g,\beta}\rangle_{f_g}-\langle\mathbf{v}_{p,\beta}\rangle_{f_p})/\tau_p \tag{8}$$

where τ_p is the Stokes time and $\langle\mathbf{v}_{g,\beta}\rangle_{f_g}$ is the filtered gas velocity resolved by the LES approach.

With the particle Reynolds dependency from Clift et al. [25], the Stokes time in Eq. (8) is

$$\tau_p = \frac{\rho_p d_p^2}{18\rho_g \nu_g} \frac{1}{1 + 0.15\,\mathrm{Re}_p^{0.687}} \tag{9}$$

Two different simple closure assumptions may be proposed to specify the statistical temperature of particle motion. The first assumption is based on "thermodynamic limit." Here we consider a fluid stochastic particle, having mass m_g and velocity $\mathbf{v}_g$, which strikes a solid particle of mass m_p, and velocity $\mathbf{v}_p$, such that the momentum of fluid particle changes much faster than its kinetic energy. After many collisions, the velocities of fluid and solid particles ultimately become statistically independent, $\langle \mathbf{v}_p \cdot \mathbf{v}_g \rangle = 0$, implying the average kinetic energy of the two must be equal, $\frac{1}{2} m_g \langle \mathbf{v}_g^2 \rangle = \frac{1}{2} m_p \langle \mathbf{v}_p^2 \rangle$, or in terms of statistical temperatures

$$T_p = T_{\mathrm{tur},g} \tag{10}$$

where $T_{\mathrm{tur},g}$ is a statistical temperature of fluid particle motion. According to kinetic definition, $T_{\mathrm{tur},g}$ may be formally written as

$$T_{\mathrm{tur},g} = \frac{2}{3} m_g \langle \mathbf{v}_g'^2 \rangle / 2 \tag{11}$$

where the mass of a fluid particle is formally defined here by the gas density and the volume of the fluid-element $m_g = \rho_g \cdot \mathrm{Vol}$, and $\langle \mathbf{v}_g'^2 \rangle / 2$ is the turbulent gas kinetic energy. With Eqs. (10) and (11), the considered hypothetical particle changes its velocity smoothly by the first term in Eq. (7). The local variation of filtered gas velocity (in terms of two-way coupling) modifies the trajectory of neighboring hypothetical particles.

Another simple closure of the first term in Eq. (7) may be given using the Tchen-Hinze theory for the particle kinetic energy in response to the kinetic energy of fluid velocity fluctuations (see also Zaichik et al. [26], Zaichik and Alipchenkov [27], Reeks [28], Wang and Stock [29])

$$\frac{T_p}{m_p} = \frac{\langle \mathbf{v}_g'^2 \rangle}{3} \frac{\tau_L}{\tau_L + \tau_p} \tag{12}$$

This paper identifies the integral Lagrangian time scale τ_L using the local time scale computed from the resolved mean kinetic energy of turbulence and viscous dissipation rate. Hereafter the computed statistics of a hypothetical particle, (7) and (8), are compared with the measured statistics of the solid one, using Eq. (10) or (12).

2.2 Computational Procedure and Results for Particle-Free Gas Flow. The LES of particle-laden fully-developed channel flow with two-way coupling was performed using conditions specified from Kulick et al. [1] and Benson and Eaton [3]. The numerical code of Pierce [30] was used for the gas-phase computation. This code resolves three-dimensional incompressible filtered Navier-Stokes equations on the staggered space-time grid. The second-order central differences in space and the Crank-Nicolson discretization in time are applied with semi-implicit numerical integration using Newton-Raphson iterations. The subgrid momentum transport term was modeled by the dynamic approach of Germano (Germano et al. [31]). The kinematic air viscosity was 1.5×10^{-5} m^2/s. We coupled this code in "two ways" with the Lagrangian particles solver, according to the motion equation (Eq. (7)) which was completed by gravitational force (see Fig. 1). The second order Runge-Kutta schema is chosen for computing the particle motion. In each time step, the gas flow was computed first, then the forces acting on particles were calculated and applied to the particle motion computations. The velocity of gas at the particle position was obtained by the second order Lagrange interpolating polynomial (27 nodes). Finally, the volume averaged aerodynamic force on each fluid computational cell was calculated with explicit updating of the fluid motion. At free boundaries, the periodic boundary conditions were implemented for gas and particulate phases. In computations, the wall was assumed to be perfectly smooth where each particle striking the wall rebounds elastically. The time step fraction required for the considered particle to contact the wall was computed using precollision quantities.

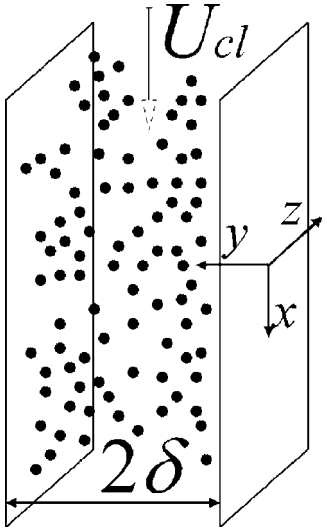

Fig. 1 Calculation configuration for channel flow

The local statistical "temperature" in Eq. (11) was defined by simply associating the volume with the control volume of the finite-difference mesh,

$$T_{\mathrm{tur},g} = \frac{2}{3} \rho_g \Delta_x \Delta_y \Delta_z \sum_{\alpha} (\mathbf{v}_{g,\alpha} - \bar{\mathbf{v}}_{g,\alpha})^2 / 2 \tag{13}$$

Figure 1 shows the computational configuration. Kulick et al. [1] experiment computations were performed at Reynolds number $\mathrm{Re}_\tau = 644$, based on friction velocity ($u_\tau = 0.49$ m/s), and channel half-width δ. This corresponds to the Reynolds number of 13,800 based on the centerline velocity and the channel half-width. We chose computation parameters similar to Wang and Squires [11], with $64 \times 66 \times 64$ grid points for the flow resolution in the x, y, and z directions, respectively, covering the computational domain $5\pi\delta/2 \times 2\delta \times \pi\delta/2$. In the streamwise and spanwise directions, the uniform grid was used ($\Delta x^+ = 80.91$, $\Delta z^+ = 20.23$ in wall coordinates). In the normal to wall direction, the nonuniform stretched grid was applied with the first velocity position at $y^+ = 0.88$. The particle radius is much smaller than the filter width except very near the wall, where the particle radius can be comparable to the wall-normal grid spacing, as seen in both Wang and Squires [11] and Yamamoto et al. [14]. Thus, the point-particle assumption is less valid near the wall.

In the case of single-phase flow, Fig. 2 shows the computed mean velocity (Fig. 2(a)) and the variance in streamwise (Fig. 2(b)) and wall-normal (Fig. 2(c)) directions. These figures compare numerical results with the experiment of Kulick et al. [1] and the results obtained by Yamomoto et al. [14] and by Wang and Squires [11]. The agreement between numerical and experimental velocities is quite good. Additionally, the results in Fig. 2 are completed with profiles computed by the LES using $192 \times 132 \times 128$ grid points for the flow resolution in the x, y, and z directions, respectively ($y^+_{\min} = 0.74$, $\Delta y^+_{\max} = 21.31$, $\Delta x^+ = 27.04$, $\Delta z^+ = 10.14$, and $\mathrm{Re}_\tau = 649$) and show that profiles from computations on refined mesh are close to those obtained on the $64 \times 66 \times 64$ grid points mesh. Comparing the distribution of kinetic turbulent energy shows that the percentage of the unresolved in the present LES kinetic energy is not significant.

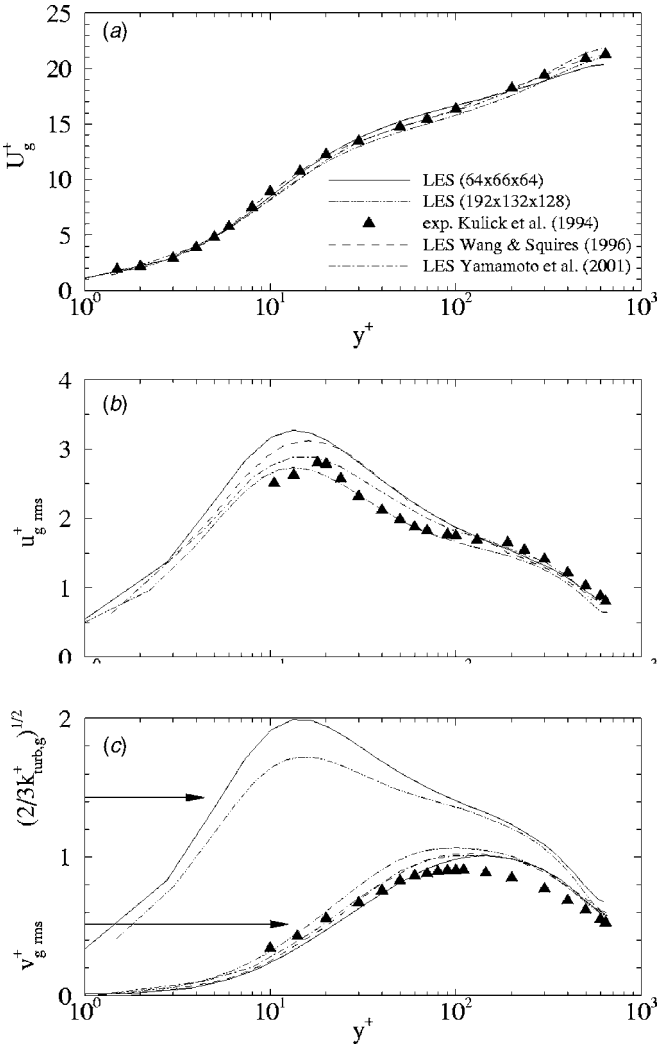

Fig. 2 Comparison of present LES and DNS in the channel single-phase flow with measurements of Kulick et al. [1] and with the LES of Yamomoto et al. [14] and Wang and Squires [11]: (*a*) mean velocity; (*b*) streamwise variance; (*c*) wall-normal variance

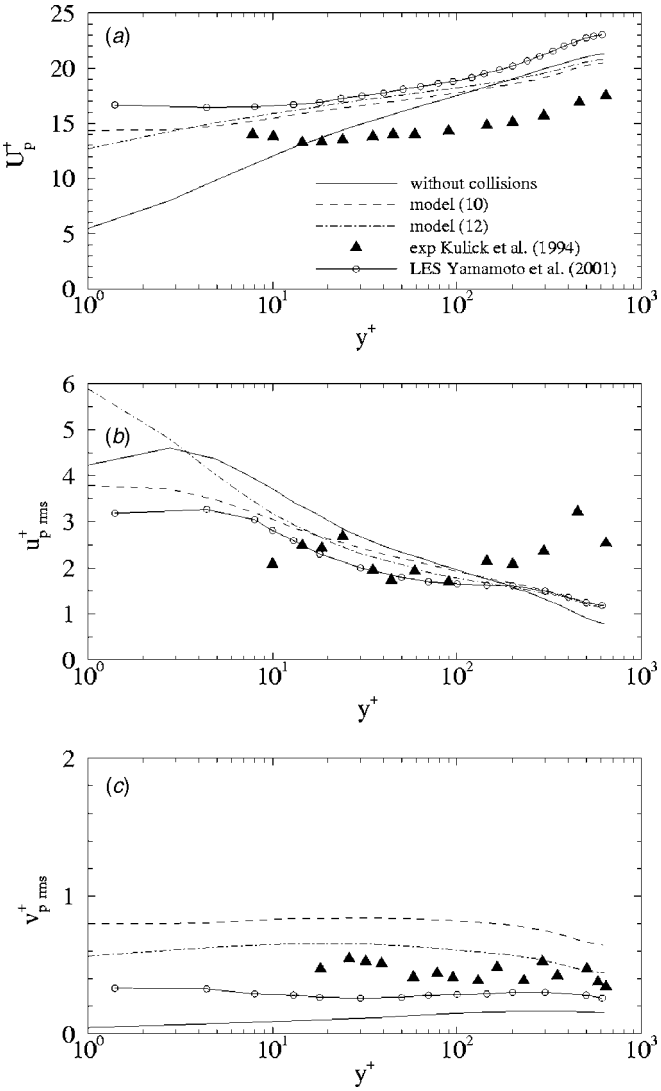

Fig. 3 Comparison of computed statistics of hypothetical particle with measured statistics of Kulick et al. [1] and the results from the LES of Yamomoto et al. [14], where binary interparticle collisions are simulated (70 μm copper particles with mass loading f=0.2): (*a*) streamwise mean velocity; (*b*) rms of streamwise velocity; (*c*) rms of wall-normal velocity. Solid line represents results without considering the interparticle collision.

3 Results of Computation of Particle Laden Channel Flow

3.1 Particle Velocity Statistics. For 70 μm copper particles, ρ_p=8800 kg/m^3 and mass loading f=0.2, Fig. 3 compares the computation of mean and rms velocity of the hypothetical particle against the experimental data of Kulick et al. [1] and the LES results of Yamamoto et al. [14]. Figure 3(*a*) shows the mean streamwise velocity profile. This figure clearly shows that, similar to Yamamoto et al. [14], both closure models for hypothetical particle motion, Eqs. (10) and (12), provide reasonably good expectations compared to the experimental profile; in mean, particles exceed the stream-wise fluid velocity in the near-wall region. Without accounting for interparticle collisions, the difference is that the mean particle streamwise velocity steeply decreases towards the wall. Figure 3(*b*) shows that the variance of streamwise velocity of the hypothetical particle matches the measured statistics, except near the channel center (analogous to Yamamoto et al. [14]). Figure 3(*c*) shows the distribution of the wall-normal rms velocity. Without accounting for interparticle collision, the wall-normal rms velocity is strongly underestimated against the measurements, while using the "thermodynamic" equilibrium closure model (Eq. (10)) overestimates the velocity. When applying the closure model (Eq. (12)), the computed wall-normal rms velocity is as predictive as the model of Yamamoto et al. [14]. Figure 4 shows the same main results comparing computed values with the measured statistics for the 50 μm glass particle with ρ_p =2500 kg/m^3 [1] and mass loading f=0.02. Using closure (Eq. (10)), the numerical and experimental distributions of mean (Fig. 4(*a*)) and rms streamwise velocity (Fig. 4(*b*)) match well, while the computed rms velocity in the wall-normal direction overestimates the measurements.

For mass loading f=0.15, Benson and Eaton [3] presented the mean and rms streamwise velocity for 150 μm glass particles with ρ_p=2500 kg/m^3 (the wall-normal velocity variance distribution was not reported). In this experiment, the number of immersed glass particles was 3.6 times less than in Kulick et al. [1]. Figures 5(*a*) and 5(*b*) show the comparison with measurements in the case of perfectly smoothed walls. In the region where experimental data are provided, the variance of hypothetical particle streamwise velocity follows experimental quantities closely,

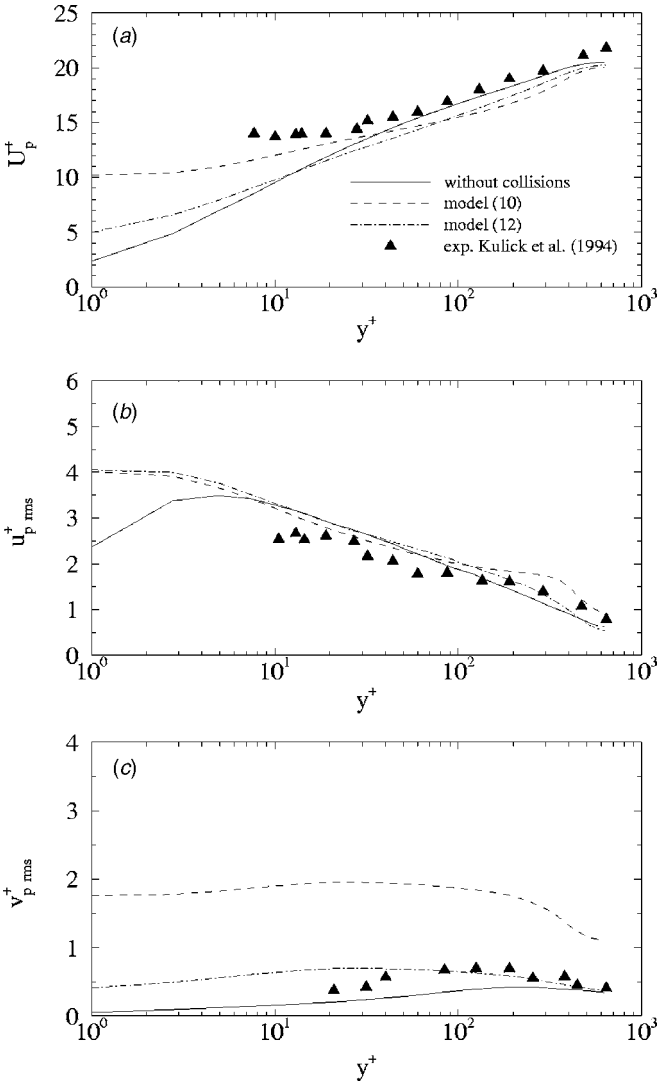

Fig. 4 Comparison of computed statistics of hypothetical particle velocity with measured statistics of Kulick et al. [1] (50 μm glass particles with mass loading $f=0.02$): (*a*) streamwise mean velocity; (*b*) rms of streamwise velocity; (*c*) rms of wall-normal velocity. Solid line represents results without considering of interparticle collision.

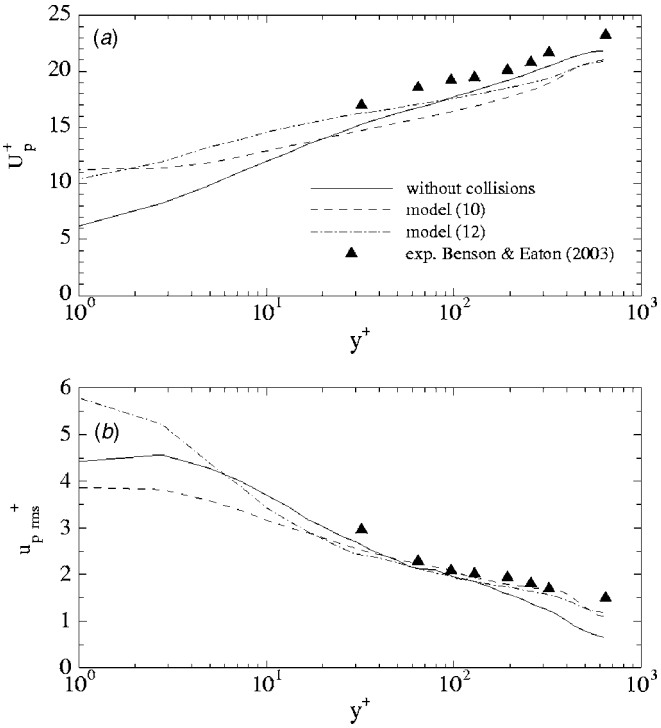

Fig. 5 Comparison of computed statistics of hypothetical particle velocity with measured statistics of Benson and Eaton [3] (150 μm glass particles with mass loading $f=0.2$; channel with perfectly smoothed walls): (*a*) streamwise mean velocity; (*b*) rms of streamwise velocity. Solid line represents results without considering the interparticle collision.

whereas computations without collisions underestimate the measurements in the center-channel region. At the same time, the computed mean streamwise velocity corresponds quite well to the reported experimental quantities, with or without accounting for particle-particle collisions.

Following the physical picture of Caraman et al. [32] in the near-wall region, strong fluctuations of streamwise velocity in the gas may produce axial fluctuations of particle velocity. Due to interparticle collision, the axial fluctuating kinetic energy of particles is redistributed in radial transport of fluctuating particle energy. As a result, particle-particle collisions change negligibly the longitudinal fluctuation of particle velocity. Our computations with collisions appear to correspond with this tendency. The mean particle velocity near the wall increases compared to the case where collisions are neglected. The rms values for wall-normal particle velocities also increase when considering interparticle collisions. The rms values for particle velocity in the axial direction are virtually unchanged. Although Eq. (6) assumes collisions with full isotropy of particle velocity, the gradient term in Eq. (7) with Eq. (10) is proportional to the energy redistribution process, from the axial fluctuating kinetic energy in the shear flow to the radial kinetic energy of the particle.

3.2 Gas Velocity Statistics. Figure 6(*a*) shows the mean streamwise gas velocity obtained in the experiment of Kulick et al. [1] and in the present computation using Eq. (10) for particle-free and particle-laden turbulent flows. The experiment was conducted for different mass loadings of 70 μm copper particles: $f=0,0.2,0.4$. Kulick et al. [1] observed that particles have little effect on the mean velocity profile. As shown by Fig. 6(*a*), the computed mean gas velocity is also not influenced by the presence of particles. Figures 6(*b*) and 6(*c*) present the turbulence intensity in streamwise and wall-normal directions. From Kulick's et al. [1] experiment, it appears that the turbulence was fairly attenuated even though the gas-phase mean velocity was unchanged by particles. The computed velocity fluctuations also predict this effect with attenuation about twice as less intensive (LES of Yamomoto et al. [14] did not predict this effect). To emphasize the effect of turbulence attenuation, Fig. 6 also displays the numerical prediction for $f=1$ (dashed line) and shows that the degree of turbulence attenuation by particles increases as the mass loading increases.

The nature of turbulence attenuation is not yet well understood. The work done in stretching a cloud of dispersed particles by energetic eddies may be manifested as an additional viscous dissipation of turbulence by particles. However, the refined measurement of Paris and Eaton [33] shows that, at the centerline, this extra dissipation is a small fraction compared to the overall turbulent dissipation. From DNS (Elghobashi and Truesdell [34]) and measurements of Paris and Eaton [33], it has been recognized that particles alter the transfer of turbulent energy across the spectrum. When turbulent flow passes through a cloud of inertial particles, the small eddies newly formed by particles may interact with incoming large scale turbulence. Such a nonlocal interaction

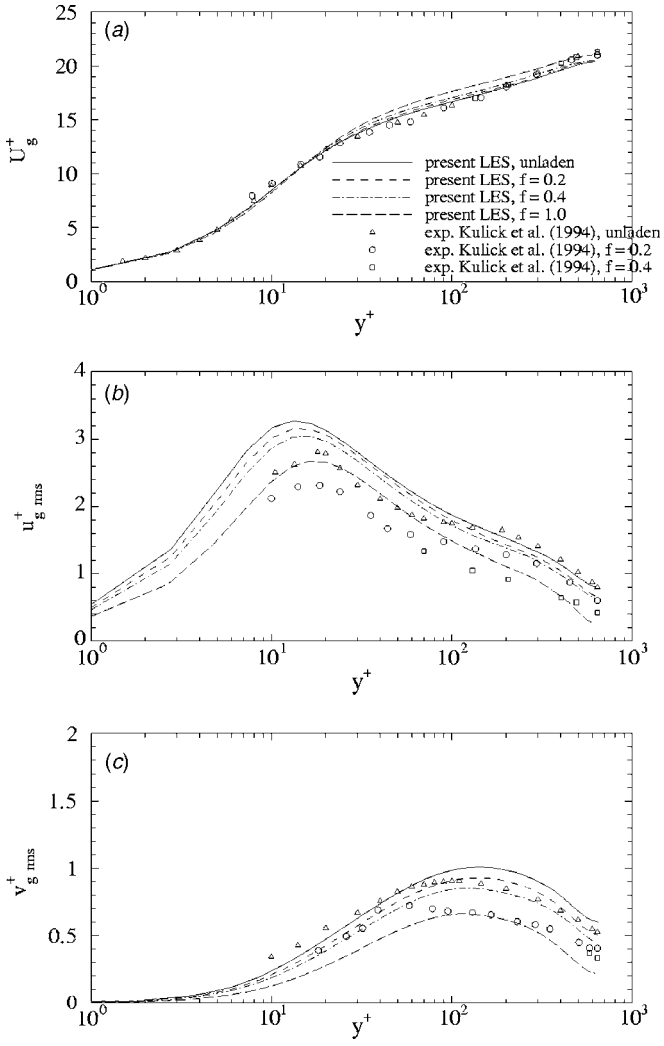

Fig. 6 Comparison of computed gas velocity profiles with measurements of Kulick et al. [1], for different mass loadings: (*a*) Streamwise mean velocity; (*b*) rms of streamwise velocity; (*c*) rms of wall-normal velocity. Additional computation for *f* =1 is presented by the long dashed line.

between large eddies and newly generated small scale turbulence may enhance the rate of turbulence decay in the large scale motion with a corresponding increase in the dissipation process. The flow power spectra, measured by Kulick et al. [1] at the channel centerline for various mass loadings also shows that particles generate turbulence at high frequencies and remove energy from the large scales of the flow. However, Kulick et al. [1] found that particles interact with flow on a preferred range of frequencies, depending on the mass loading; this finding is contrary to DNS [34].

Figure 7 shows the streamwise velocity power spectra computed in the middle point of the channel centerline for different mass loadings. Each spectra is normalized by the axial kinetic energy of free-particle flow. This figure shows that the model cannot predict the turbulence generation at small scales with, in the sequel, redistribution of turbulent energy across the spectrum of scales. The LES approach filters this physical phenomenon. Figure 7 shows that turbulent energy is reduced uniformly across a broad range of scales as a result of momentum exchange between gas flow and particles. Accounting for interparticle collision contributes significantly to this effect. Here, in the framework of the hypothetical particle approach, the turbulent field plays the role of a third body for a long range "slipping" collision between such particles. Due to interparticle collisions, each hypothetical particle smoothly changes its trajectory. In terms of two-way coupling, this induces an additional change of filtered gas velocity with a corresponding transmission of momentum to neighboring hypothetical particles. This contributes to the removal of turbulent particle energy. Figure 7(*c*) shows that, with increased mass loading, turbulence attenuation is much stronger. Figure 7(*d*) presents the experimental and computed values of kinetic energy and viscous dissipation, averaged at the centerline for different mass loadings. Turbulence strongly decreases as mass loading increases; interparticle collisions are likely a strong contributor to this effect.

4 Conclusion

This study introduces a simplified collisional microdynamic of solid particles, coupled in "two ways" with LES approach for simulating particle-laden highly turbulent shear flow. The dynamics of solid particles with discontinuous (due to collisions) phase trajectories is viewed here as the motion of an ensemble of hypothetical particles along trajectories smoothed over particle-particle collisions. In the governing equation for a hypothetical particle, the statistical temperature was closed by assuming local "thermodynamic equilibrium" with surrounding resolved turbulence. This approach does not require any additional CPU resources for considering interparticle collisions.

The simulations of a highly turbulent gas-particle channel flow were specifically conducted to compare the statistics of hypothetical particle velocity with experimental results (Kulick et al. [1] and Benson and Eaton [3]) and with LES/particle computations (Yamamoto et al. [14]) where binary collisions were modeled. The computation showed a relatively good agreement with both experiment and Yamamoto's et al. [14] results, implying that the interparticle collisions has a universal character in the high-Reynolds number channel flow and in the considered range of mass loadings. The computation yielded the effects observed in experiments from Eaton's group: (i) particles did not practically effect the mean velocity of the flow; (ii) the particles' velocity profile had a particularly flattened form; and (iii) particles attenuated turbulence. In the region where experimental data were reported, the "thermodynamic limit" closure agrees quite well with measured streamwise mean velocity and its variance but overestimates the wall-normal fluctuations. The predicted effect of turbulence attenuation by particles was almost twice as less intensive than reported from measurements, which is still fairly more pronounced than in Yamamoto et al. [14].

It must be stated that the presented computational model is too simple to be considered a real contribution to the open discussion on the nature of turbulence attenuation by particles. The computations did not predict the generation of high-frequency turbulence by particles and the redistribution of turbulent energy across the spectrum of scales found in experiments and DNS. This physics is filtered in the LES approach. In our computation, turbulence is attenuated as a result of momentum exchange between gas flow and particles. This effect becomes stronger when accounting for interparticle collisions. Each hypothetical particle, changing its velocity as a result of collective interparticle collisions, exchanges momentum with neighboring hypothetical particles through modifying turbulent energy in the gas flow.

Acknowledgment

We are indebted to Dr. V. L. Saveliev from the Institut of Ionosphere in Kazakhstan for fruitful discussions at various stages of this study.

Nomenclature

d_p = diameter of solid particle
$f(\vec{\mathbf{r}},\vec{\mathbf{v}},t)$ = distribution function
f = mass loading

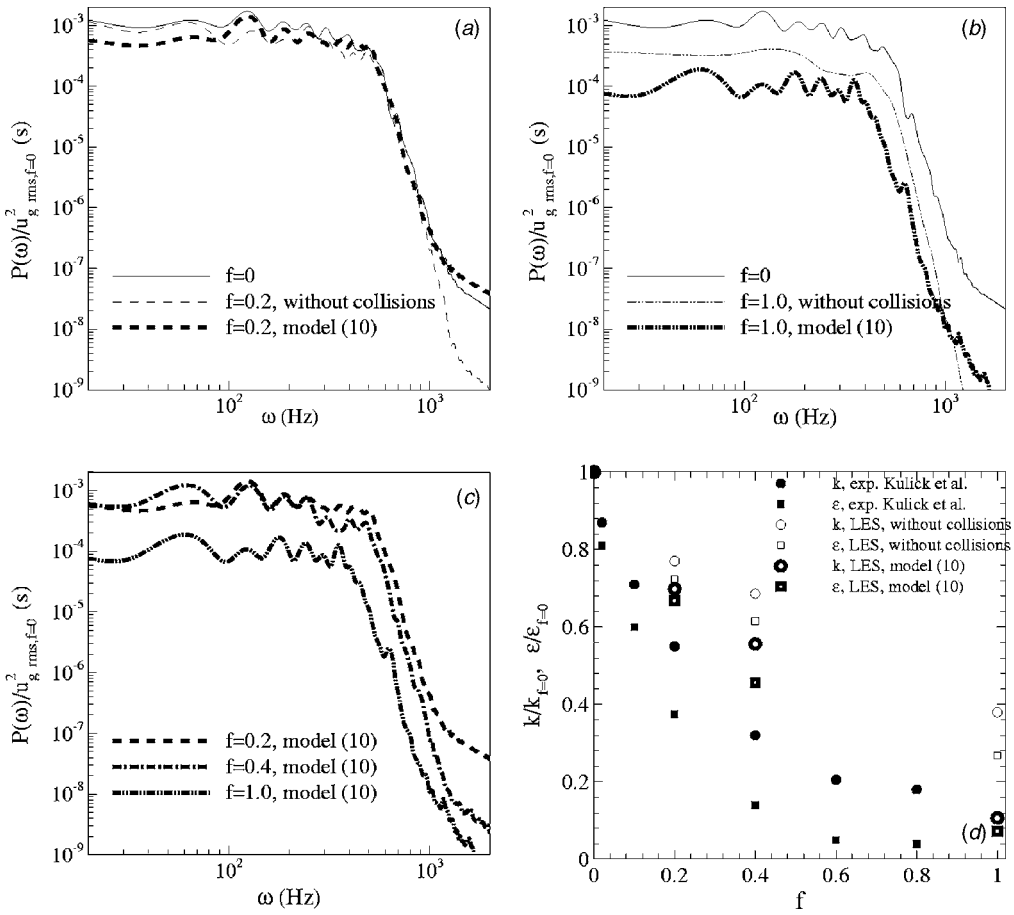

Fig. 7 Attenuation of turbulence at the channel centerline with different mass loadings of 70 μm copper particles: (*a*)–(*c*) streamwise velocity spectra in the middle of the centerline with and without considering the collision; (*d*) gas-phase turbulent kinetic energy and dissipation; filled symbols, measurements of Kulick et al. [1]

$I(f_\alpha, f_\beta)$ = collision operator
m_g = fluid particle mass
m_p = solid particle mass
n_p = solid particles number density
Re_p = solid particle Reynolds number
Re_τ = Reynolds number based on channel half-width and friction velocity
$\vec{\mathbf{r}}(x_1, x_2, x_3)$ = position vector
T_p = statistical "temperature" of solid particle
$T_{\mathrm{tur},g}$ = statistical "temperature" of fluid particle
u_τ = friction velocity
$\vec{\mathbf{v}}(\mathbf{v}_1, \mathbf{v}_2, \mathbf{v}_3)$ = velocity vector
$\bar{\mathbf{v}}_g$ = mean gas velocity
$\mathbf{v}'_g$ = fluid velocity fluctuations
$\langle \mathbf{v}'^2_g \rangle / 2$ = turbulent gas kinetic energy
$\langle \mathbf{v}_p \rangle$ = averaged solid particle velocity
$\mathbf{v}'_p$ = solid particle velocity fluctuations
Vol = volume of fluid element
x, y, z = coordinates
$\Delta_x, \Delta_y, \Delta_z$ = mesh dimension
δ = channel half-width
$\delta_{\alpha\beta}$ = Kronecker delta
ρ_g = gas density
ρ_p = density of solid particle
τ_p = solid particle Stokes time
τ_L = integral Lagrangian time scale
ν_g = dynamic gas viscosity

Subscripts

g = gas
p = solid particles

References

[1] Kulick, J. D., Fessler, J. R., and Eaton, J. K., 1994, "Particle Response and Turbulence Modification in Fully Developed Channel Flow," J. Fluid Mech., **277**, pp. 109–134.

[2] Fessler, J. R., Kulick, J. D., and Eaton, J. K., 1994, "Preferential Concentration of Heavy Particles in a Turbulent Channel Flow," Phys. Fluids, **6**(11), pp. 3742–3749.

[3] Benson, M. J., and Eaton, J. K., 2003, "The Effects of Wall Roughness on the Particle Velocity field in a Fully Developed Channel Flow," Report No. TSD-150, Mechanical Engineering Department, Stanford University, Stanford, CA.

[4] Kussin, J., and Sommerfeld, M., 2002, "Experimental Studies on Particle Behaviour and Turbulence Modification in Horizontal Channel Flow With Different Wall Roughness," Exp. Fluids, **33**(1), pp. 143–159.

[5] Sommerfeld, M., and Kussin, J., 2003, "Analysis of Collision Effects for Turbulent Gas-Particles Flow in a Horizontal Channel: Part II. Integral Properties and Validation," Int. J. Multiphase Flow, **29**, pp. 701–718.

[6] Moin, P., and Kim, J., 1982, "Numerical Investigation of Turbulent Channel Flow," J. Fluid Mech., **118**, pp. 341–377.

[7] Saveliev, V. L., and Gorokhovski, M. A., 2005, "Group-Theoretical Model of Developed Turbulence and Renormalization of Navier-Stokes Equation," Phys. Rev. E, **72**, p. 016302.

[8] Simonin, O., Deutsch, E., and Boivin, M., 1995, "Large Eddy Simulation and Second Moment Closure Model of Particle Fluctuating Motion in Two-Phase Turbulent Shear Flows," Selected Papers from the Ninth Symposium on Turbulent Shear Flows, F. Durst, N. Kasagi, B. E. Launder, F. W. Schmidt, and J. H. Whitelaw, eds., Springer-Verlag, Berlin.

[9] Boivin, M., Simonin, O., and Squires, K. D., 2000, "On the Prediction of Gas-Solid Flows With Two-Way Coupling Using Large Eddy Simulation," Phys. Fluids, **12**(8), pp. 2080–2090.

[10] Apte, S. V., Gorokhovski, M., and Moin, P., 2003, "LES of Atomizing Spray With Stochastic Modeling of Secondary Breakup," Int. J. Multiphase Flow, **29**(9), pp. 1503–1522.
[11] Wang, Q., and Squires, K., 1996, "Large Eddy Simulation of Particle-Laden Turbulent Channel Flow," Phys. Fluids, **8**, pp. 1207–1223.
[12] Simonin, O., Wang, Q., and Squires, K. D., 1997, "Comparison Between Two-Fluid Model Predictions and Large Eddy Simulation Results in a Vertical Gas-Solid Turbulent Channel Flow," ASME FEDSM'97-3625.
[13] Vance, M. W., and Squires, K. D., 2002, "An Approach to Parallel Computing in an Eulerian-Lagrangian Two-Phase Flow Model," ASME FEDSM2002-31225.
[14] Yamamoto, Y., Potthoff, M., Tanaka, T., Kajishima, T., and Tsuji, T., 2001, "Large-Eddy Simulation of Turbulent Gas-Particle Flow in a Vertical Channel: Effect of Considering Interparticle Collisions," J. Fluid Mech., **442**, pp. 303–334.
[15] Alder, B. J., and Wainwright, T. E., 1959, "Studies in Molecular Dynamics. I. General Method," J. Chem. Phys., **31**(2), pp. 459–466.
[16] Bird, G. A., 1994, *Molecular Gas Dynamics and the Direct Simulation of Gas Flows*, Oxford University Press, London, UK.
[17] Tanaka, T., and Tsuji, Y., 1991, "Numerical Simulation of Gas-Solid Two-Phase Flow in a Vertical Pipe: On the Effect of Inter-Particle Collision," ASME FED-Vol. 121, pp. 123–128.
[18] Sommerfeld, M., 1995, "The Importance of Inter-Particle Collisions in Horizontal Gas-Solid Channel Flows," ASME FED-Vol. 228, pp. 335–345.
[19] Sommerfeld, M., 2003, "Analysis of Collision Effects for Turbulent Gas-Particles Flow in a Horizontal Channel: Part I. Particle Transport," Int. J. Multiphase Flow, **29**, pp. 675–699.
[20] Sommerfeld, M., 2001, "Validation of a Stochastic Lagrangian Modeling Approach for Inter-Particle Collisions in Homogeneous Turbulence," Int. J. Multiphase Flow, **27**, pp. 1829–1858.
[21] Dukowicz, J. K., 1980, "A Particle-Fluid Numerical Model for Liquid Sprays," J. Comput. Phys., **35**(2), pp. 229–253.
[22] Gorokhovski, M., and Saveliev, V., 2003, "Analyses of Kolmogorov's Model of Breakup," Phys. Fluids, **15**, pp. 184–192.
[23] Landau, L. D., and Lifshitz, E. M., 1981, *Course of Theoretical Physics*, Butterworth-Heinemann.
[24] Saveliev, V., and Nanbu, K., 2002, "Collision Group and Renormalization of the Boltzmann Collision Integral," Phys. Rev. E, **65**, p. 051205.
[25] Clift, R., Grace, G. R., and Weber, M. E., 1978, *Bubbles, Drops and Particles*, Academic, New York.
[26] Zaichik, L. I., Simonin, O., and Alipchenkov, V. M., 2003, "Two Statistical Models for Predicting Collision Rates of Inertial Particles in Homogeneous Isotropic Turbulence," Phys. Fluids, **15**(10), pp. 2995–3005.
[27] Zaichik, L. I., and Alipchenkov, V. M., 2003, "Pair Dispersion and Preferential Concentration of Particles in Isotropic Turbulence," Phys. Fluids, **15**(6), pp. 1779–1787.
[28] Reeks, M. W., 1977, "On the Dispersion of Small Particles Suspended in an Isotropic Turbulent Fluid," J. Fluid Mech., **83**(3), pp. 529–546.
[29] Wang, L. P., and Stock, D. E., 1993, "Dispersion of Heavy Particles in Turbulent Motion," J. Atmos. Sci., **50**, pp. 1897–1913.
[30] Pierce, C. D., 2001, "Progress-Variable Approach for Large-Eddy Simulation of Turbulent Combustion," Ph.D. thesis, Stanford University, Stanford, CA.
[31] Germano, M., Piomelli, U., Moin, P., and Cabot, W. H., 1991, "A Dynamic Subgrid-Scale Eddy Viscosity Model," Phys. Fluids A, **3**(7), pp. 1760–1765.
[32] Caraman, N., Borée, J., and Simonin, O., 2003, "Effect of Collisions on the Dispersed Phase Fluctuation in a Dilute Tube Flow: Experimental and Theoretical Analysis," Phys. Fluids, **15**(12), pp. 3602–3612.
[33] Paris, A. D., and Eaton, J. K., 2001, "Turbulence Attenuation in a Particle-Laden Channel Flow," Report No. TSD-137, Mechanical Engineering Department, Stanford University, Stanford, CA.
[34] Elghobashi, S., and Truesdell, G. C., 1993, "On the Two-Way Interaction Between Homogeneous Turbulence and Dispersed Solid Particles. I: Turbulence Modification," Phys. Fluids A, **5**(7), pp. 1790–1801.

Simulation and Analysis of High-Speed Droplet Spray Dynamics

H. Shi

C. Kleinstreuer[1]
e-mail: ck@eos.ncsu.edu

Department of Mechanical and Aerospace Engineering,
North Carolina State University,
Raleigh, NC 27695-7910

An experimentally validated computer simulation model has been developed for the analysis of gas-phase and droplet characteristics of isothermal sprays generated by pressure jet atomizers. Employing a coupled Euler-Lagrange approach for the gas-droplet flow, secondary droplet breakup (based on the ETAB model), was assumed to be dominant and the k-ε model was selected for simulating the gas flow. Specifically, transient spray formation in terms of turbulent gas flow as well as droplet velocities and size distributions are provided for different back pressures. Clearly, two-way coupling of the phases is important because of the impact of significant gas entrainment, droplet momentum transfer, and turbulent dispersion. Several spray phenomena are discussed in light of low back-pressure (1 atm) *and high back-pressure* (30 atm) *environments. At low back-pressure, sprays have long thin geometric features and penetrate faster and deeper than at high back-pressures because of the measurable change in air density and hence drag force. Away from the nozzle exit under relatively high back pressures, there is no distinct droplet size difference between peripheral and core regions because of the high droplet Weber numbers, leading to very small droplets which move randomly. In contrast to transient spray developments, under steady-state conditions droplets are subject to smaller drag forces due to the fully-developed gas entrainment velocities which reduce gas-liquid slip. Turbulent dispersion influences droplet trajectories significantly because of the impact of random gas-phase fluctuations.* [DOI: 10.1115/1.2717621]

1 Introduction

Liquid sprays have a wide range of applications in fuel injection, surface coating, and drug delivery, to name a few. Spray flow can be defined as that region downstream of an injection port where a jet-like liquid column or sheet has broken up due to instabilities, leading to the formation of droplets which move relatively to the gas phase [1,2]. Figure 1 depicts a pressure jet atomizer and different phases and forms of droplet generation. An alternative, low-speed spray device is the pressure swirl atomizer used in aerosol cans, paint spraying, and nasal sprays. For all atomizers, the liquid mass flow rate, spray angle, injection velocity, nozzle design, back pressure, droplet-size distribution, and spray penetration depth are key operational parameters.

2 Reviews of Spray Breakup Mechanisms and Computer Simulations

Once the liquid jet leaves the orifice, the breakup process starts immediately. The first step is called primary breakup due to the formation of ligaments and other irregular liquid elements along the surface of the liquid column [3] (see Fig. 1(*a*)). However, those irregular liquid elements are unstable because they are subjected to relatively large drag forces exerted by the surrounding gas, which will result in droplet deformation. Droplet deformation can finally lead to different forms of breakup, called secondary breakup (see Fig. 1).

Although primary breakup is essential in the formation of sprays, it can be incorporated into the secondary breakup mechanism because those irregular liquid elements resulting from the primary breakup are highly unstable and will definitely break up during the second phase. In most previous numerical spray studies, as well as in the present study, secondary breakup is the only breakup mechanism under consideration. Numerical and experimental efforts made to investigate primary breakup can be found in works by Wu et al. [4], Mazallon et al. [5], Herrmann, et al. [6], and Yi and Reitz [7]. Thus, "breakup" implies "secondary breakup" in this study unless specified differently.

The basic droplet (secondary) breakup regime is determined by the Weber number which is generally defined as the ratio of the inertial force to surface tension. Here,

$$\mathrm{We} = \frac{\rho_g V_{\mathrm{slip}}^2 r}{\sigma} \tag{1}$$

where ρ_g is the gas density, V_{slip} is the relative velocity (slip velocity) between droplet and gas, r is the droplet radius, and σ is the liquid surface tension coefficient. Thus, the Weber number connects the gas-induced drag force, which leads to deformation to the liquid surface tension which tends to maintain a spherical droplet shape, i.e., resists deformation. If a droplet is exposed to a gas flow, significant deformation starts at a Weber number of unity. Above a certain value of the Weber number, droplet deformation leads to breakup. Based on different Weber number values, three major breakup regimes can be established [8] (see Fig. 1(*b*)):

1. Bag breakup: The liquid bulk or large droplet deforms into a thin disk normal to the flow direction, followed by a severe deformation of the center of the disk into a thin, balloon-like structure, which will finally lead to breakup.
2. Stripping breakup: It involves deflection of the periphery of the disk in the downstream direction instead of the deflection of the center of the disk. For sprays, most droplet breakups occur in the stripping breakup regime [9].
3. Catastrophic breakup: Catastrophic breakup has a similar mechanism as stripping breakup, but it involves more explosion-type breakup.

Computational fluid dynamics (CFD) simulation is a fast, detailed, and relatively low-cost tool for determining spray charac-

[1]Corresponding author.

Contributed by the Fluids Engineering Division of ASME for publication in the JOURNAL OF FLUIDS ENGINEERING. Manuscript received May 28, 2006; final manuscript received October 19, 2006. Assoc. Editor: Dimitris Drikakis.

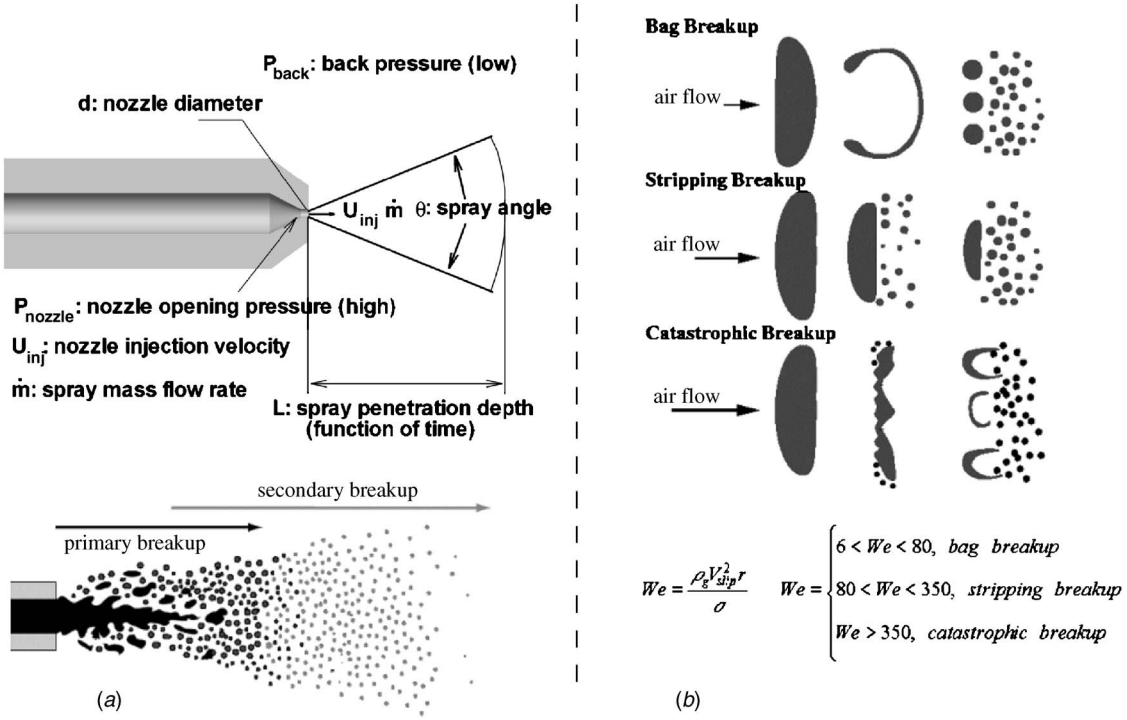

Fig. 1 Droplet spray generation: (*a*) spray device as well as primary and secondary breakups; (*b*) droplet breakup mechanism

teristics, designing new sprays, and obtaining optimal device operational conditions. To begin with, spray droplet breakup, droplet transport, and droplet/gas interaction mechanisms are the most desirable results to answer questions related to challenging spray phenomena. Commercial CFD packages have become more and more popular and effective simulation tools in both academia and industry. The present study provides spray simulation results based on the user-enhanced CFX10 solver (Ansys, Inc.). The goal is to systematically investigate the spray dynamics, especially the difference between steady-state and transient sprays.

The present model development relies on the following methods and models:

1. Lagrangian-drop Eulerian-fluid method: The most popular approach to simulate sprays is the Lagrangian-drop Eulerian-fluid method. In this kind of approach, the droplets which are formed through the atomization process of the liquid jet are tracked in a Lagrangian frame of reference through Monte Carlo methods, whereas the gas phase is described in a Eulerian frame of reference. Each computational particle is considered to represent a group of particles possessing the same characteristics such as size, composition, and so on, as originally proposed by Dukowicz [10].

   Lagrangian-liquid Eulerian-gas spray models are well established for the numerical calculation of complex two-phase flows and have generated excellent results. However, numerical convergence may be a problem due to the iterative gas-and-droplet-phase solutions. They require strong relaxation of the interphase source terms, and hence the procedure is taxing in terms of grid density and computational time [11]. The Lagrangian-liquid Eulerian-gas spray model is also, in principle, only valid for dilute sprays when the local gas void fraction is greater than 99%. This criterion is not satisfied in the region close to the injector orifice, e.g., in the case of diesel sprays [12].
2. Droplet breakup models: Among all spray dynamic mechanisms, droplet breakup received the most attention. The most popular spray breakup strategy for pressure atomizers is called the "*blob method*." In this approach [9], it is assumed that spherical droplets with uniform size, $d_p = d_{\text{nozzle}}$, are ejected from pressure jet-type atomizers and subjected to the aerodynamically induced breakup. Under the same "blob method," there are several kinds of secondary breakup models, e.g., Reitz and Diwakar [13], Reitz wave [14], TAB [15], and ETAB [16].

   Reitz and Diwakar [9,13] proposed a droplet breakup model in their fuel spray simulation where the droplet breakup was dominated by the Weber number (see Eq. (1)). Later, Reitz [14] suggested a new wave-model where new droplets are formed based on the growth rate of the fastest Kelvin-Helmholtz wave instability on the surface of the parent droplet. Successful applications of the Reitz wave-model include Shang et al. [17], Iyer and Abraham [12], and Madabhushi [18].

   O'Rourke and Amsden [15] suggested another droplet breakup model based on Taylor Analogy Breakup (TAB). The TAB model predicts the droplet breakup based on the droplet deformation in terms of the radial cross-sectional change. In order to improve the TAB model, Tanner [16] used an enhanced TAB model (ETAB), where the initial droplet deformation parameters are corrected.

   Clearly, Reitz wave and TAB or ETAB models analyze the droplet breakup from different angles. The Reitz wave model is based on the theory of Kelvin-Helmholtz (KH) wave instability on the surface of the parent droplet while TAB and ETAB models are based on the droplet deformation which is inherent in the Rayleigh-Taylor (RT) instability theory. Recently, KH-RT hybrid models [19–21] were proposed as a combination of both theories and in an effort to include the primary breakup effect. The Kelvin-Helmholtz instability model was used to predict the primary breakup of the intact liquid core of a diesel jet. The secondary breakup of the individual drops was modeled with the Kelvin-Helmholtz model in conjunction with the Rayleigh-Taylor (RT) instability model. The TAB model was used to deter-

mine the droplet deformation parameters used in the Rayleigh-Taylor (RT) instability model.

Similarly, the Kelvin-Helmholtz/droplet deformation and breakup model (KH-DDB model) was developed by Park and Lee [22]. In the KH-DDB model, the primary breakup is still simulated with the Kelvin-Helmholtz instability model while the secondary breakup is predicated with an improved TAB model by considering nonlinear effects [23].

A very different droplet breakup model relies on a stochastic approach [24–26], which is based on Kolmogorov's hypothesis [27] of viewing solid particle-breakup as a discrete random process.

3. Gas-phase modeling: During spray droplet breakup and transport, the gas phase gains significant momentum from the droplets. The k-ε turbulence model has been widely used for modeling gas-phase turbulence which is mainly produced in the shear layer between the liquid jet and surrounding gas [12]. As an exception, Apte et al., [26] conducted large-eddy simulations (LES) for atomizing sprays. The results indicate that the LES approach is computationally efficient and able to capture the dynamics of gas-phase turbulence during liquid atomization.

While certain elements of CFD spray simulations have been presented by previous investigators [16,21,22], novel contributions of the present study include the following:

1. Validation of a comprehensive spray model, which may benefit academic and industrial researchers;
2. A more systematic study on the topics of: (1) comparison of transient and steady-state spray dynamics; (2) analysis of the effect of turbulent dispersion on spray droplet transport; and (3) impact of gas entrainment velocity and turbulence kinetic energy.

3 Theory

Employing the ETAB model, spray simulations in this study will start from the point when the liquid column, i.e., jet, leaves the nozzle. Limitations of the model include:

(i) Only secondary breakup, i.e., droplet formation from irregular liquid elements, is considered. Although primary breakup has a significant impact during the formation of spray, those irregular liquid elements from primary breakup are unstable because they are subjected to relatively large drag forces exerted by the surrounding gas. As a result, secondary breakup is the eventual spray-breakup mechanism that leads to atomization.
(ii) The liquid-phase volume fraction is ignored, i.e., the effect of the volume occupied by the droplets is not included, which may reduce computational accuracy in the region close to the nozzle.
(iii) Droplet collision and agglomeration effects are not considered under the assumption that breakup is the major mechanism in the region of interest.
(iv) Isothermal and constant gas density conditions.

Assumptions (ii) and (iii) are based on the facts that, according to [3], atomization involves primary breakup into bulks at the liquid core surface near the nozzle, followed by secondary breakup into smaller drops with very low liquid volume fractions and negligible effects of collision.

3.1 Spray Breakup Model. In the present study, the Enhanced Taylor Analogy Breakup (ETAB) model was employed because of its accuracy and stability [16]. In the ETAB model, droplet deformation is expressed by the dimensionless deformation $y=2(x/r)$, where x describes the deviation of the droplet equator from its underformed position, and r is the effective droplet radius. Breakup occurs if y exceeds unity. Model details may be found in Refs. [15,16].

3.2 Droplet Transport and Droplet/Gas Interaction Model (Lagrangian-Liquid Eulerian-Gas Model). Under the consideration of accuracy and reasonable model complexity, the Lagrangian-liquid Eulerian-gas spray models with an embedded k-ε turbulence model were selected for the numerical calculation of complex disperse two-phase flows. The gas containing the particles is assumed to be incompressible. This is a practical choice since most sprays are highly subsonic flows [10]. The basic equations are

Continuity

$$\frac{\partial \alpha_g}{\partial t} + \frac{\partial \alpha_g u_i}{\partial x} = 0 \tag{2}$$

Momentum

$$\frac{\partial \alpha_g u_i}{\partial t} + u_j \frac{\partial \alpha_g u_i}{\partial x_j} = -\frac{\alpha_g}{\rho_g}\frac{\partial p}{\partial x_i} + \frac{\partial}{\partial x_j}\left[\alpha_g(v+v_T)\left(\frac{\partial u_i}{\partial x_j}+\frac{\partial u_j}{\partial x_i}\right)\right] + \frac{1}{\alpha_g \rho_g} M_p \tag{3}$$

where α_g is the gas-phase volume fraction, u is the gas velocity, ρ_g is the gas density, g is the acceleration of gravity, p is the pressure, v is the kinematic viscosity, and v_T is the eddy viscosity, and M_p is the term defining momentum exchange with the particles, per unit volume, defined in Eq. (13). As an approximation, α_g is set to one, which is reasonable for most spray regions (i.e., $\alpha_g > 0.99$).

The turbulence kinetic energy and dissipation transport equations for the k-ε model read

$$\frac{\partial k}{\partial t} + u_j \frac{\partial k}{\partial x_j} = \tau_{ij}\frac{\partial u_i}{\partial x_j} - \varepsilon + \frac{\partial}{\partial x_j}\left[(v+\sigma_k v_T)\frac{\partial k}{\partial x_j}\right] \tag{4}$$

$$\frac{\partial \varepsilon}{\partial t} + u_j \frac{\partial \varepsilon}{\partial x_j} = \alpha \frac{\varepsilon}{k}\tau_{ij}\frac{\partial u_i}{\partial x_j} - \beta\frac{\varepsilon^2}{k} + \frac{\partial}{\partial x_j}\left[(v+\sigma_\varepsilon v_T)\frac{\partial \varepsilon}{\partial x_j}\right] \tag{5}$$

where τ_{ij} is the stress tensor, ε is the turbulence dissipation rate, k is the turbulence energy, and

$$v_T = \frac{c_\mu k^2}{\varepsilon} \tag{6a}$$

$$c_\mu = 0.09;\ \alpha = 1.44;\ \beta = 1.92;\ \sigma_k = 1.0;\ \sigma_\varepsilon = 1.3 \tag{6b}$$

For droplet transport, the instantaneous gas velocity rather than its average is more relevant. The instantaneous gas velocity is recovered using Reynold's decomposition

$$U_g = u_g + u_g' \tag{7}$$

where the time-averaged velocity $u_g = u_i$ in Eqs. (2) and (3), and u_g' is the turbulent (random) component of the gas velocity. Each particle representing a group of particles possessing the same characteristics, individually labeled by subscript p, is assumed to obey the following equations [28]:

$$\frac{dx_p}{dt} = u_p \tag{8}$$

$$m_p \frac{du_p}{dt} = \frac{1}{8}\pi \rho_g d_p^2 C_D (U_g - u_p)|U_g - u_p| \tag{9}$$

where x_p is the particle position, u_p is the particle velocity, m_p is the particle mass, ρ_g is the gas density, and C_D is the drag coefficient. The droplet drag coefficient can be written as [29]

$$C_D = \begin{cases} 24(1 + 0.15\,\mathrm{Re}_p^{0.687})/\mathrm{Re}_p & \text{for } 0.0 < \mathrm{Re}_p \le 1000 \\ 0.44 & \text{for } 1000 < \mathrm{Re}_p \end{cases} \tag{10}$$

where Re_p is defined as

$$\mathrm{Re}_p = \frac{\rho_g |U_g - u_p| \cdot d_p}{v_g} \tag{11}$$

To account for the enhanced drag force coefficient of the deformed droplets in the spray breakup model, a correction formula is used [8]

$$C_{D,\mathrm{droplet}} = C_{D,\mathrm{sphere}}(1 + 2.632y) \quad 0 < y < 1 \tag{12}$$

where $C_{D,\mathrm{sphere}}$ is the drag force coefficient of a spherical droplet (see Eq. (10)).

As a result, the momentum transfer from the droplets to the gas phase can be written as (see Eq. (3))

$$M_p = -\frac{1}{dV}\sum_{1}^{NP}\left(\frac{1}{8}\pi d_p^2 C_D(U_g - u_p)|U_g - u_p|\right) \tag{13}$$

where NP is the number of total particles in the cell and dV is the cell volume.

To account for the effect of turbulent dispersion, the turbulence structure of the gas flow field is modeled by a random process along the droplet trajectories. The model assumes that a particle is always within a single turbulent eddy. Each eddy has a characteristic fluctuating velocity, u_g', lifetime, t_e, and length, l_e. When a particle enters the eddy, the fluctuating velocity for that eddy is added to the local mean gas velocity to obtain the instantaneous fluid velocity (see Eq. (7)), used in Eq. (9). This turbulent gas velocity is assumed to prevail as long as the particle/eddy interaction time is less than the eddy lifetime and the displacement of the particle relative to the eddy is less than the eddy length. If either of these conditions is exceeded, the particle is assumed to be entering a new eddy with new characteristics, i.e., fluctuating velocity, u_g', lifetime, t_e, and length, l_e. The quantities are [30,31]

$$u_g' = \Gamma\left(\frac{2k}{3}\right)^{0.5} \tag{14}$$

$$l_e = \frac{C_\mu^{0.75} k^{1.5}}{\epsilon} \tag{15}$$

$$t_e = \frac{l_e}{(2k/3)^{0.5}} \tag{16}$$

where k and ε are the local turbulence kinetic energy and dissipation, respectively, C_μ is an empirical turbulence constant, and Γ represents random numbers with zero-mean, variance of one, and normal distribution.

4 Numerical Method

The numerical solutions of the continuity equation, momentum equation, the k-ε turbulence model equations, droplet breakup, and droplet tracking were carried out with a user-enhanced commercial finite-volume based program, i.e., CFX 10.0 from Ansys Inc. (Canonsburg, PA).

All variables, including velocity components, pressure, and droplet concentrations are located at the centroids of the control volumes. A first-order upwind scheme was used to model the fluid flow fields to accelerate convergence. It was found that using a second-order scheme, fully-coupled turbulent fluid-particle simulations using the k-ε turbulence model occasionally encountered convergence problems. Hence, the spray simulation results with a first-order upwind scheme were compared to available converged results with a second-order scheme. The difference was less than 2%. For the time-derivative term, a second-order backward Euler scheme was used.

The final mesh topology, using ICEM (ICEM-CFD Engineering Inc., Berkeley, CA), was determined by refining the mesh until grid independence of the results was achieved. The numerical accuracy was enhanced with a highly refined mesh density along the nozzle axis. Specifically, reducing or increasing the mesh density by a factor of 2.0 had a negligible effect on all results. The simulations were conducted in a cylindrical domain (10 cm in diameter, 10 cm in height). The nozzle center was located axially at a point 1 cm above the bottom center to eliminate a possible influence of the opening at the bottom of the cylinder. The basic boundary conditions were as follows (see Fig. 2):

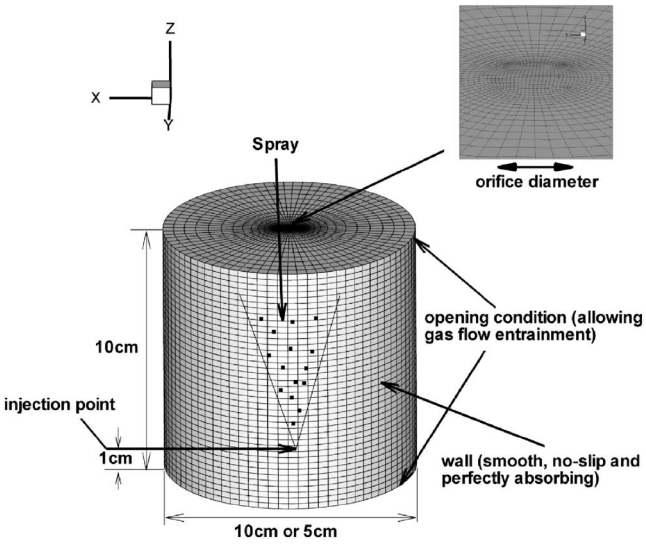

Fig. 2 Mesh generation for the computational flow domain

1. Nozzle exit (1 cm above the center of the cylinder bottom): initial droplet size equal to the nozzle diameter ("blob" method), initial droplet (injection) velocity, spray angle, and spray mass flow rate.
2. Open bottom and top of the cylinder: opening condition allowing for gas flow entrainment.
3. Cylinder wall: no-slip, smooth, and perfectly absorbing (if droplets deposit).

All computations were performed on an IBM Linux Cluster at NCSU's High-Performance Computing Center (Raleigh, NC) and a local dual Xeon Intel 3.0G Dell desktop (CFPD Laboratory, Department of Mechanical and Aerospace Engineering, NC State University). The solutions at steady state or at each time step for transient computations of the flow field were assumed to be converged when the dimensionless mass and momentum residual ratios were <0.0001. Improving the convergence criteria to <0.00001 had a negligible effect on the simulation results.

5 Model Validations and Physical Insight

Two sets of experimental measurements [32,33] for pressure atomizers were selected for model validation purposes. Basic experimental conditions are summarized in Table 1. The spray angle was estimated based on the empirical formula (Eq. (17)) given by Dukowicz [10]

$$\tan\frac{\theta}{2} = A\left(\frac{\rho_g}{\rho_d}\right)^{0.5} \tag{17}$$

The constant A is a function of the nozzle internal geometry. In the present study, A was taken to be 0.4 [10] which is a good choice for jet sprays in the parameter range of interest.

The data sets of case studies 1a, 1b, and 2 (see Table 1) were selected to validate the ETAB model and the Lagrangian-liquid Eulerian-gas model (see Sec. 3). All experiments were conducted at room temperature, for which evaporation effects were minor [12] considering the short travel time of jet droplets, i.e., milliseconds in the present study.

Table 1 Experimental conditions

Sources	Injected liquid	Spray parameters	Gas (nitrogen) parameters
Case 1a[a]	Material: diesel fuel oil Density: 840 kg/m^3 Viscosity: 2.1E-3 kg/(m s) Surface tension: 0.0295 N/m Boiling temp.: 180–410°C	Nozzle diameter: 0.3 mm Mass flow rate: 0.007 kg/s Velocity: 122.2 m/s Spray angle (estimated): 1.68 deg	Pressure: 1 atm Temp.: 20–25 deg
Case 1b[a]		Nozzle diameter: 0.3 mm Mass flow rate: 0.006 kg/s Velocity: 102.5 m/s Spray angle (estimated): 9.14 deg	Pressure: 30 atm Temp.:20–25 deg
Case 2[b]	Material: *n*-hexane Density: 665 kg/m^3 Viscosity: 3.2E-4 kg/(m s) Surface tension: 0.0184 N/m Boiling temp.: 69°C	Nozzle diameter: 0.127 mm Mass flow rate: 0.001 kg/s Velocity: 127 m/s Spray angle (estimated): 3.56 deg	Pressure: 14.8 atm Temp.: 20–25 deg

[a]Cases 1a and 1b: Hiroyasu and Kadota [32].
[b]Case 2: Wu et al. [33].

Figure 3 compares the simulation results with the experimental data of Hiroyasu and Kadota [32] and Wu et al. [33]. The simulation result in Fig. 3(*b*) gives the axial velocity profile as a function of radial distance at axial location $x/D=600$ downstream of the orifice, where D is the nozzle diameter and x is the downstream axial distance from the orifice.

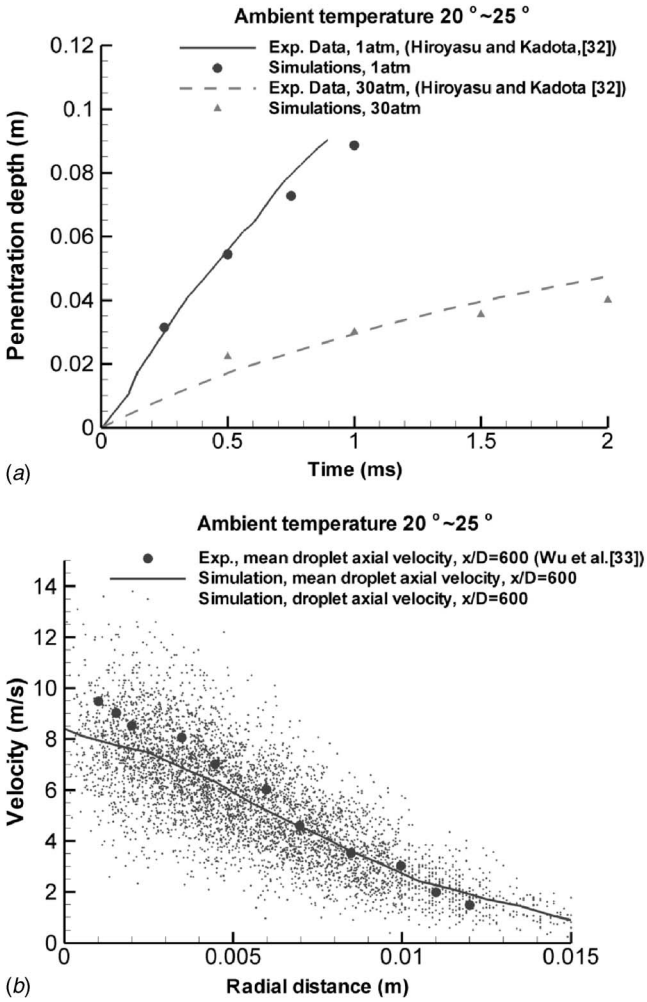

Fig. 3 Computer model validation with experimental spray data

In general, the simulations match the experimental results reasonably well. Discrepancies may stem from several factors:

(1) Droplet agglomeration effects which were not included in the present simulation. Excluding droplet agglomeration may underestimate the penetration depth and the axial velocity due to a lower particle-inertia effect.
(2) Empirically estimated spray conditions, i.e., actual spray angle and spray mass flow rate may deviate from ones assumed for the simulations.
(3) Unknown factors, for example, the spray droplet velocity is very sensitive to the realistic instantaneous liquid mass flow rate, surrounding conditions, and other device factors generating experimental uncertainties which cannot be included in the simulations.

6 Results and Discussion

6.1 Transient Spray Dynamics. Spray dynamics is a time-evolution process. To investigate transient spray dynamics which involves instantaneous gas/droplet interactions, operational data for case 1a and case 1b (see Table 1) were employed for the following simulations:

Spray penetration depth: One of the most important parameters related to time evolution is spray penetration depth, which is defined as the distance between nozzle and spray front tip (see Figs. 1(*a*) and 3(*a*)). Due to the relatively large drag force and spray breakup effect, especially under high back gas pressure, the spray velocity will decay rapidly after leaving the nozzle. Spray penetration depth is greatly affected by the back pressure. Back pressure normally refers to the pressure in the spray chamber or the environment. Back pressure can be as high as 50 atm, e.g., for the diesel-engine-type spray or only atmospheric, e.g., for spray-paint and nasal spray applications.

As shown in Fig. 3(*a*), spray penetrates much faster and further under lower back pressure (1 atm) than under higher back pressure (30 atm). The reason lies in Eq. (9) where the drag force is proportional to the gas density ρ_g and $\rho_g \sim p$ according to the ideal gas law. Hence, larger drag forces on the droplets will decrease the droplet velocity more sharply, and hence decrease the spray penetration depth. To overcome this problem, sprays working in a high back-pressure environment need to have very high injection velocities, sometimes $u_{in} > 200$ m/s.

Droplet velocity and spray breakup: Figures 4 and 5 show mid-

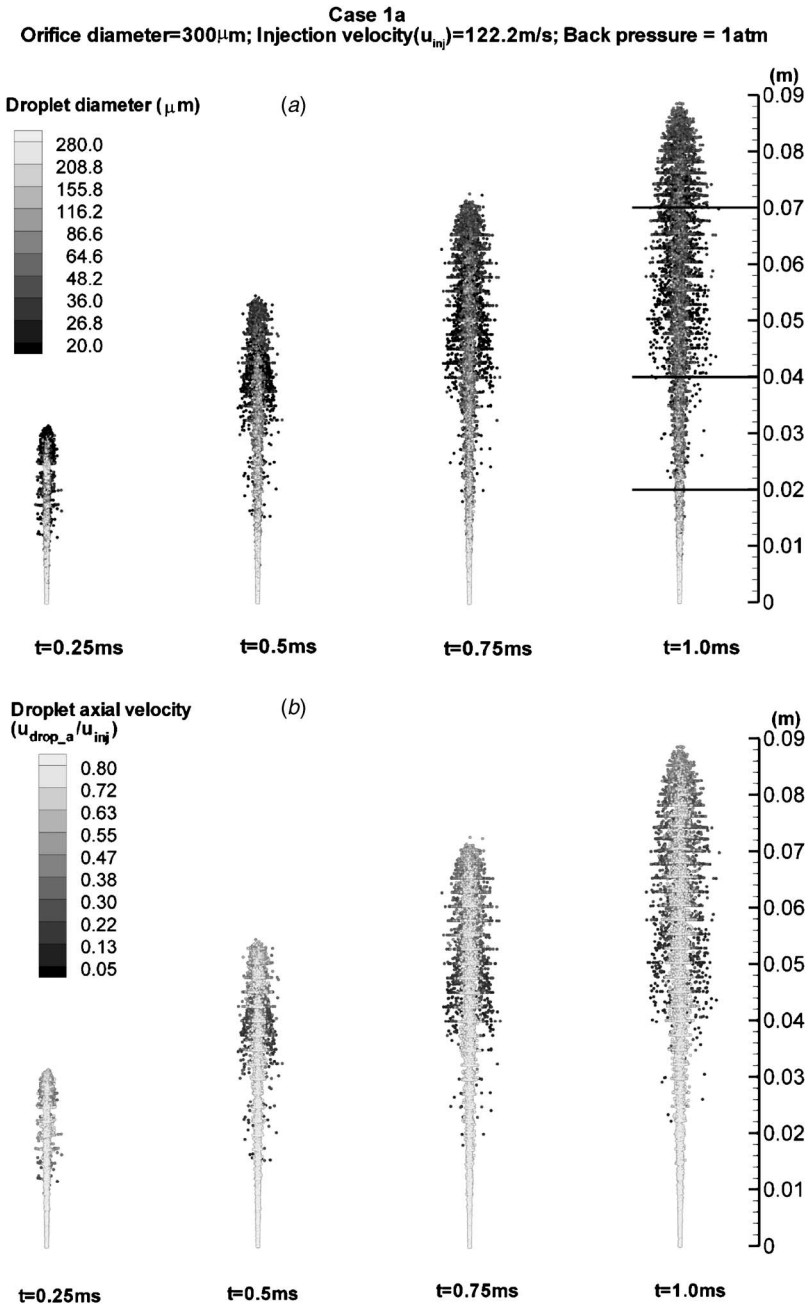

Fig. 4 Spray droplet size and axial velocity patterns for case 1a at different times (i.e., t=0.25 ms, 0.5 ms, 0.75 ms, and 1.0 ms)

plane views of the sprays' particle sizes and droplet velocities for case 1a (1 atm back pressure) and case 1b (30 atm back pressure) to illustrate the dynamics of spray developments. Clearly, Figs. 4 and 5 demonstrate the effect of back pressure on the penetration depth. A spray with a low back pressure (1 atm) shows a long and thin geometric cone compared to a spray with high back pressure (30 atm). Comparing Figs. 4(*b*) and 5(*b*), it can be seen that, although the injection velocities for the two cases are approximately the same, droplets in case 1a decelerate and break up much slower than those in case 1b. As mentioned, this is due to the different drag forces which are proportional to the gas density ρ_g. Figure 4 also shows that the droplets with the smallest size and lowest velocity always lie in the peripheral region of the spray cone. The reason is, the peripheral droplets have larger gas-droplet slip velocities when compared to the droplets in the spray core where significant entrainment gas velocities exist. Thus, the peripheral droplets experience larger drag forces, i.e., larger Weber numbers, which will make droplets decelerate and break up rapidly. Each new smaller child droplet inherits only a very small amount of momentum of the parent droplet. Thus, they will be surpassed by the droplets in the core and left behind by the spray front.

For the high back pressure case (30 atm, Fig. 5), it can be still seen that the droplets with lowest velocities always lie in the peripheral region of the spray cone (Fig. 5(*b*)). However, such an observation does not imply a distinct droplet size distribution (Fig. 5(*a*)). The major reason is that sprays with high back pressure exhibit much higher Weber numbers. As a result, in Eq. (1) the gas density is more dominating than the slip velocity to produce a large Weber number. So, almost all droplets either in the core or

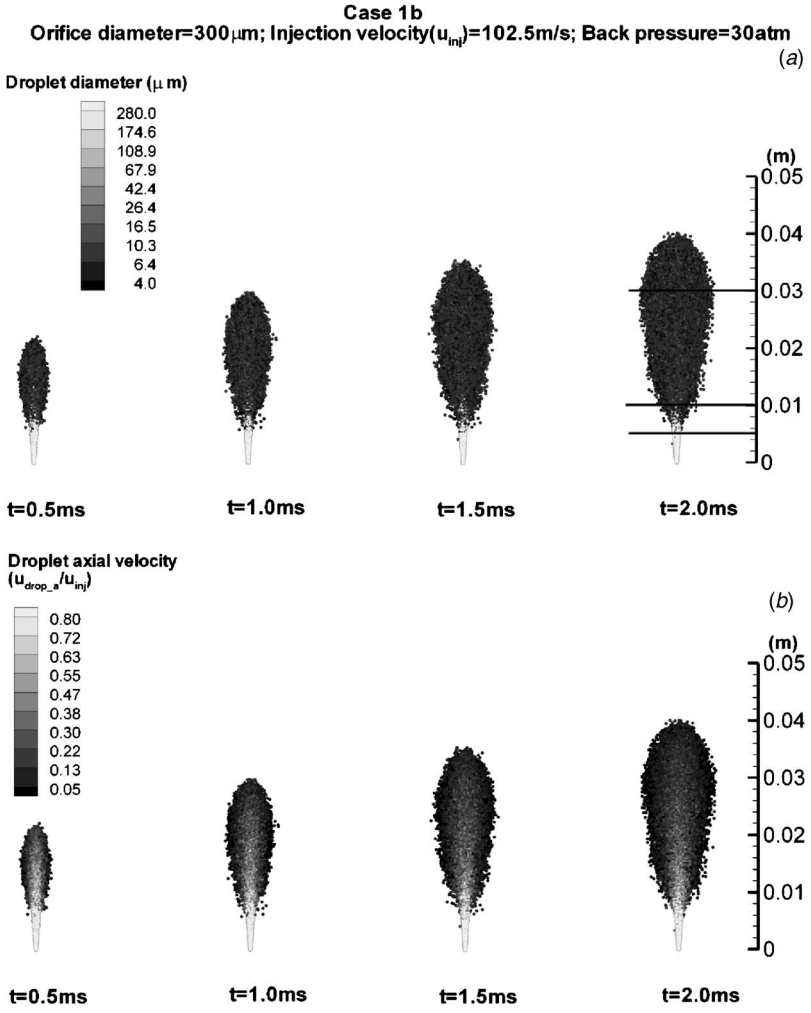

Fig. 5 Spray droplet size and axial velocity patterns for case 1b at different times (i.e., t=0.5 ms, 1.0 ms, 1.5 ms, and 2.0 ms)

the peripheral regions of the spray cone break up to tiny droplets very quickly. Tiny droplets are easily affected by turbulent dispersion, resulting in an indistinct droplet size difference between peripheral and core regions.

All experimental measurements and simulations so far indicated that the *droplet velocity* decreases with radial distance as shown in Figs. 4 and 5. However, in terms of the trend of *droplet size* as a function of radial distance, experimental data and numerical simulations are contradictory. Some experiments [34,35] reported that the droplet size is at a minimum along the spray centerline and increases with radial distance. They attributed this observation to two reasons [34–36]: (i) Due to the shear force, the droplets near the centerline move outward. As a result, collisions between droplets become more frequent, which will increase the size of droplets in the peripheral region. (ii) Large droplets are easily centrifuged to the spray periphery due to large-scale vortices. In contrast, the experiments by Lee and Park [21] indicated a reduction of droplet size with radial distance, which is in agreement with some previous spray simulation results [16,21,22,26] and the present study, as explained in the last paragraph. Nevertheless, the disagreements and contradictions among spray studies indicate that key spray mechanisms may not be fully understood and hence further experimental and computational analyses are necessary.

Droplet size distribution: Figures 6 and 7 include information on droplet size distribution for two cases. Figures 6(a) and 7(a) show the droplet volume mean diameter profiles as a function of axial distance at time levels of 1.0 ms and 2.0 ms for case 1a (1 atm) and case 1b (30 atm), respectively. It clearly shows that in case 1b the droplets and gas reach their equilibrium, i.e., no breakup is occurring, in a much shorter distance than in case 1a. For case 1b, the volume mean droplet diameter stays quasistable after 0.010 m in contrast to about 0.07 m for case 1a. It can also be seen that, the equilibrium droplet diameter of case 1a is around 50 μm, i.e., much larger than 10 μm as in case 1b. As explained before, due to the higher gas density, the drag force in case 1b (30 atm) is much larger than in case 1a. For larger drag forces, droplets will break up more quickly and thoroughly to smaller droplets.

Figures 6(b)–6(d) and 7(b)–7(d) depict the droplet number density functions, which are classified on an interval of 5 μm and plotted as histograms, at different axial places (marked in Figs. 4 and 5) for two cases. First, Fig. 7 supports that droplets in case 1b reach equilibrium at around 0.01 m because the droplet number density functions in Figs. 7(c) and 7(d) are almost identical. It is also interesting to note that, after reaching equilibrium, the droplet density function is a normal-distribution type. Normal distributions or normal-like distributions are found in most spray applications [3,37,38]. Meanwhile, in case 1a (1 atm, Fig. 6), it seems that droplets reach equilibrium at about 0.07 m, where the droplet-size distribution is normal again. In summary, for both cases droplet-size evolves from a "disordered" distribution (Figs. 6(b) and 7(b)) at the start of the breakup to a normal distribution

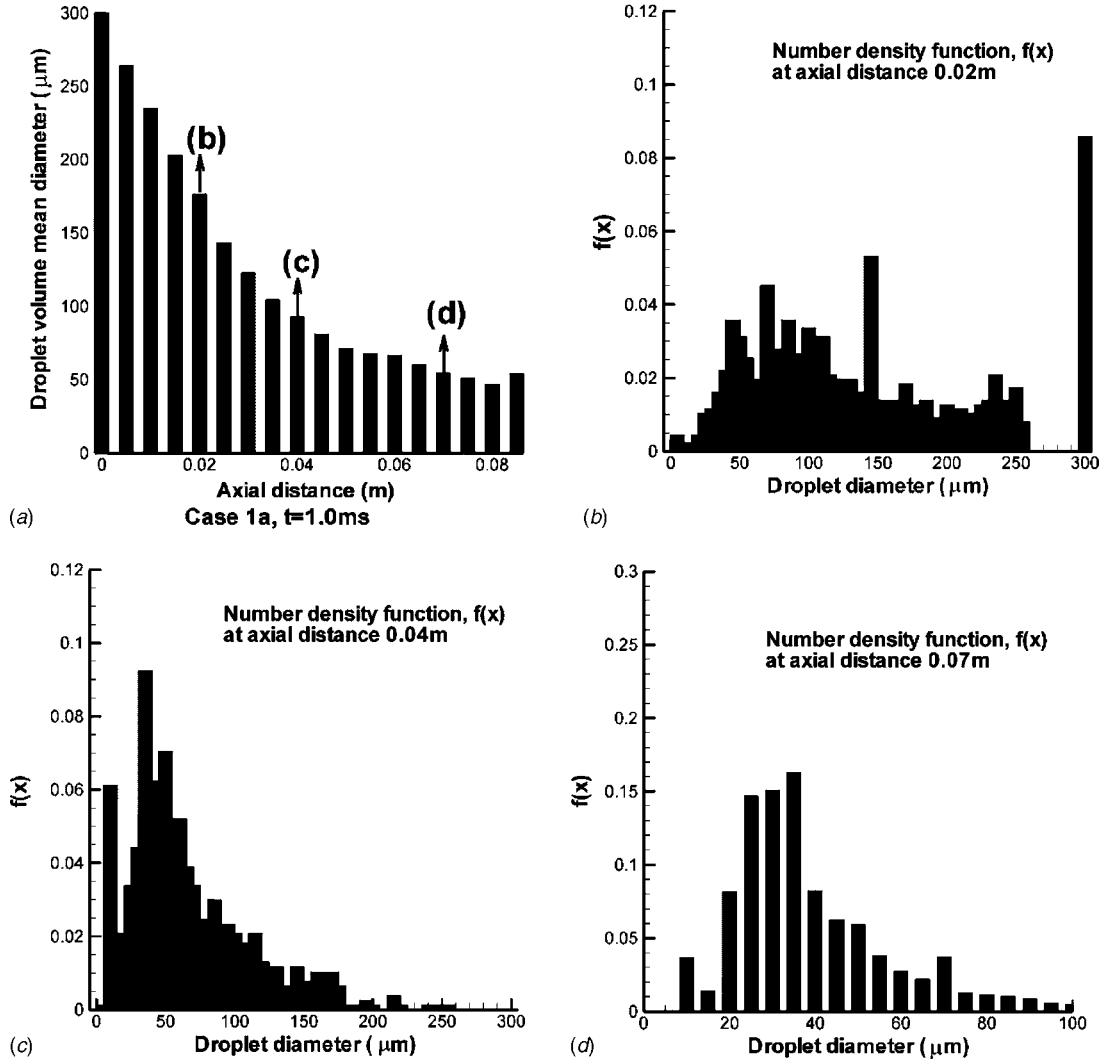

Fig. 6 Droplet size distribution for case 1a (transient)

at the end of breakup. The droplet size distribution after reaching equilibrium is normal-like, instead of uniformly distributed. The reason that droplet size is normally distributed may stem from the fact that the turbulent velocity distribution is assumed to be normal (see Eqs. (9) and (14)), which consequently leads to normally distributed droplet size.

Gas velocity and turbulence kinetic energy: During the interaction between droplets and gas, the gas phase also gains momentum from droplets. Clearly, when a droplet spray is injected into a quiescent gas reservoir, large entrainment velocities are generated. The gas entrainment velocity in case 1a (Fig. 8(*a*)) is much larger than that in case 1b (Fig. 9(*a*)) because of the lower gas density. Meanwhile, Fig. 8(*a*) shows that, at the very beginning of injection, the gas entrainment velocity near the nozzle can almost be as high as the droplet injection velocity, but will decrease as the spray proceeds to its steady state. The possible reason is that right after the first group of droplets come out of the nozzle, droplets immediately experience a tremendous drag force due to the static air, which will make droplets break up rapidly as well as exchange momentum with the gas. The gas near the nozzle will gain relatively large amounts of momentum resulting in significant gas velocities. Because of the continuous discharge, the later droplets will encounter a smaller drag force, or Weber number, since the gas near the nozzle already has some entrainment velocity. As a result, succeeding droplets will exchange relatively small amounts of momentum with the local gas field. As a result, the gas entrainment velocity near the nozzle will decrease to seek a momentum equilibrium with the appearing droplets, while more and more ambient gas attains an entrainment velocity as the spray spreads. For case 1b, such a trend is insignificant because case 1b has a much higher gas-phase density, i.e., by a factor of 30, than case 1a. As a result, the momentum exchange from the droplets to the gas does not lead to variation in gas entrainment velocity as high as for case 1a at the beginning of injection.

Figures 8(*b*) and 9(*b*) show the gas turbulence kinetic energy. Gas turbulence kinetic energy is mainly produced and transported by the shear stress on the gas caused by the momentum exchange. As expected, case 1a produces much larger turbulent effects on the gas phase because of smaller gas densities. Similar to the gas velocity, the gas turbulence energy is more intense closer to the nozzle. Roughly speaking, the gas turbulence energy is also intense closer to the axial centerline except that the kinetic energy right along the centerline is smaller than the nearby side areas. Experiments [33] and some other numerical studies [12,17] observed a similar trend. Because the spray gas velocity has an axisymmetric distribution and reaches its maximum on the center-

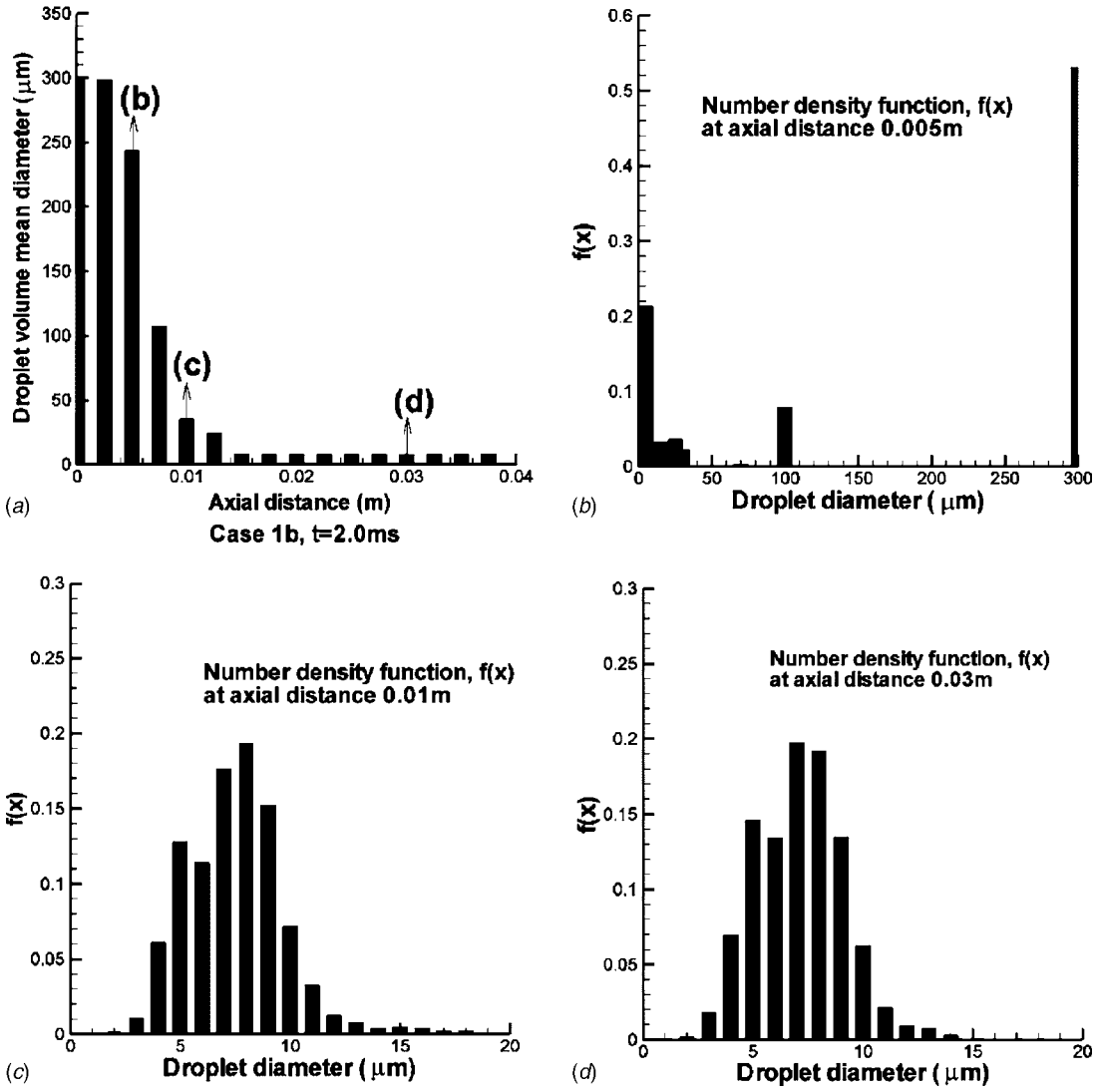

Fig. 7 Droplet size distribution for case 1b (transient)

line (see Figs. 8(*a*) and 9(*a*)), the shear stress on the centerline is a minimum because $\tau \sim \partial \mathbf{v}/\partial y$. Although the centerline always has the largest velocity in its axial plane, the kinetic energy along the centerline will decay faster than in its nearby region.

6.2 Steady-State Spray Dynamics. After liquid is injected from the nozzle, it takes a short time to reach a steady state. For example, Wu et al. [33] reported that the characteristic time for steady-state in their tests is about 30 ms. In this section, two steady-state simulations of sprays, i.e., case 1a and case 2, are conducted to investigate the dynamics of sprays.

Steady versus transient sprays: In Sec. 6.1, the dynamics of spray evolution after injection was discussed. Now, a steady-state simulation was performed for case 1a data to study the difference between transient and steady sprays. The basic observations for the droplet axial velocity, droplet diameter, gas axial velocity, and gas turbulence kinetic energy under steady-state conditions (case 1a) are similar to those made for the transient case. We compared steady-state spray dynamics with the situation at $t=1.0$ ms for case 1a, where the $t=1.0$ ms was selected because its spray has propagated long enough downstream. Referring to Fig. 10 showing the droplet size distribution, it was found that for steady state (Fig. 10(*a*)), the droplet mean volume diameter is larger along the axial direction than in the transient case ($t=1.0$ ms) after 0.02 m from the nozzle. Similar to Figs. 6(*c*) and 6(*d*) when $t=1.0$ ms for case 1a, Figs. 10(*c*) and 10(*d*) (i.e., steady-state results for case 1a) indicate that droplets relatively close to the nozzle have an irregular droplet size distribution due to the incomplete breakup process. When comparing the size distributions (see Fig 10(*d*)), for the steady-state case it is more like a normal distribution than in the transient case. The differences are explained in Fig. 11.

Figure 11 shows the droplet mean axial velocity, gas velocity, and droplet volume mean diameter for both steady-state and transient simulations as a function of radial distance at the axial location of 0.07 m from the nozzle. The droplet velocities of steady and transient sprays start from the same value at the centerline. Then the droplet velocities at steady state become more elevated than for the transient spray as the radial distance increases. For those peripheral spray droplets, their steady-state velocities are almost twice that of the transient case. It means that droplets in transient sprays experience higher momentum loss during their journey, because droplets in transient sprays have to overcome more resistance, i.e., the drag force from the static gas. In contrast,

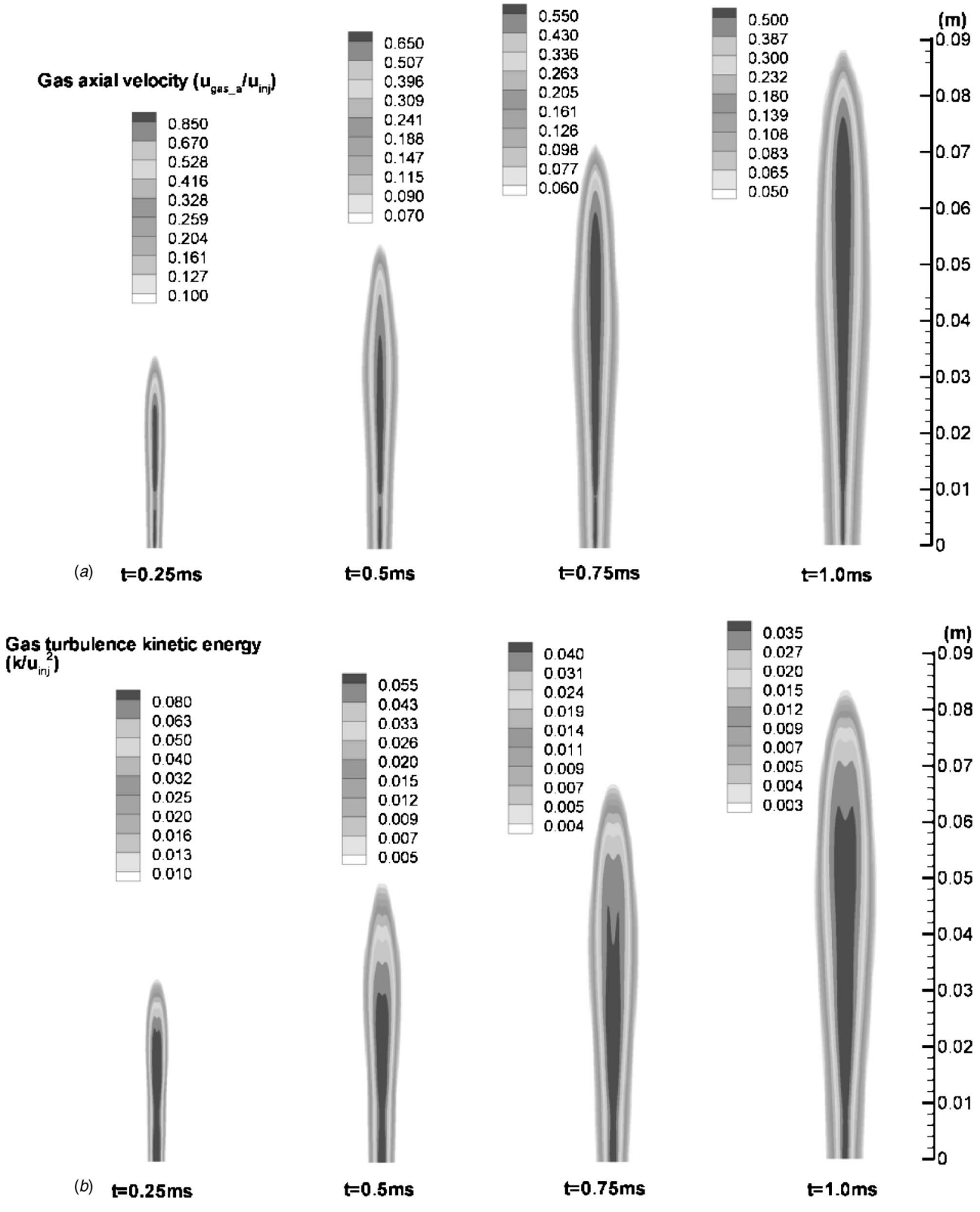

Fig. 8 Gas entrainment velocity and turbulence kinetic energy distributions for case 1a at different times (i.e., t=0.25 ms, 0.5 ms, 0.75 ms, and 1.0 ms)

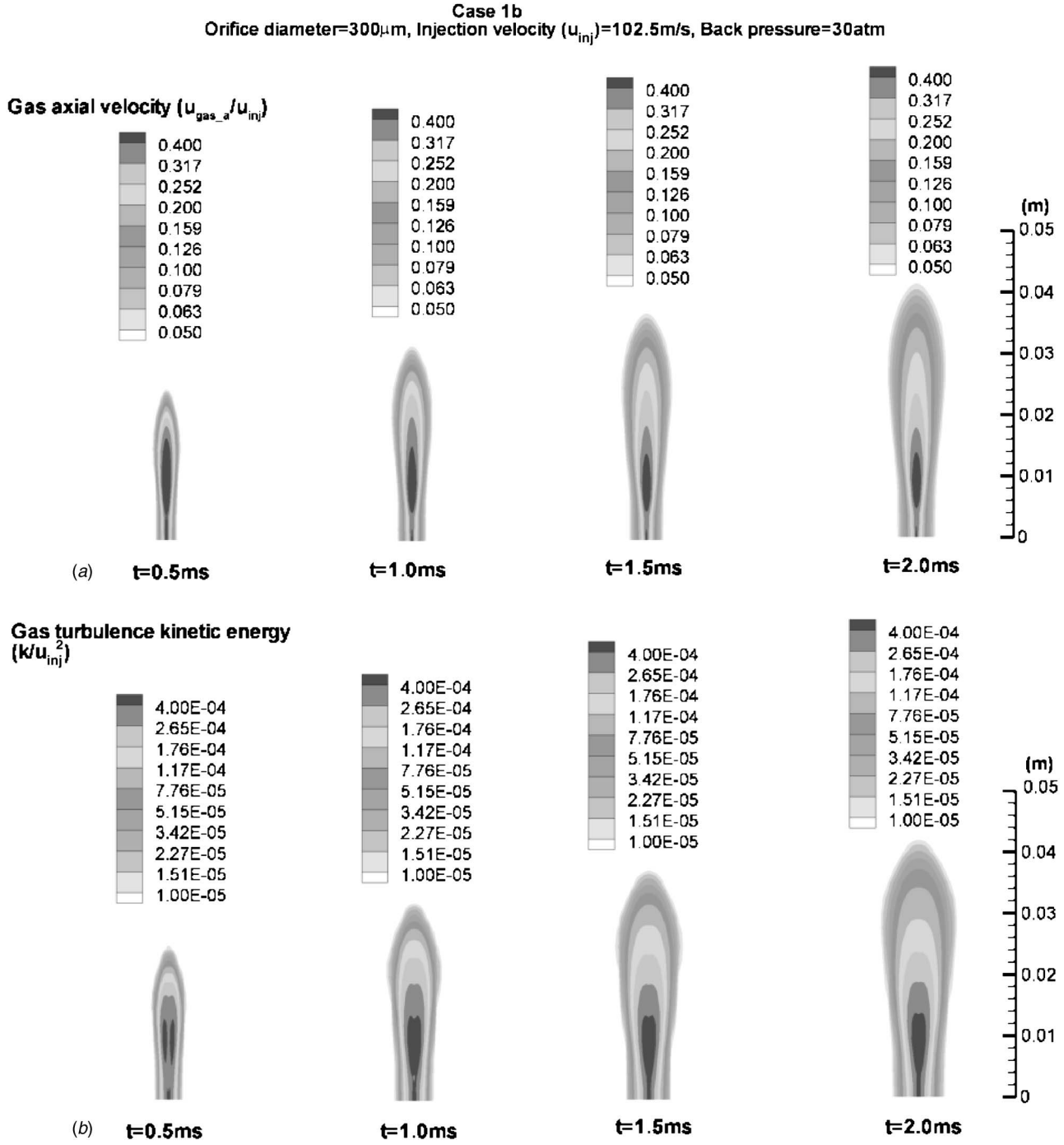

Fig. 9 Gas entrainment velocity and turbulence kinetic energy distributions for case 1b at different times (i.e., t=0.5 ms, 1.0 ms, 1.5 ms, and 2.0 ms)

steady-state sprays spread in a gas with their fully entrained velocity. As a result, droplets in transient sprays also experience more breakup and become smaller (see Figs. 10 and 11(b)) due to relatively large Weber numbers (see Eq. (1)). Meanwhile, the gas entrainment velocity for a transient spray is higher at the centerline, and will reduce with a lower center velocity and higher peripheral velocity to reach the final steady-state, i.e., a fully developed situation.

Wu et al. [33] reported that the characteristic time for steady-state in their tests is about 30 ms. In the present simulation for case 1a, such a time is also approximately 30 ms. As indicated in Fig. 11(a), both gas and droplet velocities between the steady-state case and the t=30 ms case are very close.

Turbulent dispersion effect on spray droplet transport: The steady-state case 2 simulation was performed to validate the computer model with experimental measurements [33]. Wu et al. [33] provided the droplet mean axial velocity as well as the root mean-square-value of the fluctuating axial droplet velocity component as a function of radial distance $\boldsymbol{r}$ at the axial station 0.0762 m (x/D=600) from the nozzle. A similar measurement was not available in [32]. The validation with [33] involves a better understanding of turbulent dispersion on droplet transport.

Figure 3(b) depicts the axial velocity of each droplet (5000

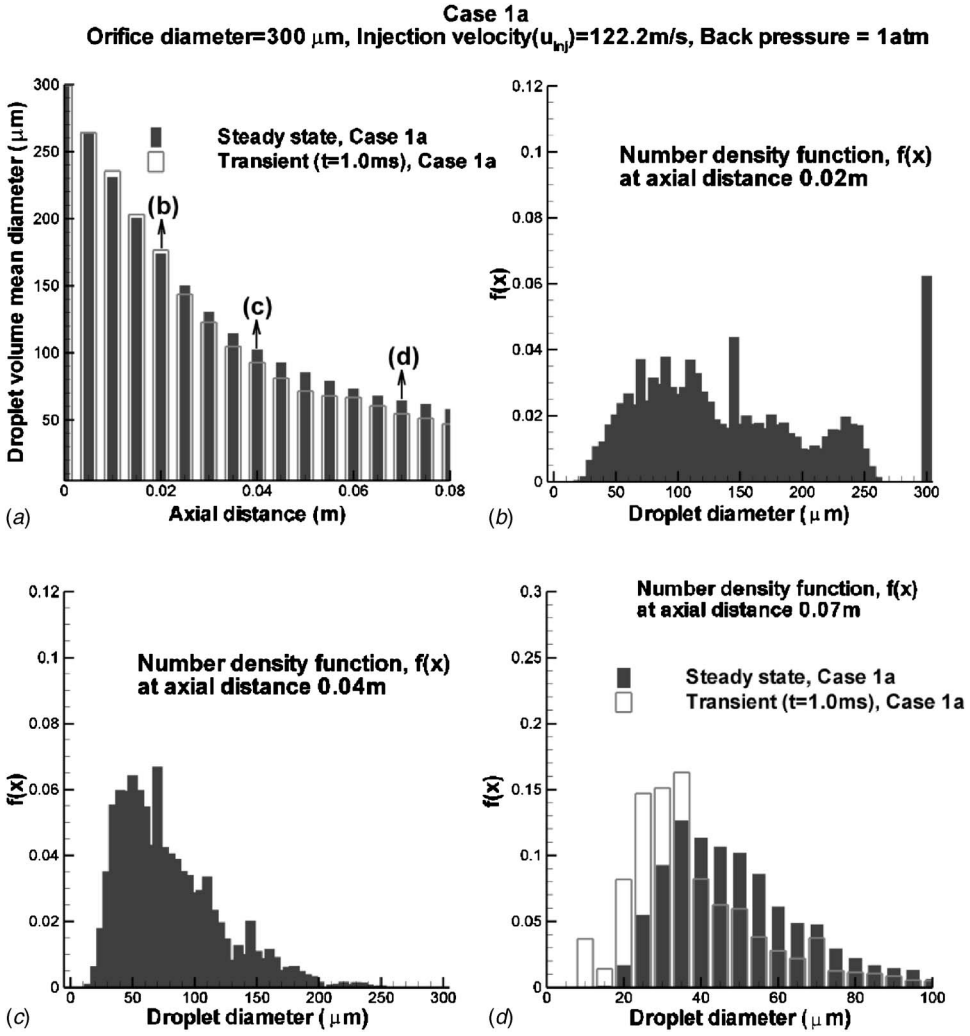

Fig. 10 Droplet size distribution for case 1a under steady-state condition

droplets considered) and their average values in the radial direction. The simulation and experiments match very well. It is noticed that, although the mean axial velocity decreases as the radial distance increases, for one particular radial position the droplet axial velocity range is large. For example, near the axial centerline the droplet axial velocity can be as high as 13 m/s and as low as only 5 m/s. This phenomenon is due to turbulent dispersion (see Eqs. (14)–(16)). As a result, it is not surprising to see the wide range of droplet velocities in radial direction.

7 Conclusion

The following conclusions can be drawn from the present study:

1. Spray penetration depth is highly related to the back pressure level. Spray penetrates faster and deeper under *lower* back pressure than under high back pressure (see Figs. 3–5) due to the lower gas density which will reduce the drag force.
2. Under relatively low back pressure, the droplets with lowest velocity and size always lie in the peripheral region of the spray cone (see Figs. 4 and 5) because the peripheral droplets are subject to larger drag forces (and hence larger slip velocities) compared to the droplets in the spray core, and hence will have shorter lifetimes and break up more rapidly.
3. All experimental measurements and simulations so far indicate that the *droplet velocity* decreases with radial distance as shown in Figs. 4 and 5. However, in terms of the trend of *droplet size* as a function of radial distance, experimental data and numerical simulations so far are contradictory.
4. Under relatively high back pressure, there is no distinct droplet size difference between peripheral and core regions downstream of the nozzle because droplets with high back pressure have much higher Weber numbers. Almost all droplets either in the core or the peripheral spray-cone regions break up to tiny droplets very quickly in a short distance and travel randomly under the effect of dispersion.
5. The droplets and gas with high back pressure reach their equilibrium, i.e., no breakup occurring, in much shorter distances than under low back pressure due to the fast breakup process brought by elevated gas pressure (see Figs. 6 and 7).
6. After the droplets and gas reach their equilibrium, i.e., no breakup occurring, the droplet size distribution of sprays will be a normal-distribution-type.
7. The gas turbulence kinetic energy right along the nozzle axis is smaller than in the nearby regions (see Figs. 8(*b*) and 9(*b*)) due to the lack of shear stress which is critical for the transport of kinetic energy.
8. During steady state, the droplet mean volume diameter is larger than in the transient case (Fig. 10) because, under steady state, droplets are subject to smaller drag forces due to the fully-developed gas entrainment velocities which will reduce the slip velocities (see Eq. (9)).
9. Turbulent dispersion is very important for droplet transport

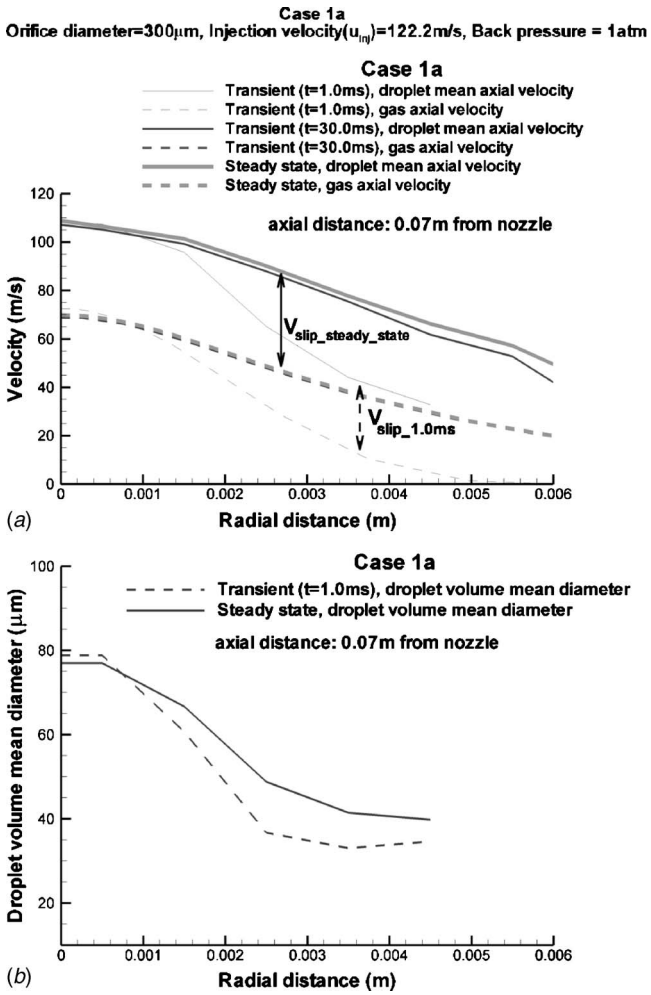

Fig. 11 Comparison of droplet axial velocity, gas axial velocity, and droplet volume mean diameter as a function of radial distance between transient simulation and steady-state simulation for case 1a

trajectory simulations because droplets in sprays may have significant fluctuating velocity components (see Fig. 3(*b*)).

Acknowledgment

The use of CFX and ICEM-CFD software from Ansys Inc. (Canonsburg, PA) and the IBM Linux Cluster at the High Performance Computing Center at North Carolina State University (Raleigh, NC) are gratefully acknowledged.

References

[1] Sirignano, W. A., 1999, *Fluid Dynamics and Transport of Droplets and Sprays*, Cambridge University Press, Cambridge, UK.
[2] Archambault, A., Edwards, C. F., and MacCormack, R. W., 2003, "Computation of Spray Dynamics by Moment Transport Equations I: Theory and Development," Atomization Sprays, **13**, pp. 63–87.
[3] Faeth, G. M., Hsiang, L. P., and Wu, P. K., 1995, "Structure and Breakup Properties of Sprays," Int. J. Multiphase Flow, **21**(Suppl), pp. 99–127.
[4] Wu, P. K., Miranda, R. F., and Faeth, G. M., 1995, "Effects of Initial Flow Conditions on Primary Breakup of Nonturbulent and Turbulent Round Liquid Jets," Atomization Sprays, **5**, pp. 175–196.
[5] Mazallon, J., Dai, Z., and Faeth, G. M., 1999, "Primary Breakup of Nonturbulent Round Liquid Jets in Gas Crossflows," Atomization Sprays, **9**, pp. 291–311.
[6] Herrmann, M., 2003, "Modeling Primary Breakup: A Three-Dimensional Eulerian Level Set/Vortex Sheet Method for Two-Phase Interface Dynamics," Center for Turbulence Research, Annual Research Briefs, pp. 185–196.
[7] Yi, Y., and Reitz, R. D., 2005, "Modeling the Primary Breakup of High-Speed Jets," Atomization Sprays, **14**, pp. 53–79.
[8] Liu, B, Mather, D., and Reitz, R. D., 1993, "Effects of Drop Drag and Breakup on Fuel Sprays," SAE Technical Paper No. 930072.
[9] Reitz, R. D., and Diwakar, R., 1986, "Effect of Droplet Breakup on Fuel Sprays," SAE Technical Paper No. 860469.
[10] Dukowicz, J. K., 1980, "A Particle-Fluid Numerical Model for Liquid Sprays," J. Comput. Phys., **35**, pp. 229–253.
[11] Burger, M., Klose, G., Rottenkolber, G., Schmehl, R., Giebert, D., Schafer, O., Koch, R., and Wittig, S., 2002, "A Combined Eulerian and Lagrangian Method for Prediction of Evaporating Sprays," ASME J. Eng. Gas Turbines Power, **124**, pp. 481–488.
[12] Iyer, V., and Abraham, J., 2003, "An Evaluation of a Two-Fluid Eulerian-Liquid Eulerian-Gas Model for Diesel Sprays," ASME J. Fluids Eng., **125**, pp. 660–669.
[13] Reitz, R. D., and Diwakar, R., 1987, "Structure of High-Pressure Fuel Sprays," SAE Technical Paper No. 870598.
[14] Reitz, R. D., 1987, "Modeling Atomization Processes in High-Pressure Vaporizing Sprays," Atomization and Spray Technology, **3**, pp. 309–337.
[15] O'Rourke, P. J., and Amsden, A. A., 1987, "The Tab Method for Numerical Calculation of Spray Droplet Breakup," SAE Technical Paper Series No. 872089.
[16] Tanner, F. X., 1997, "Liquid Jet Atomization and Droplet Breakup Modeling of Nonevaporating Diesel Fuel Sprays," SAE Technical Paper Series No. 970050.
[17] Shang, H. M., Kim, Y. M., Chen, C. P., and Wang, T. S., 1994, "Numerical Studies of Droplet-Turbulence Interactions," Appl. Math. Comput., **65**, pp. 63–78.
[18] Madabhushi, R. K., 2003, "A Model for Numerical Simulation of Breakup of Liquid Jet in Crossflow," Atomization Sprays, **13**, pp. 413–424.
[19] Beale, J. C., and Reitz, R. D., 1999, "Modeling Spray Atomization With the Kelvin-Helmholtz/Rayleigh-Taylor Hybrid Model," Atomization Sprays, **9**, pp. 623–650.
[20] Su, T. F., Patterson, M. A., Reitz, R. D., and Farrell, P. V., 1996, "Experimental and Numerical Studies of High Pressure Multiple-Injection Sprays," SAE Technical Paper Series No. 960861.
[21] Lee, C. S., and Park, S. W., 2002, "An Experimental and Numerical Study on Fuel Atomization Characteristics of High-Pressure Diesel Injection Sprays," Fuel, **81**(18), pp. 2417–2423.
[22] Park, S. W., and Lee., C. S., 2004, "Investigation of Atomization and Evaporation Characteristics of High-Pressure Injection Diesel Spray Using Kelvin-Helmholz Instability/Droplet Deformation and Break-Up Competition Model," Proc. Inst. Mech. Eng., Part D (J. Automob. Eng.), **218**, pp. 767–777.
[23] Ibrahim, E. A., Yang, H. Q., and Przekwas, A. J., 1993, "Modeling of Spray Droplets Deformation and Breakup," J. Propul. Power, **9**, pp. 651–654.
[24] Gorokhovski, M. A., 2001, "The Stochastic Lagrangian Model of Drops Breakup in the Computation of Liquid Sprays," Atomization Sprays, **11**, pp. 505–520.
[25] Gorokhovski, M. A., and Saveliev, V. L., 2003, "Analyses of Kolmogorov's Model of Breakup and its Application into Lagrangian Computation of Liquid Sprays Under Air-Blast Atomization," Phys. Fluids, **15**, pp. 184–192.
[26] Apte, S. V., Gorokhovski, M., and Moin, P., 2003, "LES of Atomizing Spray With Stochastic Modeling of Secondary Breakup," Int. J. Multiphase Flow, **29**, pp. 1503–1522.
[27] Kolmogorov, A. N., 1941, "On the Log-Normal Distribution of Particles Sizes During Breakup Process," Dokl. Akad. Nauk SSSR, **2**, pp. 99–101.
[28] Kleinstreuer, C., 2003, *Two-Phase Flow: Theory and Applications*, Tayler & Francis, NY.
[29] Clift, R., Grace, J. R., and Weber, M. E., 1978, *Bubble, Drops and Particles*, Academic Press, NY.
[30] Gosman, A. D., and Ioannides, E., 1983, "Aspects of Computer Simulation of Liquid-Fueled Combustors," J. Energy, **7**, pp. 482–490.
[31] Ansys Inc., 2004, CFX 10 Solver Theory. 168-169 Ansys Inc., Canonsburg, PA.
[32] Hiroyasu, H., and Kadota, T., 1974, "Fuel Droplet Size Distribution in Diesel Combustion Chamber," SAE Paper No. 740715.
[33] Wu, K. J., Santavicca, D. A., and Bracco, F. V., 1984, "LDV Measurements of Drop Velocity in Diesel-Type Sprays," AIAA J., **22**(9), pp. 1263–1270.
[34] Wu, K. J., Reitz, R. D., and Bracco, F. V., 1986, "Measurements of Droplet Size at the Spray Edge Near the Nozzle in Atomizing Liquid Jets," Phys. Fluids, **29**, pp. 941–951.
[35] Labs, J., and Parker, T., 2003, "Diesel Fuel Spray Droplet Sizes and Volume Fractions From the Region 25 mm Below the Orifice," Atomization Sprays, **13**, pp. 425–442.
[36] Kosaka, H., Suzuki, T., and Kamimoto, T., 1995, "Numerical Simulation of Turbulent Dispersion of Fuel Droplets in an Unsteady Spray Via Discrete Vortex Method," SAE Technical Paper No. 952433.
[37] Hsiang, L. P., and Faeth, G. M., 1993, "Drop Properties After Secondary Breakup," Int. J. Multiphase Flow, **19**, pp. 721–735.
[38] Cheng, Y. S., Holmes, T. D., Gao, J., Guilmette, R. A., Li, S., Surakitbanharn, Y., and Rowlings, C., 2001, "Characterization of Nasal Spray Pumps and Deposition Pattern in a Replica of the Human Nasal Airway," Journal of Aerosol Medicine: Deposition, Clearance, and Effects in the Lung, **14**(2), pp. 267–280.

Near-Wall Turbulent Pressure Diffusion Modeling and Influence in Three-Dimensional Secondary Flows

E. Sauret

I. Vallet
e-mail: vallet@ccr.jussieu.fr

Institut d'Alembert,
Université Pierre et Marie Curie,
75005 Paris, France

The purpose of this paper is to develop a second-moment closure with a near-wall turbulent pressure diffusion model for three-dimensional complex flows, and to evaluate the influence of the turbulent diffusion term on the prediction of detached and secondary flows. A complete turbulent diffusion model including a near-wall turbulent pressure diffusion closure for the slow part was developed based on the tensorial form of Lumley and included in a re-calibrated wall-normal-free Reynolds-stress model developed by Gerolymos and Vallet. The proposed model was validated against several one-, two, and three-dimensional complex flows. [DOI: 10.1115/1.2723811]

1 Introduction

The turbulent pressure diffusion term in Reynolds-stress transport equations is, in general, neglected not only because of the lack of experimental or direct numerical simulation (DNS) data, but also because this term does not seem important in plane channel flow [1]. Nevertheless, recent DNS computations over a backward-facing step have shown its importance in detached flows, especially close to the wall [2].

The most widely used turbulent diffusion models are the Daly-Harlow [3] proposal (hereafter DH), and the Hanjalić-Launder [4] model (hereafter HL), which corresponds also to the Hirt [5] model with a coefficient re-optimization. However, these two models were initially proposed to model only the part corresponding to velocity fluctuations (divergence of the triple-velocity correlation d_{ij}^{u}), neglecting the pressure fluctuations part. Furthermore, contrary to the HL model, which respects the tensorial symmetry of the triple-velocity correlation, the DH proposal is not symmetric in all three indices. The exact turbulent diffusion term exhibits the same asymmetry, which means that a pressure diffusion part is certainly included in the DH model, as suggested by Lumley [6] and by Launder [7]. We have recently shown [8] that the HL model improves the prediction of boundary-layer entrainment for developing flow in a square duct [9], and that the DH model substantially improves the prediction of skin friction in the reattachment and relaxation regions in two-dimensional (2D) supersonic shock-compression ramps [10,11].

These results suggested the design of a model that would combine the advantages of both the DH and HL closures. Such a model requires improvement of the closure used for the turbulent diffusion and should include, explicitly, a model for pressure diffusion.

Numerous previous assessments for the triple-velocity correlation [12–16] based on a priori comparisons to experimental or DNS data, have shown that the HL [4] and the Lumley [17] models give the best overall results, in one-dimensional (1D) plane channel flow [1,18] and in three-dimensional (3D) boundary layer [19]. Demuren and Sarkar [20], in an a posteriori assessment, compared for fully developed plane channel flow [21], the DH [3], HL [4], and Mellor-Herring [22] (hereafter MH) models, using the Speziale-Sarkar-Gatski [23] pressure-strain model with wall functions, and concluded that the MH model gives the best agreement with experimental data.

Concerning the pressure-velocity correlation, the only theoretical proposal for the slow part, in homogeneous flows, was established by Lumley [17]. The Lumley [17] model was however used in inhomogeneous flows by several authors [24,25]. Fu [24] successfully validated the Lumley [17] model in a 2D plane and round jets [26,27] by using a basic Reynolds-stress closure and the DH model for the triple-velocity correlation. Straatman [25] used the Speziale-Sarkar-Gatski [23] and the Demuren-Sarkar [20] pressure-strain models, and compared the DH, the Lumley, and a modified version of the Lumley model (coefficients recalibrated based on the analysis of zero-mean-shear turbulence), for fully developed channel flow at $\mathrm{Re}_\tau=180$ [1] and for flow over backward-facing step [28]. The modified Lumley model performed better than the original version whose predictions were close to the DH model. Gatski [16] reached the opposite conclusion for 1D turbulent channel flow at $\mathrm{Re}_\tau=590$ [18] with an a priori assessment. Nevertheless, it is difficult to generalize these results because Straatman [25] used second-moment closures with wall functions.

More recently, Suga [29] proposed a rapid-part pressure-diffusion model and used the DH proposal to model both the triple-velocity correlation and the slow-part pressure-diffusion terms. Based on the Craft-Launder [30] second-moment closure, which is wall-normal free, the Suga [29] pressure-diffusion model improved the prediction of the recirculating flow region behind a rectangular trailing edge [31]. There are other proposals for the pressure-diffusion term, but these models were essentially developed for the near-wall region [30] and some of them contain geometric normals to the wall [32,33].

In the present study, the flow is modeled by the compressible Favre-Reynolds-averaged Navier-Stokes equations using the near-wall second-moment closure of Gerolymos-Vallet [34] (hereafter GV-RSM), which is completely independent of wall topology, i.e., of the distance from the wall and of the normal-to-the-wall orientation. The coefficient $C_2^{\mathrm{H}}(A,\mathrm{Re}_{\mathrm{T}})$ present in the rapid pressure-strain redistribution model was slightly recalibrated to make the model less prone to separation (hereafter GV-C_2^{H}-modified RSM), and a complete turbulent diffusion model, including a near-wall turbulent pressure-diffusion closure, was developed from the Lumley [17] model and added to the GV-C_2^{H}-modified RSM.

Contributed by the Fluids Engineering Division of ASME for publication in the JOURNAL OF FLUIDS ENGINEERING. Manuscript received July 19, 2006; final manuscript received September 14, 2006. Assoc. Editor: Ugo Piomelli.

2 Near-Wall Turbulence Modeling

2.1 Reynolds-Stress Equations Modeling. The exact transport equations for the Favre-Reynolds-averaged Reynolds-stresses can be written symbolically

$$C_{ij} = d_{ij} + P_{ij} + \phi_{ij} - \bar{\rho}\varepsilon_{ij} + K_{ij} + \frac{2}{3}\phi_p\delta_{ij} \tag{1}$$

where the convection C_{ij} and the production P_{ij} are exact terms. Diffusion d_{ij} due to molecular d_{ij}^{μ} and turbulent d_{ij}^{T} transport

$$d_{ij} = d_{ij}^{\mu} + d_{ij}^{\mathrm{T}}; \quad d_{ij}^{\mu} \cong \frac{\partial}{\partial x_\ell}\left[\breve{\mu}\frac{\partial\widetilde{u_i''u_j''}}{\partial x_\ell}\right] \tag{2}$$

pressure-strain redistribution ϕ_{ij}, and dissipation $\bar{\rho}\varepsilon_{ij}$ terms require modeling. where $\breve{\mu}$ is the molecular dynamic viscosity determined by using Sutherland law [34]. The symbol $\breve{(\cdot)}$ is used to denote a function of average quantities that is neither a Reynolds-averaged (denoted $\overline{(\cdot)}$) nor a Favre-average (denoted $\tilde{(\cdot)}$). In the present work, we used the wall-normal-free GV-RSM closure, where direct compressibility effects K_{ij} and pressure-dilatation correlation ϕ_p terms were neglected,

$$K_{ij} \cong 0; \quad \phi_p \cong 0 \tag{3}$$

Neglecting the compressibility effects on turbulence (Eq. (3)) is tantamount to neglecting density fluctuations $\rho' \cong 0$, so that Favre and Reynolds averages are approximately equal

$$\rho' \ll \bar{\rho}; \quad \tilde{u}_i \cong \bar{u}_i; \quad \widetilde{u_i''u_j''} \cong \overline{u_i'u_j'} \tag{4}$$

The redistribution ϕ_{ij} and the dissipation $\bar{\rho}\varepsilon_{ij}$ terms were modeled together as the sum of a homogeneous part (denoted by H), an inhomogeneous part (denoted by I) and the isotropic part of the dissipation term

$$\begin{aligned}
\phi_{ij} - \bar{\rho}\varepsilon_{ij} &= \left[\phi_{ij} - \bar{\rho}\left(\varepsilon_{ij} - \frac{2}{3}\delta_{ij}\varepsilon\right)\right] - \frac{2}{3}\delta_{ij}\bar{\rho}\varepsilon \\
&= \phi_{ij1}^{\mathrm{H}} + \phi_{ij2}^{\mathrm{H}} + \phi_{ij1}^{\mathrm{I}} + \phi_{ij2}^{\mathrm{I}} - \frac{2}{3}\delta_{ij}\bar{\rho}\varepsilon \\
&\cong -C_1^{\mathrm{H}}\bar{\rho}\varepsilon a_{ij} - C_2^{\mathrm{H}}\left(P_{ij} - \frac{1}{3}\delta_{ij}P_{\ell\ell}\right) \\
&\quad + C_1^{\mathrm{I}}\frac{\varepsilon}{k}\left[\bar{\rho}\overline{u_k'u_m'}e_{\mathrm{I}_k}e_{\mathrm{I}_m}\delta_{ij} - \frac{3}{2}\bar{\rho}\overline{u_k'u_i'}e_{\mathrm{I}_k}e_{\mathrm{I}_j} - \frac{3}{2}\bar{\rho}\overline{u_k'u_j'}e_{\mathrm{I}_k}e_{\mathrm{I}_i}\right] \\
&\quad + C_2^{\mathrm{I}}\left[\phi_{km2}^{\mathrm{H}}e_{\mathrm{I}_k}e_{\mathrm{I}_m}\delta_{ij} - \frac{3}{2}\phi_{ik2}^{\mathrm{H}}e_{\mathrm{I}_k}e_{\mathrm{I}_j} - \frac{3}{2}\phi_{jk2}^{\mathrm{H}}e_{\mathrm{I}_k}e_{\mathrm{I}_i}\right] - \frac{2}{3}\delta_{ij}\bar{\rho}\varepsilon
\end{aligned} \tag{5}$$

where ϕ_{ij1}^{H} and ϕ_{ij1}^{I} contain also the anisotropic part of the dissipation tensor $(\varepsilon_{ij} - (2/3)\delta_{ij}\varepsilon)$. As usual [17,35] both the homogeneous and the inhomogeneous parts are split into a slow part (denoted by 1) and a rapid part (denoted by 2). The anisotropic part of the dissipation term is included in the slow homogeneous part ϕ_{ij1}^{H} through the particular form of the coefficient function C_1^{H} (Eq. (6)) proposed by Launder-Shima [36]

$$C_1^{\mathrm{H}} = 1 + 2.58AA_2^{1/4}\left[1 - \mathrm{e}^{-(\mathrm{Re_T}/150)^2}\right] \tag{6}$$

$$A_2 = a_{ik}a_{ki}; \quad A_3 = a_{ik}a_{kj}a_{ji}; \quad A = \left[1 - \frac{9}{8}(A_2 - A_3)\right]$$

$$a_{ij} = \frac{\overline{u_i'u_j'}}{k} - \frac{2}{3}\delta_{ij} \tag{7}$$

where A_2 and A_3 are respectively the second and third invariant of the anisotropy tensor a_{ij} and A is the flatness parameter introduced by Lumley [17].

Although the inhomogeneous terms have a form similar to the classically used echo terms, they do not contain any topology parameter. A unit vector $\vec{e}_{\mathrm{I}} = e_{\mathrm{I}_i}\vec{e}_i$ pointing in the turbulence inhomogeneity direction was developed in order to replace the geometric normal to the wall present in classical redistribution echo terms [8]

$$\vec{e}_{\mathrm{I}} = \frac{\mathrm{grad}\left\{\dfrac{\ell_{\mathrm{T}}[1 - \mathrm{e}^{-(\mathrm{Re_T}/30)}]}{1 + 2\sqrt{A_2} + 2A^{16}}\right\}}{\left\|\mathrm{grad}\left\{\dfrac{\ell_{\mathrm{T}}[1 - \mathrm{e}^{-(\mathrm{Re_T}/30)}]}{1 + 2\sqrt{A_2} + 2A^{16}}\right\}\right\|} \tag{8}$$

$$\ell_T = \frac{k^{3/2}}{\varepsilon}; \quad \mathrm{Re_T} = k^2(\breve{\nu}\varepsilon)^{-1} \tag{9}$$

where ℓ_T is the turbulence length scale, $\mathrm{Re_T}$ is the turbulent Reynolds number. The distance-from-the-wall effects are included in the coefficient functions C_1^{I} and C_2^{I} by using turbulence quantities gradients, which replace the geometric distance from the wall present in classical echo terms (Table 1).

We chose the simple models proposed by Rotta [37] for the slow homogeneous part ϕ_{ij1}^{H} and by Naot et al. [38] for the rapid homogeneous part ϕ_{ij2}^{H}, preferring to focus on the coefficient function C_2^{H}. The particular form of $C_2^{\mathrm{H}}(A, \mathrm{Re_T})$ developed by Gerolymos-Vallet [34] (Eq. (10), Fig. 1) is directly responsible of the ability of the model to predict separation and its precise functional dependence on A controls the size of the separation zone. Furthermore, this form improves the prediction of the turbulence structure [8].

Table 1 GV-C_2^{H} and GV-C_2^{H}-modified inhomogeneous redistribution coefficients

$$C_1^{\mathrm{I}} = 0.83\left[1 - \frac{2}{3}(C_1^{\mathrm{H}} - 1)\right]\left\|\mathrm{grad}\left\{\frac{\ell_{\mathrm{T}}[1 - \mathrm{e}^{-\mathrm{Re_T}/30}]}{1 + 2A_2^{0.8}}\right\}\right\|$$

$$C_2^{\mathrm{I}} = \max\left[\frac{2}{3} - \frac{1}{6C_2^{\mathrm{H}}}, 0\right]\left\|\mathrm{grad}\left\{\frac{\ell_{\mathrm{T}}[1 - \mathrm{e}^{-\mathrm{Re_T}/30}]}{1 + 1.8A_2^{\max(0.6,A)}}\right\}\right\|$$

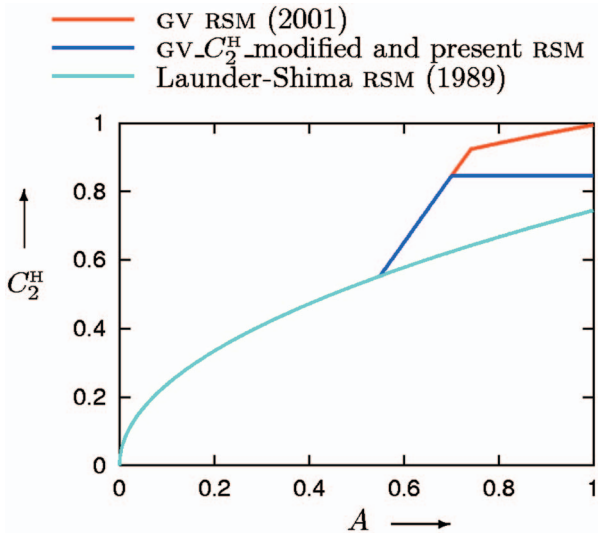

Fig. 1 Redistribution coefficient $C_2^{\mathrm{H}}(A)$

$$C_2^{\mathrm{H}} = C_{2\ \mathrm{GV}}^{\mathrm{H}} = \min\{1, 0.75 + 1.3\ \max[0, A - 0.55]\} \times A^{\{\max(0.25, 0.5 - 1.3\ \max[0, A - 0.55])\}} \left[1 - \max\left(0, 1 - \frac{\mathrm{Re_T}}{50}\right)\right] \tag{10}$$

Nevertheless, the GV-RSM slightly overestimates the size of the 3D separation zone, especially for 3D confined flows. Indeed, the GV-RSM does not accurately model compressibility and thermal effects, which can influence the size of the recirculation zone prediction. Therefore, the function C_2^{H} was slightly reoptimized (Eq. (11), Fig. 1).

$$C_2^{\mathrm{H}} = C_{2\ \mathrm{GV\ modified}}^{\mathrm{H}} = \min(0.85, C_{2\ \mathrm{GV}}^{\mathrm{H}}) \tag{11}$$

The particular form of C_2^{H} (Fig. 1) proposed by Gerolymos-Vallet [34] used the proposal of Launder-Shima [36] until $A=0.55$, which corresponds approximately to the logarithmic zone, and then is sharply raised to a value of 1 when the flatness parameter A tends to unity, which corresponds to the outer part of the boundary layer where turbulence is near isotropic. This choice was motivated by the experimental observation that in separated flow regions, the flatness parameter A approaches unity [34,39]. The various forms used for $C_2^{\mathrm{H}}(A, \mathrm{Re_T}=\infty)$ depend mainly on two parameters (Fig. 1), the slope at $A=0.55$ and the value at $A=1$. Increasing these two parameters, increases the predicted size of the recirculation size so that the GV-RSM predicts a larger separation zone than the GV-C_2^{H}-modified RSM, which separates more than the Launder-Shima RSM. Note that the calibration of this coefficient could be reoptimized according to further modification of the modeling of various terms.

2.2 Turbulent Diffusion Modeling. The turbulent diffusion d_{ij}^T is due to velocity fluctuations d_{ij}^u and to pressure fluctuations d_{ij}^p

$$d_{ij}^T = d_{ij}^u + d_{ij}^p = \frac{\partial}{\partial x_\ell}(-\overline{\rho u_i' u_j' u_\ell'}) + \frac{\partial}{\partial x_\ell}(-\overline{p' u_j'}\,\delta_{i\ell} - \overline{p' u_i'}\,\delta_{j\ell}) \tag{12}$$

In the GV and the GV-C_2^{H}-modified Reynolds-stress closures, turbulent diffusion transport was modeled by using the HL model (Eq. (13)) and the pressure diffusion term was neglected ($d_{ij}^p \cong 0$).

$$d_{ij}^u = \frac{\partial}{\partial x_\ell}(-\overline{\rho u_i' u_j' u_\ell'}) = \frac{\partial}{\partial x_\ell}\left[C_s \frac{k}{\varepsilon}\left(\overline{\rho u_i' u_m'}\frac{\partial \overline{u_j' u_\ell'}}{\partial x_m} + \overline{\rho u_j' u_m'}\frac{\partial \overline{u_\ell' u_i'}}{\partial x_m} + \overline{\rho u_\ell' u_m'}\frac{\partial \overline{u_i' u_j'}}{\partial x_m}\right)\right]; \quad C_s = 0.11 \tag{13}$$

Previous a posteriori assessments of triple-velocity correlation models on several configurations [8,40] have shown little difference between the HL, the Lumley [17], the Cormack-Leal-Seinfeld [12], the Magnaudet [41], and the Younis-Gatski-Speziale [42] models, with due allowance for fine tuning of the model coefficients. Indeed, an erroneous coefficient can change the size of recirculation zone, for example, and this is especially true if the second-moment closure used is able to correctly predict large separation [8]. Taking into account that these models are in majority bilinear in the Reynolds stresses and their gradients, Gatski [16] did not consider this conclusion surprising. Nevertheless, it should be noted that, (i) the Younis-Gatski-Speziale [42] model contains mean-flow velocity gradients, but we found very little difference with the HL model in an a priori assessment for fully developed plane channel flow [1] and (ii) the dissipation-rate ε gradient present in the Magnaudet [41] proposal in his original form (and the Cormack-Leal-Seinfeld [12] model as well) should be removed not only to avoid numerical instabilities close to the wall, in the reattachment zone [43], but also because it overestimates the triple-velocity correlations for 1D plane channel flow [15].

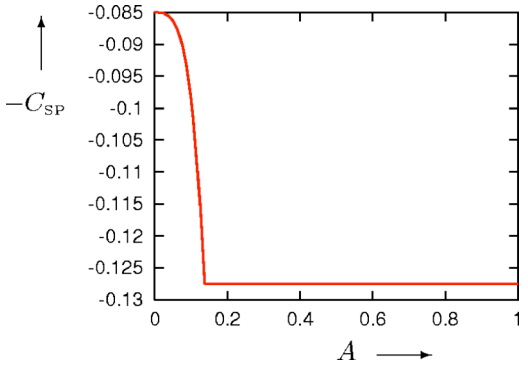

Fig. 2 Turbulent pressure-diffusion coefficient C_{SP}

In the present study, we have chosen for the turbulent diffusion transport the model proposed by Lumley [17]

$$-\overline{\rho u_i' u_j' u_\ell'} = C_{S1}\overline{\rho}\frac{k}{\varepsilon}G_{ij\ell} + C_{S2}\overline{\rho}\frac{k}{\varepsilon}[G_{imm}\delta_{j\ell} + G_{jmm}\delta_{i\ell} + G_{\ell mm}\delta_{ij}]$$

$$G_{ij\ell} = \overline{u_i' u_k'}\frac{\partial \overline{u_j' u_\ell'}}{\partial x_k} + \overline{u_j' u_k'}\frac{\partial \overline{u_i' u_\ell'}}{\partial x_k} + \overline{u_k' u_\ell'}\frac{\partial \overline{u_i' u_j'}}{\partial x_k} \tag{14}$$

$$d_{ij}^p = \frac{\partial}{\partial x_\ell}(C_{SP}\overline{\rho u_j' u_m' u_m'}\delta_{i\ell} + C_{SP}\overline{\rho u_i' u_m' u_m'}\delta_{j\ell}) \tag{15}$$

whose first term of the triple-velocity correlation corresponds to the HL proposal (Eq. (14)) and that includes a model for the slow part of the pressure-velocity correlation (Eq. (15)).

The coefficient C_{SP} of the pressure diffusion model was modified in the present work to account for near-wall effects by using a function of the flatness parameter of Lumley (Eq. (16))

$$C_{SP} = 0.085[1 + \min(0.5, A^{\max[0.25, 2(1-6A)]})] \tag{16}$$

Indeed, the original value proposed by Lumley [17] $C_{SP}=0.2$, which means that the pressure-diffusion contribution equals to −20% of the triple-velocity correlation, was determined from mathematical developments for homogeneous flows, and in consequence this value is too high close to the wall. Furthermore, the coefficient C_{SP} cannot be zero near the wall because the pressure-diffusion term is important in this zone in detached flows [2]. The proposed coefficient C_{SP} value is 0.1275, except close to the wall where it is sharply damped to a value of 0.085 (Eq. (16), Fig. 2). Then, the coefficients C_{S1} and C_{S2} (Eqs. (14) and (17)) were recalibrated for improved prediction of separated flows (the original values proposed by Schwarz-Bradshaw [14] were $C_{S1}=0.098$, $C_{S2}=0.01265$)

$$C_{S1} = 0.0935; \quad C_{S2} = 0.0115 \tag{17}$$

The coefficients C_1^{I} and C_2^{I} were also slightly modified (Table 2)

Table 2 Present model

$$C_1^{\mathrm{I}} = 0.83\left[1 - \frac{2}{3}(C_1^{\mathrm{H}} - 1)\right]\left\|\mathrm{grad}\left\{\frac{\ell_{\mathrm{T}}[1 - \mathrm{e}^{-(\mathrm{Re_T}/30)}]}{1 + 2.05A_2^{0.8}}\right\}\right\|$$

$$C_2^{\mathrm{I}} = \max\left[\frac{2}{3} - \frac{1}{6C_2^{\mathrm{H}}}, 0\right]\left\|\mathrm{grad}\left\{\frac{\ell_{\mathrm{T}}[1 - \mathrm{e}^{-(\mathrm{Re_T}/30)}]}{1 + 1.5A_2^{\max(0.6, A)}}\right\}\right\|$$

Table 3 Present model without pressure diffusion ($d_{ij}^p=0$)

$$C_1^{\mathrm{I}} = 0.83\left[1-\frac{2}{3}(C_1^{\mathrm{H}}-1)\right]\left\|\mathrm{grad}\left\{\frac{\ell_{\mathrm{T}}[1-\mathrm{e}^{-(\mathrm{Re_T}/30)}]}{1+1.52A_2^{0.75}}\right\}\right\|$$

$$C_2^{\mathrm{I}} = \max\left[\frac{2}{3}-\frac{1}{6C_2^{\mathrm{H}}},0\right]\left\|\mathrm{grad}\left\{\frac{\ell_{\mathrm{T}}[1-\mathrm{e}^{-(\mathrm{Re_T}/30)}]}{1+1.25A_2^{\max(0.6,A)}}\right\}\right\|$$

to give the correct near-wall turbulence structure and the correct logarithmic law for flat plate boundary layer [44]. These two coefficients C_1^{I} and C_2^{I} are systematically recalibrated, for different variants of the wall-normal-free RSM closures, to obtain the correct near-wall prediction of zero-pressure-gradient turbulent boundary layer [8]. Finally, to investigate the influence of the pressure-diffusion term, a version of the present model without pressure diffusion ($d_{ij}^p=0$) was developed, and the calibrated coefficients C_1^{I} and C_2^{I} are given in Table 3.

3 Validation

The present model was then validated against experimental or DNS data for several flows (i) fully developed plane channel turbulent-flow of Kim et al. [1], (ii) incident oblique shock-wave/boundary-layer interaction of Reda and Murphy [45], (iii) 3D transonic channel of Ott et al. [46], and (iv) high-subsonic annular cascade with large separation of Doukelis et al. [47]. Computations were carefully checked for grid convergence and for conformity with experimental inflow and boundary conditions [48]. The numerical method used in the present work [49,50] shows no significant CPU-time differences between various Reynolds-stress models and only 26% overhead per iteration for seven-equation (RSM) computations compared to two-equations (k-ε) computations.

3.1 Plane Channel. Various triple-velocity correlations models were compared with DNS data (Fig. 3) for fully developed plane channel flow [1] both a priori (Lumley and HL models) and a posteriori (various wall-normal-free Reynolds stress models). Note that the present model (with and without pressure-diffusion term d_{ij}^p) uses the Lumley proposal (Eq. (14), the difference between the coefficients C_{S1},C_{S2} proposed and the original values is too small to change substantially the a priori assessment in this test case) and that the CV-C_2^{H}-modified RSM uses the HL proposal (Eq. (13)) offering a comparison of a priori and a posteriori predictions with the same triple-velocity correlations closure. It is quite easy to evaluate triple-velocity correlation models by conducting an a priori comparison to DNS data in 1D plane channel flow. Nevertheless, it is difficult to choose the best proposal since the HL model gives the best asymptotic behavior for the $u'v'v'$ and the $v'v'v'$ components, whereas the Lumley model is better away from the wall (Fig. 3).

An a posteriori comparison between the present model with and without pressure-diffusion term d_{ij}^p indicates that the model proposed for the slow-part of the pressure-velocity correlation is essentially significant in the outer part of the boundary layer (Fig. 3). All turbulence models (using the HL or the Lumley model) give similar results for this simple flow. They all underestimate the level of $\overline{u'u'v'}$ and $\overline{u'v'v'}$ maxima at $y^+\cong 50$, and they all predict an erroneous sign near the wall ($y^+<40$) for the $\overline{w'w'v'}$ component. Nevertheless, note that $\overline{w'w'v'}$ component is one order of magnitude lower than $\overline{u'u'v'}$, and that in this simple flow, where most turbulence closures were calibrated, the most important component is the $\overline{u'v'v'}$ present in the shear-stress equation. Furthermore, only the divergence of the triple-velocity correlations enters the Reynolds-stress transport equation (Eq. (12)). If

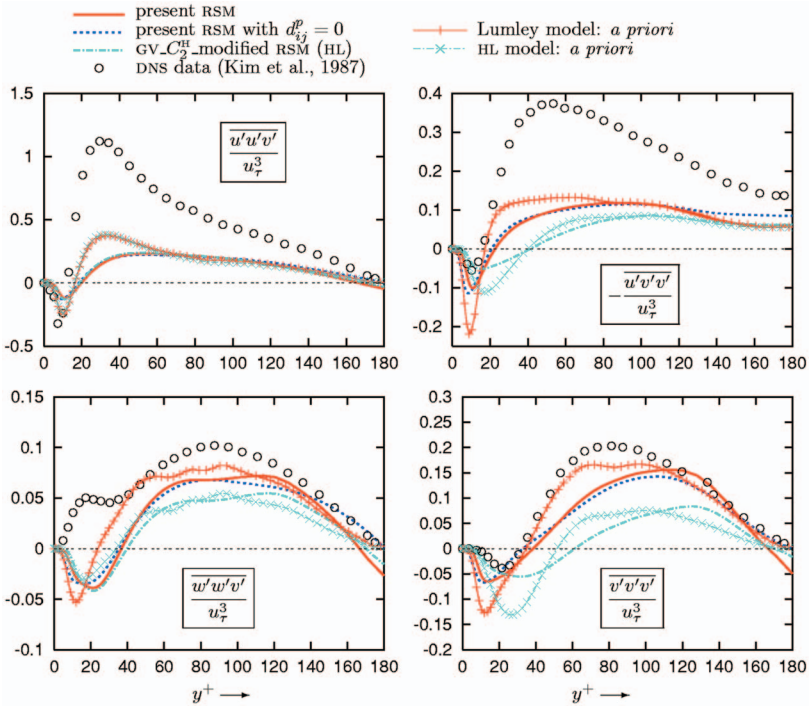

Fig. 3 Comparison of a priori prediction, and of computed results (a posteriori prediction) using the present model with and without pressure diffusion and the GV-C_2^{H}-modified RSM, with DNS data [1] of triple-velocity correlations for plane channel flow ($\mathrm{Re}_\tau=180$, $C_f=8.18\times10^{-3}$, $\mathrm{Re_B}=5600$)

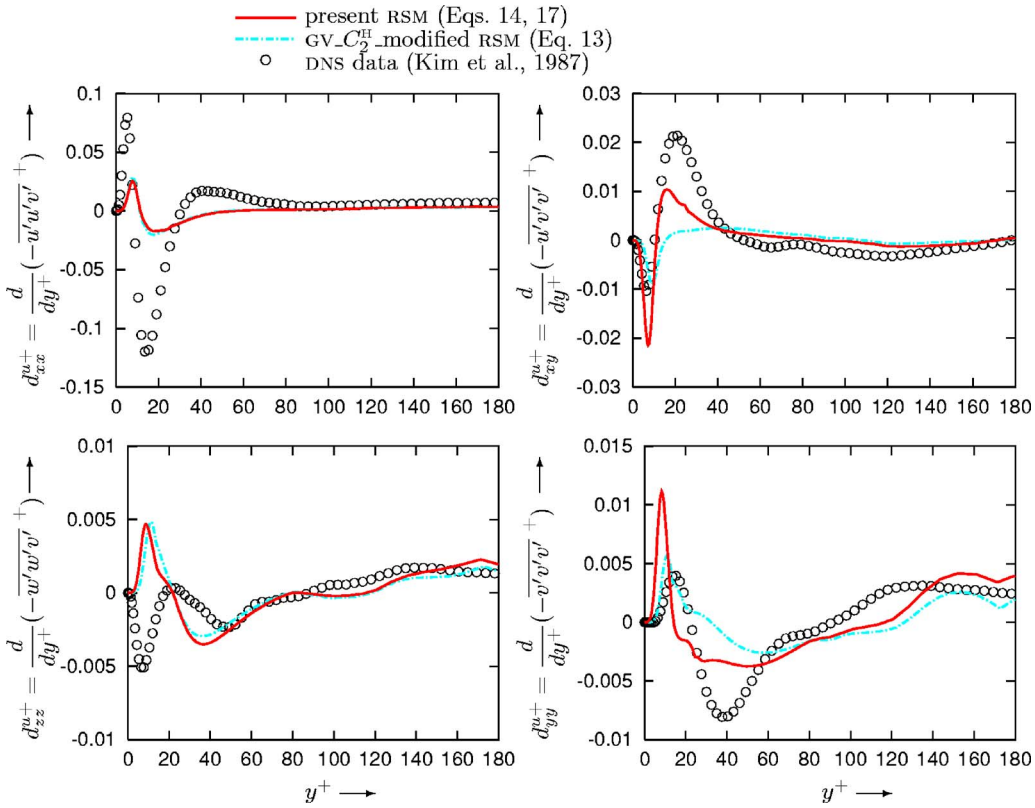

Fig. 4 Comparison of computational results using the present model and the GV-C_2^H-modified RSM, with DNS data [1] of turbulent diffusion due to velocity fluctuations d_{ij}^u for plane channel flow (Re_τ =180, C_f=8.18×10^{-3}, Re_B=5600)

we consider the four nonzero components of the turbulent diffusion due to velocity fluctuations d_{ij}^u (Eq. (12)), the present RSM (Eqs. (14) and (17)) and the GV-C_2^H-modified RSM (Eq. (13)) predict quite similar d_{ij}^u profiles except for the shear-stress d_{xy}^{u+} and the normal d_{yy}^{u+} components. The present RSM gives better agreement with DNS data, but overpredicts the peak near the wall while those in the buffer-layer zone are underpredicted (Fig. 4).

The pressure diffusion of the $\overline{u'v'}$ component d_{xy}^{p+} is in quite good agreement with DNS data (Fig. 5). However, the present RSM gives a profile that vanishes at the wall contrary to the DNS data, and the peak near the wall of the d_{yy}^{p+} component is not correct. This is due to the pressure-diffusion closure of the present RSM (the pressure-diffusion term is neglected in the GV-C_2^H-modified RSM), which is only function of the triple-velocity correlation. Further developments are required, in particular, on the echo-part and rapid-part modeling [35], which are missing, to improve the prediction near the wall.

3.2 Oblique Shock-Wave/Boundary-Layer Interaction. This configuration, experimentally studied by Reda and Murphy [45], consists of an oblique shock-wave M_{SW}=2.9 and $\Delta\vartheta_{SW}$ =13 deg impinging on a flat-plate turbulent boundary-layer. The inflow boundary conditions were chosen to fit the available experimental data [45]

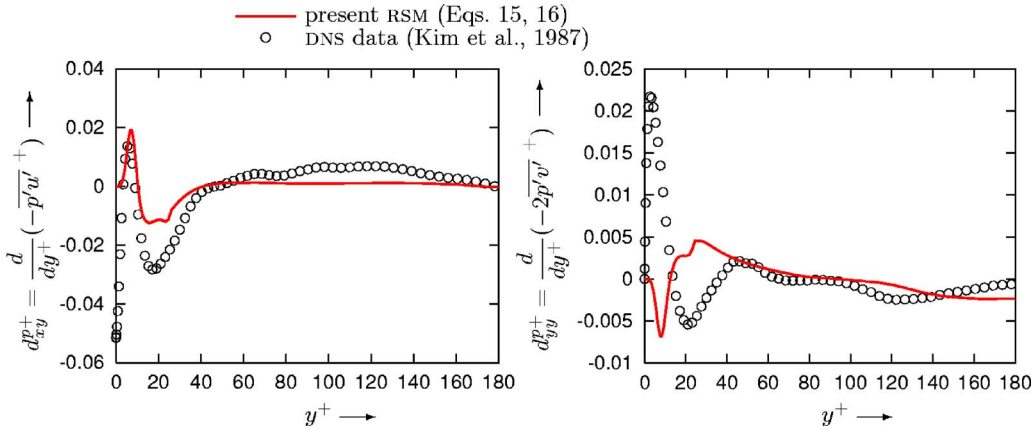

Fig. 5 Comparison of computational results using the present model with DNS data [1] of pressure diffusion term d_{ij}^p for plane channel flow (Re_τ=180, C_f=8.18×10^{-3}, Re_B=5600)

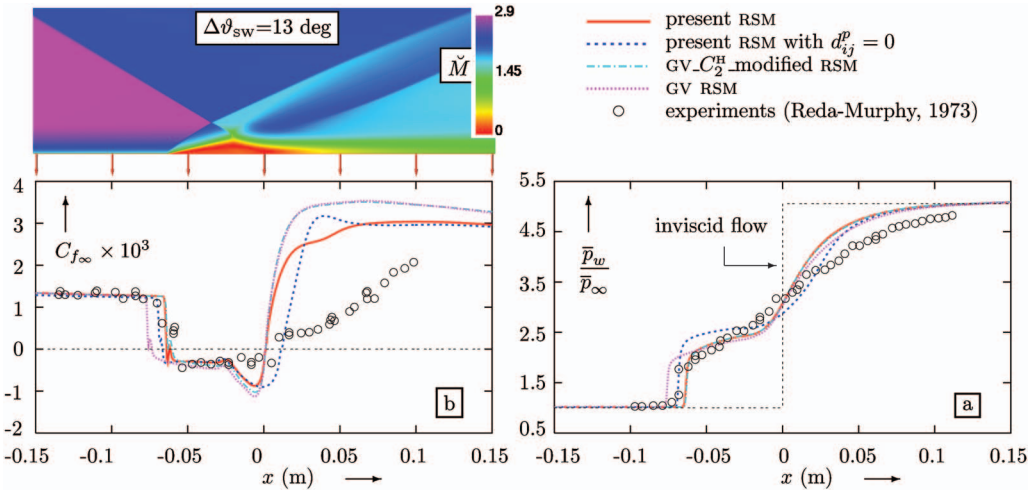

Fig. 6 Comparison of grid-converged computations with measurements [45] of wall-pressure (*a*) and skin-friction (*b*) *x*-wise distributions, for Reda-Murphy [45] incident-shock-wave interaction (M_∞=2.9, $Re_{\delta_0}=0.97\times10^6$, $\Delta\vartheta_{sw}$=13 deg) using the present model with and without turbulent pressure diffusion d^p_{ij}, the GV and GV-C_2^H-modified RSMs (iso-Machs computed with the present RSM)

$$p_{t_i}=689{,}010\ \text{Pa};\quad T_{t_i}=291\ \text{K};\quad T_w=271\ \text{K} \tag{18}$$

and only grid-converged results are presented (details on grid-convergence studies and on the influence of boundary conditions are given in Refs. [10,48].

Comparison of skin-friction distribution for the oblique-shock-wave/boundary-layer interaction (Fig. 6) highlights the importance of the pressure-velocity correlation in the reattachment region. Indeed, we note that the pressure-diffusion term is directly responsible for improving the skin-friction shape prediction in the reattachment region by removing the peak located at $x\simeq0.04$ m (Fig. 6(*b*)). This improvement is independent of the recirculation zone prediction since the present model and the GV-C_2^H-modified RSM predict identical wall-pressure distributions (the C_{S1} and C_{S2} coefficients of the present model, were calibrated to this purpose) and the GV model, which overestimates the recirculation zone, gives the same skin-friction prediction in the reattachment zone as the GV-C_2^H-modified RSM. Furthermore, previous assessments [8] have shown that the DH [3] model for the triple-velocity correlation improves the skin-friction prediction in the same way. Since the very simple DH proposal is asymmetric in all of the three indices, such as the exact turbulent-diffusion term (Eq. (12)), these results corroborate the thesis that the DH proposal should be considered as a model for the turbulent-diffusion term. This idea was previously suggested by Lumley [6] and Launder [7].

Note that the use of a triple-velocity correlation model without a suitable coefficient calibration can change the size of the recirculation zone as we can see by comparing the present model with and without pressure diffusion d^p_{ij} (Fig. 6(*a*)). Previous studies have shown a dramatic overestimation of the recirculation zone by using a too high C_{S1} coefficient in a strong shock-wave/boundary-layer interaction on a compression ramp [8]. The GV RSM slightly overpredicts the size of the recirculation zone and the GV-C_2^H-modified RSM seems to underestimate this region. However, this configuration is not free of 3D effects and probably contains compressibility and thermal effects (wall temperature was not measured), which are not taken into account. Consequently, since it is possible to adjust the size of the pressure plateau through the particular form of the redistribution function C_2^H, there is no need in dwelling on the accuracy of the upstream influence prediction (Fig. 6), as far as pressure diffusion modeling is concerned.

3.3 3D Transonic Channel. The 3D transonic channel configuration, studied experimentally by Ott et al. [46], is an interesting test case to evaluate the capacity of a model to predict solid corner secondary flow with shock-induced recirculation. A shock wave is created by adapting the outflow static pressure $\bar{p}_o$ with a cylindrical rod located 480 mm downstream the throat. The two extreme positions of the rod (horizontal and vertical), which correspond to outflow-static-to-inflow-total-pressure ratio $\pi_{S\text{-}T}=\bar{p}_o/p_{t_i}=0.636,0.669$, induce a shock wave whose position is respectively the most upstream and the most downstream in the test section. The computational domain, which corresponds to 1/4 of the symmetric nozzle, is $L_x\times L_y\times L_z=264\times40\times20$ mm. The grid used is $N_i\times N_j\times N_k=N_x\times N_y\times N_z=241\times121\times97$ with $y^+_w\sim z^+_w\sim0.65$. The computational grid used was uniform in the streamwise direction. On the solid walls, the $N_{j_s}=80\%N_j$ and the $N_{k_s}=80\%N_k$ points are geometrically stretched with ratio $r_y=1.08$ and $r_z=1.09$ in the y and z directions respectively, while the remaining points are uniformly distributed. The computational grid was chosen from previous grid studies [49,51] and for all of the turbulence closures used, convergence of the computations was obtained in about 20 h CPU time on NEC SX-8 with the numerical method developed by Gerolymos-Vallet [50]. Note that monogrid computations were performed due to the important difference between boundary layer thicknesses δ_{y_i} and δ_{z_i} at the inlet. At inflow ($x=-100$ mm), the experimentally determined conditions [46] were applied

$$p_{t_i}=168{,}600\ \text{Pa};\quad T_{t_i}=323\ \text{K};\quad \delta_{y_i}=0.2\ \text{mm};\quad \delta_{z_i}=2\ \text{mm}$$

$$T_{u_i}=2\ \%\ ;\quad \ell_{T_i}=20\ \text{mm} \tag{19}$$

The boundary layer thickness δ_{y_i} and δ_{z_i} are different because of the presence of slots on the nozzle liners which cut off the boundary layer.

Comparison of isentropic-wall-number distributions (Fig. 7) indicate that the GV and the GV-C_2^H-modified Reynolds-stress models predict a too large pressure plateau behind the shock-wave/boundary-layer interaction (which does not appear experimentally) whose size varies homothetically with the shock-wave intensity (the detached zone is more pronounced with $\pi_{S\text{-}T}=0.669$). From this, it may be deduced that a simple adjustment of the C_2^H function, the particular form of which is able to control the size of the recirculation zone, cannot give a good agreement with experimental data for both outflow-static pressures. On the other

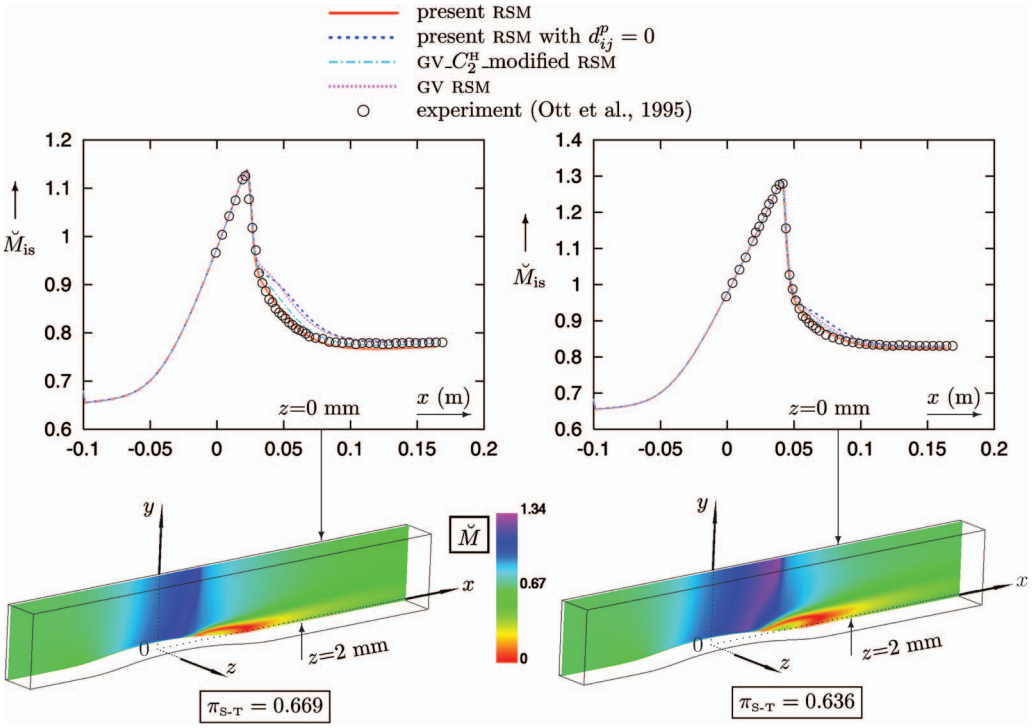

Fig. 7 Comparison of computations with measurements [46] of isentropic-wall Mach number $\breve{M}_{is}$ on the sidewall (z=0) at the y-symmetry plane (y=40 mm) of the transonic square nozzle configuration of Ott et al. [46] (only 1/4 of the symmetric nozzle is shown) for two outflow-static-to-inflow-total pressure ratios π_{S-T}=0.636, 0.669 (T_{u_i}=2%; ℓ_{T_i}=0.020 m; 241×121×97 grid), using the present model with and without turbulent pressure diffusion d_{ij}^p, the GV and the GV-C_2^H-modified RSMs; iso-Machs computed with the present RSM at z=2 mm

hand, the present model is in perfect agreement with experimental data contrary to its version without pressure diffusion modeling. This means that only explicit pressure-diffusion modeling is able to improve the corner secondary flow prediction and to adjust its size in accordance with the shock-wave intensity.

This is certainly combined with the improvement of the corner secondary flow prediction, which influences the shock-induced recirculation at the corner and the isentropic-wall-number distribution on the sidewall (z=0) at midheight (y=40 mm) of the nozzle. Indeed, the surface on which $\breve{M}$=0.1 (Fig. 8) clearly shows a substantial difference between the present model and the present RSM with d_{ij}^p=0 predictions. The lower outflow-static-to-inflow-total pressure ratio (π_{S-T}=0.636) induces the stronger shock wave, which restricts the size of the corner secondary flow. As a result, the overestimation of the corner secondary flow obtained by using the model with d_{ij}^p=0 has not as influence on the isentropic-wall Mach number $\breve{M}_{is}$ prediction as the π_{S-T}=0.669 simulation (Fig. 8). In that case (π_{S-T}=0.669), taking into account of the pressure-diffusion process d_{ij}^p reduces substantially the size of the corner secondary flow.

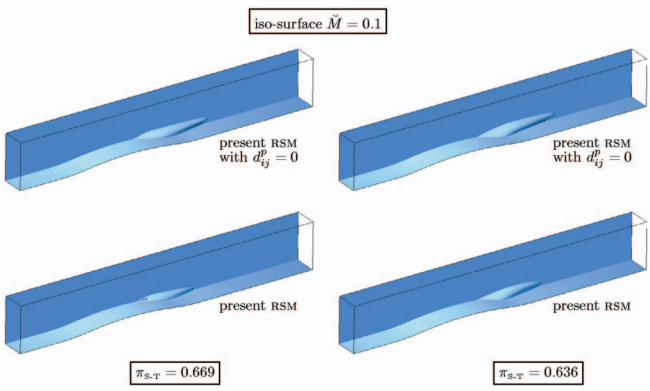

Fig. 8 Mach number isosurface at a value of $\breve{M}$=0.1 for the transonic square nozzle configuration of Ott et al. [46] (only 1/4 of the symmetric nozzle is shown) for two outflow-static-to-inflow-total pressure ratios π_{S-T}=0.636, 0.669, using the present model with and without turbulent pressure diffusion d_{ij}^p.

3.4 High-Subsonic Annular Cascade. The stator of 19 blades, which was studied experimentally by Doukelis et al. [47], was simulated on an H–O–H grid of 2.75×10^6 points [49] discretizing one blade passage with pitchwise periodicity conditions ([52], where it is shown that this grid is reasonably grid converged).

The spanwise distribution of inflow angle (generated by the presence of an upstream scroll [47]), induces a large separation zone at the hub of the cascade (Fig. 9). The present model (Fig. 9) gives the correct prediction of the pitchwise-averaged flow-angle α_M along the span ς at the outlet of the cascade ($\varsigma = (R - R_{HUB})/(R_{TIP} - R_{HUB})$, where R_{HUB} and R_{TIP} are respectively the radius at the hub and the tip of the cascade). The correct prediction of this angle is directly related to the correct prediction of the large corner stall observed in this cascade (α_M=90 deg corresponds to purely circumferential flow). If the pressure diffusion term is neglected (present model with d_{ij}^p=0), the results are less satisfactory. However, we can note that the GV-C_2^H-modified RSM is in quite good agreement with experiment and a slight recalibration of the C_2^H coefficient should give perfect results. Nevertheless, this new recalibrated RSM would not be satisfactory for the previous test cases. Furthermore, previous studies [8]

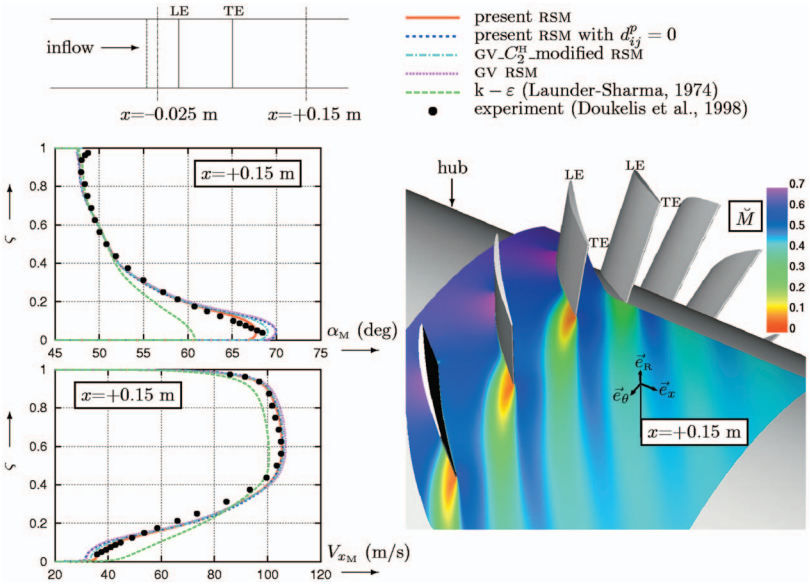

Fig. 9 Partial view of the NTUA annular cascade [47], illustrating Mach levels near the hub (the $xR\theta$ frame is located at the x= +0.15 m station), and comparison of measured [47] and computed spanwise (ζ) distributions of pitchwise-averaged flow angle α_M and axial velocity component V_{x_M} at the outlet (x= +0.15 m), using the present model with and without pressure diffusion d_{ij}^p, the GV and the GV-C_2^H-modified RSMs, and the Launder-Sharma k-ε closure [53] ($\dot{m}$=13.2 kg s^{-1}; T_{u_i}=4%; ℓ_{T_i}=0.04 m; grid_DE [49])

have shown that turbulent diffusion models, which only include the triple-velocity correlation, do not have a major effect on this flow. Thus, for this complex detached flow, the turbulent-diffusion process d_{ij}^T seems to have little influence compared to the redistribution term ϕ_{ij}. That is why a basic linear eddy-viscosity model where the redistribution term does not appear (here, the linear k-ε model of Launder-Sharma [53]) completely fails in predicting this 3D flow (Fig. 9).

4 Conclusion

In the present work, a complete turbulent-diffusion closure, which includes a model for the slow part of the pressure-velocity correlation, was proposed and included in a recalibrated version of the Reynolds-stress model developed by Gerolymos-Vallet [34]. The closure for the pressure-diffusion term was based on the Lumley proposal and coefficients were reoptimized to take into account near-wall effects.

Comparison to experimental measurements for the 2D shock-wave/boundary-layer interaction showed that the present model improves the skin-friction distribution in the reattachment and the relaxation zones without modification of the prediction of wall-pressure distribution, as did the DH model (studies presented in a previous paper [8]), which confirm that the DH model takes into account a part of pressure diffusion, and actually models the complete turbulent transport term. Unfortunately, the DH model uses a very restrictive tensorial form and fails improving the prediction of 3D complex flows, contrary to the Lumley model, whose tensorial basis is more general. Then, the DH model should be used only for simple flows as suggested by Lumley [6]. Furthermore, being advised by recent works [54] of the skin-friction measurement-technique sensitivity (and related unsteadiness shock-wave effects) in reattachment region, the pressure-diffusion model was not calibrated to conform with experimental data. However, in this kind of 2D separated flow, the pressure-diffusion term seems to be significant only downstream the interaction without any influence on the size of the recirculation zone.

The present model was validated in 3D flows by comparing computations with experiments for a 3D transonic channel and a high-subsonic annular cascade. Explicit modeling of the pressure-diffusion term based on the tensorial form of Lumley, improves the prediction of the corner secondary flow in the 3D transonic channel for both the weak and strong shock waves. Although the present model is in quite good agreement with experimental data for the annular cascade, the turbulent-diffusion model seems less important than the redistribution for the prediction of a large recirculation zone.

Acknowledgment

The computations presented in this work were performed at the Institut pour le Développement des Ressources en Informatique Scientifique (IDRIS), where computer ressources were made available by the Comité Scientifique. The authors are listed alphabetically.

References

[1] Kim, J., Moin, P., and Moser, R., 1987, "Turbulence Statistics in Fully Developed Channel Flow at Low-Reynolds-Number," J. Fluid Mech., **177**, pp. 133–166.
[2] Le, H., Moin, P., and Kim, J., 1997, "Direct Numerical Simulation of Turbulent Flow Over a Backward-Facing Step," J. Fluid Mech., **330**, pp. 349–374.
[3] Daly, B. J., and Harlow, F. H., 1970, "Transport Equations in Turbulence," Phys. Fluids, **13**, pp. 2634–2649.
[4] Hanjalić, K., and Launder, B. E., 1972, "A Reynolds Stress Model of Turbulence and Its Application to Thin Shear Flows," J. Fluid Mech., **52**, pp. 609–638.
[5] Hirt, C. W., 1969, "Generalized Turbulence Transport Equations," Int Sem. of Int. Center for Heat and Mass Transfer, Herceg Novi, Yugoslavia.
[6] Lumley, J. L., 1979, "Second Order Modeling of Turbulent Flows," *Prediction Methods for Turbulent Flows*, VKI Lecture Series, von Kármán Institute for Fluid Dynamics, Rhode-sur-Génèse, Jan.
[7] Launder, B. E., Reynolds, W. C., Rodi, W., Mathieu, J., and Jeandel, D., 1984, *Turbulence Models and Their Applications II*, No. 56 in Collection de la Direction des Etudes et Recherches d'Electricite de France, Eyrolles, Paris.
[8] Gerolymos, G. A., Sauret, E., and Vallet, I., 2004, "Contribution to the Single-Point-Closure Reynolds-Stress Modelling of Inhomogeneous Flow," Theor. Comput. Fluid Dyn., **17**(5–6), pp. 407–431.
[9] Gessner, F. B., and Emery, A. F., 1981, "The Numerical Prediction of Devel-

oping Turbulent Flow in Rectangular Ducts," ASME J. Fluids Eng., **103**, pp. 445–455.
[10] Gerolymos, G. A., Sauret, E., and Vallet, I., 2004, "Oblique-Shock-Wave/Boundary-Layer Interaction Using Near-Wall Reynolds-Stress Models," AIAA J., **42**(6), pp. 1089–1100.
[11] Settles, G. S., Vas, I. E., and Bogdonoff, S. M., 1976, "Details of a Shock-Separated Turbulent Boundary-Layer at a Compression Corner," AIAA J., **14**(12), pp. 1709–1715.
[12] Cormack, D. E., Leal, L. G., and Seinfeld, J. H., 1978, "An Evaluation of Mean Reynolds Stress Turbulence Models: The Triple Velocity Correlation," ASME J. Fluids Eng., **100**, pp. 47–54.
[13] Amano, R. S., and Goel, P., 1986, "Triple-Velocity Products in a Channel With Backward-Facing Step," AIAA J., **24**(6), pp. 1040–1043.
[14] Schwarz, W. R., and Bradshaw, P., 1994, "Term-by-Term Tests of Stress-Transport Turbulence Models in a 3-D Boundary-Layer," Phys. Fluids, **6**(2), pp. 986–998.
[15] Hanjalić, K., 1994, "Advanced Turbulence Closure Models: A View of Current Status and Future Prospects," Int. J. Heat Fluid Flow, **15**, pp. 178–203.
[16] Gatski, T. B., 2004, "Constitutive Equations for Turbulent Flows," Theor. Comput. Fluid Dyn., **18**(5), pp. 345–369.
[17] Lumley, J. L., 1978, "Computational Modeling of Turbulent Flows," Adv. Appl. Mech., **18**, pp. 123–176.
[18] Moser, R. D., Kim, J., and Mansour, N. N., 1999, "Direct Numerical Simulation of Turbulent Channel Flow up to Re_τ=590," Phys. Fluids, **11**(4), pp. 943–945.
[19] Schwarz, W. R., and Bradshaw, P., 1993, "Measurements in a Pressure-Driven 3-D Turbulent Boundary-Layer During Development and Decay," AIAA J., **31**(7), pp. 1207–1214.
[20] Demuren, A. O., and Sarkar, S., 1993, "Perspective: Systematic Study of Reynolds Closure Models in the Computations of Plane Channel Flows," ASME J. Fluids Eng., **115**, pp. 5–12.
[21] Laufer, J., 1950, Investigation of Turbulent Flow in a 2-D Channel, NACA Report No. 1053: (supersedes NACA Tech. Note 2123 (1950)).
[22] Mellor, G. L., and Herring, H. J., 1973, "A Survey of the Mean Turbulent Field Closure Models," AIAA J., **11**(5), pp. 590–599.
[23] Speziale, C. G., Sarkar, S., and Gatski, T. B., 1991, "Modelling the Pressure-Strain Correlation of Turbulence: An Invariant Dynamical Systems Approach," J. Fluid Mech., **227**, pp. 245–272.
[24] Fu, S., 1993, "Modelling of the Pressure-Velocity Correlation in Turbulence Diffusion," Comput. Fluids, **22**, pp. 199–205.
[25] Straatman, A. G., 1999, "A Modified Model for Diffusion in Second-Moment Turbulence Closures," ASME J. Fluids Eng., **121**, pp. 747–756.
[26] Ramaprian, B. R., and Chandrasckhara, M. S., 1985, "LDA Measurements in Plane Turbulent Jets," ASME J. Fluids Eng., **107**, pp. 264–271.
[27] Taulbee, D. B., Hussein, H., and Capp, S., 1987, The Round Jet: Experiment and Inferences on Turbulence Modelling, 6th Symposium on Turbulence Shear Flows, Toulouse, Sept.
[28] Kim, J., Kline, S. J., and Johnson, J. P., 1980, "Investigation of a Reattaching Turbulent Shear Layer: Flow Over a Backward-Facing Step," ASME J. Fluids Eng., **102**, pp. 302–308.
[29] Suga, K., 2004, "Modeling the Rapid Part of the Pressure-Diffusion Process in the Reynolds Stress Transport Equation," ASME J. Fluids Eng., **126**, pp. 634–641.
[30] Craft, T. J., and Launder, B., 1996, "A Reynolds-Stress Model Designed for Complex Geometries," Int. J. Heat Fluid Flow, **17**, pp. 245–254.
[31] Yao, Y. F., Thomas, T. G., and Sandham, N. D., 2001, "Direct Numerical Simulation of Turbulent Flow Over a Rectangular Trailing Edge," Theor. Comput. Fluid Dyn., **14**(5–6), pp. 337–358.
[32] Launder, B. E., and Tselepidakis, D. P., 1994, "Application of a New Second-Moment Closure to Turbulent Channel Flow Rotating in Orthogonal Mode," Int. J. Heat Fluid Flow, **15**, pp. 2–10.
[33] So, R. M. C., and Yuan, S. P., 1999, "A Geometry Independent Near-Wall Reynolds-Stress Closure," Int. J. Eng. Sci., **37**, pp. 33–57.
[34] Gerolymos, G. A., and Vallet, I., 2001, "Wall-Normal-Free Near-Wall Reynolds-Stress Closure for 3-D Compressible Separated Flows," AIAA J., **39**(10), pp. 1833–1842.
[35] Chou, P. Y., 1945, "On Velocity Correlations and the Solutions of the Equations of Turbulent Fluctuations," Q. Appl. Math., **3**, pp. 38–54.
[36] Launder, B. E., and Shima, N., 1989, "2-Moment Closure for the Near-Wall Sublayer: Development and Application," AIAA J., **27**(10), pp. 1319–1325.
[37] Rotta, J., 1951, "Statistische Theorie nichthomogener Turbulenz—1. Mitteilung," Z. Phys., **129**, pp. 547–572.
[38] Naot, D., Shavit, A., and Wolfshtein, M., 1970, "Interactions Between Components of the Turbulent Velocity Correlation Tensor Due to Pressure Fluctuations," Isr. J. Technol., **8**(3), pp. 259–269.
[39] Pot, T., Délery, J. M., and Quelin, C., 1991, Interactions Onde-de-choc/Couche-limite dans un Canal Transsonique 3-d. Rap. Tech. 92-7078-AY-116-A, ONERA.
[40] Sauret, E., 2004, "Analyse et Développement de Modèles de Turbulence au Second-Ordre Procheparoi," Doctorat, Université Pierre-et-Marie-Curie, Paris, Sept.
[41] Magnaudet, J., 1993, "Modelling of Inhomogeneous Turbulence in the Absence of Mean Velocity Gradients," Appl. Sci. Res., **51**, pp. 525–531.
[42] Younis, B. A., Gatski, T. B., and Speziale, C. G., 2000, "Towards a Rational Model for the Triple Velocity Correlations of Turbulence," Proc. R. Soc. London, Ser. A, **456**, pp. 909–920.
[43] Gerolymos, G. A., and Vallet, I., 1999, "Effect des Modèles de Diffusion Turbulente et de Redistribution du Tenseur de Reymolds en Ecoulement Transsonique Décollé," In Actes (CD-Rom) du 14, Congrès Français de Mécanique, 30 aug–3 sep 1999, Toulouse, ENSAE (Paper No. 5049).
[44] Klebanoff, P. S., 1955, "Characteristics of Turbulence in a Boundary-Layer With Zero Pressure Gradient," NACA, Report No. 1247.
[45] Reda, D. C., and Murphy, J. D., 1973, "Shock-Wave/Turbulent-Boundary-Layer Interactions in Rectangular Channels," AIAA J., **11**(2), pp. 139–140 (also AIAA Paper No. 72-715, 1972).
[46] Ott, P., Bölcs, A., and Fransson, T. H., 1995, "Experimental and Numerical Study of the Time-Dependent Pressure Response of a Shock-Wave Oscillating in a Nozzle," ASME J. Turbomach., **117**(1), pp. 106–114.
[47] Doukelis, A., Mathioudakis, K., and Papailiou, K. D., 1998, "The Effect of Tip Clearance Gap Size and Wall Rotation on the Performance of a High-Speed Annular Compressor Cascade," ASME Paper No. 98-GT-38.
[48] Gerolymos, G. A., Sauret, E., and Vallet, I., 2004, "Influence of Inflow-Turbulence in Shock-Wave/Turbulent-Boundary-Layer Interaction Computations," AIAA J., **42**(6), pp. 1101–1106.
[49] Chassaing, J. C., Gerolymos, G. A., and Vallet, I., 2003, "Efficient and Robust Reynolds-Stress Model Computation of 3-D Compressible Flows," AIAA J., **41**(5), pp. 763–773.
[50] Gerolymos, G. A., and Vallet, I., 2005, "Mean-Flow-Multigrid for Implicit Reynolds-Stress-Model Computations," AIAA J., **43**(9), pp. 1887–1898.
[51] Gerolymos, G. A., Vallet, I., Bölcs, A., and Ott, P., 1996, "Computation of Unsteady 3-D Transonic Nozzle Flows Using k-ε Turbulence Closure," AIAA J., **34**(7), pp. 1331–1340.
[52] Gerolymos, G. A., Neubauer, J., Sharma, V. C., and Vallet, I., 2002, "Improved Prediction of Turbomachinery Flows Using Near-Wall Reynolds-Stress Model," ASME J. Turbomach., **124**(1), pp. 86–99.
[53] Launder, B. E., and Sharma, B. I., 1974, "Application of the Energy Dissipation Model of Turbulence to the Calculation of Flows Near a Spinning Disk," Lett. Heat Mass Transfer, **1**, pp. 131–138.
[54] Schülein, E., 2006, "Skin-Friction and Heat Flux Measurements in Shock/Boundary-Layer Interaction Flows," AIAA J., **44**(8), pp. 1732–1741.

An Application of a Gradient Theory With Dissipative Boundary Conditions to Fully Developed Turbulent Flows

Gerhard Silber
Institute for Materials Science and Center of Biomedical Engineering (CBME), University of Applied Sciences, Frankfurt am Main, Germany
e-mail: silber@fb2.fh-frankfurt.de

Uwe Janoske
University of Cooperative Education, Mosbach, Germany; and Center of Biomedical Engineering (CBME)

Mansour Alizadeh
University of Science and Technology, Teheran, Iran

Guenther Benderoth
Institute for Material Science and Center of Biomedical Engineering (CBME), University of Applied Sciences, Frankfurt am Main, Germany

The paper presents a complete gradient theory of grade two, including new dissipative boundary conditions based on an axiomatic conception of a nonlocal continuum theory for materials of grade n. The total stress tensor of rank two in the equation of linear momentum contains two higher stress tensors of rank two and three. In the case of isotropic materials, both the tensors of rank two and three are tensor valued functions of the second order strain rate tensor and its first gradient. So the vector valued differential equation of motion is of order four, where the necessary dissipative boundary conditions are generated by using porosity tensors. An application to hydrodynamic turbulence by a linear theory is shown, whereby fully developed steady turbulent channel flows with fixed walls and one moving wall are also examined. The velocity distribution parameters are identified by a numerical optimization algorithm, using experimental data of velocity profiles of channel flow with fixed walls from the literature. These profiles were compared with others given in the literature. With these derived parameters, the predicted velocity gradient of a channel flow agrees well with data from the literature. In addition all simulations were successfully carried out using the finite difference method.
[DOI: 10.1115/1.2720476]

1 Introduction

It is well known that turbulence is the result of dynamic instability of shearing flows and that turbulent flows exhibit internal kinematic structure in the form of eddies. Osborne Reynolds recognized that turbulence is, in essence, a problem of statistical dynamics and proposed a probabilistic averaging technique to obtain the fundamental equations governing the average flow. Conventional statistical theory of hydrodynamic turbulence is based on the Reynolds stress averaging of the classical Navier-Stokes equations. In this paper the phenomenon of fully developed turbulence is not described by the kinematical aspect of instabilities based on the classical Newtonian framework (Navier-Stokes equations). There is, however, a proposal for analyzing this by non-Newtonian fluid effects based on adequate constitutive equations fulfilling the second law of thermodynamics.

Such problems can also be described by continuum theories based on nonclassical continua. In contrast to the classical theory, the kinematical status in any material point is not only characterized by the velocity vector but is considered to have additional kinematical variables like vorticity, microrotation, etc. Various types of Cosserat theories and theories for fluids with microstructures were generated in this way. Theories of microfluids with microrotations and/or microstretching were first introduced by Eringen [1–3] in the sixth decade of the last century and the following decades [4–6].

Maugin [7] gives a very comprehensive review about continuum thermodynamics based on the principle of virtual power with application to the theory of coupled fields in deformable continua and other important areas of physics. A fundamental analysis of gradient theories of the *n*th order is also presented in this paper.

There are quite a few studies applying these theories to turbulent flows and it has been shown in various papers, that the application of micropolar theories for calculating turbulent flows gives an adequate description [4,8–12]. Ariman et al. [13] gave an important and very interesting comprehensive review of possible applications of microcontinuum theories to fluids. On the basis of Eringen's micropolar model Ahmadi [14] presented a study to describe turbulent shear flows employing the regular averaging technique.

Other possible ways of describing turbulent flows are so-called gradient theories dealing with a classical continuum with only one vector for each material point—in the case of fluids the velocity vector—but taking into consideration higher gradients of the velocity field in the constitutive equations. These kinds of theories with applications to elasticity of solids were first introduced by Mindlin [15] in the 1960s and by Eringen [4,5] and Cheverton and Beatty [16] in the 1970s.

In the comprehensive review of Maugin [7] one can also find a separate section which presents a fundamental analysis of the *n*th order gradient theories of continua. Another important paper of Drouot and Maugin [17] deals with higher velocity gradients for describing polymer diffusions and contains a critical study of some corresponding flows. In the second part of this work, a second-order gradient theory is directly introduced to describe a nonhomogeneous flow, where the characterization of the fluid particles (macromolecules) is described by a vectorial internal variable. These theories were also called polar and/or nonlocal field theories or theories of nonsimple materials.

In this paper we choose for the description of a fully developed steady turbulent channel flow, a gradient theory of grade two, as introduced by Trostel in the 1980s [18,19] based on an axiomatic conception using the first law of thermodynamics and the principles of rational mechanics (determinism, objectivity, neighborhood). This basic continuum mechanical concept from Trostel is very similar to the concepts of Mindlin [15], Eringen [4,5], and Maugin [7] but gives concrete ideas for generating the necessary constitutive equations and dissipative boundary conditions with porosity tensors. These tensors take a certain roughness of the

Contributed by the Fluids Engineering Division of ASME for publication in the JOURNAL OF FLUIDS ENGINEERING. Manuscript received August 25, 2005; final manuscript received December 22, 2006. Assoc. Editor: Dennis Siginer.

boundary into consideration. The higher "sensitiveness" of the body, or fluid, having the kinematic phenomenom of turbulence, is considered, using a modification of the principle of local neighborhood. This means that not only the first but also higher velocity-gradients are admitted in the kinematical description. Hence, there are sets of dynamical and kinematical variables in the form of stress tensors and dual strain-rate tensors not only of second but also higher ranks depending on the grade of the model used. It should be remarked that there are certain relations between polar theories and gradient theories in the order of differential equations of motion. For instance, Silber [20] has shown for certain kinematical restrictions that there are correlations and comparable sensitivities between a grade two gradient fluid and a simple Cosserat fluid.

Another motivation, or indication for using gradient theories, to describe turbulent flows, may be the fact that already in the 1950s one can find proposals by Prandtl, v. Kármán, and Schlichting [21], that not only the first, but also the second gradient of the average velocity v of turbulent flows should be considered. So v. Kármán suggests a dependence of the turbulent apparent shear stress on a function of the form $\sqrt{v'^2+\kappa^2 v''^2}$ where $\kappa=$const. [21].

2 Theory

2.1 Field Equations of Linear Gradient Theory for Fluids of Grade Two. For generating gradient theories, the usage of the principles of rational mechanics, especially determinism, objectivity, modified local neighborhood, and the second law of thermodynamics lead to the field equations of linear and angular momentum as well as to the constitutive forms for the set of stress tensors. Generally, for a material of grade n, there are n higher stress tensors from rank two up to rank $n+1$ which depend on the second order strain rate tensor (symmetric part of velocity gradient) and its gradients up to grade $n-1$ [18,19,22,23]. The equation of linear momentum has the same structure as in the case of an ordinary continuum ($n=1$) but within a total stress tensor of rank two containing all higher stress tensors up to rank $n+1$ in the form of a function series. The conservation of angular momentum is reduced to the requirement for the total stress tensor to be symmetric, hence all higher stress tensors are symmetric in the last two right-side indices. For a grade three theory, the constitutive equations for the three viscosity stress tensors of rank-two up to four for isotropic materials are developed by Silber [22] in the form of power series representation. Generally, the tensors are tensor-valued isotropic functions of rank two up to four of tensor valued arguments of rank two up to four [23].

In the case of a grade-two theory ($n=2$) based on the concept of the principles of rational mechanics and the first law of thermodynamics the specific dissipative power is a functional of the first and second gradient of the velocity field [18,19], so the two kinematical tensor valued variables are the strain-rate tensor $\boldsymbol{D}$ and its gradient in the following forms (for tensor notation see Appendix)

$$\boldsymbol{D} := \frac{1}{2}(\boldsymbol{\nabla v} + \boldsymbol{v}\,\boldsymbol{\nabla})$$

and

$$\boldsymbol{\nabla D} := \frac{1}{2}(\boldsymbol{\nabla\nabla v} + \boldsymbol{\nabla v}\,\boldsymbol{\nabla}) \tag{1}$$

where $\boldsymbol{v}$ is the velocity vector and $\boldsymbol{\nabla}$ is the NABLA-operator. The equation of linear momentum and conservation of mass have the classical forms

$$\boldsymbol{\nabla}\cdot\boldsymbol{S}_\Sigma + \rho\boldsymbol{k} = \rho\dot{\boldsymbol{v}}$$

and

$$\dot{\rho} + \rho\,\boldsymbol{\nabla}\cdot\boldsymbol{v} = 0 \tag{2}$$

with the total stress tensor of rank-two $\boldsymbol{S}_\Sigma$, the body force per unit mass $\boldsymbol{k}$ and the density ρ (the dot at the velocity vector means the material time derivative). The total stress tensor in $(2)_1$ reads

$$\boldsymbol{S}_\Sigma := -p\boldsymbol{I} + \overset{(2)}{\boldsymbol{S}}_R - \boldsymbol{\nabla}\cdot\overset{(3)}{\boldsymbol{S}}_R \tag{3}$$

where p is the hydrostatic pressure, $\boldsymbol{I}$ is the unit tensor of rank-two and $\boldsymbol{S}_R^{(i)}$ $(i=2,3)$ are the two stress tensors of rank-two and three. For a linear theory of grade-two the constitutive equations for these two stress tensors adopt the following forms of second and third order tensor functions in the two kinematical tensors $\boldsymbol{D}$ and $\boldsymbol{\nabla D}$ [22,23]

$$\begin{aligned}
\overset{(2)}{\boldsymbol{S}}_R &= \nu_1(\operatorname{tr}\boldsymbol{D})\boldsymbol{I} + \nu_2\boldsymbol{D} \\
\overset{(3)}{\boldsymbol{S}}_R &= \left(\nu_3\,\boldsymbol{\nabla}\operatorname{tr}\boldsymbol{D} + \frac{\nu_4}{2}\boldsymbol{\nabla}\cdot\boldsymbol{D}\right)\boldsymbol{I} + \frac{\nu_4}{4}[\boldsymbol{I}(\boldsymbol{\nabla}\operatorname{tr}\boldsymbol{D}) + \overset{(4)}{\boldsymbol{I}}_2\cdot(\boldsymbol{\nabla}\operatorname{tr}\boldsymbol{D})] \\
&\quad + \frac{\nu_5}{2}[\boldsymbol{I}(\boldsymbol{\nabla}\cdot\boldsymbol{D}) + \overset{(4)}{\boldsymbol{I}}_2\cdot(\boldsymbol{\nabla}\cdot\boldsymbol{D})] + \nu_6\,\nabla\boldsymbol{D} + \frac{\nu_7}{2}(\boldsymbol{D}\,\boldsymbol{\nabla})\cdot\cdot(\overset{(4)}{\boldsymbol{I}}_1 + \overset{(4)}{\boldsymbol{I}}_2)
\end{aligned} \tag{4}$$

In (4) ν_i $(i=1,2,\ldots,7)$ are material coefficients, $\boldsymbol{I}_1^{(4)}$ and $\boldsymbol{I}_2^{(4)}$ are isotropic tensors of rank-four (see Appendix), tr$(\bullet)$ means the trace-operator, $\boldsymbol{\nabla}(\bullet)\equiv\operatorname{grad}(\bullet)$ and $\boldsymbol{\nabla}\cdot(\bullet)\equiv\operatorname{div}(\bullet)$ are the gradient and divergence operators and "$\cdot\cdot$" means the double-scalar product (see Appendix).The relations (4) are based on the theory of isotropic tensor functions, so there are no terms of the gradient of $\boldsymbol{D}$ within the stress tensor of rank two and vice versa of the strain rate tensor $\boldsymbol{D}$ itself within the stress tensor of rank three possible (isotropic tensor-valued tensor functions are built up of isotropic tensors only, see Appendix). Inserting (4) into (3) one gets with regard to (1) the following representation of the total stress tensor as a second-order tensor function of the first and third gradients of the velocity field;

$$\begin{aligned}
\boldsymbol{S}_\Sigma &= [-p(\rho) + \kappa_1^0\,\boldsymbol{\nabla}\cdot\boldsymbol{v} + \kappa_2^0\Delta(\boldsymbol{\nabla}\cdot\boldsymbol{v})]\boldsymbol{I} + \kappa_3^0\,\boldsymbol{\nabla}\boldsymbol{\nabla}(\boldsymbol{\nabla}\cdot\boldsymbol{v}) \\
&\quad + \kappa_1(\boldsymbol{\nabla v} + \boldsymbol{v}\,\boldsymbol{\nabla}) - \kappa_2\Delta(\boldsymbol{\nabla v} + \boldsymbol{v}\,\boldsymbol{\nabla})
\end{aligned} \tag{5}$$

where Δ is the Laplacian-operator and κ_i^0 and κ_j are material coefficients which are defined by

$$\begin{aligned}
&\kappa_1^0 := \nu_1 \quad \kappa_2^0 := -\frac{1}{2}(2\nu_3 + \nu_4) \quad \kappa_3^0 := -\frac{1}{2}(\nu_4 + \nu_5 + \nu_7) \\
&\kappa_1 := \frac{\nu_2}{2} \quad \kappa_2 := \frac{1}{4}(\nu_5 + 2\nu_6 + \nu_7)
\end{aligned} \tag{6}$$

From (5) the Newtonian fluid results for $\kappa_2^0=\kappa_3^0=\kappa_2\equiv 0$. Inserting (5) into the balance of linear momentum (2) one gets with regard to a conservative field of external body force $\rho\boldsymbol{k}=-\boldsymbol{\nabla}U$ the following vector valued differential equation of the fourth order for the velocity field:

$$\mu_1^0\,\boldsymbol{\nabla}(\boldsymbol{\nabla}\cdot\boldsymbol{v}) + \mu_2^0\Delta[\boldsymbol{\nabla}(\boldsymbol{\nabla}\cdot\boldsymbol{v})] + \kappa_1\Delta\boldsymbol{v} - \kappa_2\Delta\Delta\boldsymbol{v} - \boldsymbol{\nabla}(p+U) = \rho\dot{\boldsymbol{v}} \tag{7}$$

with newly defined material coefficients

$$\mu_1^0 := \kappa_1^0 + \kappa_1 \quad \mu_2^0 := \kappa_2^0 + \kappa_3^0 - \kappa_2 \tag{8}$$

The specific dissipative power reads

$$\begin{aligned}
\rho\dot{D} &= \nu_1\operatorname{tr}^2\boldsymbol{D} + \nu_2\operatorname{tr}\boldsymbol{D}^2 + \nu_3(\boldsymbol{\nabla}\operatorname{tr}\boldsymbol{D})\cdot(\boldsymbol{\nabla}\operatorname{tr}\boldsymbol{D}) \\
&\quad + \nu_4(\boldsymbol{\nabla}\cdot\boldsymbol{D})\cdot(\boldsymbol{\nabla}\operatorname{tr}\boldsymbol{D}) + \nu_5(\boldsymbol{\nabla}\cdot\boldsymbol{D})\cdot(\boldsymbol{\nabla}\cdot\boldsymbol{D}) \\
&\quad + \nu_6(\boldsymbol{\nabla D})\cdots(\boldsymbol{D}\,\boldsymbol{\nabla}) + \nu_7(\boldsymbol{D}\,\boldsymbol{\nabla})\cdots(\boldsymbol{D}\,\boldsymbol{\nabla}) \geqslant 0
\end{aligned} \tag{9}$$

or in terms of the velocity gradient

$$\rho\dot{D} = \nu_1(\nabla\cdot\boldsymbol{v})^2 + \frac{\nu_2}{2}(\nabla\boldsymbol{v})\cdot\cdot(\nabla\boldsymbol{v}+\boldsymbol{v}\,\overleftarrow{\nabla}) + \frac{1}{4}(4\nu_3+2\nu_4+\nu_5)$$
$$\times(\nabla\nabla\cdot\boldsymbol{v})\cdot(\nabla\nabla\cdot\boldsymbol{v}) + \frac{1}{2}(\nu_4+\nu_5)(\Delta\boldsymbol{v})\cdot(\nabla\nabla\cdot\boldsymbol{v})$$
$$+\frac{\nu_5}{4}(\Delta\boldsymbol{v})\cdot(\Delta\boldsymbol{v}) + \frac{1}{4}(2\nu_6+\nu_7)(\nabla\nabla\boldsymbol{v})\cdots(\boldsymbol{v}\,\overleftarrow{\nabla}\,\overleftarrow{\nabla}) \geqslant 0 \tag{10}$$

For incompressible fluids in the previous equations $\mathrm{tr}\,\boldsymbol{D}=\nabla\cdot\boldsymbol{v}=0$ has to be considered.

2.2 Dissipative Boundary Conditions for Gradient Fluids of Grade Two. One can generally get the necessary boundary conditions for the solutions of the field equation (7) from the mechanical power $P_{\Sigma O}$ at the surface $O(V)$ of the continuum which reads for a theory of grade-two [18,19,22]

$$P_{\Sigma O} = \int_{O(V)} \left(\boldsymbol{\sigma}_0\cdot\boldsymbol{v} + \boldsymbol{\sigma}_1\cdot\frac{\partial\boldsymbol{v}}{\partial s_n}\right)dO \tag{11}$$

where the two stress vectors $\boldsymbol{\sigma}_0$ and $\boldsymbol{\sigma}_1$ at the surface of the body are defined by

$$\boldsymbol{\sigma}_0 := \boldsymbol{n}\cdot\boldsymbol{S}_\Sigma - (\nabla_2 + 2H\boldsymbol{n}^*)\cdot(\boldsymbol{n}\cdot\overset{(3)}{\boldsymbol{S}}_R), \quad \boldsymbol{\sigma}_1 := \boldsymbol{n}\boldsymbol{n}\cdot\cdot\overset{(3)}{\boldsymbol{S}}_R \tag{12}$$

with the planar part ∇_2 of the NABLA operator $\nabla=\nabla_2+\boldsymbol{n}\partial/\partial s_n$, the unit normal vector at the surface area $\boldsymbol{n}$, and the middle bend of the surface area H (for local-convex area $\boldsymbol{n}^*=-n$ and for local-concave area $\boldsymbol{n}^*=\boldsymbol{n}$). Two classes of boundary conditions are possible: in the case of ideal boundary conditions (so-called isoenergetic conditions), the power of surface vanishes ($P_{\Sigma\cdot}\equiv 0$). For real, respectively dissipative boundary conditions with $P_{\Sigma\cdot}\neq 0$ Trostel [19] developed a conception using so-called porosity tensors and Alizadeh [24] gave a particular formulation for dissipative boundary conditions for fluids of grade three.

2.2.1 Flow With Velocity-Slip. In the case of a gradient theory of grade two considering a velocity-slip at the boundary with

$$\boldsymbol{v}_W - \boldsymbol{v}_F \neq 0 \quad \text{respectively } \boldsymbol{v}_W \neq \boldsymbol{v}_F \tag{13}$$

we get from [24] the following two dynamical boundary conditions:

$$\boldsymbol{\sigma}_0\cdot\boldsymbol{I}_2 := \left[\lambda_{vv}(\boldsymbol{v}_W-\boldsymbol{v}_F) + \lambda_{vv'}\frac{\partial(\boldsymbol{v}_W-\boldsymbol{v}_F)}{\partial s_n}\right]\cdot\boldsymbol{I}_2$$
$$\boldsymbol{\sigma}_1\cdot\boldsymbol{I}_2 := \left[\lambda_{vv'}(\boldsymbol{v}_W-\boldsymbol{v}_F) + \lambda_{v'v'}\frac{\partial(\boldsymbol{v}_W-\boldsymbol{v}_F)}{\partial s_n}\right]\cdot\boldsymbol{I}_2 \tag{14}$$

where the indices F and W denote fluid and wall, λ_{vv} to $\lambda_{v'v'}$ are so-called porosity coefficients, and $\boldsymbol{I}_2=\boldsymbol{I}-\boldsymbol{n}\boldsymbol{n}$ is the planar unit tensor of rank-two. Satisfying the non-negative specific dissipation energy of a thin layer at the boundary consisting of fluid and wall simultaneously leads to the following restrictions from [24]:

$$\lambda_{vv}\geqslant 0 \quad \lambda_{v'v'}\geqslant 0 \quad \lambda_{vv}\lambda_{v'v'}\geqslant\lambda_{vv'}^2 \tag{15}$$

Together with (12)–(14) one gets the complete dynamical boundary conditions

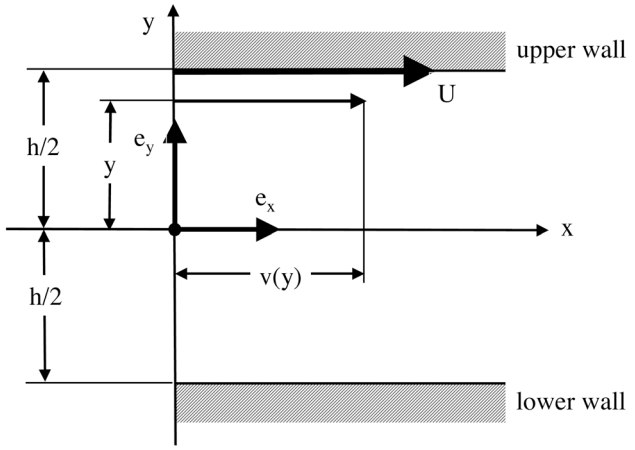

Fig. 1 One-dimensional channel flow with moving upper wall

$$[\boldsymbol{n}\cdot\boldsymbol{S}_\Sigma - (\nabla_2+2H\boldsymbol{n}^*)\cdot(\boldsymbol{n}\cdot\overset{(3)}{\boldsymbol{S}}_R)]\cdot\boldsymbol{I}_2$$
$$\overset{!}{=}\left[\lambda_{vv}(\boldsymbol{v}_W-\boldsymbol{v}_F) + \lambda_{vv'}\frac{\partial(\boldsymbol{v}_W-\boldsymbol{v}_F)}{\partial s_n}\right]\cdot\boldsymbol{I}_2$$
$$(\boldsymbol{n}\boldsymbol{n}\cdot\cdot\overset{(3)}{\boldsymbol{S}}_R)\cdot\boldsymbol{I}_2 \overset{!}{=}\left[\lambda_{vv'}(\boldsymbol{v}_W-\boldsymbol{v}_F) + \lambda_{v'v'}\frac{\partial(\boldsymbol{v}_W-\boldsymbol{v}_F)}{\partial s_n}\right]\cdot\boldsymbol{I}_2 \tag{16}$$

where on the left-hand sides of (16) $\boldsymbol{S}_\Sigma$ has to be taken by (5) and $\boldsymbol{S}_R^{(3)}$ by $(4)_1$ with regard to (1), so that the expressions (16) are complete functions of the velocity vectors $\boldsymbol{v}_W$ and $\boldsymbol{v}_F$ at the boundary only.

2.2.2 Flow Without Velocity-Slip. If there is no velocity-slip at the boundary, the kinematical and dynamical boundary conditions are [24]

$$\boldsymbol{v}_W-\boldsymbol{v}_F=\boldsymbol{0}, \quad \text{respectively } \boldsymbol{v}_W=\boldsymbol{v}_F$$
$$(\boldsymbol{n}\boldsymbol{n}\cdot\cdot\overset{(3)}{\boldsymbol{S}}_R)\cdot\boldsymbol{I}_2 \overset{!}{=} -\left(\lambda_{v'v'}\frac{\partial\boldsymbol{v}_F}{\partial s_n}\right)\cdot\boldsymbol{I}_2 \tag{17}$$

.

2.3 One-Dimensional Steady Channel Flow of Incompressible Gradient Fluids of Grade Two. Let x be the coordinate for the flow direction and y the cross-sectional coordinate of the gap of the channel, then for a one-dimensional steady pressure driven channel flow between parallel plates the velocity field has the form of

$$\boldsymbol{v}(\boldsymbol{x},t) = v(y)\boldsymbol{e}_x \tag{18}$$

where v is the only nonzero velocity coordinate in the axis direction $\boldsymbol{e}_x$ (see Fig. 1).

With regard to (18) one gets from (5) respectively (7) the constitutive equation for the (total) shear stress τ_{xy} respectively the equation of motion of a fluid of grade two in the forms of

$$\tau_{xy} = \kappa_1\frac{dv}{dy} - \kappa_2\frac{d^3v}{dy^3} \equiv \frac{d}{dy}\left(\kappa_1 v - \kappa_2\frac{d^2v}{dy^2}\right) \tag{19}$$

and

$$\kappa_1\frac{d^2v}{dy^2} - \kappa_2\frac{d^4v}{dy^4} \equiv \frac{d^2}{dy^2}\left(\kappa_1 v - \kappa_2\frac{d^2v}{dy^2}\right) = A$$

$$A := \frac{d}{dx}(p+U) = \text{const} < 0 \tag{20}$$

Satisfying the non-negative specific dissipation energy (9) respectively (10) the two material coefficients κ_1 and κ_2 with regard to (6) have to fulfill the following restrictions

$$\kappa_1 \geqslant 0 \quad \text{and } \kappa_2 \geqslant 0 \tag{21}$$

The general solution of (20) adopts the form

$$v(y) = C_1 \sinh \lambda y + C_2 \cosh \lambda y + C_3 y + C_4 + \frac{A}{2\kappa_1} y^2 \quad \lambda^2 := \frac{\kappa_1}{\kappa_2} \tag{22}$$

where λ is a newly defined material coefficient.

2.3.1 Channel Flow Without Velocity-Slip. In the case of a channel flow with fixed walls, the symmetry condition $v(y)-v(-y)=0$ has to be fulfilled, so that with regard to (22) $C_1=C_3=0$. From (17) we get the following kinematical and dynamical boundary conditions:

$$\nu = 0$$

and

$$\frac{\lambda_{\nu'\nu'}}{\kappa_1}\frac{d\nu}{dy} + \frac{1}{\lambda^2}\frac{d^2\nu}{dy^2} = 0 \quad \text{at } y = \frac{h}{2} \tag{23}$$

Together with (22) and (23) the closed form of the velocity field then reads

$$v(\eta) = -B\left[1 - \eta^2 - 2\frac{\Pi}{\Lambda^2}\left(1 - \frac{\cosh \Lambda\eta}{\cosh \Lambda}\right)\right] \quad \Pi := \frac{1+\alpha_3\Lambda^2}{1+\alpha_3\Lambda\tanh\Lambda} \tag{24}$$

with the following definitions for B, the nondimensional parameters Λ and α_3 and the nondimensional cross-section coordinate η

$$B := \frac{A}{2\kappa_1}\left(\frac{h}{2}\right)^2 < 0 \quad \Lambda := \lambda\frac{h}{2} \quad \alpha_3 := \frac{\lambda_{v'v'}}{\kappa_1 h/2} \quad \eta := \frac{y}{h/2} \tag{25}$$

The restrictions for these parameters derived from (15) and (21) with regard to $(22)_2$ read

$$\Lambda < 0 \quad \text{or } \Lambda > 0 \quad \text{and } \alpha_3 > 0 \tag{26}$$

2.3.2 Channel Flow With Velocity-Slip. With regard to the symmetry condition $v(y)-v(-y)=0$ the two dynamical boundary conditions derived from (16) read

$$\frac{\lambda_{vv}}{\kappa_1}v + \left(1 + \frac{\lambda_{vv'}}{\kappa_1}\right)\frac{dv}{dy} - \frac{1}{\lambda^2}\frac{d^3v}{dy^3} = 0 \quad \text{at } y = \frac{h}{2}$$
$$\frac{\lambda_{vv'}}{\kappa_1}v + \frac{\lambda_{v'v'}}{\kappa_1}\frac{dv}{dy} + \frac{1}{\lambda^2}\frac{d^2v}{dy^2} = 0 \quad \text{at } y = \frac{h}{2} \tag{27}$$

With regard to (22) and (27) the following closed form of velocity field can be generated

$$v(\eta) = B\left[\eta^2 + \frac{2}{M}\left(F + \Omega\frac{\cosh\Lambda\eta}{\cosh\Lambda}\right)\right] \tag{28}$$

where

$$M := \alpha_1 - \xi\Lambda\tanh\Lambda \quad \xi := \alpha_2^2 - \alpha_1\alpha_3$$

$$F := \left(\frac{\xi}{2} - \alpha_3 + \frac{\alpha_2}{\Lambda^2}\right)\Lambda\tanh\Lambda - \xi - \frac{\alpha_1}{2}\left(1 - \frac{2}{\Lambda^2}\right) - (1+2\alpha_2)$$

$$\Omega := \xi + \alpha_2 - \frac{\alpha_1}{\Lambda^2} \quad \alpha_1 := \frac{\lambda_{vv}}{\kappa_1}\frac{h}{2} \quad \alpha_2 := \frac{\lambda_{vv'}}{\kappa_1} \tag{29}$$

and B, Λ, η, and α_3 are defined in (25) and the following restrictions derived from (15) and (21) have to be fulfilled

$$\Lambda < 0 \quad \text{or } \Lambda > 0 \quad \text{and } \alpha_1 > 0 \ \alpha_3 > 0 \ \alpha_2^2 - \alpha_1\alpha_3 < 0 \tag{30}$$

2.3.3 Channel Flow With Moving the Upper Wall Without Velocity-Slip. In the following case the upper wall ($\mathbf{0}=h/2$) of the channel is moving with constant velocity U and the lower wall ($y=-h/2$) is fixed (see Fig. 1). With regard to (17) the four kinematical and dynamical boundary conditions read

$$v = 0 \quad \text{and } -\frac{\lambda_{v'v'}}{\kappa_1}\frac{dv}{dy} + \frac{1}{\lambda^2}\frac{d^2v}{dy^2} = 0 \quad \text{at } y = -\frac{h}{2}$$
$$v = U \quad \text{and } +\frac{\lambda_{v'v'}}{\kappa_1}\frac{dv}{dy} + \frac{1}{\lambda^2}\frac{d^2v}{dy^2} = 0 \quad \text{at } y = +\frac{h}{2} \tag{31}$$

With regard to (31) one gets from (22) the following closed form of the velocity field;

$$v(\eta) = -B\left[1 - \eta^2 - 2\frac{\Pi}{\Lambda^2}\left(1 - \frac{\cosh\Lambda\eta}{\cosh\Lambda}\right)\right] + \frac{U}{2}\left[1 + \eta + \Xi\left(\eta - \frac{\sinh\Lambda\eta}{\sinh\Lambda}\right)\right] \tag{32}$$

with

$$\Xi := \frac{\alpha_3}{1 - \alpha_3(1 - \Lambda\coth\Lambda)} \tag{33}$$

where B, η, α_3, and Λ are defined by (25) and the restrictions (26) have to be fulfilled. For $U\equiv 0$ the solution (32) leads to the special case of channel flow with fixed plates (24).

2.3.4 Channel Flow With Moving the Upper Wall and Velocity-Slip. With regard to (16) the four dynamical boundary conditions read:

$$\frac{\lambda_{vv}}{\kappa_1}v - \left(1 + \frac{\lambda_{vv'}}{\kappa_1}\right)\frac{dv}{dy} + \frac{1}{\lambda^2}\frac{d^3v}{dy^3} = 0 \quad \text{at } y = -\frac{h}{2}$$
$$\frac{\lambda_{vv'}}{\kappa_1}v - \frac{\lambda_{v'v'}}{\kappa_1}\frac{dv}{dy} + \frac{1}{\lambda^2}\frac{d^2v}{dy^2} = 0 \quad \text{at } y = -\frac{h}{2} \tag{34}$$

and

$$\frac{\lambda_{vv}}{\kappa_1}(v-U) + \left(1 + \frac{\lambda_{vv'}}{\kappa_1}\right)\frac{dv}{dy} - \frac{1}{\lambda^2}\frac{d^3v}{dy^3} = 0 \quad \text{at } y = +\frac{h}{2}$$
$$\frac{\lambda_{vv'}}{\kappa_1}(v-U) + \frac{\lambda_{v'v'}}{\kappa_1}\frac{dv}{dy} + \frac{1}{\lambda^2}\frac{d^2v}{dy^2} = 0 \quad \text{at } y = +\frac{h}{2} \tag{35}$$

With regard to (34) and (35) one gets from (22) for the closed form of the velocity field

$$v(\eta) = B\left[\eta^2 + \frac{2}{M}\left(F + \Omega\frac{\cosh\Lambda\eta}{\cosh\Lambda}\right)\right] + \frac{U}{2}\left\{1 + \frac{1}{N}\left[Q\eta + (\xi+\alpha_2)\frac{\sinh\Lambda\eta}{\sinh\Lambda}\right]\right\} \tag{36}$$

with

$$N := 1 + \xi + \alpha_1 + 2\alpha_2 - (\xi - \alpha_3)\Lambda\coth\Lambda, \quad Q := (\alpha_1 - \xi\Lambda)\coth\Lambda \tag{37}$$

where F, B, α_1, α_2, α_3, ξ, η, Λ, Ω, and M are defined by (25) respectively by (29) fulfilling the restrictions (26). For $U\equiv 0$ the

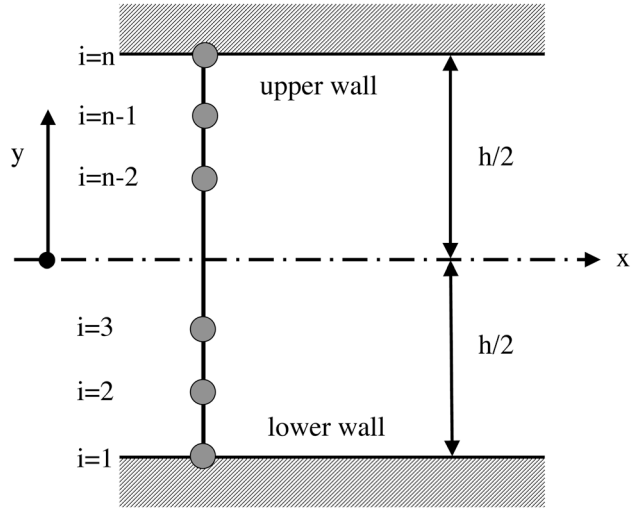

Fig. 2 Discretization of the gap (channel flow)

solution (36) leads to the special case of channel flow with fixed plates (28).

3 Finite Difference Method

Besides the analytical solution, the differential equations were solved using a finite-difference method. The discretization of the gap with n grid points is shown in Fig. 2. The distance between the grid points is Δy. The discretization of the differential Eq. (20) then reads

$$a_1 v_{i+2} + a_2 v_{i+1} + a_3 v_i + a_4 v_{i-1} + a_5 v_{i-2} = A \tag{38}$$

with the coefficients

$$a_1 = a_5 = -\frac{\kappa_2}{\Delta y^4} \quad a_2 = a_4 = \frac{\kappa_1}{\Delta y^2} + \frac{4\kappa_2}{\Delta y^4} \quad a_3 = -\frac{2\kappa_1}{\Delta y^2} - \frac{6\kappa_2}{\Delta y^4} \tag{39}$$

Expression (38) leads to a system of linear equations for the unknown velocities v_i. The gradients at the walls are obtained by fitting the function to an interpolated curve and then differentiating this curve. The gradients for $y=-h/2$ can be expressed by the values of v_i, whereby the equations for $y=+h/2$ take analogous forms,

$$\left[\frac{\partial v}{\partial y}\right]_{y=-h/2} = -\frac{1}{4}\frac{v_5}{\Delta y} + \frac{4}{3}\frac{v_4}{\Delta y} - 3\frac{v_3}{\Delta y} + 4\frac{v_2}{\Delta y} - \frac{25}{12}\frac{v_1}{\Delta y}$$

$$\left[\frac{\partial^2 v}{\partial y^2}\right]_{y=-h/2} = \frac{11}{12}\frac{v_5}{\Delta y^2} - \frac{14}{3}\frac{v_4}{\Delta y^2} + \frac{19}{2}\frac{v_3}{\Delta y^2} - \frac{26}{3}\frac{v_2}{\Delta y^2} + \frac{35}{12}\frac{v_1}{\Delta y^2}$$

$$\left[\frac{\partial^3 v}{\partial y^3}\right]_{y=-h/2} = -\frac{3}{2}\frac{v_5}{\Delta y^3} + 7\frac{v_4}{\Delta y^3} - 12\frac{v_3}{\Delta y^3} + 9\frac{v_2}{\Delta y^3} - \frac{30}{12}\frac{v_1}{\Delta y^3} \tag{40}$$

Introducing these gradients into the boundary condition (34) and (35), the values v_1 and v_2 can be expressed by v_3, v_4, and v_5. Solving the equations with the finite difference method is used as the basis for further simulations taking two-dimensional domains into account.

4 Application to Fully Developed Turbulent Flows

In the following application to fully developed steady turbulent channel flows, the velocity field $\boldsymbol{v}$ in all above equations has to be understood as a mean velocity field $\bar{\boldsymbol{v}}$ in the form of a quantity average at a location $\boldsymbol{x}$ over a certain period of time Δt, which is large enough so that $\bar{\boldsymbol{v}}$ is time independent,

$$\bar{\boldsymbol{v}}(\boldsymbol{x}) := \frac{1}{\Delta t}\int_{t=t_0}^{t_0+\Delta t} \boldsymbol{v}(\boldsymbol{x},t)dt \tag{41}$$

To simplify the notation in the rest of this article the symbol $\boldsymbol{v}(\boldsymbol{x})$ will be used for the mean velocity $\bar{\boldsymbol{v}}(\boldsymbol{x})$.

4.1 Optimization Routine. In the subsequent analysis, a numerical identification of the material parameters was carried out by using the model for a channel flow with fixed walls. With these calculated parameters a prediction for a measured velocity gradient and a simulation of channel flows with an upper moving plate was calculated.

For describing the experimental data of channel flow, the parameters within the velocity distributions (24) and (28) have to be determined such that these functions predict the experimental data in a satisfactory way. This is obtained by using a quality function χ^2 of the following form

$$\chi^2 := \frac{1}{n}\sqrt{\sum_{i=1}^{n}[v(y_i;\Lambda,\alpha_1,\alpha_2,\alpha_3) - v(y_i)]^2} \stackrel{!}{=} \min \tag{42}$$

where $v(y;\Lambda,\alpha_1,\alpha_2,\alpha_3)$ is the velocity distribution with the model parameters Λ, α_1, α_2, and α_3, $v(y_i)$ is the measured velocity value at the position y_i and n is the number of data points. Because all parameters within the velocity distributions appear in a nonlinear way, a nonlinear optimization routine has to be used for minimizing the quality function (42). The goal of the numerical optimization process is to find the global minimum of this function. Apart from linear optimization for a nonlinear procedure, one can only be sure in certain special cases as for convex quality functions that such a routine will find the global minimum. To ensure at least a certain probability for finding a global minimum, a stochastic routine was employed. This routine is known as "Simulated Annealing" algorithm [25].

4.2 Parameter Identification Based on Channel Flow Data. Using the experimental data of [26] the following nondimensional form of the velocity profile is given by

$$V(\eta) := \frac{v(\eta)}{v(0)} \quad \text{with} \quad V(0) = 1 \tag{43}$$

4.2.1 Parameter Identification Without Velocity Slip. With (24) and (43) one gets

$$V(\eta) = \frac{1 - \eta^2 - 2\dfrac{\Pi}{\Lambda^2}\left(1 - \dfrac{\cosh \Lambda\eta}{\cosh \Lambda}\right)}{1 + 2\dfrac{\Pi}{\Lambda^2}\dfrac{1-\cosh\Lambda}{\cosh\Lambda}} \quad \Pi := \frac{1+\alpha_3\Lambda^2}{1+\alpha_3\Lambda\tanh\Lambda} \tag{44}$$

For experimental data from [26], by using the previously described optimization algorithm, disregarding the restriction $(26)_2$, the following values for the two parameters α_3 and Λ in expression (44) can be determined ($\chi^2 = 0.26496 \times 10^{-3}$),

$$\alpha_3 = -2.4424634 \times 10^{-2} < 0 \quad \Lambda = 40.265075 \tag{45}$$

Using the parameter restriction $(26)_2$ one gets for the optimal quality function ($\chi^2 = 0.1335144$):

$$\alpha_3 = 2.185455 > 0 \quad \Lambda = -565.97459 \tag{46}$$

A satisfactory reproduction of the experimental data can only be obtained by the parameter set given in (45). Unfortunately this set does not fulfill the restriction (26), because the value of the parameter α_3 is negative thus violating the dissipation postulate (10).

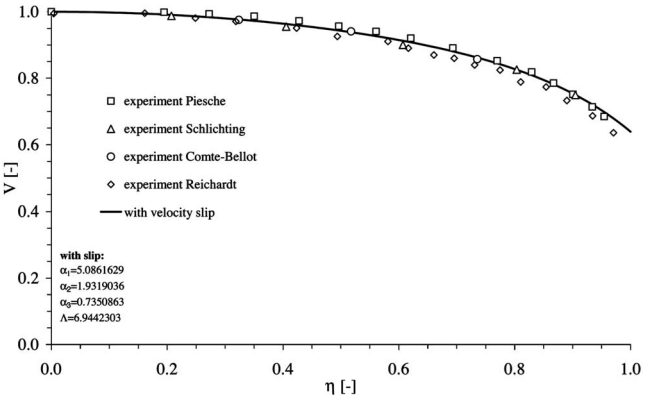

Fig. 3 Comparison of experimental data (dots) and theoretical predicted velocity profile (solid line) of a steady channel flow with velocity slip

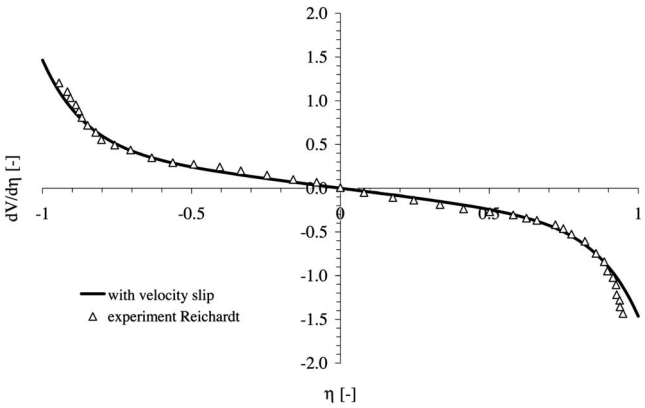

Fig. 4 Comparison of experimental data by Reichardt [32] (dots) and theoretical predicted velocity gradient (solid line) of steady channel flow with velocity slip

Otherwise, if the postulate (10) is fulfilled, the optimal parameter set (46) does not meet the experiment efficiently. So both solutions are inadmissible. This seems to prove that boundary conditions without velocity-slip in the context of the above model do not adequately describe the experimental data.

4.2.2 Parameter Identification With Velocity Slip. With (28) and (43) the velocity profile in dimensionless form is obtained by

$$V(\eta) = \frac{F + \frac{M\eta^2}{2} + \Omega\frac{\cosh\Lambda\eta}{\cosh\Lambda}}{F + \frac{\Omega}{\cosh\Lambda}} \tag{47}$$

On the basis of the experimental data of [26] the parameters α_i $(i=1,2,3)$ and Λ in expression (47) with a χ^2 of 0.10289×10^{-3} were derived, by using the optimization algorithm. Expression (48) shows the resulting numerical values

$$\alpha_1 = 5.0861629 \quad \alpha_2 = 1.9319036 \quad \alpha_3 = 0.73508637$$

$$\Lambda = 6.944230 \tag{48}$$

In contrast to (45), these parameters fulfill the restrictions (30) and are thus admissible in the sense of the dissipation postulate (10). Figure 3 shows a comparison of the calculated velocity profile with the above given parameters and the experimental data of Piesche and the data of Schlichting [27], Comte-Bellot [28,29], and Reichardt [30]. The velocity-slip at the boundary of about 60% is comparable with earlier calculations given by Trostel [18,19], Silber [22], Alexandru [31]. But these calculations were based on "field-boundary conditions," since the dissipative boundary conditions of this analysis were not available at that time. On the basis of those "field-boundary conditions," the possibility of decreasing velocity-slip with higher gradient models can be obtained. Indeed, the velocity-slip of a gradient grade three theory was lower than one of a grade two [22]. There may exist a kind of "convergence," whereby a certain gradient model can give an accurate slip at the boundary. Therefore further investigations with higher gradient models are desirable.

Because the parameters (45) are inadmissible in the sense of the dissipation postulate (10) and the parameters (46) do not describe the problem in an adequate way (no slip condition), these parameter sets will not be considered in the following analysis.

4.3 Prediction of Velocity Gradient Measurements of Steady Channel Flow. Differentiating the velocity field (47) in the case of channel flow with velocity-slip regarding the nondimensional cross section coordinate η the following nondimensional form of velocity gradient is obtained

$$\frac{dV(\eta)}{d\eta} = \frac{M\eta + \Lambda\Omega\frac{\sinh\Lambda\eta}{\cosh\Lambda}}{F + \frac{\Omega}{\cosh\Lambda}} \tag{49}$$

In Fig. 4 a comparison of experimental data and the prediction of velocity gradient (49) using the parameter set (48) is shown. The course of the model shows clearly that the prediction by the slip-theory is suitable. This indicates the necessity of using velocity-slip-condition, at least in the case of the presented theory. Moreover curvatures given in Fig. 4 generated by the finite difference method (see Sec. 3) are congruent with those derived from theory.

4.4 Simulation of Steady Channel Flows With One Moving Wall. In Fig. 5 different scenarios of channel flows with moving upper wall on the basis of the optimized model parameters (48) are shown. For the nondimensional representations V of the velocity profiles with slip conditions by obeying (36) for $B>0$ one gets

$$V := \frac{v(\eta)}{v(0)} = \frac{a(\eta) + \frac{2F}{M} + \Theta\left[1 + \frac{P(\eta)}{N}\right]}{a(0) + \frac{2F}{M} + \Theta} \qquad \Theta := \frac{U}{2B} \tag{50}$$

with

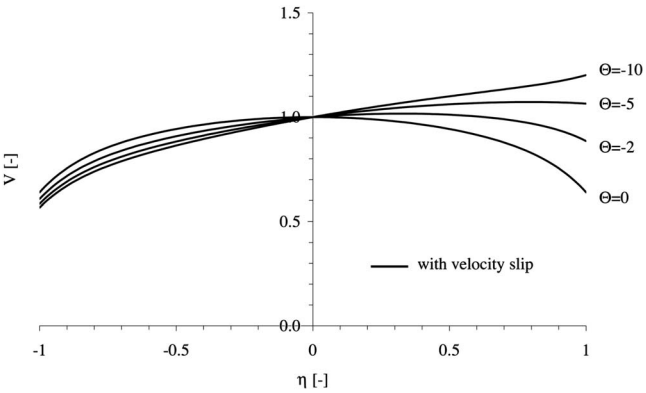

Fig. 5 Velocity distributions of steady channel flow with moving upper wall for varying Θ

$$a(\eta) := \eta^2 + \frac{\Omega}{M}\frac{\cosh \Lambda \eta}{\cosh \Lambda} \quad P(\eta) := Q\eta + (\xi + \alpha_2)\frac{\sinh \Lambda \eta}{\sinh \Lambda} \tag{51}$$

To generate different scenarios, the parameter $\Theta := U/2B$ is varied and the predicted velocity distributions with slip condition should create an idea of the flow behavior.

4.5 Mean Shear Stress of Channel Flow With Fixed Walls and Friction Reynolds Number. Finally, a comparison of the shear stresses and Reynolds number will be discussed. With regard to (19) and (43) one gets the following nondimensional representation for the mean shear stress as a function of the nondimensional velocity gradients

$$\hat{\tau}(\eta) := \frac{h/2}{\kappa_1 v(0)}\tau_{xy} = \frac{dV(\eta)}{d\eta} - \frac{1}{\Lambda^2}\frac{d^3V(\eta)}{d\eta^3} \tag{52}$$

Inserting (49) into (52) leads to the following linear expression of the nondimensional coordinate η

$$\hat{\tau}(\eta) = \frac{M\eta}{F + \dfrac{\Omega}{\cosh \Lambda}} \tag{53}$$

From (52) and (53) one gets with regard to (29) and the optimized parameters (48) the value for dimensionless wall shear stress in the case of channel flow of a grade two fluid with velocity slip condition in the following form:

$$\hat{\tau}_W = \hat{\tau}(\eta = -1) = \frac{h/2}{\kappa_1 \nu(0)}\tau_{xy}(y = -h/2) = -\frac{M}{F + \dfrac{\Omega}{\cosh \Lambda}} = 0.423 \tag{54}$$

Unfortunately, we could not find any data of wall shear stresses in the literature. Only Reichardt gives some formulas for its calculation. In Reichardt [30] one can find the relations $u^* = \tau_0/\rho$ and

$$\frac{v_{\max}}{u^*} = 2.5 \ln\left[\frac{\dfrac{h v_{\max}}{\nu}}{\left(\dfrac{v_{\max}}{u^*}\right)^{-1}}\right]$$

where ρ is the density of the fluid, τ_0 is the wall shear stress, $v_{\max}$ is the velocity in the channel axis, and ν is the kinematic viscosity. With the relevant values ($h = 24.6$ cm, $v_{\max} = 365.5$ cm/s, $\rho = 10^{-3}$ kg/cm^3 for water) one gets $u^* = 15,2$ cm/s and $\tau_0 = 2.3104 \times 10^{-3}$ N/cm^2. With these values, taking the dynamic viscosity of water as $\mu = 1.1 \times 10^{-5}$ kg/cm^{-1} s^{-1} one can calculate the nondimensional wall shear stress $\hat{\tau}_W := (h/2/\mu v_{\max})\tau_0 = 7.1$. The comparison of these values with those calculated by the gradient theory shows that the wall shear stress formulas calculated by Reichardt are one order of magnitude higher. Lacking further information these results are only mentioned but not discussed further.

For a final discussion including the Reynolds number, the friction Reynolds number Re_τ and the friction velocity u_τ can be defined in the common way,

$$\mathrm{Re}_\tau := \frac{\rho u_\tau h/2}{\mu}$$

and

$$u_\tau := \sqrt{\frac{\tau_W}{\rho}} \tag{55}$$

With regard to (54) the wall shear stress τ_W is

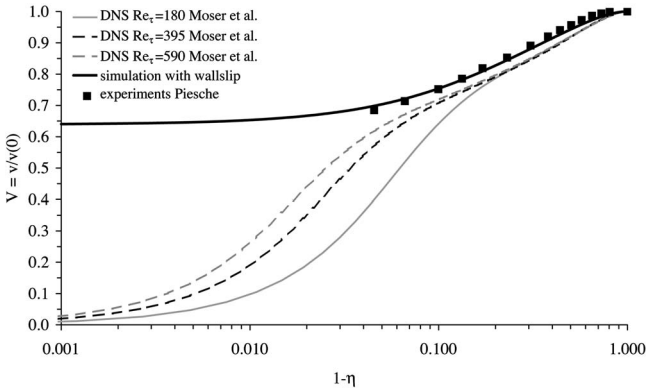

Fig. 6 Comparison of mean velocity profiles by experiments and gradient theory with wall slip condition

$$\tau_W := \tau_{xy}(y = -h/2) = \frac{\kappa_1 \nu(0)}{h/2}\hat{\tau}_W \tag{56}$$

Regarding (54) and (56) and the definition of the Reynolds number $\mathrm{Re} := [\rho \nu(0) h/2]/\mu$ one gets the following final expression for the friction Reynolds number:

$$\mathrm{Re}_\tau = \sqrt{\mathrm{Re}}\sqrt{\frac{\kappa_1}{\mu}\tau_W} = \sqrt{\mathrm{Re}}\sqrt{0.423\frac{\kappa_1}{\mu}} \tag{57}$$

For getting a certain numeric range of the friction Reynolds number, it is assumed that the material coefficient κ_1 in (57) can probably be interpreted as the classical (molecular) dynamic viscosity μ (with regard to $(22)_2$ and $(25)_2$ the other material coefficients κ_2 and Λ can be interpreted as kinds of correction factors with respect to the classical Newtonian concept (see also the expressions (19) and (20))). The expression (57) finally leads to

$$\mathrm{Re}_\tau = \sqrt{0.423}\sqrt{\mathrm{Re}} \tag{58}$$

Figure 6 shows a comparison between the numerical results by [33] with the results of the gradient theory analysis presented here. The results of [33] are based on a direct numerical simulation (DNS) where a no slip condition at the wall $\nu(\eta = 1) = 0$ is assumed. It can be seen, that the dimensionless velocity distribution in the case of the gradient theory is very close to the numerical data given by Moser et al. [33] and the experimental data by Piesche [26] except in the region close to the wall. The aberration in the near-wall region is apparent, since in the gradient theory a dissipative boundary condition (slip condition) was used. Moser et al. [33] found on the basis of DNS, that the (dimensionless) velocity profiles of fully-developed turbulent channel flow do not change their form ($U^+ - y^+$ -diagram), when the friction Reynolds number passes 395. So it is probably possible that the presented theory is suitable for describing turbulent channel flows particularly for friction Reynolds numbers higher than 395, because the dimensionless velocity profile (50) is independent of the pressure gradient A respectively B (for pure channel flows the wall velocity $U \equiv 0$ and thus $\Theta \equiv 0$).

Measurements of flow velocity by Piesche [26] (using hot wire anemometer) and Adrian et al. [34] (using PIV, data not plotted in Fig. 6) are only available for wall distances in which the results of the models with velocity slip at the wall are the same. Thus a final validation of the gradient theory with wall slip is currently not possible.

Adrian et al. [34] and Moser et al. [33] describe the turbulent velocity fluctuations and the formation of the turbulent structures in a detailed way. A comparison, e.g., of the turbulent velocity fluctuations with results of the gradient theory is not possible, because the gradient theory takes into account an average value of

the flow velocity only. Furthermore the gradient theory is based on a steady-state approach, e.g., time-averaged velocity profiles are used.

5 Conclusion

The objective of this study was to investigate the appropriateness of a continuum mechanical gradient theory to describe measurements of fully developed steady turbulent channel flows. Therefore a grade two gradient theory based on an axiomatic conception of Trostel [18,19] is presented. The differential equation of motion in the case of a linear theory derived from the equation of linear momentum is of the fourth order. Two cases have been discussed: channel flow with fixed walls and channel flow with one moving wall both with velocity slip at the wall. The necessary boundary conditions include material parameters as well as so called porosity parameters. These parameters characterize a certain roughness of the boundary of the flow region.

For describing turbulent flows, the velocity field is identified with the average velocity field in the form of a quantifiable average at a location over a certain period of time. The identification of the model parameters in the velocity distributions was carried out by a numerical algorithm called Simulated Annealing based on experimental data of fully developed steady channel flow with fixed walls from the literature [26]. The predictions with such derived parameter sets were compared with different experimental data from the literature [27,29,30,32]. It could be shown that a model without using velocity slip as boundary conditions, did not fulfill the restrictions derived from the dissipation postulate (8). Therefore all solutions of the velocity field are inadmissible. In the case of a theory with velocity-slip, all parameters fulfill the dissipation postulate and the predictions show accordance with all experimental data used in this analysis. The calculated value of velocity-slip at about 60% is comparable with earlier analyses without using a closed systematic form of dissipative boundary conditions [19,22,31]. Furthermore it is remarkable that the predicted velocity gradient of channel flow with fixed walls, which is based on optimized parameters from the measurement data of [26], describes almost precisely the experimental data of velocity gradient by Reichardt. This result again supports the necessity to use velocity slip condition at least in the light of the presented theory.

Supplementary, the results of the presented gradient theory are compared with numerical calculations by Moser et al. [33] based on a direct numerical simulation (DNS). Thereby the predicted velocity distribution on the basis of the gradient theory is in accordance with the data of Moser except in the near-wall region. This abberation is apparent, because in the gradient theory a dissipative boundary condition in the form of a slip condition was used. Finally an explicit expression for the calculation of the friction Reynolds number in the case of a gradient fluid of grade two is generated to dicuss its relevance.

Furthermore the simulations of channel flows with one moving wall show exclusive velocity distribution scenarios using varying wall velocities and pressure gradients. As expected the results derived by the finite difference method are in accordance with the results calculated by the theory.

Appendix: Tensor Notation

An arbitrary tensor of rank n is presented in the form $\boldsymbol{A}^{(n)}$. With exceptions tensors of rank-two are always written as $\boldsymbol{A}^{(2)} \equiv \boldsymbol{A}$. The so-called dyadic product of two vectors $\boldsymbol{a}$ and $\boldsymbol{b}$ results in a tensor of rank two $\boldsymbol{A}$ and is defined by

$$\boldsymbol{A} := \boldsymbol{ab} \tag{A1}$$

In general the "k-times scalar product" between a tensor $\boldsymbol{A}^{(m)}$ of rank m and a tensor $\boldsymbol{B}^{(n)}$ of rank n results in a tensor $\boldsymbol{C}^{(p)}$ of rank $p := m+n-2k$, so that

$$\overset{(m)}{\boldsymbol{A}}\underbrace{\cdots \quad \cdots}_{\text{k-times}}\overset{(n)}{\boldsymbol{B}} = \overset{(m+n-2k)}{\boldsymbol{C}} \qquad \text{with } k \leqslant m \text{ and/or } k \leqslant n \tag{A2}$$

Isotropic tensors of rank $2n$ are written in the form $\boldsymbol{I}^{(2n)}{}_i$ and fulfill the tensor transformation

$$\overset{(2n)}{\boldsymbol{I}_i} = \overset{(4n)}{\boldsymbol{Q}}\underbrace{\cdots \quad \cdots}_{\text{2n-times}}\overset{(2n)}{\boldsymbol{I}_i} \tag{A3}$$

with (the summation convention of Einstein is considered)

$$\overset{(4n)}{\boldsymbol{Q}} := \boldsymbol{e}_{\alpha_1}\boldsymbol{e}_{\alpha_2}\cdots\cdots\cdot\boldsymbol{e}_{\alpha_{2n}}(\boldsymbol{e}_{\alpha_{2n}}\cdot\boldsymbol{Q})\cdots\cdots\cdot(\boldsymbol{e}_{\alpha_2}\cdot\boldsymbol{Q})(\boldsymbol{e}_{\alpha_1}\cdot\boldsymbol{Q})$$

$$\underbrace{\overset{(4n)}{\boldsymbol{Q}^T}\cdots\cdots}_{\text{2n-times}}\overset{(4n)}{\boldsymbol{Q}} = \overset{(4n)}{\boldsymbol{Q}}\underbrace{\cdots\cdots\overset{(4n)}{\boldsymbol{Q}^T}}_{\text{2n-times}} = \overset{(4n)}{\boldsymbol{I}}_1 \tag{A4}$$

where $\mathbf{Q}$ are orthogonal transformations. In the case of rank two there exists only one isotropic tensor $\boldsymbol{I}$ with the following well-known property

$$\overset{(2)}{\boldsymbol{I}} \equiv \boldsymbol{I} = \boldsymbol{e}_i\boldsymbol{e}_i = \boldsymbol{I}^T \quad \text{with} \quad \boldsymbol{I}\cdot\boldsymbol{a} = \boldsymbol{a}\cdot\boldsymbol{I} = \boldsymbol{a} \tag{A5}$$

In the case of rank four there exist three tensors $\overset{(4)}{\boldsymbol{I}}_i (i=1,2,3)$ with the following properties:

$$\overset{(4)}{\boldsymbol{I}}_1 = \boldsymbol{e}_i\boldsymbol{e}_j\boldsymbol{e}_j\boldsymbol{e}_i = \overset{(4)}{\boldsymbol{I}_1^T} \quad \text{with} \quad \overset{(4)}{\boldsymbol{I}}_1\cdot\cdot\boldsymbol{A} = \boldsymbol{A}\cdot\cdot\overset{(4)}{\boldsymbol{I}}_1 = \boldsymbol{A} \tag{A6}$$

$$\overset{(4)}{\boldsymbol{I}}_2 = \boldsymbol{e}_i\boldsymbol{e}_j\boldsymbol{e}_i\boldsymbol{e}_j = \overset{(4)}{\boldsymbol{I}_2^T} \quad \text{with} \quad \overset{(4)}{\boldsymbol{I}}_2\cdot\cdot\boldsymbol{A} = \boldsymbol{A}\cdot\cdot\overset{(4)}{\boldsymbol{I}}_2 = \boldsymbol{A}^T \tag{A7}$$

$$\overset{(4)}{\boldsymbol{I}}_3 = \boldsymbol{e}_i\boldsymbol{e}_i\boldsymbol{e}_j\boldsymbol{e}_j \equiv \boldsymbol{II} = \overset{(4)}{\boldsymbol{I}_3^T} \quad \text{with} \quad \overset{(4)}{\boldsymbol{I}}_3\cdot\cdot\boldsymbol{A} = \boldsymbol{A}\cdot\cdot\overset{(4)}{\boldsymbol{I}}_3 = (\operatorname{tr}\boldsymbol{A})\boldsymbol{I} \tag{A8}$$

References

[1] Eringen, A. C., 1964, "Mechanics of Micromorphic Materials," in *Proceedings of the 11th International Congress of Applied Mechanics*, H. Gortler, ed., Springer Verlag, pp. 131–138.
[2] Eringen, A. C., 1966, "Linear Theory of Micropolar Elasticity," J. Math. Mech. **16**(6), pp. 909–923.
[3] Eringen, A. C., 1966 "Theory of Micropolar Fluids," J. Math. Mech. **16**(1), pp. 1–18.
[4] Eringen, A. C., 1974, "Polar and Nonlocal Theories of Continua," Bogazici University, Turkey, p. 137.
[5] Eringen, A. C., 1976, *Continuum Physics-Polar and Nonlocal Field-Theories*, Academic, New York.
[6] Eringen, A. C., 2001, *Microcontinuum Field Theories II: Fluent Media*, Springer.
[7] Maugin, G. A., 1980, "The Method of Virtual Power in Continuum Mechanics: Application to Coupled Fields," Acta Mech., **35**, pp. 1–70.
[8] Eringen, A. C., 2003, "Incompressible Micromorphic Fluid Model for Turbulence," Int. J. Eng. Sci., **41**, pp. 1041–1057.
[9] Eringen, A. C., 2005, "On a Rational Theory of Turbulence," Int. J. Eng. Sci., **43**, pp. 209–221.
[10] Kirwan, A. D., Newman, N., and Chang, M.-S., 1976, "On Microdeformable Fluids: A Special Case of Microfluids,"Int. J. Eng. Sci., **14**, pp. 673–684.
[11] Liu, C. Y., 1970, "On Turbulent Flow of Micropolar Fluids," Int. J. Eng. Sci., **8**, pp. 457–466.
[12] Peddieson, J., 1972, "An Application of the Micropolar Fluid Model to the Calculation of a Turbulent Shear Flow," Int. J. Eng. Sci., **10**, 23–32.
[13] Ariman, T., Turk, M. A., and Sylvester, N. D., 1973, "Microcontinuum Fluid Mechanics—A Review," Int. J. Eng. Sci., **11**, pp. 905–930.
[14] Ahmadi, G., 1975, "Turbulent Shear Flow of Micropolar Fluids," Int. J. Eng. Sci., **13**, pp. 959–964.
[15] Mindlin, R. D., 1965, "Second Gradient of Strain and Surface-Tension in Linear Elasticity," Int. J. Eng. Sci., **1**, pp. 417–438.
[16] Cheverton, K. J., and Beatty, M. F., 1975, "On the Mathematical Theory of the Mechanical Behavior of Some Non-Simple Materials," Arch. Ration. Mech. Anal., **60**, pp. 1–16.
[17] Drouot, R., and Maugin, G. A., 1983, "Phenomenological Theory for Polymer Diffusion in Nonhomogeneous Velocity-Gradient Flows," Rheol. Acta, **22**, pp. 336–347.
[18] Trostel, R., 1985, "Gedanken zur Konstruktion mechanischer Theorien," Beiträge zu den Ingenieurwissenschaften, Universitäts-Bibliothek der TU Berlin.
[19] Trostel, R., 1988, "Gedanken zur Konstruktion mechanischer Theorien II," Forschungsbericht Nr. 7, Universitäts-Bibliothek der TU Berlin.

[20] Silber, G., 1988, "Nichtlokal Nichtpolar Oder Lokalpolar mit Kinematischem Zwang?" Mechanik-Beiträge zur Theorie und Anwendungen, Universitäts-Bibliothek der TU Berlin, pp. 270–284.
[21] Schlichting, H., 1958, *Grenzschicht-Theorie*, G. Braun, Karlsruhe, dritte edition.
[22] Silber, G., 1986, *Eine Systematik Nichtlokaler Kelvinhafter Fluide vom Grade drei auf der Basis eines Klassischen Kontinuummodelles*, Vol. 18/No. 26. VDI-Verlag, Düsseldorf.
[23] Silber, G., 1990, "Darstellung Höherstufig-Tensorwertiger Isotroper Funktionen," Z. Angew. Math. Mech., **70**(9), pp. 381–393.
[24] Alizadeh, M., 2001, "Eine Randwertsystematik für Gradientenfluide vom Grade drei auf der Basis von Porositätstensoren," Online dissertation, http://edocs.tuberlin.de/diss/2001/alizadeh_mansour.pdf; Ph.D. thesis, TU Berlin.
[25] Otten, R. H. J. M., and van Ginneken, L. P. P. P., 1990, *The Annealing Algorithm*, Kluwer.
[26] Piesche, M., 1983, "Strömungs-und Wärmetransportvorgänge im Einlaufbereich Eines Ebenen Spaltes mit Relativ Zueinander Bewegten Wänden," Strömungsmechanik und Strömungsmaschinen, **33**, pp. 1–58.
[27] Schlichting, H., 1964, *Grenzschicht-Theorie*, G. Braun, Karlsruhe, fünfte edition.
[28] Comte-Bellot, G., 1968, "Turbulent Flow Between Two Parallel Planes II," Z. Phys., **209**, pp. 440–444.
[29] Comte-Bellot, G., 1965, "Écoulement Turbulent Entre Deux Parois Parallèles," Publ. Scientifiques et Techniques du Ministère de l'Air, **419**.
[30] Reichardt, H., 1951, "Vollstïdige Darstellung der turbulenten Geschwindigkeitsverteilung in glatten Leitungen," Z. Angew. Math. Mech., **31**(7), pp. 208–219.
[31] Alexandru, C., 1989, *Systematik Nichlokaler Kelvinhafter Fluide vom Grade zwei auf der Basis Eines Cosserat Kontinuummodelles*, VDI-Verlag, Düsseldorf, Vol. 18, No. 61.
[32] Reichardt, H., 1956, "Über die Geschwindigkeitsverteilung in Einer Geradliniegen Turbulenten Couette-Strömung," Z. Angew. Math. Mech., **36**, Sonderheft, 1956, pp. 26–29.
[33] Moser, R. D., Kim, J., and Mansour, N. N., 1999, "Direct Numerical Simulation of Turbulent Channel Flow up to Re=590," Phys. Fluids, **4**, (11), pp. 943–945.
[34] Adrian, R. J., Meinhart, C. D., and Tomkins, C. D., 2000, "Vortex Organization in the Outer Region of the Turbulent Boundary Layer," J. Fluid Mech., **422**, pp. 1–54.

Christian H. Bischof

H. Martin Bücker
e-mail: buecker@sc.rwth-aachen.de

Arno Rasch

Emil Slusanschi

Institute for Scientific Computing,
RWTH Aachen University,
D-52056 Aachen, Germany

Bruno Lang
Bergische Universität Wuppertal,
D-42097 Wuppertal, Germany

Automatic Differentiation of the General-Purpose Computational Fluid Dynamics Package FLUENT

Derivatives are a crucial ingredient to a broad variety of computational techniques in science and engineering. While numerical approaches for evaluating derivatives suffer from truncation error, automatic differentiation is accurate up to machine precision. The term automatic differentiation comprises a set of techniques for mechanically transforming a given computer program to another one capable of evaluating derivatives. A common misconception about automatic differentiation is that this technique only works on local pieces of fairly simple code. Here, it is shown that automatic differentiation is not only applicable to small academic codes, but scales to advanced industrial software packages. In particular, the general-purpose computational fluid dynamics software package FLUENT is transformed by automatic differentiation.
[DOI: 10.1115/1.2720475]

1 Introduction

Approximating derivatives by finite differences is a subtle, and often annoying, task. In particular, it usually takes several runs of the program until a suitable stepsize is found, and even then it is difficult to estimate the truncation error that is inherent to this way of evaluating derivatives. Therefore we would like to have an efficient and easy-to-use alternative that eliminates the concept of a stepsize and does not involve any truncation error at all. In fact there is a technique called automatic or algorithmic differentiation (AD) which is capable of efficiently evaluating accurate derivatives of functions implemented by arbitrarily complex computer programs.

In applying AD to FLUENT,[1] one of the leading commercial computational fluid dynamics (CFD) software packages, we show that AD is not only applicable to small academic programs, but scales to large industrial simulation codes. Thus, by providing derivatives without truncation error, AD accelerates the transition from large-scale simulation to optimization. A shift from a pure simulation to a systematic approach of determining design variables or model parameters by some kind of optimization framework is one of the major trends in today's computational science. Examples include multidisciplinary design optimization, parameter identification, and other inverse problems. Derivative information is also crucial for analyzing the sensitivity of simulation outputs with respect to physical or model parameters.

After a brief introduction into the elementary concepts of automatic differentiation, we report on the results of applying the AD technology to the FLUENT code consisting of approximately 1.6 million lines of Fortran. From two case studies, the reader may get a feeling for the additional information provided by an automatically "differentiated" CFD code.

2 Automatic Differentiation

Automatic differentiation refers to a set of techniques for transforming a given computer program P into a new program P' capable of computing derivatives in addition to the original output. More precisely, if P implements some function

$$f:\mathbb{R}^n \to \mathbb{R}^m$$

mapping an input x to an output $y=f(x)$, the transformed program P' computes not only the function value y but also the $m \times n$ Jacobian matrix

$$J = \frac{\partial y}{\partial x}$$

at the same point x. The AD-generated program P' is called the *differentiated* program.

The basic idea behind AD is the fact that the execution of P is nothing but a—potentially very long—sequence of elementary arithmetic operations such as binary addition, multiplication, or intrinsic functions like $\sin(\cdot)$ or $\cos(\cdot)$. The partial derivatives of all these elementary functions are known and, following the chain rule of differential calculus, can be combined in a step-wise manner to yield the overall derivative of the entire program.

To illustrate the basic idea behind AD, consider the following simple code fragment and keep in mind that the technique is also applicable to larger codes. The sample Fortran fragment is given by

```
u = x(1) + x(2)
v = sin(u)
y = v * x(1),
```

and computes the scalar output $y=\sin(x_1+x_2)\cdot x_1$ from a given two-dimensional input vector $x=(x_1,x_2)^T$ using the intermediate variables u and v. We introduce a straightforward strategy of automatic differentiation called the *forward mode* by studying the transformation of the sample code fragment. In the forward mode, a gradient object ∇w is associated to every scalar variable w appearing in the original code. In the differentiated code, this gradient object ∇w is used to store the partial derivatives of the variable w with respect to the input variables of interest, i.e., $\nabla w = \partial w / \partial x$, and additional statements for updating ∇w are executed whenever the value of w changes. Suppose that we would like to obtain derivatives of y with respect to x_1 and x_2. Note that the forward mode follows the control flow of the original program, i.e., the differentiated code computes y and ∇y from given values of x_1, x_2 and $\nabla x_1, \nabla x_2$. Thus, in mathematical notation the above code segment would be augmented to

$$\nabla u = \nabla x_1 + \nabla x_2; \quad u = x_1 + x_2$$

[1] FLUENT is a registered trademark of Fluent Inc.

Contributed by the Fluids Engineering Division of ASME for publication in the JOURNAL OF FLUIDS ENGINEERING. Manuscript received May 12, 2005; final manuscript received October 12, 2006. Assoc. Editor: Ye Zhou.

$$\nabla v = \cos(u) \cdot \nabla u; \quad v = \sin(u)$$

$$\nabla y = \nabla v \cdot x_1 + v \cdot \nabla x_1; \quad y = v \cdot x_1$$

If we are interested in partial derivatives with respect to n input variables then the code produced by the forward mode contains a length-n loop for each operation with a gradient object. More precisely, the AD-generated code implementing the above forward-mode equations is given by the following:

```
do i=1,n
    g_u(i)=g_x(i,1)+g_x(i,2)
enddo
u=x(1)+x(2)
do i=1,n
    g_v(i)=cos(u)*g_u(i)
enddo
v=sin(u)
do i=1,n
    g_y(i)=g_v(i)*x(1)+v*g_x(i,1)
enddo
y=v*x(1)
```

Here, the gradients are implemented by arrays, for instance, ∇u is represented by `g_u(1:n)`. In this simple example, we are interested in derivatives with respect to $n=2$ scalar input variables. If the code is initialized with $\nabla x_1=(1,0)$ and $\nabla x_2=(0,1)$, then it is easy to check that the differentiated code computes $\nabla y = (\partial y/\partial x_1, \partial y/\partial x_2)$.

Because of the associativity of the chain rule, there are different ways to combine the partial derivatives of the elementary functions leading to different algorithms for AD. In exact arithmetic, all techniques deliver the same results but may differ significantly in time and space complexity. The complexity of an AD-generated program is typically measured in terms of the complexity of the original program. One is interested in how much more time and storage are consumed by the AD-generated program than by the original program. To this end, let T_f and M_f denote the execution time and memory requirement, respectively, of the original program evaluating some function $f:\mathbb{R}^n \to \mathbb{R}^m$. Similarly, let T_J and M_J denote time and memory of the AD-generated program capable of computing not only f but also its $m \times n$ Jacobian matrix J. If we were to improve the performance of the original code, we would try to minimize T_f and M_f as a function of n and m. In AD, however, the original code is taken as input so that T_f and M_f are given quantities. Rather, one is interested in minimizing the ratios T_J/T_f and M_J/M_f. That is, one is trying to reduce the overhead incurred by the derivative computation, compared to the computation of the function to be differentiated.

Comparing the original code P for computing f and the AD-generated code P' for computing f and J, one can see from the above example that the execution time and storage requirement of the forward mode roughly grow with the number of directional derivatives, n. That is, the ratios T_J/T_f and M_J/M_f depend linearly on n, and these ratios are independent of m.

Notice that the time complexity of the forward mode of AD corresponds to that of numerical differentiation by divided differencing. For instance, approximating the Jacobian of the function f by first-order forward divided differences

$$\frac{\partial f}{\partial x_i} \approx \frac{f(x+he_i)-f(x)}{h} \quad i=1,\ldots,n$$

needs $n+1$ evaluations of f. Here, $e_i \in \mathbb{R}^n$ denotes the ith canonical unit vector, and h is the step size. Thus, for first-order forward differences, we have $T_J/T_f=n+1$.

In contrast, there is a so-called reverse mode where the time complexity, relative to the original program, depends on m, but not on n. Therefore, the reverse mode is preferable when computing gradients of scalar functions depending on many input variables since its time complexity is a small multiple of the time to run the original code, independent of the length of the gradient.

In contrast to symbolic differentiation which is typically provided by computer algebra packages like Maple [1] or Mathematica [2], AD is applicable to large computer codes with loops, conditional branches, and subroutine calls. AD generates a program for evaluating derivatives rather than a mathematical formula. Yet the results obtained by AD-generated code are accurate up to machine precision due to the absence of any numerical approximation scheme.

There is a growing number of tools for automatically differentiating computer programs written in languages like Fortran77/90/95, C, C++, and Matlab. Examples include ADIFOR [3], TAMC/TAF [4], TAPENADE [5], ADIC [6], ADOL-C [7], ADIMAT [8], ADMIT [9], and MAD [10]. See www.autodiff.org for a more detailed overview of currently available AD software. The books by Griewank [11] and Rall [12] give a thorough introduction to automatic differentiation.

3 FLUENT

FLUENT, developed by Fluent Inc., is a general-purpose computer program for simulating fluid flow, heat transfer, and chemical reactions in two and three space dimensions. It is used in a broad variety of industrial branches and academic research including the automotive and aerospace industries, metallurgy, and power generation. In the present case studies we use version 4.5.2 of the FLUENT code which is essentially written in Fortran 77 with some additional Fortran 90 language elements that are mainly used for dynamic memory management. The whole source code consists of more than 2 million lines of Fortran, including comments. Furthermore there are approximately 50,000 lines of C code primarily concerned with the graphical user interface and system calls. However most of the C code is not relevant for the computational part of FLUENT.

4 Automatic Differentiation of FLUENT

In this section, we describe the extension of the functionality of FLUENT by automatic differentiation. The sheer size of the FLUENT source code requires a reliable and robust automatic differentiation tool for the code transformation process. For this task we use version 2.1 of the ADIFOR [3] software tool which has been successfully used in numerous applications from various scientific disciplines, e.g., Refs. [13–17]. ADIFOR (Automatic differentiation of Fortran) is capable of transforming a given Fortran 77 program into a new program that computes the same function as the original code and additionally evaluates certain derivatives that have been specified before. ADIFOR only accepts standard Fortran 77 as input language, with the exception of some additional commonly used language extensions like, e.g., `DO…ENDDO`, `INCLUDE`, and `IMPLICIT NONE`. Therefore we first create a modified version of FLUENT containing no Fortran 90 constructs. In this version the memory is allocated statically and all statements involving dynamic memory management have been disabled. A number of minor modifications are necessary, correcting nonstandard Fortran 77 programming techniques that typically arise during many years of program development. A few subroutines, mainly responsible for input/output (I/O), have been explicitly excluded from the AD process. Furthermore we remove the graphical user interface for the sake of simplicity. The resulting modified version of FLUENT consists of roughly 1.6 million lines of Fortran (550,000 without comments) in 1845 subroutines and functions. The C part of the code has been reduced to 5000 lines.

After this "code massaging" we apply ADIFOR to the slightly modified FLUENT package. As variables, for which derivatives are desired, we choose velocity and pressure. ADIFOR carries out an interprocedural dependency analysis in order to determine

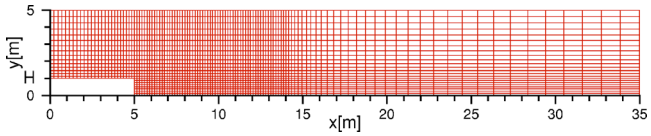

Fig. 1 Schematic picture of the backward-facing step and the grid

those routines for which derivative code is to be generated. Here, 1070 subroutines and 200 functions are automatically selected to be transformed by AD. From these, ADIFOR eventually generates approximately 1.6 million lines of Fortran code (700,000 without comments). The remaining subroutines and functions are left unchanged because they perform no computational work relevant for the computations of the selected derivatives. Furthermore, we need a small driver for the initialization of the differentiated program. The whole source code consists of roughly 2.2 million lines of code (950,000 without comments).

Although the process of applying AD is conceptually easy, typically taking only a few manhours for small or medium-sized programs, the human effort to transform FLUENT is considerable. The reason for this increased amount of human work is that a certain knowledge of the internal program structure is necessary. For someone who is completely unfamiliar with FLUENT, it may take several weeks or months to get a differentiated version of FLUENT.

In the sequel, we present two case studies of derivative computations using typical examples from the FLUENT tutorial [18]. We show that accurate derivative information can be computed by the AD technology and stress that, in contrast to numerical differentiation, these derivative values are free from truncation error. Thus, by eliminating the tedious and sometimes difficult process of determining a suitable stepsize, AD significantly facilitates computing derivative information in a reliable way.

5 Case Study 1: Flow Over a Backward Facing Step

In the first example, we consider the simulation of a two-dimensional flow over a backward-facing step, a common benchmark problem for CFD codes. More precisely, we look at a rectangular domain, 35 m long and 5 m high, whose geometry is schematically depicted in Fig. 1. We assume a step height of $H=1$ m and a flow from left to right. At the inlet, $x=0$, we specify a flat velocity profile with a horizontal component $u_x=1$ m/s and vertical component $u_y=0$ m/s. The fluid density is 1.0 kg/m^3 and the dynamic viscosity is 3.57×10^{-5} kg/(m s). Based on the step height the Reynolds number is 2.8×10^4. The flow is assumed to be incompressible and turbulent with an inlet turbulence intensity of 2.0%. The characteristic length of the flow is supposed to be the height of the upstream channel, 4 m.

The basic equations describing the flow in FLUENT are the conservation of mass and the conservation of momentum. In the general form, the conservation of mass in direction x_i, $i=1,2$ ($x_1=x$ and $x_2=y$) at time t, is given by

$$\frac{\partial \varrho}{\partial t}+\frac{\partial}{\partial x_i}(\varrho u_i)=0$$

where ϱ is the density and u_i is the velocity in direction i. The conservation of momentum is described by

$$\frac{\partial}{\partial t}(\varrho u_i)+\frac{\partial}{\partial x_j}(\varrho u_i u_j)=-\frac{\partial p}{\partial x_i}+\frac{\partial \tau_{ij}}{\partial x_j}+\varrho g_i$$

in which p denotes the pressure; τ_{ij} is the stress tensor; and g_i is the gravitational acceleration in direction i.

For predicting the flow under these conditions one could use the standard k-ε turbulence model. However, in the FLUENT tutorial guide where this example is taken from, a variant of the standard k-ε turbulence model, namely the renormalization group (RNG) k-ε model [19] is preferred.

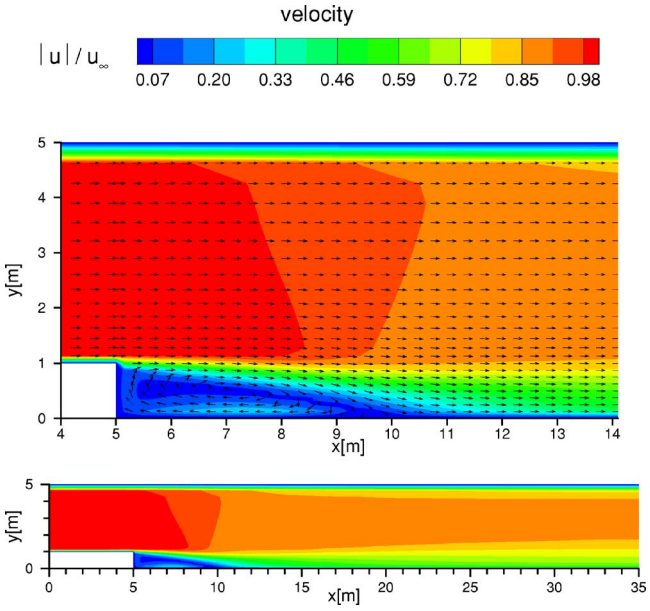

Fig. 2 Scaled velocity of the fluid, $|u|/u_\infty$, over the complete domain (bottom) and a detailed view of the vicinity of the step (top)

The computational grid consists of approximately 3000 cells (see Fig. 1). The result of the simulation is shown in Fig. 2. The colors indicate the absolute values of the resulting velocities, i.e., $\sqrt{u_x^2+u_y^2}$, scaled by the instream velocity, u_∞. Here, u_x and u_y are the horizontal and vertical components of the velocity vector (u_x,u_y), respectively, and $u_\infty=1$ m/s. In this benchmark example one is typically interested in the length of the separation bubble behind the backward facing step, the so-called recirculation zone. Figure 3 shows the streamtraces for the recirculation zone which ends at approximately $x=10$ m.

The length of the recirculation zone is determined by the height of the step, H. We are now interested in the change of the recirculation zone when varying the step height. That is, we would like to get the sensitivity of a result of a FLUENT simulation with respect to one of its inputs. In particular, we are looking for the derivative of the flow field u with respect to the step height H. ADIFOR is used to transform the FLUENT package into a differentiated version capable of computing $\partial u/\partial H$ along with the original simulation. The resulting derivative vectors are shown in Fig. 4. Similar to the original vector field, the colors indicate the ab-

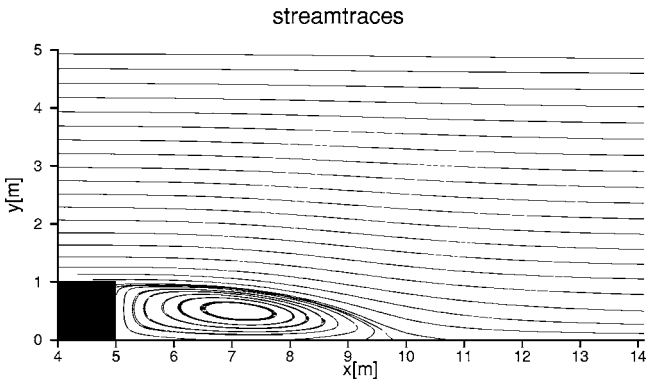

Fig. 3 Streamtraces in the vicinity of the step

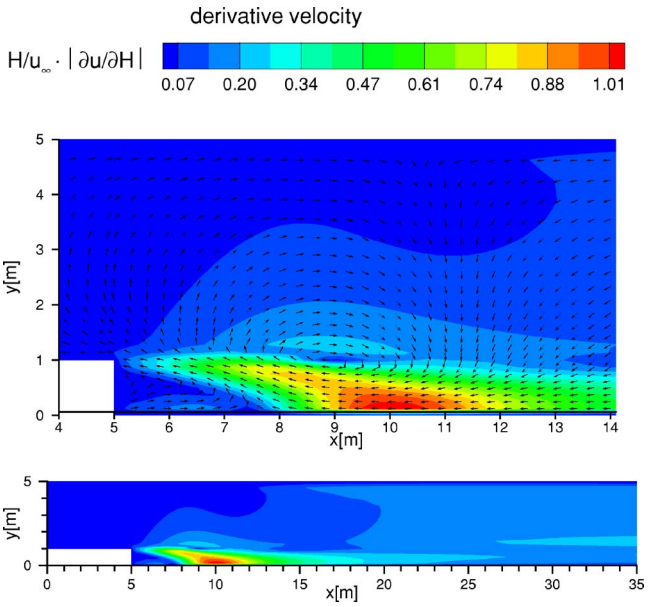

Fig. 4 Scaled derivatives, $H/u_\infty \cdot |\partial u/\partial H|$, over the complete domain (bottom) and a detailed view of the vicinity of the step (top)

solute values of the derivative velocity vectors, i.e., $\sqrt{(\partial u_x/\partial H)^2+(\partial u_y/\partial H)^2}$, scaled by H/u_∞. Note that the largest derivative values occur in the vicinity of the reattachment point, about 5 m downstream of the step at $x=10$ m, showing the strong influence of the step height on the length of the recirculation zone. On the other hand, the computed sensitivities for the remainder of the flow field are relatively small, in particular upstream of the step.

A corresponding analysis can be carried out with the derivative of the pressure. In Fig. 5 the static pressure p, scaled by p_∞, is depicted. We use the pressure at the inlet as the reference value $p_\infty=0.031$ kg/(m s^2). Figure 6 shows the derivative of the pressure p with respect to the step height H, scaled by H/p_∞. Near the reattachment point the scaled derivatives are negative with relatively large absolute values. Furthermore we observe relatively

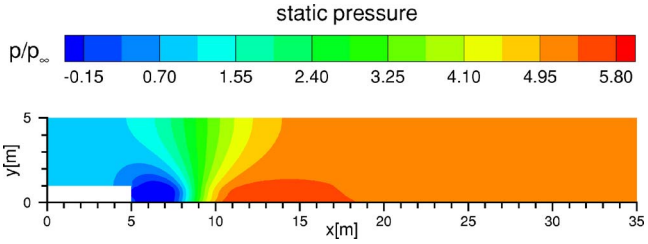

Fig. 5 Static pressure of the fluid, p/p_∞, over the complete domain

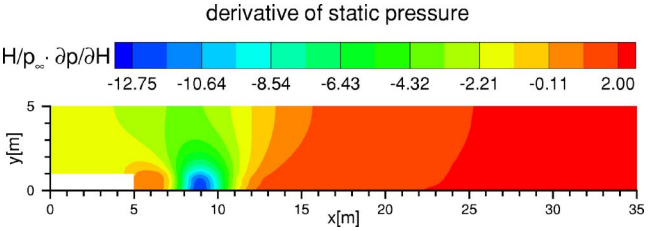

Fig. 6 Scaled derivative of the pressure, $H/p_\infty \cdot \partial p/\partial H$, over the complete domain

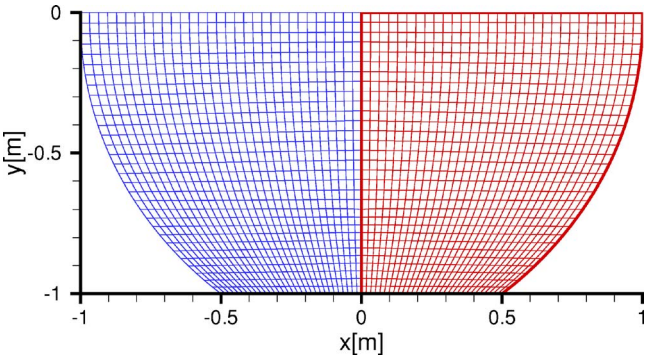

Fig. 7 Schematic picture of the bowl and the grid

small positive and small negative derivatives downstream and upstream of the step, respectively. Directly behind the step the derivative $H/p_\infty \cdot \partial p/\partial H$ is almost zero.

The CPU time requirements for the differentiated version compared to the original code increase by a factor of $T_J/T_f=2.1$. More precisely, it takes approximately 16.8 s of CPU time on a 900 MHz UltraSPARC III processor to compute the original flow over the backward facing step. Using the differentiated version of FLUENT, the original flow field *and* the derivative with respect to the step height are computed in 35.5 s. Note that it would need at least two runs of the original FLUENT program in order to compute a first-order approximation of the gradient using divided differences. The differentiated version computes the gradient without truncation error in approximately the same time. The overall storage requirements (physical memory) for the differentiated FLUENT program are 38 MB, compared to 22 MB for the original code, i.e., $M_J/M_f=1.7$.

6 Case Study 2: Water and Air in a Spinning Bowl

As a second example we choose a time-dependent flow problem from the FLUENT tutorial guide. In this problem, we consider a large bowl, which is one-third filled with water. The physical constants for density (ϱ) and viscosity (μ) of air and water are given by

$$\varrho_{\text{air}} = 1.0\ \frac{\text{kg}}{\text{m}^3} \quad \mu_{\text{air}} = 2\times 10^{-5}\ \frac{\text{kg}}{\text{m s}}$$

$$\varrho_{\text{water}} = 1000\ \frac{\text{kg}}{\text{m}^3} \quad \mu_{\text{water}} = 9\times 10^{-4}\ \frac{\text{kg}}{\text{m s}}$$

The bowl has a radius of 1 m and spins with an angular frequency of 3 rad/s. The geometry of the bowl is shown in Fig. 7. Due to the symmetry of the problem, only half of the bowl is modeled where the computational grid consists of approximately 1100 cells. Initially, the angular velocity of the fluid is assumed to be 3 rad/s throughout the entire domain. Based on the rotating water the Reynolds number is about 10^6, so the present problem is turbulent with a free surface. A turbulence intensity of 1.0% and a characteristic length of 1 m are assumed.

For the solution we use the time-dependent volume of fluid model [20] with time steps of 1 ms. For modeling turbulence the standard k-ε model [21–23] is used. The standard k-ε model is an eddy-viscosity model consisting of two equations for the turbulent kinetic energy k and its dissipation rate ε. More precisely, the additional transport equations in direction x_i at time t that are solved for k and ε are given by

$$\frac{\partial}{\partial t}(\varrho k)+\frac{\partial}{\partial x_i}(\varrho u_i k)=\frac{\partial}{\partial x_i}\left(\frac{\mu_t}{\sigma_k}\frac{\partial k}{\partial x_i}\right)+G_k-\varrho\varepsilon \qquad (1)$$

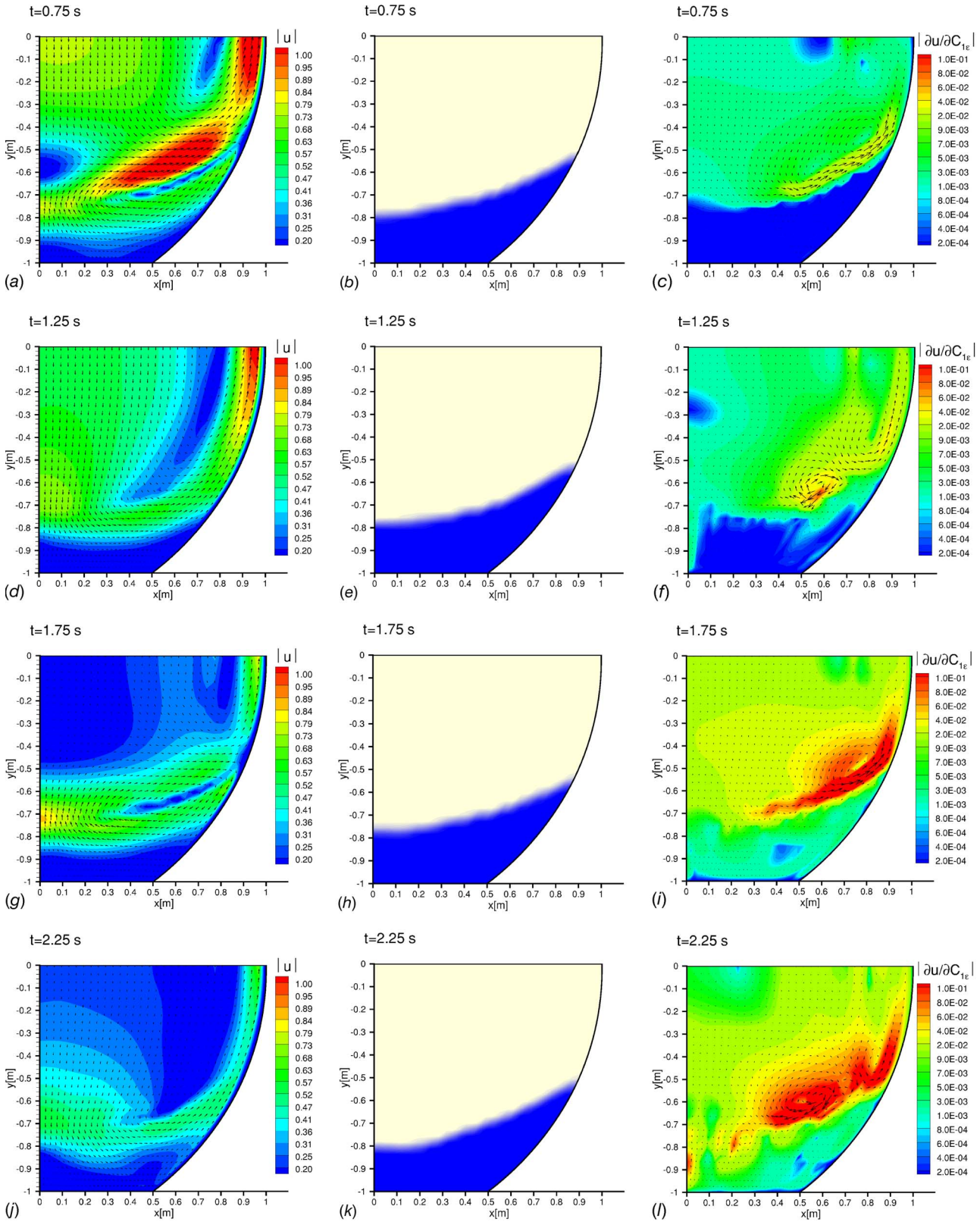

Fig. 8 Spinning bowl. Each row corresponds to one time step, showing the velocity (left), the volume fraction (middle), and the derivative of the velocity with respect to the turbulence parameter $C_{1\varepsilon}$ (right)

$$\frac{\partial}{\partial t}(\varrho\varepsilon)+\frac{\partial}{\partial x_i}(\varrho u_i\varepsilon)=\frac{\partial}{\partial x_i}\left(\frac{\mu_t}{\sigma_\varepsilon}\frac{\partial\varepsilon}{\partial x_i}\right)+C_{1\varepsilon}\frac{\varepsilon}{k}G_k-C_{2\varepsilon}\varrho\frac{\varepsilon^2}{k} \quad (2)$$

Here, ϱ and u_i denote the density and the velocity in direction i, respectively. Furthermore, the turbulent viscosity is given by

$$\mu_t=C_\mu\varrho\frac{k^2}{\varepsilon}$$

and

$$G_k=\mu_t\left(\frac{\partial u_j}{\partial x_i}+\frac{\partial u_i}{\partial x_j}\right)\frac{\partial u_j}{\partial x_i}$$

represents the rate of production of the turbulent kinetic energy. In these equations, the coefficients $C_{1\varepsilon}$, $C_{2\varepsilon}$, C_μ, σ_k, and σ_ε are parameters of the standard k-ε model which have the following empirically derived values, that are also used in FLUENT as defaults

$$C_{1\varepsilon}=1.44, \quad C_{2\varepsilon}=1.92, \quad C_\mu=0.09, \quad \sigma_k=1.0, \quad \sigma_\varepsilon=1.3 \quad (3)$$

The reader is referred to Refs. [21–23] for more details of the underlying assumptions involved in the standard k-ε model.

We are looking for the derivatives of the flow field with respect to the five constant coefficients, $C_{1\varepsilon}$, $C_{2\varepsilon}$, C_μ, σ_k, and σ_ε. To adapt the k-ε turbulence model for a particular kind of problem, engineers are interested in the sensitivities of the solution with respect to the constant coefficients in the transport equations. Such derivative information can be useful when the coefficients should be modified in order to improve the reliability of the k-ε model for specific applications [24].

In other words, we consider a *parameterized* k-ε model with parameters $C_{1\varepsilon}$, $C_{2\varepsilon}$, C_μ, σ_k, and σ_ε which are to be adjusted such that the model best mimics the physical behavior observed in reality. This task is often called parameter identification and usually yields an optimization problem. Since many numerical optimization methods employ derivative-based search strategies, the availability of accurate derivative information is essential for fast convergence. Therefore we use automatic differentiation to obtain derivatives of the velocity with respect to the five model parameters of the k-ε model. The differentiated FLUENT code computes all five derivatives, together with the original function. The ratio of the CPU time consumption of the differentiated version and the original version is $T_J/T_f=6.3$ which is still a good result since numerical differentiation using divided differences would need at least six function evaluations to compute derivative approximations of potentially relatively low accuracy. The physical memory requirements of FLUENT and its differentiated version are 17 MB and 65 MB, respectively, which is an increase by a factor $M_J/M_f=3.8$.

The results of the simulation are depicted in Fig. 8. Each row corresponds to a snapshot at a certain time step. The first row corresponds to the simulated flow at $t=0.75$ s. In each row, the original velocity field is shown in the left picture, whereas the rightmost picture, shows the sensitivity of the velocity field with respect to turbulence parameter $C_{1\varepsilon}$. The colors indicate the absolute values of the velocity vectors and the derivative velocity vectors, respectively. Note that the scale for the derivatives is logarithmic. For better orientation, the current shape of the free surface is displayed in the middle column. At $t=0.75$ s the derivative velocity is relatively small. Later in time, at $t=1.25$ s, $t=1.75$ s, or $t=2.25$ s, the derivatives become more significant indicating a growing influence of the turbulence parameter $C_{1\varepsilon}$. Note that the greatest derivative values appear near the shear layer.

In Table 1, the maximum absolute values of the derivatives of the velocity with respect to of all five turbulence parameters are given. For each value, the number of the corresponding grid point and its coordinates (x and y) are also given, indicating the location where the maximum occurs. For all four time steps, the velocity is most sensitive with respect to C_μ. The location where these maximum derivative values, $\max|\partial u/\partial C_\mu|$, occur, differs from time step to time step. Notice also that, at time step $t=1.25$ s, the maximum derivative values occur at the same position, $(x,y)=(0.3694,-0.7281)$, for the parameters $C_{2\varepsilon}$, C_μ, σ_k, and σ_ε.

Table 1 The table shows, for various time steps (first column), the maximum absolute values of the derivatives $\partial u/\partial c_i$ with respect to the five turbulence parameters c_i, where $c_1=C_{1\varepsilon}$, $c_2=C_{2\varepsilon}$, $c_3=C_\mu$, $c_4=\sigma_k$, $c_5=\sigma_\varepsilon$ (third column), and the corresponding grid point where the maximum occurs (fourth column). The fifth and sixth columns indicate the location of the point, i.e., the (x,y) position where the maximum occurs

Time step	i	$\max\lvert\frac{\partial u}{\partial c_i}\rvert$	Point no.	x	y
$t=0.75$ s	1	0.0287	911	0.8091	−0.5046
	2	0.0220	911	0.8091	−0.5046
	3	0.1067	976	0.8519	−0.5394
	4	0.0016	991	0.5118	−0.9761
	5	0.0006	991	0.5118	−0.9761
$t=1.25$ s	1	0.0903	723	0.5864	−0.6352
	2	0.2584	502	0.3694	−0.7281
	3	1.9713	502	0.3694	−0.7281
	4	0.0011	502	0.3694	−0.7281
	5	0.0004	502	0.3694	−0.7281
$t=1.75$ s	1	0.3637	880	0.7665	−0.5378
	2	0.8123	374	0.2709	−0.7275
	3	6.0418	374	0.2709	−0.7275
	4	0.0043	880	0.7665	−0.5378
	5	0.0022	786	0.6544	−0.6030
$t=2.25$ s	1	0.4077	722	0.5999	−0.6023
	2	1.4933	312	0.2081	−0.7841
	3	6.2194	312	0.2081	−0.7841
	4	0.0094	817	0.6961	−0.5703
	5	0.0054	753	0.6404	−0.5695

If one is interested in the order of magnitude of the sensitivities rather than in their precise values, one may analyze the scaled derivatives $c_i\cdot(\partial u/\partial c_i)$. Considering the fact that C_μ is about an order of magnitude smaller than the other four parameters in Eq. (3), the scaled sensitivities with respect to the first three parameters, $C_{1\varepsilon}$, $C_{2\varepsilon}$, and C_μ, are nearly equal within an order of magnitude for all four time steps, whereas the sensitivities with respect to σ_k and σ_ε are between one and two orders of magnitude less than the first three sensitivities. However, these differences are not large enough to construct a new model omitting the parameters σ_k and σ_ε without further analysis.

7 Conclusions

Automatic differentiation is a powerful technology for computing accurate derivatives of arbitrary functions given in the form of a computer program. In this paper we reported on a successful application of AD to FLUENT, a widely used commercial CFD code. Although in principle there is no difference between automatic differentiation of small or large codes, applying this technology to a complex CFD package consisting of 1.6 million lines of source code is still a challenging task and, to the best of our knowledge, FLUENT is by far the largest code to which AD has been applied to date.

This result highlights the usability of AD in general and the power of the AD tool ADIFOR in particular. However, not everything is fully automatic: a fair amount of work, in particular clean-

ing up the original code in order to make it conform to the language standard, was necessary before AD could be applied.

The extended functionality of the differentiated simulation code offers a variety of possibilities for the community of computational scientists and engineers since many applications going beyond pure simulation rely heavily on the availability of accurate derivatives. Examples include sensitivity analysis, parameter identification, and design optimization. Hence we believe that automatic differentiation, delivering accurate and fast derivatives of arbitrarily large codes, will become an indispensable tool in the rapid prototyping cycle, providing deeper insight into computer models and enabling numerical optimization approaches employing these models.

Acknowledgment

The authors would like to thank Jakob W. Risch for his valuable contribution during the initial stage of this project. This research is partially supported by Deutsche Forschungsgemeinschaft (DFG) within Grant No. SFB 540 "Model-based experimental analysis of kinetic phenomena in fluid multi-phase reactive systems," Aachen University, Germany. We are grateful to Ulrich Renz and his team of the Institute of Heat Transfer and Air Conditioning for a fruitful collaboration within Grant No. SFB 540. Finally, we would like to thank the anonymous referees whose comments helped to improve our manuscript.

References

[1] Heck, A., 2003, *Introduction to Maple*, 3rd ed., Springer, New York.
[2] Wolfram, S., 2003, *The Mathematica Book*, 5th ed., Wolfram Media, Champaign, IL.
[3] Bischof, C., Carle, A., Khademi, P., and Mauer, A., 1996, "ADIFOR 2.0: Automatic Differentiation of Fortran 77 Programs," IEEE Comput. Sci. Eng., **3**(3), pp. 18–32.
[4] Giering, R., and Kaminski, T., 1998, "Recipes for Adjoint Code Construction," ACM Trans. Math. Softw., **24**(4), pp. 437–474.
[5] Hascoët, L., 2004, "TAPENADE: A Tool for Automatic Differentiation of Programs," Proceedings of the 4th European Congress on Computational Methods in Applied Sciences and Engineering, ECCOMAS 2004, Jyväskylä, Finland, July 24–28.
[6] Bischof, C., Roh, L., and Mauer, A., 1997, "ADIC—An Extensible Automatic Differentiation Tool for ANSI-C," Softw.: Pract. Exp., **27**(12), pp. 1427–1456.
[7] Griewank, A., Juedes, D., and Utke, J., 1996, "ADOL-C, A Package for the Automatic Differentiation of Algorithms Written in C/C++," ACM Trans. Math. Softw., **22**(2), pp. 131–167.
[8] Bischof, C. H., Bücker, H. M., Lang, B., Rasch, A., and Vehreschild, A., 2002, "Combining Source Transformation and Operator Overloading Techniques to Compute Derivatives for MATLAB Programs," *Proceedings of the Second IEEE International Workshop on Source Code Analysis and Manipulation (SCAM 2002)*, Los Alamitos, CA, IEEE Computer Society, pp. 65–72.
[9] Coleman, T. F., and Verma, A., 2000, "ADMIT-1: Automatic Differentiation and MATLAB Interface Toolbox," ACM Trans. Math. Softw., **26**(1), pp. 150–175.
[10] Forth, S. A., 2006, "An Efficient Overloaded Implementation of Forward Mode Automatic Differentiation in MATLAB," ACM Trans. Math. Softw., **32**(2), pp. 195–222.
[11] Griewank, A., 2000, *Evaluating Derivatives: Principles and Techniques of Algorithmic Differentiation*. SIAM, Philadelphia, PA.
[12] Rall, L. B., 1981, *Automatic Differentiation: Techniques and Applications, Lecture Notes in Computer Science*, Vol. 120, Springer, Berlin, Germany.
[13] Bischof, C., Corliss, G., Green, L., Griewank, A., Haigler, K., and Newman, P., 1992, "Automatic Differentiation of Advanced CFD Codes for Multidisciplinary Design," Comput. Syst. Eng., **3**(6), pp. 625–637.
[14] Carle, A., Green, L. L., Bischof, C. H., and Newman, P. A., 1994, "Applications of Automatic Differentiation in CFD," Proceedings of the 25th AIAA Fluid Dynamics Conference, Colorado Springs, CO, June 20–23, AIAA Paper No. 94–2197.
[15] Le Dimet, F.-X., Navon, I. M., and Daescu, D. N., 2002, "Second-Order Information in Data Assimilation," Mon. Weather Rev., **130**(3), pp. 629–648.
[16] Bischof, C. H., Bücker, H. M., and an Mey, D., 2002, "A Case Study of Computational Differentiation Applied to Neutron Scattering," *Automatic Differentiation of Algorithms: From Simulation to Optimization*, G. Corliss, C. Faure, A. Griewank, L. Hascoët, and U. Naumann, eds., Computer and Information Science, Springer, New York, pp. 69–74.
[17] Bischof, C. H., Bücker, H. M., Lang, B., Rasch, A., and Risch, J. W., 2003, "Extending the Functionality of the General-Purpose Finite Element Package SEPRAN by Automatic Differentiation," Int. J. Numer. Methods Eng., **58**(14), pp. 2225–2238.
[18] Fluent Inc., 1997, *FLUENT 4.4 Tutorial Guide*, 2nd ed., Lebanon, NH.
[19] Yakhot, V., and Orszag, S. A., 1986, "Renormalization Group Analysis of Turbulence, I. Basic Theory," J. Sci. Comput., **1**(1), pp. 1–51.
[20] Hirt, C. W., and Nichols, B. D., 1981, "Volume of Fluid (VOF) Method for the Dynamics of Free Boundaries," J. Comput. Phys., **39**, pp. 201–225.
[21] Launder, B. E., and Spalding, D. B., 1972, *Lectures in Mathematical Models of Turbulence*, Academic Press, London, UK.
[22] Launder, B. E., and Spalding, D. B., 1974, "The Numerical Computation of Turbulent Flows," Comput. Methods Appl. Mech. Eng., **3**, pp. 269–289.
[23] Mohammadi, B., and Pironneau, O., 1993, *Analysis of the K-Epsilon Turbulence Model*, Wiley, Chichester, UK.
[24] Bischof, C. H., Bücker, H. M., and Rasch, A., 2005, "Sensitivity Analysis of Turbulence Models Using Automatic Differentiation," SIAM J. Sci. Comput., **26**(2), pp. 510–522.

Journal of Fluids Engineering

Technical Brief

Conditionally-Sampled Turbulent and Nonturbulent Measurements of Entropy Generation Rate in the Transition Region of Boundary Layers

Edmond J. Walsh

Kevin P. Nolan

Stokes Research Institute,
Department of Mechanical and Aeronautical Engineering,
University of Limerick,
Limerick, Ireland

Donald M. McEligot
Idaho National Laboratory (INL),
Idaho Falls, ID 83415-3885

Ralph J. Volino
United States Naval Academy,
Department of Mechanical Engineering,
Annapolis, MD 21402

Adrian Bejan
Department of Mechanical Engineering and Materials Science,
Duke University,
Durham, NC 27708-0300

Conditionally-sampled boundary layer data for an accelerating transitional boundary layer have been analyzed to calculate the entropy generation rate in the transition region. By weighing the nondimensional dissipation coefficient for the laminar-conditioned-data and turbulent-conditioned-data with the intermittency factor γ the average entropy generation rate in the transition region can be determined and hence be compared to the time averaged data and correlations for steady laminar and turbulent flows. It is demonstrated that this method provides, for the first time, an accurate and detailed picture of the entropy generation rate during transition. The data used in this paper have been taken from detailed boundary layer measurements available in the literature. This paper provides, using an intermittency weighted approach, a methodology for predicting entropy generation in a transitional boundary layer. [DOI: 10.1115/1.2717622]

Keywords: boundary layer, transition, turbulence, entropy generation

Contributed by the Fluids Engineering Division of ASME for publication in the JOURNAL OF FLUIDS ENGINEERING. Manuscript received September 30, 2005; final manuscript received January 8, 2007. Review conducted by Joseph Katz.

Introduction

Efficiency is one of the key concerns in the development of modern turbomachines, as modest improvements result in significant gains in cost savings and pollution reduction. The continued increases in efficiency over the years have come in part from an elevation of turbine inlet temperatures and increased pressure ratios. However, such strategies are becoming more and more difficult to implement, as the gas temperature in modern gas turbines is well in excess of the melting temperature of the blade material. Thus, other ways to increase efficiency are continually sought. To elucidate these sources, the designer must understand the characteristics and sources of various loss mechanisms. Entropy generation minimization (EGM) is a method of thermodynamic optimization of real systems that owe their thermodynamic imperfection to heat transfer, fluid flow, and mass transfer irreversibilities [1]. Denton [2] noted that entropy creation is a direct measure of lost work and is therefore the key to understanding loss mechanisms in turbomachinery flows. With the help of such knowledge it may be possible to achieve improvements of component efficiency, thereby offering advantages to the designer. Such an analysis is not restricted to turbomachinery and is applicable to all fluid flow systems.

EGM is especially important when considering the boundary layer. It is stated throughout the literature that boundary layers are a key loss generating mechanism in turbomachinery. Bejan [1] noted that for a flat plate boundary layer the near wall region, $Y^+ < 30$, is where the generation of entropy is concentrated. Much work has focused on understanding and accurately predicting both the laminar and turbulent boundary layer loss mechanisms, with reasonable success. For the laminar boundary layer Truckenbrodt [3] integrated the Pohlhausen [4] family of velocity profiles and showed that the nondimensional entropy generation rate per unit surface is inversely proportional to Re_θ. For turbulent boundary layers, Schlichting [5] demonstrated that the nondimensional entropy generation rate is only weakly dependent on the Reynolds number of the flow. Both of these results have withstood the test of time with a number of authors showing good agreement between measurements and predictions.

An important boundary layer phenomenon is the transition process from a laminar to a turbulent boundary layer, this topic being the focus of numerous experimental and theoretical investigations. The transition region may be small relative to the wetted surface at low Reynolds numbers, where the flow is predominantly laminar, and high Reynolds numbers where the flow is predominantly turbulent. However, at Reynolds and Mach numbers found in turbomachinery, through hot film measurements in a linear cascade,

Walsh and Davies [6] demonstrated that the transition process extends over a relatively large proportion of the suction surface. The understanding and prediction of this region has plagued researchers for over a century, with an abundance of investigators addressing the prediction of transition onset and length over a diverse range of flow conditions [7–12].

The intermittent nature of transitional boundary layers has also been studied extensively, notably by Emmons [13] and Dhawan and Narasimha [14]. More recently, work on conditional sampling and intermittency has focused on the effects of free stream turbulence intensity [15–17] and passing wakes [18] on transition and the resulting structures of the transitional boundary layers. However, very limited experimental or theoretical work has been devoted to the entropy generation rate within the transition region, and no work has been presented where the transitional entropy generation rate has been calculated based on the intermittency factor γ. Stieger [19] showed ensemble-averaged and time-averaged dissipation coefficient data for a diffusing boundary layer flow over a flat plate subject to a passing wake. It was observed that the time averaged data lie between the laminar and turbulent correlations and a somewhat erratic evolution of dissipation coefficient C_D during transition from laminar to turbulent flow was seen.

Detailed hot wire measurements for the transition region of an accelerating boundary layer have been made available by Volino et al. [17]. This work contains nonconditionally sampled and conditionally sampled data, which consists of laminar and turbulent conditioned data in an accelerating transitional boundary layer. This means the flow within the turbulent spots and the calmed regions of the transitional boundary layer are identified first and then the data for each are separated and processed. Hence, the data are sampled based on the state of the boundary layer; laminar or turbulent. The favorable pressure gradient resulted in an extended transition region which gave improved measurement resolution in the transition region. Detailed entropy generation calculations from these data have been carried out and the conditionally-sampled data are compared with the nonconditionally-sampled data in the literature, as seen by Stieger [19]. This is the first time that dissipation has been characterized in a transitional boundary layer using the conditionally averaged approach. It should be noted that in such work care must be taken when using intermittency weighted averages of conditionally sampled data. This is because deviations of quantities identified as "laminar-like" and "turbulent-like" from actual laminar and turbulent characteristics can affect the success of the method [20]. The resultant distribution of entropy generation rate in the transition region is the first to shed light on the entropy production rate within a boundary layer as the flow transitions from a laminar to turbulent state.

Entropy Generation

The dissipation function [5] can be used to determine the volumetric entropy generation rate for steady, two-dimensional, incompressible adiabatic flows,

$$\dot{S}'''_{\text{gen}} = \underbrace{\frac{\mu}{T}\left[\frac{\partial \bar{u}}{\partial y}\right]^2}_{\substack{\text{viscous}\\ \text{dissipation}}} - \underbrace{\frac{\rho\overline{u'v'}}{T}\left[\frac{\partial \bar{u}}{\partial y}\right]}_{\substack{\text{Reynolds stress}\\ \text{dissipation}}} \tag{1}$$

For laminar flow Reynolds stresses are assumed to be negligible and the second term of Eq. (1) may be ignored. It is convenient to write $\dot{S}'''_{\text{gen}}$ in the nondimensional form of the dissipation coefficient,

$$C_D = \frac{T}{\rho u_e^3}\int_0^\delta \dot{S}'''_{\text{gen}} dy \tag{2}$$

Denton [2] noted that for turbulent boundary layers the dissipation coefficient is much less dependent on the state of the boundary layer than the more widely used skin friction coefficient, C_f with about 90% of entropy generation occurring within the inner part of the boundary layer. Denton [2] also details a method by Truckenbrodt [3] based on an inverse relationship between dissipation coefficient and momentum thickness Reynolds number, given in Eq. (3),

$$C_{D_{\text{LAM}}} = \beta\,\text{Re}_\theta^{-1} \tag{3}$$

where β has a range of $0.151 \leqslant \beta \leqslant 0.22$ for a Pohlhausen pressure gradient shape factor of $-12 \leqslant \Lambda \leqslant 12$. Schlichting [5] reports a correlation for turbulent boundary layers with a shape factor H_{12} between 1.2 and 2, and a Re_θ between 10^3 and 10^5,

$$C_{D_{\text{TURB}}} = 0.0056\,\text{Re}_\theta^{-1/6} \tag{4}$$

Denton [2] noted reasonable agreement between Eq. (4) and data for Re_θ between 500 and 1000 for accelerating, constant pressure, and diffusing boundary layers.

For the transition region no correlation exists to describe the distribution of the dissipation coefficient with varying Re_θ. Emmons [13] presumed that since the flow in the transition region is part of the time laminar ($\gamma=0$) and part of the time turbulent ($\gamma=1$), the average flow at any streamwise position is given by

$$f = (1-\gamma)f_{\text{LAM}} + \gamma f_{\text{TURB}} \tag{5}$$

Here f is a boundary layer flow related quantity with f_{LAM} and f_{TURB} as its local laminar and fully turbulent values. Such a linear combination method, although relatively simple, has proven to be an effective and useful transition model. Dhawan and Narasimha [14] showed that this equation gives reasonable approximations for the boundary layer thicknesses and shape factor. Dhawan and Narasimha [14] also showed that the skin friction coefficient C_f may be substituted into Eq. (5) to give good agreement with experimental data. Dey [21] has shown that the momentum imbalance due to the method is small enough to be negligible. The dissipation coefficient C_D is inserted into Eq. (5) in a similar manner to yield

$$C_D = (1-\gamma)C_{D_{\text{LAM}}} + \gamma C_{D_{\text{TURB}}} \tag{6}$$

This equation will be used to determine the intermittency weighted entropy generation rate in the transition region from the conditionally sampled data.

Transition Region Experimental Data

All the calculations presented in this paper are based on data presented by Volino et al. [17] in which detailed information regarding the experimental apparatus and method can be found. A brief summary of the experimental data is given here. The data are hot wire measurements from ten measurement stations that extend the length of the transition region of an accelerating boundary layer subject to a velocity gradient of 13.9 s^{-1}. The streamwise free-stream turbulence intensity is 8.8% at the test section inlet and drops to 2% at station 10. Data were taken for 26 s at a 20 kHz sampling rate for each measurement point using a boundary layer type hot wire probe, a boundary layer cross-wire probe, and a constant temperature hot wire anemometer control system. Distance from the wall is known to within 25 μm. The data were low-pass filtered at 10 kHz. Uncertainties in mean and rms fluctuating velocities are 3–5%. Uncertainty in the Reynolds shear stresses $-\overline{u'v'}$ is 10%. Uncertainty in skin friction coefficient C_f is 8%. Uncertainties in the momentum and displacement thicknesses are 10%. Uncertainty in the shape factor H_{12} is 7%. Intermittency was calculated from both u' and $u'v'$ with good agree-

Table 1 Boundary layer data [17]

Station	x (m)	U_∞ (m/s)	$\frac{\bar{u'}_\infty}{U_\infty}$ (%)	$\frac{\bar{v'}_\infty}{U_\infty}$ (%)	$K \times 10^6$	γ_{pk} (%)	$\delta_{99.5}$ (mm)
1	0.1182	6.22	6.4	6.4	5.32	4.1	4.04
2	0.1895	7.12	4.9	5.5	4.04	3.0	3.99
3	0.2677	7.99	3.9	4.8	3.25	4.7	4.52
4	0.3449	9.13	3.2	4.2	2.53	8.9	5.16
5	0.4231	10.35	2.7	3.8	1.97	17.0	4.72
6	0.5033	11.38	2.4	3.4	1.63	34.4	5.28
7	0.5805	12.49	2.1	3.2	1.33	56.0	5.67
8	0.6587	13.63	1.9	2.9	1.13	71.4	5.80
9	0.7353	14.62	1.7	2.7	0.97	86.2	6.58
10	0.8165	15.89	1.5	2.5	0.83	93.2	7.92

ment found between the two. The correlation coefficients between the u' and $-u'v'$ data were above 0.9 for 95% of the measurement locations, with 0.8 as the lowest value. Uncertainty in the intermittency is 10%. Volino et al. [17] refer to the laminar conditioned data as "nonturbulent" due to elevated fluctuations in the laminar region of transition and to the unconditioned data as "composite." A summary of the measurements at each station is given in Tables 1 and 2. Uncertainty in the laminar-conditioned dissipation coefficient data is calculated at 6%. The uncertainties in turbulent-conditioned and nonconditionally sampled dissipation coefficient data where the Reynolds shear stresses are included are calculated at 10%.

Entropy Calculations

Figure 1 shows the mean velocity profiles for stations 1–9 in wall coordinates. For the turbulent conditioned data there is good agreement with the Von Kármán empirical correlation. The Reynolds shear stresses for the turbulent conditioned data for measurement stations 1–9 are also shown in Fig. 1, nondimensionalized with the turbulent friction velocity u_τ^2. The $-u'v'$ fluctuations for the laminar conditioned data are significantly smaller than the turbulent conditioned data and have been neglected in the laminar dissipation coefficient calculations. The Reynolds shear stresses for the turbulent conditioned data and the nonconditionally sampled data were fitted with a sixth order polynomial set to zero at the wall. This was found to sufficiently fit the data. This polynomial equation was used to represent the Reynolds shear stresses in Eq. (1) for each of the mean velocity profiles. The peaks in the $-u'v'$ profiles are around $Y^+ \approx 30$, in broad agreement with classical data available in the literature, Roach and Brierley [22] with peak $-u'v'$ found in $Y^+ \approx 30-40$ for fully developed turbulent boundary layers. Some scatter is observed in the turbulent Reynolds shear stresses at low Reynolds numbers. This is due to the low intermittency level in this region.

Detailed near wall measurements are needed in order to calculate the dissipation coefficient accurately. The mean boundary layer velocity profiles were fitted with a linear approximation in the near-wall region ($Y^+ = U^+$) with an overlapping sixth order polynomial to the remainder of velocity profile. This method is considered to be more accurate than applying a single high order polynomial fit as it exploits the law of the wall in the viscous sublayer where $Y^+ = U^+$. It was found that the overlap between the linear and nonlinear portions of the velocity profiles was at approximately $Y^+ \approx 5$ (±2), in agreement with the "universal law" of the wall. This result gives confidence in the validity of the measurements and the methodology proposed to determine the entropy generation rate. The velocity profile curve fits are also set to zero at the wall. The entropy generation rates calculated for station 5 are shown in Fig. 2. A large difference between the laminar conditioned data and the total turbulent conditioned data is visible. Using Eq. (1) the total turbulent nondimensional entropy generation rate can be calculated by summing the viscous and Reynolds shear stress contributions. The flat regions of both the laminar and turbulent conditioned viscous data are a result of the linear curve fits where $\partial u/\partial y$ is constant. Since the linear curve fit of the velocity profile must pass through the origin in accordance with the zero slip condition, the linear curve fit may be forecasted back to the wall when integrating the curves to determine the dissipation coefficient.

The conditionally-sampled and nonconditionally sampled $\dot{S}'''_{\text{gen}}$ plots for all the measurement stations given in Tables 1 and 2 are shown in the form of nondimensional contour plots in Fig. 3. $\dot{S}'''_{\text{gen}}$ is nondimensionalized by $(\dot{S}'''_{\text{gen}})^* = \dot{S}'''_{\text{gen}}\theta T/\rho U_\infty^3$, where the length scale θ is the nonconditionally-sampled momentum thickness. The plots are smoothed with a spline interpolation between data points.

Figure 3 shows (a) laminar data which represents the flow between the turbulent spots, (b) turbulent data which represent the flow in the turbulent spots, and (c) intermittently weighted data, which are intermittency weighted representations of the flow field at each measurement station calculated by inserting the data from

Table 2 Conditionally sampled boundary layer data [17]

	Re_θ	H	Re_θ	H	Re_θ	H
Station	Composite		Nonturbulent		Turbulent	
1	136	1.96	136	1.97	90	1.97
2	149	1.98	149	1.99	135	1.72
3	169	1.94	168	1.94	186	1.59
4	196	1.87	193	1.89	244	1.51
5	221	1.82	212	1.86	293	1.48
6	263	1.76	239	1.86	366	1.46
7	324	1.66	264	1.86	432	1.46
8	372	1.58	278	1.82	474	1.43
9	457	1.49	297	1.81	580	1.39
10	580	1.43	364	1.69	745	1.35

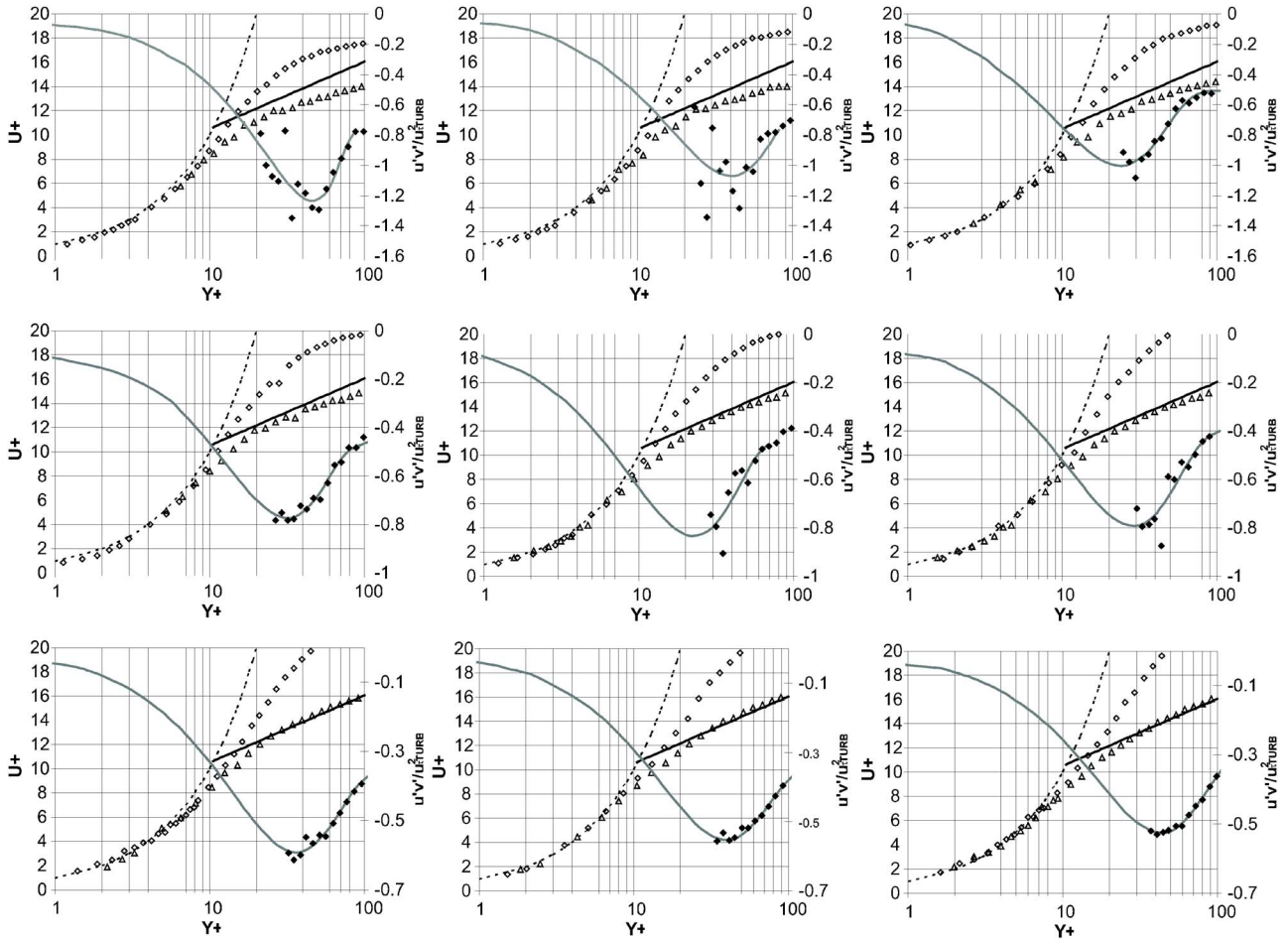

Fig. 1 Conditionally-sampled velocity profiles and Reynolds shear stresses for stations 1–9: ○, laminar-conditioned data; △, turbulent-conditioned data; ♦, turbulent-conditioned Reynolds shear stresses; ---, law of the wall, $Y^+ = U^+$; —, Von Kármán empirical correlation $U^+ = 2.4 \ln Y^+ + 5$; —, sixth order polynomial fit of turbulent-conditioned Reynolds shear stress data

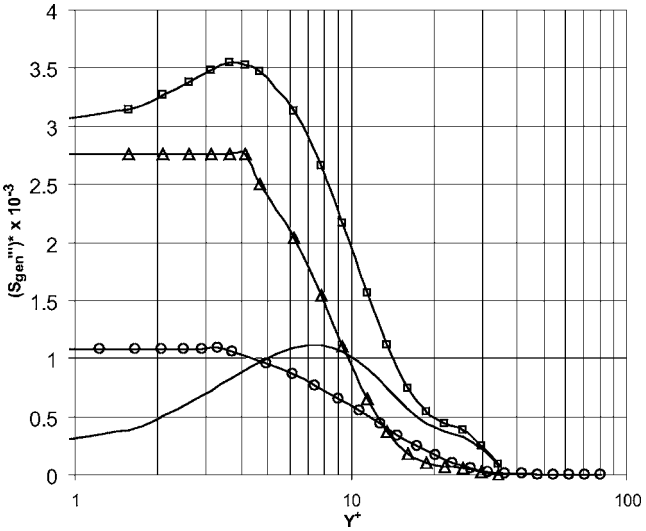

Fig. 2 Entropy generation rate profiles for station 5: ○, laminar-conditioned data; △, viscous turbulent conditioned data; —, Reynolds shear stress turbulent-conditioned data; □, total turbulent-conditioned data

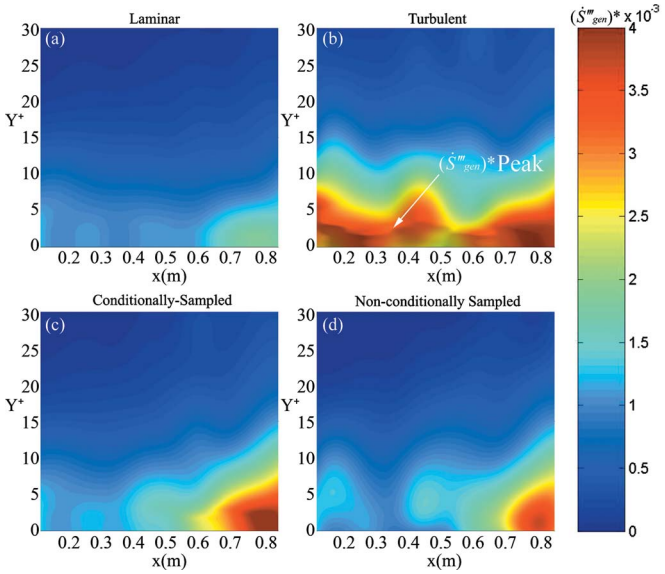

Fig. 3 Contours of nondimensional volumetric entropy generation rate for (*a*) laminar conditionally-sampled, (*b*) turbulent conditionally-sampled, (*c*) intermittency weighted data, and (*d*) nonconditionally sampled

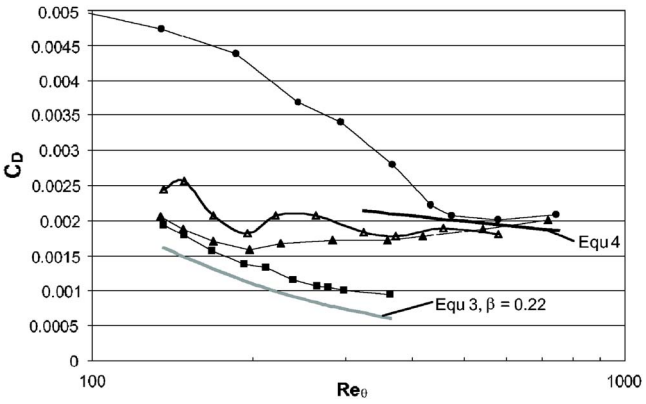

Fig. 4 Dissipation coefficient vs Re_θ: ■, laminar-conditioned data; ●, turbulent-conditioned data (note: station 1 data point for turbulent-conditioned data are located at Re_θ=90); ▲, intermittency weighted data; △, unconditionally sampled data

(a) and (b) into Eq. (6). A nonconditionally sampled, time-averaged picture of the flow field (d) is also shown.

The dissipation coefficient, Eq. (2), results obtained for each measurement station given in Tables 1 and 2 are shown in Fig. 4. This figure is obtained by integrating the contours of Fig. 3 across the boundary layer thickness at each measurement station. The data are presented in a similar manner to Fig. 3. with the laminar-conditioned data and turbulent-conditioned data representing the flow conditions due to intermittent turbulent spot passage and the intermittency weighted and nonconditionally sampled data showing the difference between the intermittency weighted and time averaged interpretations of the flow field. The data are plotted against Re_θ for the respective data set. Re_θ for the intermittently averaged data were calculated by applying Eq. (5) to the Re_θ values for laminar and turbulent conditionally sampled data. The existing laminar and turbulent correlations, Eqs. (3) and (4), are included as references in Fig. 4.

Discussion

High levels of entropy generation rates per unit volume in the near wall region are a common feature found in the literature [1,2,20] and are present in the current data as seen in Fig. 3. This trend is found in both the laminar and turbulent profiles throughout the transition region. From the entropy generation profiles in the turbulent region of Fig. 2 and Fig. 3(*b*), we find a consistent peak entropy generation rate per unit volume away from the wall in the region $2 \leqslant Y^+ \leqslant 3$; this peak is a result of the linear velocity profile up to the $Y^+ \approx 5$ region combined with increasing Reynolds stresses in this region. This visibility of the peak in Fig. 3(*b*) is enhanced with the addition of a 3D light source. The peak associated with station 5 occurs at $Y^+=4$ as a result of a shallower entropy generation rate profile. This shallower profile is found to be a result of the higher Reynolds shear stress contribution to the entropy generation rate for station 5. Unfortunately conditionally sampled data are rare in the literature preventing a comparison of this behavior with other such data.

For the laminar-conditionally sampled data of Fig. 4, we find a trend of decreasing dissipation coefficient with increasing Reynolds number based upon the momentum thickness, which is in qualitative agreement with the long standing correlation of Truckenbrodt [3], Eq. (3), also shown in Fig. 4. In terms of magnitude, with a value of $\beta=0.22$, which is the maximum using the limits imposed on the pressure gradient parameter by Schlichting [5], the curve falls consistently 25% below the measured data. The reason for this may be that the acceleration parameter in the current data is greater than the maximum allowed by the Pohlhausen family of velocity profiles from which the β value is obtained. It is likely that it is also partly due to the laminar region directly behind a turbulent spot where the dissipation coefficient levels are high before relaxing to the laminar level; readjusting after the turbulent spot has passed the measurement location. Either way calculating β using the Pohlhausen pressure gradient shape factor Λ for the current data, as described by Denton [2], gives $\beta=0.27$ giving excellent agreement with the current data, with an average difference from measurements of less than 5%.

In the conditionally sampled turbulent data very high levels of dissipation coefficient are deduced in the region of low intermittency. These high dissipation levels may be due to the high velocity gradients found in a relatively thin turbulent boundary layer. At low momentum thickness Reynolds numbers the magnitude of the values are approximately twice those correlated by Schlichting [5], Eq. (4). However as the intermittency increases we find good agreement with the correlation of Schlichting [5] at $Re_\theta > 500$ in agreement with the observations of Denton [2].

There is a large amount of scatter observed in the turbulent conditioned Reynolds shear stresses at stations 1 and 2 where the intermittency is between 3% and 4%. As a result very little turbulent data are recorded during the 26 s sampling time. Perhaps better results may be obtained if the sampling time is selected based on the intermittency factor to ensure adequate sampling of such short scale temporal events. Such measurements are further hampered by the relatively bulky cross wire probes used to measure the Reynolds shear stresses in a thin accelerating unsteady boundary layer.

The intermittency weighted data are a combination of the conditionally sampled laminar and turbulent flow, Eq. (6), and are the first such representation of the dissipation coefficient in the transition region. It is found that the dissipation coefficient follows a similar trend to that of the widely employed skin friction coefficient in the transition region and thus presents a number of established techniques to allow its prediction. The difficulty lies in predicting the laminar and turbulent dissipation coefficient distributions initially. This task is made more difficult by the limited amount of these types of measurements available in the literature.

For the nonconditionally sampled data of Fig. 4 there is up to a 20% higher dissipation coefficient calculated at low Reynolds numbers when compared to the intermittency weighted conditionally sampled data. Two distinct peaks are seen in the distribution of the dissipation coefficient. Similar peaks were also found in the time averaged data of Stieger [19] and O'Donnell [23]. As shown above, these peaks are in fact not representative of the dissipation coefficient in a transitional boundary layer and are misleading in determining the sources of thermodynamic loss. The peaks are caused by the time averaging technique employed in the data processing, where large Reynolds stresses are inferred from measurements. These large fluctuations are not the result of local Reynolds stresses, but due to the intermittent nature of the boundary layer. Hence these fluctuations do not contribute to the entropy generation rate because they are short term temporal events and cannot simply be time averaged. Furthermore as the conditioned and nonconditioned data imply the time averaging approach is particularly inappropriate in regions of low intermittency. This is unfortunate as most of the existing data are of the time averaged, and not conditionally sampled type.

In summary, this paper presents the first look at the entropy generation rate in a conditionally sampled transitional boundary layer. This is important, because it is the first step towards developing a predictive technique for the entropy generation rate in the transition region to accompany the long-standing laminar and turbulent correlations. Such correlations are necessary for the advancement of boundary layer codes.

Conclusions

In this paper entropy generation measurements in a transitional boundary layer weighted on intermittency have been calculated successfully for the first time. There is a significant difference

between the time averaged data with the intermittency weighted data in both magnitude and distribution with up to a 20% deviation between the two. A more gradual transition from the laminar to the turbulent state is seen in the conditionally sampled data rather than the somewhat erratic time averaged data, which exhibited a double peak caused by the passing of turbulent spots over the sensor. Agreement with the trend of the laminar correlation of Truckenbrodt [3] is reasonable for all Reynolds numbers considered but the experimental data is consistently 25% higher than the prediction. Calculating the Pohlhausen pressure gradient shape factor for the current data gives a value of $\beta=0.27$, and gives excellent agreement with the experimental data, although this β value is outside the recommended range of the Truckenbrodt correlation. The turbulent correlation also agrees well with the data in the turbulent region. In summary, using this technique with conditionally sampled data, a more accurate representation of the thermodynamic losses is made possible and is the first step in code development for predicting the thermodynamic loss in the transition region.

Acknowledgment

This publication has emanated from research conducted with the financial support of the Science Foundation of Ireland. The INL contribution was partly supported via DOE Idaho Operations Office Contract No. DE-AC07-05ID14517.

Nomenclature

C_D = dissipation coefficient
C_f = skin friction coefficient
H_{12} = boundary layer shape factor (δ^*/θ)
K = acceleration parameter
Re_θ = momentum thickness Reynolds number
Re_x = streamwise coordinate Reynolds number
$\dot{S}'''$ = entropy generation rate per unit volume, W m^{-3} K
T = absolute temperature, K
u = x direction velocity, m s^{-1}
U_e = boundary layer edge velocity ($0.99U_\infty$), m s^{-1}
U_∞ = free-stream velocity, m s^{-1}
u' = instantaneous streamwise fluctuating velocity, m s^{-1}
U^+ = local mean streamwise velocity in wall coordinates
u_τ = friction velocity, m s^{-1}
v' = instantaneous cross-stream fluctuating velocity, m s^{-1}
x = streamwise coordinate, distance from the leading edge, m
y = cross-stream coordinate, distance from the wall, m
Y^+ = distance from the wall in wall coordinates

Greek Symbols

δ = boundary layer thickness, m
δ^* = displacement thickness, m
μ = dynamic viscosity, N s m^{-2}
Λ = Pohlhausen pressure gradient shape factor
γ = intermittency
θ = momentum thickness, m
ρ = density, kg m^{-3}
ν = kinematic viscosity, m^2 s^{-1}

Subscripts

LAM = laminar condition
TURB = turbulent condition

References

[1] Bejan, A., 1982, *Entropy Generation Through Heat and Fluid Flow*, Wiley, NY.
[2] Denton, J. D., 1993, "Loss Mechanisms in Turbomachines," ASME J. Turbomach., **115**, pp. 621–656.
[3] Truckenbrodt, E., 1952, "A Method of Quadrature for the Calculation of the Laminar and Turbulent Boundary Layer in Case of Plane and Rotational Symmetric Flow," NACA TM 1379, 1955 (Translated as Ing.-Arch., **20**(4), pp. 211–228).
[4] Pohlhausen, K., 1921, "Zur Näherungsweisen Integration der Differentialgleichung der Laminaren Reibungsschicht," Z. Angew. Math. Mech., **1**, 252–268.
[5] Schlichting, H., 1979, *Boundary Layer Theory*, 7th ed., Mc-Graw Hill, NY.
[6] Walsh, E. J., and Davies, M. R. D., 2005, "Measurements in the Transition Region of a Turbine Blade Profile Under Compressible Conditions," ASME J. Fluids Eng., **127**, pp. 400–403.
[7] Mayle, R. E., 1991, "The Role of Laminar-Turbulent Transition in Gas Turbine Engines," ASME J. Turbomach., **113**, pp. 509–537.
[8] Walsh, E. J., and Davies, M. R. D., 2003 "Measurement and Prediction of Transition on the Suction Surface of Turbine Blade Profiles," *Proceedings of the 5th European Conference on Turbomachinery*, Fluid Dynamics and Thermodynamics, Prague, Czech Republic, Paper No. TT01-201.
[9] Gostelow, J. P., Blunden, A. R., and Walker, G. J., 2004 "Effects of Free Stream Turbulence and Adverse Pressure Gradients on Boundary Layer Transition," ASME J. Turbomach., **116**, pp. 392–404.
[10] Boyle, R. J., and Simon, F. F., 1999, "Mach Number Effects on Turbine Blade Transition Length Prediction," J. Turbomach., **121**, pp. 694–702.
[11] Suzen, Xiong, Y.B., G., and Huang, P. G., 2002, "Predictions of Transitional Flows in Low-Pressure Turbines using Intermittency Transport Equation," AIAA J., **40**, pp. 254–266.
[12] Abu-Ghannam, B. J., and Shaw, R., 1980, "Natural Transition of Boundary Layers-The Effect of Turbulence, Pressure Gradient and Flow History," J. Mech. Eng. Sci., **22**, pp. 213–228.
[13] Emmons, H. W., 1951, "The Laminar-Turbulent Transition in a Boundary Layer," J. Aeronaut. Sci., **18**, pp. 490–498.
[14] Dhawan, S., and Narasimha, R., 1958, "Some Properties of Boundary Layer Flow During the Transition From Laminar to Turbulent Motion," J. Fluid Mech., **3**, pp. 418–436.
[15] Kim, J., and Simon, T. W., 1991, "Free-Stream Turbulence and Concave Curvature Effects on Heated, Transitional Boundary Layers" Final Report, Minnesota University, Minneapolis, Department of Mechanical Engineering, Vol. I, NASA CR 187150 and Vol. II, NASA CR 187151.
[16] Wang, T., and Zhou, D., 1998, "Conditionally Sampled Flow and Thermal Behaviour of a Transitional Boundary Layer at Elevated Free-Stream Turbulence," Int. J. Heat Fluid Flow, **19**, pp. 348–357.
[17] Volino, R. J., Schultz, M. P., and Pratt, C. M., 2003, "Conditional Sampling in a Transitional Boundary Layer under High Free-Stream Turbulence Conditions," ASME J. Fluids Eng., **125**, pp. 28–37.
[18] Schobeiri, M. T., Read, K., and Lewalle, J., 2003, "Effect of Unsteady Wake Passing Frequency on Boundary Layer Transition, Experimental Investigation, and Wavelet Analysis," ASME J. Fluids Eng., **125**, pp. 251–266.
[19] Stieger, R. D., 2002, "The Effects of Wakes on Separating Boundary Layers in Low Pressure Turbines," Ph.D. dissertation, Engineering Department, Cambridge University, Cambridge, UK.
[20] Kim, J., Simon, T. W., and Kestoras, M., 1994, "Fluid Mechanics and Heat Transfer Measurements in Transitional Boundary Layers Conditionally Sampled on Intermittency," ASME J. Turbomach., **116**, pp. 405–416.
[21] Dey, J., 2000, "On the Momentum Balance in Linear-Combination Models for the Transition Zone," ASME J. Turbomach., **122**, pp. 587–588.
[22] Roach, P. E., and Brierley, D. H., 1990, "The Influence of a Turbulent Free Stream on Zero Pressure Gradient Transitional Boundary Layer Development. Part 1: Test Cases T3A and T3B," *Numerical Simulation of Unsteady Flows and Transition to Turbulence*, Cambridge University Press, pp. 319–347.
[23] O'Donnell, F. K., 2000, "The Measurement of Aerodynamic Entropy Generation in a Turbine Blade Boundary Layer," Ph.D. thesis, Mechanical and Aeronautical Department, University of Limerick, Ireland.

Journal of Fluids Engineering

Discussion

Comments on "Liquid Film Atomization on Wall Edges-Separation Criterion and Droplets Formation Model"

Askar Gubaidullin
Consulting Engineer
4 Rue Boileau,
Vélizy, 78140, France

In an intriguing paper [1], Maroteaux, Llory, Le Coz, and Habchi presented a separation criterion for a liquid film from sharp edges in a high-speed air flow. According to their model, the film of thickness h_f and velocity U_f separates from a sharp edge of angle α if $\alpha > \alpha_{\text{crit}}$. The relation obtained for the critical angle is

$$\alpha_{\text{crit}} = \frac{U_f}{\omega_{\max} h_f} \log\left(\frac{\delta}{\delta_0}\right)_{\text{crit}} \tag{1}$$

where δ/δ_0 is the amplitude ratio of the final to the initial perturbation of the film surface. When the wave amplitude reaches a critical value, the film stripping from an edge occurs. The critical value $(\delta/\delta_0)_{\text{crit}}$ is set equal to 20 as the best fit for their experimental data. The frequency $\omega_{\max}$ is defined as the most unstable perturbation growth rate that causes the film separation. This maximum frequency is computed from the dispersion relation of Jain and Ruckenstein (JR) [2]. The results of 12 tests with dodecane film flowing on springboard or straight step are reported. The geometrical edge angle α is equal to 135 deg for all tests. The maximum film thickness h_f is measured while the film velocity U_f is estimated. The fact of stripping is established from the visual observations. If the critical angle, computed from Eq. (1), takes values that are inferior to 135 deg, the theory assumes to predict stripping. The experimental data are summarized in Table 1.

Let us analyze this separation criterion. First, consider the JR study: JR investigated the rupture mechanism for *stagnant ultrathin* (less than a nanometer) films on a solid surface. In their case, the instability arises due to molecular interaction forces between the film and the surrounding fluid or gas. For the case of the negligible surrounding gas viscosity and the absence of the surface active agent, the dispersion relation is expressed as

$$\omega = -\left(\frac{\sigma_{\text{eff}}}{2\mu h_0}\right) \times \left[\frac{(kh_0)\sinh(kh_0)\cosh(kh_0) - (kh_0)^2}{\cosh^2(kh_0) + (kh_0)^2}\right] \tag{2}$$

Here, h_0 is the mean film thickness, k is a wave number, and σ_{eff} is the effective surface tension, which is defined as the sum of the surface tension σ and a term due to London/van der Waals interaction

$$\sigma_{\text{eff}} = \sigma + \frac{1}{k^2}\left(\frac{\partial \Phi}{\partial h}\right)_{h=h_0} \tag{3}$$

The film is unstable to small perturbations if $\omega > 0$, i.e., when $\sigma_{\text{eff}} < 0$. Critical thickness, below which the water film breaks up, is found to be about 10^{-2} microns and films thicker than that critical value are stable.

Maroteaux et al. have employed this relation by substituting the body force Φ by the force due to "normal acceleration" equal to $\Phi = -\Delta\rho h_f a$. This acceleration is expressed as

$$a = \frac{U_f^2}{R} \tag{4}$$

with the radius estimated as

$$R = h_f\left(\frac{\pi}{\alpha} + 1\right)$$

We will not present the analysis of the arguments that lead to formulas (1), (3), and (4)—even if those seem to be controversial—and will only point out a few apparent inconsistencies. Consider the experiment when dodecane film negotiates the edge without stripping: $h_f = 17$ microns, $\alpha \cong 2.4$ (135 deg), $U_f = 2.3$ m/s (see Table 1, test No.1). Then, Eq. (4) results in the unrealistic value for the acceleration, $a \cong 1.35 \times 10^5$ m/s. In fact, it represents the expression for the centripetal acceleration of an element that moves with a constant velocity magnitude along the arc of radius R. In Ref. [1] this acceleration is denoted as a "normal acceleration" directed "towards the gas," i.e., outwards. As is well known, the centripetal acceleration is directed inwards or to the center, as its name suggests. Obviously, it does not represent correctly the acceleration of the film. Hence, the force $\Phi = -\Delta\rho h_f a$ does not have much of physical sense especially if employed in the dispersion relation derived for stagnant nanofilms. Indeed, a transposition of JR results to this very different physical phenomenon is questionable.

Furthermore, the values for maximum wave-growth frequency $\omega_{\max} \cong 64 \times 10^3$ s^{-1} and the corresponding wave number $k \cong 39 \times 10^3$ m^{-1} are not realistic either. This frequency corresponds to the ultrasound range that is hardly characteristic for this case. Nevertheless, the critical angle computed from Maroteaux's formula is $\alpha_{\text{crit}} = 364 > 135$ deg, and the theory corresponds to the experiment. Finally, note that the angle of an edge has not been varied in the tests. Thus, the separation criterion based on the critical angle does not seem to be appropriate.

The film stripping is a very complex phenomenon that may depend on the film flow rate, surface tension, viscosity, gravity, wavy motion, interfacial shear, surface wettability, and geometry (slope inclination, edge angle). Simple physical considerations lead to an assumption that the film stripping occurs when the disruptive aerodynamic forces dominates over the adhesive capillary forces. The film inertia and its viscosity are important as well. These effects are represented by the Weber and Reynolds numbers, which are defined as

Contributed by the Fluids Engineering Division of ASME for publication in the JOURNAL OF FLUIDS ENGINEERING. Manuscript received November 15, 2005; final manuscript received April 14, 2006. Review conducted by Joseph Katz.

Table 1 Summary of experiments[a]

No.	$h_{f,\max}$ (μm)	U_g (m/s)	U_f (m/s)	α^0_{crit} (from [1])	Re	We	Experimental observation
1	17	80	2.3	⋯	21.7	4.9	no stripping
2	23	80	3.2	128	40.8	6.5	some droplets
3	28	80	3.8	94	59.0	7.8	established stripping
4	21	60	2.5	174	29.1	3.3	rare droplets
5	29	60	2.9	118	46.7	4.5	some droplets
6	38	60	2.6	87	54.8	6.0	established stripping
7	26	80	2.05	⋯	29.6	7.6	no stripping
8	26	80	2.4	158	34.6	7.5	rare droplets
9	32	80	3.2	99	56.8	9.1	established stripping
10	34	60	1.8	165	34.0	5.5	no stripping
11	37	60	1.8	160	37.0	6.0	no stripping
12	41	60	2.25	115	51.2	6.6	established stripping

[a]Reference [1].

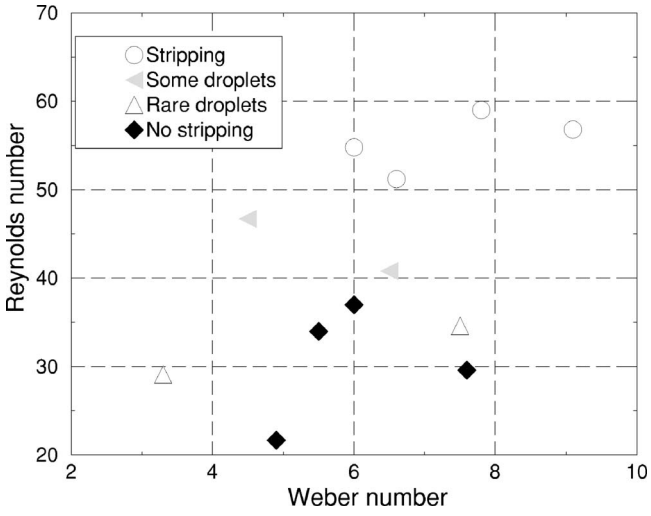

Fig. 1 Experimental data plotted as a function of the Weber and Reynolds numbers

$$\text{We} = \frac{\rho_g (U_g - U_f)^2 h_f}{\sigma}$$

and

$$\text{Re} = \frac{\rho_f U_f h_f}{\mu_f}$$

respectively. The estimated values for each test of We and Re are presented in Table 1. Unfortunately, mean values of the film thickness and velocity have not been measured in [1]. Note that those are more appropriate to define the dimensionless parameters. The dodecane physical properties are taken to be $\mu_f = 1.35 \times 10^{-3}$ kg/m s, $\rho_f = 749$ kg/m^3, $\sigma = 0.025$ N/m (not specified in [1]) and the density of air is $\rho_g = 1.2$ kg/m^3. It can be seen that a zone of stripping corresponds to the elevated values of Re, We, and is clearly separated from that where no stripping occurs in (We, Re) coordinates (see Fig. 1). These considerations, however, by no means represent a complete dimensional analysis of the phenomenon. More detailed and accurate experimental data obtained for fluids with varied physical properties are desired to establish a reliable correlation. It should be noted that this approach is somewhat similar to that developed by Nigmatulin and co-workers in their study of the droplet entrainment in annular flows [3].

Furthermore, the separation may strongly depend on the wave characteristics. Thus, accurate experimental measurements of those are required. Additionally, under certain conditions the shear-driven film motion is governed by large amplitude nonlinear waves. The linear stability analysis cannot be applied in such a case.

References

[1] Maroteaux, F., Llory, D., Le Coz, J.-F., and Habchi, C., 2002, "Liquid Film Atomization on Wall Edges-Separation Criterion and Droplets Formation Model," ASME J. Fluids Eng., **124**, pp. 565–575.

[2] Jain, R. E., and Ruckenstein, E., 1976, "Stability of Stagnant Viscous Films on a Solid Surface," J. Colloid Interface Sci., **54**(1), pp. 108–116.

[3] Nigmatulin, R. I., 1991, *Dynamics of Multiphase Media*, Hemisphere, Vol. 2.

Journal of Fluids Engineering

Announcement

Interested in Cavitation Erosion?

ASTM's Subcommittee G02.10 on Erosion would like to hear from you if you have any interest in cavitation erosion testing. Do you (or your organization):

- Use (or have used) ASTM Method G 32 for cavitation erosion testing?
- Use (or have used) any other cavitation erosion, or liquid impingement erosion, test method? (For example, ASTM G 73 or G 134.)
- Have any concern with cavitation erosion as a field problem or research topic?

If any of above apply, please contact the following with a brief explanation:

Frank J. Heymann, task group chairman
25 Thornton Way # 205, Brunswick, ME 04011, USA
Email: marseah@gwi.net
Phone: 207-725-7073

The objective of this effort is to help us determine the degree of interest in, and importance of, cavitation erosion test methods at the present time. If you respond, we will send you a questionnaire and hope you will be willing to reply to that also!

Paul A. Swanson
Subcommittee G02.10 chairman

